

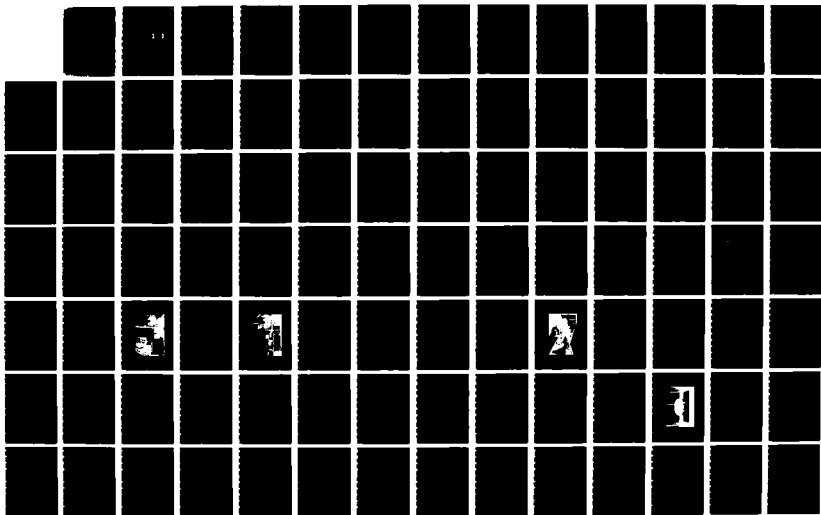
AD-A182 227

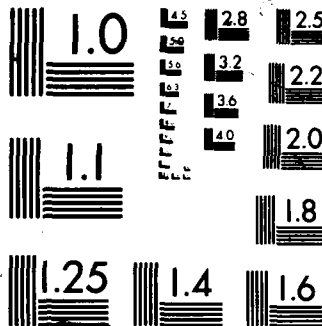
LANDMINE DETECTION BY SCATTER RADIATION RADIOGRAPHY(U)
ARMY MILITARY PERSONNEL CENTER ALEXANDRIA VA
J G CAMPBELL 02 JUL 87

1/6

UNCLASSIFIED

F/G 15/6 6 NL





PHOTOCOPY RESOLUTION TEST CHART

AD-A182 227

LANDMINE DETECTION BY SCATTER RADIATION RADIOGRAPHY

JOHN G. CAMPBELL, LTC
HQDA, MILPERCEN (DAPC-OPA-E)
200 Stovall Street
Alexandria, VA 22332

Final Report, 2 July 1987

DTIC
ELECTE
JUL 09 1987
S D

Approved for public release; distribution is unlimited.

A dissertation submitted to the University of Florida, Gainesville, Florida, in partial fulfillment of the requirements for the degree of Doctor of Philosophy.

UNCLASSIFIED

SECURITY CLASSIFICATION OF THIS PAGE (When Data Entered)

REPORT DOCUMENTATION PAGE		READ INSTRUCTIONS BEFORE COMPLETING FORM
1. REPORT NUMBER	2. GOVT ACCESSION NO. AD-A182227	3. RECIPIENT'S CATALOG NUMBER
4. TITLE (and Subtitle) LANDMINE DETECTION BY SCATTER RADIATION RADIOGRAPHY		5. TYPE OF REPORT & PERIOD COVERED Final Report, 2 July 1987
		6. PERFORMING ORG. REPORT NUMBER
7. AUTHOR(s) John G. Campbell		8. CONTRACT OR GRANT NUMBER(s)
9. PERFORMING ORGANIZATION NAME AND ADDRESS Student, HQDA, MILPERCEN (DAPC-OPA-E) 200 Stovall Street Alexandria, VA 22332		10. PROGRAM ELEMENT, PROJECT, TASK AREA & WORK UNIT NUMBERS
11. CONTROLLING OFFICE NAME AND ADDRESS HQDA, MILPERCEN, ATTN: DAPC-OPA-E 200 Stovall Street Alexandria, VA 22332		12. REPORT DATE 2 July 1987
		13. NUMBER OF PAGES 563
14. MONITORING AGENCY NAME & ADDRESS (if different from Controlling Office)		15. SECURITY CLASS. (of this report) Unclassified
		15a. DECLASSIFICATION/DOWNGRADING SCHEDULE
16. DISTRIBUTION STATEMENT (of this Report) Approved for public release; distribution is unlimited.		
17. DISTRIBUTION STATEMENT (of the abstract entered in Block 20, if different from Report)		
18. SUPPLEMENTARY NOTES Document is a dissertation submitted to the University of Florida, Gainesville, FL.		
19. KEY WORDS (Continue on reverse side if necessary and identify by block number) landmine mine warfare antitank mine detection Monte Carlo x ray scattering imaging radiation transport detector response, x-ray spectra, backscatter nonmetallic mine		
20. ABSTRACT (Continue on reverse side if necessary and identify by block number) The application of scatter radiation radiography to the detection of buried nonmetallic antitank landmines is examined. A combination of calculations and measurements is used to address the problem. The primary calculation tool is a Monte Carlo photon transport code. Measurements are made with an x-ray source, sodium iodide detector, and soil box positioning system. The soil box containing a model of a nonmetallic antitank mine is moved beneath the x-ray source to simulate both the forward motion of a vehicle transporting		

DD FORM 1 JAN 73 1473

EDITION OF 1 NOV 65 IS OBSOLETE

UNCLASSIFIED

SECURITY CLASSIFICATION OF THIS PAGE (When Data Entered)

UNCLASSIFIED

SECURITY CLASSIFICATION OF THIS PAGE(When Data Entered)

the detection system and raster of the beam to search a path of sufficient width to allow safe passage. Measurements are used to validate the calculation results for a small detector and produce images of buried mines. The calculations are extended to large area detectors which are required to provide path searches of approximately three meter widths. Environmental parameters, such as height sensitivity, soil density and moisture content, and inhomogeneities are examined in both calculations and measurements. Calculations are used to suggest mine detection mechanisms and to optimize geometric parameters and x-ray beam quality. Power requirements are also addressed.

UNCLASSIFIED

SECURITY CLASSIFICATION OF THIS PAGE(When Data Entered)

LANDMINE DETECTION BY
SCATTER RADIATION RADIOGRAPHY

by

JOHN G. CAMPBELL

Accession For	
NTIS CRA&I	<input checked="" type="checkbox"/>
DTIC TAB	<input type="checkbox"/>
Unannounced	<input type="checkbox"/>
Justification	
By	
Distribution /	
Availability Codes	
Dist	Avail and/or Spec
A-1	

A DISSERTATION PRESENTED TO THE GRADUATE SCHOOL
OF THE UNIVERSITY OF FLORIDA IN
PARTIAL FULFILLMENT OF THE REQUIREMENTS
FOR THE DEGREE OF DOCTOR OF PHILOSOPHY

UNIVERSITY OF FLORIDA

1987



ACKNOWLEDGMENTS

A number of individuals and organizations have played an important role in my research. First and foremost, I thank my wife, Becky, for her support, understanding, and patience.

Dr. Alan Jacobs, who was my research advisor, was always willing to help, whether the assistance required discussion of new ideas or manual labor. The basic concept of the project, using imaging techniques for mine detection, was his. The generous amount of time he took from a very busy schedule is greatly appreciated. I thank the other members of my committee, Dr. Edward Carroll, Dr. Edward Dugan, Dr. John Staudhammer, and Dr. Mark Yang, for their time and guidance.

Two graduate students, who worked on other aspects of the research problem, also contributed to my efforts. Captain Dale Moss designed the soil box positioning system and its computer control. Linda Hipp was an equal partner in the assembly of the positioning system and spent many long hours performing measurements.

I thank Bill Coughlin of the Radiation Control Department for the loan of an ionization chamber for the exposure rate transmission experiments, and Harvey Norton,

of the same organization, for the use of a calibration set of radionuclide sources. Dr. William Ellis provided the filter sets used in the measurements.

The electronics skills and untiring efforts of Ken Fawcett were solely responsible for keeping an old x-ray machine in operation for the measurements. His expertise was crucial to this research.

I thank Lois Carroll, who typed this manuscript, for her professional and always cheerful assistance.

Gary Melocik of Bicron Corporation provided details on the composition and geometry of the NaI(Tl) detector used in the experiment. Dr. William Frank, 3M Corporation, provided information on the composition of the Trimax 12 rare earth intensifying screens. Without their assistance, the detector response calculations could not have been performed.

Andrew Lickly of Applied Reasoning Corporation, and David Hampton of Seattle Telecom and Data, Inc., ran benchmark versions of the Monte Carlo code on their accelerator boards. Two graduate students of the Nuclear Engineering Sciences Department also helped test the code. Samer Kahook ran a benchmark on the IBM PC/AT. Kiratadas Kutikkad ran a mine detection problem on the Cray X-MP/48 using the MCNP code.

I thank the United States Army for allowing me the opportunity to continue my education and for financial support during the research effort. The measurements portion of this work was supported by the U.S. Army Belvoir Research

and Development Center under contract, DAAK 70-86-K-0016. I thank those individuals associated with the administration of the contract for their active interest in the research. Of those individuals, I particularly thank Edward Ostrosky for his participation in the early measurements, and Dr. Robert Moler for his reviews of the progress of the work.

TABLE OF CONTENTS

	<u>Page</u>
ACKNOWLEDGMENTS	ii
LIST OF TABLES.	xi
LIST OF FIGURES	xv
ABSTRACT.	xxxi
 CHAPTERS	
I INTRODUCTION	1
II BACKSCATTER MINE DETECTION AND IMAGING . .	4
Previous Uses of Scattered Radiation . . .	5
Backscattered Photon Mine Detection. . . .	8
Fluorescence Emission	8
Rayleigh Scattering	9
Compton Scattering.	10
Backscatter Radiation Radiography.	13
Genesis of Current Research Effort. . . .	13
Improvements on Previous X-Ray	
Backscatter Efforts	17
Research Goals.	17
III EQUIPMENT AND MATERIALS.	20
Equipment.	20
X-Ray Source.	20
Soil Box and Positioning System	27
Detector and Related Electronics. . . .	30
Computer Control System	36
Materials.	38
Soils	38
Nonmetallic Antitank Mine Model	39
Materials Tests	46
IV RADIATION TRANSPORT.	52
Photon Interactions.	52
Coherent Scattering	52
Incoherent Scattering	59
Photoelectric Effect.	67
Mass Interaction Coefficients	71

TABLE OF CONTENTS - continued

CHAPTERS		Page
	Single Scatter Model	73
	Computation Scheme.	73
	Interaction Modeling.	78
	Monte Carlo Model.	78
	Problem Parameters and Data	80
	Random Number Generators.	81
	Computation Scheme.	83
	Modelling Scattering Interactions	87
	Russian Roulette.	89
	Code Output	89
	Validation of the Monte Carlo Codes.	90
	Number and Energy Albedo Calculations	91
	Energy Spectra Comparisons.	91
	Comparison with Buried Mine Calculations.	91
	Testing the Scattering Routines	99
V	X-RAY SOURCE	105
	Kramers' Formula Method.	105
	Kramers' Formula.	106
	Time Dependent Accelerating Potential	107
	Characteristic X-Ray Production.	108
	Attenuation by Materials in the Beam Path.	109
	Anode Self-Attenuation.	111
	Effects Neglected in Model.	116
	General Features of the Calculated Spectra	117
	Testing the Modified Kramers' Formula Model.	119
	Exposure Rate Transmission Measurements.	119
	Comparisons with Published Spectra.	122
	Other Methods to Determine X-Ray Spectra	126
	Measurement	126
	Monte Carlo Calculation	130
	Laplace Transform Pair Method	130
VI	DETECTOR RESPONSE.	139
	Plane Detector Code.	141
	Assumptions in the Plane Detector Response Calculation	144
	Energy Deposition.	146
	Case of Zero Degree Incidence	146
	Case of Large Angle Incidence	149
	Counts Per Incident Photon	151

TABLE OF CONTENTS - continued

CHAPTERS		<u>Page</u>
	Discriminator Setting Corresponding to 0 MeV.	151
	Discriminator Setting Corresponding to Energies Greater Than 0 MeV.	153
	Validation of the Plane Detector Response Calculations	157
	Iodine Escape Ratio	157
	Measured Energy Spectra	163
	Shield and Edge Effects.	163
	Calculation of the Correction Factor.	163
	Results of the Correction Factor Calculation	166
VII	MINE DETECTION MECHANISMS.	169
	Backscattered Photon Signal Differences.	169
	Fluence	170
	Energy Fluence.	176
	Spatial Distribution.	182
	Angular Distribution.	186
	Energy Spectra.	194
	Edge Effects.	198
	Conclusions Based on Signal Differences	204
	Irradiation Geometry and Optimum Energy.	208
	Height of Detector.	208
	Angle of Incidence.	209
	Raster Gap Size	216
	Detector Collimator Length.	222
	Detector Panel Dimensions	223
	Segmented Detector Geometry	227
	Source Beam Collimation	229
	Source Energy Optimization.	232
	Depth of Burial	241
	Polyenergetic Sources	244
	Conclusions Based on Optimizations.	246
VIII	APPLICATION TO IMAGING	248
	Comparisons with Measurements.	249
	Spatial Distribution of Detector Response.	249
	Detector Response with Mine Present	251
	Edge Effects.	258
	Energy Window Detector.	262
	Environmental Parameters	266
	Height Sensitivity.	266
	Soil Density Variation.	272
	Soil Moisture Content	277
	Inhomogeneities	283

TABLE OF CONTENTS - continued

CHAPTERS	Page
Imaging.	287
Monte Carlo Generated Images.	287
Measured Images	296
Dual Energy Subtraction Technique	342
Power Requirements	347
Variables	348
Fraction of Source Photons Reaching the Detector.	350
Source Flux	350
Pixel Dwell Time.	353
Calculation Technique	353
Power Calculations.	357
IX CONCLUSIONS.	363
APPENDICES	
A CHARACTERISTICS OF LANDMINES	368
Mine Classification.	368
Metallic or Nonmetallic	371
Antitank or Antipersonnel	372
Conventional or Scatterable	372
Surface or Buried	373
Fuzing Type	375
Employment of Landmines.	376
B HISTORICAL EXAMPLES OF MINE WARFARE	378
Mine Development	378
Forerunners of Modern Mines	378
Mines of World War II	379
Countermine Warfare in World War II	380
Mine Employment.	380
North Africa.	380
Eastern Front	382
Korea and Vietnam	383
C OTHER MINE DETECTION AND NEUTRALIZATION METHODS.	385
Detector Technologies	385
General Considerations.	385
Microwaves.	386
Neutrons.	388
Magnetic Resonance Techniques	390
Trace Gases	391
Animals	392
Biochemical Methods	392
Infrared Methods.	393

TABLE OF CONTENTS - continued

APPENDICES		Page
	Neutralization	394
	Mechanical Systems.	394
	Explosive Methods	395
	Magnetic Signature Duplication.	396
D	X-RAY TRANSMISSION MEASUREMENTS.	397
E	GADOLINIUM OXYSULFIDE DETECTOR	414
	Detector Description	414
	Detector Design	414
	Screen Composition.	417
	Detector Response Matrix Calculation	422
	Calculation Technique	422
	General Results of Calculations	425
	Description of the Detector Response	
	Matrix.	428
	Perpendicular Incidence	429
	45 Degree Incidence	436
	75 Degree Incidence	444
	Comparison with Published Results	449
	Response Matrix Relationship to	
	Detector Electronics	450
	Shortcomings of the Detector	455
	Sensitivity	456
	Fluorescence Decay Constant	460
	Corrective Actions.	463
	Comparison of Measured and Calculated	
	Responses.	464
	Calculation Technique	464
	Measurements.	465
F	X-RAY SPECTRA USED IN MEASUREMENTS	470
G	COMPUTER CODES	484
	Computer Hardware.	484
	Personal Computers and Monte	
	Carlo Calculations.	484
	Computer Selection.	485
	Comparison with Cray X-MP/48	
	Supercomputer	487
	Computer Software.	489
	Computer Languages.	489
	Radiation Transport Codes	489
	X-Ray Spectra Codes	491
	Detector Response Codes	492
	Imaging Codes	493
	Utility Codes	494
	Photon Interaction Data Files	496
	Commercial Software	497

TABLE OF CONTENTS - continued

APPENDICES	<u>Page</u>
H MONTE CARLO TECHNIQUES	501
Angular Scattering Distributions	501
Momentum Transfer Variable.	501
Incoherent Scattering	502
Sampling the Klein-Nishina Distribution.	504
Coherent Scattering	506
Random Number Generators	509
MCPHOT.PAS Generator	509
MCPHOT.P Generator	509
Fluorescent Emission	510
Application to Polyenergetic Sources . . .	512
Available Methods	512
Application of the Fit Method	513
LIST OF REFERENCES.	516
BIOGRAPHICAL SKETCH	527

LIST OF TABLES

TABLES	Title	<u>Page</u>
III.1	Geometry of the Sodium Iodide Detector and Shield.	32
III.2	Sources Used in Determining Lower Level Discriminator Setting	35
III.3	Composition of Soil Types.	40
III.4	Characteristics of Common Warsaw Pact Nonmetallic Antitank Mines.	42
III.5	Ratios of the Linear Interaction Coefficients of Sucrose to TNT.	47
IV.1	Energy Mesh Structure for Mass Interaction Coefficients.	74
IV.2	Energy at Which Photoelectric and Incoherent Scattering Mass Interaction Coefficients Are Equal.	76
IV.3	Comparison of Number and Energy Albedo Calculations for Iron	92
IV.4	Comparison of Number Albedo Calculations for Concrete	93
IV.5	Comparison of Energy Albedo Calculations for Concrete	94
IV.6	Comparison of Number Albedo Calculations for FTB Soil and Buried DNB Mines.	101
V.1	Energies of Tungsten K Characteristic X Rays.	110
V.2	Comparison of Exit Path Lengths from Tungsten Anodes	115
VI.1	Energies of Iodine Fluorescent Emission X Rays Used in the Detector Response Calculations	143

LIST OF TABLES - continued

TABLES		<u>Page</u>
VII.1	Comparison of the Linear Relationship Between the Ratio of Number to Energy Albedo and Source Energy at Perpendicular Incidence	180
VII.2	Mine to Soil Response Ratios at Selected Beam Angles of Incidence.	211
VII.3	Front to Back Panel Fluence Ratios of the Collimated Detector for 100 keV Photon Beams Incident at 60 Degrees . .	214
VII.4	Results of Calculations for the Geometric Parameters of the Collimated Fluence Detector.	220
VII.5	Mine to Soil Fluence Ratio Dependence on Panel Width and Raster Gap Size for an Uncollimated Detector	226
VII.6	Optimum Source Energies for the Uncolli- mated Fluence Detector.	235
VII.7	Comparison of the Segmented and Unseg- mented Uncollimated Fluence Detectors .	238
VII.8	Mine to Soil Fluence Ratio at Selected Depths of Burial of the TST Mine. . . .	242
VII.9	Mine to Soil Fluence Ratios Versus Depth of Mine Burial for the Energy Window Detector with Source Energy of 100 keV.	245
VIII.1	Parameters for Spatial Distribution Comparison.	250
VIII.2	Comparison of Calculated and Measured Mine to Soil Detector Response/Ratio with the TST Mine at 0.0 cm	257
VIII.3	Energy Window Measurements for the TST Mine at 2.54 cm Depth of Burial	265
VIII.4	Mine to Soil Fluence Ratio from the Collimated Detector with Recently Buried Mines.	276
VIII.5	Mine to Soil Fluence Ratio from the Energy Window Detector with Recently Buried Mines.	278

LIST OF TABLES - continued

TABLES		<u>Page</u>
VIII.6	Mine to Soil Fluence Ratio of the Uncollimated Fluence Detector for Three Water Contents of HTL Soil with the TST Mine at 2.5 cm Depth of Burial	280
VIII.7	Mine to Soil Fluence Ratio of the Collimated Fluence Detector for Two Water Contents of HTL Soil with the TST Mine at 2.5 cm Depth of Burial	281
VIII.8	Mine to Soil Fluence Ratio of the Energy Window Detector for Three Water Contents of HTL Soil with the TST Mine at 2.5 cm Depth of Burial.	282
VIII.9	Object to Soil Fluence Ratio from the Collimated Detector for Selected Inhomogeneities.	286
VIII.10	Object to Soil Fluence Ratio from the Energy Window Detector for Selected Inhomogeneities.	288
VIII.11	Operational Requirements for a Vehicle-Mounted Antitank Mine Detection System.	349
VIII.12	Photon Output of the GE Maxitron 300 X-Ray Therapy Unit.	352
VIII.13	Imaging Quantities Necessary to Fulfill Operational Requirements.	354
VIII.14	Power and Signal to Noise Ratio Requirements for Imaging and Mine Detection with the Uncollimated Detector.	358
VIII.15	Power and Signal to Noise Ratio Requirements for Imaging and Mine Detection with the Collimated Detector.	362
E.1	Gadolinium Oxysulfide Screen Model	423
E.2	Energies of Fluorescent Photons Used in the DETECT.PAS Code.	426
E.3	Calculated Ratios of Radiation Field Quantities, ^{133}Ba to ^{137}Cs	466

LIST OF TABLES - continued

TABLES		<u>Page</u>
G.1	Benchmarks for Monte Carlo Transport Codes.	488
G.2	Photon Interaction Data Files.	498
H.1	Fluorescent Emission Probabilities	511

LIST OF FIGURES

FIGURES	Title	Page
II.1	Conceptual large area backscatter detector system.	18
III.1	X-ray source, soil box and positioning system and detector	22
III.2	Detector electronics, computer and x-ray source console.	24
III.3	Lead shield for tube head and detector . .	29
III.4	Geometry of sodium iodide detector and shield.	31
III.5	Components of the counting system.	37
III.6	Soil mass attenuation coefficients	41
III.7	TST mine used in measurements.	45
III.8	Transmission comparison for TNT and substitute.	49
III.9	Transmission comparison for NSL and local soil.	51
IV.1	Atomic form factor versus momentum transfer variable.	55
IV.2	Solid angle differential coherent scattering cross section versus scattering angle.	57
IV.3	Coherent cross section versus photon energy.	58
IV.4	Fractional energy of Compton scattered photons versus incident photon energy .	60
IV.5	Solid angle differential Klein-Nishina cross section versus scattering angle .	62

LIST OF FIGURES - continued

FIGURES		<u>Page</u>
IV.6	Incoherent scattering function versus momentum transfer variable.	64
IV.7	Comparison of the solid angle differential Klein-Nishina and incoherent scattering cross sections.	65
IV.8	Incoherent scattering cross section versus photon energy	66
IV.9	Photoelectric interaction cross section versus photon energy.	69
IV.10	Probability of K shell fluorescence versus atomic number.	70
IV.11	Energies of K fluorescent photons versus atomic number	72
IV.12	Mass interaction coefficients of aluminum versus photon energy.	75
IV.13	Boundaries and materials of Monte Carlo calculations.	84
IV.14	Number albedo versus energy for concrete .	95
IV.15	Backscattered energy spectrum, 0.200 MeV on aluminum	96
IV.16	Backscattered energy spectrum, 0.6616 MeV on aluminum	97
IV.17	Backscattered energy spectrum, 0.6616 MeV on iron	98
IV.18	Comparison of calculations of the solid angle differential coherent cross section	101
IV.19	Comparison of calculations of the solid angle differential incoherent cross section	102
V.1	Transmission curve without anode self- attenuation	112
V.2	Typical x-ray spectrum calculation	118

LIST OF FIGURES - continued

FIGURES		<u>Page</u>
V.3	Heel effect displayed by spectra	120
V.4	Heel effect displayed by half value thickness	121
V.5	Typical transmission curve comparison. . .	123
V.6	Spectrum comparison with Epp and Weiss at 80 kVp	124
V.7	Spectrum comparison with Epp and Weiss at 105 kVp.	125
V.8	Spectrum comparison with Fewell and Shuping at 70 kVp	127
V.9	Spectrum comparison with Fewell and Shuping at 80 kVp	128
V.10	Spectrum comparison with Fewell and Shuping at 90 kVp	129
V.11	Archer-Wagner method fit to measured transmission data	134
V.12	Comparison of modified Kramers' method and the Archer-Wagner method at 80 kVp.	136
V.13	Comparison of modified Kramers' method and the Archer-Wagner method at 150 kVp	137
VI.1	Fraction of incident energy absorbed perpendicular incidence	147
VI.2	Fraction of incident energy absorbed 75 degree incidence	150
VI.3	Plane detector response, discrimination less than 0.03317 MeV	152
VI.4	Plane detector response, discrimination greater than 0.03317 MeV	156
VI.5	Iodine escape peak ratio versus energy . .	158
VI.6	Measured and calculated NaI(Tl) spectra. .	164
VI.7	Plane detector response.	167

LIST OF FIGURES - continued

FIGURES		<u>Page</u>
VI.8	Detector response with edge and shield correction.	168
VII.1	Number albedos versus energy for HTL soil and two TST mine cases.	172
VII.2	Number albedo ratios versus energy for the TST mine at 0.0 cm in three soils . . .	174
VII.3	Number albedo ratios versus energy for the TST mine at 2.5 cm in three soils . . .	175
VII.4	Energy albedos versus energy for HTL soil and two TST mine cases.	177
VII.5	Multiple scatter fraction versus energy for HTL soil and two TST mine cases . .	179
VII.6	Ratio of number to energy albedo for HTL soil and two TST mine cases	181
VII.7	Spatial distribution of backscattered fluence from 100 keV photons perpendicularly incident on HTL soil . . .	183
VII.8	Spatial distribution of backscattered fluence from 100 keV photons perpendicularly on the center of the TST mine at 0.0 cm.	184
VII.9	Spatial distribution of mine to soil ratio of backscattered fluence from perpendicularly incident 100 keV photons	185
VII.10	Spatial distribution of the single scattered mine to soil ratio from perpendicularly incident 100 keV photons	187
VII.11	Angular distribution of backscattered fluence from 100 keV photons perpendicularly incident on HTL soil and two TST mine cases.	188
VII.12	Angular distribution of the multiple scattered fluence from 100 keV photons perpendicularly incident on HTL soil and two TST mine cases.	189

LIST OF FIGURES - continued

FIGURES		<u>Page</u>
VII.13	Mine to soil fluence ratio versus collimator acceptance angle for 100 keV photons perpendicularly incident on the TST mine at 0.0 cm in HTL soil .	191
VII.14	Mine to soil fluence ratio versus collimator acceptance angle for 100 keV photons perpendicularly incident on the TST mine at 2.5 cm in HTL soil .	192
VII.15	Multiple scatter fraction versus collimator acceptance angle for 100 keV photons perpendicularly incident on the TST mine at 0.0 cm in HTL soil. . .	193
VII.16	Differential energy spectra for 100 keV photons perpendicularly incident on HTL soil and two TST mine cases	195
VII.17	Ratios of mine and soil integral energy spectra for two TST mine cases in HTL soil.	197
VII.18	Edge effect geometries	199
VII.19	Spatial distribution of the single scattered fluence from a 100 keV photon beam perpendicularly incident on the inside edge of the TST mine	201
VII.20	Spatial distribution of the single scattered mine to soil fluence response ratio for a 100 keV photon beam perpendicularly incident on the inside edge of the TST mine	202
VII.21	Spatial distribution of the single scattered mine to soil fluence response ratio for a 100 keV photon beam perpendicularly incident on the outside edge of the TST mine	203
VII.22	NaI(Tl) detector response and fluence response versus source beam energy. . .	206
VII.23	Ratio of NaI(Tl) detector response to fluence response as a function of source energy	207

LIST OF FIGURES - continued

FIGURES		<u>Page</u>
VII.24	Ratios of integral energy spectra for 100 keV photons incident on the TST mine at 2.5 cm in NSL soil for the cases of 0 to 60 degree incidence . . .	212
VII.25	Spatial distribution of the fluence response from a 100 keV beam incident at 60 degrees on the TST mine at 2.5 cm in NSL soil	215
VII.26	Fluence response versus distance from beam axis for 100 keV photons perpendicularly incident on the TST mine at 2.5 cm in NSL soil.	217
VII.27	Relationship between the raster gap size, the length of the collimator, and the spacing of the first collimator element required to exclude single scattered Photons from the detector	224
VII.28	Geometry of the segmented fluence detector.	228
VII.29	Fluence response ratio matrices for the segmented detector for perpendicularly incident 150 keV photon beams on the TST mine at 2.5 cm in HTL soil.	231
VII.30	Source energy optimization curve for the uncollimated fluence detector with mine depth of burial of 5 cm in NSL soil . .	234
VII.31	Source energy optimization curve for the segmented fluence detector with mine depth of burial of 2.5 cm in NSL soil .	237
VII.32	Source energy optimization curve for the energy window detector with mine depth of burial of 5 cm in NSL soil . .	240
VIII.1	Calculated and measured spatial distribution of detector response from back-scatter from sandy soil at 100 kVp. . .	252
VIII.2	Calculated and measured spatial distribution of detector response from back-scatter from sandy soil at 150 kVp. . .	253

LIST OF FIGURES - continued

FIGURES		<u>Page</u>
VIII.3	Calculated and measured spatial distribution of detector response from back-scatter from sandy soil at 200 kVp. . .	254
VIII.4	Comparison of the number albedos of sucrose and TNT	256
VIII.5	Three dimensional image diagram of measured detector response for the lucite annulus experiment	260
VIII.6	Two dimensional image diagram of measured detector response for the lucite annulus experiment	261
VIII.7	Three dimensional image diagram of measured detector response for the steel annulus experiment.	263
VIII.8	Two dimensional image diagram of measured detector response for the steel annulus experiment.	264
VIII.9	Fluence response as a function of height above the soil surface for selected panel widths of the uncollimated detector	268
VIII.10	Fluence response as a function of height above the soil surface for selected acceptance angles of the collimated detector	270
VIII.11	Fluence response as a function of height above the soil surface for the energy window detector.	273
VIII.12	Ratio of fluence responses for two densities of HTL soil with the TST mine at selected depths of burial as a function of source energy for the uncollimated detector	274
VIII.13	Object to soil fluence response ratio for selected materials as a function of source energy for the uncollimated detector.	284

LIST OF FIGURES - continued

FIGURES		<u>Page</u>
VIII.14	Monte Carlo generated image for the TST mine buried flush to an NSL soil surface for the uncollimated fluence detector.	290
VIII.15	Monte Carlo generated image for the TST mine buried flush to an HTL soil surface for the uncollimated fluence detector.	291
VIII.16	Monte Carlo generated image for the TST mine buried flush to an MCL soil surface for the uncollimated fluence detector.	292
VIII.17	Monte Carlo generated image for the TST at 2.5 cm depth of burial in NSL soil for the uncollimated fluence detector .	294
VIII.18	Low pass filtered Monte Carlo image for the TST mine at 2.5 cm depth of burial in NSL soil for the uncollimated fluence detector.	295
VIII.19	Monte Carlo generated image for the TST mine at 5.0 cm depth of burial in NSL soil for the uncollimated fluence detector.	297
VIII.20	Monte Carlo generated image for a simulated water puddle on HTL soil with 20% water content by weight for the uncollimated fluence detector	298
VIII.21	Monte Carlo generated image for an iron disk buried flush to the surface of NSL soil for the uncollimated fluence detector.	299
VIII.22	Three dimensional image diagram of the measured uncollimated detector response to a 100 kVp source beam filtered by Pb for the TST mine buried flush to the soil surface.	301
VIII.23	Two dimensional image diagram of the measured uncollimated detector response to a 100 kVp source beam filtered by Pb for the TST mine buried flush to the soil surface.	302

LIST OF FIGURES - continued

FIGURES	Page
VIII.24 Three dimensional image diagram of the measured uncollimated detector response to a 200 kVp source beam filtered by Pb for the TST mine buried flush to the soil surface.	303
VIII.25 Three dimensional image diagram of the measured uncollimated detector response to a 100 kVp source beam filtered by Pb for the TST mine at a depth of burial of 2.54 cm	304
VIII.26 Low pass filtered image diagram of the measured uncollimated detector response to a 100 kVp source beam filtered by Pb for the TST mine at a depth of burial of 2.54 cm	306
VIII.27 Three dimensional image diagram of the measured uncollimated detector response to a 200 kVp source beam filtered by Pb for the TST mine at a depth of burial of 2.54 cm	307
VIII.28 Low pass filtered image diagram of the measured uncollimated detector response to a 200 kVp source beam filtered by Pb for the TST mine at a depth of burial of 2.54 cm	308
VIII.29 Three dimensional image diagram of the measured uncollimated detector response to a 100 kVp source beam filtered by Pb for the TST mine laid on the soil surface	309
VIII.30 Two dimensional image diagram of the measured uncollimated detector response to a 100 kVp source beam filtered by Pb for the TST mine laid on the soil surface	310
VIII.31 Three dimensional image diagram of the measured collimated detector response to a 200 kVp source beam filtered by Al for the TST mine at a depth of burial of 2.54 cm	311

LIST OF FIGURES - continued

FIGURES		<u>Page</u>
VIII.32	Two dimensional image diagram of the measured collimated detector response to a 200 kVp source beam filtered by Al for the TST mine at a depth of burial of 2.54 cm	312
VIII.33	Three dimensional image diagram of the measured collimated detector response to a 200 kVp source beam filtered by Al for the TST mine at a depth of burial of 7.62 cm	314
VIII.34	Three dimensional image diagram of the measured collimated detector response to a 200 kVp source beam filtered by Al for the TST mine laid on the soil surface	315
VIII.35	Two dimensional image diagram of the measured collimated detector response to a 200 kVp source beam filtered by Al for the TST mine laid on the soil surface	316
VIII.36	Three dimensional image diagram of the measured uncollimated detector response to a 100 kVp source beam filtered by Al for the TST mine at a depth of burial of 2.54 cm with overlying rock array	318
VIII.37	Three dimensional image diagram of the measured uncollimated detector response to a 150 kVp source beam filtered by Al for the TST mine at a depth of burial of 2.54 cm with overlying rock array	319
VIII.38	Three dimensional image diagram of the measured uncollimated detector response to a 150 kVp source beam filtered by Sn for the TST mine at a depth of burial of 2.54 cm with overlying rock array	321
VIII.39	Three dimensional image diagram of the measured uncollimated detector response to a 200 kVp source beam filtered by Sn for the TST mine at a depth of burial of 2.54 cm with overlying rock array	322

LIST OF FIGURES - continued

FIGURES		<u>Page</u>
VIII.40	Three dimensional image diagram of the measured collimated detector response to a 150 kVp source beam filtered by Al for the TST mine at a depth of burial of 2.54 cm with overlying rock array	323
VIII.41	Three dimensional image diagram of the measured collimated detector response to a 200 kVp source beam filtered by Al for the TST mine at a depth of burial of 2.54 cm with overlying rock array	324
VIII.42	Irregular soil surface used in measurements	326
VIII.43	Three dimensional image diagram of the measured uncollimated detector response to a 200 kVp source beam filtered by Pb for the TST mine at a depth of burial of 2.54 cm with irregular soil surface	327
VIII.44	Two dimensional image diagram of the measured uncollimated detector response to a 200 kVp source beam filtered by Pb for the TST mine at a depth of burial of 2.54 cm with irregular soil surface	328
VIII.45	Three dimensional image diagram of the measured collimated detector response to a 100 kVp source beam filtered by Al for the TST mine at a depth of burial of 2.54 cm with irregular soil surface	330
VIII.46	Three dimensional image diagram of the measured collimated detector response to a 150 kVp source beam filtered by Al for the TST mine at a depth of burial of 2.54 cm with irregular soil surface	331
VIII.47	Three dimensional image diagram of the measured collimated detector response to a 200 kVp source beam filtered by Al for the TST mine at a depth of burial of 2.54 cm with irregular soil surface	332

LIST OF FIGURES - continued

FIGURES		<u>Page</u>
VIII.48	Two dimensional image diagram of the measured collimated detector response to a 200 kVp source beam filtered by Al for the TST mine at a depth of burial of 2.54 cm with irregular soil surface	333
VIII.49	Three dimensional image diagram of the measured uncollimated detector response to a 100 kVp source beam filtered by Pb for a wood disk buried flush to the soil surface.	334
VIII.50	Three dimensional image diagram of the measured collimated detector response to a 200 kVp source beam filtered by Al for a wood disk buried flush to the soil surface.	335
VIII.51	Three dimensional image diagram of the measured uncollimated detector response to a 100 kVp source beam filtered by Pb for a steel disk buried flush to the soil surface.	336
VIII.52	Three dimensional image diagram of the measured collimated detector response to a 200 kVp source beam filtered by Al for a steel disk buried flush to the soil surface.	337
VIII.53	Three dimensional image diagram of the measured uncollimated detector response to a 100 kVp source beam filtered by Pb for water contained in a thin plastic container buried flush to the soil surface	339
VIII.54	Three dimensional image diagram of the measured collimated detector response to a 200 kVp source beam filtered by Al for water contained in a thin plastic container buried flush to the soil surface.	340
VIII.55	Three dimensional image diagram of the measured collimated detector response to a 200 kVp source beam filtered by Al for a hole filled with loose soil. .	341

LIST OF FIGURES - continued

FIGURES	Page
VIII.56 Failure of the dual energy subtraction technique	345
VIII.57 Two dimensional image diagram of the measured uncollimated detector response to a 100 kVp source beam filtered by Pb for the TST mine at a depth of burial of 2.54 cm with irregular soil surface.	346
A.1 Typical antitank mine.	370
D.1 X-ray fluence spectrum, 80 kVp, 2.00 mm Al.	398
D.2 Measured and calculated transmission of exposure rate, 80 kVp, 2.00 mm Al.	399
D.3 X-ray fluence spectrum, 80 kVp, 2.24 mm Al.	400
D.4 Measured and calculated transmission of exposure rate, 80 kVp, 2.24 mm Al.	401
D.5 X-ray fluence spectrum, 100 kVp, 2.00 mm Al.	402
D.6 Measured and calculated transmission of exposure rate, 100 kVp, 2.00 mm Al.	403
D.7 X-ray fluence spectrum, 100 kVp, 2.24 mm Al.	404
D.8 Measured and calculated transmission of exposure rate, 100 kVp, 2.24 mm Al.	405
D.9 X-ray fluence spectrum, 150 kVp, 3.00 mm Al.	406
D.10 Measured and calculated transmission of exposure rate, 150 kVp, 3.00 mm Al.	407
D.11 X-ray fluence spectrum, 150 kVp, 3.34 mm Al.	408
D.12 Measured and calculated transmission of exposure rate, 150 kVp, 3.34 mm Al.	409
D.13 X-ray fluence spectrum, 200 kVp, 3.00 mm Al.	410

LIST OF FIGURES - continued

FIGURES	Page
D.14 Measured and calculated transmission of exposure rate, 200 kVp, 3.00 mm Al. . .	411
D.15 X-ray fluence spectrum, 200 kVp, 3.34 mm Al.	412
D.16 Measured and calculated transmission of exposure rate, 200 kVp, 3.34 mm Al. . .	413
E.1 Gadolinium oxysulfide based detector . . .	416
E.2 Active region of the detector.	418
E.3 Spectrum and transmission curve at 115 kVp	421
E.4 Fraction of incident energy absorbed, perpendicular incidence	430
E.5 Fraction of incident energy absorbed in each screen, perpendicular incidence	431
E.6 Fraction of incident energy reflected, perpendicular incidence	432
E.7 Fraction of incident energy transmitted perpendicular incidence	433
E.8 Fraction of incident energy absorbed, 45 degree incidence	437
E.9 Fraction of incident energy absorbed in each screen, 45 degree incidence . .	438
E.10 Fraction of incident energy reflected, 45 degree incidence	440
E.11 Fraction of incident energy transmitted, 45 degree incidence	441
E.12 Fraction of incident energy absorbed, 75 degree incidence	445
E.13 Fraction of incident energy absorbed in each screen, 75 degree incidence. . . .	446
E.14 Fraction of incident energy reflected, 75 degree incidence	447

LIST OF FIGURES - continued

FIGURES		Page
E.15	Fraction of incident energy transmitted, 75 degree incidence	448
E.16	Emission spectrum of gadolinium oxysulfide with 0.3 atom % terbium. . .	452
E.17	Emission spectrum of 3M Trimax 12 screens.	453
E.18	Average number of visible photons produced per incident x-ray photon. . .	454
E.19	Dark pulse count rate versus time.	459
E.20	Measured pulse height spectra.	462
E.21	Response versus distance for ^{137}Cs	468
E.22	Response versus distance for ^{133}Ba	469
F.1	X-ray fluence spectrum, 100 kVp, 1.01 mm Al.	471
F.2	X-ray fluence spectrum, 150 kVp, 1.01 mm Al.	472
F.3	X-ray fluence spectrum, 200 kVp, 2.67 mm Al.	473
F.4	X-ray fluence spectrum, 100 kVp, 9.52 mm Al.	474
F.5	X-ray fluence spectrum, 150 kVp, 9.52 mm Al.	475
F.6	X-ray fluence spectrum, 150 kVp, 1.85 mm Sn.	476
F.7	X-ray fluence spectrum, 200 kVp, 1.85 mm Sn.	477
F.8	X-ray fluence spectrum, 100 kVp, 0.25 mm Al, 0.24 mm Pb.	478
F.9	X-ray fluence spectrum, 100 kVp, 0.75 mm Pb.	479
F.10	X-ray fluence spectrum, 150 kVp, 0.25 mm Al, 0.75 mm Pb.	480

LIST OF FIGURES - continued

FIGURES	<u>Page</u>
F.11 X-ray fluence spectrum, 200 kVp, 0.75 mm Pb.	481
F.12 X-ray fluence spectrum, 200 kVp, 0.25 mm Al, 0.75 mm Pb.	482
F.13 X-ray fluence spectrum, 200 kVp, 0.25 mm Al, 1.35 mm Pb.	483
H.1 The fit technique.	514

Abstract of Dissertation Presented to the Graduate School
of the University of Florida in Partial Fulfillment of the
Requirements for the Degree of Doctor of Philosophy

LANDMINE DETECTION BY SCATTER
RADIATION RADIOGRAPHY

By

John G. Campbell

August 1987

Chairman: Alan M. Jacobs
Major Department: Nuclear Engineering Sciences

The application of scatter radiation radiography to the detection of buried nonmetallic antitank landmines is examined. A combination of calculations and measurements is used to address the problem. The primary calculation tool is a Monte Carlo photon transport code. Measurements are made with an x-ray source, sodium iodide detector, and soil box positioning system. The soil box containing a model of a nonmetallic antitank mine is moved beneath the x-ray source to simulate both the forward motion of a vehicle transporting the detection system and raster of the beam to search a path of sufficient width to allow safe passage. Calculations are used to suggest mine detection mechanisms and to optimize geometric parameters and x-ray beam quality. Measurements are used to validate the calculation results for a small detector and produce images of buried mines. The calculations are extended to large

area detectors which are required to provide path searches of approximately three meter widths. Environmental parameters, such as height sensitivity, soil density and moisture content, and inhomogeneities are examined in both calculations and measurements. Power requirements are also addressed.

A system based upon detector collimation to emphasize differences in the multiple scattered components, characteristic of soil and the explosive found in mines, is found to be capable of mine detection at depths of burial of at least 7.5 cm at power levels compatible with portability, and at speeds, path widths, detection probabilities and false alarm probabilities consistent with operational requirements. Detection at greater depths is possible in soil recently disturbed by mine burial.

Images of holes refilled with loose soil can be distinguished from those of buried mines by their characteristic features. However, the refilled hole images bear some resemblance to those of mines laid on the soil surface. A compound detector, consisting of both collimated and uncollimated regions, can be used to overcome this problem and increase the probability of detection of mines buried at shallow depths.

CHAPTER I

INTRODUCTION

This research studies the use of backscattered x rays to detect and image buried nonmetallic antitank mines. A source of x-ray photons is directed at the soil surface. After interacting with soil or a buried object, backscattered photons strike a detector located above the soil surface producing a response. Detection of a buried object depends upon differences between the photon interaction characteristics of soil and the object. The x-ray source is rastered over the soil surface producing an array of responses, each of which carries information related to the materials through which photons passed before reaching the detector. This array of detector responses is manipulated to produce an image characteristic of those materials. Calculations are performed to optimize the detection and imaging process. A variety of detector geometries and types are examined by these calculations. Measurements are made with a small sodium iodide scintillation detector to examine the predictions of the calculations and to produce images of buried objects.

Chapter II provides a summary of the use of scattered x-ray and gamma-ray photons to provide information about

materials they irradiate. The general concepts for the mine detection and imaging system are also introduced in this chapter. Three related appendices (A, B and C) provide background on the characteristics of landmines, a short history of landmine warfare, and a description of other technologies which have been applied to mine detection.

Chapter III describes the equipment and materials used in the research. Included in this chapter are descriptions of soil and mine materials used in the calculations and measurements.

Chapter IV describes the photon interaction characteristics important to the mine detection problem. The single scatter and Monte Carlo photon transport codes used in the calculations are also described. Validation of the Monte Carlo calculation method is presented.

Chapter V describes the method used to produce calculations of the x-ray source spectrum and the validation of the technique. Other source calculation methods are discussed. A related appendix (D) provides a graphical display of one of the validation methods. Appendix F provides graphs of spectra used in experiments.

Chapter VI describes the method used to calculate the response function of the sodium iodide scintillation crystal used in the experiments. Validation of the calculated response function is provided. Response calculation for a detector based on terbium activated gadolinium oxysulfide is described in a related appendix (E). Detectors similar to

this could prove useful for covering the large areas necessary to find vehicle paths through minefields.

In Chapter VII, results of the application of the Monte Carlo transport code to the physics and geometry of mine detection employing backscattered radiation are provided. Based on these calculations, several detector types are selected for further investigation. Optimization of the geometry and source energy is made for each type of detector selected.

Chapter VIII applies the results of the previous chapter to producing images of mines. Calculated and measured images are examined. The effects of environmental parameters on images are discussed, and power requirements are estimated.

Chapter IX presents conclusions derived from this research effort along with recommendations for directions for future work.

CHAPTER II

BACKSCATTER MINE DETECTION AND IMAGING

Conventional radiography uses the transmission of photons through an irradiated object to produce an image. The image depends upon the photon attenuation properties of the internal structure of the object. Conventional radiography cannot be used to examine objects buried in soil, such as mines, because of the obvious inability to locate the detector below the object. Backscatter radiography, which depends upon differences in the photon scattering properties of irradiated objects to produce an image, is suited to the geometry of mine detection. Photons can originate and be detected above the soil surface. Scattered radiation has been used in medical and engineering applications to determine properties and form images of irradiated objects. Nonmetallic mine detectors using backscattered radiation have been constructed and tested, but have not been considered useful enough for actual field use. The detection and imaging principles investigated in this research are designed to overcome problems inherent in the previous work.

Previous Uses of Scattered Radiation

The first suggested use of Compton (incoherent) scattering to determine characteristics of a material was by Odeblad and Norhagen (1956). They showed that the intensity of the scattered radiation for a fixed source energy and scattering angle depends on the electron density of the scattering medium. In a small volume of uniform composition, the electron density is proportional to the material density. Using a collimated ^{60}Co gamma-ray source and a collimated scintillation detector, they were able to measure the relative electron densities of materials in the small volume defined by the intersection of the fields of view of the detector and source collimators.

Lale (1959) used a collimated ^{192}Ir source and a collimated detector positioned to receive forward scattered Compton photons to measure electron density within transverse cross sections in rabbits and guinea pigs. The subjects were moved with respect to the beam to produce an image of density variation. The process was very slow, and subject to considerable quantum noise and attenuation of the incident and scattered beams, but demonstrated that air in organs would provide a large change in measured electron density in images. In an extension of this work, Lale (1968) used 5.6 MV x rays to reduce attenuation losses. A patient platform was lowered through the beam. Forward scattered photons were detected with a liquid scintillator.

Kondic and Hahn (1970) suggested the use of Compton scattering to measure density variations in two-phase flow. They examined collimated sources used with both collimated and uncollimated detectors. With the uncollimated detector, energy discrimination was used to determine the path taken by a scattered photon. The relationship between energy and angle in a Compton single scattering event determines the position along the source beam from which the photon is scattered, and the intensity (corrected for attenuation) at that energy determines the electron density of the material at that point. Farmer and Collins (1971) independently used the same uncollimated detector technique in a medical application. They used a collimated ^{137}Cs source and an uncollimated Ge(Li) detector to examine cross sectional structure. Rather than move the patient or scan the beam, the energy discrimination technique was used to determine origin of the scattered photons. Problems with this method are attenuation of both the primary and scattered photons, and resolution reduction caused by detection of multiply scattered photons. Extensions of this method (Farmer and Collins, 1974) using two higher resolution Ge(Li) detectors, above and below the patient, and focused to the plane of interest, also suffered from attenuation and multiple scatter. Reiss and Shuster (1972) and Dohring et al. (1974) used collimated ^{137}Cs sources and collimated detectors with patient motion to determine lung function and measure lung density. Problems with multiple scattering were again noted.

Clarke and Van Dyke (1973) and Garnett et al. (1973) developed a two-source method to determine bone density. The two source technique is used to eliminate the problem of attenuation by tissue above the bone. The second source is of the same energy as the single scattered beam of the first for a selected scattering angle. Measurements of both transmitted and scattered beams are made in two orientations to allow correction for attenuation.

Battista et al. (1977) examined the physics of scatter imaging and described the two major limitations to be attenuation of the single scattered photon fluence and contamination by multiply scattered photons. They provide methods for obtaining a correction for the multiple scattering problem. Battista and Bronskill (1978) extended this investigation and concluded that multiple scatter is an inherent limitation whose effect can be reduced, but not eliminated, by improving the energy resolution of the detector. They also showed that the use of forward scattered components both reduces dose to patients and the effects of multiple scatter. Anghaie (1982) showed that predictions of the multiple scattered component could be used to improve image resolution by subtracting it from the total signal.

Hanson et al. (1983) successfully used heavily filtered x-ray beams in the two source densitometry method, taking advantages of the high intensities and well-defined beams available from x-ray machines. Errors from contamination by multiple scattering were found to exceed those due to the polychromatic nature of the source.

Jacobs et al. (1979) proposed an imaging scheme much different than those discussed thus far. A collimated scanning x-ray source with an uncollimated detector was used to view large angle backscattered photons. Energy modulation of the source was used to produce two images. The image at the lower source energy is characteristic of the overlying materials. When subtracted from the higher energy image (after multiplication by an appropriate factor), the result is an image characteristic of deeper layers within the irradiated object. The technique was found to be sensitive to regions of air within the object. This dual energy approach was shown to allow irregular surface features to be removed from the final image.

Backscattered Photon Mine Detection

A number of attempts have been made to use backscattered photons to detect buried nonmetallic mines. With only one exception, the published descriptions are from efforts sponsored by the United States military. Detailed accounts of these mine detection systems are contained in classified documents. The descriptions provided here are from unclassified summaries (Roder, 1975; Nolan et al., 1980). The wide range of other technologies which have been examined as possible mine detection methods are described in Appendix C.

Fluorescence Emission

Although fluorescent emission is not a backscatter technique, attempts to use it as a mine detection mechanism are similar. Between 1954 and 1957, the Armour Research

Foundation used a 150 kVp x-ray source to attempt to produce fluorescent emission from the lead or mercury contained in mine fuzes. These elements are found in approximately one gram quantities of lead azide, lead styphnate or mercury fulminate (U.S. Department of the Army, 1986). High resolution detectors were used to look for the energies of the characteristic x rays of lead or mercury. The Compton scattered fluence was found to completely obscure any fluorescent emission signal which might be present. Additional efforts using more modern detectors produced this same result, and the technique was deemed infeasible.

Rayleigh Scattering

From 1958 to 1961, Tracerlab, Inc. attempted to use Rayleigh (coherent) scattering from these same high atomic number components of the mine fuze as a detection mechanism. Because the probability of Rayleigh scattering decreases and the direction of scattering becomes more forward peaked as incident energy increases, the technique is limited to shallow depths of burial. A 120 kVp x-ray source was employed, in an attempt to produce Rayleigh scattered photons when the beam struck the high atomic number materials in the fuze. Because the incident beam was polyenergetic, the Rayleigh scattered photons were also produced in a spectrum of energies. Compton scattering was again the dominant source of the detected signal. Two rastering detectors were tightly collimated to focus on a very small volume which might contain the mine fuze. Detection was signaled by a small shift

in the backscattered spectrum to higher energies. The very small sampled volume, which led to scans on the order of hours per square foot, was the cause for termination of this effort. Unfortunately, this detection system was not tested with a real mine. Had it been employed in such a fashion, a large difference between cases of irradiation of soil only and of soil containing a buried mine would have resulted. The mine detection mechanism would have been the difference between the photoelectric cross sections of soil and mine. The higher photoelectric absorption of photons striking soil results in fewer photons capable of being backscattered than in the mine present case.

Compton Scattering

The first attempt to examine the contrast mechanism afforded by the difference photoelectric cross sections of soil and mine materials was made by the Naval Ordnance Laboratory in 1960 to 1961. Unfortunately, 2 and 10 MV bremsstrahlung sources were selected for the experiments. At these energies the photoelectric cross sections of soil and mine materials are both very small. The dominant interaction is Compton scattering, and the respective material cross sections for this interaction at these energies are nearly the same. Additionally, the material densities of soil and explosive are similar. As a result no contrast mechanism existed and only negative results were obtained.

Beginning in 1967 and extending until 1973, Texas Nuclear Corporation conducted experiments to produce non-metallic mine detection systems using backscatter of gamma or x rays. These experiments culminated in a nonmetallic antitank mine detector. A less successful nonmetallic anti-personnel mine detector was also produced. Both systems used vertically collimated sources and vertically collimated detectors. Low energy x-ray sources were used to enhance the photoelectric contrast between mine and soil. The antitank mine detector used a 130 kVp x-ray source mounted on the front of a 1/4-ton truck and four CsI(Tl) scintillation detectors. It was capable of operation at several miles per hour. Field tests were conducted at a variety of military installations with U.S. and Soviet mines filled with dinitrobenzene (a nonexplosive substitute for trinitrotoluene). Although depths of detection of up to 10 cm were achieved, a number of conditions of the test were optimized to enhance the mine detection process. The tests were conducted in areas free of buried organic material, such as tree roots, whose response was known to produce false alarms in the detector. The areas of the tests were also fairly level, minimizing sensitivity to irregular surfaces. Deep ruts or depressions comparable to the size of a mine were also capable of producing false alarms. The test areas were free of vegetation, which if present would have lowered the contrast between soil and soil with mine, and if nonuniform, could have produced false alarms. The

extent of coverage was also a problem; mines located midway between two detectors were missed unless they were on the surface. A final objection to the system involved soil density. It was found that the detector was sensitive to density changes whether a mine was present or not. Concern was expressed that dummy minefields could be produced by simply digging and refilling holes. The act of emplacing a mine significantly alters the soil density, reducing it, on the average, to 75% of the undisturbed value (Roder, 1975). After weathering had returned the soil to its normal density, detection was no longer possible at 10 cm, and the response difference at 7.5 cm was much reduced. Further work on this detection system was terminated primarily as a result of the apparent superiority of a competing technology, and secondarily as a result of the inadequacies described (Nolan et al., 1980).

Coleman (1971) performed Monte Carlo calculations for several cases in support of this effort. They are discussed in Chapter IV. These calculations and the majority of Texas Nuclear experiments were conducted with solid blocks of dinitrobenzene. The mines used in the field tests were filled with dinitrobenzene, but it is unclear whether any air space, characteristic of real mines (described in Appendix A), was provided.

Preiss and Livnat (1973), working in Israel, provide the only non-U.S. military publication of research on the detection of nonmetallic mines by the backscatter of

ionizing radiation. The system consisted of an uncollimated ^{75}Se source with a NaI(Tl) detector collimated to view a 10 cm diameter circle at the soil surface at a fixed detector height. The system was placed on a cart and pushed by the operator over dirt road surfaces. The electronic components of the detector were carried by backpack. This research effort was the first to consider the effect of the air space which exists at the top of mines. Experiments with solid explosive filling the mine and with an actual mine, containing an air space, revealed completely different effects. In the case of the solid mine, the ratio of the detector response with mine present to mine absent (soil only) was found to be greater than 1.00. In the case of the mine with air space, the ratio was less than 1.00. Mine detection was accomplished by selecting an energy range in the backscattered spectrum which enhanced the reduction in response with the mine present.

Backscatter Radiation Radiography

Genesis of Current Research Effort

A high priority has been placed on research into the detection of landmines (West et al., 1985; U.S. Department of the Army, 1986). The increased interest in this research is based upon a combination of factors, driven by the implementation of a new dynamic operational concept by the U.S. Army. This new concept, termed the AirLand Battle, is oriented primarily to the threat of a Warsaw Pact attack into Western Europe. The superseded defensive concept,

termed the Active Defense, concerned itself with attrition of numerically superior attacking forces by use of defensive positions prepared in depth on the battlefield (DePuy, 1984; Holder, 1985). Simulations indicated that this concept would be successful against the first echelon of a Warsaw Pact attack, but without extensive, rapid reinforcement would be of doubtful utility against the following echelons. The AirLand battle concept emphasizes the use of aggressive engagement of the attacking force using both fire and maneuver at varying depths on the battlefield. Counterattacks into the flanks of the attacking force and into rear supply and transport areas are encouraged to disrupt the rigid plans and time tables characteristic of Soviet military operations. These maneuvers are also designed to enhance one of the few perceived advantages of Western military forces in conventional combat with Soviet forces: the capability of Western leaders of virtually any size unit to use their initiative in fluid situations compared to the discouragement (at least until recently) of any deviation from detailed plans, regardless of tactical situation, applied to Soviet leaders, especially of smaller sized units (Suvorov, 1984; Walker, 1986; Baxter, 1986). Another key factor in the development of the AirLand Battle concept is the advent of a series of technological advances and equipment modernizations which make rapid maneuver feasible (RisCassi, 1986).

The landmine represents a serious challenge to rapid maneuver. The employment of mines by the attacking force to protect its flanks and rear areas could do much to neutralize the new operational concepts. The effectiveness of landmines is high. More than 20% of Allied tank casualties in World War II were caused by mines. United Nations tank casualties in the Korean conflict were as high as 70% in offensive operations. In Vietnam (through 1970) 70% of all U.S. vehicle losses were due to mines (U.S. Department of the Army, 1973). The keystone manual of the U.S. Army, FM 100-5, Operations (U.S. Department of the Army, 1982), emphasizes synchronized execution. Clearly, the capability of mines to produce delays and disruptions is inconsistent with the new maneuver oriented operational concepts.

Adding to this concern is the mine warfare capability and experience of the Soviet Army, which is unsurpassed by any army in history (Honeywell, 1981). Appendix B provides examples of the Soviet experience with mines. The primary mission assigned to Soviet engineer units is to insure the momentum of maneuver mobility by rapidly overcoming natural and manmade obstacles, while at the same time hindering enemy force movement (Sidorenko, 1973). The second portion of this mission, directly affecting the new U.S. Army operational concepts, is accomplished by Mobile Obstacle Detachments, which provide countermobility support by laying minefields and establishing other expedient obstacles along enemy avenues of approach (Plyaskin et al., 1973; Uli,

1986). In short, the Soviet Army is aware of its vulnerabilities on its flanks and in its rear areas, and is organized to address the threat, in part, by employing mines. Soviet doctrine has long included the rapid emplacement of mines on the surface without burial (U.S. Department of the Army, 1979a). In the 1970's, mechanical minelayers and mine dispensing chutes for vehicles and helicopters were fielded to allow rapid minefield emplacement. More recently fielded scatterable mine systems further enhance the capability to respond to the new U.S. operational concepts (West et al., 1985).

Aside from manual probing, a hand-held nonmetallic mine detector of questionable capability (the hand-held metallic detector works well), and actual mine detonation in an adverse encounter, the U.S. Army has no method for detecting buried nonmetallic mines (U.S. Department of the Army, 1986). These slow or adverse detection mechanisms are incompatible with the advent of new operational concepts which rely upon maneuver mobility. Accordingly, reviews of all previous detection technologies have been conducted by the U.S. Army in an attempt to find systems which might be made to work. One such review (Moler, 1985) examined the range of nuclear techniques (x-ray backscatter is included within this category, even though it is actually an atomic technique). This review recommended imaging using x-ray backscatter as the highest priority nuclear technique for additional research.

Improvements on Previous X-Ray Backscatter Efforts

The shortcomings of the Texas Nuclear Corporation research effort, described above, provide the basis for improvements in the x-ray backscatter technique. The concepts investigated in this dissertation differ from the previous efforts in a number of areas. The major difference is the examination of the formation of images of buried objects, rather than detection based upon a single difference between soil and soil with buried object. Creating an image requires capabilities that were unavailable in the past. X-ray sources capable of long linear scans and the image processing technology to allow real time analysis of data have been developed since the Texas Nuclear Corporation efforts. An image provides the important capability to discriminate between buried mines and other buried objects which have photon interaction characteristics similar to mine materials. Coupling the scanning x-ray beam with a detector large enough to assure coverage of width of the largest vehicle which must traverse a mined area eliminates another shortcoming of the previous effort. A diagram of a conceptual detector is shown in Figure II.1.

Research Goals

The goals of this research effort are to optimize the design parameters of a large area, x-ray backscatter imaging system and to examine the effect of environmental parameters on the detection and imaging process. The design parameters available for optimization are the energies of

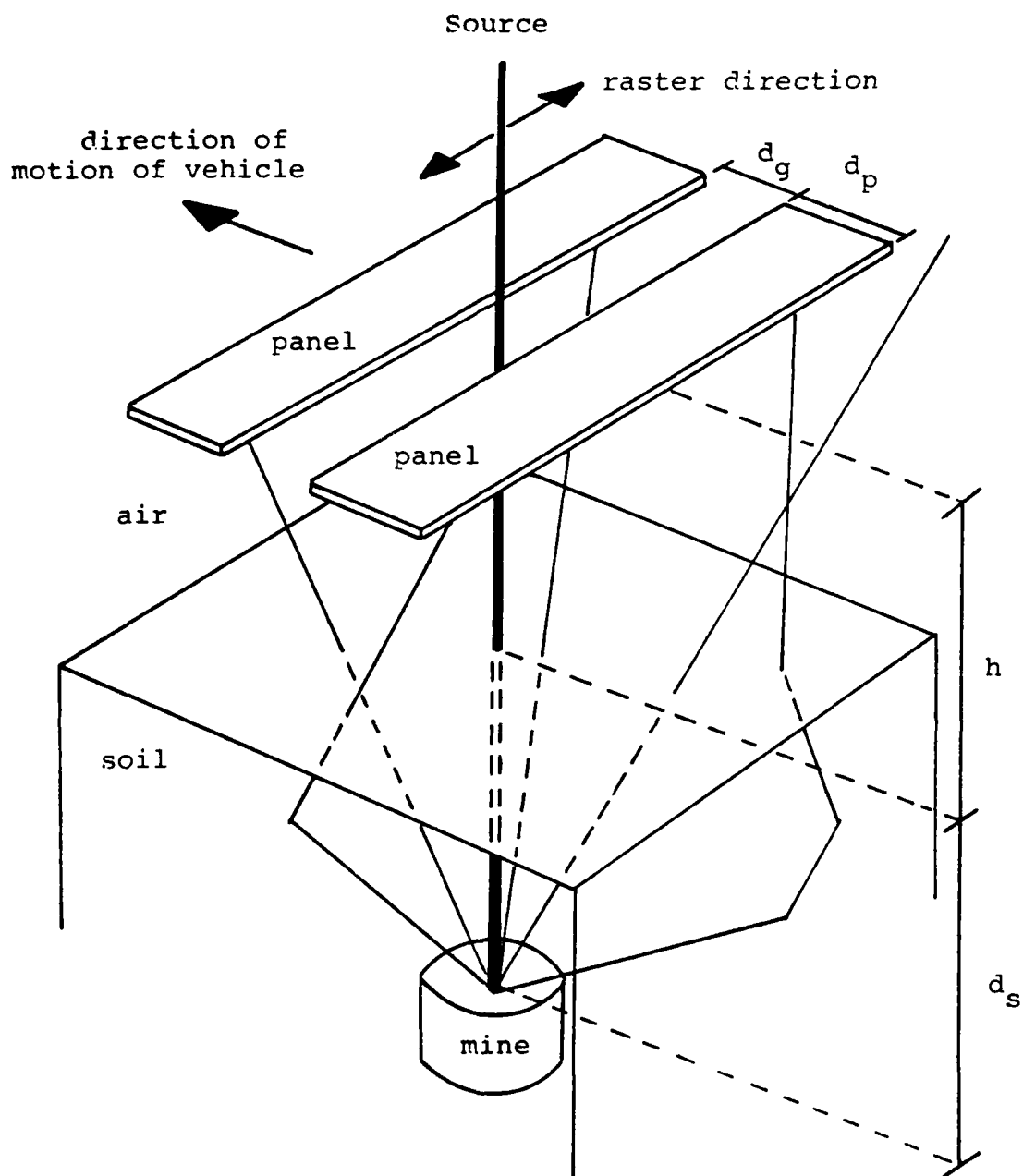


Figure II.1. Conceptual large area backscatter detector system. A pencil, incident x-ray beam strikes the soil surface. The beam is scattered as it penetrates the soil and mine. Some of the photons scattering within the mine reach the panels of the detector after single or multiple scatters. Distances indicated on the diagram are the height of the detector above the soil, h ; the depth of burial of the mine, d ; the size of the gap between the two panels, d_g ; and the width of a panel, d_p .

the x-ray beams, beam angle of incidence, beam size, beam collimation, detector geometry, and detector collimation. Environmental parameters are soil type, soil density, soil moisture content, inhomogeneities with the soil, surface irregularities, mine geometry, and mine depth of burial. The method for examining parameters is a combination of calculations and measurements. The primary calculation tool is a Monte Carlo photon transport code written specifically for the mine detection problem. Measurements are made with a small NaI(Tl) detector to validate the Monte Carlo predictions, allowing extension of the code to large area detector configurations.

CHAPTER III

EQUIPMENT AND MATERIALS

The apparatus used to perform measurements is designed to simulate the raster of the x-ray beam across a soil surface which may contain buried objects. This raster simulation is accomplished by moving a soil box under a fixed x-ray beam. The complete simulation system consists of the x-ray machine, the soil box and its positioning system, the detector and its related electronics, and the computer control devices. Figure III.1 shows the x-ray source, soil box and positioning system, and detector. Figure III.2 shows the detector electronics, computer control and x-ray source control systems. Materials used for soil and buried objects are selected to simulate those items found under field conditions.

Equipment

X-Ray Source

An x-ray machine is selected as the source of the photons for backscatter imaging applications because of its capability to produce intense photon beams which can be rastered. Extremely high activity radionuclide sources would be required to produce similar intensities in the collimated beams necessary for the imaging process. Such

Figure III.1 X-ray source, soil box and positioning system, and detector. The GE Maxitron 300 x-ray generator (top center) is held in a fixed position while the soil box (center) is moved in raster mode by drive screws powered by DC motors with controlled clutch/brakes. The positioning interface to the controlling computer is on the right side of the photograph.

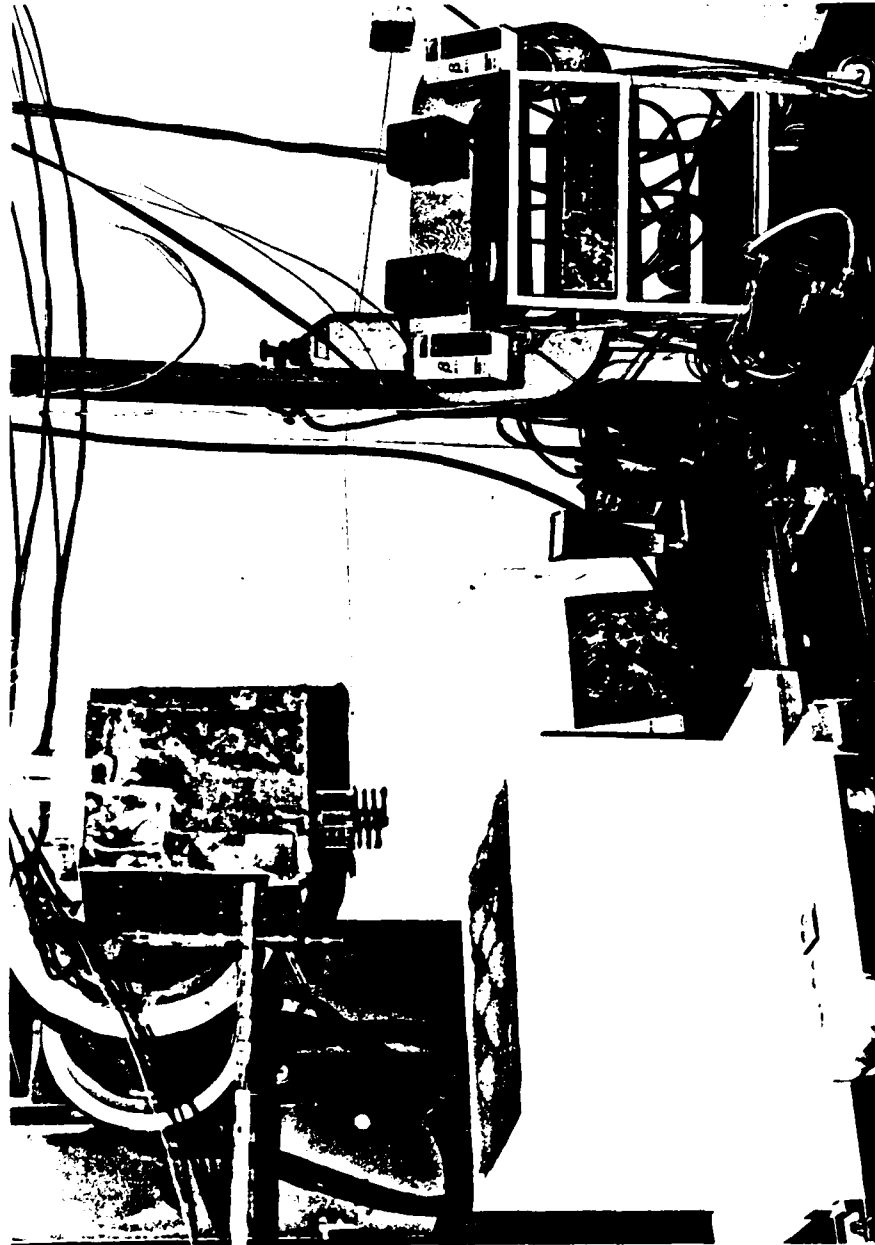
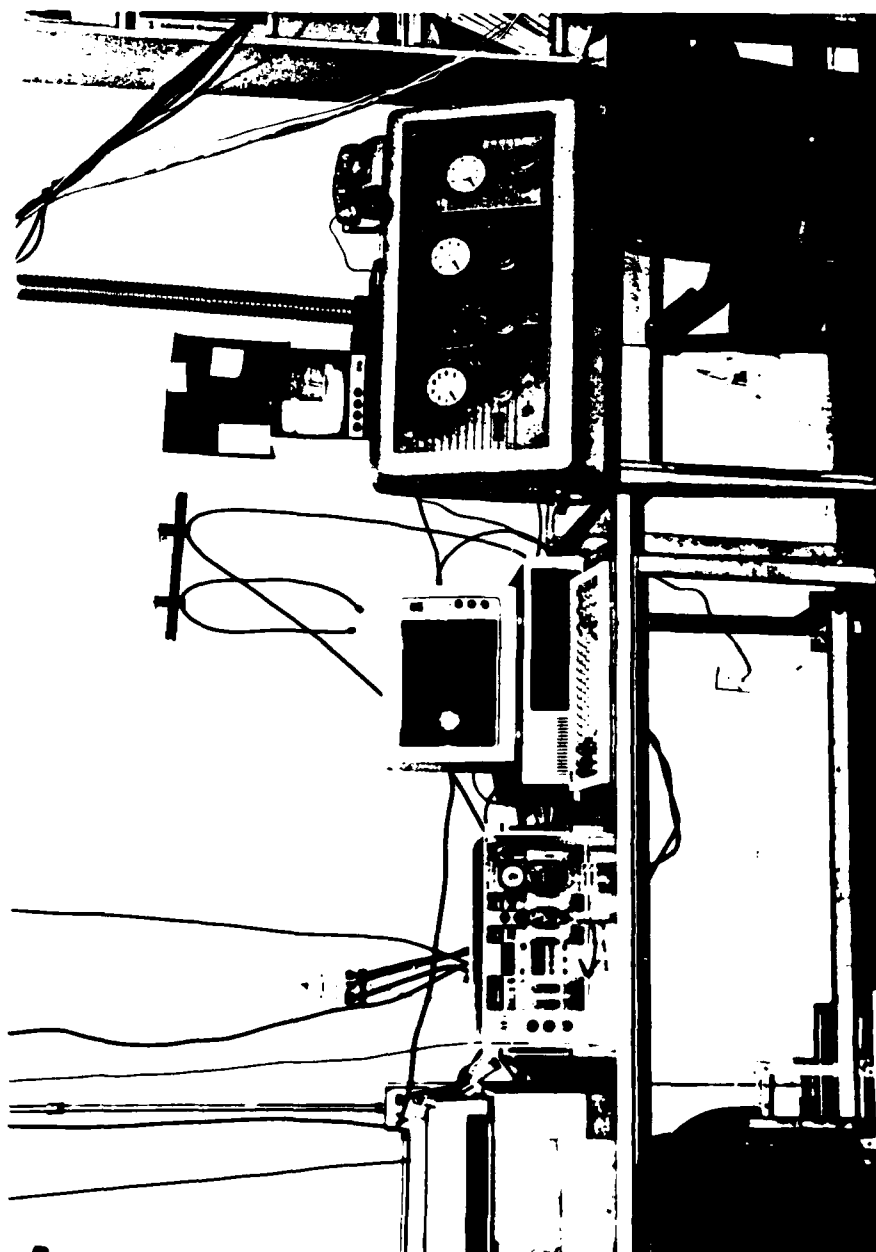


Figure III.2. Detector electronics, computer and x-ray source console. This photograph shows, from left to right, the detector high voltage supply, scaler and timer, amplifier and single channel analyzer, count rate meter, the IBM PC computer, and the GE Maxitron 300 control console with remote TV picture of exposure room.



sources require heavy shielding at all times and pose a constant radiological safety concern. An x-ray machine poses the same hazard only when in operation. Since the mine detection problem requires a minimum path width equal to the widths of following vehicles (on the order of 3 meters), rastering of the beam is required. Mechanical systems are not practical for rastering a radionuclide source at the speeds required for the imaging problem (on the order of 10^3 m/s), or alternatively, moving a collimator along a line source at those speeds. The electron beam of an x-ray machine can be scanned along an extended anode at very high speeds to provide the raster required. An additional advantage of an x-ray machine is the capability to alter intensities by varying beam current and to alter beam quality by varying tube voltage or filtration. Separate radionuclide sources would be required to accomplish such alterations.

The source of the photons used in the backscatter imaging experiments is a General Electric Maxitron 300 X-Ray Therapy Unit (General Electric, 1962). The unit is capable of producing continuous beams of 70 to 300 kVp at beam currents between 5 and 20 mA. The primary voltage waveform accelerating the electrons to the anode is single phase, self-rectified at approximately 1200 Hz. The accelerated electrons strike a 45 degree angle tungsten anode. If the electron energy exceeds that of the K shell binding energy of tungsten, K characteristic x rays are produced in

addition to the continuous x rays produced at all energies. All beams pass through a 4.75 mm thick beryllium window. Additional filtration can be provided both within and outside the head of the unit. Adjustable internal, rectangular collimators are employed to shape the beam. When an external filter is used, an additional external collimator is employed to prevent the majority of scattered or fluorescent photons produced within the external filter from reaching the soil plane.

The shielding of the head of the x-ray unit is supplemented by a 0.16 cm (1/16 inch) thick layer of lead. This additional shielding was found to be required when measurements were performed using an uncollimated detector with a heavily filtered beam at higher accelerating potentials. The higher accelerating potentials produce photons more likely to penetrate the standard shielding of the unit. This fact, combined with low intensity fields produced by heavily filtered beams, results in a significant fraction of the detector response being caused by head leakage scatter. The lead shielding reduces the probability of head leakage photons reaching the soil and subsequently scattering into the detector. The shielding employed does not entirely eliminate the problem, requiring two sets of measurements to be made at high energies when an uncollimated detector is used. The first image scan is made with the desired beam filtration. A second scan is then made with a very thick lead external filter which prevents beam photons from

reaching the soil. This second image scan is, therefore, the result of the head leakage scatter. Subtraction of the second scan from the first corrects the imaging data for the head leakage scatter. Structural constraints caused by the weight of the shield prevent thicker layers from being used. Figure III.3 shows lead shielding covering the head of the x-ray machine.

Soil Box Positioning System

The soil box positioning system was constructed according to a design by Moss (1986). The control system was constructed by Moss. The soil box is positioned in the x-y plane (the plane parallel to the floor of the exposure room) beneath the source by a two level linear bearing system driven by ball screws which are powered by DC motors with controlled clutch/brakes. The scan motion is boustrophedonic. Both local and remote control of the positioning system are available. Local control is used to provide the initial beam-soil intercept position prior to irradiation. Remote control of the soil box motion is through an RS-232 serial interface bus. It is used in the imaging process to move the soil box through the array of measurement positions. Two soil boxes of dimensions of 66 cm by 66 cm by 45 cm deep and 122 cm by 91 cm by 45 cm deep are used. The larger box is required for measurements with a collimated detector. Both are filled with locally obtained sandy soil typical of North Central Florida.

Figure III.3. Lead shield for tube head and detector. The detector within its shield and the shielding of the head of the x-ray generator are viewed from below. The shielding is required to attenuate x-ray leakage from the generator head in directions other than that of the beam. The filter holder with filter and external collimator is also shown.



Detector and Related Electronics

Two types of detectors have been used in the imaging measurements. The x-ray sensing portion of the first detector is based on terbium activated gadolinium oxysulfide rare earth intensifying screens. This device was constructed to provide an inexpensive, sensitive, large area detector. For reasons detailed in Appendix E, this detector is found to be unsuitable for the detection and imaging tasks. It is replaced by Bicron Model .5M.390/.5L-X, sodium iodide detectors. This detector type is used in all imaging measurements. The geometry of this detector is shown in Figure III.4. Also included in this diagram is a composite shield designed to allow the detector, when operated in an uncollimated mode, to simulate small regions of a large area plane detector by permitting photons to enter only through the exposed face. Several regions of the detector (labeled 3, 4, 5 and 6 in Figure III.4) are not identified in the diagram. Bicron Corporation, the manufacturer of the detector, provided the compositions and densities for these materials with the understanding that they would not be published due to their proprietary nature (Melocik, 1986). They are included in the Monte Carlo calculations performed to determine the detector response function (described in Chapter VI). Table III.1 provides the dimensions of the materials shown in Figure III.4.

Because a large area, plane detector is a possible candidate for an actual fielded system (Chapter II), it is

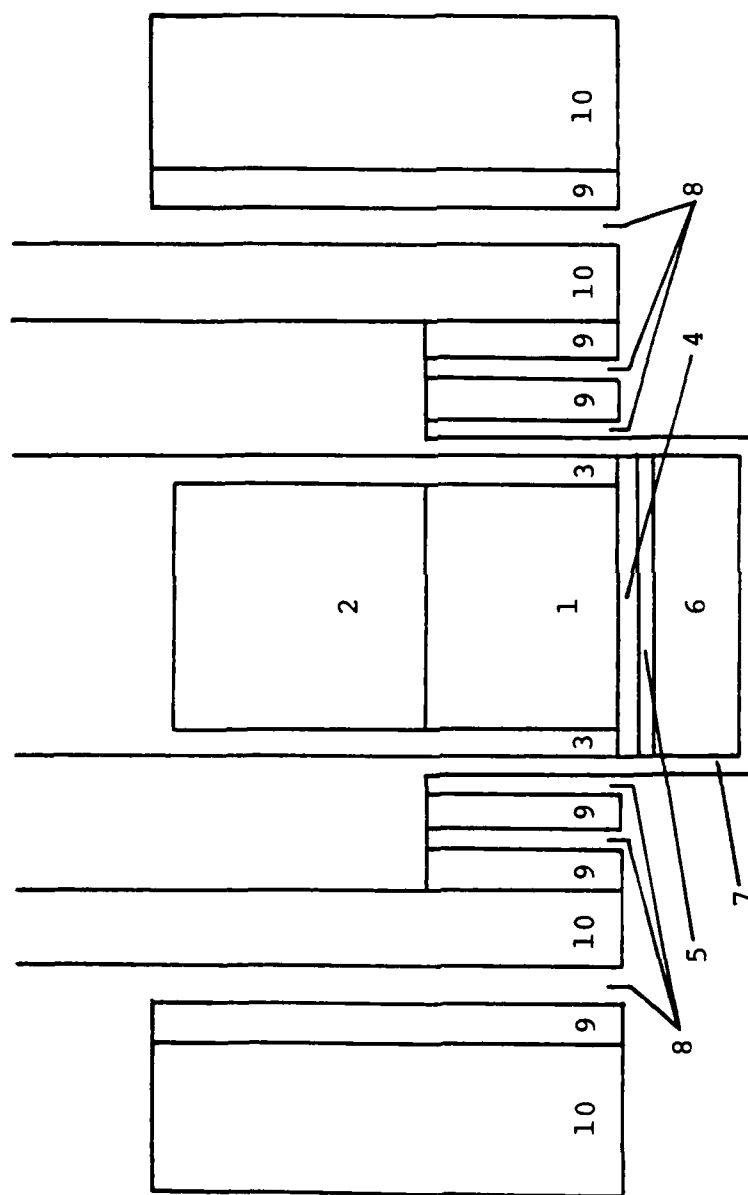


Figure III.4. Geometry of the sodium iodide detector and shield. A cross section of the Bicron Model .5M.39Q/.5L-X NaI(Tl) detector (Melocik, 1986), and locally fabricated shield is shown (not to scale). Numbers in detector and shield regions correspond to materials and dimensions provided in Table III.1.

TABLE III.1
Geometry of the Sodium Iodide
Detector and Shield

#	Material	Diameter or Width	Thickness (cm)
1	NaI(Tl) crystal	1.2700	0.9906
2	Quartz light pipe	1.2700	1.2700
3	Bicron proprietary	0.1588	a
4	Bicron proprietary	1.5875	a
5	Bicron proprietary	1.5875	a
6	Bicron proprietary	1.5875	a
7	Aluminum housing (face)	1.6383	0.0254
8 inner	Air space	0.04	1.0643
9 inner	Tin	0.07	1.0643
8 mid	Air space	0.06	1.0643
9 mid	Tin	0.07	1.0643
10 inner	Lead	0.1588	15.0343
8 outer	Air space	0.08	2.3343
9 outer	Tin	0.07	2.3343
10 outer	Lead	0.3175	2.3343

Dimensions of the Bicron Model .5M.390/.5L-X NaI(Tl) detector and locally fabricated shield used in measurements and calculations. Numbers (#) in the table are keyed to Figure III.4.

^a Materials and thicknesses are proprietary information of Bicron Corporation.

desirable to retain as much similarity to such a configuration as possible. The shield is employed to assist in retaining this similarity in the small sodium iodide detector by preventing large numbers of photons from striking the sides of the crystal. The responses of a small detector, taken at a number of positions, can then be used to simulate a large detector. Additionally, considerably greater detail is available with a small detector than with a large detector which averages detailed response information over its greater area. The purpose of the tin inner layer of the shield is to prevent K fluorescent x rays produced in the lead of the shield from entering the sides of the detector. If this layer were not present and a lead layer was adjacent to the detector, lead K fluorescent x rays from the lip of the layer would enter through the side of the detector. The high photoelectric cross section of tin at these energies (72.794 to 87.343 keV) makes it an attractive material for shielding lead x rays. The lower level discriminator of the counting system is set high enough to preclude counting of tin K fluorescent x rays (25.042 to 29.106 keV) (Storm and Israel, 1970). The face of the NaI(Tl) crystal and the bottom of the shield are at the same level to preclude collimation of the detector. Collimators are attached to the detector shield when such a configuration is desired. A detailed description of the modeling of the detector response function, including correction for edge effects and the shield, is provided in Chapter VI.

The usual purpose of the lower level discriminator setting of the counting system is to preclude pulse height events corresponding to electronic noise. As described above, an additional purpose in this detector system is to prevent tin K fluorescent x rays, which could enter through the sides of the detector, from being counted. A set of radioactive sources is used to determine the relationship between photon energy and lower level discriminator setting (in combination with a fixed detector high voltage supply, and amplifier and preamplifier settings). Sources and energies used for this calibration are given in Table III.2. A discriminator setting corresponding to 35 keV was selected to prevent counting of spillover of the tin K ray peak as a result of the resolution of the detector. Based upon the Monte Carlo spectral and number albedo calculations (Chapter IV provides examples), this setting results in only a small reduction of the total detector response compared to the case when no discrimination is used. The fluence spectral calculations show that only when the source energy is small is there any significant contribution below 35 keV. The number albedo (the fraction of incident photons which are reflected from a surface) calculations show that low energy source photons produce significantly less backscatter than high energy photons (this is true up to about 300 keV). Additionally, results of the detector response calculation, provided and described in Chapter VI show that low energy photons produce a much lower response than all others except

TABLE III.2
Sources Used in Determining Lower
Level Discriminator Setting

Source	Energy (keV) ^a
¹⁰⁹ Cd (Ag K _{α1} x ray)	22.162
¹³³ Bs (Cs K _{α1} x ray)	30.970
¹³⁷ Cs (Ba K _{α1} x ray)	32.191
¹³³ Ba (gamma)	80.999
¹⁰⁹ Cd (gamma from ^{109m} Ag)	88.037
⁵⁷ Co (gamma)	122.06135

^aPhoton energy data are from Lederer and Shirley (1978).

very high energy photons (which pass through the detector without significant interaction). The 35 keV value also provides some safeguard for the lower level discriminator setting determination from non-linearities observed in the low energy response of NaI(Tl) (Aitken et al., 1967). The light output and hence pulse height is not proportional to the amount of energy deposited in the NaI(Tl) crystal for low photon energies. Figure III.3 shows the detector and shield. The slotted wooden structure supporting the detector allows the distance between the beam axis and the detector to be varied.

The detector is operated in a pulse counting mode. The detector high voltage is supplied at -900 volts. Figure III.5 provides a diagram of the components of the counting system. Remote control of the counting system is by an IEEE-488 General Purpose Interface Bus (GPIB).

Computer Control System

An IBM PC personal computer controls both the RS-232 serial interface bus, which operates the soil box positioning system, and the IEEE-488 GPIB, which operates the counting system. Software for these two functions was provided by Moss (1986). The RS-232 serial interface bus transmits the direction, distance and axis of motion to the motor controllers. The GPIB controls the counting channel and time through the counter/timer. The two systems are integrated by the computer to allow complete automation of the scanning and counting tasks required to produce an

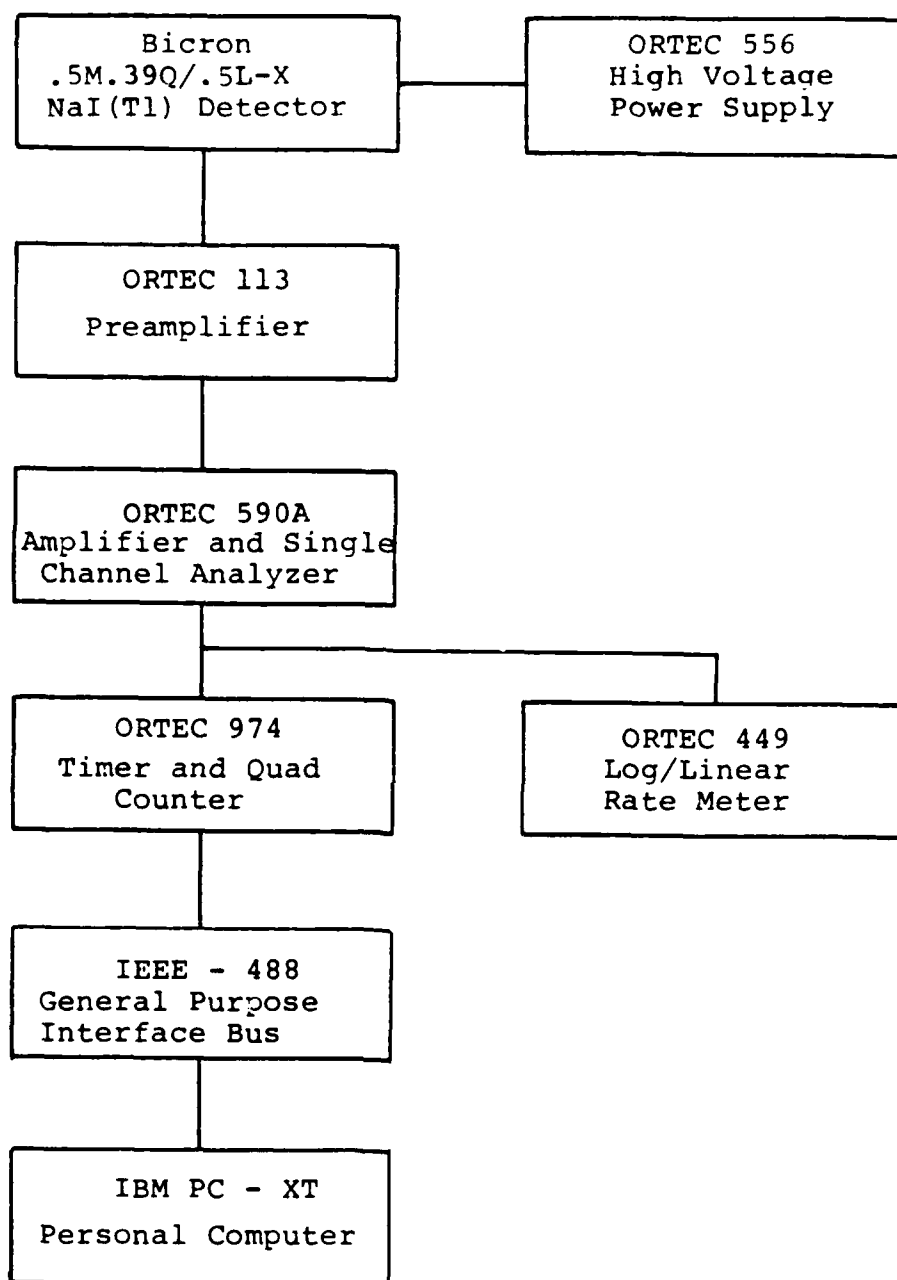


Figure III.5. Components of the counting system.

image. Independent operation of the positioning and counting systems is also possible.

Simple graphical display programs, written in Turbo Pascal (Borland, 1985), are used to rapidly analyze the image data. These programs accept the data files produced by the counting system control program.

Materials

Soils

Three soil types are selected for calculations to represent a range of soil properties. Norfolk sandy loam (Jaeger, 1975) has a high silicon dioxide content and is similar to the North Central Florida sandy soil used in the measurements. Hagerstown loam (Bear, 1955) is close to the average of all soil types examined in elemental composition. Malatula clay loam is a lateritic soil with high iron content. Lateritic soils are produced under conditions of high rainfall and high temperatures. These conditions, over geologic periods of time, lead to the decomposition of organic materials and selected minerals. The result is a soil low in silicon dioxide and high in hydrated oxides of iron and aluminum (Bear, 1955). A global average soil constructed from the average elemental composition of the crust of the earth is also used in some calculations (Jaeger, 1975). This global average soil is very similar in its photon interaction properties to Hagerstown loam. Hereafter, these soils will be referred to as NSL (Norfolk sandy loam), HTL (Hagerstown loam), MCL (Malatula clay loam) and GAD (global

average). The elemental compositions, densities and weight percentages of water of these soils are given in Table III.3. A comparison of the mass attenuation coefficients of the NSL, HTL and MCL soils is given in Figure III.6. The coefficients are calculated from Hubbell's data (1982).

Nonmetallic Antitank Mine Model

Nonmetallic antitank mines of the Warsaw Pact are the subject of the mine detection effort. Nonmetallic mines are important subjects for study because of the difficult problem they present to all current mine detector types and because their implications to changes in U.S. operational doctrine. Metallic mines are not considered since other techniques are more applicable to their detection. While nonmetallic antipersonnel mines are also very difficult to detect, they are a secondary concern for mounted armor combat operations. Also, while buried, surface laid, and scatterable mines would be employed in any large scale conflict in Europe, this study concerns itself primarily with the buried mine, the more difficult detection problem. Table III.4 provides characteristics of several common conventional Warsaw pact nonmetallic landmines. The TST mine, listed in the table for the purpose of comparison, is the model used in experiments and calculations. As indicated by the table, it is representative of common Warsaw pack nonmetallic antitank mines.

The TST model consists of a lucite, right circular cylinder, with 0.635 cm thick walls and outside diameter of

TABLE III.3
Composition of Soil Types

Element	Weight Percentage of Elements in Dry Soils ^a			
	NSL	HTL	GAD	MCL
H	0.070	0.185	-	-
C	0.502	1.320	-	-
O	52.627	49.637	47.330	38.702
Na	0.082	0.629	2.840	0.052
Mg	0.054	0.674	2.110	0.784
Al	1.095	6.236	8.240	18.955
Si	44.142	34.330	28.100	1.730
P	0.026	0.086	-	0.493
S	0.028	0.162	-	-
K	0.083	2.327	2.640	0.075
Ca	0.278	0.688	3.650	0.129
Ti	0.425	0.626	-	8.035
Mn	0.008	0.040	-	0.504
Fe	0.580	3.061	5.090	30.578

^aData for NSL and GAD are from Jaeger (1975). Data for HTL and MCL are from Bear (1955).

Density and Moisture Ranges

Soil Type	Density Range ^b	Moisture Range ^b
	(g/cm ³)	(%)
NSL	1.40 - 1.96	5 - 25
HTL	0.96 - 2.17	8 - 25
GAD	0.96 - 2.17	10 - 30
MCL	0.080 - 1.80	15 - 30

^bData from Hough (1957) and Chilton et al. (1984).

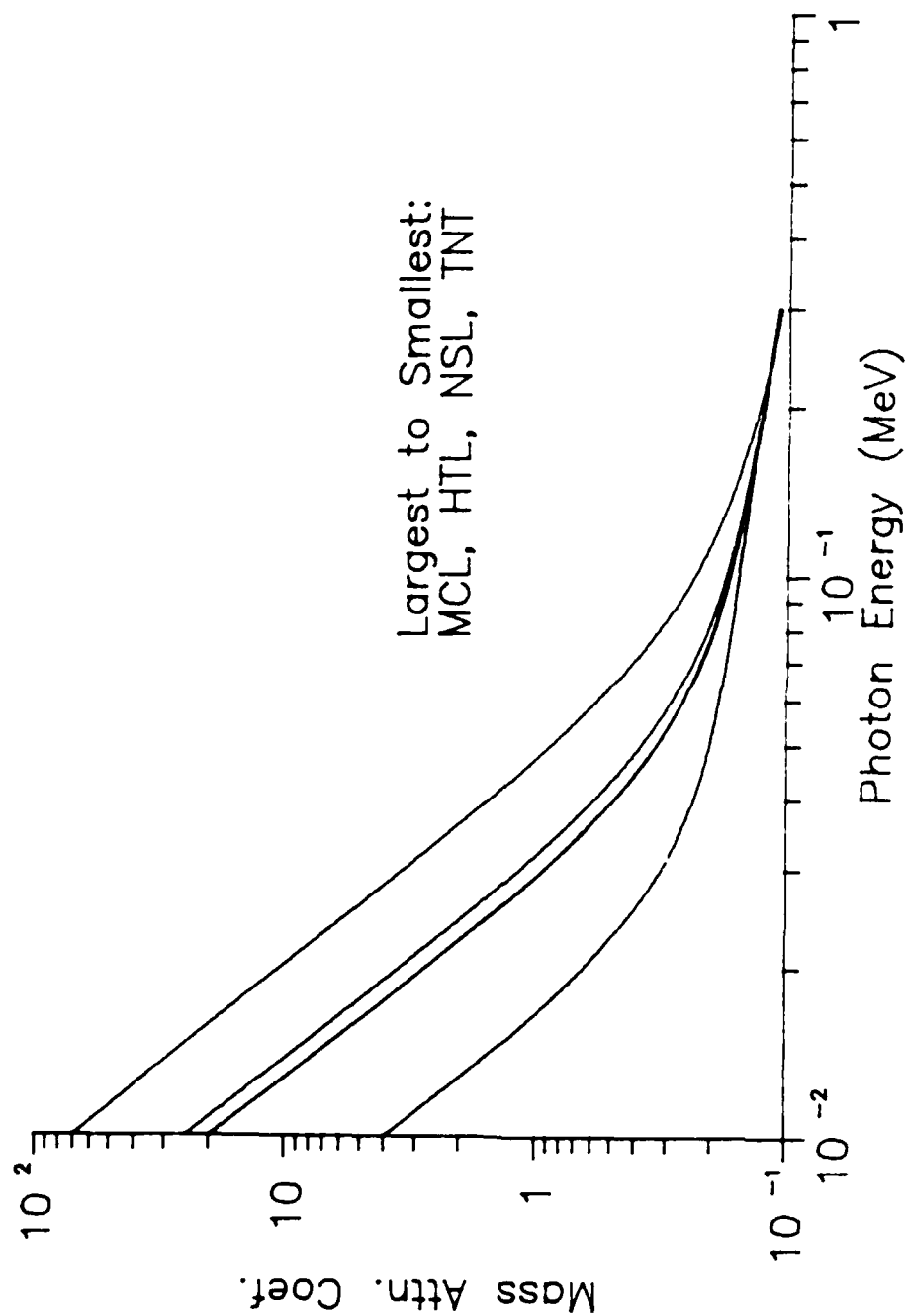


Figure III.6. Soil mass attenuation coefficients. The mass attenuation coefficients (cm^2/g) of the three soils used in the majority of the calculations, Malatula clay loam (MCL), Hagerstown loam (HTL), and Norfolk sandy loam (NSL) are displayed. The mass attenuation coefficients for trinitrotoluene (TNT), the explosive contained in most mines, are also shown for comparison.

TABLE III.4
 Characteristics of Common Warsaw Pact
 Nonmetallic Antitank Mines

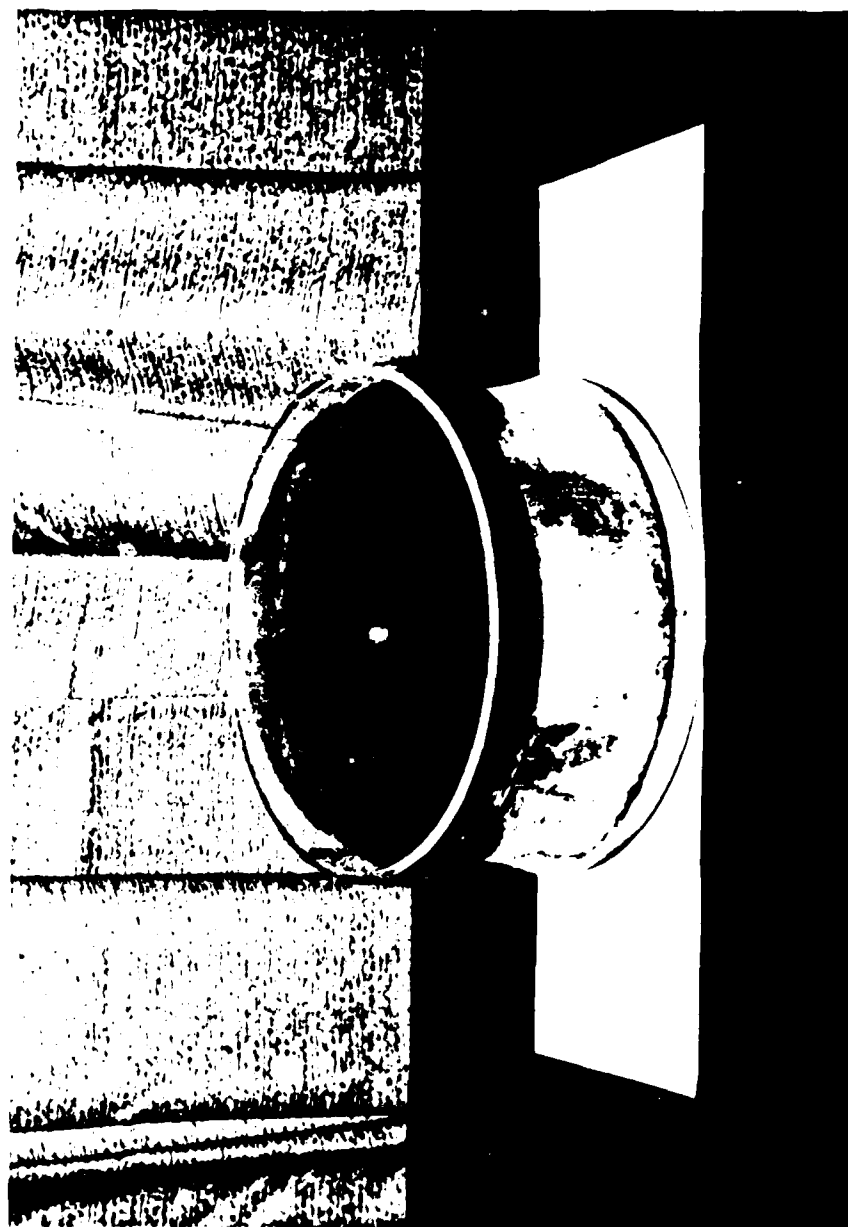
Mine	Country	Mass (kg)	Diameter (cm)	Height (cm)	Expl. Type	Expl. Mass (kg)
PM-60	GDR	11.3	32	12	TNT	8.6
TM-60	USSR	11.3	32	11.7	TNT	7.5
TMB-2	USSR	7.0	27.4	15.5	TNT or AMATOL	5.0
PT-Mi- Ba-III	CZECH	9.9	32.2	10.2	TNT	5.6
TST	N/A	10.3	30.2	variable	sucrose	7.5

Table adapted from U.S. Department of the Army, TRADOC Threat Monograph, Comparison of Selected NATO and Warsaw Pact Engineer Organizations and Equipment (U.S. Army Training and Doctrine Command, Fort Monroe, VA, 1979b), p. 88.

30.16 cm. The cylinder is 14.60 cm high and has two 0.635 cm thick covers for the top and bottom. An aluminum cylinder with 0.24 cm thick walls, outside diameter of 28.89 cm and height of 8.57 cm fits inside the lucite cylinder and holds the explosive substitute material. Only the top 7.50 cm of the aluminum cylinder is filled with explosive material. Its lower portion is separated from this material by a 0.24 cm thick base plate. The 0.83 cm high curtain below the aluminum base plate is drilled with three holes at 120 degree intervals. These holes align with five sets of three holes in the lucite cylinder and are used to allow variable setting of the air gap located between the top lucite cover and the explosive substitute material. The aluminum container of the model provides structural support for the heavy explosive substitute portion of the mine. Additionally, it served as the mold for the molten substitute material when it was prepared. Aluminum is very similar to soil in its photon scattering properties, and, as such, is an acceptable wall material for the backscatter radiation method of mine detection. Due to its metallic content, it would be an unacceptable model for many other detection methods. Figure III.7 shows the TST mine used in the measurements.

Since actual explosive materials present safety and administrative problems, a substitute material is required. Since TNT is the most commonly used explosive in landmine, it serves as the standard against which substitute materials

Figure III.7. TST mine used in measurements. The TST mine is designed to simulate nonmetallic antitank mines. The upper layer of the mine cylinder, whose thickness can be varied, contains air. The lower portion contains the explosive substitute material. A detailed description of the geometry and materials of the TST mine is provided in the text.



are compared. Previous studies made use of dinitrobenzene as a TNT substitute. Unfortunately, this material is toxic. Evaluation of a number of common nontoxic materials is made by comparing linear interaction coefficients with those of TNT. Sucrose is selected as the substitute. Table III.5 shows the comparison of the interaction coefficients of TNT and sucrose.

The explosive substitute is solidified KaroTM Light Corn Syrup. While this material is not sucrose, it has similar elemental composition and photon interaction characteristics. Upon heating, a portion of the fructose contained in the syrup is converted to sucrose. A number of test batches of the substitute are made by removing water from the syrup by heating. When the capability to consistently obtain the same material density (1.56 g/cm^3) is achieved, samples are used in the tests described below and found to be an acceptable substitute for TNT.

Materials Tests

Tests of photon interaction characteristics of the explosive substitute and soil materials are conducted to insure that the cross section sets used in the Monte Carlo photon transport calculations are adequate. As described above, the TNT substitute is solidified KaroTM Light Corn Syrup with a density of 1.56 g/cm^3 . The soil used in the experiments is obtained locally. Its high sand content suggests that it is similar to the Norfolk Sandy Loam (NSL) soil described above. Samples of each of these materials

TABLE III.5
 Ratios of the Linear Interaction
 Coefficients of Sucrose to TNT

Energy (MeV)	Interaction Coefficient Ratios ^a			Total
	Coherent	Incoherent	Photoelectric	
0.010	0.9379	1.0257	0.9505	0.9524
0.015	0.9346	1.0171	0.9520	0.9581
0.020	0.9336	1.0117	0.9528	0.9652
0.030	0.9335	1.0062	0.9540	0.9789
0.040	0.9334	1.0037	0.9545	0.9873
0.050	0.9334	1.0024	0.9547	0.9919
0.060	0.9334	1.0017	0.9559	0.9944
0.080	0.9334	1.0008	0.9548	0.9967
0.100	0.9335	1.0004	0.9571	0.9978
0.150	0.9333	1.0000	0.9571	0.9987
0.200	0.9338	0.9998	0.9572	0.9991
0.300	0.9338	0.9997	0.9572	0.9994
0.400	0.9339	0.9996	0.9572	0.9994
0.500	0.9339	0.9996	0.9583	0.9995
0.600	0.9339	0.9996	0.9586	0.9995
0.800	0.9340	0.9996	0.9581	0.9995
1.000	0.9339	0.9996	0.9583	0.9996

^aSucrose density: 1.588 g/cm³; TNT density: 1.654 g/cm³ (Weast, 1967). For the purpose of backscatter radiation effects, the two interaction coefficient ratios of the most importance in evaluating a substitute material are the incoherent and total coefficients. Coefficient data are from Hubbell et al. (1975) and Hubbell (1982).

are placed in the beams of various spectra produced by the GE Maxitron 300 X-Ray Therapy Unit. Before the materials tests are conducted, each of the four energy spectra utilized in the measurements is itself tested using exposure attenuation by added aluminum filtration as described in Chapter V. The conditions required for formal half value layer measurements are observed in these measurements and in the materials tests (Johns and Cunningham, 1983). The transmission of exposure rate is also calculated using the method described in Chapter V for NSL (three sets of data for NSL at different density and moisture contents) and TNT.

Seven thicknesses of the solidified KaroTM Light Corn Syrup are each subjected to the four spectra: 80, 100, 150, and 200 Kvp, each filtered by 4.75 mm of beryllium inherent filtration, 0.25 mm aluminum equivalent monitor chamber, 3.19 mm of aluminum added filtration, and an air path of 67.31 cm. Figure III.8 compares the measured exposure rate transmissions with those calculated. Perfect agreement would occur if the ratio for each sample of measurement to calculation is 1.00 or, in terms of the figure, if the plotted points lie on the line of slope equal to 1.00. Agreement is very good, and the explosive substitute is deemed adequate.

For each of the four beam energies listed above, three sets of five soil samples are prepared (60 samples in total). Multiple samples are used because of the variability in composition, density and moisture content characteristic

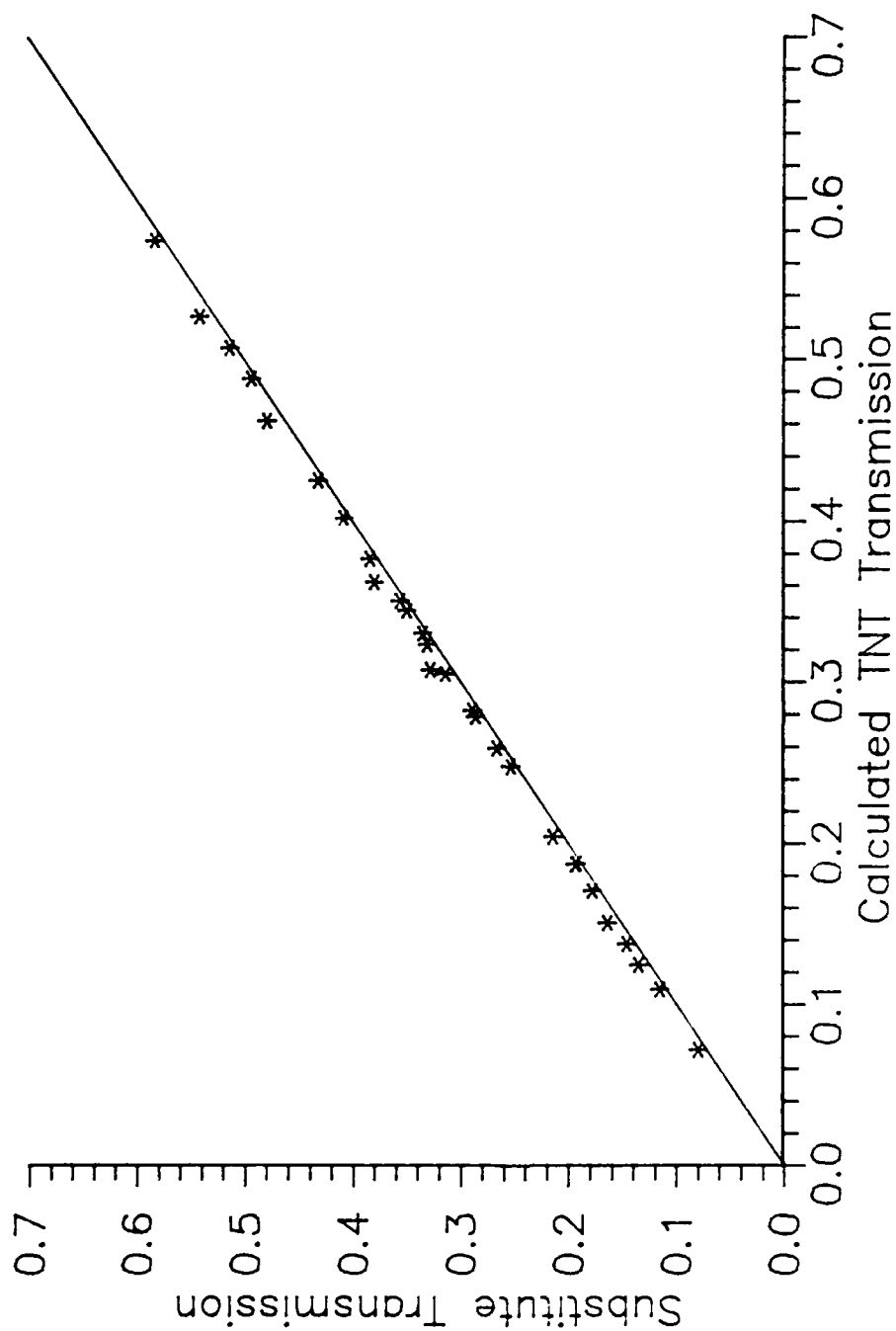


Figure III.8. Transmission comparison for TNT and substitute. A comparison of the measured transmission of exposure rates produced by samples of the explosive substitute material, and the calculated attenuation of exposure rates of TNT for the same thicknesses as the substitute samples is shown. Calculations were performed by the XRSPEC.PAS code (described in Chapter V).

of the soil. Two of the sets of samples differed only in density; the compacted set density is measured to be 1.579 g/cm^3 and the loose soil set, 1.450 g/cm^3 . Both have an average moisture content of 3.26%. The third set differs both in moisture content and density. It is prepared by heating the soil to remove all moisture. The density of this soil is 1.62 g/cm^3 . The increase in density with loss of water is a result of combustion of low density organic matter in the soil during heating. All samples are of the same thickness. Exposure transmission measurements and calculations are compared in Figure III.9. Agreement is very good, indicating that the local soil is, as suspected, close to NSL soil in its photon interaction properties.

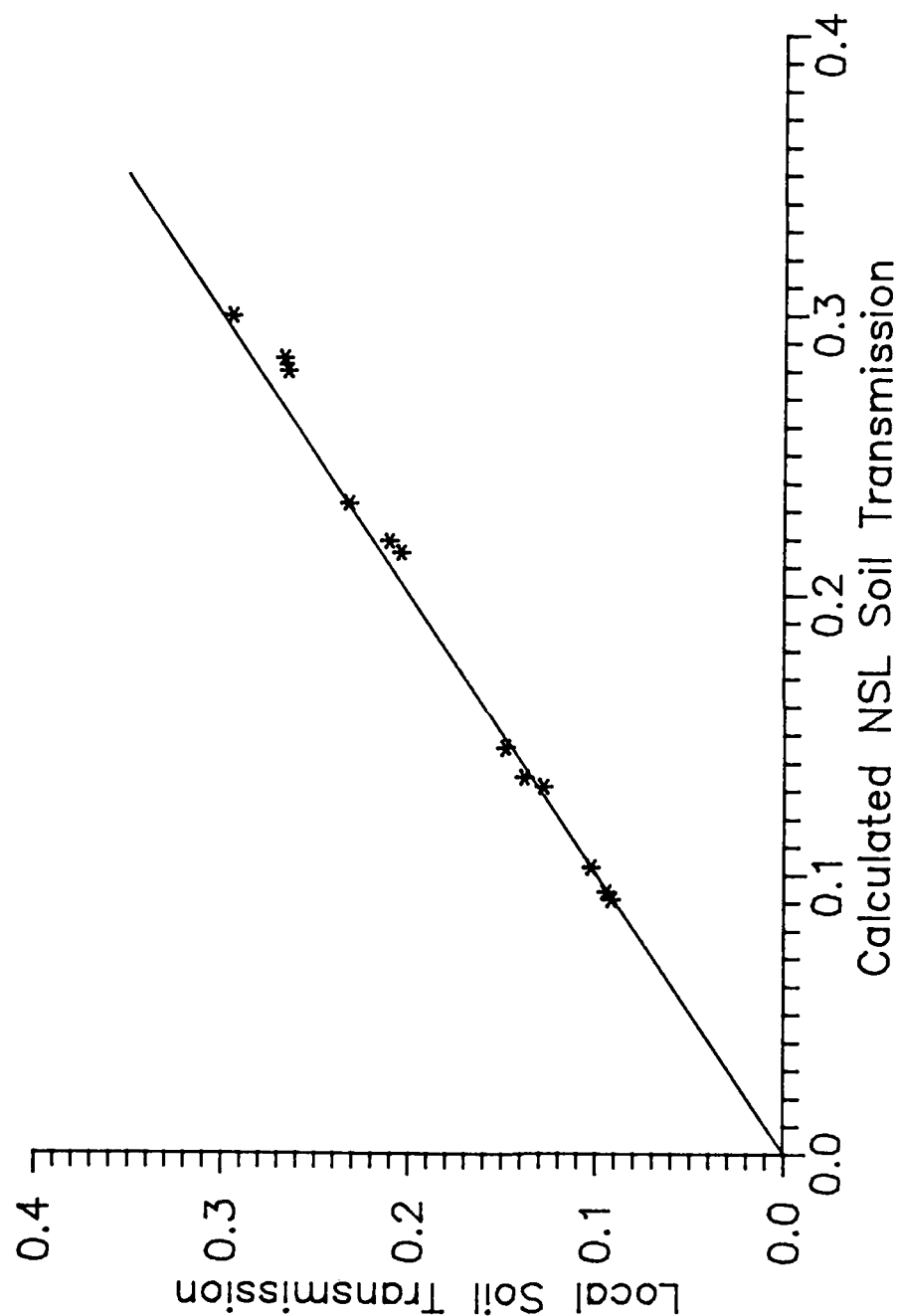


Figure III.9. Transmission comparison for NSL and local soil. A comparison of the measured transmission of exposure rates produced by sets of samples of the locally available soil, and the calculated attenuation of exposure rates of NSL soil for the same thicknesses as the local soil samples is shown. Calculations were performed by the XRSPEC.PAS code (described in Chapter V).

CHAPTER IV

RADIATION TRANSPORT

In the mine detection system, photons, originating from an x-ray source, travel through air, and strike the soil. The photons then undergo interactions with the soil and objects buried within it. Some photons are scattered back through the soil surface and strike the detector. This chapter describes the fundamental photon interactions of importance to the mine detection problem, the radiation transport models used to simulate those interactions, and their validation.

Photon Interactions

Photons interact with matter through a variety of mechanisms. The energy range of interest for mine detection and imaging (described in Chapter VII) results in only three photon interactions of importance: coherent scattering, incoherent scattering and the photoelectric effect. A brief description of each of these interaction types is provided.

Coherent Scattering

Thomson gave the first description of the interaction of an electromagnetic wave with a free electron (Jammer, 1966). Applying purely classical physics to the interaction, he showed that the time varying electric field

associated with the electromagnetic wave would cause the electron to oscillate with the same frequency as the field. The resulting accelerated charged particle would then radiate an electromagnetic wave of this same frequency. Since the frequency of the photon is unchanged, there is no change in photon energy as a result of the coherent scattering interaction. This elastic scattering process is known as Thomson scattering. The solid angle differential cross section (the probability of scatter into a unit solid angle per electron per unit fluence incident on the electron) for Thomson scattering is given by

$$\frac{d\sigma_T}{d\Omega} = \frac{r_e^2}{2} (1 + \cos^2 \theta_s) ,$$

where $\frac{d\sigma}{d\Omega}$ is the solid angle differential Thomson scattering cross section,
 r_e is the classical radius of the electron,
 θ_s is the scattering angle.

When the photon energy is such that its associated wavelength is comparable in size to the atoms in the material in which it scatters, the interaction can no longer be considered to be with a single free electron. The interaction is now collectively with all the electrons of an atom. These atomic electrons oscillate and radiate in phase. The process is called coherent or Rayleigh scattering. In this case the solid angle differential cross section becomes

$$\frac{d\sigma_{\text{coh}}}{d\Omega} = \frac{r_e^2}{2} (1 + \cos^2 \theta_s) F^2(x, Z) ,$$

where $\frac{d\sigma_{\text{coh}}}{d\Omega}$ is the solid angle differential coherent scattering cross section,

$F(x, Z)$ is the atomic form factor, which depends upon the atomic number, Z , of the material, and the momentum transfer variable, x , given by

$$x = \frac{\sin \frac{\theta_s}{2}}{\lambda} ,$$

where λ is the wavelength of the photon.

The integral of the solid angle differential coherent cross section gives the probability of coherent scattering per atom per unit incident fluence,

$$\sigma_{\text{coh}} = \pi r_e^2 \int_0^\pi (1 + \cos^2 \theta_s) \sin \theta_s F^2(x, Z) d\theta_s ,$$

where σ_{coh} is the total coherent scattering cross section per atom. Coherent scattering cross sections and atomic form factors are provided in tabular form for all elements by Hubbell et al. (1975). The square of the atomic form factor represents the probability that the electrons of an atom take up the recoil momentum of the interaction without absorbing any of the incident photon's energy. Figure IV.1 shows a graph of the atomic form factors of aluminum ($Z=13$)

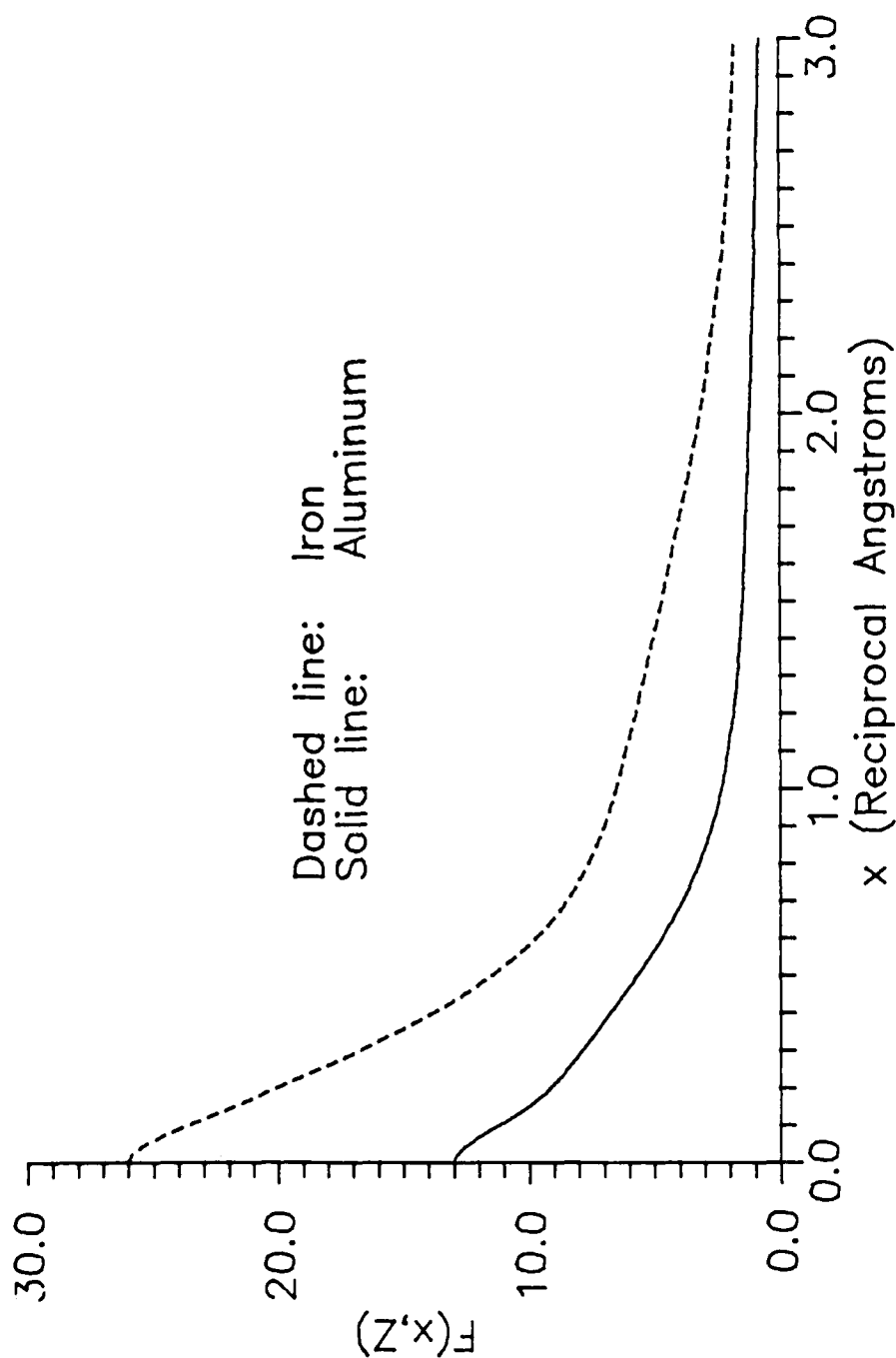


Figure IV.1. Atomic form factor versus momentum transfer variable. Atomic form factors for aluminum and iron are shown as a function of the momentum transfer variable. Data are from Hubbell et al. (1975).

and iron ($Z=26$) as a function of x . At large values of x , the atomic form factor and, hence, the probability of coherent interaction, is small. Large values of x correspond to small photon wavelengths or high photon energies. The higher the atomic number of the material, the larger the atomic form factor at a given energy and scattering angle. Hence, at a given energy, coherent scattering is more probable in high Z materials than in low Z materials. The effect of the atomic form factor term is to strongly peak the coherent scattered photons in the forward direction. This forward peaking is largest in low Z materials and at high energies. Figure IV.2 displays these effects. Because of the forward peaking and lack of change in energy, the typical coherently scattered photon closely resembles the incident photon, and many calculations ignore this interaction mechanism. In terms of the mine detection problem, coherent backscatter will be important only at relatively low energies, and will have a larger effect in the soils containing the highest portion of high Z elements. Figure IV.3 shows the coherent cross section of aluminum and iron as a function of photon energy.

It should be noted that atomic form factors are available only for individual atoms and a very few compounds. Since coherent scattering is a cooperative process involving all the electrons of an atom and the spatial distribution of the electron density about an atom in a molecule is altered relative to the free atom, the use of the available atomic

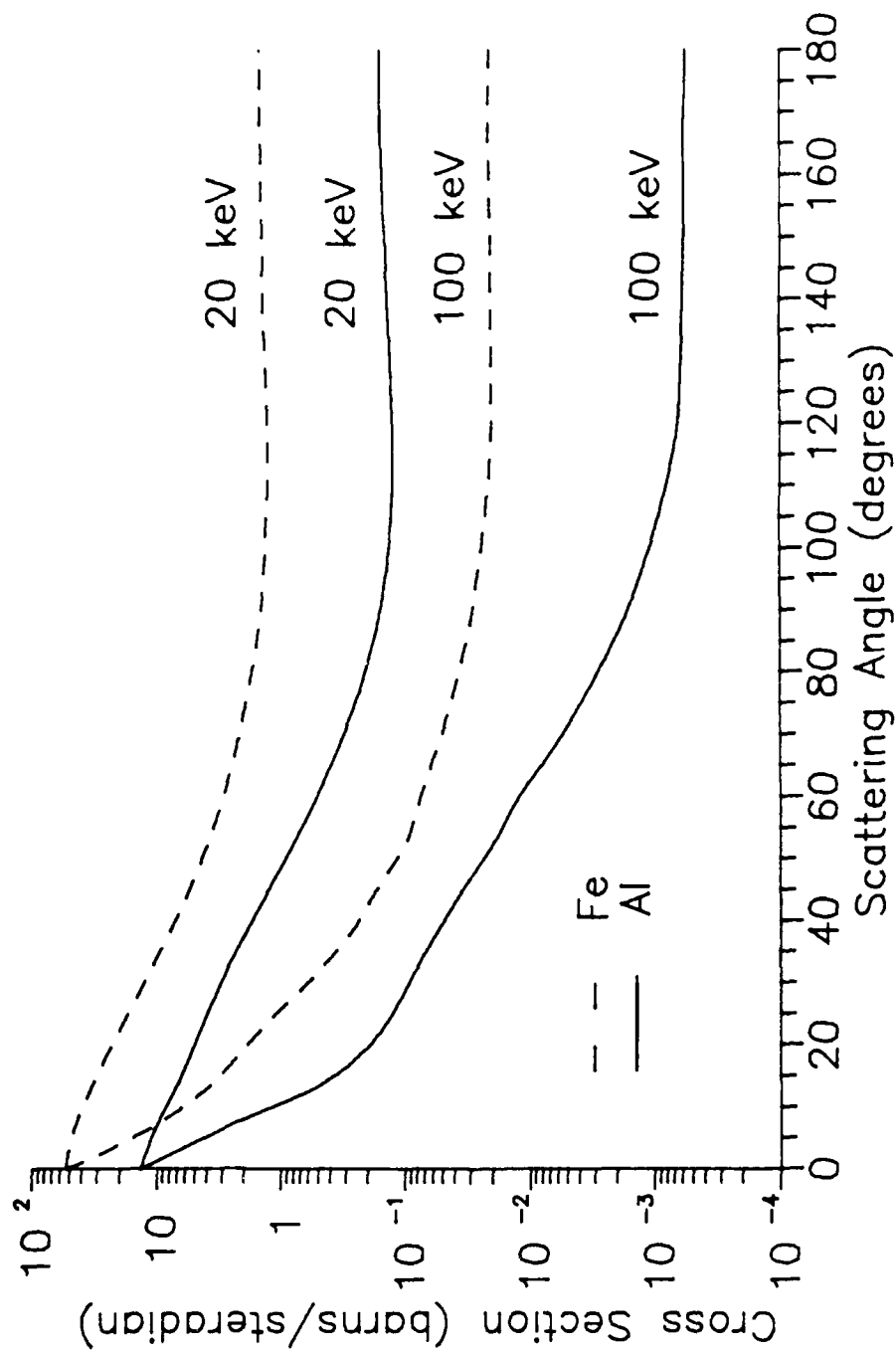


Figure IV.2. Solid angle differential coherent scattering cross section versus scattering angle. The graph shows that for a given material, coherent scattering is more forward peaked at higher energy, and for a given energy, coherent scattering in any direction is greatest in the material with the higher atomic number.

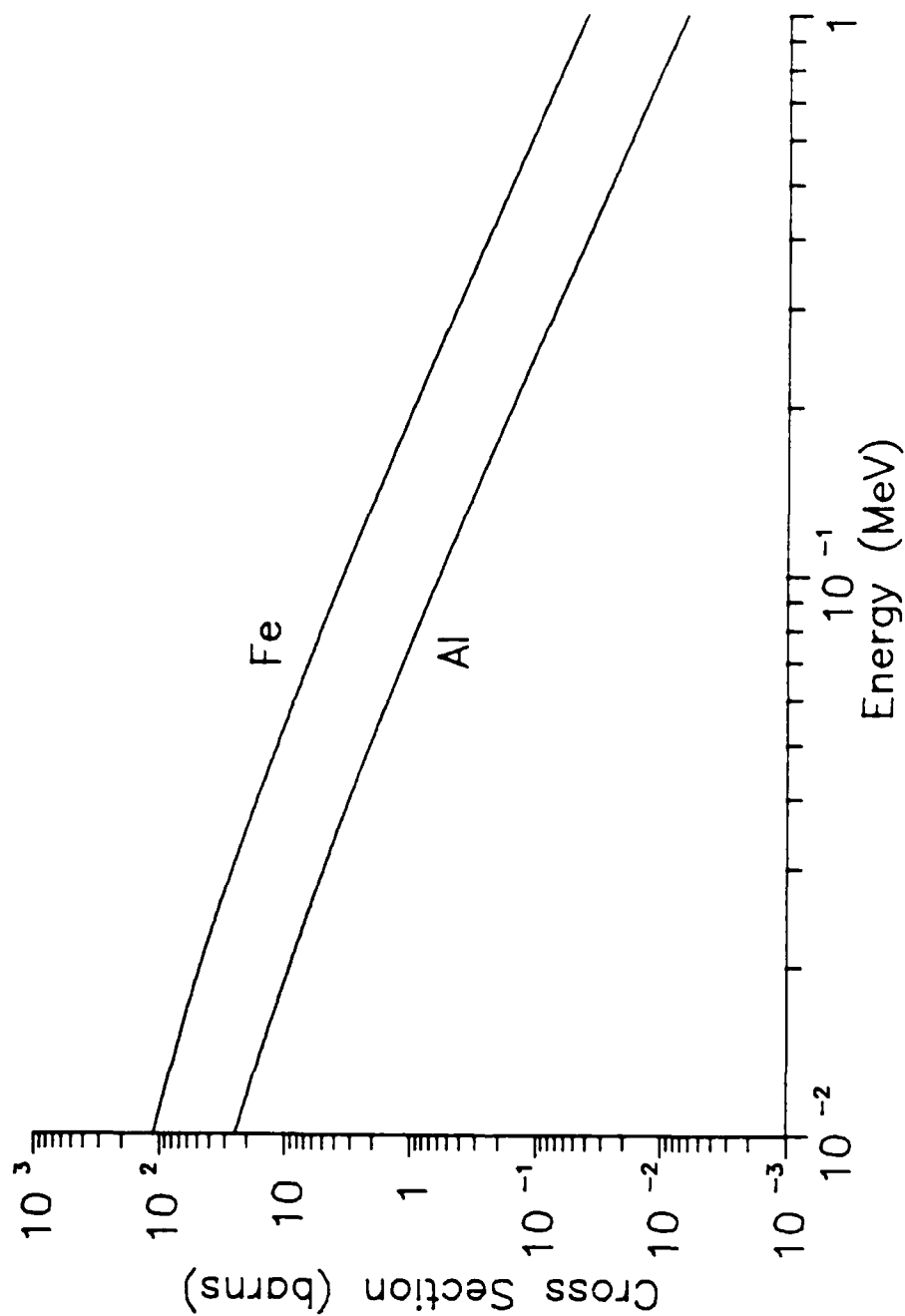


Figure IV.3. Coherent cross section versus photon energy. The coherent scattering cross section of aluminum and iron are shown. The material having the higher atomic number has the higher coherent scattering cross section at all energies. Data for the graph are from Hubbell et al. (1975).

form factors for compounds is only an approximation to physical reality.

Incoherent Scattering

Compton (1923) first described photon inelastic scattering from a free electron. In his model of this interaction, the photon strikes a free, stationary electron producing a new, lower energy, scattered photon and a recoil electron. This free electron case will be approximately correct if the energy of the incident photon is very large in comparison with the binding energy of the electron to its atom. Compton's formula for the dependence of the scattered photon's energy on the energy of the incident photon and the scattering angle is

$$E' = \frac{E}{1 + \alpha(1 - \cos\theta_s)} ,$$

where E' is the energy of the scattered photon,

E is the energy of the incident photon,

θ_s is the scattering angle, and

$\alpha = E/m_e c^2$, where $m_e c^2$ is the rest mass energy of the electron (0.511 MeV).

This relationship plays a very important role in the mine detection problem. Figure IV.4 shows the fractional energy (E'/E) in a Compton interaction as a function of incident photon energy for several scattering angles. The fractional loss is greatest at high energies, and at a fixed energy, for large scattering angles (backscattering). Since

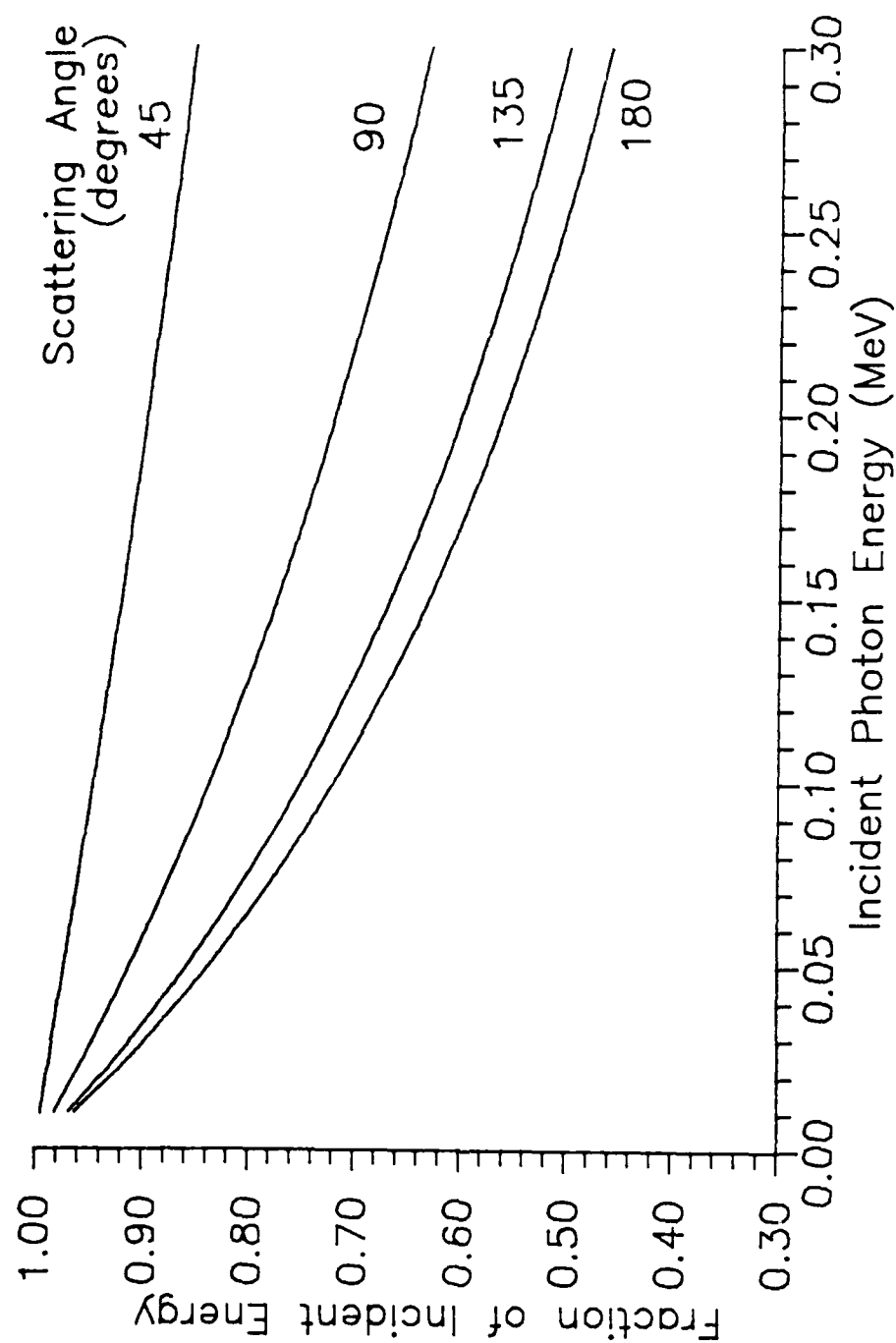


Figure IV.4. Fractional energy of Compton scattered photons versus incident photon energy. The graph shows that the fraction of energy retained by the scattered photon is greatest for small scattering angles, and for low incident photon energies.

high photon energies are required for deep penetration, these two factors combine to make backscatter from significant depths in the soil difficult.

The Klein-Nishina formula (Evans, 1955) gives the solid angle differential scattering cross section for the inelastic scattering of an unpolarized photon from a free electron,

$$\frac{d\sigma_{KN}}{d\Omega} = \frac{r_e^2}{2} \left\{ \frac{1 + \cos^2 \theta_s}{[1 + \alpha(1 - \cos \theta_s)]^2} + \frac{\alpha^2 (1 - \cos \theta_s)^2}{[1 + \alpha(1 - \cos \theta_s)]^3} \right\} .$$

In this equation $\frac{d\sigma_{KN}}{d\Omega}$ is the solid angle differential Klein-Nishina cross section per electron. Figure IV.5 shows the differential Klein-Nishina cross section as a function of scattering angle for three energies. At low energies forward scatter and backscatter are approximately equally probable. As energy increases, scattering becomes more forward peaked. This fact increases the difficulty of the backscatter detection of mines. The use of higher energy photons, which are capable of penetrating to great depths in soil, will eventually lead to a lower backscattered signal due to this forward peaking and the two factors discussed above with respect to Compton's energy/angle relation.

In reality, photons are bound, and there are threshold energies at which the incident photon energy is equal to the binding energy of the electron.

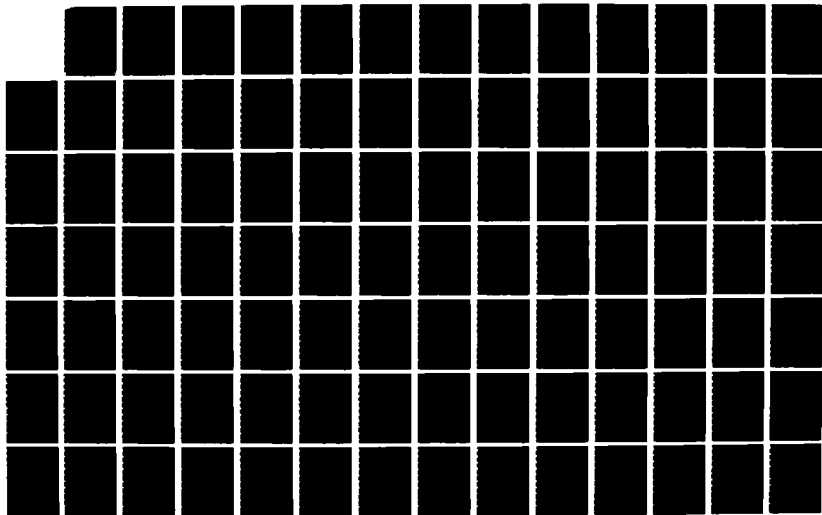
AD-A182 227

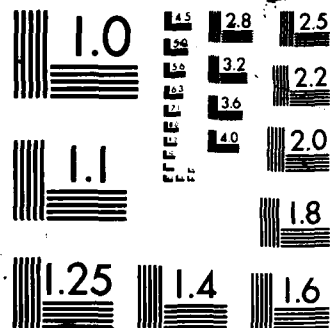
LANDMINE DETECTION BY SCATTER RADIATION RADIOGRAPHY(U)
ARMY MILITARY PERSONNEL CENTER ALEXANDRIA VA
J G CAMPBELL 82 JUL 87

2/6

UNCLASSIFIED

F/G 15/6 6 NL





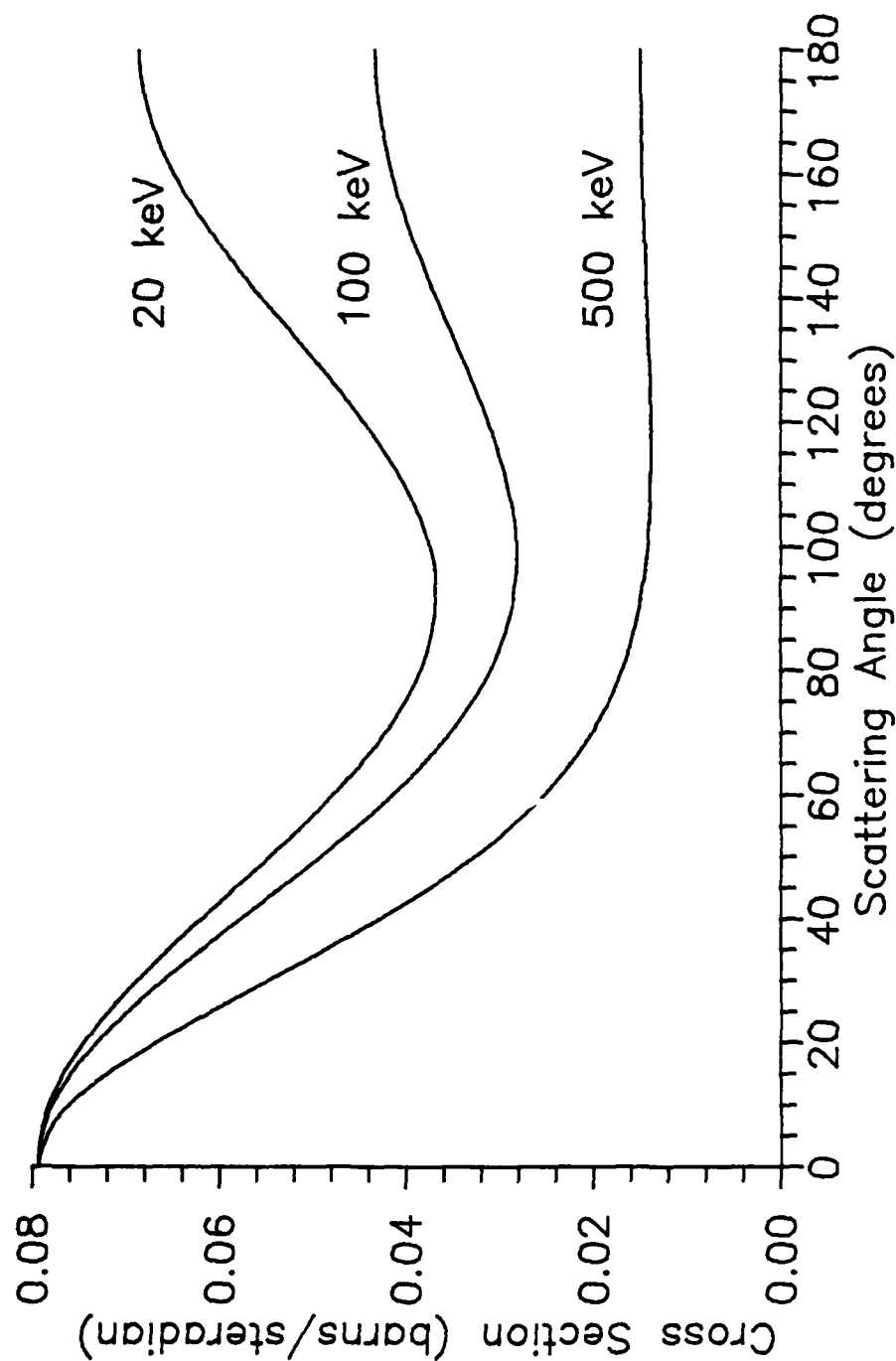


Figure IV.5. Solid angle differential Klein-Nishina cross section versus scattering angle. The variation of the cross section with scattering angle is shown for three incident photon energies. As the incident energy increases, backscattering becomes less probable.

large compared to the atomic binding energy are not correctly accounted for by the Klein-Nishina formula. The Klein-Nishina formula is corrected by multiplication by the incoherent scattering function, $S(x,Z)$,

$$\frac{d\sigma_{inc}}{d\Omega} = \frac{d\sigma_{KN}}{d\Omega} S(x,Z) ,$$

where $\frac{d\sigma_{inc}}{d\Omega}$ is the solid angle differential incoherent scattering cross section.

The incoherent scattering function represents the probability that an atomic electron struck by a photon will absorb energy and be excited or removed from the atom. Figure IV.6 shows the incoherent scattering function for aluminum and iron as a function of the momentum transfer variable. The function has the effect of decreasing the Klein-Nishina cross section (per electron) with the reduction being greatest at low energies and in high Z materials. Figure IV.7 displays these effects. The incoherent scattering cross section is given by the integral over solid angle of the differential cross section

$$\sigma_{inc} = \int_0^{2\pi} \int_0^{\pi} \frac{d\sigma_{KN}}{d\Omega} S(x,Z) \sin\theta_s d\theta_s d\phi ,$$

where σ_{inc} is the total incoherent scattering cross section per atom.

Tabulated values of the incoherent scattering cross section are provided by Hubbell et al. (1975). Figure IV.8

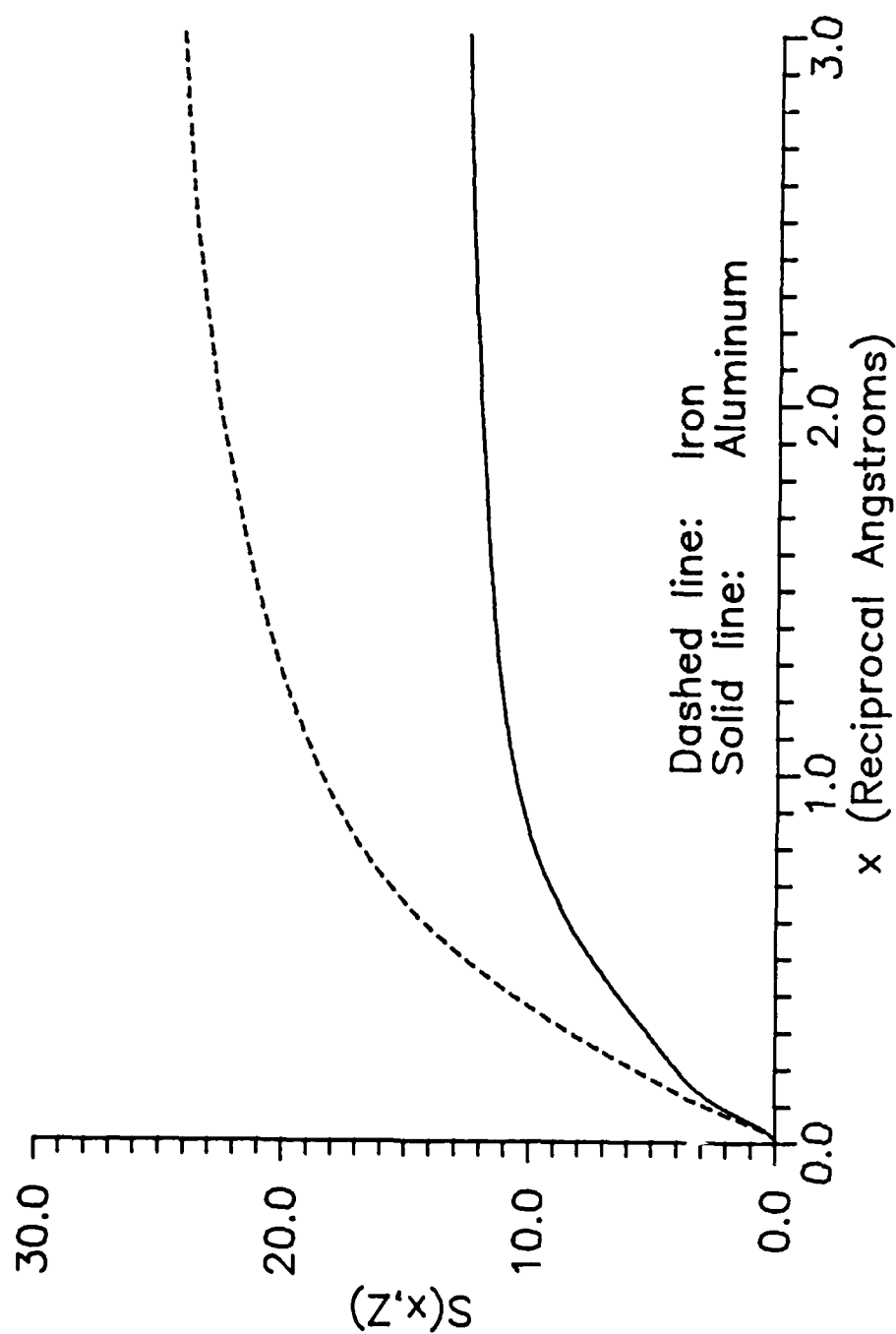


Figure IV.6. Incoherent scattering function versus momentum transfer variable. To account for incoherent scattering from bound electrons, the Klein-Nishina cross section is multiplied by the incoherent scattering function. Data are from Hubbell et al. (1975).

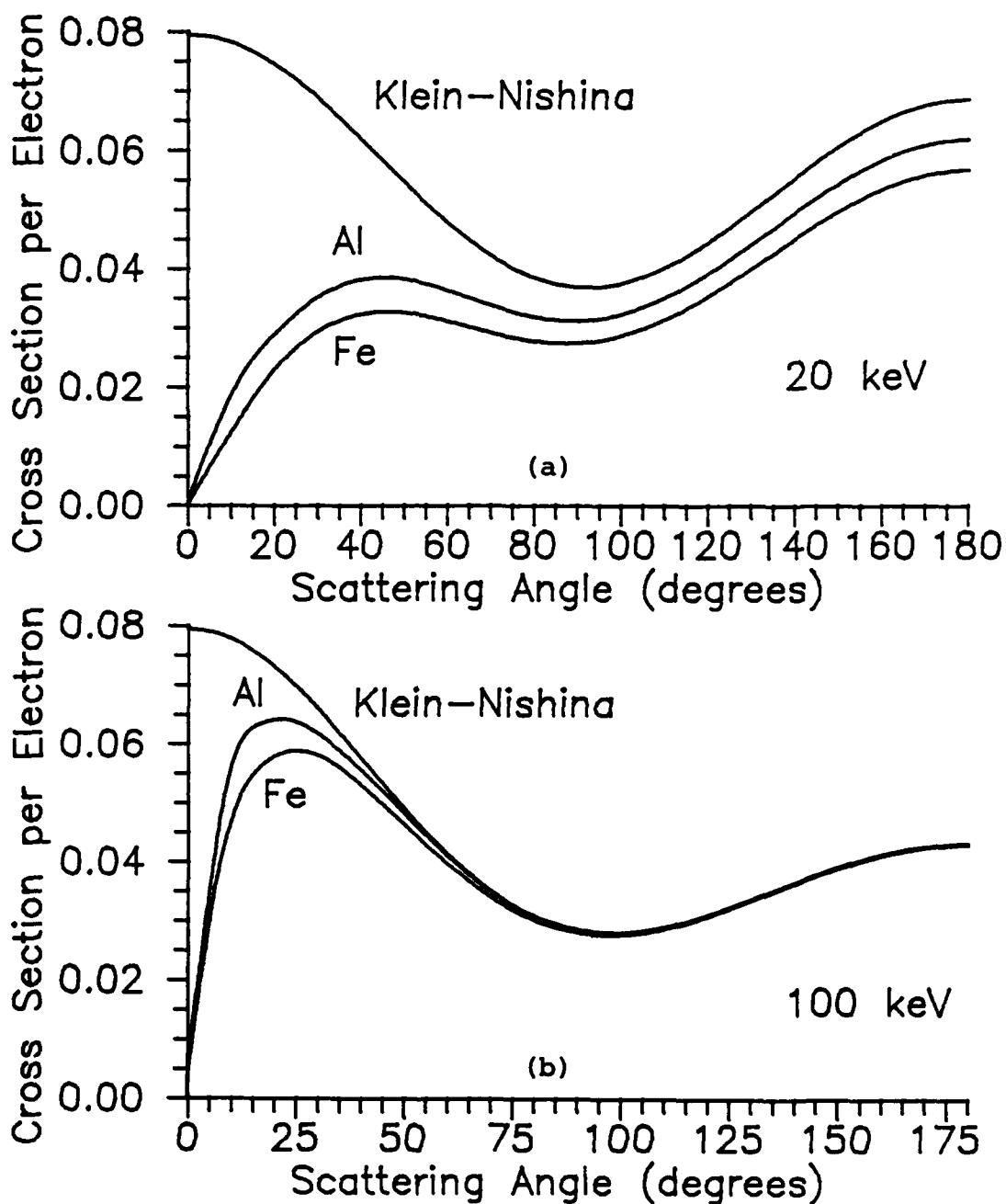


Figure IV.7. Comparison of the solid angle differential Klein-Nishina and incoherent scattering cross sections. The solid angle differential Klein-Nishina and incoherent scattering cross sections per electron (in units of barns per steradian per electron) of aluminum and iron are compared at 20 keV (a) and 100 keV (b).

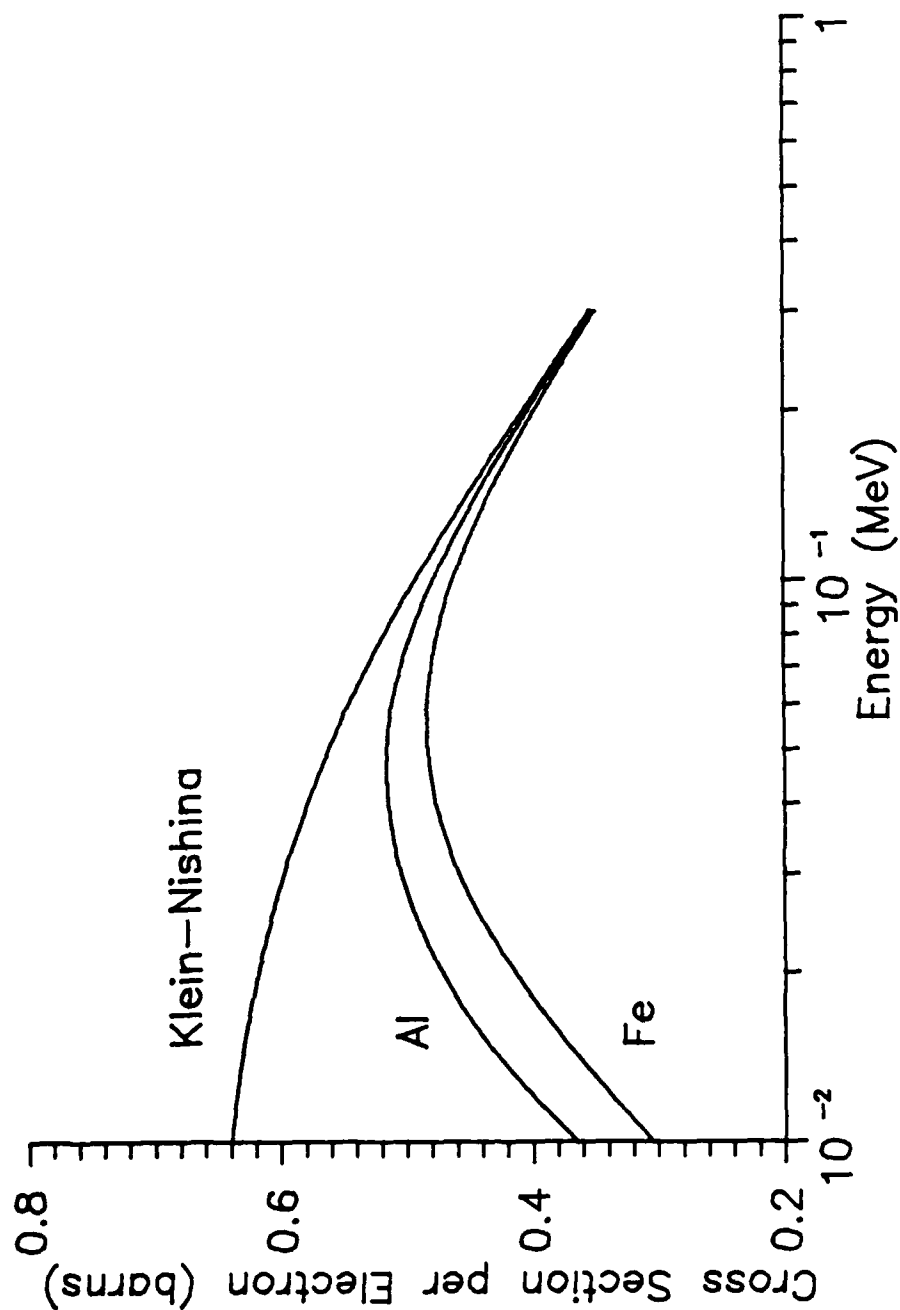


Figure IV.8 Incoherent scattering cross section versus photon energy. The incoherent scattering cross section per electron of aluminum and iron are compared to the Klein-Nishina cross section. The reduction from the Klein-Nishina cross section is greatest at low energy and in the material with the higher atomic number. Data are from Hubbell et al. (1975).

shows the incoherent scattering cross section per electron of aluminum and iron, and that calculated from the integral of the unmodified Klein-Nishina formula. The Klein-Nishina cross section overestimates the true incoherent cross section at low energy. The error in the Klein-Nishina cross section is larger in high Z materials. Because the effect of the incoherent scattering function is important only at low energies, it is often neglected in calculations. The same caveat described in the discussion of the atomic form factor, regarding atomic and molecular electron density configurations, applies to the incoherent scattering function.

Photoelectric Effect

In the photoelectric effect, an incident photon strikes an atomic electron and is completely absorbed. The electron is emitted from the atom with kinetic energy equal to the difference in the incident photon energy and the binding energy of the electron to the atom. If the interaction is with an inner shell electron, the vacancy remaining after the interaction will be filled, either producing a fluorescent emission photon(s) or Auger electrons. In the energy region of interest to the mine detection problem, the cross section per atom for the photoelectric interaction varies approximately as

$$Z^n/E^3$$

where n varies between 4.0 and 5.0 depending on photon energy (Anderson, 1984). This approximation indicates the

photoelectric cross section will be large at low energies and in high atomic number materials. Figure IV.9 shows the variation of the photoelectric cross section of iodine ($Z=53$), gadolinium ($Z=64$) and lead ($Z=82$) as a function of photon energy (each of these materials plays a role in this research). Superimposed on the variation with atomic number and energy, discussed above, are edges. These sharp discontinuities in the cross sections are the result of the discrete binding energies of electrons in their atomic shells. Below an edge energy, the incident photon does not possess sufficient energy to overcome the binding energy of the electrons in a particular shell. As photon energy increases to just above the edge energy, this is no longer the case and the cross section increases dramatically as a result of the capability to remove the newly available electrons. As a result of these edges, a lower atomic number material may have a higher cross section for the photoelectric interaction in an energy range below the edge energy of a higher atomic number material.

Figure IV.10 shows the probability of K shell fluorescent emission following the filling of a vacancy in the inner atomic shell. In low atomic number materials, this probability is small; the alternate radiationless emission of Auger electrons dominates (Evans, 1955). Since soil and explosive materials contain generally low atomic number elements, fluorescent emission from these materials is not very probable. Even in those few instances in which

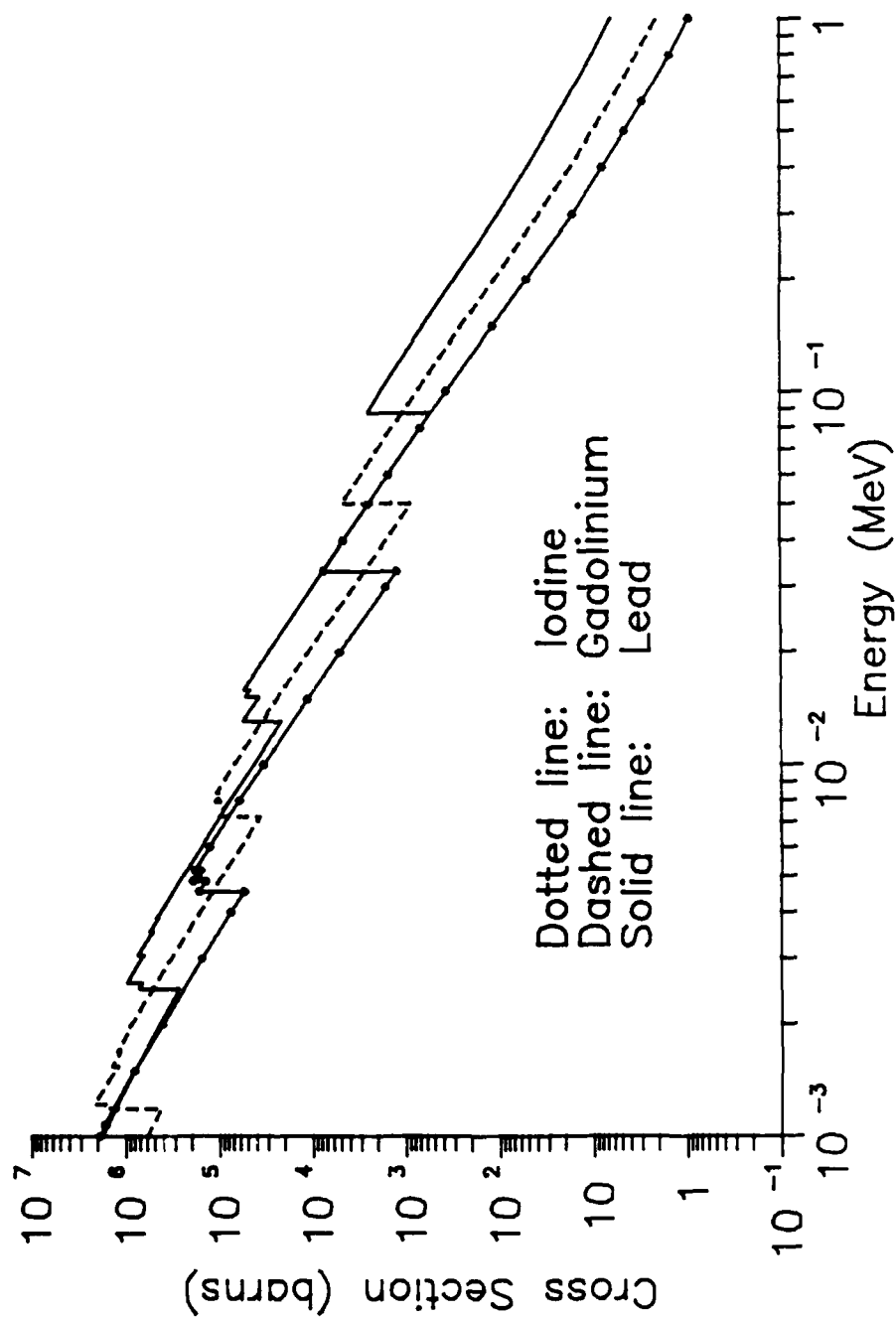


Figure IV.9. Photoelectric interaction cross section versus photon energy. The photoelectric interaction cross sections of iodine, gadolinium and lead are shown. K, L and M edges of gadolinium and lead, and K and L edges of iodine occur within the energy range of the graph. Data are from Storm and Israel (1970).

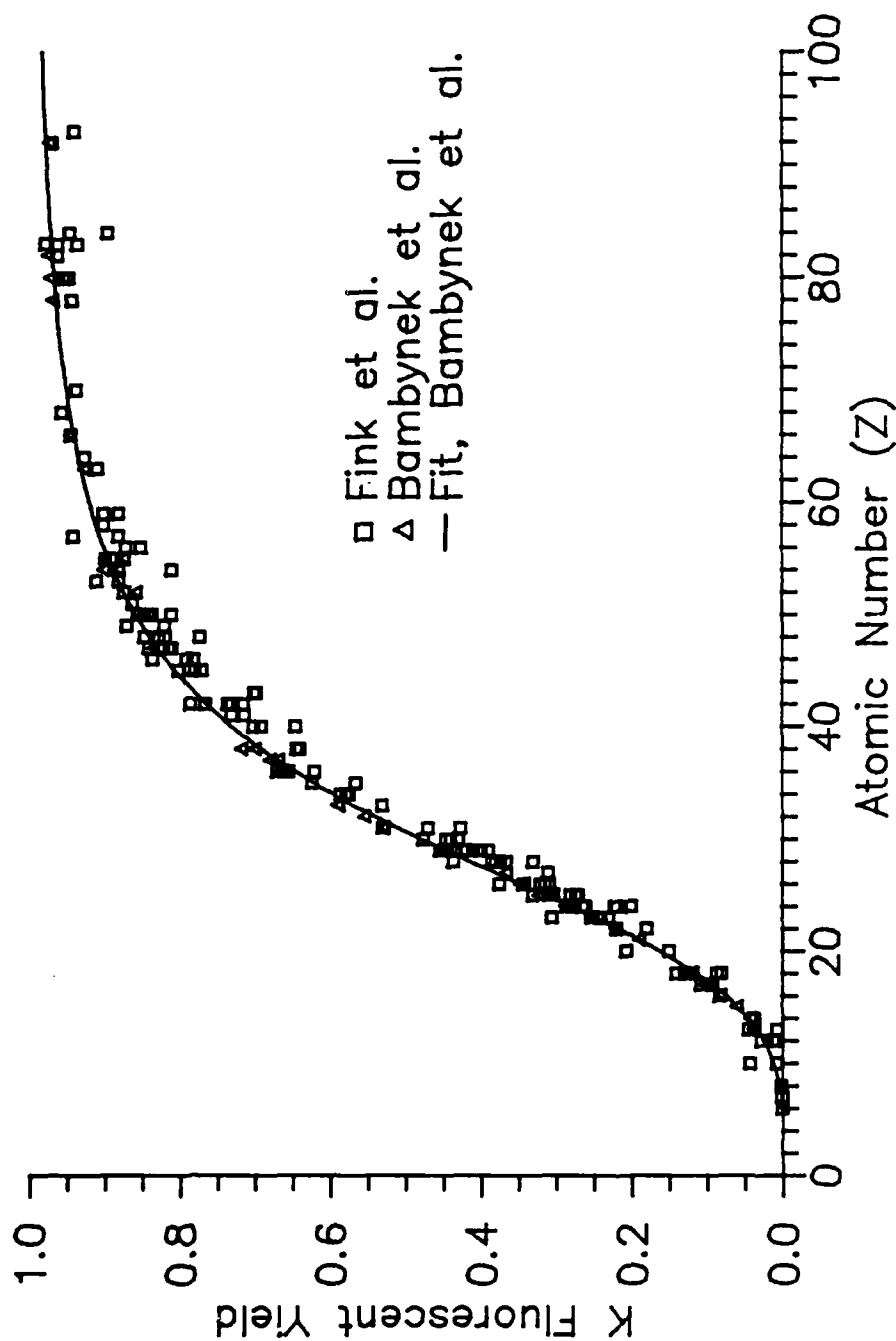


Figure IV.10. Probability of K shell fluorescence versus atomic number. Data for this graph are taken from reviews of measurements of the K fluorescent yield by Fink et al. (1966) and Bambynek et al. (1972). The solid line is an empirical fit to the data Bambynek et al. consider most reliable.

fluorescent emission does occur, the emitted photons will be very low in energy due to the small binding energy of K shell electrons in low Z materials. Figure IV.11 shows this effect. These very low energy photons will be rapidly absorbed near their point of origin and produce a negligible contribution to the backscattered fluence. In materials such as those of Figure IV.9, fluorescent emission plays an important role and cannot be neglected. These materials are associated with the detection of the scattered photons and are discussed in Chapter VI and Appendix E. Emission of fluorescent photons is isotropic.

Mass Interaction Coefficients

The interaction cross sections described above are converted into mass interaction coefficients for use in the transport models. For compounds and mixtures, the cross section data from Hubbell et al. (1975) and elemental weight fractions are used to construct the mass interaction coefficients. In cases where edge effects are important, the photoelectric data of Storm and Israel (1970) are also used. These sets of mass interaction data are then expanded by cubic spline interpolation into fine energy mesh tables for use in the models. In cases where edge effects are important, the cubic spline interpolations are performed separately above and below the edges and then merged. The mass interaction coefficient tables cover an energy range from 1 keV to 1 MeV. The mesh structure used is given in

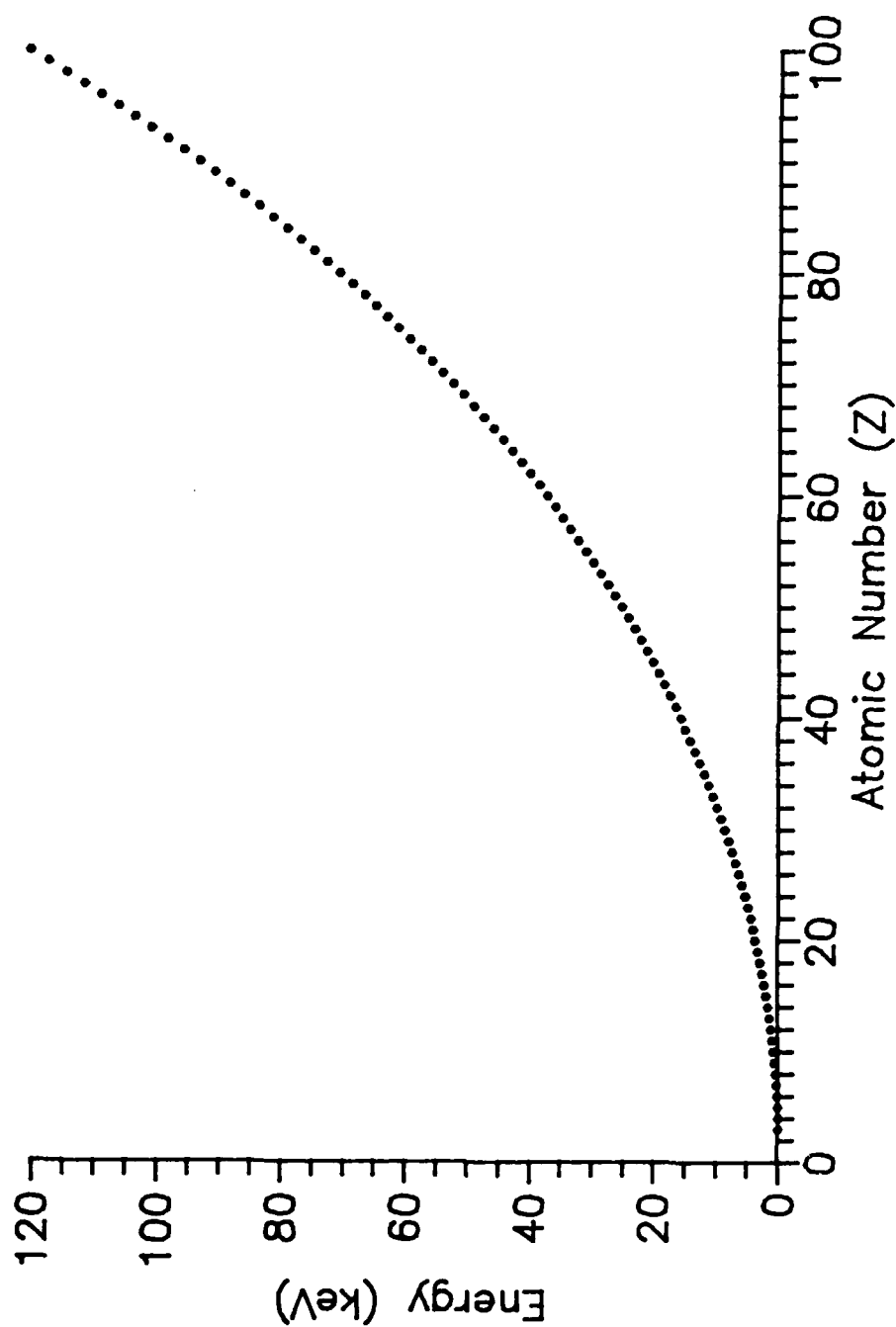


Figure IV.11. Energies of K_{α} fluorescent photons versus atomic number. The K_{α} x ray is the most probable fluorescent photon to be emitted. Data are from Storm and Israel (1970).

Table IV.1. Supplementing this structure are table entries for energies just above and just below edges.

Figure IV.12 shows the mass interaction coefficients of aluminum as a function of photon energy. The energy ranges of dominance of the interactions are dependent on the atomic number of the absorber. The photoelectric effect dominates at low energies; incoherent scattering, at higher energies. In no case does coherent scattering dominate. Table IV.2 gives the approximate energy at which the photoelectric and incoherent mass interaction coefficients are equal for materials of interest to the mine detection problem.

Single Scatter Model

A single scatter photon transport computer code, SGLMIN.PAS, written in Turbo Pascal (Borland, 1985) provides a simple introduction to the variables associated with the mine detection problem. While multiple scatter plays a very important role, this simple model has been used to provide insights into many aspects of the mine detection problem.

Computation Scheme

The code computes the single scattered fluence to an array of detector positions located above and parallel to the soil surface. The parameters which can be varied in calculations are energy of the incident photon beam, angle of incidence of the beam, height of the detector plane above the soil, soil type and density, depth of burial of the mine, and the beam/soil/mine intercept position. For each position in the array in the detector plane, the code

TABLE IV.1

Energy Mesh Structure for
Mass Interaction Coefficients

Energy Range (MeV)	Energy Increment (MeV)
0.001 to 0.050	0.001
0.050 to 0.300	0.005
0.300 to 1.000	0.010

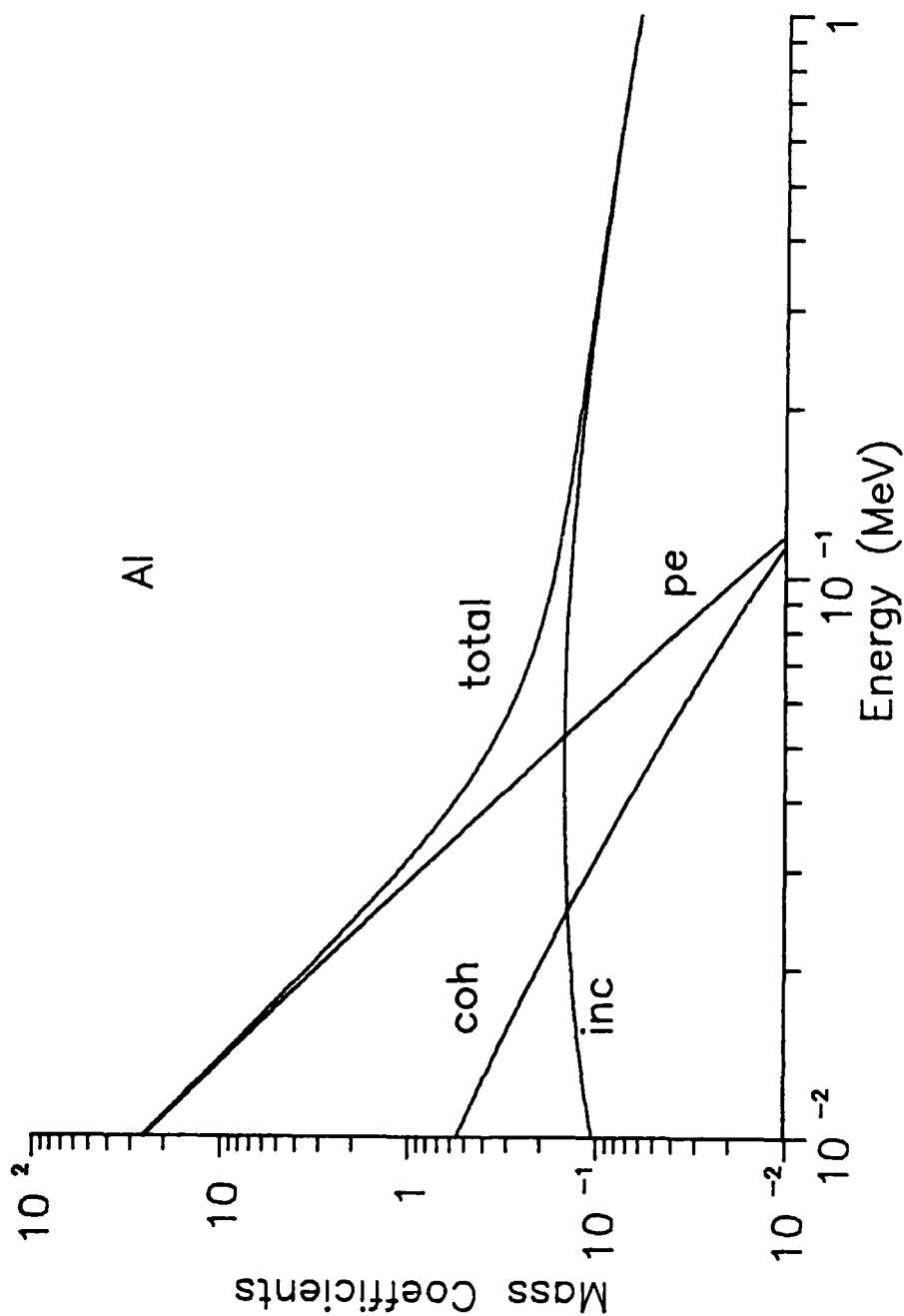


Figure IV.12. Mass interaction coefficients of aluminum versus photon energy. Mass interaction coefficients (in units of cm^2/g) for coherent scattering (coh), incoherent scattering (inc), and photoelectric interaction (pe) of aluminum are shown. The sum of these coefficients is the mass scatter coefficient total).

TABLE IV.2

Energy at Which Photoelectric
and Incoherent Scattering Mass Interaction
Coefficients Are Equal

Material	Effective Z	Energy (MeV)
Wood	6.525	0.025
Sucrose	6.704	0.026
TNT	6.919	0.026
Air	7.374	0.029
Quartz	10.805	0.046
NSL soil	10.905	0.048
HTL soil	11.381	0.053
Concrete	11.576	0.055
GAD soil	11.912	0.055
Aluminum	13.000	0.052
MCL soil	15.856	0.080
Iron	26.000	0.115
Sodium iodide	46.558	0.260
Lead	82.000	0.550

computes the fluence per incident photon. This quantity is obtained by calculating a series of probabilities. These probabilities are of survival while passing through air from the source to the soil plane, of survival while passing through soil or mine to a scattering point, of undergoing an incoherent scattering interaction in a small incremental volume about a scattering point, of scattering into an incremental solid angle about a point in the detector array, of survival while passing from the scattering point through the soil or mine towards a point in the detector plane, and of survival while passing through air from the soil plane to a point in the detector plane. The product of these probabilities gives the desired fluence per incident photon at a single point in the detector plane from a single incremental scattering volume. The summation of such results from increments along the photon's path to a depth where the incremental response is negligible gives the total single scattered fluence per incident photon at a single point in the detector array. This process is carried out for all points in the detector array. Typically, the array consists of 421 points at a 10 cm increment within a 200 cm by 200 cm detector plane. A geometry routine calculates the distances along the photon path through the various materials encountered. A full three dimensional representation of the TST mine with air and explosive layers is included in the geometry routine. Output of results of calculations is

optionally to the computer terminal screen, hardcopy, disk file and three-dimensional graphical display.

Interaction Modelling

The code uses the fine energy mesh mass interaction coefficient data described previously in this chapter. Log-log interpolation is used to determine values of the coefficients at energies not provided within the fine mesh tables. Coherent scattering is not included in the model. Incoherent scattering includes modification of the Klein-Nishina distribution by the incoherent scattering function. Contributions due to fluorescent emission from soils or mine following photoelectric interactions are neglected based upon their low probability of occurrence in low Z materials, and the very low energies (and, therefore, high attenuation) characteristic of such photons when an infrequent emission occurs. For example, the probability of K fluorescent emission following a photoelectric interaction of a photon, whose energy exceeds the K edge energy, with an aluminum atom in soil is less than 2%. If a fluorescent photon were produced (part of the less than 2%), its energy would be 1.486 keV (Storm and Israel, 1970) and would have a mean free path of about 2×10^{-4} cm in soil.

Monte Carlo Model

The majority of the calculations supporting this research have been made with Monte Carlo computer codes. Two versions of the radiation transport code have been used. MCPHOT.PAS is written in Turbo Pascal (Borland, 1985) for

use on personal computers. MCPHOT.P is written in Green Hills Pascal (Green Hills, 1984) for use with the Definicon DSI-32 coprocessor (Marshall et al., 1985) which provides increased speed of calculation. Appendix G provides additional information about this device. The two codes are essentially identical in most respects, although calculations of angular spectra are included in the MCPHOT.P code to support computations for collimated detectors.

The Monte Carlo transport codes follow the histories of monoenergetic photons from their source to the detector plane. The detector response function, described in detail in Chapter VI, which is also the result of a Monte Carlo calculation, couples directly to the energies and angles of incidence of the photons striking the detector plane. The results of the calculation of the x-ray spectrum, described in Chapter V, are used to weight the monoenergetic Monte Carlo transport calculations to account for polychromatic sources. This technique allows the monoenergetic calculations to be used with any x-ray source spectrum, producing a considerable reduction in computation time from the alternative of sampling of a spectrum within the transport calculation.

Appendix H provides details for the techniques used to sample the more complex probability density functions encountered in the Monte Carlo code. Also included in this appendix are details concerning the random number generators used in the Monte Carlo codes and the technique for applying the monoenergetic source results to polychromatic sources.

Problem Parameters and Data

Each of the Monte Carlo codes begins with the input of problem data. These inputs are the photon interaction data of air, soil and explosive, material densities, mine geometry, and problem parameters. The photon interaction data are the mass interaction coefficient files for coherent scattering, incoherent scattering and the photoelectric effect, the atomic form factors, incoherent scattering functions and an integral used for sampling the coherent scattering distribution (described in Appendix H). The mass interaction data are read from files constructed using the fine energy mesh described previously. The atomic form factors and incoherent scattering functions are read from files constructed in the same 45 value format as the tables which appear in Hubbell et al. (1975). The integral associated with coherent scattering is also read from files arranged in a 45 value format. Interactive input provides the parameters for the particular problem. The parameters available are initial photon energy, angle of incidence, source height, beam geometry, soil type, height and extent of detector plane, mine type, explosive type, depth of burial of mine, beam/soil/mine intercept position, and number of photon histories to be followed. Three beam geometries are allowed: parallel beam, diverging circular beam and diverging rectangular beam.

Random Number Generators

The Monte Carlo codes are prolific users of random numbers uniformly distributed on an interval between 0 and 1. For example, tests at 150 keV with the TST mine at 1.5 cm depth of burial in HTL soil showed that an average of 80 random number calls were made per photon. Since calculations employing 200,000 photons are not unusual, it is apparent that the period of the random number generator used should be long. Random number generators are not actually random; all follow fixed rules for producing a sequence of numbers with a cycle length characteristic of the technique used. The period of the generator refers to how many random numbers can be generated before the sequence repeats. Problems with short periods of random number generators employed on personal computers are common (Whitney, 1984; Wichmann and Hill, 1987). In the interest of speed of computation, multiplicative and linear congruential random number generators are used. Implementations of these types of random number generators, which use integer arithmetic, are efficient and fast, but subject to machine dependent period constraints. The general form of these generators is

$$I_{j+1} = [aI_j + c] \text{ mod } m ,$$

where m is the modulus, a is the multiplier and c is the increment. The modulus operator (mod) requires division of the bracketed quantity by m and retention of the remainder.

To obtain a random number between 0 and 1, the result of the above operation is divided by $m + 1$. In a multiplicative congruential generator, c is equal to zero. Unless care is taken to avoid improper selection of the values of the constants, seriously flawed generators can be produced (Press et al., 1986). The constants used in the random number generators (detailed in Appendix H) in the MCPHOT.PAS and MCPHOT.P codes are well established and recommended.

The Compaq Deskpro (Compaq, 1984a) used for the MCPHOT.PAS calculations is based upon the Intel 8086 computer chip. The 16 bit words of this machine allow only 65,535 distinct integer values. Employment of a linear congruential method on such a machine results in a maximum period of the same size, provided optimum values of a , c , and m are chosen. This is clearly unacceptable for the problem at hand. The method selected for use in the MCPHOT.PAS code is a multiplicative congruential form, which uses real numbers, suggested by Cheney and Kincaid (1980). An 8087 math coprocessor (8087-2 for the Compaq Deskpro) and the 8087 supported version of Turbo Pascal must be employed with this method to obtain 16 digit real precision (Borland, 1985) required by the algorithm. The maximum period of this generator is on the order of one billion (2^{30}) random numbers (Cheney and Kincaid, 1980). The penalty paid for this long period is reduced speed due to real number arithmetic (Norton, 1986). The Definicon DSI-32 coprocessor used with the MCPHOT.P code is based upon the National Semiconductor 32032 computer chip

(Definicon Systems, 1986). This machine allows for more than four billion distinct integers ($2^{32}-1$), and makes the use of fast, integer based random number generators with long periods possible. The algorithm selected is a linear congruential method suggested by Dyck et al. (1984). The maximum period of this generator is approximately one-half billion (Forsythe et al., 1977).

Computation Scheme

Based upon selection of a particular beam geometry and angle of incidence, photons are individually started from the source position. Random numbers are used to determine the position, and in the case of diverging beams, the direction of the photon within the beam. Each photon begins its history with the initial energy assigned in the input, a weight of 1.00, and series of integer codes which indicate that it has not yet been involved in a scattering event, that it is initially traveling in air, and that it is not at any of the material boundaries of the problem.

Based upon the photon's position and direction of travel, the distance to the next material boundary is computed. In the case of the photon just emitted from the source, this first boundary is the soil, but thereafter any of seven boundaries are possible. Figure IV.13 shows the boundaries and material indices used in the calculation. A series of geometry routines determine which of the boundaries the photon will intercept if it continues on its path

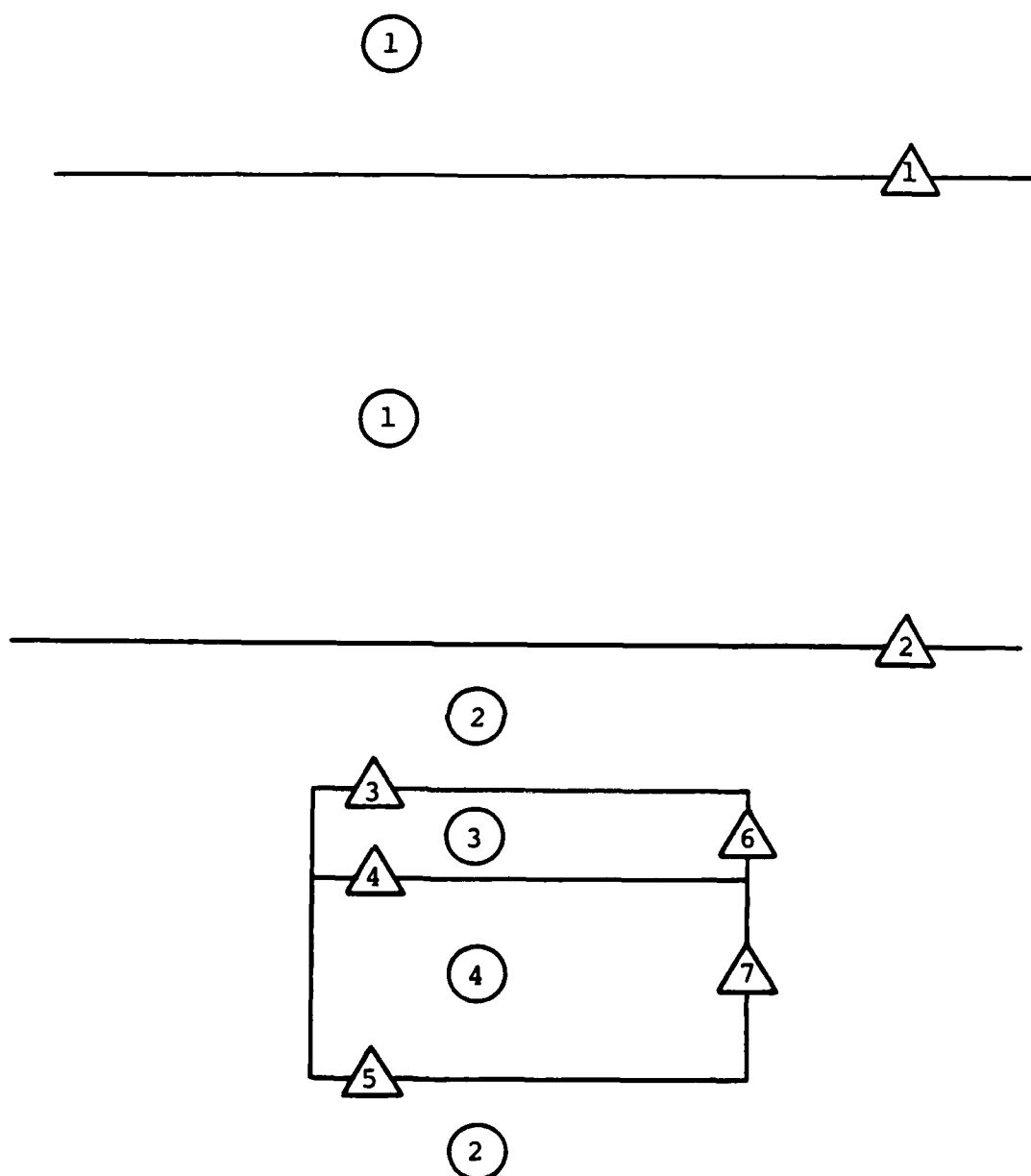


Figure IV.13. Boundaries and materials of Monte Carlo calculations. Triangles indicate boundaries; circles, materials. The boundaries are the detector plane (1), the soil surface (2), the top of the mine (3), the air-explosive interface in the mine (4), the bottom of the mine (5), the cylinder wall in the air region of the mine (6), and the cylinder wall in the explosive region of the mine (7). The materials are air above the soil (1), soil (2), air within the mine (3), and explosive (4). The detector plane boundary exists only for photons travelling upward, away from the soil plane.

without interaction, and then, which of those boundaries is closest and its distance.

Based upon the material in which the photon is traveling, a calculation of the distance to interaction is made. While the distance any single photon travels before interacting is not predictable, the distribution of the distances for a large number of photons is

$$p(x) = \mu \exp(-\mu x),$$

where $p(x)$ is the probability density function describing the distribution of distances travelled to an interaction,

μ is the linear attenuation coefficient for the material in which the photon travels at the photon's energy,

x is the distance to first interaction.

This distance distribution is sampled using random numbers by the relationship

$$x = -(1.0/\mu) \ln(rn),$$

where rn is a random number uniformly distributed between 0 and 1. The linear attenuation coefficient is obtained by summing the mass interaction coefficients at the photon energy for the appropriate material and then multiplying by the material density.

The distances to the next boundary and to interaction are then compared. If the boundary distance is smaller, the photon is placed at the boundary and allowed to continue in

the same direction of travel in the new material. A routine in the code determines the new material index by examining the position and direction of travel of the photon. This is true unless the boundary is that of the detector plane. In this case the photon is scored. A number of pieces of information are extracted during the scoring process. They include the weight and energy of the photon, the detector response produced by the photon, the number of scattering events the photon has undergone, the position in the detector plane of the photon intercept, and the angle of incidence of the photon on the detector plane.

If the interaction distance is smaller, the position of interaction is calculated, and the type of interaction is determined. Because photoelectric effect interactions cannot contribute to the scattered fluence at the detector, and fluorescent emission is not important, a weighting technique is used to force all photons to scatter, greatly increasing the efficiency of the calculation. The weighting factor applied at each scattering event is given by

$$\frac{\mu_{\text{coh}} + \mu_{\text{inc}}}{\mu} ,$$

where each of the interaction coefficients is found by table look-up at the photon energy in the material of the interaction. This weighting factor represents the probability that the interaction is a scattering event and is, therefore, a number less than one. Since incoherent scattering events lower the energy of the resulting photon and

since the cross section for the photoelectric effect becomes larger as energy decreases, the weighting factor decreases with each incoherent scattering interaction. The type of interaction is forced by this weighting procedure to either be a coherent or incoherent scattering event. The type of interaction is determined by finding the ratio,

$$\frac{\mu_{\text{coh}}}{\mu - \mu_{\text{pe}}} ,$$

and comparing it to a random number. In this ratio, μ_{pe} is the linear photoelectric interaction coefficient. This ratio is the probability that the scattering event is coherent. If the random number is less than the ratio, the interaction is a coherent scattering event; otherwise, it is an incoherent scattering event.

Modeling Scattering Interactions

If the interaction is determined to be a coherent scattering event, the probability density function,

$$p(\Omega) = \frac{\frac{d\sigma_{\text{coh}}}{d\Omega}}{\sigma_{\text{coh}}} ,$$

must be sampled to determine the direction of the scattered photon. Conventional rejection techniques are inefficient for sampling this distribution (Williamson, 1983a). The technique used is a combination of inversion and rejection sampling (Carter and Cashwell, 1977; Williamson and Morin, 1983a). It is described in detail in Appendix H.

If the interaction is determined to be an incoherent scattering event, a rejection method described by Carter and Cashwell (1977) is used to sample the direction of scatter. The probability density function to be sampled is given by the ratio of the differential incoherent scattering cross section to the total incoherent scattering cross section,

$$p(\Omega) = \frac{\frac{d\sigma_{inc}}{d\Omega}}{\sigma_{inc}} \quad .$$

As described in Appendix H, this technique requires that the Klein-Nishina distribution be sampled for scattering direction as a first step in the method. The Kahn method (Kahn, 1956) for performing this sampling is selected based upon efficiency and calculation speed comparisons by Bloomquist and Gelbard (1983).

Regardless of the type of scattering event which occurs, the routines in the codes return a scattering angle (in terms of the cosine of the scattering angle) with respect to the initial direction of the photon. The energy of a coherently scattered photon is unchanged; that of an incoherently scattered photon is altered by the Compton energy/scattering angle relationship. The scattering angle specifies the polar angle with respect to the initial photon direction. The azimuthal angle is uniformly distributed and is sampled by selecting a random number and multiplying by 2π . Given these two angles, the direction cosines with respect to the initial photon direction are defined. A

routine in the Monte Carlo codes then uses the precollision direction cosines and the scatter direction cosines with respect to the initial direction to calculate the new direction cosines with respect to the coordinate system of the problem. An algorithm given by Carter and Cashwell (1977) is used for this purpose.

Russian Roulette

Before allowing a scattered photon to recycle through the scheme described, the photon is examined to determine if Russian roulette should be played. The criteria for subjecting the photon to Russian roulette are that the photon be located well outside or below the mine and be moving away from the mine, or that the photon be at least 1 cm below the soil surface and have an energy of 20 keV or less, or that the photon has a weight of 0.05 or less. The Russian roulette method used in the code selects a random number and compares it to 0.5. If the random number is less than 0.5, the photon's weight is increased by a factor of two, and it is allowed to travel to the next boundary or interaction. If the random number is greater than 0.5, the photon is terminated and a new photon is started. The Russian roulette routine is used to save computation time from being applied to photons which are not likely to contribute significantly to the backscattered fluence.

Code Output

Code output is to terminal screen, printer, and diskette files. The hardcopy output includes a recapitulation

of the problem parameters, summary statistics, energy spectrum of the backscattered fluence, and angular spectral information to support calculations for collimated detector geometries (MCPHOT.P only). The diskette file output is the spatial distribution of the backscattered fluence and detector response.

Validation of the Monte Carlo Codes

The MCPHOT.PAS and MCPHOT.P codes include detailed consideration of coherent and incoherent scattering because of the importance of low energy photons to the backscatter mine detection problem. Published literature on backscatter effects is rarely concerned with the low energy regime of interest in this research. When such results at low energy are published, these detailed effects are ignored. In order to allow comparison with published results, the more sophisticated coherent and incoherent scattering routines must be replaced by routines which neglect coherent scatter entirely and use the Klein-Nishina distribution for incoherent scatter. Two separate comparisons are made with published results. One is made at the simplified level; a second, with the fully developed scattering routines employed. This dual comparison also provides information on the range of applicability of the simplified approach. The fully developed scattering routines are validated separately from the Monte Carlo transport codes, and by comparison with a general purpose, mainframe computer code.

Number and Energy Albedo Calculations

Number and energy albedos are the fractions of the number and energy of source photons which are reflected from a surface. Berger and Raso (1960) and Raso (1963) provide results of Monte Carlo calculations for number and energy albedos. Table IV.3 compares the results of their calculations for iron with those of the MCPHOT.PAS code without the full coherent and incoherent scattering routines. Tables IV.4 and IV.5 compare the same published data for concrete (Chilton et al., 1984) with those of the MCPHOT.PAS code, both with and without the fully developed scattering routines. As is apparent from the tables, comparisons are excellent for the simplified codes. Figure IV.14 compares the number albedo calculations for concrete by the MCPHOT.PAS code with and without the fully developed scattering routines. The differences are significant only at low energies.

Energy Spectra Comparisons

Minato (1973) provides energy spectra of the back-scattered fluence from aluminum and iron at several energies. Figures IV.15 through IV.17 show comparisons of Minato's spectra with calculations by the MCPHOT.PAS code. Agreement is very good.

Comparison with Buried Mine Calculations

Coleman (1971) provides results of Monte Carlo calculations at three energies for buried mines. The mine model used in these calculations is a right circular cylinder with a radius of 11.43 cm and a thickness of 8.636 cm (Coleman,

TABLE IV.3
Comparisons of Number and Energy
Albedo Calculations for Iron

Perpendicular Incidence		
Energy (MeV)	Number Albedo	
	Berger and Raso (1960)	Simple ^a MCPHOT.PAS
0.10	0.042 ± 0.003	0.042 ± 0.002
0.20	0.106 ± 0.004	0.105 ± 0.003
0.50	0.149 ± 0.005	0.146 ± 0.004
1.00	0.141 ± 0.005	0.135 ± 0.003
Energy (MeV)	Energy Albedo	
	Berger and Raso (1960)	Simple ^a MCPHOT.PAS
0.10	0.032 ± 0.004	0.032 ± 0.003
0.20	0.063 ± 0.005	0.062 ± 0.004
0.50	0.054 ± 0.004	0.053 ± 0.003
1.00	0.031 ± 0.002	0.030 ± 0.002

^aSee text for description.

TABLE IV.4
Comparisons of Number
Albedo Calculations for Concrete

Perpendicular Incidence				
Energy (MeV)	Number Albedo			
	Berger and Raso (1960)	Raso (1963)	Simple ^a MCPHOT.PAS	Full ^a MCPHOT.PAS
0.01	-	-	0.0018 ±0.0002	0.0039 ±0.0003
0.015	-	-	0.0047 ±0.0004	0.0074 ±0.0005
0.020	0.008 ±0.002	-	0.0084 ±0.0003	0.0119 ±0.0004
0.03	-	-	0.0225 ±0.0015	0.0285 ±0.0015
0.04	-	-	0.0457 ±0.0013	0.0529 ±0.0012
0.05	0.076 ±0.004	-	0.0761 ±0.0011	0.0808 ±0.0012
0.07	-	-	0.1386 ±0.0024	0.1419 ±0.0025
0.10	0.213 ±0.006	-	0.2098 ±0.0022	0.2243 ±0.0034
0.15	-	-	0.2647 ±0.0010	0.2638 ±0.0032
0.20	0.285 ±0.006	0.285 ±0.006	0.2873 ±0.0026	0.2891 ±0.0032
0.25	-	-	0.2901 ±0.0032	0.2992 ±0.0046
0.50	0.268 ±0.006	0.275 ±0.006	0.2810 ±0.0040	-
1.00	0.221 ±0.006	0.207 ±0.006	0.2140 ±0.0040	-

^aSee text for description.

TABLE IV.5
Comparisons of Energy
Albedo Calculations for Concrete

Perpendicular Incidence				
Energy (MeV)	Energy Albedo			
	Berger and Raso (1960)	Raso (1963)	Simple ^a MCPHOT.PAS	Full ^a MCPHOT.PAS
0.01	-	-	0.0018 ±0.0004	0.0038 ±0.0006
0.015	-	-	0.0045 ±0.0008	0.0072 ±0.0010
0.02	0.008 ±0.004	-	0.0078 ±0.0006	0.0113 ±0.0007
0.03	-	-	0.0204 ±0.0027	0.0261 ±0.0019
0.04	-	-	0.0403 ±0.0023	0.0469 ±0.0025
0.05	0.065 ±0.006	-	0.0650 ±0.0018	0.0692 ±0.0021
0.07	-	-	0.1105 ±0.0039	0.1133 ±0.0040
0.10	0.153 ±0.008	-	0.1515 ±0.0031	0.1630 ±0.0050
0.15	-	-	0.1640 ±0.0013	0.1633 ±0.0032
0.20	0.154 ±0.007	-	0.1556 ±0.0028	0.1564 ±0.0022
0.25	-	-	0.1406 ±0.0031	0.1429 ±0.0044
0.50	0.085 ±0.004	0.087 ±0.004	0.0880 ±0.0030	-
1.00	0.041 ±0.002	0.038 ±0.002	0.0410 ±0.0020	-

^aSee text for description.

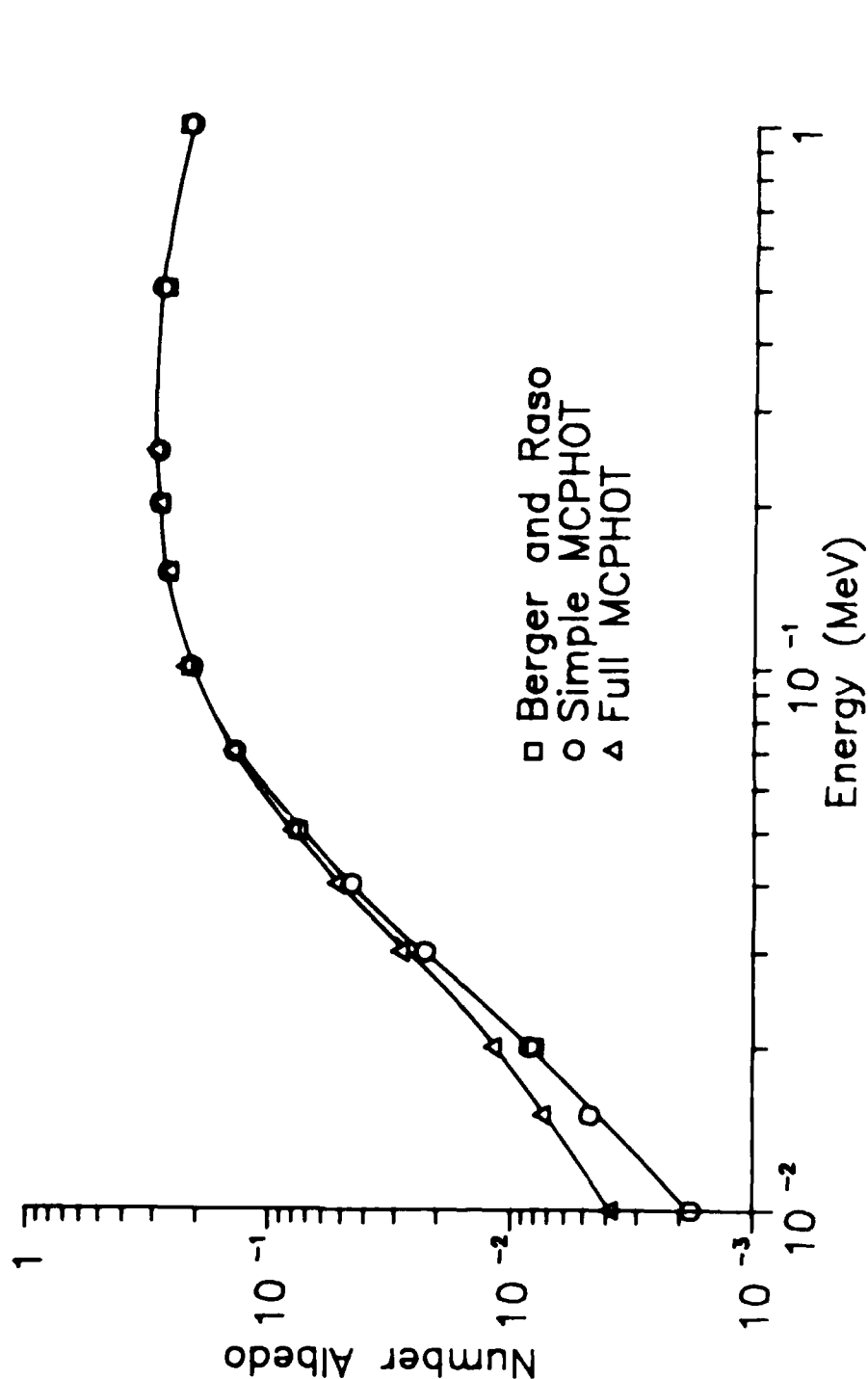


Figure IV.14. Number albedo versus energy for concrete. Calculated values of the number albedo for the case of perpendicular incidence as a function of incident photon energy are compared. The Berger and Raso (1960) values agree well with the simple MCPHOT code calculations. Both neglect coherent scattering, and use only the Klein-Nishina scattering distribution. The full MCPHOT code calculation includes coherent scattering and incoherent scattering from bound electrons.

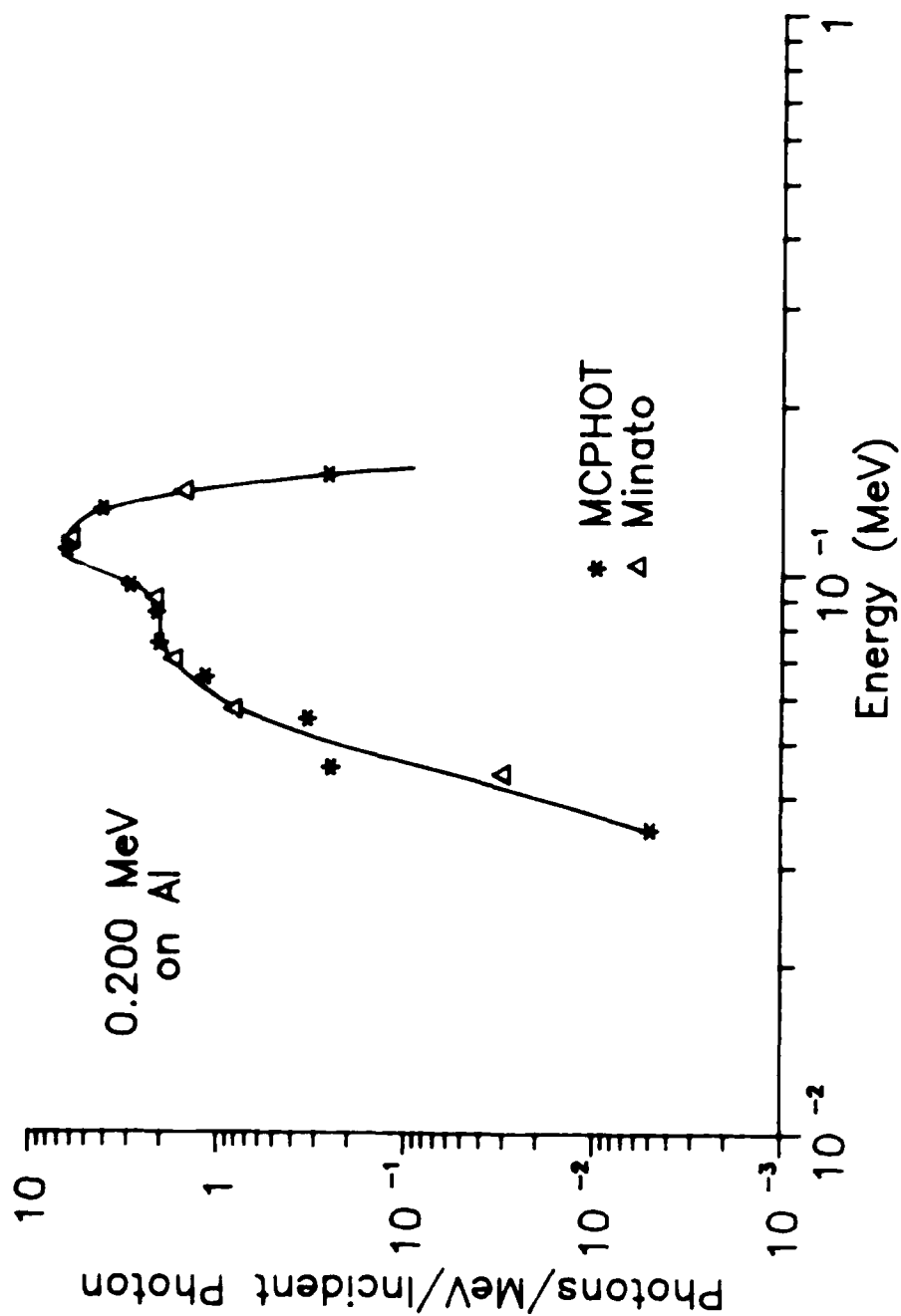


Figure IV.15. Backscattered energy spectrum, 0.200 MeV on aluminum. Calculations are for perpendicular incidence of 0.200 MeV photons on aluminum by Minato (1973) and the simple MCPHOT are compared.

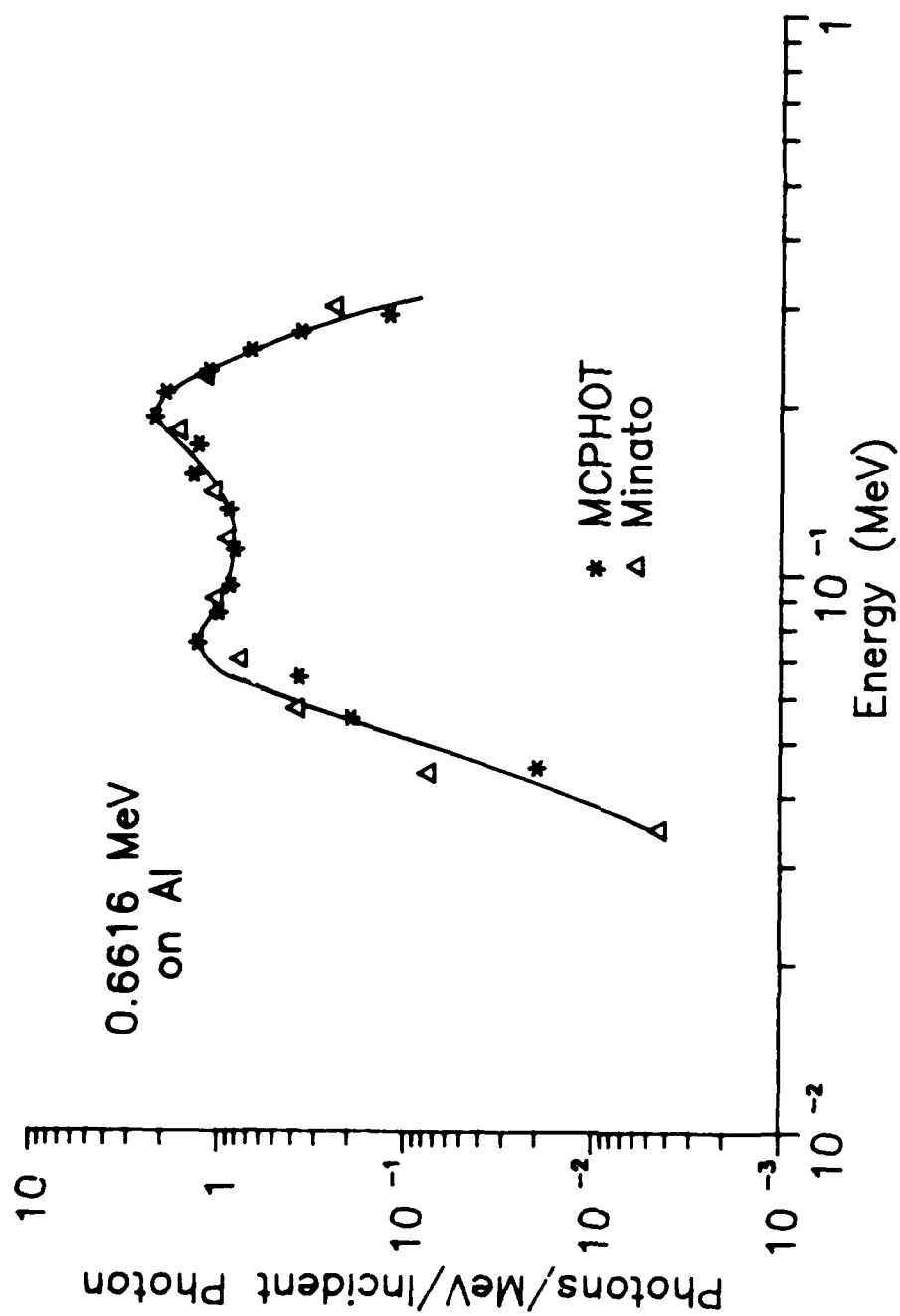


Figure IV.16. Backscattered energy spectrum, 0.6616 MeV on aluminum. Calculations are for perpendicular incidence of 0.6616 MeV photons on aluminum by Minato (1973) and the simple MCPHOT are compared.

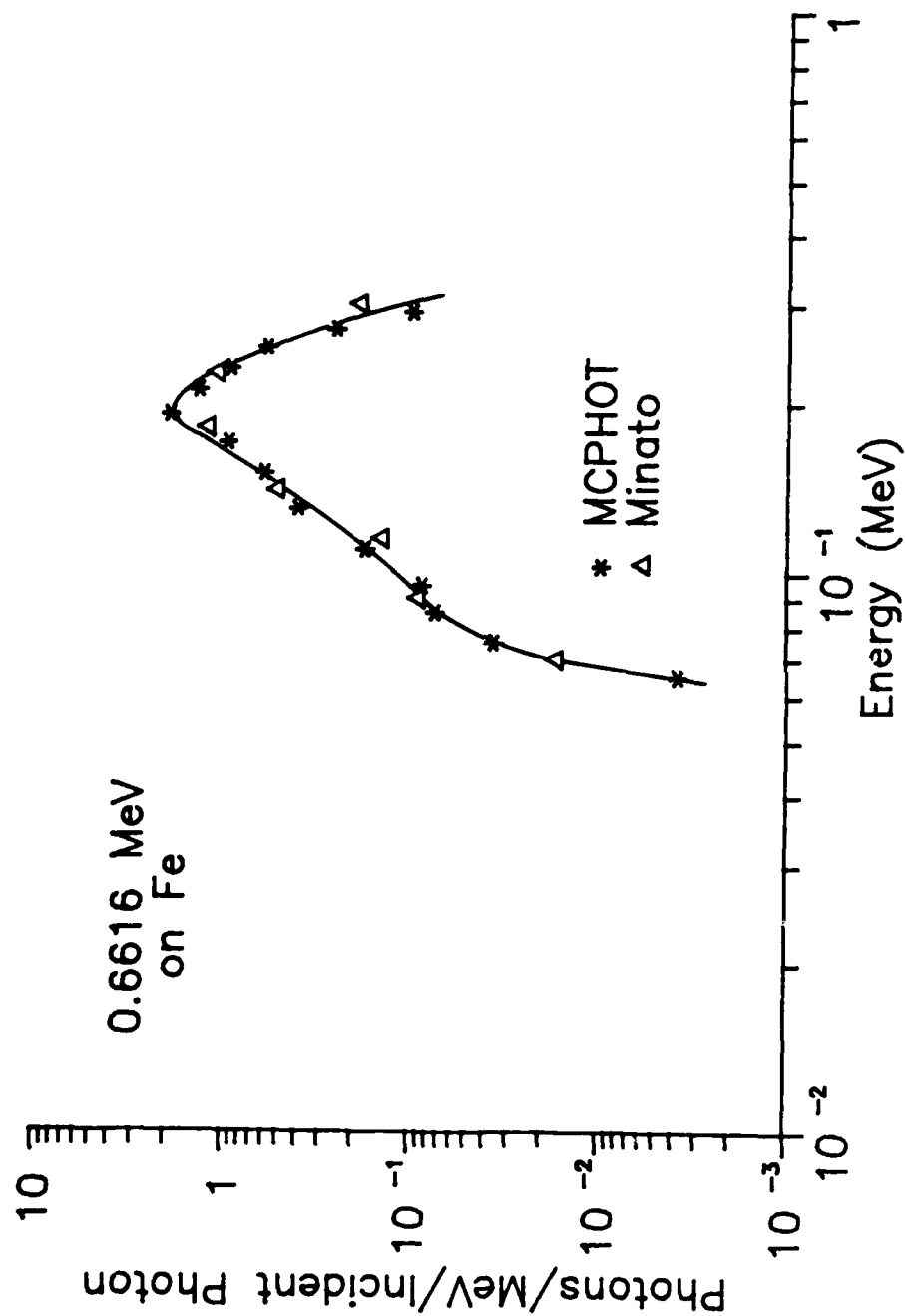


Figure IV.17. Backscattered energy spectrum, 0.6616 MeV on iron. Calculations are for perpendicular incidence of 0.6616 MeV photons on iron by Minato (1973) and the simple MCPHOT are compared.

1971) or 8.890 cm (Roder and Van Konyenburg, 1975). The mine is composed entirely of dinitrobenzene (DNB) at a density of 1.44 g/cm^3 ; no air space is considered. The soil (hereafter identified as FTB) composition used in the calculations is from samples taken at Fort Belvoir, Virginia. The soil density used is 1.30 g/cm^3 . The code used for the calculations does not consider coherent scattering and uses the Klein-Nishina distribution without modification by the incoherent scattering factor. Photon interaction data sets were constructed for FTB soil and DNB to allow calculations using the MCPHOT.P code. Coleman's values of the number albedo from soil only and with mine present are compared with calculations by the MCPHOT.P code in Table IV.6. The comparisons are very good.

Testing the Scattering Routines

The sampling techniques used for coherent and incoherent scattering are tested by comparison with analytical calculations of the respective solid angle differential scattering cross section as a function of the cosine of the scattering angle. The same routines employed in the MCPHOT.PAS and MCPHOT.P codes are used to sample the cosine of the scattering angle for coherent and incoherent scattering. These codes are run for 100,000 samples with the cosines of the scattering angles binned in increments of 0.02. Figures IV.18 and IV.19 compare the analytical and Monte Carlo calculations of the solid angle differential scattering cross section as a function of the cosine of the scattering angle

TABLE IV.6

Comparisons of Number Albedo
Calculations for FTB Soil and Buried DNB Mines

Energy (MeV)	Depth of Burial (cm)	Number Albedo	
		Coleman (1971)	MCPHOT.P
0.070	Soil only	0.117 \pm 0.002	0.1162 \pm 0.0110
0.120	Soil only	0.215 \pm 0.003 ^a	0.2094 \pm 0.0014
0.130	Soil only		0.2274 \pm 0.0015
0.200	Soil only	0.256 \pm 0.004	0.2634 \pm 0.0016
0.070	5.08	0.119 \pm 0.002	0.1196 \pm 0.0011
0.120	5.08	0.227 \pm 0.003 ^a	0.2257 \pm 0.0015
0.130	5.08		0.2380 \pm 0.0009
0.200	10.16	0.259 \pm 0.004	0.2627 \pm 0.0016

^aColeman provides a calculation for a range between 0.120 and 0.130 MeV with uniform distribution of source energies.

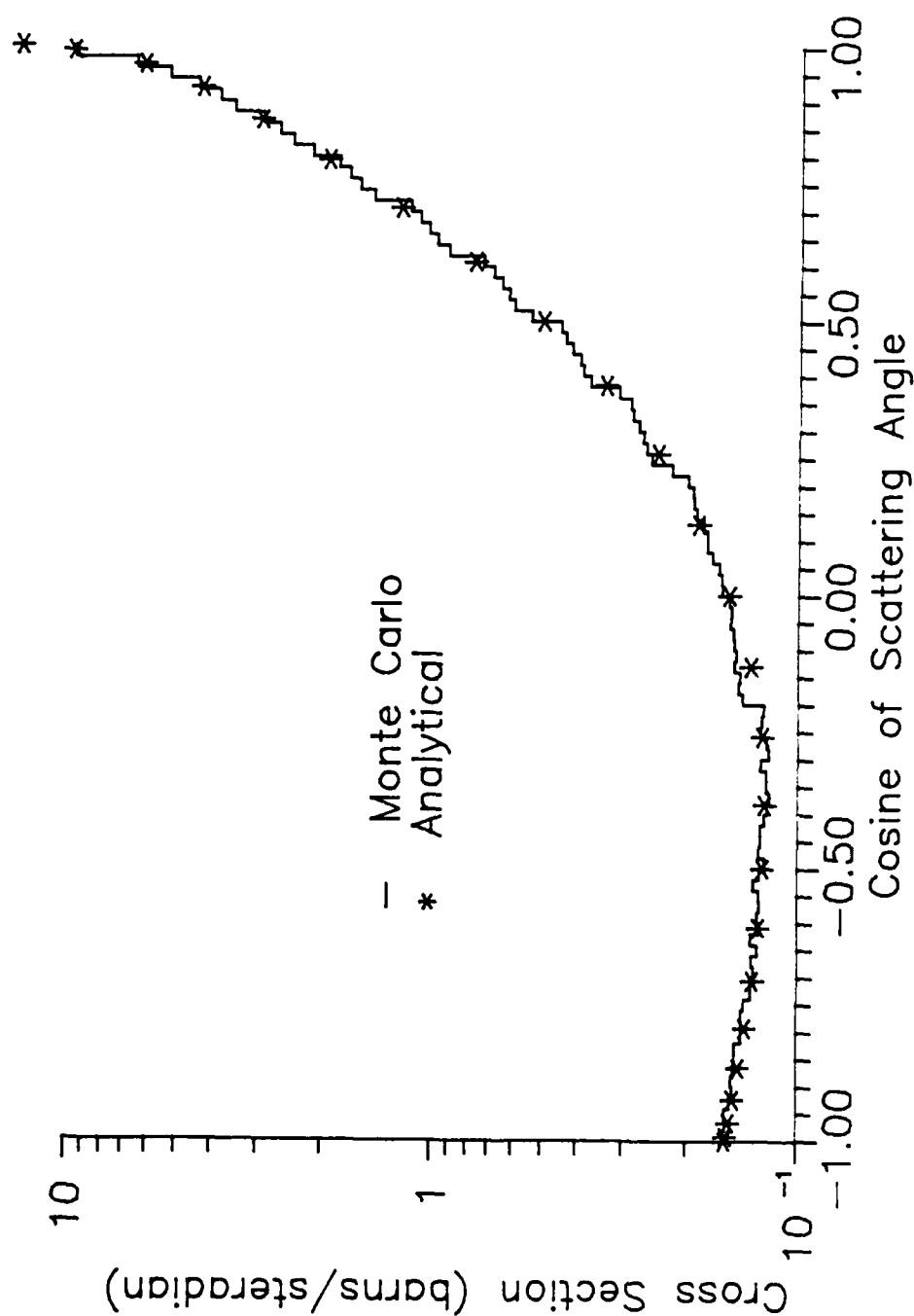


Figure IV.18. Comparison of calculations of the solid angle differential coherent cross section. Analytical and Monte Carlo calculations of the solid angle coherent scattering cross section are compared for 20 keV photons on aluminum. The Monte Carlo sampling technique used here is also employed in the MCPHOT codes. 100,000 photon histories are used in the Monte Carlo calculation.

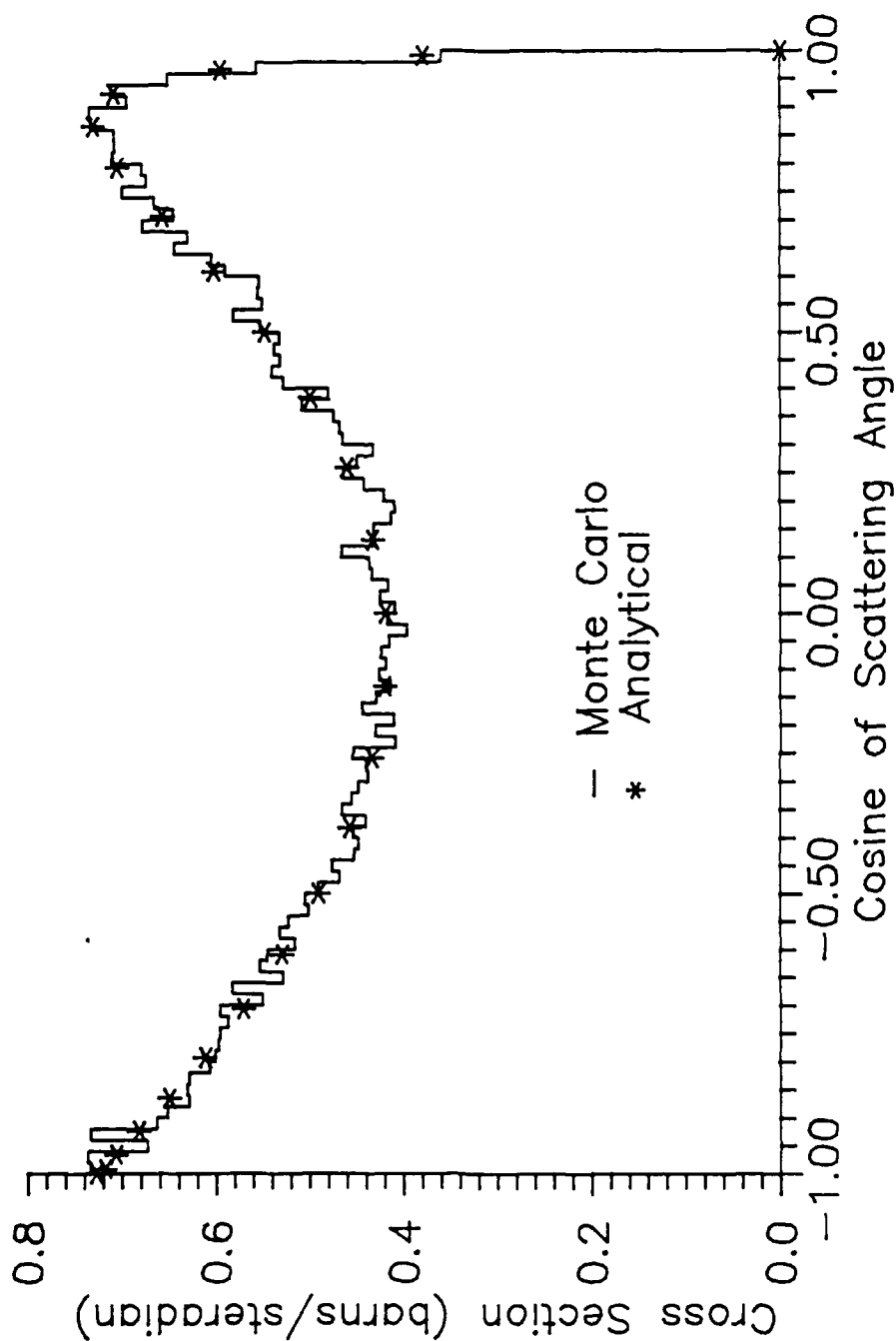


Figure IV.19. Comparison of calculations of the solid angle differential incoherent cross section. Analytical and Monte Carlo calculations of the solid angle incoherent scattering cross section are compared for 50 keV photons on aluminum. The Monte Carlo sampling technique used here is also employed in the MCPHOT codes. 100,000 photon histories are used in the Monte Carlo calculation.

for coherent and incoherent scattering. The comparisons are very good.

An additional test of the scattering routines and the entire code was made by comparing MCPHOT.P results with those of the MCNP code (Briesmesiter, 1986). MCNP is a general purpose Monte Carlo code developed at Los Alamos National Laboratory for neutron and photon transport. It is a widely accepted standard code for mainframe computer use in nuclear engineering and weapons applications. An option in the MCNP code allows full treatment of photon scattering using atomic form factors and the incoherent scattering function. A buried mine problem was run using the MCNP code on a Cray X-MP/48 computer and compared to the same calculation using the MCPHOT.P code on the Definicon DSI-32. In order to conserve central processing unit time on the Cray computer, the problem was limited to a cylinder of 50 cm radius about the beam axis. The MCPHOT.P code was modified for this same constraint. The only difference between the two calculations was to allow the MCNP code to model photoelectric interactions with subsequent fluorescent emissions. This was done to test the assumption in the MCPHOT.P code that fluorescent emission from soil and mine materials could be ignored. Comparisons were made with the number of photons striking a 50 cm radius disk above the soil, the total energy of those photons and their energy spectrum. In each case the comparison was excellent. Differences in the number and energy of photons striking the disk are less than

1.5%. With the exception of one low energy bin, all energy spectra results are within expected statistical variation. The fractional contribution of fluorescent emission photons to the fluence at the disk was found to be 0.00027, justifying their neglect in the MCPHOT.P code. Further, since these photons appeared in the 5 to 10 keV bin of the energy spectrum, and most real detectors employ some type of discrimination against low energy noise, these photons would not be detected.

CHAPTER V

X-RAY SOURCE

A number of techniques are available for determining or modelling the spectra produced by x-ray machines. The method selected for use in the mine detection calculations is presented and other techniques are discussed.

Kramers' Formula Method

The technique selected for calculating the x-ray spectra of the GE Maxitron 300 Therapy Unit is based upon a modification of Kramers' formula (Kramers, 1923). The model is implemented by an interactive computer code, XRSPEC.PAS, written in Turbo Pascal (Borland, 1985) for use on personal computers. The code calculates 1 keV increment spectra for fluence, energy fluence and exposure, and the integrals of these quantities. The relative values of integral quantities calculated by varying the amount of attenuating material in the beam can be used to simulate transmission experiments, which can then be checked against actual measurements. Since the values are relative, it is equally valid to consider the calculated quantities to be fluence rate, energy fluence rate and exposure rate. Fluence files created for use with the photon transport calculations of the mine detection problem are normalized so that the integrated fluence is 1.00 photons/(source photon - cm^2).

Kramers' Formula

Kramers' formula is a simple relationship between the energy associated with an electron accelerating potential and the intensity or energy fluence spectrum of the x rays produced when the electrons strike a target, in this case the anode of an x-ray machine. The formula is based upon the nonrelativistic, semiclassical physics of electron energy loss, neglecting electron scattering. It applies only to the continuous portion of the x-ray spectrum produced by the bremsstrahlung process. Despite these simplifying assumptions, its use in calculations of x-ray spectra is well established. The International Commission on Radiological Units and Measurements (1964) finds the method to perform well over a wide range of energies, provided that modifications for self-absorption in the anode and attenuation by other materials in the path of the beam are made.

One form of Kramers' formula is

$$I(E) = k (E_0 - E),$$

where I is the intensity or energy fluence of x-ray photons of energy, E ,

k is a constant of proportionality dependent on the anode material,

E_0 is the energy of the electrons striking the anode, and

E is the energy of an x-ray photon within the spectrum.

Since electron energy is related to accelerating potential by the relation

$$E = e V,$$

where e is the charge of the electron, and

V is the accelerating potential,

Kramers' formula is alternatively written as

$$I(V) = k' (V_0 - V),$$

where k' is k/e .

Application of this formula results in an unattenuated bremsstrahlung spectrum which declines linearly from a maximum of $k'V_0$ at V equal to zero, to a value of zero when V is equal to V_0 . In order to apply Kramers' formula to the case of the GE Maxitron 300 Therapy Unit, a number of modifications are necessary. These modifications are described in the following paragraphs.

Time Dependent Accelerating Potential

Since the accelerating potential of the GE Maxitron 300 is self-rectified, single phase, it varies in time. As a result, the V_0 term in Kramers' formula must be replaced with an expression which accounts for the time dependence of the accelerating potential. This time dependence is modeled as a sinusoid based upon waveforms associated with the GE Maxitron 300 (General Electric, 1962). The expression used to model the single phase nature of the accelerating voltage is

$$V_0 = V_{\max} \cos\pi(t/200), \quad t = -100, \dots, 100,$$

where V_o is the time dependent accelerating potential of electrons striking the anode, and

V_{max} is the maximum accelerating potential of electrons striking the anode or the peak tube potential.

To account for the self-rectified nature of the potential, the value of the cosine is permitted to take on only positive values by constraining its argument to $-\pi/2$ to $\pi/2$. The resulting 201 values of the intensity are summed in 1 keV intervals. Negative values of the quantity, $V_o - V$, result in no contribution to the intensity.

Characteristic X-Ray Production

If the energy of the accelerated electrons exceeds the binding energy of electrons of the anode material, characteristic x rays may be produced. Only K characteristic photon emission from the tungsten anode is modelled by the XRSPEC.PAS code; that is, only interactions with the K or inner shell atomic electrons of tungsten are considered. This presents no problem as long as sufficient filtration of the beam is applied to remove the low energy L characteristic radiation. For the mine detection application, even this filtration requirement is unnecessary, since virtually no L x rays survive interaction with the soil to contribute to the scattered fluence. The filtration is important, however, in tests of the code which rely on transmission measurements of the uncollided beam in which thin layers of attenuating material are employed.

The ratio of the intensity (or energy fluence) of K characteristic radiation to the intensity of the continuous spectrum as a function of electron energy, and the relative intensities of the various K x rays are provided by Dyson (1975). Because the characteristic to continuous ratio is a function of electron energy, and because that energy is changing in time for the GE Maxitron 300, characteristic x-ray production is time dependent. The sinusoidal model of the accelerating potential described for the time dependent continuous x-ray production is again employed. Table V.1 provides a listing of the energies of the K characteristic x rays used in the computer code. Because the $K_{\beta 1}$ and $K_{\beta 3}$ x rays are stored in the same energy interval in the 1 keV increment scheme of the code, only four distinct K x ray energy channels appear in code output. Additionally, since the $K_{\alpha 1}$ and $K_{\alpha 2}$ x rays are in adjacent energy intervals, graphs of spectra appear to show only three K rays.

Attenuation by Materials in the Beam Path

All calculated spectra for the GE Maxitron 300 normally include a minimum of four materials in the path of the beam. These are the beryllium window of the x-ray tube, a monitor ionization chamber, the filter required to remove L x rays of tungsten, and air. Sets of mass attenuation coefficients for these materials and others used in experiments are calculated by cubic spline fits of the data of Hubbell (1982). Attenuation coefficients include the effect of coherent scattering. In cases where detailed information concerning

TABLE V.1
Energies of Tungsten K Characteristic X Rays

X Ray	Actual Energy ^a (keV)	Code Energy Bin (keV)
K _{α1}	59.321	59
K _{α2}	57.984	58
K _{β1}	67.244	67
K _{β2}	69.081	69
K _{β3}	66.950	67

^aActual energies of K characteristic x rays are from Storm and Israel (1970).

the L and K edges is required, the cross section data of Storm and Israel (1970) are used. The mass attenuation data are constructed for energies between 1 and 300 keV with a 1 keV increment. These data sets have been constructed for the following materials: tungsten, beryllium, aluminum, copper, iron, lead, lucite, air, gadolinium oxysulfide, sucrose, TNT and a soil type (Norfolk sandy loam) similar to that used in the mine detection and imaging experiments.

Anode Self-Attenuation

Since x-ray photons are produced by electron interactions within the anode, they are subjected to attenuation by tungsten as they exit. Correction for anode attenuation is accomplished using the method suggested by Soole (1971). Soole compares calculations using Kramers' formula without correction for anode self-attenuation to published exposure transmission data. He finds the resulting calculated exposure transmission curves to indicate a softer (lower energy) spectrum than the measured values implied. Figure V.1 shows a typical calculation by the XRSPEC.PAS code without anode self-attenuation. The figure shows measured and calculated exposure rate transmission produced by placing varying thicknesses of aluminum in the x-ray beam. The geometry of the measurements conforms to the requirements for formal half value layer determination (Johns and Cunningham, 1983). The discrepancy between the calculation and measurement is the same as is observed by Soole. The steeper slope of the calculated curve implies a softer beam, that is, one which

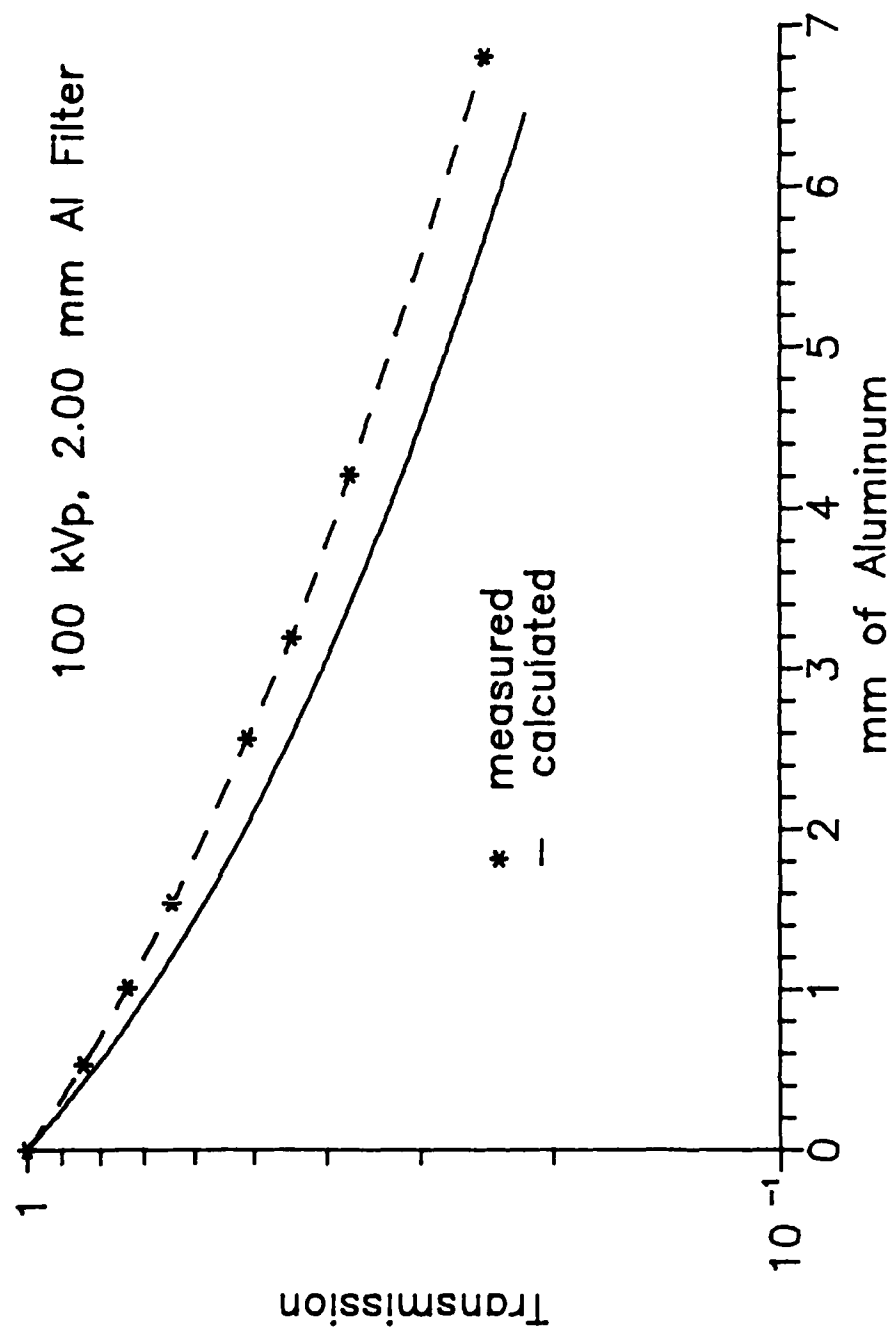


Figure V.1. Transmission curve without anode self-attenuation. A typical measured transmission of exposure rate is compared to a calculation by the XRSPEC.PAS code without anode self-attenuation. The source spectrum was produced by the GE Maxitron 300 X-Ray Therapy Unit operated at 100 kVp with 4.75 mm beryllium inherent filtration, 2.00 mm aluminum added filtration (includes 0.25 mm aluminum equivalent monitor ionization chamber), and air path length of 91.44 cm.

is more strongly attenuated. Soole shows that uncertainties in the amount of characteristic radiation produced cannot account for the discrepancy, and concludes that self-attenuation in the anode is the cause. The high photoelectric interaction cross section of tungsten preferentially removes the lower energy components resulting in the harder spectrum. Soole makes use of the concept of mean effective depth of production of x rays, originally presented by Hanson and Salem (1961). While x rays are not produced at a single point at depth within the anode, Hanson and Salem show that for the purpose of calculations, a mean effective depth can be defined. This depth is very small, on the order of microns for tungsten. Soole independently determines this depth using Kramers' formula by iteratively adding small amounts of tungsten to materials through which the beam passes. The mean effective depth is that which provides the least squares deviation between calculated and measured transmission data. His tungsten depths, derived in this manner, are somewhat higher than published mean effective depths (in mg/cm^2 of any target material). The published data are for a variety of smooth surface metal targets, but do not include tungsten. The surface of a tungsten anode, especially one which has been in operation for an extended period of time, is far from smooth at the micron level, so the differences are not surprising.

The least squares fitting technique employed by Soole and described above, is used with exposure transmission

measurements on the GE Maxitron 300 and calculations using Kramers' formula with the modifications described to determine the mean effective depths of x-ray production associated with the unit. Because the source of Soole's exposure transmission data used a constant potential machine, it was expected that the effective depths calculated for the single phase GE Maxitron 300 would be smaller for the same kVp and filtration. The opposite is found to be the case. While this may be due to differences in wear on the surfaces of the respective anodes (the GE Maxitron 300 is approximately 25 years old), a somewhat different point of view provides results which are more compatible. Since the hardening of the beam is due to preferential removal of softer components as they pass through the tungsten anode, it is not actually the depth of penetration which is paramount, but rather, the length of the exit path the photons must traverse. Calculations of this exit path distance from Soole's work (19 degree anode angle) and that of the GE Maxitron 300 (45 degree anode angle) are compared in Table V.2. The values are similar. It should be noted that this correction technique may account for other factors which affect beam hardness, such as variation of the shape of the primary waveform with peak kilovoltage.

To use the exit path data within the XRSPEC.PAS computer code, a least squares fit of the tungsten exit thickness versus maximum energy of the beam is made. The resulting energy dependent thickness is then included in the materials through which the beam passes.

TABLE V.2

Comparison of Exit Path Lengths Through Tungsten
Anodes Which Provide the Best Fit to Measured
Exposure Rate Transmission Data as Calculated
Using Kramers' Formula.

Beam Energy (kVp)	Filtration (mm of Al)	Exit Path Length (microns)	
		Soole (1971)	GE Maxitron 300
80	2.00	6.99	5.63
80	2.24	-	5.86
80	3.00	6.01	-
100	2.00	6.99	5.81
100	2.24	-	5.75
100	3.00	4.04	-
150	3.00	-	5.20
150	3.34	-	5.32
150	3.44	-	5.79
200	3.00	-	4.07
200	3.34	-	4.90

Effects Neglected in the Model

In addition to the simplifying assumptions inherent in Kramers' formula, several other effects are neglected. These include the effect of the filter in producing secondary photons in the beam, and the effect of the external collimator in preferentially hardening the outer portions of the beam.

When a photon interacts in the filter, a number of outcomes are possible. The XRSPEC.PAS model, by its use of simple attenuation coefficients, assumes that any interacting photon is removed from the beam. In reality, coherent scatter, incoherent scatter and fluorescent emission photons can be produced and may contribute to the beam. The external collimator exists to remove these photons, but it cannot fulfill this function if the photons pass through the collimator opening.

Since the walls of the collimator are parallel to the centerline of the beam, and the beam is diverging, a higher fraction of photons striking the lower walls will penetrate the collimator. This results in an unwanted penumbra about the defined beam, which will be spectrally harder than the center.

These effects are highly dependent upon the geometry and materials involved. Detailed calculations made for the actual geometry and materials used in the mine detection experiments show the effects to be negligible, producing a maximum shift in the average energy of a spectral distribution of 20 eV.

General Features of the Calculated Spectra

Figure V.2 shows a typical spectrum calculation. The low energy components are removed by aluminum filtration, producing the maximum in the continuous portion of the spectrum. K characteristic x-ray peaks are present since the maximum accelerating potential exceeds 69.508 keV, the binding energy of the inner shell electrons of tungsten (Storm and Israel, 1970). A less obvious feature in the spectrum also occurs at this energy. A close examination of the continuous portion of the spectrum reveals a discontinuity at the tungsten K edge energy. This discontinuity is somewhat obscured by the nearby characteristic x rays. The drop in the fluence is due to the discontinuous increase in the photoelectric cross section of tungsten at its K edge energy. Photons having energies just below that of the edge and exiting the anode are less attenuated than those of energies just above the edge energy. Examples of this feature also occur in published spectra (Sundararaman et al., 1973; Stanton et al., 1979).

Another well known feature of x-ray measurements, the heel effect, is demonstrated by the XRSPEC.PAS code. The heel effect refers to the spectral hardening of portions of the beam which pass through greater thicknesses of the anode, and thus suffer greater self-attenuation. Portions of the beam located closest to the anode are, therefore, the hardest. Since increased attenuation is largest for low energy photons, the result is a variation of hardness within

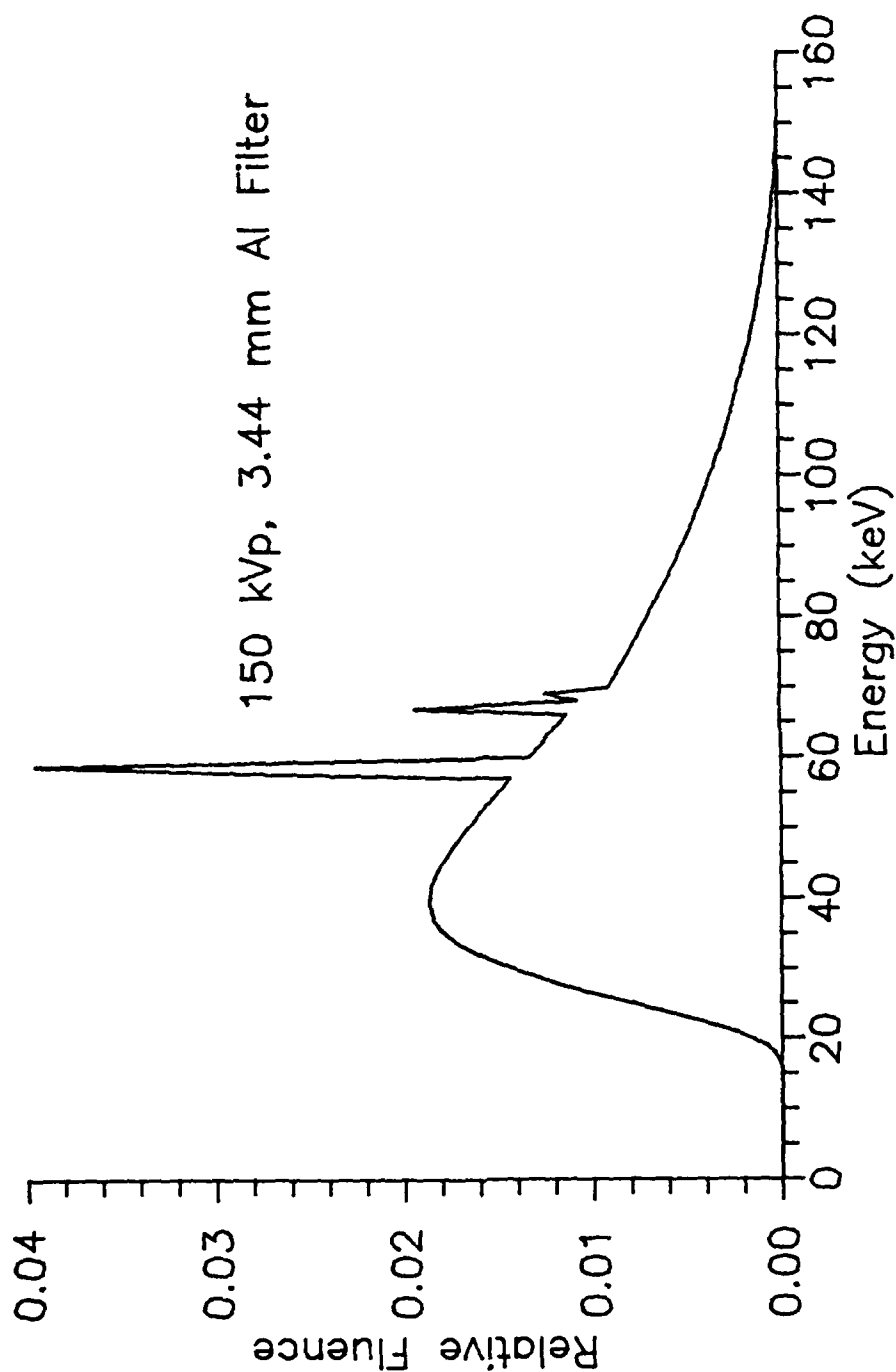


Figure V.2. Typical x-ray spectrum calculation. The fluence spectrum (in units of photons per cm^2 per keV) at 150 kVp calculated by the XRSPEC.PAS code for the GE Maxitron 300 X-Ray Therapy Unit with 4.75 mm beryllium inherent filtration, 3.44 mm aluminum added filtration (includes 0.25 mm aluminum equivalent monitor ionization chamber) and air path length of 90.07 cm is shown. Total fluence is normalized to 1 photon per cm^2 .

the beam. Calculations using the XRSPEC.PAS code show this feature. Figure V.3 shows the results of calculations of the fluence spectra for three portions of an x-ray beam generated at 80 kVp. The spectrum associated with the portion of the beam nearest the anode is reduced in magnitude and shifted to higher energies by the heel effect. Figure V.4 displays the effect in a form often found in medical physics texts (Hendee, 1984). Here the effect is shown in the variation of half value thickness, the thickness of material (aluminum in this case) required to reduce the exposure rate of the x-ray beam by a factor of two. The calculation of this figure uses the geometry required for formal half value measurements (Johns and Cunningham, 1983). As shown in the figure, greater thicknesses of aluminum are required for portions of the beam nearest the anode.

Testing the Modified Kramers' Formula Model

The validity of the modified Kramers' formula method for calculating x-ray spectra is tested by comparisons with exposure rate transmission measurements and published measurements of spectra.

Exposure Rate Transmission Measurements

The transmission of exposure rate of x-ray beams produced by the GE Maxitron 300 is measured for a variety of combinations of maximum accelerating potentials and filtrations. Beams produced by these energy and filtration combinations are transmitted through varying thicknesses of aluminum to develop transmission curves. These measured

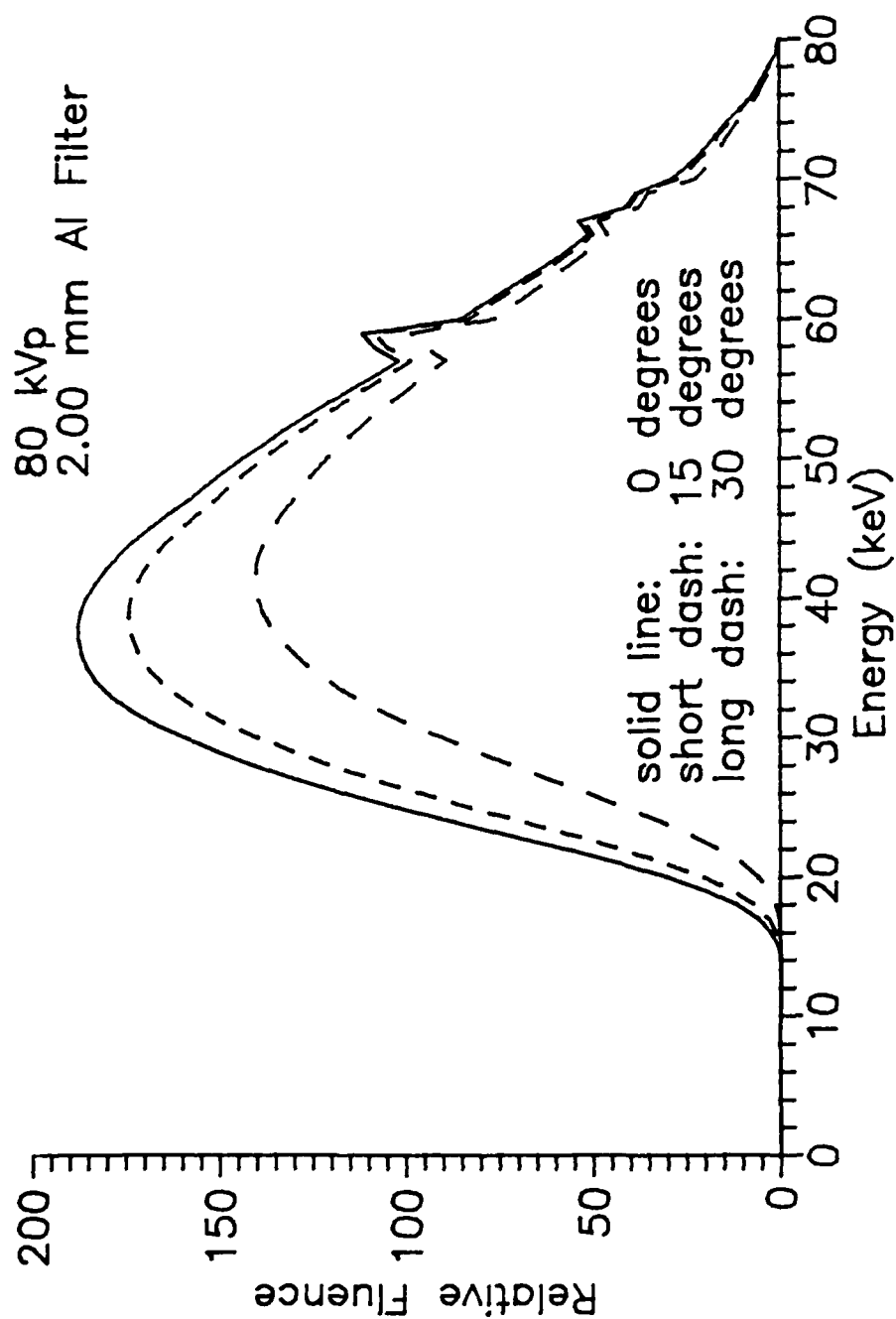


Figure V.3. Heel effect displayed by spectra. A comparison of x-ray spectra for three beam angles generated at 80 kVp calculated by the XRSPEC.PAS code for the GE Maxitron 300 X-Ray Therapy Unit. Fluence units are relative number of photons per cm^2 per keV.

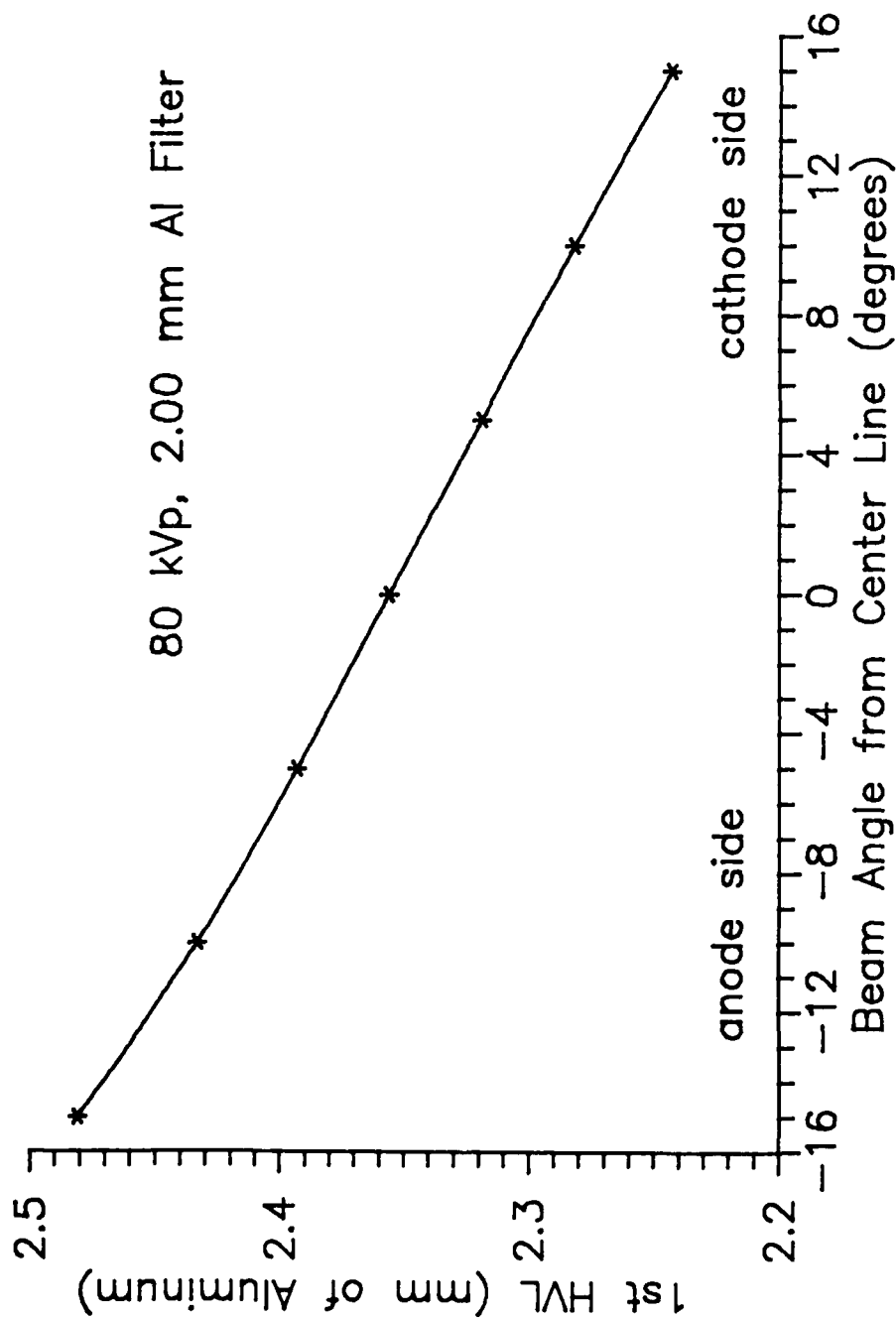


Figure V.4. Heel effect displayed by half value thickness. A comparison of first half value layers (mm of aluminum) of 80 kVp beams as a function of beam angle is shown. Values were calculated by the XRSPEC.PAS code for the GE Maxitron 300 X-Ray Therapy Unit.

results are then compared to calculations for the same transmission experiment simulated by the XRSPEC.PAS code. Figure V.5 shows the results of such a comparison for the spectrum shown in Figure V.2. Other comparisons are provided in Appendix D. Figures in the appendix show the calculated spectra, and the associated measured and calculated transmission of exposure rate. Measurements are made with an MDH Industries, Inc. 1015 X-Ray Monitor, which has a flat energy response to below 20 keV. As can be seen by the comparisons, the agreement between calculations and measurements is very good.

Comparisons with Published Spectra

Comparisons with published measurements of x-ray spectra are also performed. Fewell and Shuping (1977) reviewed published spectral measurements and recommend their own work and that of Epp and Weiss (1966) as the best available. In doing so, they indicate that serious discrepancies exist in other published spectra. Accordingly, comparisons are made with these two recommended sets of published spectra.

Figures V.6 and V.7 show the comparison between the XRSPEC.PAS fluence spectrum calculation and the measurements of Epp and Weiss. The voltage waveform used in the Epp and Weiss measurements is considerably different from that of the GE Maxitron 300. The XRSPEC.PAS code is modified to model this new waveform, which is a constant potential term plus a 120 Hz component with a peak to peak amplitude equal

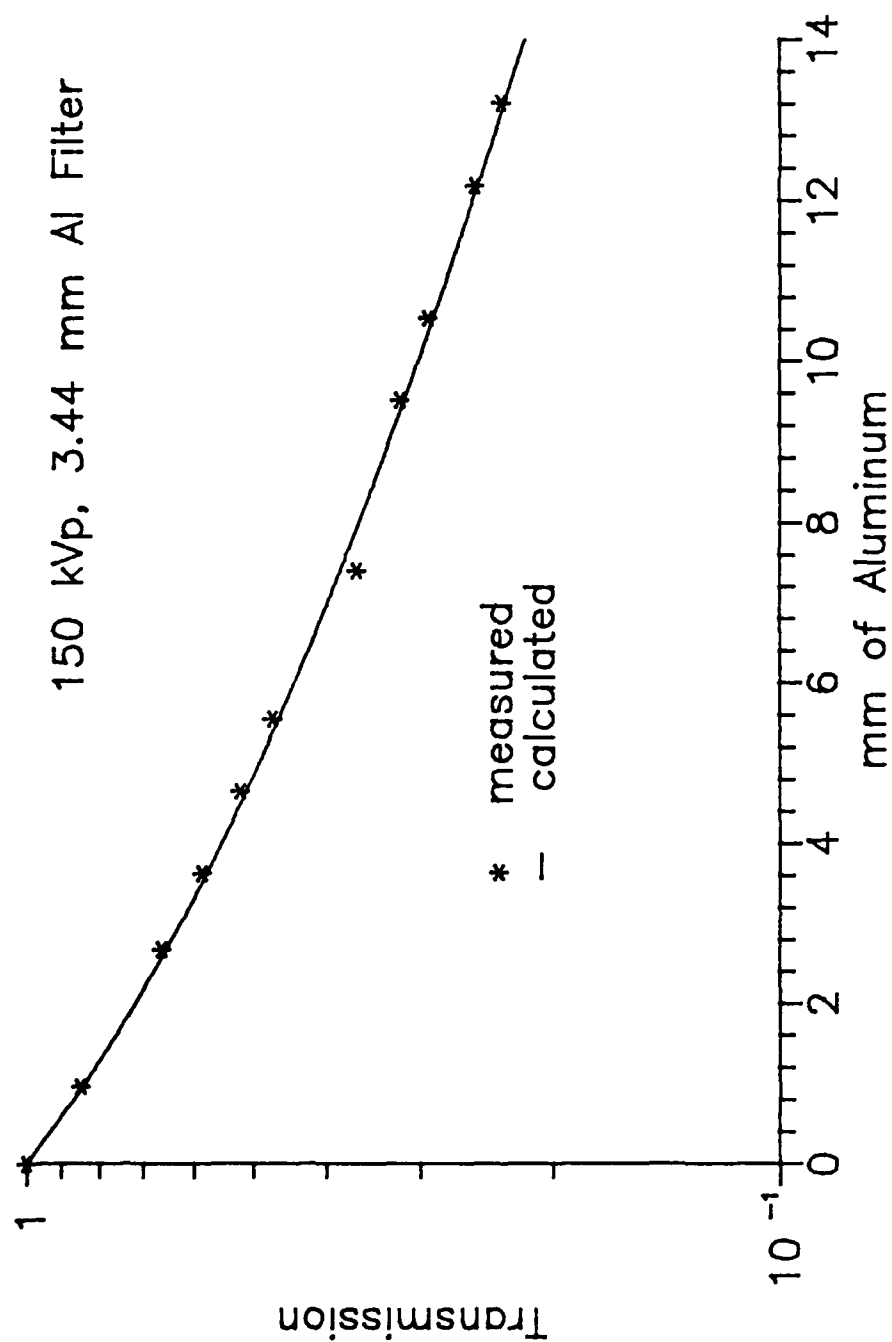


Figure V.5. Typical transmission curve comparison. A comparison of measured and calculated transmission of exposure rate of a 150 kVp beam produced by the XRSPEC.PAS code for the GE Maxitron 300 X-Ray Therapy Unit with 4.75 mm beryllium inherent filtration, 3.44 mm aluminum added filtration (includes 0.25 mm aluminum equivalent monitor ionization chamber) and air path length of 91.44 cm.

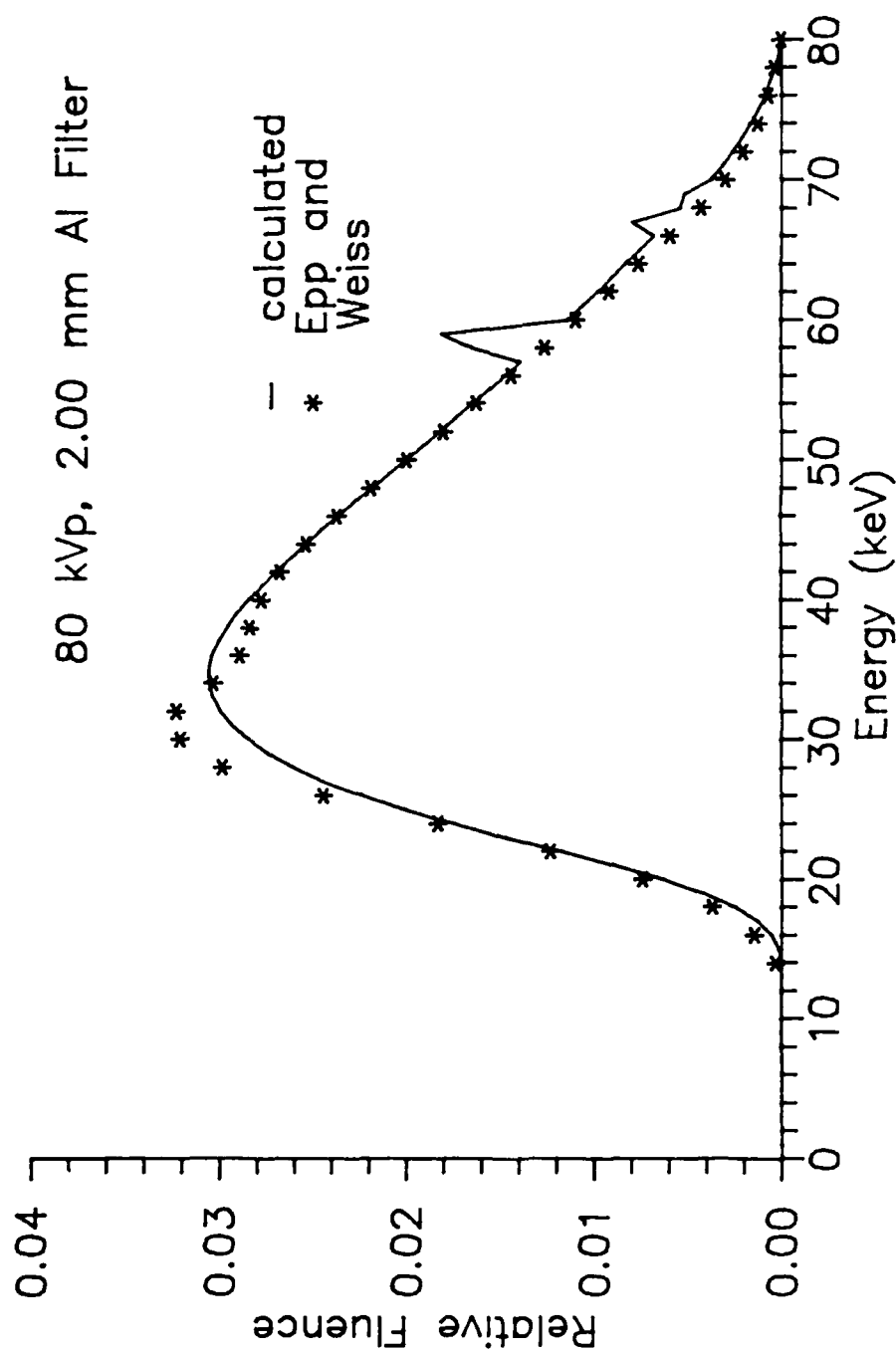


Figure V.6. Spectrum comparison with Epp and Weiss at 80 kVp. The measured spectrum, from Epp and Weiss (1966), is generated by a diagnostic x-ray unit operated at 80 kVp with 0.5 mm inherent aluminum filtration, 2.00 mm aluminum added filtration and an air path length of 2.13 m. Fluence units are photons per cm^2 per keV. The calculated spectrum is generated by the XRSPEC.PAS code. Total fluence is normalized to 1 photon per cm^2 .

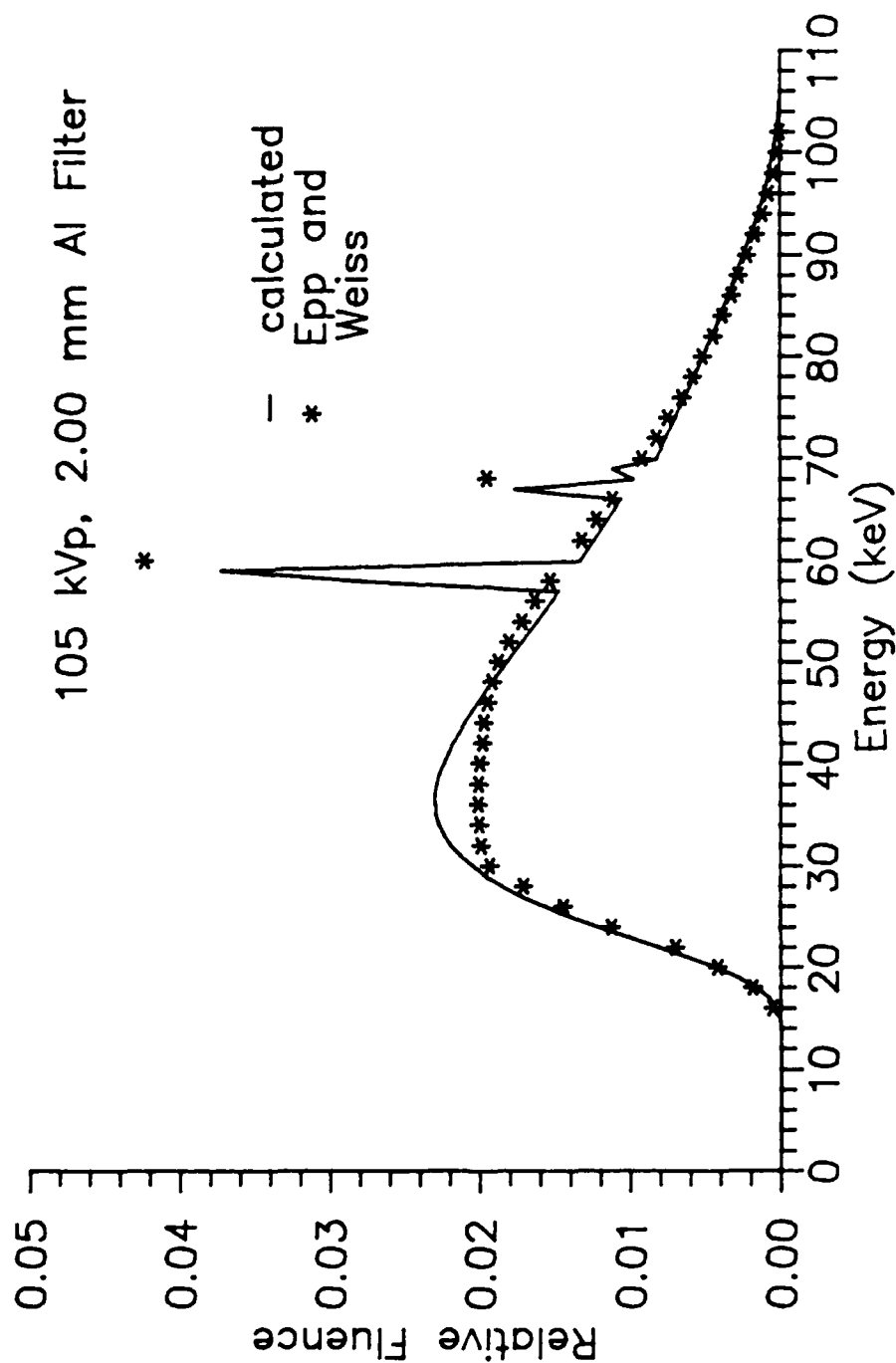


Figure V.7. Spectrum comparison with Epp and Weiss at 105 kVp. The measured spectrum, from Epp and Weiss (1966), is generated by a diagnostic x-ray unit operated at 105 kVp with 0.5 mm inherent aluminum filtration, 2.00 mm aluminum added filtration and an air path length of 2.13 m. Fluence units are photons per cm^2 per keV. The calculated spectrum is generated by the XRSPEC.PAS code. Total fluence is normalized to 1 photon per cm^2 .

to 25% of the constant potential term. This waveform would be expected to produce a harder spectrum than the single phase waveform of the GE Maxitron 300 when operated at the same peak kilovoltage. Comparisons at 80 and 105 kVp are shown. The lack of characteristic x rays in the measured 80 kVp spectrum casts some doubt on the quality of these measurements. The characteristic x rays should be more intense in this spectrum than in the corresponding GE Maxitron 300 spectrum as a result of the waveform. Overall, however, the comparisons are generally good.

Figures V.8, V.9 and V.10 show the comparison with the measurements of Fewell and Shuping (1977). The voltage waveform of the x-ray machine used in these measurements is single phase, as is the GE Maxitron 300. Comparisons are made at 70, 80 and 90 kVp. The comparisons in all three cases are excellent. The presence of characteristic x rays in the measured 80 kVp spectrum reinforces the lack of confidence in the Epp and Weiss measurements described above.

Other Methods to Determine X-Ray Spectra

Several other methods are frequently applied to the problem of determining x-ray spectra.

Measurement

The most direct method for determining x-ray spectra is measurement. Unfortunately, this method is an extremely difficult, expensive, and time consuming endeavor requiring highly specialized equipment and detailed corrections for

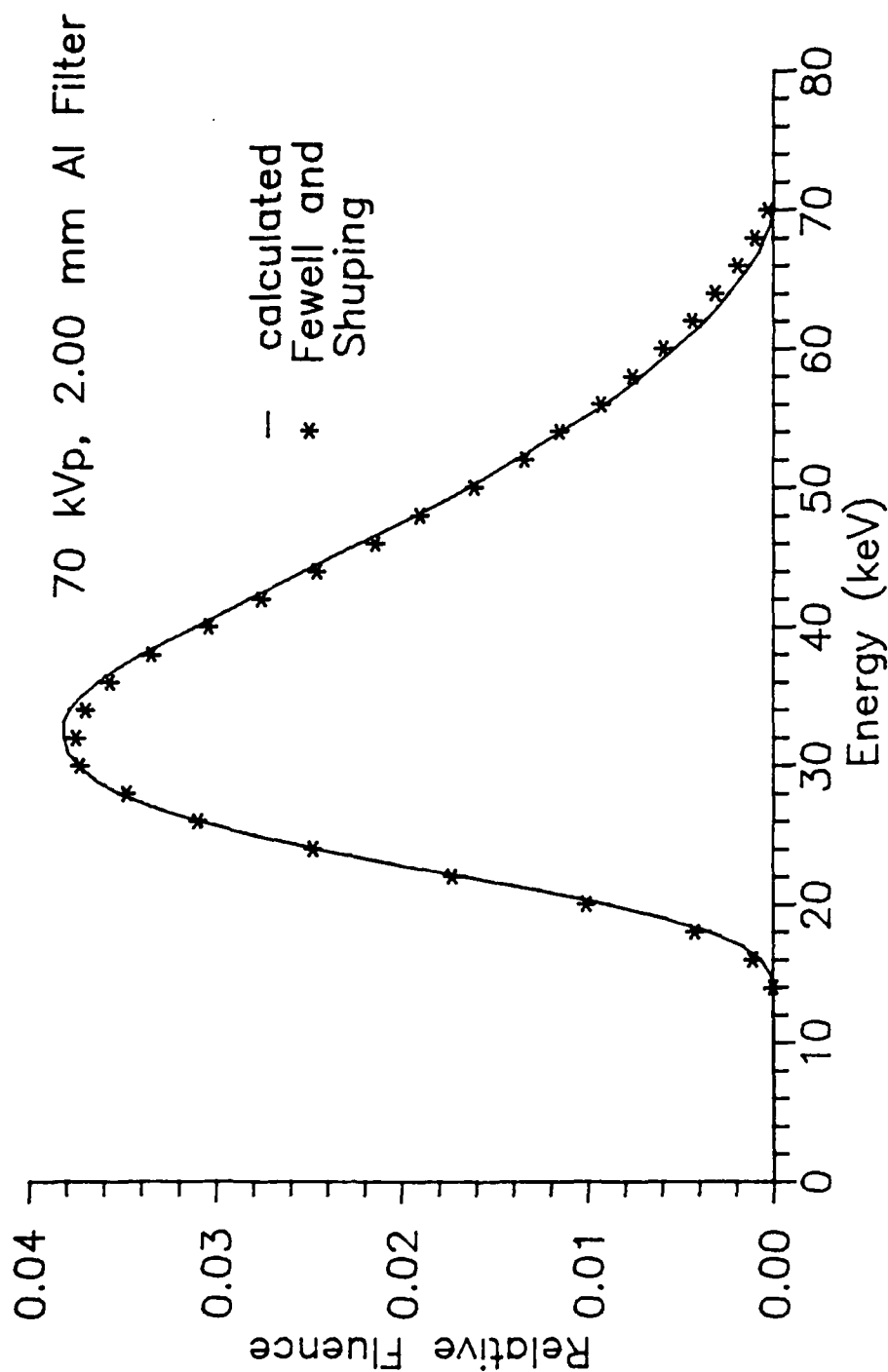


Figure V.8. Spectrum comparison with Fewell and Shuping at 70 kVp. The measured spectrum, from Fewell and Shuping (1977), is generated by a diagnostic x-ray unit operated at 70 kVp with 0.7 mm aluminum equivalent inherent filtration, 2.00 mm aluminum added filtration and an air path length of 100 cm. Fluence units are photons per cm² per keV. The calculated spectrum is generated by the XRSPEC.PAS code. Total fluence is normalized to 1 photon per cm².

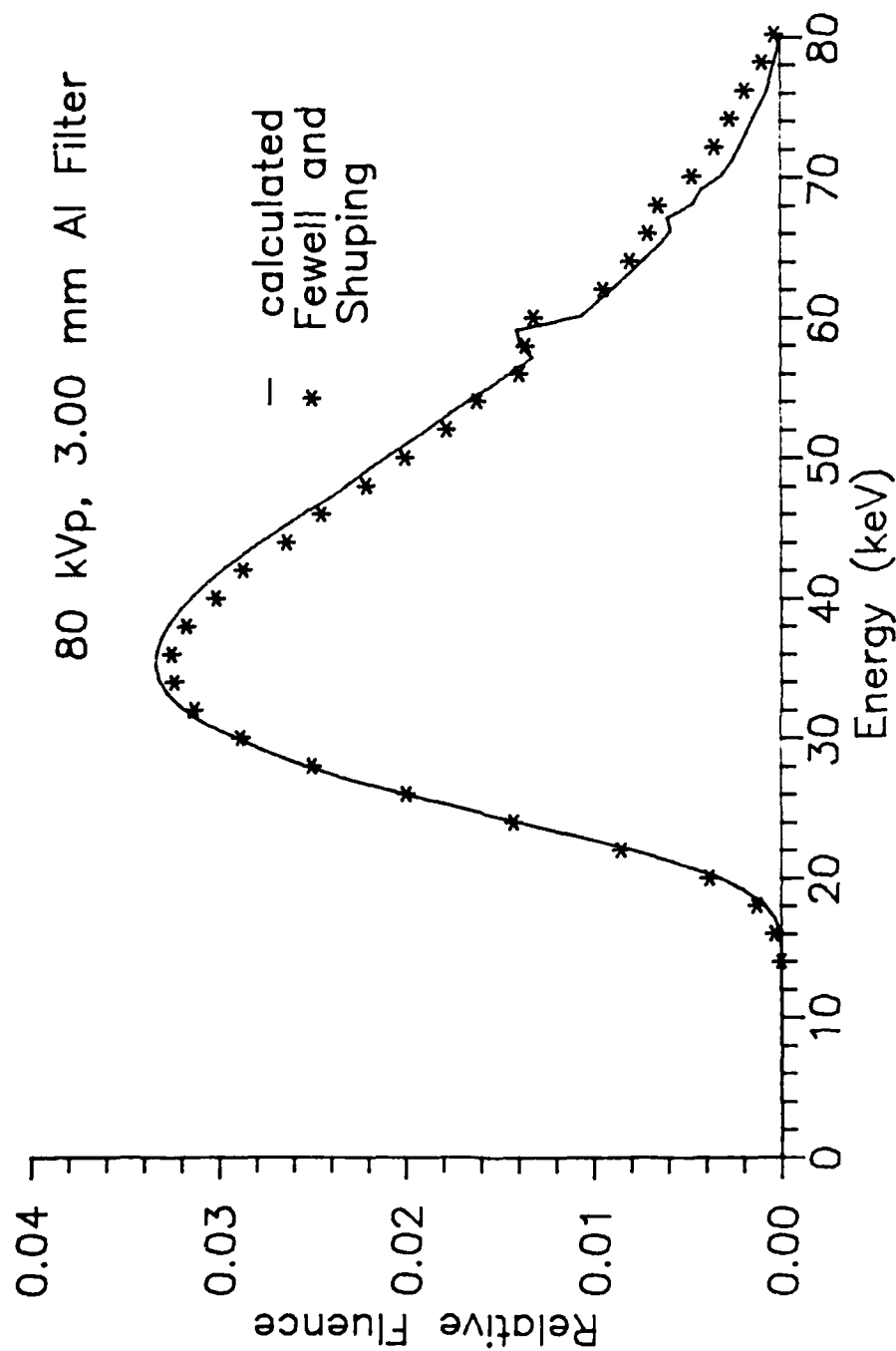


Figure V.9. Spectrum comparison with Fewell and Shuping at 80 kVp. The measured spectrum, from Fewell and Shuping (1977), is generated by a diagnostic x-ray unit operated at 80 kVp with 0.7 mm aluminum equivalent inherent filtration, 3.00 mm aluminum added 2 filtration and an air path length of 100 cm. Fluence units are photons per cm^2 per keV. The calculated spectrum is generated by the XRSPEC.PAS code. Total fluence is normalized to 1 photon per cm^2 .

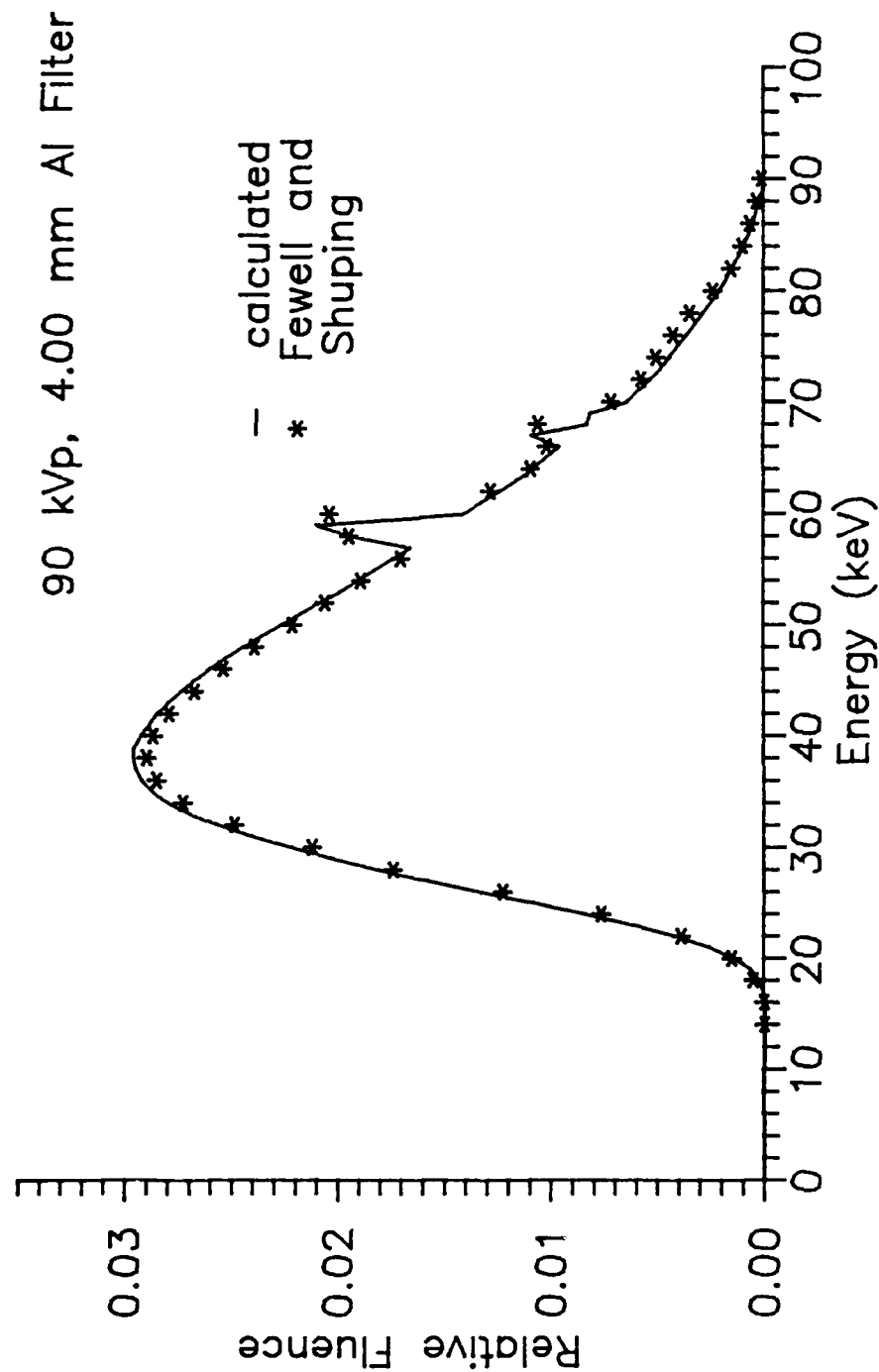


Figure V.10. Spectrum comparison with Fewell and Shuping at 90 kVp. The measured spectrum, from Fewell and Shuping (1977), is generated by a diagnostic x-ray unit operated at 90 kVp with 0.7 mm aluminum equivalent inherent filtration, 4.00 mm aluminum added₂ filtration and an air path length of 100 cm. Fluence units are photons per cm² per keV. The calculated spectrum is generated by the XRSPEC.PAS code. Total fluence is normalized to 1 photon per cm².

the response of the detector employed in the measurement (Baird, 1981). As noted above, serious discrepancies in published measurements of x-ray spectra are noted in the literature (Fewell and Shuping, 1977), indicating that the relative difficulty of the technique is high. For these reasons, a measurement technique is not selected. However, as described above, comparisons of calculated results with published measurements of spectra, which have been determined by reviewers to be reliable, have been useful in testing the modified Kramers' formula method.

Monte Carlo Calculation

Implementation of a Monte Carlo code to calculate x-ray spectra requires a good understanding of the bremsstrahlung interaction cross sections for thick targets. Unfortunately, these cross sections are not well known for the diagnostic and therapeutic x-ray energy ranges which are of interest in the mine detection problem (Koch and Motz, 1959). Results of Monte Carlo calculations of x-ray spectra are generally considered inferior to other techniques (Huang et al., 1981). As a result this method is not selected.

Laplace Transform Pair Method

This technique was first introduced by Silberstein (1932, 1933). It requires that exposure transmission measurements be made by placing varying thicknesses of materials in the path of the beam (usually aluminum or copper). The resulting exposure rate transmission versus thickness data is then fit to a function of the attenuation coefficient of

the material which has a known inverse Laplace transform. This inverse transform function, multiplied by the derivative of the attenuation coefficient with respect to energy to transform variables from attenuation coefficient to energy, constitutes the x-ray spectrum. Silberstein provided the first such Laplace transform pair.

Significant improvements to Silberstein's original transform pair were made by Bell (1936) and Jones (1940) to account for the known physics of x-ray spectra and photon attenuation. Greening (1947) provided an approximation technique for accounting for the characteristic portion of the x-ray spectrum and also produced the first definition of the general properties required of other Laplace transform pairs for use in spectral reconstruction (Greening, 1950). The original Silberstein pair, though modified by additional parameters, continued to be used even though its fits to transmission data were often not particularly good. Better Laplace transform pairs were identified (Saylor, 1969; Huang et al., 1981; Archer and Wagner, 1982), but with their use, the capability to approximate the characteristic portion of the spectrum was lost. Baird (1981) provides a theoretical analysis of the general Laplace transform pair technique. Ahuja et al. (1986), provide a summary of the Laplace transform pair models which have been used up to 1986. The International Commission on Radiological Units and Measurements (1964) cautions that the usefulness of this technique depends upon the accuracy of measurement of the

transmission curve and the number of parameters used in fitting the curve.

The Archer-Wagner method (Archer and Wagner, 1982) is generally accepted as the most accurate transform pair available today (Rubio and Mainardi, 1984; Archer, 1985, Ahuja et al., 1986). Joseph (1975) establishes the physical basis for the form used in the Archer-Wagner fitting function, accounting for its accuracy in approximating transmission data. The Archer-Wagner method does not include characteristic x-ray contributions, but can be used to check spectral calculations for cases in which the characteristic x-ray component is negligible or absent. Mathematically, it is the most complex of the sets of transform pairs that have been used. The function used in fitting the exposure rate transmission measurements is of the form

$$X(\xi) = \left[\frac{ab}{(\xi+a)(\xi+b)} \right]^v \exp(-\mu_0 \xi)$$

where $X(\xi)$ is the ratio of exposure (or exposure rate) after passing through ξ g/cm² of attenuating material to the exposure (or rate) without any attenuating material,

μ_0 is the mass attenuation coefficient of the attenuating material at the maximum energy in the spectrum, and

a, b, v are the fitting parameters to be determined.

The associated fluence spectrum is given by

$$F(E) = \frac{\pi^{1/2} (ab)^v}{\Gamma(v)} \left[\frac{\mu - \mu_0}{a-b} \right]^{v-1/2} \exp \left[- \frac{(a+b)}{2} (\mu - \mu_0) \right] I_{v-1/2} \left[\frac{1}{2} (a-b) (\mu - \mu_0) \right] \left(- \frac{d\mu}{dE} \right)$$

where $F(E)$ is the fluence as a function of energy,
 μ is the mass attenuation coefficient of the attenuating material at energy, E ,
 Γ is the gamma function,
 I is the modified Bessel function, and
 $\frac{d\mu}{dE}$ is the derivative of the mass attenuation coefficient with respect to energy at energy, E .

In order to implement the Archer-Wagner method, a nonlinear parameter fitting computer program was written using the Levenberg-Marquardt method (Press et al., 1986). Figure V.11 shows an example of the excellent capability of the Archer-Wagner formula to fit measured transmission data. For spectra generated at 100 kVp and below (where characteristic radiation does not play a major role), the worst fit data point in four cases examined was less than 0.8%. Once the parameters are determined, a second program computes the fluence spectrum at a 1 keV increment. The previously assembled mass attenuation coefficient data for aluminum

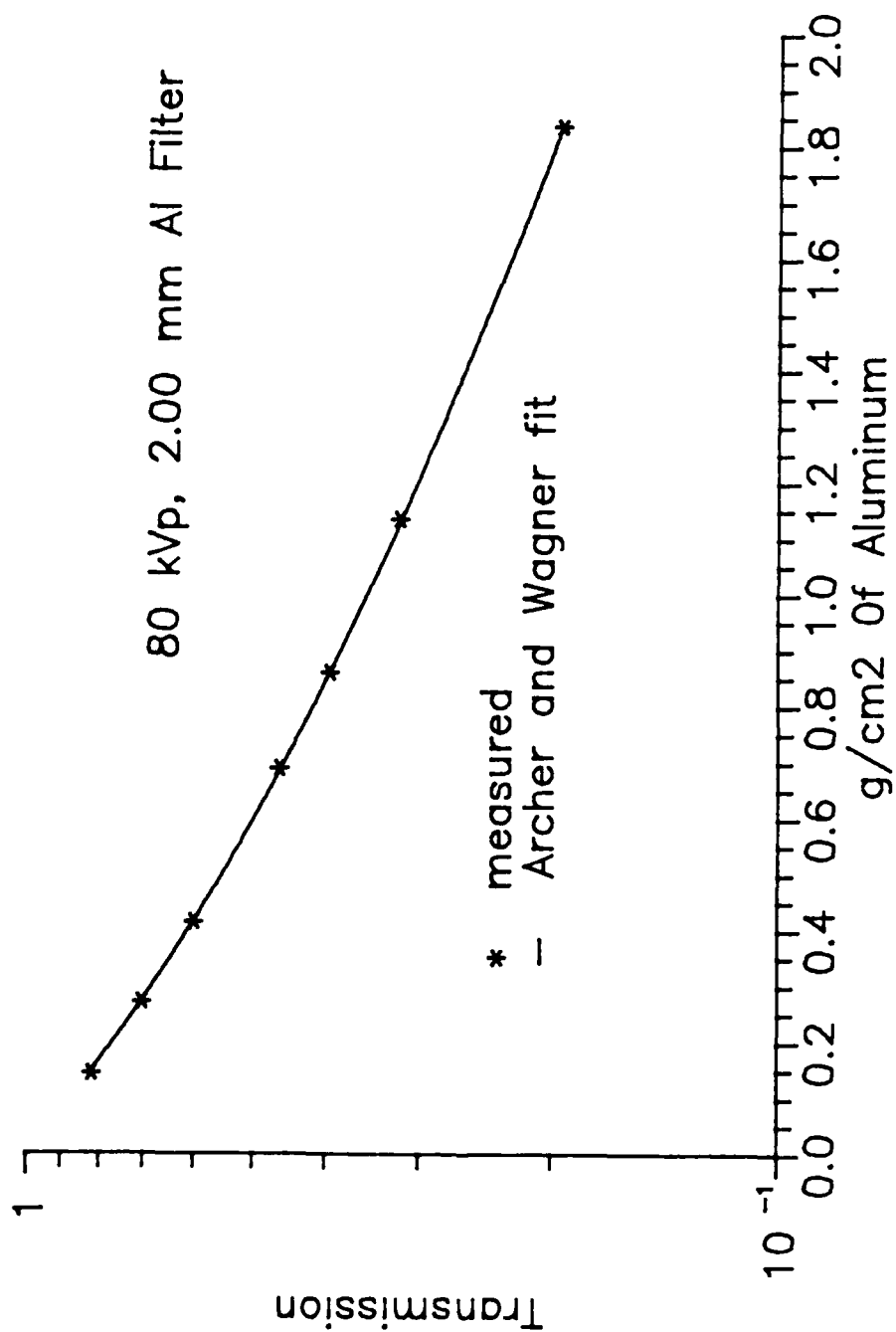


Figure V.11. Archer-Wagner method fit to measured transmission data. The excellent capability of the Archer-Wagner fitting equation (Archer and Wagner, 1982) is demonstrated.

(any material can be used as the attenuator in the technique) were numerically differentiated to provide the derivative required to support the calculation. Algorithms used for computing the gamma function and modified Bessel function are from Press et al. (1986). Figure V.12 compares the results of fluence spectra calculations at 80 kVp by the modified Kramers' formula method and by the Archer-Wagner method. While some differences exist due to the minor characteristic x-ray contribution, the agreement is seen to be good. Figure V.13 shows the same comparison at 150 kVp where the characteristic contribution is large. The comparison is now poor, highlighting the reason for rejection of this otherwise excellent technique.

Rubio and Mainardi (1984) have attempted to extend the Archer-Wagner method to include characteristic x rays. The extension involves adding exponential terms with parameter coefficients to the fitting function, resulting in delta functions in the inverse Laplace transform. In their paper, Rubio and Mainardi use published measured fluence spectra to calculate exposure transmission data. These calculated data are then applied to a fitting function, which allows for only two K x rays in the inverse transform. Calculated spectra are produced which predict the characteristic components to between 10 and 15% of the measured values. No demonstration of spectral reconstruction from actual transmission data, subject to random error found in any actual experimental measurement, is made. Attempts to apply this

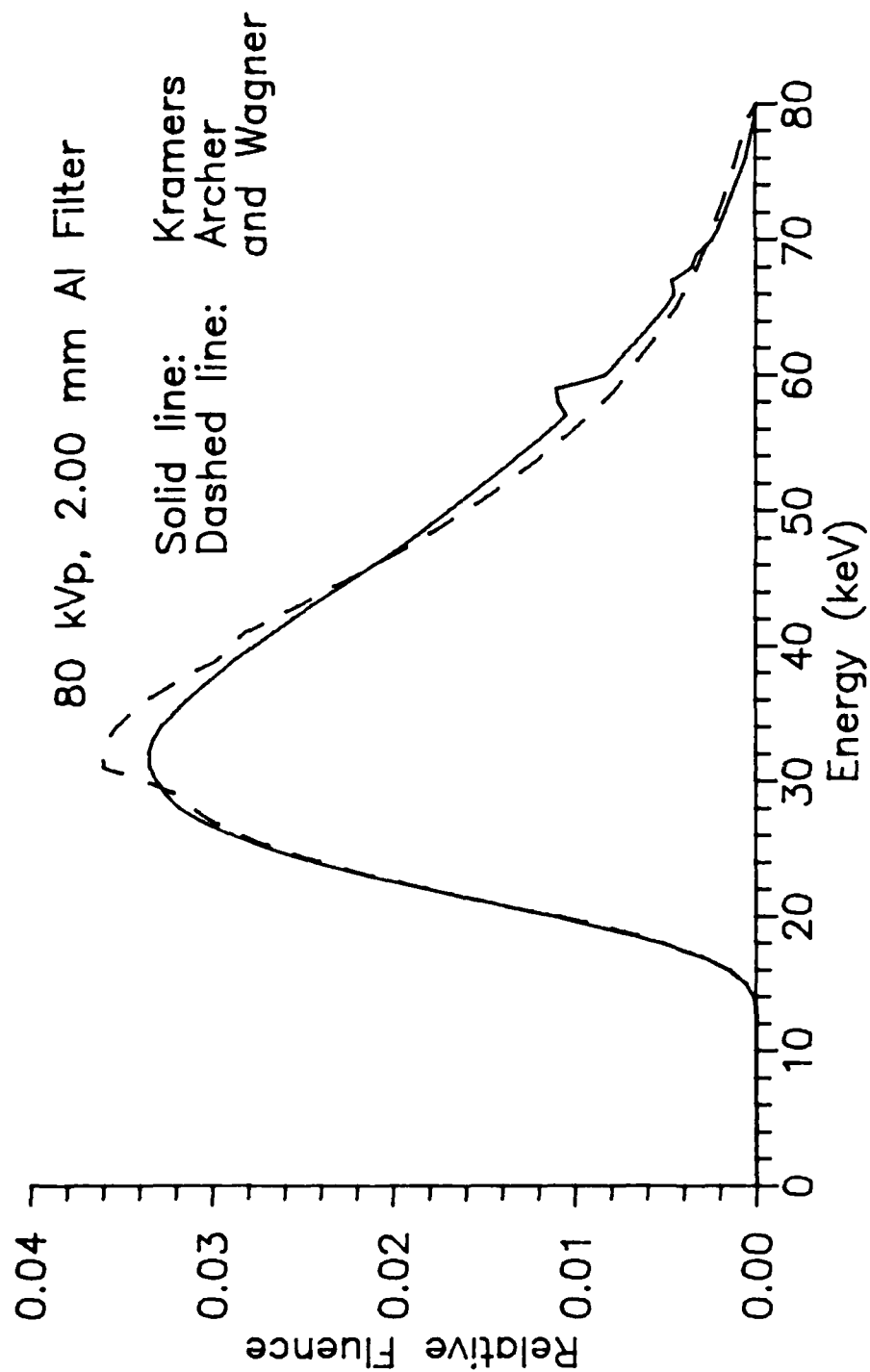


Figure V.12. Comparison of modified Kramers' method and the Archer-Wagner method at 80 kVp. A comparison of two calculated x-ray spectra for an 80 kVp beam generated by the GE Maxitron 300 X-Ray Therapy Unit with 4.75 mm beryllium inherent filtration, 2.00 mm aluminum added filtration (includes 0.25 mm aluminum equivalent monitor ionization chamber₂), and an air path length of 90.17 cm is shown. Fluence units are photons per cm² per keV. Total fluence is normalized to 1 photon per cm².

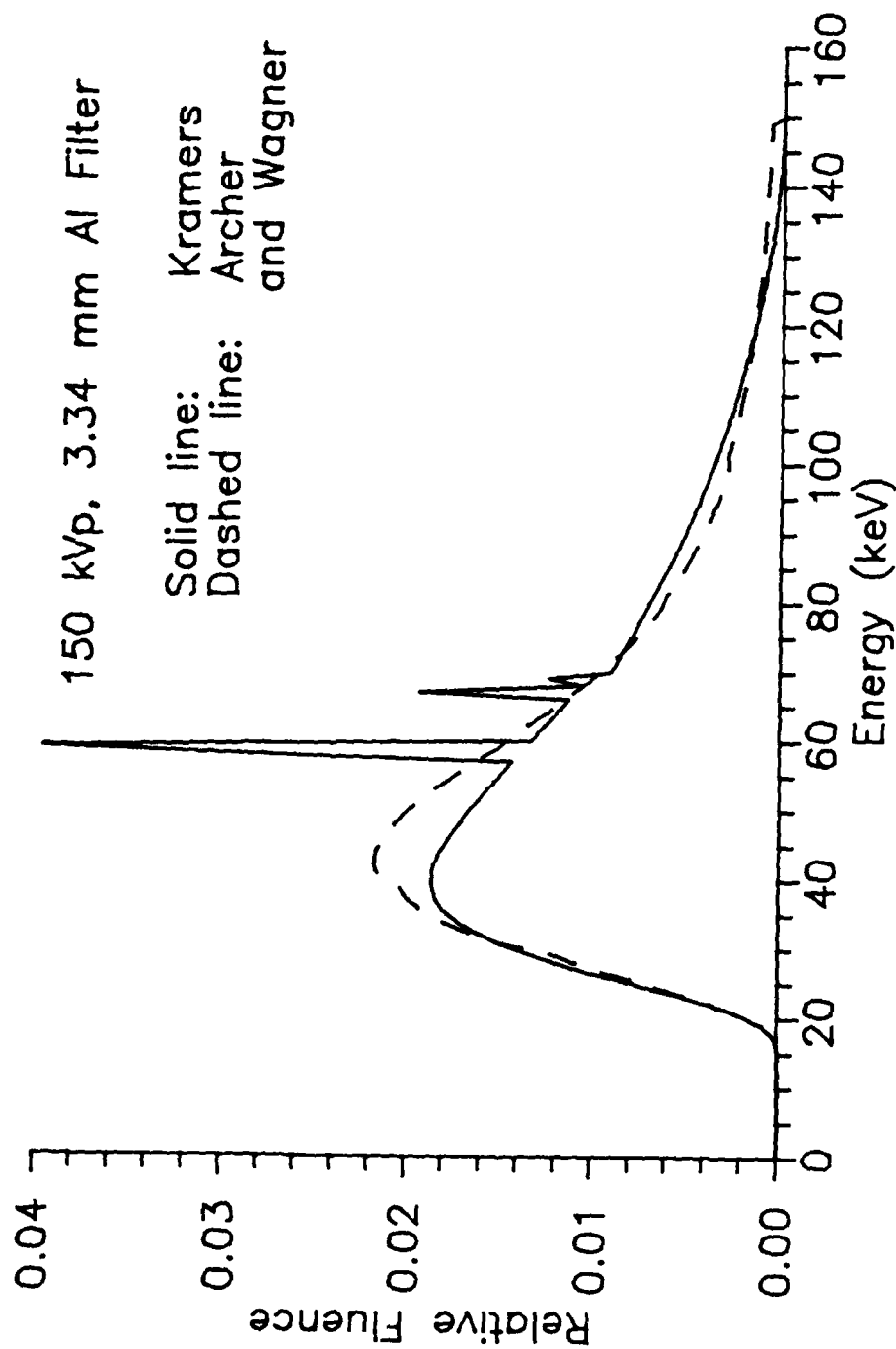


Figure V.13. Comparison of modified Kramers' method and the Archer-Wagner method at 150 kVp. A comparison of two calculated x-ray spectra for a 150 kVp beam generated by the GE Maxitron 300 X-Ray Therapy Unit with 4.75 mm beryllium inherent filtration, 3.44 mm aluminum added filtration (includes 0.25 mm aluminum equivalent monitor ionization chamber), and an air path length of 90.17 cm is shown. Fluence units are photons per cm^2 per keV. Total fluence is normalized to 1 photon per cm^2 .

technique as a part of this dissertation research effort with four K characteristic x rays failed when applied to real data. Values of the fluence for a characteristic x-ray energy are as likely to be negative (without physical meaning) as not. Conclusions regarding the limitation of the usefulness of the Archer-Wagner method to cases of little or no characteristic radiation are unchanged by the extension proposed by Rubio and Mainardi.

CHAPTER VI

DETECTOR RESPONSE

Several types of detectors have been used in the mine detection calculations. Early in the course of the work, a detector based on terbium activated gadolinium oxysulfide was constructed for measurements. For a variety of reasons described in Appendix E, this detector is judged to be unsuitable for the mine detection effort. Nevertheless, this general type of detector has some very positive features for specific detection techniques. Appendix E provides a description of this detector, its response function, and its shortcomings.

Several configurations of large area detectors similar to those envisioned in a working system have also been used in calculations. In these cases, since a detector material has not been selected, fluence response is used. These detectors are discussed in Chapter VII.

The detector employed in imaging and detection experiments is a small sodium iodide scintillation crystal. This small detector allows detailed examination of response features, which would be lost by integration in a large area detector. As a result, it also provides rigorous tests of analytical predictions. The structure of the detector and

its shield are described in detail in Chapter III. This chapter discusses the response function calculation for the detector and its validation.

Considerable work has been performed by many researchers on the detector response of NaI(Tl). The amount of research on NaI(Tl) response at the low photon energies of interest in the mine detection problem is considerably smaller than that at high energies, but is still adequate to provide checks of the computer code used in calculating the response matrix for this research. The usual application of a NaI(Tl) scintillation detector is to perform spectral measurements rather than counting, which is done in this effort. As a result, most of the validation checks available involve features of the spectral response, that is, peak ratios and shapes of energy spectra. Accordingly, these features are examined in assessing the computer code. The approach used in developing the detector response matrix is to begin with an infinite plane detector consisting of (from face towards photomultiplier) the outer aluminum can thickness, the three materials between the can and sodium iodide crystal (as explained in Chapter III, these materials, thicknesses and densities were provided by the manufacturer for the purpose of this calculation, but cannot be published because of their proprietary nature), the sodium iodide crystal, and the quartz light pipe (see Figure III.4). The response of this detector is calculated for a mesh of 24 energies, ranging from 10 to 300 keV, and 9

angles of incidence, ranging from 0 to 89.9 degrees. Ten thousand photon histories are followed for each energy/angle mesh point. A correction to this response matrix is then calculated for the effect of the shield and edge leakage for the same energy/angle mesh.

Plane Detector Code

The plane detector response is calculated by the DETNAI.P code, written in Green Hills Pascal (Green Hills Software, 1984) and implemented on the DSI-32 coprocessor (Marshall et al., 1985). Cross sections for all materials are calculated for a fine energy mesh by cubic spline interpolation of data by Hubbell et al. (1975), Hubbell (1982), and Storm and Israel (1970) when detailed information concerning photoelectric edge effects is required. Full coherent, incoherent and photoelectric interactions, including fluorescent emission from iodine are included. The atomic form factors and incoherent scattering factors are from Hubbell (1975). Implementation of the coherent scattering routine is based on the techniques of Carter and Cashwell (1977), and Williamson and Morin (1983a, 1983b). Implementation of the incoherent scattering routine is also based on the recommendations of Carter and Cashwell (1977), utilizing the Kahn method (1956) for sampling the Klein-Nishina relationship as a first step in the technique. The atomic fluorescent yield of iodine is from Bambynek et al. (1972). Four iodine fluorescent emission K x rays and one L x ray are allowed, in accordance with the recommendations of

Carter and Cashwell (1977). Secondary L fluorescence following $K_{\alpha 1}$ or $K_{\alpha 2}$ emission is also allowed. Table VI.1 provides the energies of these fluorescent x rays.

The response function calculation for the gadolinium oxysulfide detector (Appendix E) is primarily concerned with the gross amount of energy deposited in the phosphor layer by x-ray photon interactions in the phosphor, which is then converted to light photons. Because of the faster response time of NaI(Tl), it is the sum of the energies of all the interactions of a single x-ray photon and its progeny, which are deposited in the crystal, that is of importance. For each photon, this sum is compared to the energy corresponding to the lower level discriminator setting of the counting system. Only if the energy deposited in the NaI(Tl) exceeds the discriminator energy is a count recorded. The response is the number of counts per incident photon at a given energy and angle of incidence as opposed to the amount of energy deposited per incident photon at a given energy and angle of incidence in the case of the gadolinium oxysulfide based detector. The DETNAI.P code calculates this response for nine discriminator settings ranging from 0 to 45 keV. A derivative of the DETNAI.P code, NAISPEC.PAS, computes the spectrum of energies deposited in the NaI(Tl) crystal.

TABLE VI.1

Energies of Iodine Fluorescent Emission X Rays
Used in the Detector Response Calculations

X Ray	Energy (keV)
Weighted average of 3 L x rays	4.206
$K_{\alpha 1}$	28.613
$K_{\alpha 2}$	28.318
$K_{\beta 1}'$: weighted average of M2, M3, M4 to K transitions	32.276
$K_{\beta 2}'$: weighted average of N2, N3 to K transitions	33.041

Assumptions in the Plane Detector
Response Calculation

Knoll (1979) addresses a number of complications in calculations of response functions for NaI(Tl) detectors. These complications are described below, along with the assumptions used for handling them in this research and their rationale.

In any energy deposition event, photon energy is converted to kinetic energy of electrons (and the energy required to overcome electron binding, which is generally negligible for x-ray photons). It is the kinetic energy of electrons which ultimately produces the visible light photons which strike the photocathode of the photomultiplier tube and begin the process of producing a voltage pulse. If the ranges of these secondary electrons are large with respect to the crystal dimensions, a significant fraction would leak out of the crystal without having their energies absorbed. This effect is ignored in the DETNAI.P calculations because of the very short ranges of secondary electrons produced by low energy photons. The effect is important only for high energy gamma rays which produce high energy secondary electrons. The effect of electron escape at these energies is unimportant (Berger and Seltzer, 1972).

Bremsstrahlung radiation is produced when charged particles are accelerated in an electric field (the same process producing the continuous portion of the x-ray spectrum in an anode of the x-ray tube). In the NaI(Tl)

crystal, the charged particles of interest are again the secondary electrons described above, and the electric field is primarily that of the nuclei of iodine atoms. In the energy range of interest in the mine detection problem, the probability of producing bremsstrahlung photons is small. Any bremsstrahlung produced would be of very low energy resulting in rapid local reabsorption. For these reasons, bremsstrahlung escape is not considered in the detector response calculations of the DETNAI.P code.

Fluorescent emissions following photoelectric interactions near the surface of the NaI(Tl) crystal may escape the crystal. This effect is included in the DETNAI.P code (and in NAISPEC.PAS). It plays an important role in the shape of the response function and serves as a method for checking the response calculations against published values of the iodine escape ratio (described below). This effect is more important for low energy photons (above the K edge of iodine) because high photoelectric cross sections make interactions near the surface of the crystal and the subsequent fluorescent escape more probable.

Scatter of source photons from surrounding materials will obviously effect the detector response if not accounted for. Shielding the head of the x-ray machine and the sides of the detector reduces this effect. The DETNAI.P code assumes no scatter off of surrounding materials. As is described in Chapter VIII, the initial problem in reconciling measured and calculated response was determined to be caused

by scatter of head leakage photons. The detector response calculation played the key role in identifying this previously unnoticed scatter path.

If two pulses arrive during the resolving time of the detector, the sum of the pulses will be detected, resulting in a single count at an incorrect energy. This is avoided by measuring at count rates where such sum events are improbable. One of the criteria for selection of the energy/filtration combinations being used is to avoid high count rate situations.

Energy Deposition

As explained above, gross energy deposition is not the primary quantity of interest in NaI(Tl) response. It is, however, instructive to examine the energy absorption process to obtain a better physical feel for the nature of the interactions occurring in the detection process.

Case of Zero Degree Incidence

Figure VI.1 shows the fraction of the incident photon energy absorbed in the NaI(Tl) crystal as a function of incident photon energy for the case of 0 degree incidence on the outer aluminum layer of the detector. The shape of the curve is explained by examining the photon interaction characteristics of the crystal.

At low energy the fraction of incident energy absorbed is low due to absorption of photons in the material layers in front of the crystal. As incident energy increases, more photons are capable of penetrating the front layers and

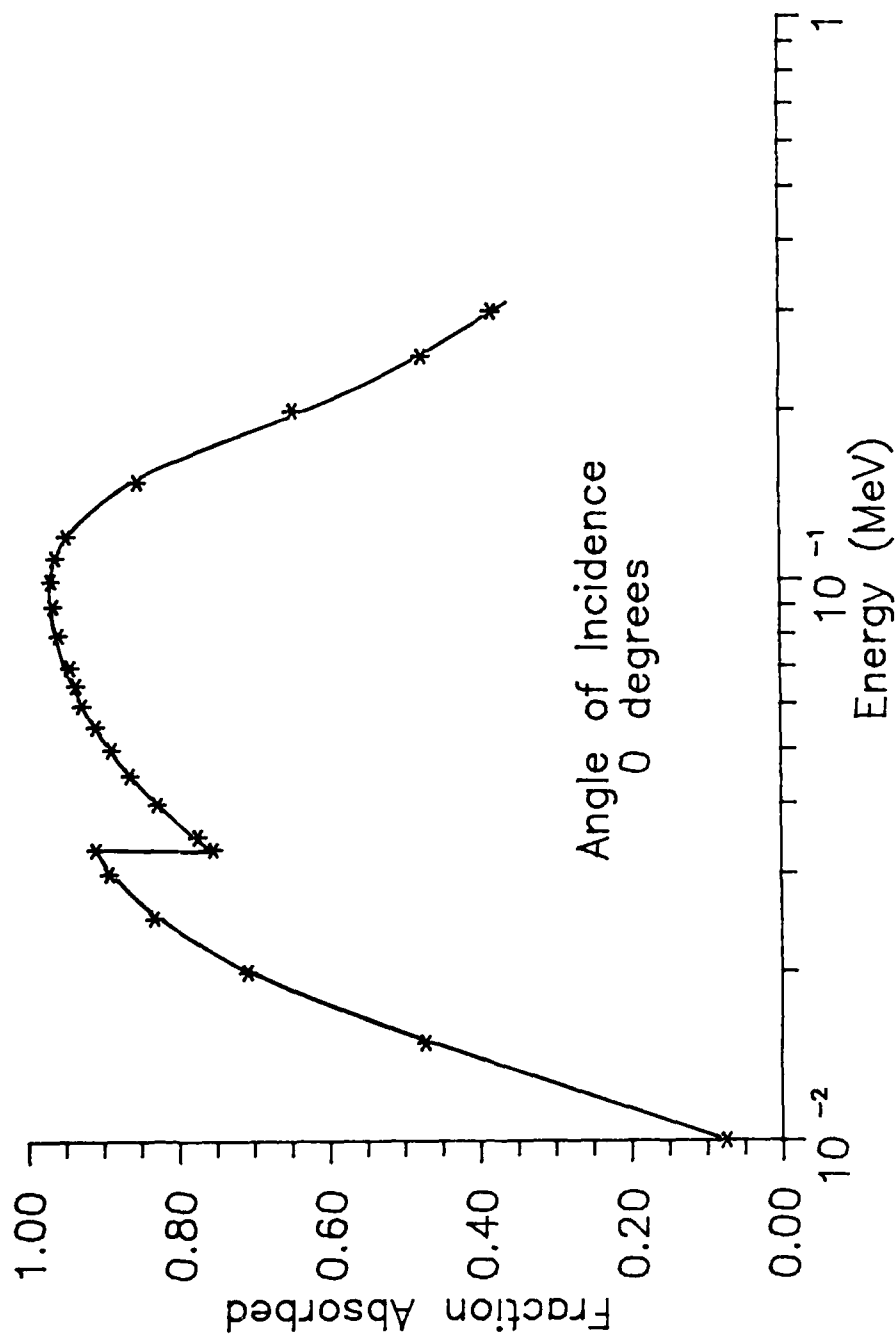


Figure VI.1. Fraction of incident energy absorbed, perpendicular incidence. The calculated fraction of incident photon energy absorbed in the NaI(Tl) crystal of a plane model of a Bicron Model .5M.39Q/.5L-X detector for the case of zero degree incidence is shown. Calculations were performed by the DETNAI.P Monte Carlo code.

reaching the NaI(Tl) crystal, resulting in an increase in the fraction of energy absorbed in the crystal.

At the K edge of iodine (0.03317 MeV), there is a discontinuous decrease in the fraction of energy absorbed in the NaI(Tl) crystal. Below this energy, incident photons are unable to remove K shell electrons in iodine; above it, they are. The removal of a K shell electron is frequently followed by emission of a K fluorescent x ray (radiationless Auger electron emission is also possible). The decrease in the fraction of energy absorbed in the crystal at the K edge energy is caused by the escape of these iodine K fluorescent x rays from front surface of the crystal.

Above the K edge, the absorbed fraction increases to a maximum at about 0.100 MeV. This increase is due primarily to the increasing depth of penetration of the incident photons. The deeper into the NaI(Tl) crystal that photons interact, the more difficult it is for the K fluorescent x rays to escape the crystal. As depth of penetration increases, they are reabsorbed in the crystal with increasing efficiency. A secondary mechanism for the increase in absorbed fraction is the enhanced capability for penetration of the material layers in front of the crystal.

As incident energy increases above the peak at approximately 0.100 MeV, there is a decrease in the absorbed fraction. This is primarily a result of transmission of photons through the crystal without interaction and small angle (forward) Compton scattering events in which the scattered

photon escapes the rear of the crystal, depositing only a small fraction of its original energy. These transmission losses are moderated somewhat by backscatter into the crystal from the quartz light pipe located on the back side of the crystal.

Case of Large Angle Incidence.

The Figure VI.2 shows the fraction of incident energy absorbed within the NaI(Tl) crystal for photons incident at 75 degrees. The general shape of the curve remains similar to that of the zero degree incidence case. Differences between the cases are again explained by examining the physical processes occurring within the detector. In the low energy region, the fraction absorbed in the crystal is much reduced as compared to the zero degree incidence case. This is primarily caused by the much higher absorption of energy in the material layers in front of the crystal, which is a result of the long slant paths through these materials. A secondary cause is a greater fraction of the incident photons being backscattered from these layers without reaching the NaI(Tl) crystal.

The effect at the iodine K edge has the same explanation as in the zero degree incidence case. Above the K edge, the two factors discussed in the zero degree incidence case are both again present, although the increased penetration of the layer in front of the crystal plays a much larger role for the large angle of incidence case.

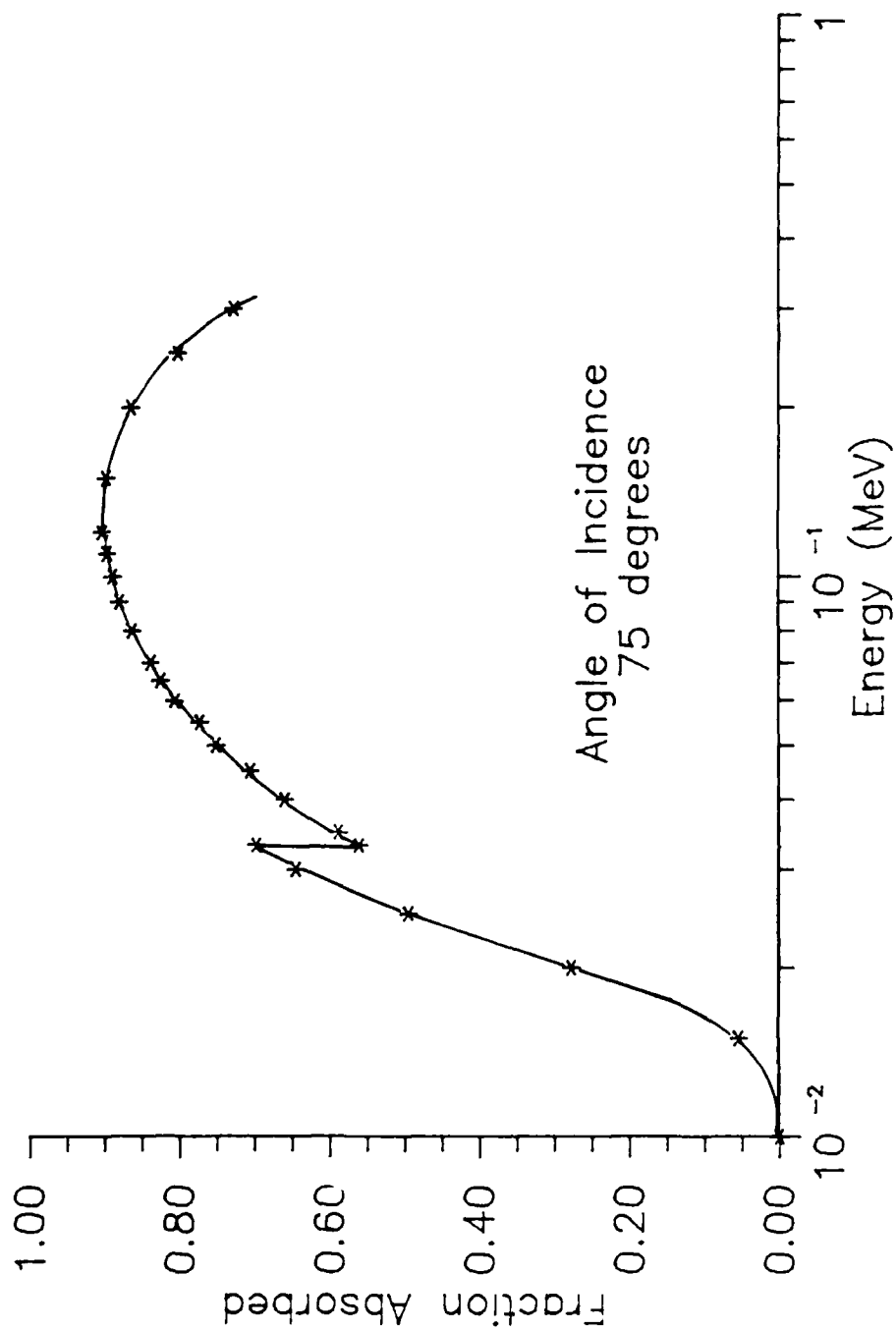


Figure VI.2. Fraction of incident energy absorbed, 75 degree incidence. The calculated fraction of incident photon energy absorbed in the NaI(Tl) crystal of a plane model of a Bicron Model .5M.39Q/.5L-X detector for the case of 75 degree incidence is shown. Calculations were performed by the DETNAI.P Monte Carlo code.

At high energies, the decrease in fraction absorbed is much less than in the zero degree incidence case. This is a result of the much thicker NaI(Tl) layer seen by an uncollided photon (long slant path through the crystal). Few, if any, photons are transmitted through the crystal without interaction. The primary transmission mechanism becomes Compton scatter.

Counts Per Incident Photon

As described above, it is not the gross energy absorbed which determines the number of counts recorded, but the total energy absorbed in the crystal as a result of all interactions of each individual incident photon and its progeny. A further modification to the number of counts recorded is the setting of the lower level discriminator. Figure VI.3 shows the response of the plane detector in counts per incident photon striking the outer case of the detector for two discriminator level settings corresponding to 0 and 0.025 MeV.

Discriminator Setting Corresponding to 0 MeV

This discriminator setting results in a count being recorded for any energy depositing photon event occurring in the crystal. The effect of the iodine K edge, so prominent in the energy deposition curves, is removed by this criterion. Any deviation from a value of 1.00 counts per incident photon is a result of photons completely missing the crystal or undergoing only coherent interactions in the crystal. Several mechanisms are responsible for such misses.

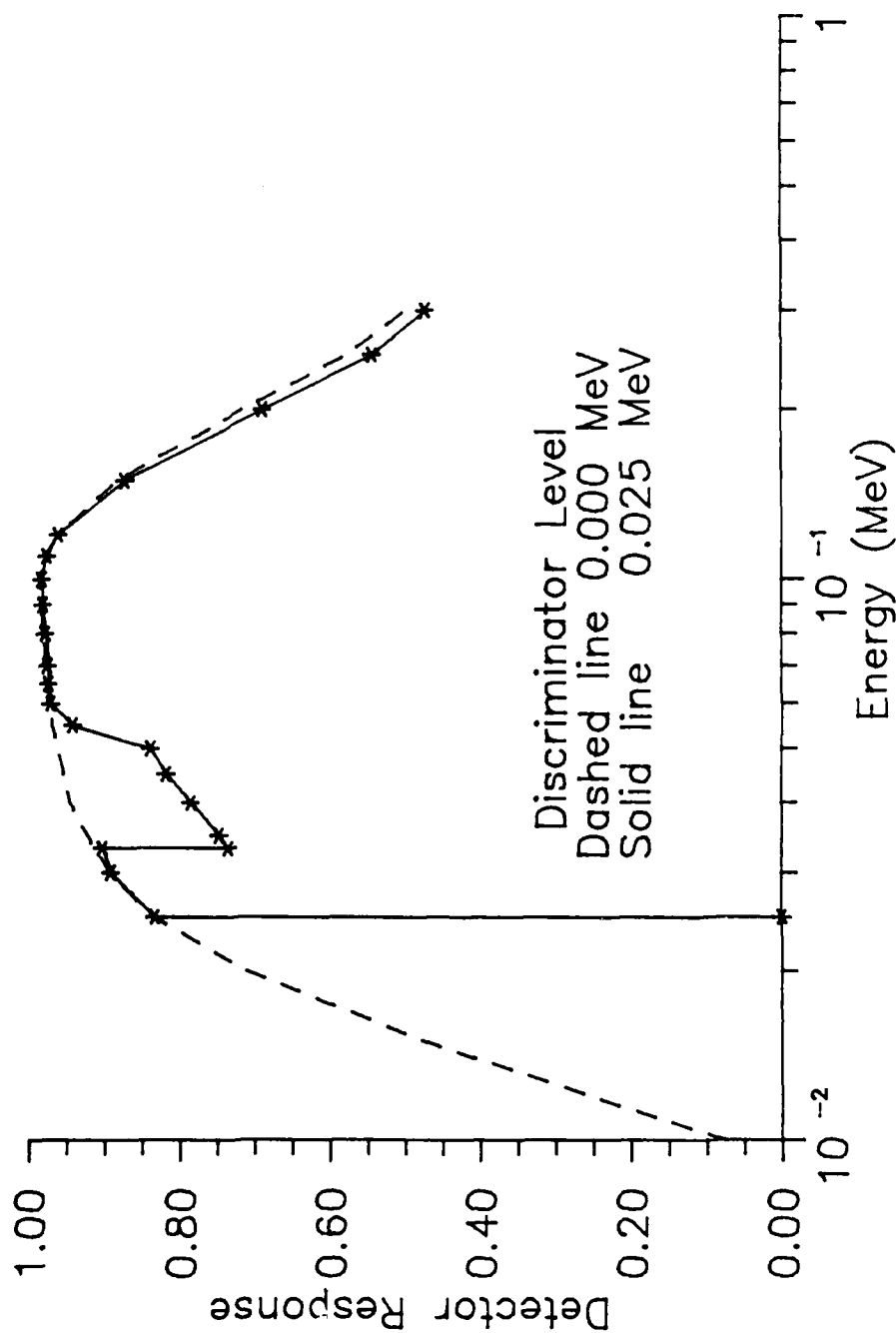


Figure VI.3. Plane detector response, discrimination less than 0.03317 MeV. The calculated detector response (number of counts per incident photon striking the detector) for the case of perpendicular incidence on a plane model of a Bicron Model .5M.39Q/.5L-X detector is shown. The calculation was performed by the DETNAI.P Monte Carlo code for the cases of lower level discriminator settings corresponding to 0.000 and 0.025 MeV.

Complete absorption of the photon energy in a single event in the material layers in front of the crystal is the primary reason for the low response at low energy. It is caused by photoelectric interactions. Partial absorption of the photon energy in the material layers in front of the crystal with subsequent scatter away from the crystal or absorption in non-crystal layers also does not produce a count. The initial interaction is a Compton scattering event. This series of interactions occurs at all photon energies, having its largest effect at higher energies and large angles of incidence. Coherent interactions with any part of the detector followed by transmission through the crystal, scatter away from the crystal, or absorption in non-crystal layers also produce a miss. This effect is more likely at lower incident photon energies. Transmission without interaction through the crystal is the primary cause for the decrease in response at high energy.

Discriminator Level Setting Corresponding to Energies Greater Than 0 MeV.

At first consideration, it might be thought that the effect of any discriminator setting would be simply to remove all energy deposition events below that setting from contributing to the counts recorded. The effect, however, extends beyond the energy corresponding to the discriminator setting. Two manifestations of the extended effect are possible, dependent upon whether the discriminator level corresponds to an energy above or below the K edge of iodine.

Figure VI.3 also displays the detector response versus incident energy for a discriminator setting (0.025 MeV) below the iodine K edge (0.03317 MeV). Below the energy corresponding to the discriminator level setting (0.025 MeV, in this example), there is no response as would be expected by the definition of the purpose of the discrimination process. Between the discriminator setting and the K edge, the response closely resembles that of the no discrimination case. It is actually very slightly smaller as a result of Compton interactions which deposit less than 0.025 MeV in the crystal and then scatter out of the crystal. The incoherent cross section is low at these energies in comparison with the cross section for photoelectric interaction, so these events are relatively rare.

Above the K edge energy, there is a "notch" in the response curve. This "notch" is a result of photoelectric events in the crystal which are followed by the emission and escape of iodine K fluorescent x rays. In this region of the curve, for such events, the total energy deposited by an incident photon in the NaI(Tl) crystal is less than that required by the discriminator setting and no count is recorded. Eventually, an incident photon energy is reached at which the energy deposited in the crystal exceeds that required by the discriminator setting regardless of whether a fluorescent photon escapes or not. When this occurs the response curve once again becomes very similar to that of the case of no discrimination. In actuality, the transition

back to the response curve without discrimination is a staircase because several different K fluorescent photons are emitted by iodine. The transition energies are easily calculated by simply adding the various K x ray energies to the energy corresponding to the discriminator level setting. In this example, the transition energies are 0.053318, 0.053613, 0.057276, and 0.058041 MeV.

At high energies, the detector response deviates slightly, but noticeably from the no discrimination case. This deviation is caused by Compton scattering events in the crystal which deposit less than the energy required by the discriminator level setting and then scatter out of the crystal. These events are much more probable at higher energies where the incoherent cross section is large relative to the cross section for photoelectric interaction.

Figure VI.4 compares the response curve for perpendicular incidence on the plane detector with discriminator settings of 0 and 0.035 MeV. A major difference from the case with a discriminator setting corresponding to energies less than the K edge energy of iodine is apparent: the low energy edge of the "notch" is missing. This is because even the lowest energy photon, capable of recording a count, is also capable of emitting iodine K fluorescent x rays. The transition energies back to (approximately) the response curve without discrimination are now shifted to higher energies: 0.063318, 0.063613, 0.067276, and 0.068041 MeV.

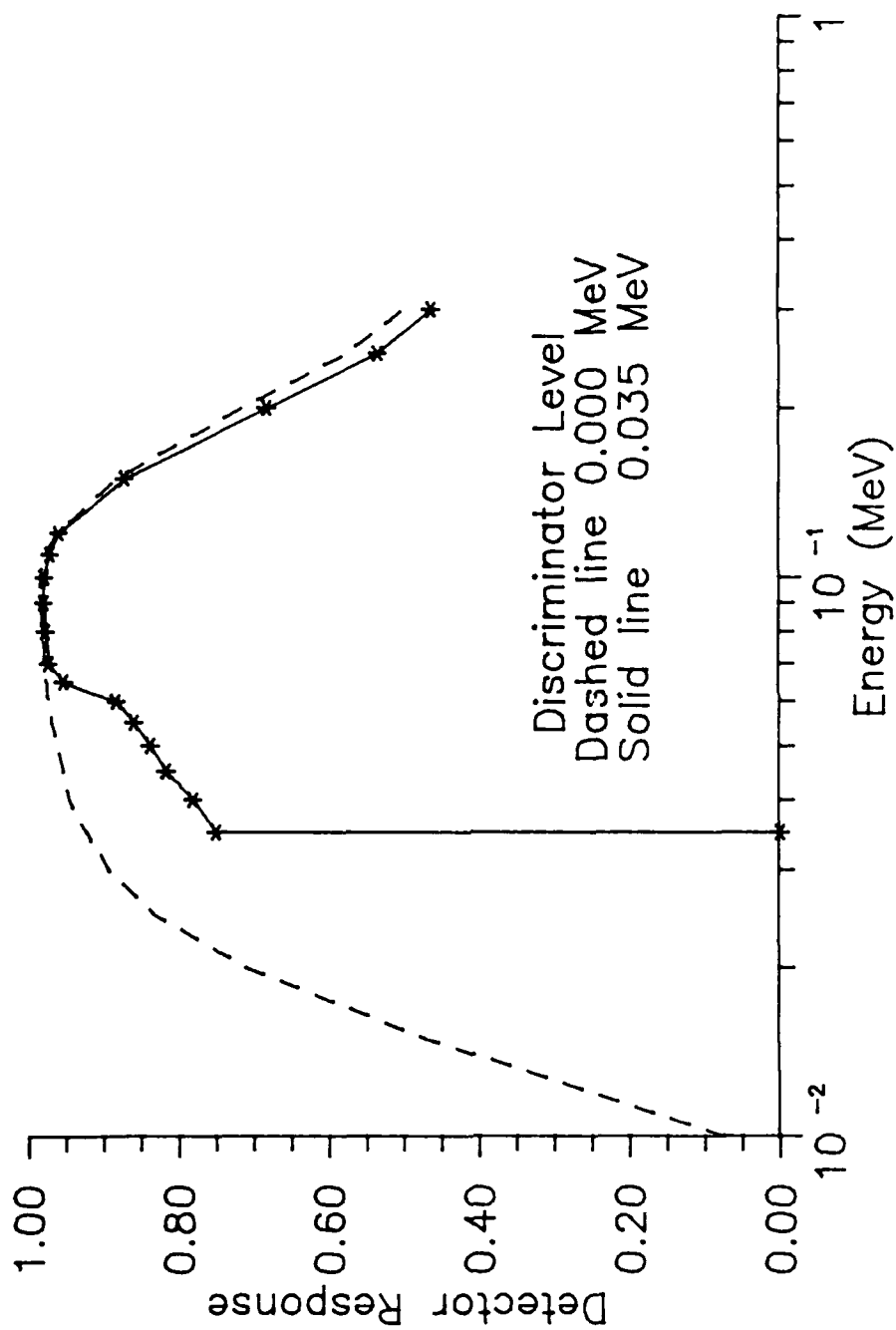


Figure VI.4. Plane detector response, discrimination greater than 0.03317 MeV. The calculated detector response (number of counts per incident photon striking the detector) for the case of perpendicular incidence on a plane model of a Bicron Model .5M.39Q/.5L-X detector is shown. Calculations were performed by the DETNAI.P Monte Carlo code for the cases of lower level discriminator settings corresponding to 0.000 and 0.035 MeV.

Validation of the Plane Detector Response Calculations

Published measurements and calculations are used to verify the detector response calculations.

Iodine Escape Ratio

A number of researchers have made calculations and measurements of the iodine escape ratio for NaI(Tl). In a NaI(Tl) energy spectrum, this is the ratio of the area under the iodine K fluorescent x ray escape peak to that of the full energy deposition peak (often referred to as the photo-peak). Counts falling within the iodine escape peak are a result of photons having photoelectric interactions within the NaI(Tl) crystal after which iodine K fluorescent photons escape the crystal. The iodine escape peak is actually composed of the several peaks because several different energy iodine K x rays are emitted and can escape. The energies of these peaks are simply the energy of the incident photon (which is equal to the energy of the full energy deposition peak) minus the energy of the escaping x rays. Because of the relatively poor resolution of NaI(Tl), these individual escape peaks are smeared into a single peak in any real energy spectrum measurement.

Figure VI.5 compares calculations of the NAISPEC.PAS code to two other sets of Monte Carlo calculations of the iodine escape peak ratio (Dell and Ebert, 1969; Sharma et al., 1972). Those two sets of calculations have been found to compare well to measurements of the iodine escape ratio.

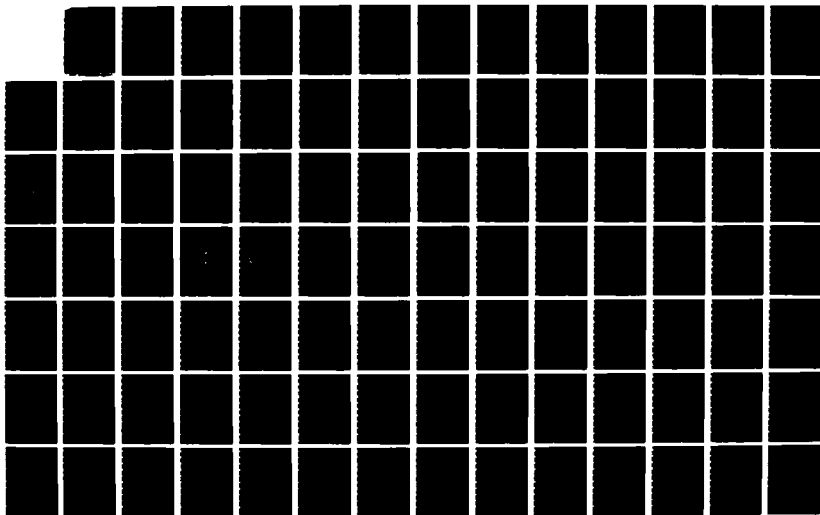
AD-A182 227

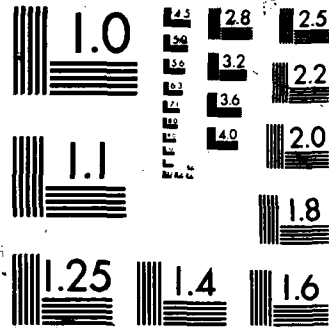
LANDMINE DETECTION BY SCATTER RADIATION RADIOGRAPHY(U)
ARMY MILITARY PERSONNEL CENTER ALEXANDRIA VA
J G CAMPBELL 02 JUL 87

3/6

UNCLASSIFIED

F/G 15/6 6 NL





XEROCOPY RESOLUTION TEST CHART

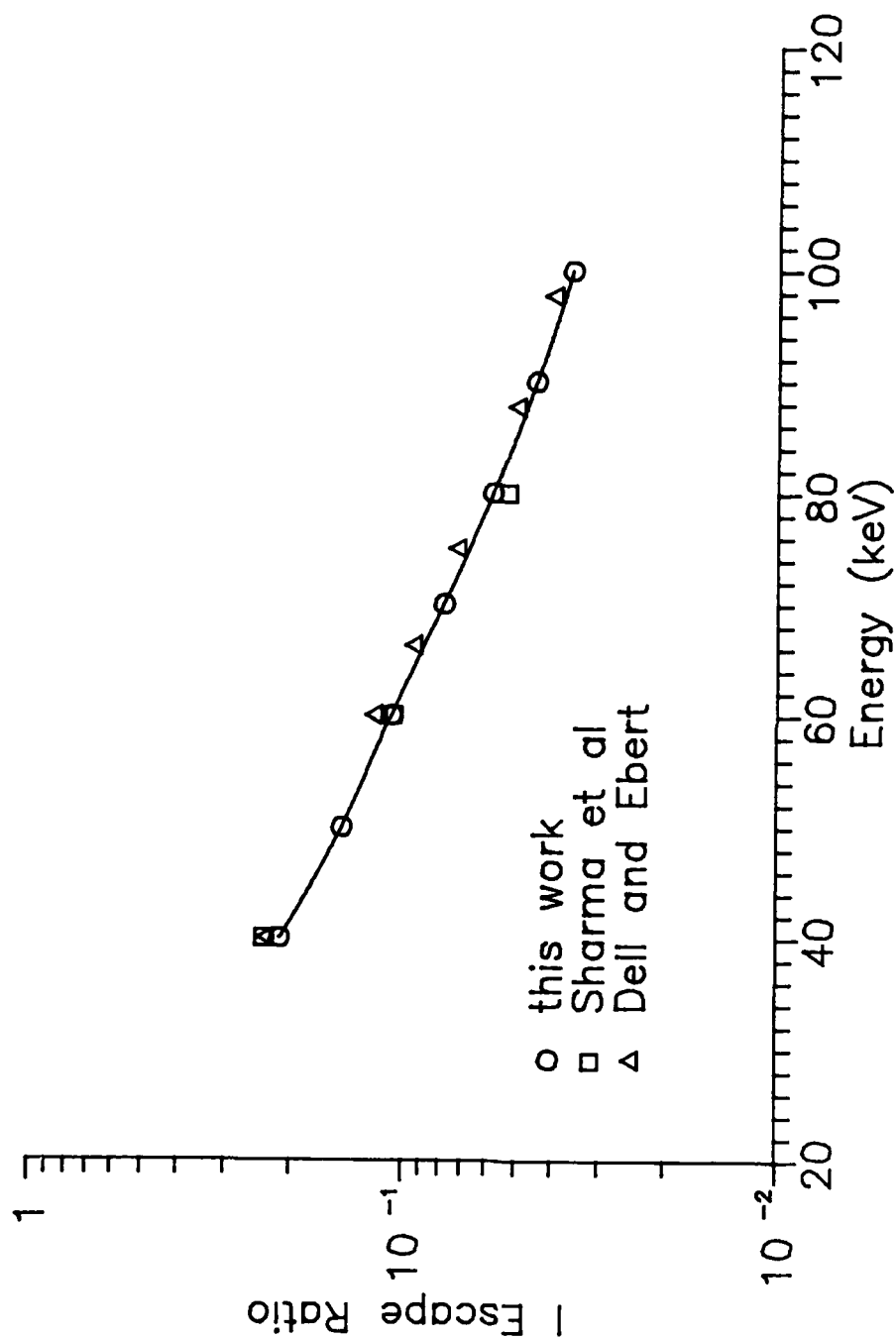


Figure VI.5. Iodine escape peak ratio versus energy. A comparison of Monte Carlo calculations of the iodine escape peak ratio for perpendicular incidence on NaI(Tl) as a function of incident photon energy is shown. The results of Dell and Ebert (1969), Sharma et al. (1972), and the NAISPEC.PAS codes are compared.

ratio. Calculations performed for this comparison modelled the detector used by Dell and Ebert (1969) in the experimental portion of their work. This detector consisted of a 2.5 cm (diameter) by 2.5 cm (thickness) NaI(Tl) crystal with a 0.013 cm beryllium window. All photon beams were tightly collimated, small in diameter and incident perpendicularly on the center of the face of the detector. These conditions, combined with the low energies of the photons used (40 to 100 keV), make scatter out of the crystal negligible. Therefore, a plane detector approximation for calculation purposes is acceptable. As shown in Figure VI.5, the NAISPEC.PAS calculations agree well with these other efforts. The discrepancies which exist are a result of differences in the basic data, assumptions, and techniques used in the calculations. The Sharma paper provides an excellent discussion of the calculation techniques they used; the Dell and Ebert calculations are poorly documented, but are probably very similar in nature to those of Sharma et al. The effect of the various differences are in some instances to increase, and others to decrease the iodine escape ratio.

Sharma et al. assume a bare NaI(Tl) crystal suspended in vacuum. The NAISPEC.PAS code models the beryllium wall suspended in air. The effect of the presence of a low atomic number material wall is to produce incoherent scatterers which alter photon directions producing interactions, on the average, closer to the surface of the NaI(Tl) crystal

(if the photons reach the crystal) and result in a greater probability of escape of K fluorescent x rays. Actually, the situation is more complicated since multiple incoherent scatters can reduce the photon energy below the K edge energy and thereby prevent the possibility of fluorescent photon emission. This effect is more important for photon energies not much greater than the iodine K edge energy.

Coherent scattering is not modelled in the Sharma calculations. Full coherent scattering with angular distributions based on the atomic form factors of Hubbell et al. (1975) is included in the NAISPEC.PAS model. Full coherent scattering will alter directions of the interacting photons, and for the reasons discussed in the paragraph above will increase the escape ratio.

The calculations of Sharma et al. use only the Klein-Nishina relationship to model the angular distribution of the scatter after a Compton event. Full incoherent scattering with angular distributions of the scattered photons modified by the incoherent scattering functions of Hubbell et al. (1975) is included in the NAISPEC.PAS code. Lower incoherent interaction rates are the result of lower cross sections. This will lower the escape ratio for the reasons discussed above.

The K fluorescent yield is the total probability of fluorescent emission following electron transition to a vacancy in the K shell. Sharma et al. use a value of 0.91 from Fink et al. (1966). The most current value, which is

used in the NAISPEC.PAS and DETNAI.PAS codes is 0.882 (Bambynek et al., 1972; Lederer and Shirley, 1978). For the NAISPEC.PAS code, this results in a larger full energy deposition peak, and, hence, a lower iodine escape ratio.

The model of Sharma et al. lumps all K fluorescent photons into a single energy (that of the most probable photon, the $K_{\alpha 1}$) and does not model L x ray emission (it follows that no secondary emission after $K_{\alpha 1}$ or $K_{\alpha 2}$ emission is modelled either). The NAISPEC.PAS code allows for four individual K x ray energies, and L x ray emission, including secondary L emission after K emission. The second most probable K x ray photon is the $K_{\alpha 2}$ which is lower in energy than the $K_{\alpha 1}$. The average K x ray is less capable of escaping the crystal and will result in a lower escape ratio.

The calculations of Sharma et al. assume any interaction of a K x ray photon is an absorption. (Dell and Ebert do not make this assumption). The NAISPEC.PAS makes no assumption about how a K x ray will interact; its history is followed until it is absorbed. This means that a photon arising from a Compton scatter of a K x ray could escape the crystal, increasing the escape ratio.

In the calculations of Sharma et al. any history of a photon whose energy falls below 10 keV is terminated. There is no termination of any history in the NAISPEC.PAS code based on an energy cutoff. The lack of a cutoff allows additional chances for very low energy photons to escape the crystal, increasing the escape ratio.

Sharma et al. use the mass interaction coefficient data of Grodstein (1957). The NAISPEC.PAS code uses the most current published interaction data (Hubbell et al., 1975; Hubbell, 1982; Storm and Israel, 1970). The incoherent interaction coefficients in the Grodstein data are simply calculated from the Klein-Nishina relationship. As a result they are too high at low energies. Additionally, below 40 keV, the photoelectric data of Grodstein is very poor (15 to 20% low). The correct (lower) incoherent data will reduce the escape ratio. The correct photoelectric data (higher) will increase the escape ratio.

The model of Sharma et al. uses the broad energy mesh of the Grodstein tables (14 energies between 10 and 300 keV) and employs linear interpolation to obtain other values. The NAISPEC.PAS code uses a fine mesh table constructed from a cubic spline interpolation of the more modern data (183 energies between 1 and 300 keV), and uses log-log interpolation to obtain other values. Linear interpolation overestimates the photoelectric interaction data in a coarse mesh table leading to interactions nearer the crystal surface. The more accurate procedure of the NAISPEC.PAS code will, therefore, lower the escape ratio.

The calculations of Sharma et al. are based on 10000 photon histories; the NAISPEC.PAS calculations are based on 50000 photon histories. The number of histories by itself has no effect on the value of the escape ratio, but on how precisely it is calculated.

Measured Energy Spectra

Figure VI.6 compares an energy spectrum measurement made by Dell and Ebert (1969) as part of their iodine escape work. The calculated energy spectrum is from the NAISPEC. PAS code and employs a gaussian distribution to smear the discrete energies calculated into the resolution of the NaI(Tl) crystal employed in the measurements. Assumptions on the variation of resolution with energy are from Berger and Seltzer (1972). Agreement between the measured and calculated spectra is seen to be good.

Shield and Edge Effects

The plane detector response described above is adjusted for two types of photon events, which occur in the real detector, but not in the plane model. These effects are caused by photons which penetrate the detector shield, enter the side wall, and deposit energy in the NaI(Tl) crystal, increasing the observed count rate above that which is predicted by the plane detector response calculations; and photons, which enter the bottom face of the detector and exit the side wall of the detector without depositing sufficient energy to produce a count, decreasing the observed count rate predicted by the plane detector response calculations.

Calculation of the Correction Factor

A computer code DETCOR.PAS was written in Turbo Pascal (Borland, 1985) to make a first order approximation of the correction factor at each energy/angle mesh point in the

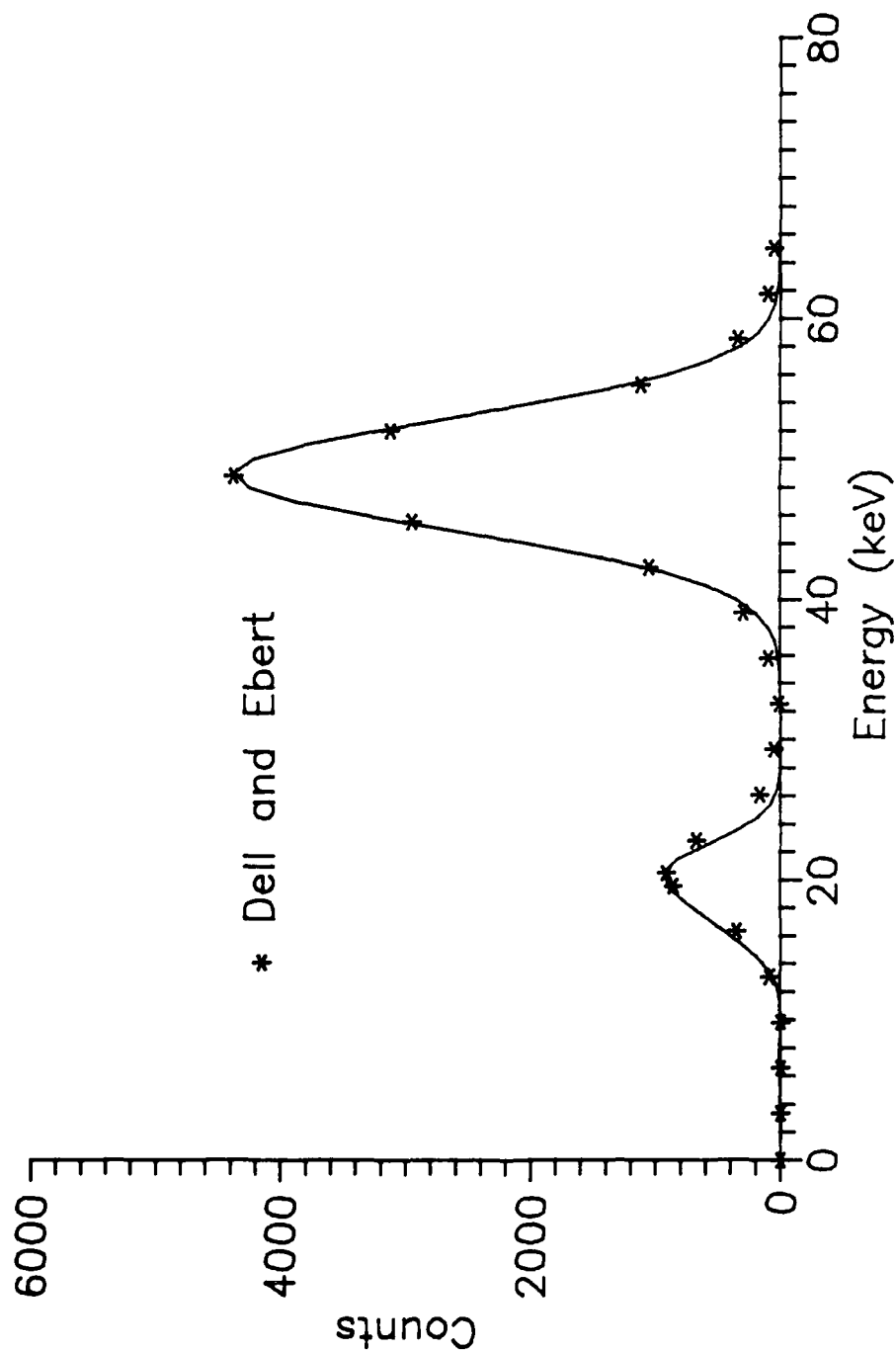


Figure VI.6. Measured and calculated NaI(Tl) spectra. A comparison of calculated NaI(Tl) spectra due to perpendicularly incident K_{α} x rays of erbium on a 2.5 cm thick crystal with a 0.013 cm thick beryllium window is shown. Measured values from Dell and Ebert (1969) and calculated values from the NAISPEC.PAS code are normalized at the maximum value of the full energy deposition peak (photopeak).

plane detector response matrix. A full correction would require a complete Monte Carlo calculation of the entire process from source through detector system for each detector position. Such calculations would be essentially impossible to perform for the range of calculations required. The small size of the detector being used merely increases the problem by requiring large numbers of photon histories to be followed to approach reasonable statistics. As will be seen in comparisons of calculations and measurements in Chapter VIII, the first order correction appears to be adequate for the problem. The DETCOR.PAS code models the full detector and shield system in three dimensions. All layers, including air spaces, are included (see Table III.1 for dimensions). Each energy/angle correction calculation entails a two-dimensional plane wave of photons, all of a given energy and angle of incidence, impinging on the space surrounding and occupied by the detector. Approximately 12000 photons with a spacing of 0.02 cm between adjacent photons in the incident plane wave, are individually attenuated through the three dimensional structure of the shield and detector to determine each photon's probability of interaction within the NaI(Tl) crystal. This probability is summed for all of the photons and compared to the same quantity for a plane detector case with entrance restricted to the size of the face of the detector. The ratio of these two probabilities is the first order correction factor. Mass attenuation coefficients for all the materials in the

calculation do not include coherent scattering, since these events do not deposit energy and, generally, do not greatly change the direction of travel of a photon. The model implicitly assumes that the variation in fluence over the size of the detector is small, which is a good approximation for the small detector being used.

Results of the Correction Factor Calculations

Results of the calculations show that except at high energies (200 keV or greater), the effect of photons penetrating the shield into the side of the crystal outweighs that of photons leaking through the side wall of the crystal, making the correction factor a number greater than 1.00. The reason for this phenomenon is twofold. Photons in the low energy range under consideration are very rapidly attenuated by the NaI(Tl) crystal, reducing the impact of leakage to only those photons which strike very close to the bottom edge of the crystal. The protrusion (see Figure III.1) of the detector face below the shield (to avoid collimation), combined with the layer of low atomic number material, which is packed around the sides of the crystal within the aluminum housing (proprietary material), plays a significant role. This side region is relatively poorly shielded and allows significant numbers of photons to penetrate into NaI(Tl) crystal through the side wall. Figure VI.7 and VI.8 display, respectively, the plane detector response function and the result of correcting it for shield and edge effects.

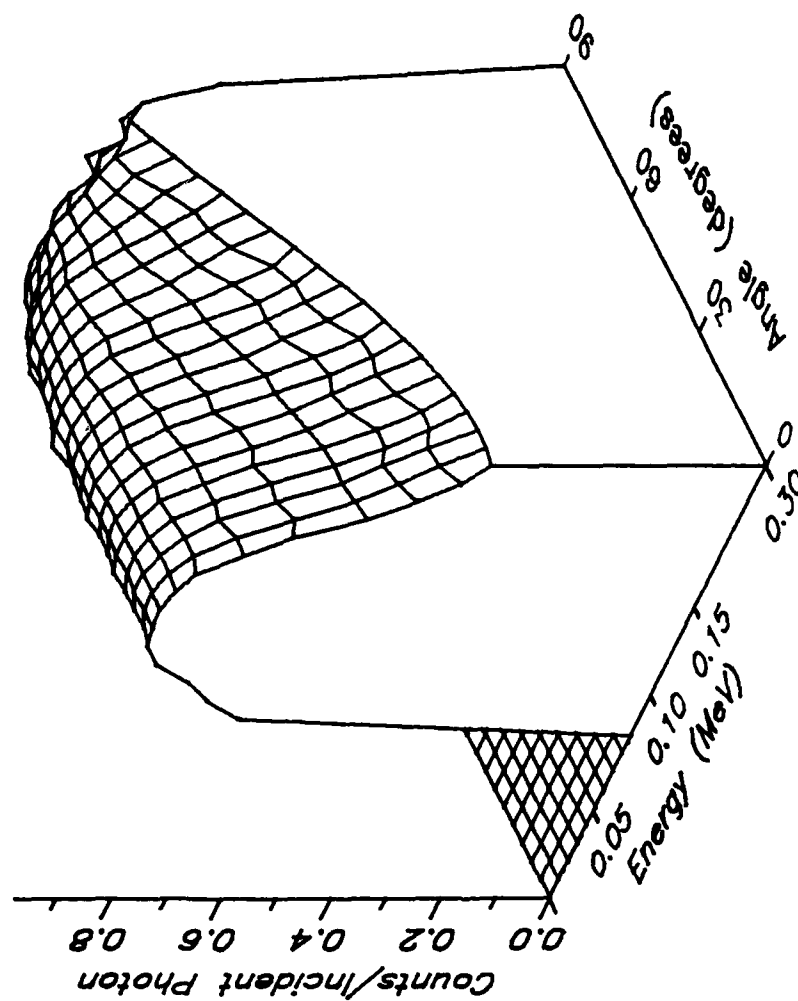


Figure VI.7. Plane detector response. The response of the plane model of a Bicron Model .5M.39Q/.5L-X NaI(Tl) detector is displayed as a function of photon energy and angle of incidence.

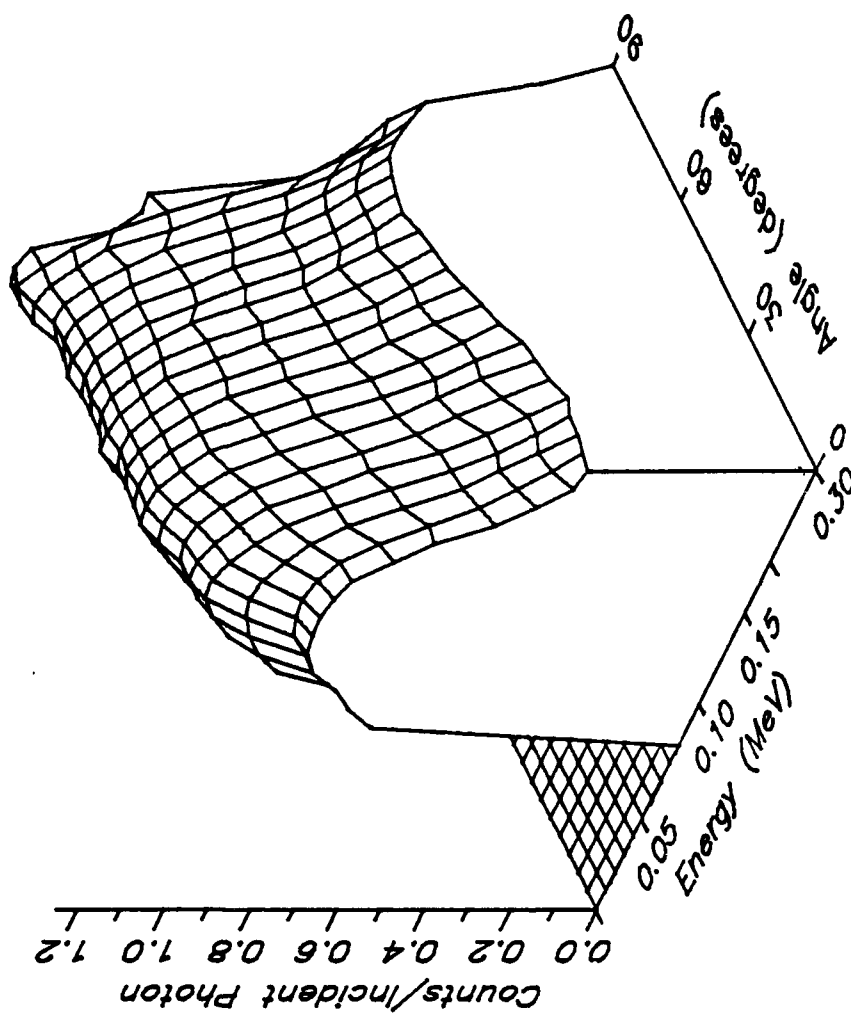


Figure VI.8. Detector response with edge and shield correction. The response of the plane model of a Bicron Model .5M.39Q/.5L-X NaI(Tl) detector, corrected for edge and shield effects, is displayed as a function of photon energy and angle of incidence.

CHAPTER VII

MINE DETECTION MECHANISMS

The detection of a buried, nonmetallic antitank mine using backscattered ionizing radiation depends upon differences between the characteristics of the reflected photons for the cases of mine present and absent. These differences derive from the simple physical characteristics of the two cases. The mine represents a low atomic number inclusion within the higher atomic number soil. Additionally, the mine has a definite geometric shape and includes a region of air near its upper surface. While soil and explosive densities are similar, the soil and air densities are very dissimilar. This chapter describes the implications of these physical differences in producing dissimilarities in the backscattered photon signals and provides the basis for mine detection mechanisms to exploit them. Results provided are from calculations using the SGLMIN.PAS and MCPHOT.P codes.

Backscattered Photon Signal Differences

The physical differences discussed above lead to dissimilarities in the fluence, energy fluence, spatial distribution, angular distribution, and energy spectra of the backscattered photon signals. Additionally, the geometry of

the mine and its air layer produce edge effects and signal variation with beam/mine intercept. Single scatter and Monte Carlo calculations are used in this section to introduce the basic detection mechanisms resulting from the physics and geometry of mine/soil system. Except for examination of angle of incidence, all calculations in this section use a perpendicularly incident source beam; and, except for the examination of edge effects, a beam intercept at the center of the mine. Justification for concentration on perpendicular incidence is provided later in the chapter. Monte Carlo generated images, which examine multiple intercepts, are described Chapter VIII.

Fluence

Because the principal scatterer in the mine, the explosive material, has a lower atomic number than the soil which surrounds it, the photon interaction characteristics in the two materials are considerably different. The lower atomic number of the explosive, at any given energy, results in a lower photoelectric interaction probability and higher incoherent scattering probability within the mine. This produces a lower rate of photoelectric absorption and a corresponding higher probability for photon backscatter. Differences will be significant only for the energy region in which the photoelectric interaction cross section of soil is also significant. Above this energy region, incoherent scattering is dominant in both materials, and is much less capable of distinguishing between soil and explosive.

Figure VII.1 shows number albedos as a function of source beam energy for perpendicular incidence on HTL soil, and the centers of TST mines buried in HTL soil with their top surfaces 0.0 (flush to the surface) and 2.5 cm below the ground. The number albedo, representing the fraction of all incident photons which are reflected, is directly proportional to the backscattered fluence. In all three cases, the shapes of the number albedo curves are similar. The number albedo is low at low energies because photoelectric interactions are dominant. At these energies, photons are much more likely to be absorbed than scattered. As source photon energy increases, the probability of incoherent scattering increases, accounting for the rise in the number albedo. At higher energies the rate of increase slows and the curves level off. This is a result of the preference in incoherent scattering for forward scatter as energy increases. The case of the mine buried flush with the surface shows the greatest difference from the soil alone. This is expected since it presents the low atomic number explosive directly to the beam. The difference for the case of the mine buried at 2.5 cm is much smaller. At low energy there is little difference from the soil only case. This is a result of the inability of the low energy photons to penetrate the soil layer in both entrance and exit directions. As energy increases, photons are able to penetrate, but soil attenuation reduces the backscattered signal. Since the incoherent cross section per electron is only weakly

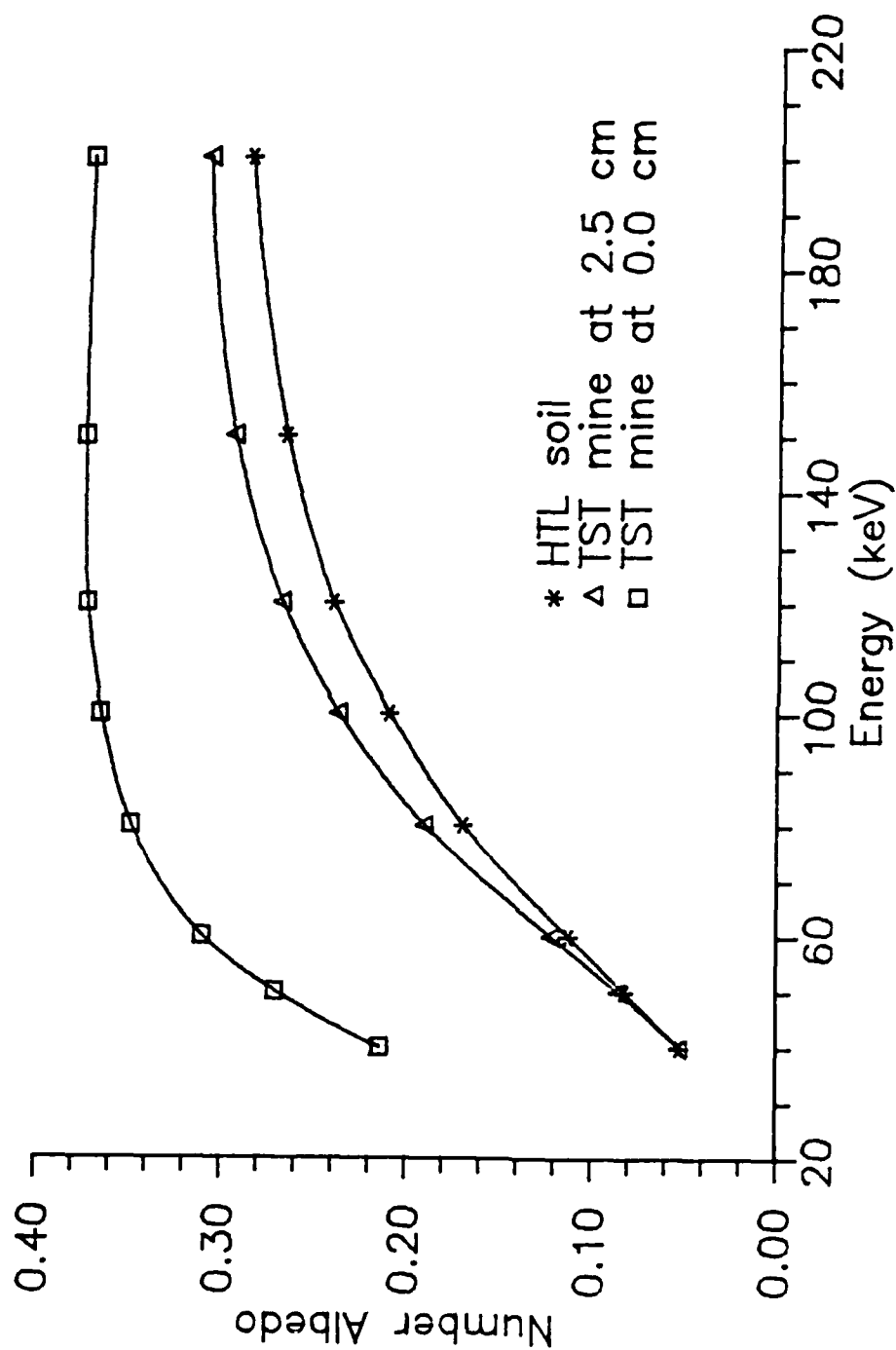


Figure VII.1. Number albedos versus energy for HTL soil and two TST mine cases. The number albedos displayed in this figure are for perpendicularly incident photons beams. The depth of burial of 0.0 cm refers to the top surface of the mine being flush with the soil surface.

dependent on atomic number, and the density of soil and explosive are similar, once the energy region of significant photoelectric interaction is exceeded, the backscattered fluences become similar. Figure VII.2 shows the ratios of the number albedos for the mine at the surface to those of the three major soils used in the research. The higher the ratio between the mine and soil cases, the greater the difference in the backscattered characteristics, and, in general, the greater the ease of mine detection. The greatest ratio occurs at low energy because the greatest difference between the photoelectric interaction cross sections of soil and explosive also occurs here. The higher atomic number soil absorbs the incident photons much more efficiently than the explosive. MCL soil with the highest atomic number of the three soils shows the greatest contrast. Figure VII.3 shows this same ratio for the three soils with the mine buried at 2.5 cm. Apparent in this figure is the existence of optimum energies for mine detection. For the reasons discussed above, the backscattered responses for the buried mine and soil cases are more similar at both low and high energy. Somewhere in between, an optimum source energy exists. This optimum energy is dependent upon the atomic number of the soil material. In NSL soil, it is about 80 keV; in HTL soil, about 100 keV; and in MCL soil, about 150 keV. This variation with soil type is simply a result of the extent of the energy region in which photoelectric interactions are important. Beyond this region the incoherent

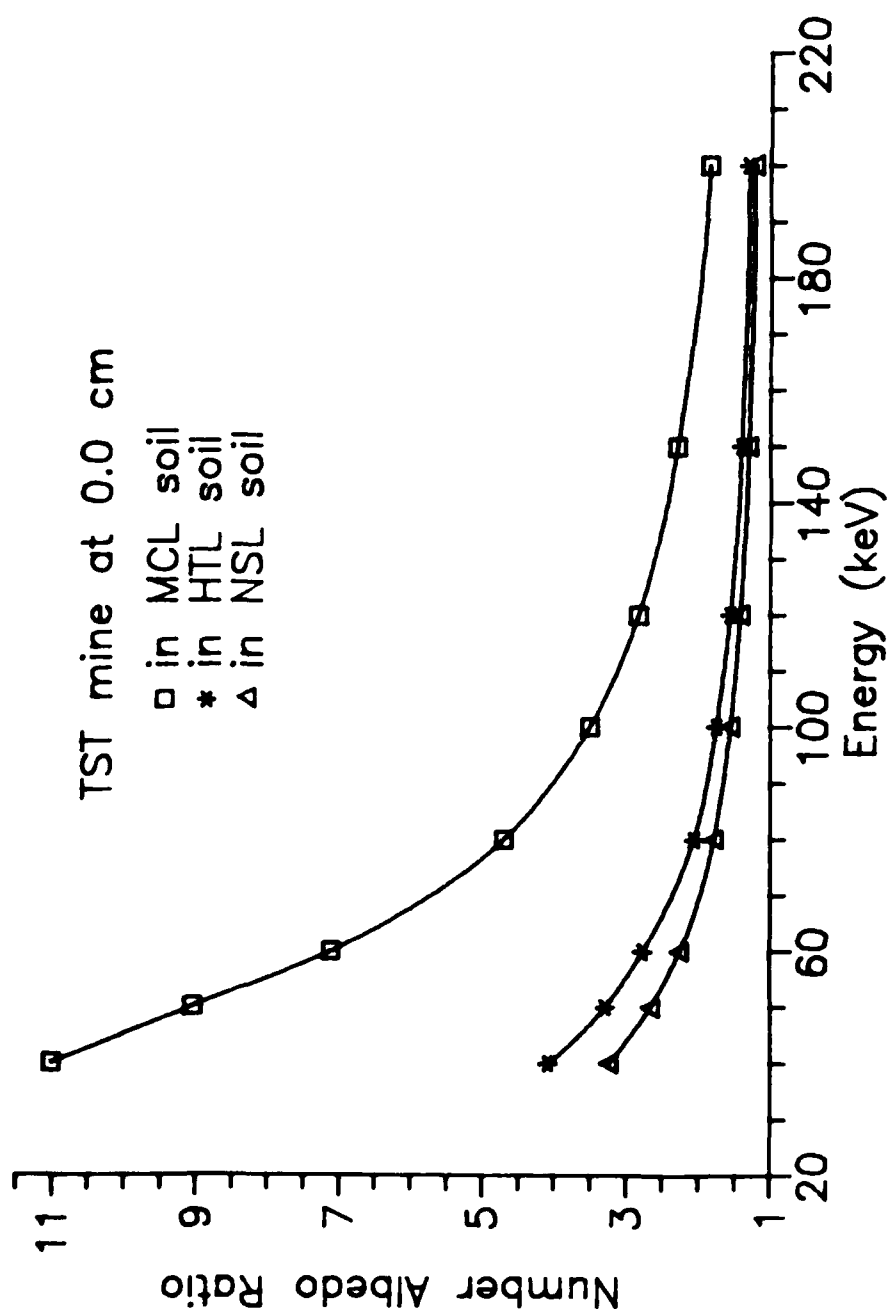


Figure VII.2. Number albedo ratios versus energy for the TST mine at 0.0 cm in three soils. The ratio of the number albedos of mine present to soil only are shown for three soil types for perpendicularly incident photon beams striking the center of the TST mine buried flush with the soil surface.

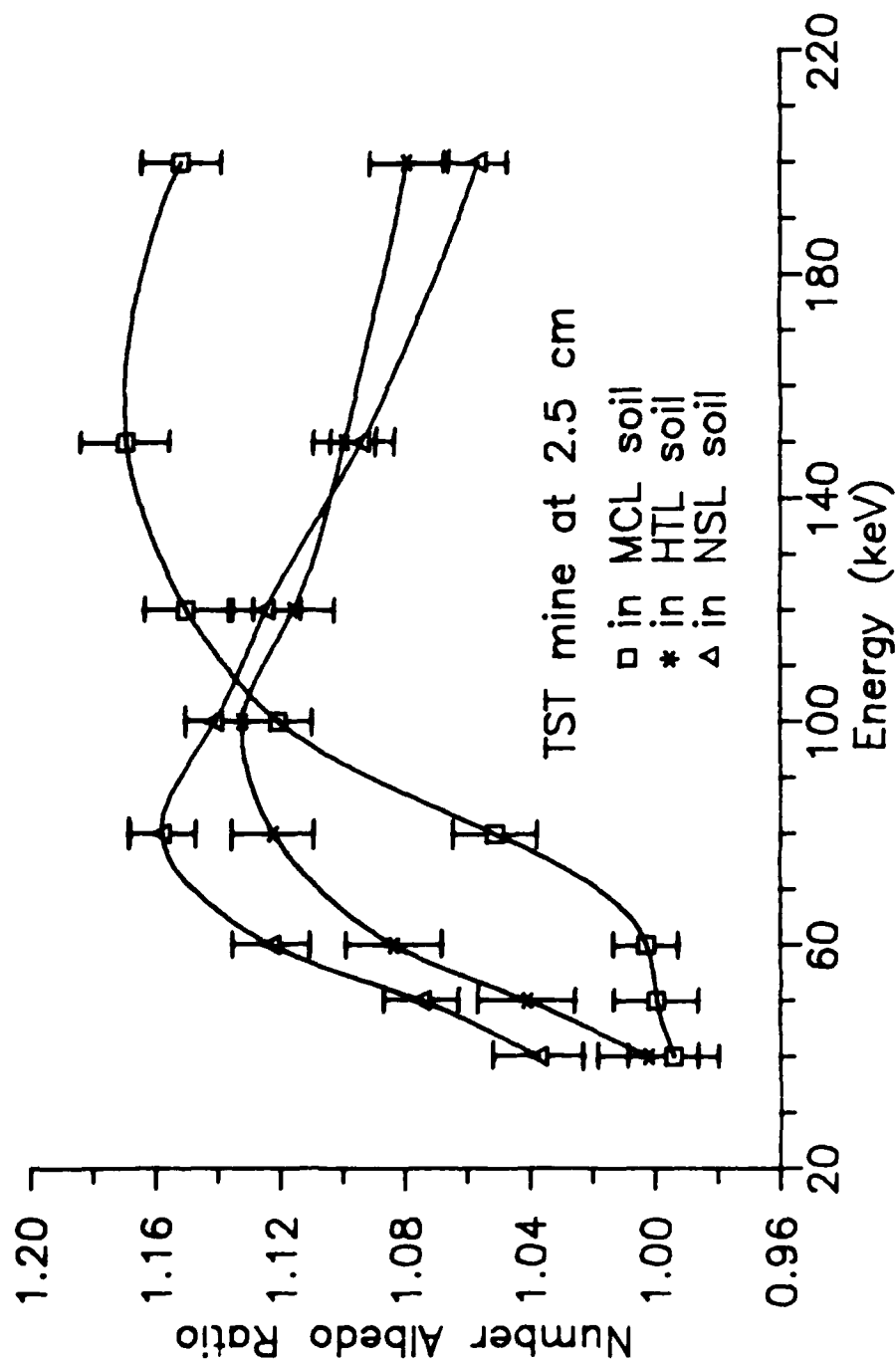


Figure VII.3. Number albedo ratios versus energy for the TST mine at 2.5 cm in three soils. The ratio of the number albedos of mine present to soil only are shown for three soil types for perpendicularly incident photon beams striking the center of the TST mine at a depth of burial of 2.5 cm.

interaction dominates and fails to significantly differentiate between soil and explosive. This region of photoelectric importance extends furthest in higher atomic number materials. Similar conclusions are reached later in this chapter for more realistic detector configurations in which energy requirements for the source are established. It is apparent that the use of high energy sources is not productive. Optimum source energies for an uncollimated fluence detector lie below 200 keV. As discussed below, this is also true for collimated detectors.

Energy Fluence

The energy albedo represents the fraction of incident photon energy reflected from a surface. It is, therefore, directly proportional to the backscattered energy fluence. Figure VII.4 shows the energy albedo as a function of source energy for the same cases examined in the preceding section. Comparison with Figure VII.1 indicates that the energy albedos are smaller in each case than the number albedos. This is a result of the loss of energy which occurs with each incoherent scattering event. The energy albedo curves also exhibit maxima in the energy region of consideration. This is a result of the nature of the energy loss phenomenon; the fractional loss in energy is greater at higher incident energy in incoherent scattering interactions. The maximum is most apparent in the lowest atomic number case, the mine buried flush to the surface. This is because the average photon undergoes more incoherent scattering

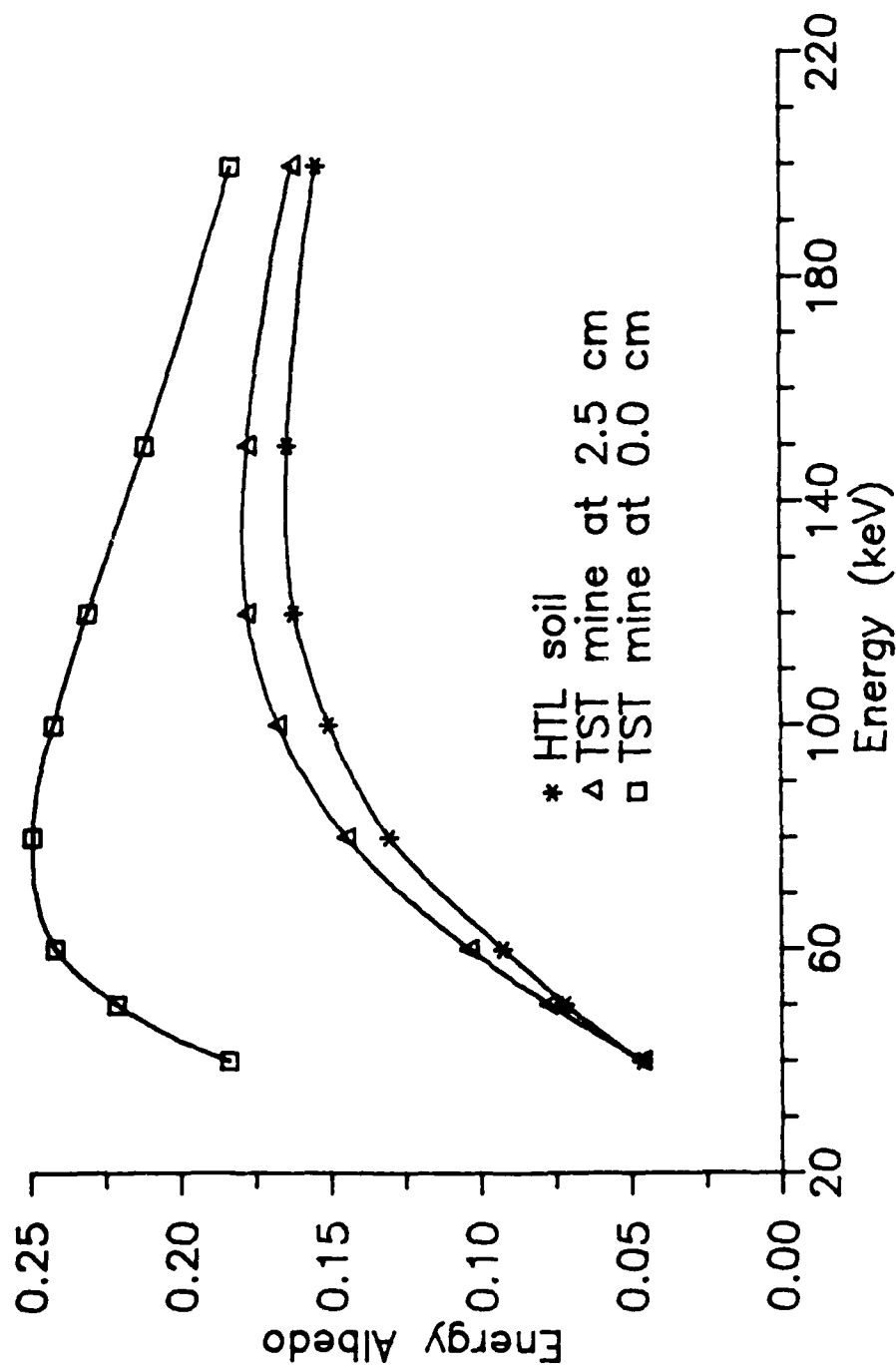


Figure VII.4. Energy albedos versus energy for HTL soil and two TST mine cases. The energy albedos displayed in this figure are for perpendicularly incident photon beams.

interactions before reflection, resulting in greater energy loss, than in the higher atomic number cases. Figure VII.5 displays this fact by showing the fraction of backscattered photons which have undergone multiple scatter for each case.

The ratio of the energy albedo of a given atomic number material to a higher atomic number material can be shown to be always less than the corresponding number albedo ratio. Bulatov and Andrushin (1967) use the calculated albedos of Berger and Raso (1960) to show that the ratio of number to energy albedo versus energy is a linear relationship in the energy range above 200 keV. The slope of the line is found to be greatest in lower atomic number materials. Table VII.1 compares the results of Bulatov and Andrushin to calculations performed by the MCPHOT codes, and recalculation from the original Berger and Raso data. Figure VII.6 shows this linear relationship below 200 keV for the three mine detection related cases. Algebraic manipulation provides

$$\frac{A_E(\text{TNT})}{A_E(\text{soil})} = \frac{A_N(\text{TNT})}{A_N(\text{soil})} \left[\frac{b(\text{soil}) + m(\text{soil}) E}{b(\text{TNT}) + m(\text{TNT}) E} \right] ,$$

where A_E is an energy albedo,

A_N is a number albedo,

b is an intercept, and

m is a slope.

Since the slope for a lower atomic number material is larger and the intercepts are nearly equal, the bracketed quantity is a number less than 1.00. Accordingly, the ratio of

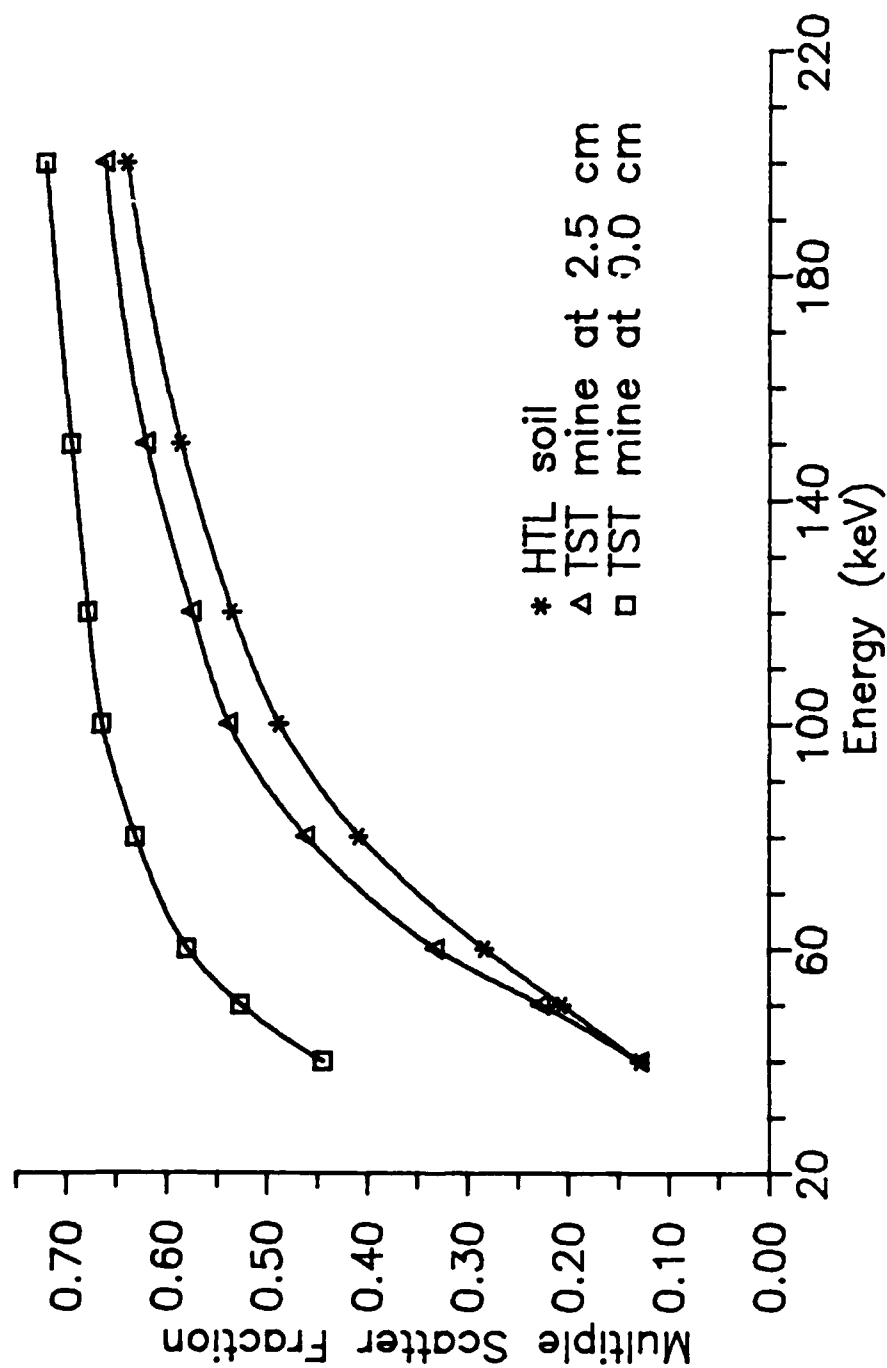


Figure VII.5. Multiple scatter fraction versus energy for HTL soil and two TST mine cases. The fraction of all backscattered photons reaching the detector, which have been multiply scattered, is compared for three scattering cases as a function of source energy.

TABLE VII.1

Comparison of the Linear Relationship
Between the Ratio of Number to Energy Albedo
and Source Energy at Perpendicular Incidence

	Bulatov and Andrushin (1967)	Berger and Raso (1960)	MCPHOT.P
Concrete slope (MeV^{-1})	4.28	4.45	4.47
intercept	1.00	0.94	0.95
Iron slope (MeV^{-1})	3.55	3.59	3.53
intercept	1.00	0.96	0.98
HTL soil slope (MeV^{-1})	-	-	4.58
intercept	-	-	0.93
HTL soil with TST mine flush with surface slope (MeV^{-1})	-	-	5.27
intercept	-	-	0.98
HTL soil with TST mine at 2.5 cm depth of burial slope (MeV^{-1})	-	-	4.78
intercept	-	-	0.94

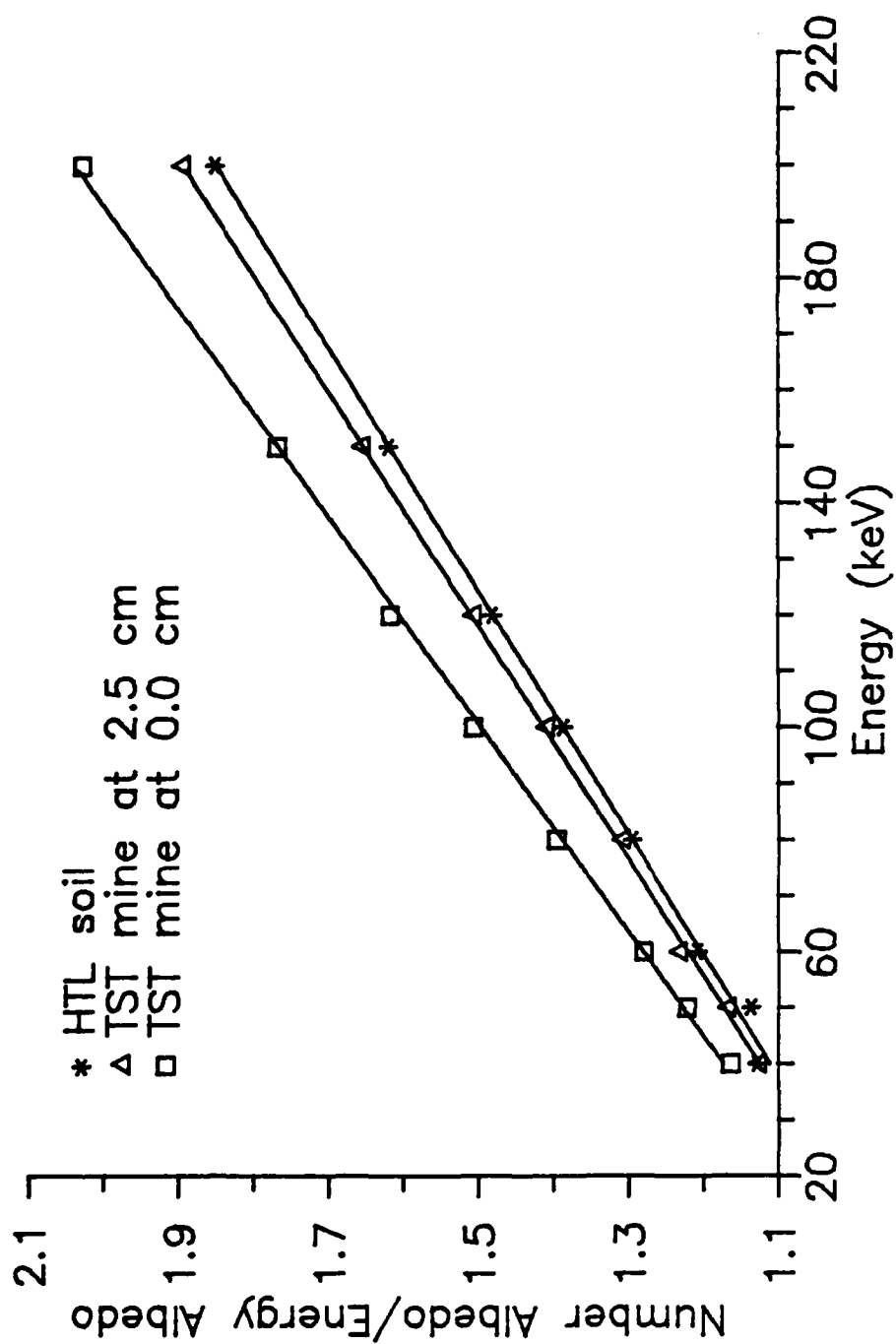


Figure VII.6. Ratio of number to energy albedo for HTL soil and two TST mine cases. The relationship between the number to energy albedo ratio as a function of energy is linear.

energy albedos in the mine detection cases is always smaller than the ratio of number albedos. This suggests that a fluence detector, such as a scintillator, would provide somewhat better discrimination between mine and soil than a detector based on energy absorption, such as an ionization chamber.

Spatial Distribution

Figures VII.7 and VII.8 show Monte Carlo calculations of the spatial distribution of the backscattered fluence intercepting a plane located 34.6075 cm (this height corresponds to that used in the measurements portion of the work) above the soil surface for the case of HTL soil alone and soil with mine buried flush to the surface. The source beam is composed of 100 keV photons (as shown later in this chapter, approximately optimum for mine detection in HTL soil) and is perpendicularly incident. Since the beam axis intercepts the plane at its center, the figure indicates that the greatest backscattering occurs directly along the source direction. This is because the shortest attenuation path out of each material is in that direction. Figure VII.9 shows the quotient of spatial distribution of the mine at 0.0 cm to that of soil. The dimensions of the display have been reduced from those of the two preceding figures, and symmetry considerations employed to eliminate large variations in the quotient resulting from very small and hence more uncertain responses. The ratio has a relative minimum in the direction of greatest backscatter. While the

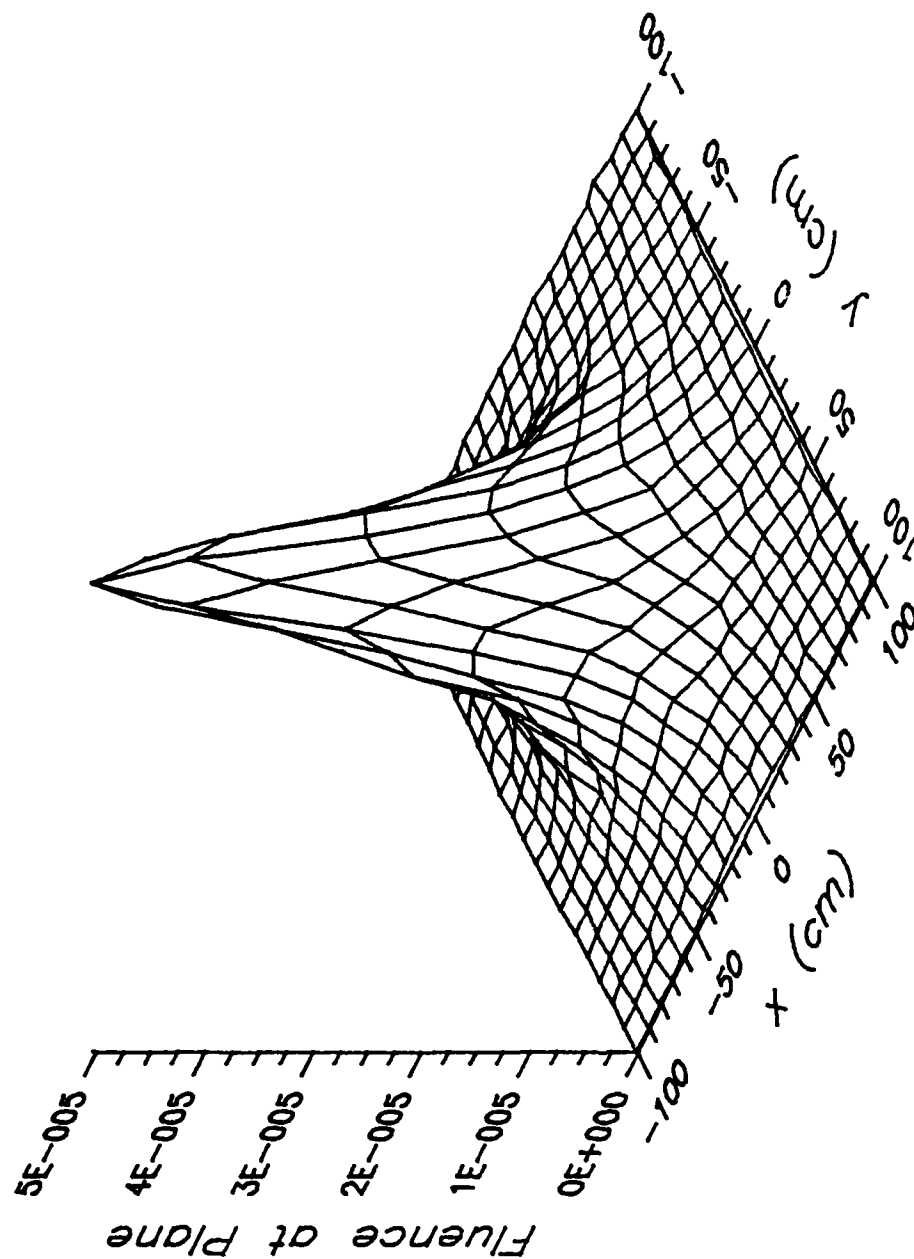


Figure VII.7. Spatial distribution of backscattered fluence from 100 keV photons perpendicularly incident on HTL soil. The fluence (photons/(incident photon-cm²)) striking a plane located 34.6075 cm above and parallel to the soil surface is shown. The source beam is incident at the origin of the x-y plane at the soil surface.

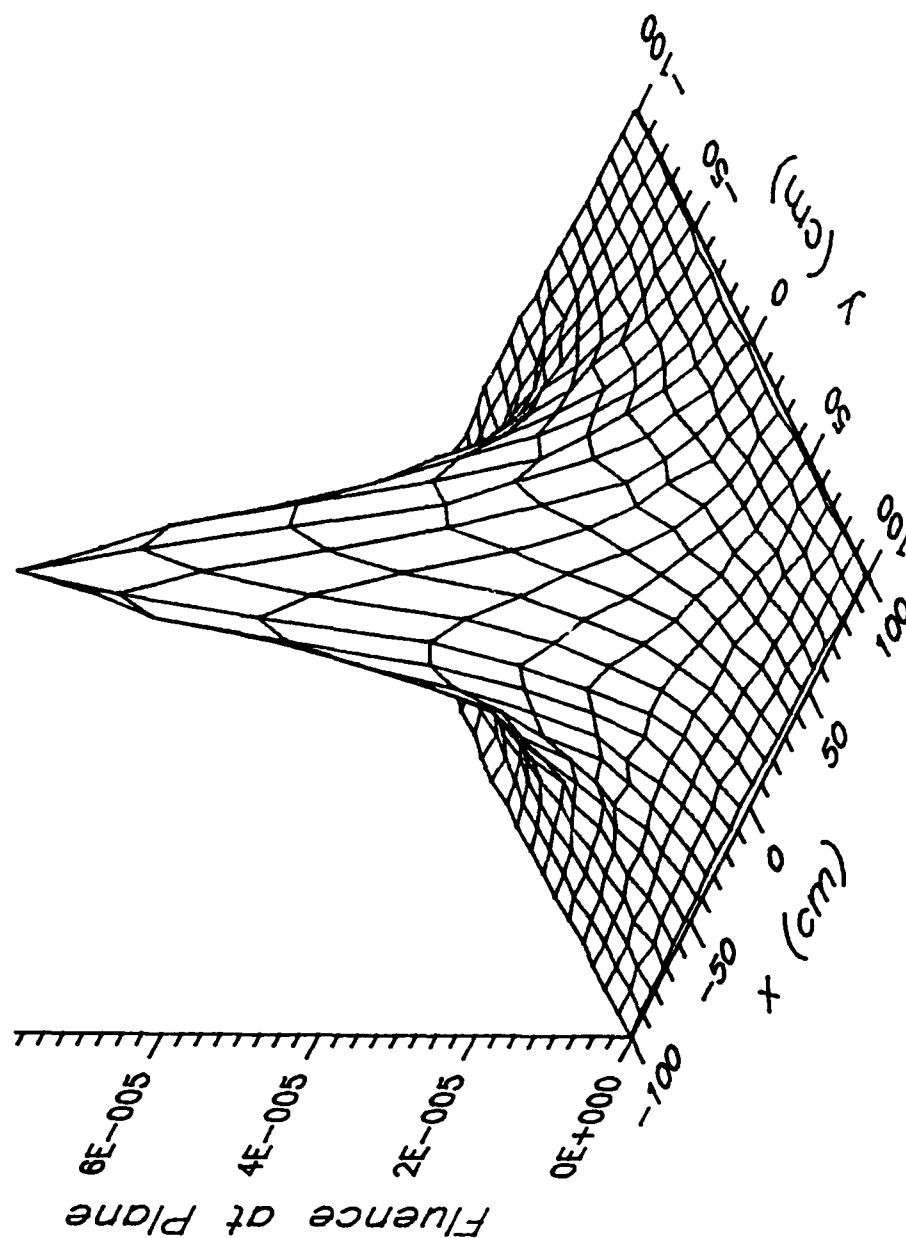


Figure VII.8. Spatial distribution of backscattered fluence from 100 keV photons perpendicularly on the center of the TST mine at 0.0 cm. The fluence (photons/(incident photon-cm²)) striking a plane located 34.6075 cm above and parallel to the soil surface is shown. The source beam is incident at the origin of the x-y plane at the soil surface, which is also the center of the top face of the mine cylinder in this example.

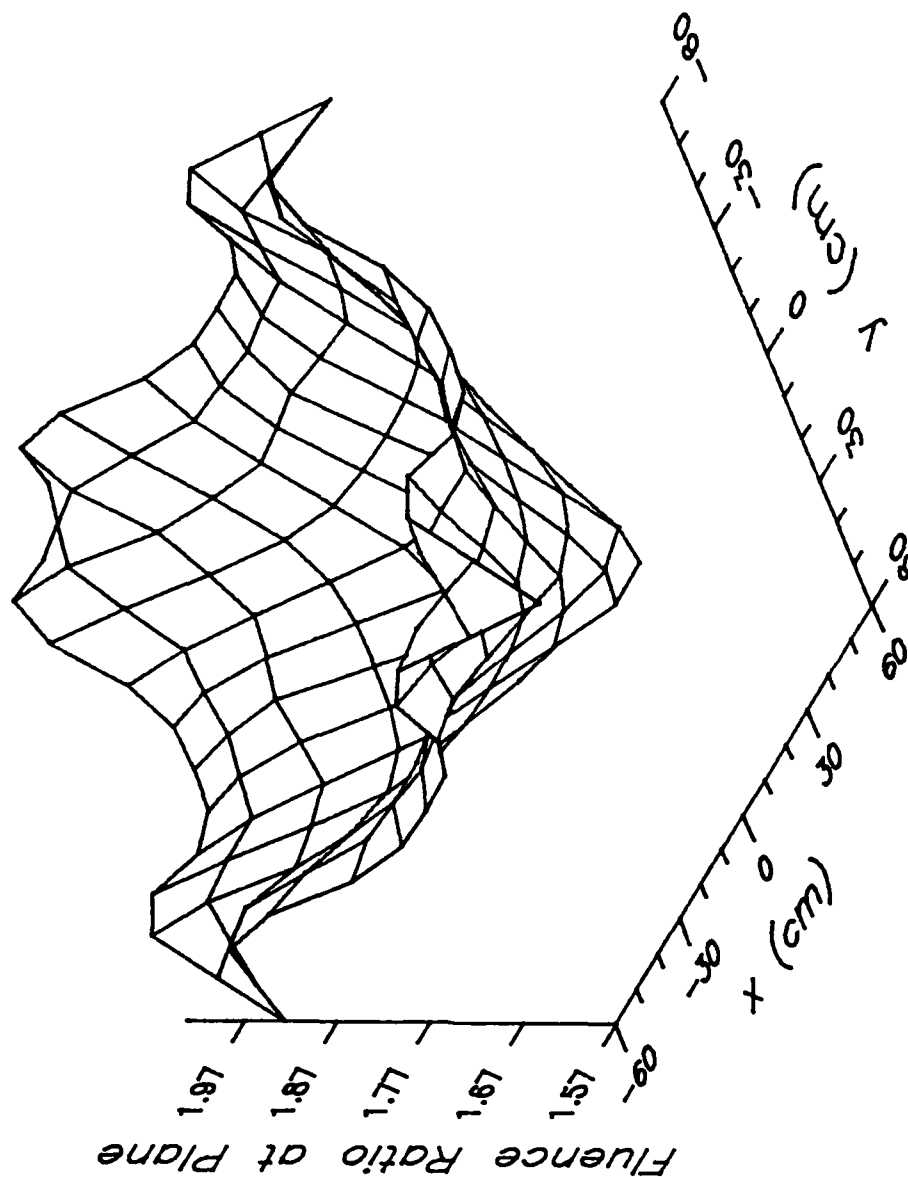


Figure VII.9. Spatial distribution of of the mine to soil ratio of backscattered fluence from perpendicularly incident 100 kev photons. This figure displays the ratio of the two preceding figures. A minimum in the ratio occurs along the direction of greatest backscatter.

ratio is greater than 1.00 everywhere, it is higher at positions further from the beam axis because, for equal slant paths through their respective materials, photons traveling through explosive are less attenuated than those travelling through soil. The existence of the central minimum is essentially due to the single scattered component. Figure VII.10 shows the same quotient for the single scattered component only, more clearly revealing its origin. This result implies that a detector will be better able to detect mines if the regions corresponding to the central minimum are not included within it. As a practical matter, part of the central region must be removed to allow raster of the beam.

Angular Distribution

The angular distribution referred to in this section is that of the photons striking a plane above the soil surface after backscatter from soil or mine. Figure VII.11 shows the differential angular spectra for the cases under discussion for a perpendicularly incident 100 keV beam. Zero radians or 0 degrees is equivalent to perpendicular incidence on the plane. Figure VII.12 shows the same spectra for the multiply scattered photons only. Greater differences in ratios between the soil and mine cases in the multiple scatter spectra suggests that a detector which is capable of removing the single scatter component would be more sensitive to mine detection. The differences in the multiple scattered spectra are a result of the much lower

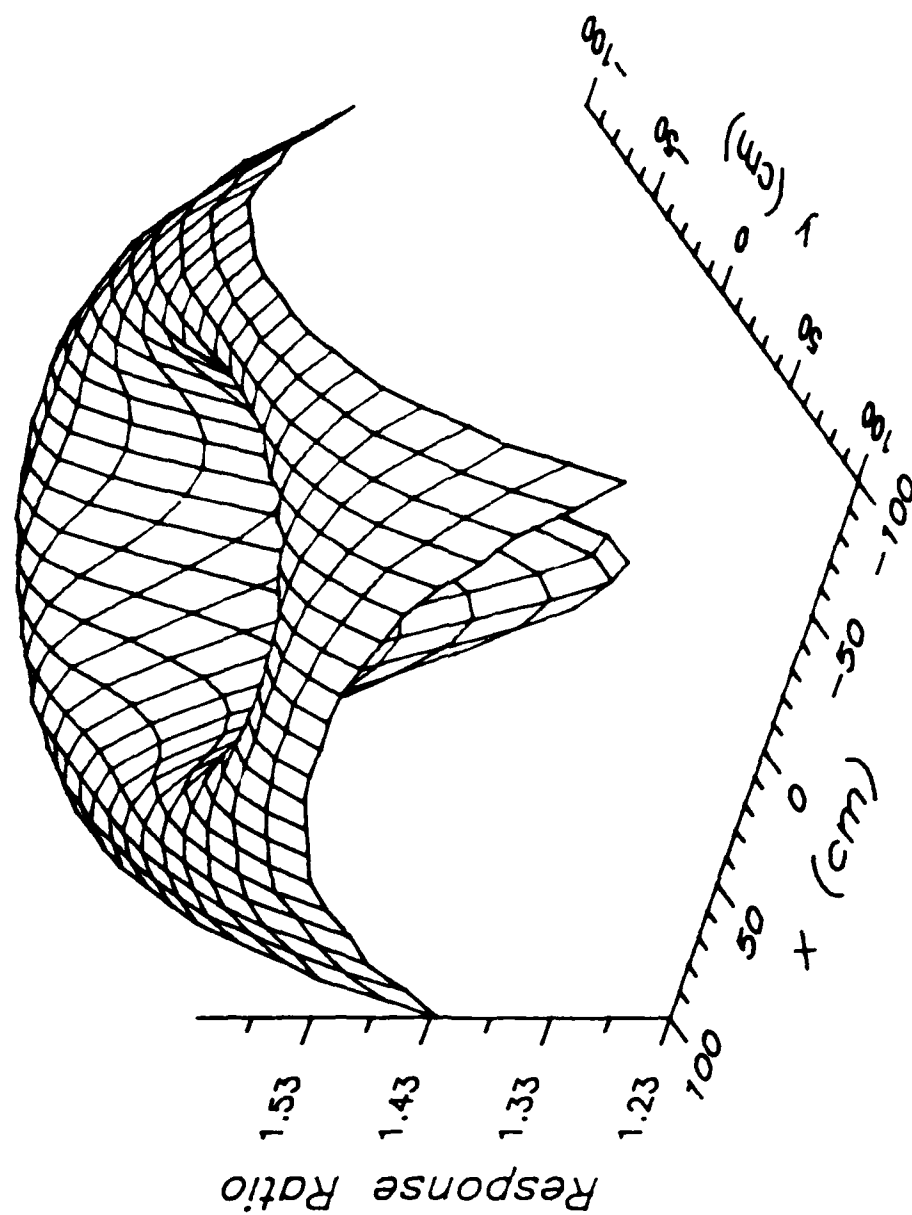


Figure VII.10. Spatial distribution of the single scattered mine to soil ratio from perpendicularly incident 100 kev photons. The single scatterer component of the mine to soil fluence ratio intercepting a plane located 34.6075 cm above and parallel to the soil surface is shown.

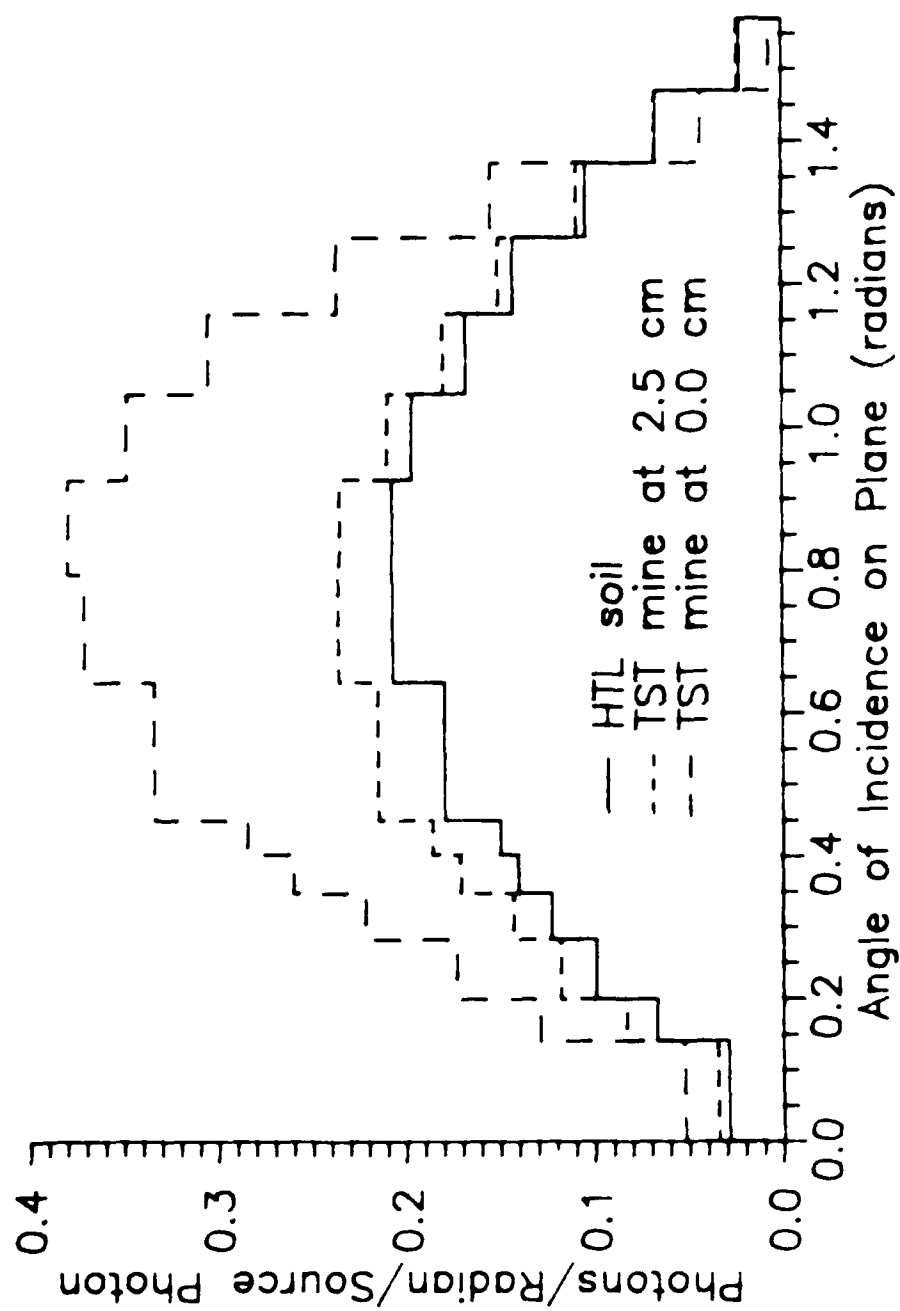


Figure VII.11. Angular distribution of backscattered fluence from 100 keV photons perpendicularly incident on HTL soil and two TST mine cases.

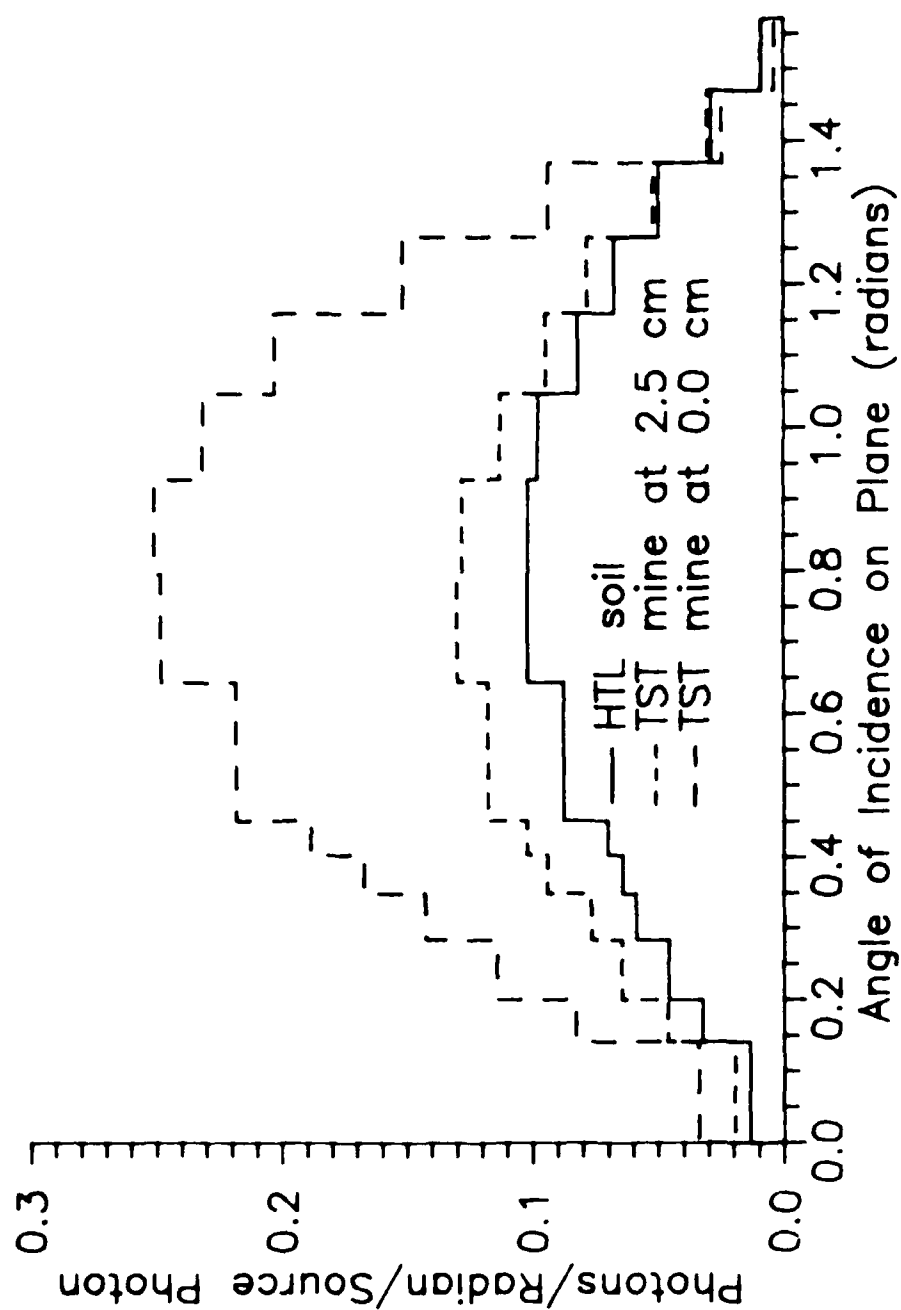


Figure VII.12. Angular distribution of the multiple scattered fluence from 100 keV photons perpendicularly incident on the HTL soil and two TST mine cases.

probability of such scatters in soil compared to that in the lower atomic number explosive. Removing the single scattered component can be accomplished by collimation of detector segments located away from the beam axis.

Figures VII.13 and VII.14 show the results of calculations for a plane of incidence parallel to the soil surface at a height of 34.6075 cm from which a central 25 cm radius about the beam axis has been removed. The results in this figure are shown in terms of the integral angular spectra. Figure VII.13 compares the ratios of the integral spectrum of the mine at 0.0 cm to that of soil for the full plane and the plane missing the central disk. Figure VII.14 shows the same results at 2.5 cm depth of burial. The ratios achieved by this new configuration are large in both cases. Figure VII.15 reveals the reason for the jump in the ratios for collimators which admit photons at angles of incidence of approximately 0.65 (37 degrees) radians or less (this angle is specific to this calculation). This collimator geometry achieves a significant exclusion of the single scattered fluence. The large ratios are a result of the much greater lateral path distance a multiple scattered photon must travel to reach the detector when it is highly collimated. Long paths through soil produce a much greater attenuation than paths through explosive. The total fluence at the detector is much reduced from the uncollimated detector calculations, as indicated by the large uncertainties associated with small acceptance angles in Figures VII.13 and VII.14.

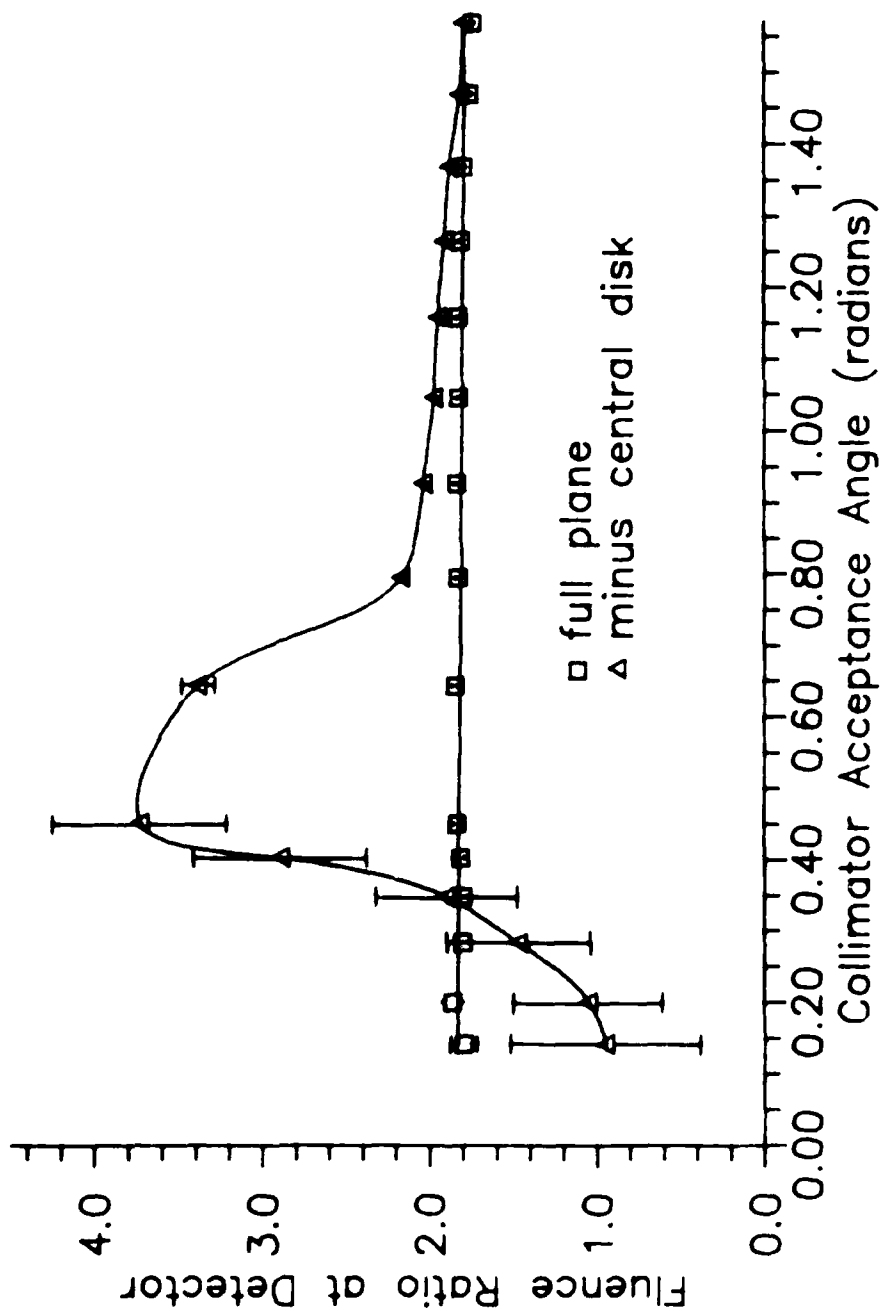


Figure VII.13. Mine to soil fluence ratio versus collimator acceptance angle for 100 keV photons perpendicularly incident on the TST mine at 0.0 cm in HTL soil. A 25 cm radius central section of the detection plane has been removed. The plane is located 34.6075 cm above and parallel to the soil surface.

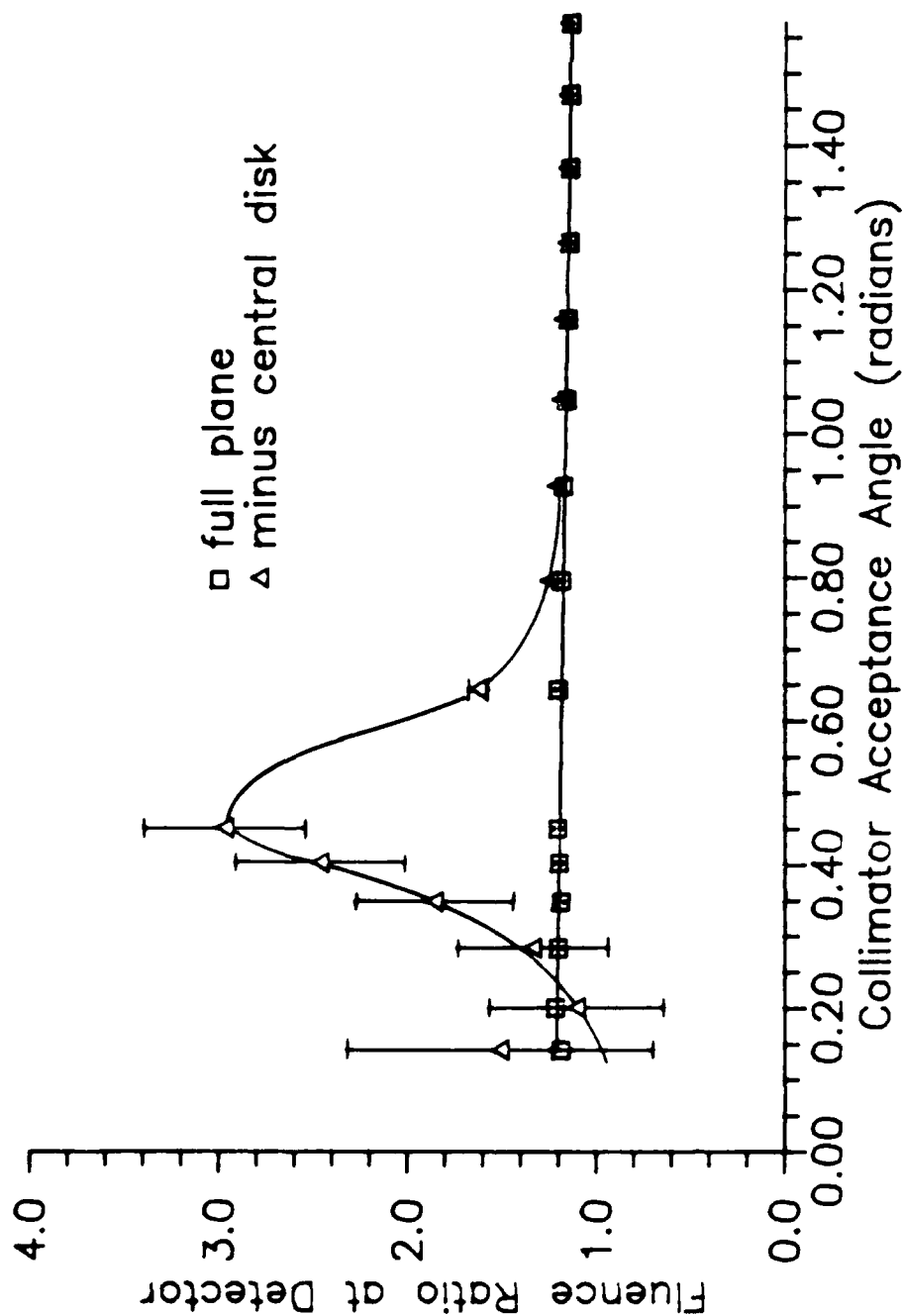


Figure VII.14. Mine to soil fluence ratio versus collimator acceptance angle for 100 keV photons perpendicularly incident on the TST mine at 2.5 cm in HTL soil. A 25 cm radius central section of the detection plane has been removed. The plane is located 34.6075 cm above and parallel to the soil surface.

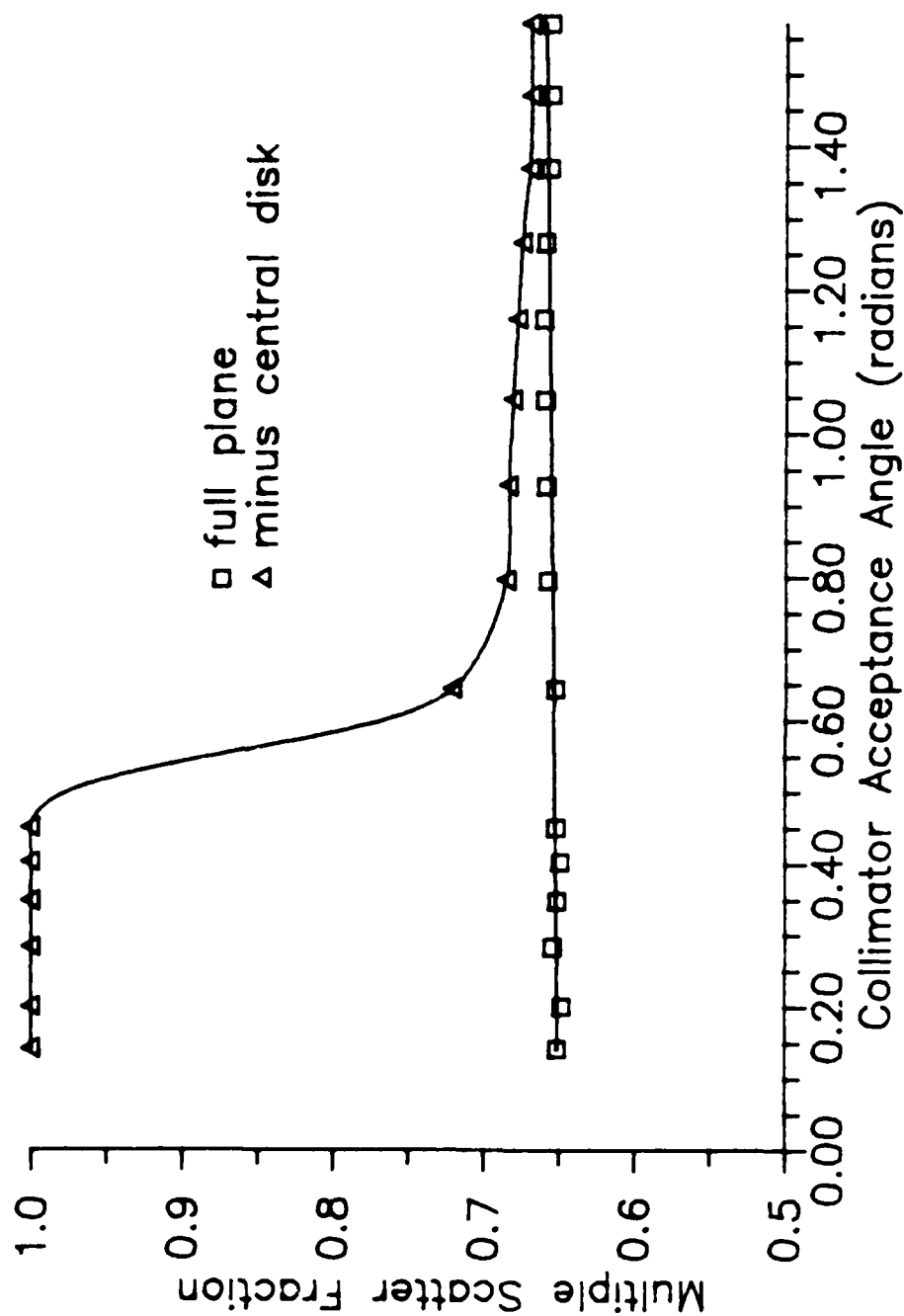


Figure VII.15. Multiple scatter fraction versus collimator acceptance angle for 100 keV photons perpendicularly incident on the TST mine at 0.0 cm in HTL soil. The fraction of backscattered photons which are multiply scattered intercepting a plane with its central 25 cm radius section missing at a height of 34.6075 cm above the soil surface is shown.

It is significant that an optimum collimation angle may occur for a particular combination of photon energy, detector height, and mine geometry. If the collimator acceptance angle is too large, single scattered photons are admitted, making the ratio low. As noted in Chapter II, many early applications of scatter imaging made use of the fact that the single scattered fluence is very nearly independent of all variables except density. Since the mine and soil densities are similar, the single scattered fluences are roughly alike. If the collimator acceptance angle is too small, the area viewed by the collimated region of the detection plane shrinks. When the geometry is such that the area viewed is at the edge of the mine, the ratio drops. This edge effect is caused by the air layer in the mine. The photons scattering in the explosive enter the soil at depths which prevent them from reaching the surface. The average photon scattering in the soil, which eventually reaches the collimated plane, is always close to the surface. In extreme cases, the ratio may fall below unity.

Energy Spectra

Figure VII.16 shows the differential energy spectra for 100 keV photons perpendicularly incident on the problem cases. The major difference in the spectral shapes with the mine present occurs in the lower energy region and is due to the increased multiple scatter in the lower atomic number materials. The break in the smoothness of the spectral curves at high energy is due to coherent backscatter. The

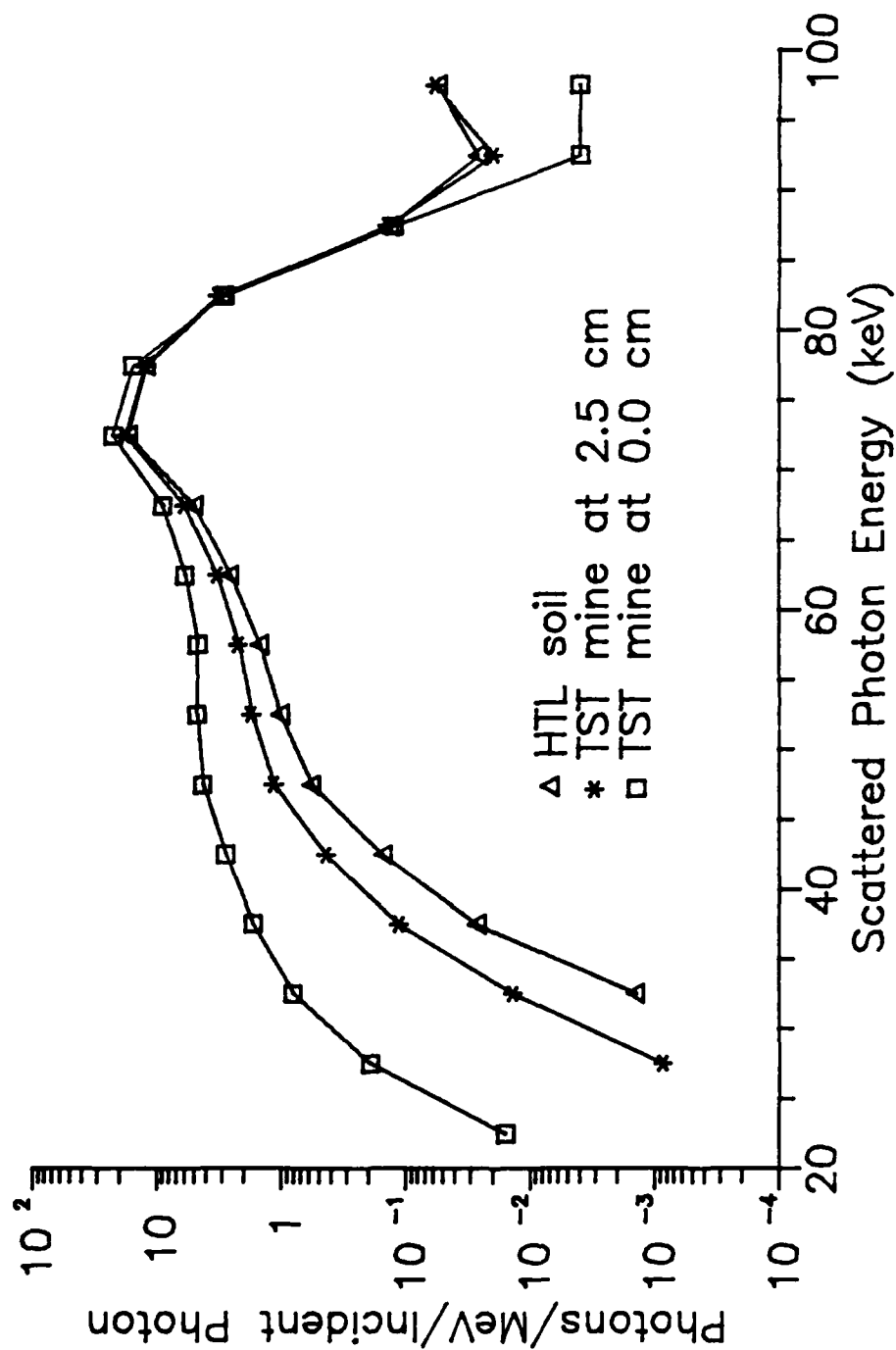


Figure VII.16. Differential energy spectra for 100 keV photons perpendicularly incident on HTL soil and two TST mine cases. Differential energy spectra (photons/(source photon - MeV)), calculated for the soil and mine present cases. The major difference between soil and mine is at low energy.

low energy differences suggest energy discrimination which removes high energy components might be useful in mine detection. Figure VII.17 shows the ratio of the integral spectra for the mine present cases to that of the soil only case. This figure emphasizes the desirability of removing the higher energy scatter components. At low energy the ratio is large; at high energy, it becomes equal to the number albedo ratio. Three significant problems exist for a detector based on this concept. First, the number of low energy backscattered photons is small, as indicated by the large uncertainties at low energy in Figure VII.17. Second, if the source contains low energy photons, as most x-ray spectra do, the backscattered spectra will also contain many low energy photons. This is because the fractional energy lost by a low energy photon in an incoherent interaction is small. X-ray spectra without low energy components can be produced by heavy filtration by high atomic number materials, but this further reduces the magnitude of an already small signal at a fixed power level of the x-ray generator, and may make source shielding leakage radiation the origin of a significant contributor to the signal. Third, if a radiation detector based on scintillation is employed and produces a significant Compton continuum, the low energy responses will be masked. Large area scintillation detectors, containing high atomic number materials would reduce this problem.

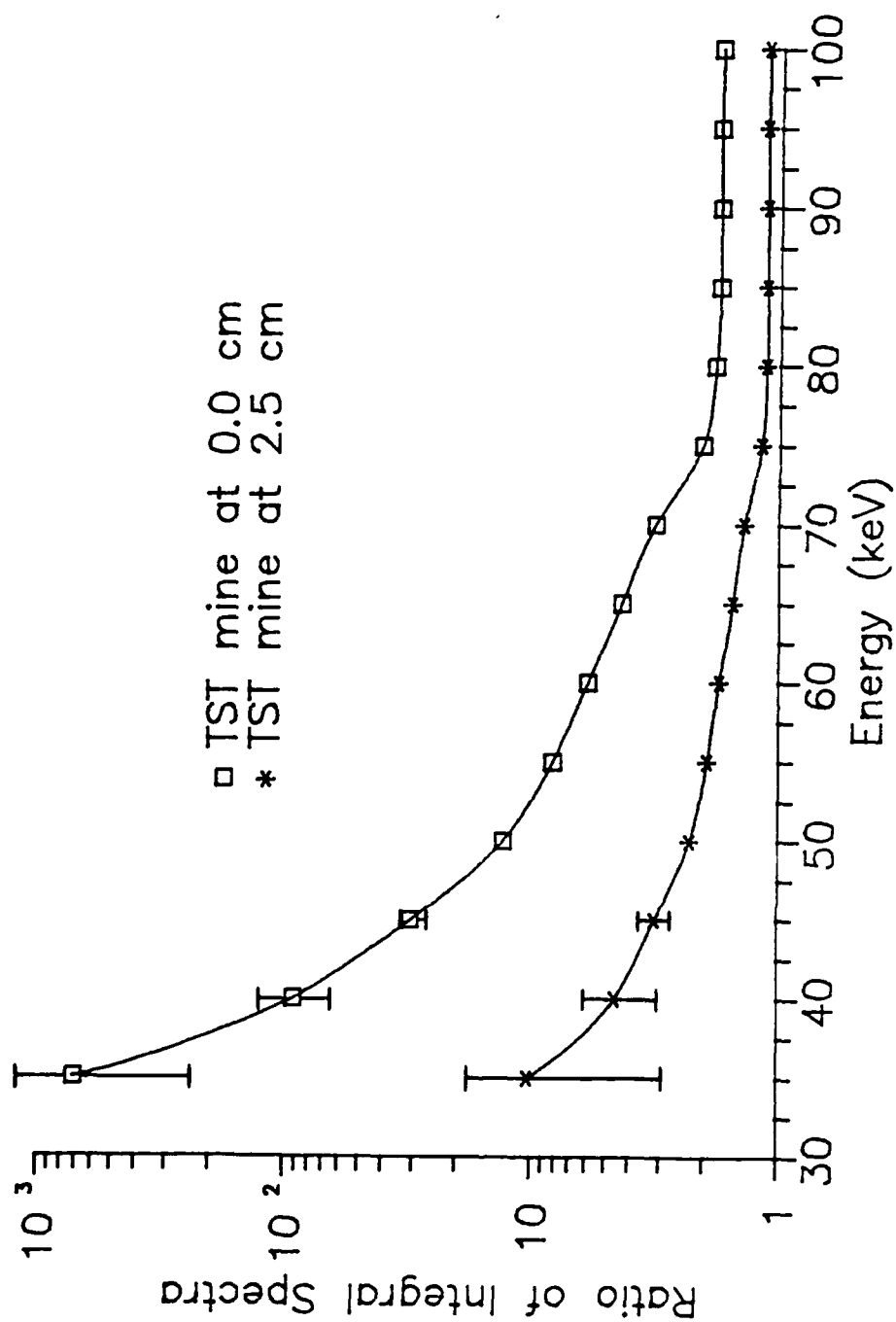


Figure VII.17. Ratios of mine and soil integral energy spectra for two TST mine cases in HTL soil. The energy value appearing in the graph is that of the upper end of the energy window with the lower end set at zero.

Edge Effects

An example of an edge effect has been discussed in the section concerning angular distributions of the backscattered fluence. The presence of the air layer in the mine is the principal cause for the edge effects. As first noted by Preiss and Livnat (1973), the air layer reduces the backscattered fluence from that produced by a mine composed of solid explosive. Preiss and Livnat used an uncollimated, high energy radionuclide source with a collimated asymmetrically located detector to enhance this reduction in response. Other edge effects are produced by the air layer when the source beam strikes just inside or outside the edge of a mine. The edge effects can be described most simply in terms of a single scatter model. Figure VII.18 shows the geometry of the edge effect phenomena. The top portion of the figure shows two photons scattering at the same polar angle, θ , but at azimuthal angles which differ by 180 degrees. These scattered photons are produced by a beam striking near the inside edge of the mine. The two detector positions, which are symmetric with respect to the beam, but not with respect to the mine center, lie in the paths of the two photons. The paths taken by the two photons are through different materials. The path on the left includes considerably more air than the path on the right. The transmission probability along the left path will be much greater than that of the right path which traverses more soil. Extension of this argument to all scattering paths for a

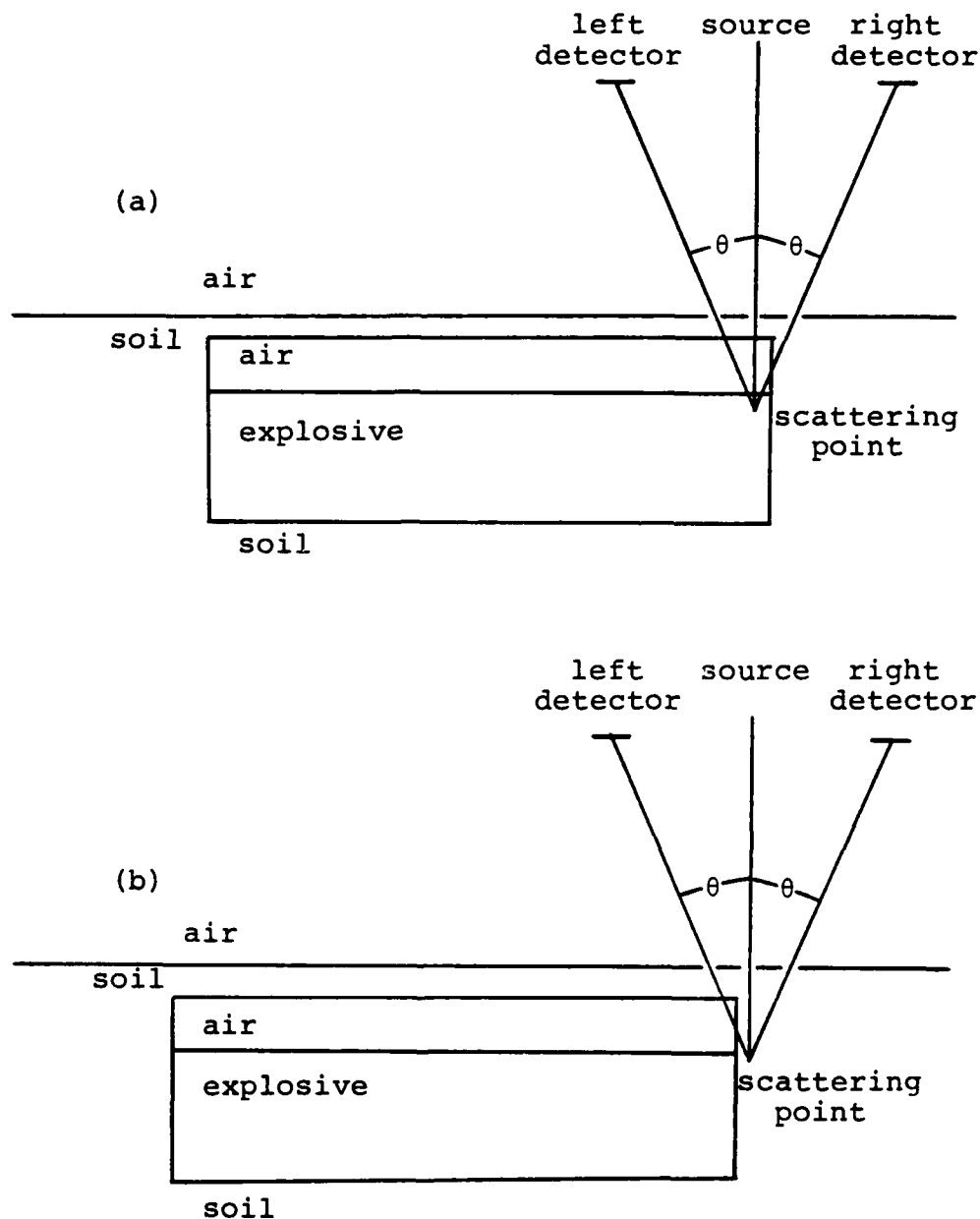


Figure VII.18. Edge effect geometries. (a) Edge effect produced by a beam intercept just inside the mine wall. (b) Edge effect produced by a beam intercept just outside the mine wall.

large number of incident photons results in the response of the detector on the left being higher than that on the right. The lower half of the figure shows the analogous basis for the edge effect of a beam striking just outside the mine. Here, the path on the left includes air, while the path on the right is entirely through soil.

Figure VII.19 shows the single scatter spatial distribution resulting from a perpendicularly incident, 100 keV photon beam striking just inside of the edge of the mine buried at 2.5 cm. Examination of this figure reveals an asymmetric spatial distribution of the backscattered fluence response. Fewer photons are backscattered into the positive y half of the plane than into the negative y portion. Figures VII.20 and VII.21 more clearly display this type of asymmetry by showing the spatial distribution of the single scatter mine to soil fluence ratios for this inside intercept, and an intercept just outside the edge. A detector occupying the left front portion of the plane of Figure VII.20 will record a response less than that of soil alone. This is a result of the air layer allowing photons to reach depths normally not attainable. These deeply located photons are then unable to reach the detector through the long slant paths through soil. The reduction in response occurs because these photons produce essentially no contribution to the backscattered fluence as they traverse the low density air.

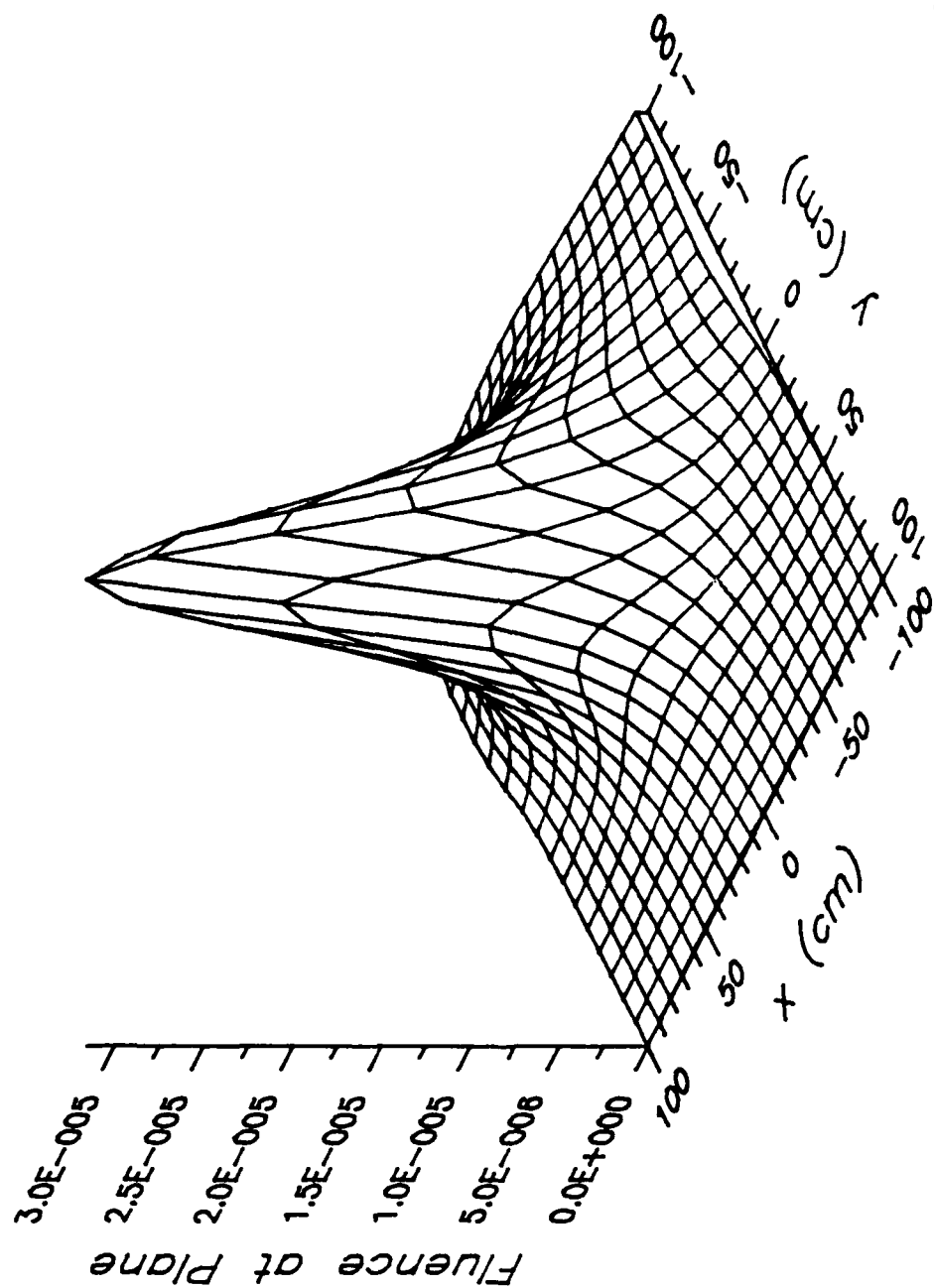


Figure VII.19. Spatial distribution of the single scattered fluence from a 100 keV photon beam perpendicularly incident on the inside edge of the TST mine. The single scattered fluence (photons/(incident photon-cm²)) striking a plane located 34.6075 cm above and parallel to the soil surface is shown. The mine is buried at a depth of 2.5 cm in NSL soil.

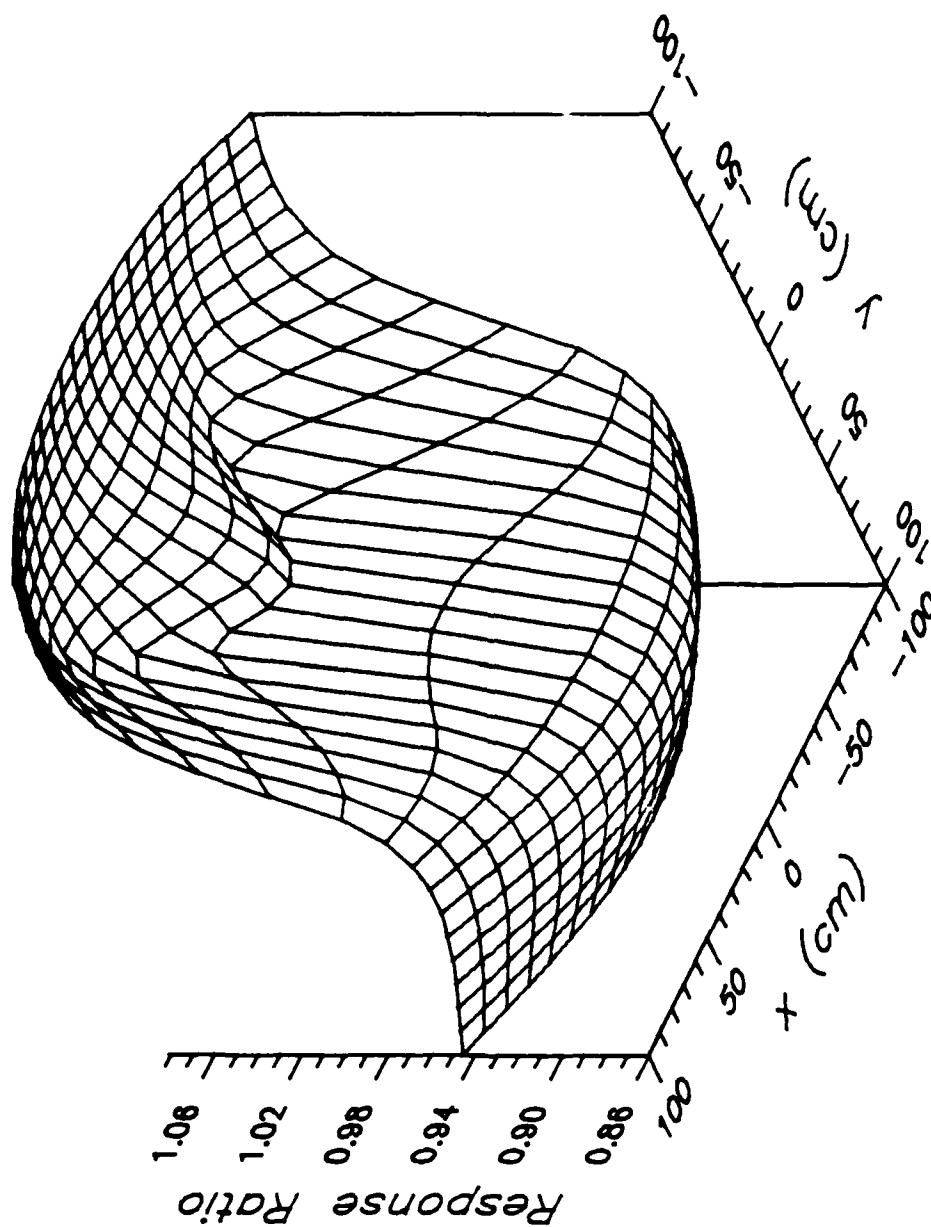


Figure VII.20. Spatial distribution of the single scattered mine to soil fluence response ratio for a 100 keV photon beam perpendicularly incident on the inside edge of the TST mine. This figure shows the ratio of the spatial distribution of single scattered fluence of Figure VII.19 with the TST mine at a depth of burial of 2.5 cm in NSL soil to that produced without a mine present.

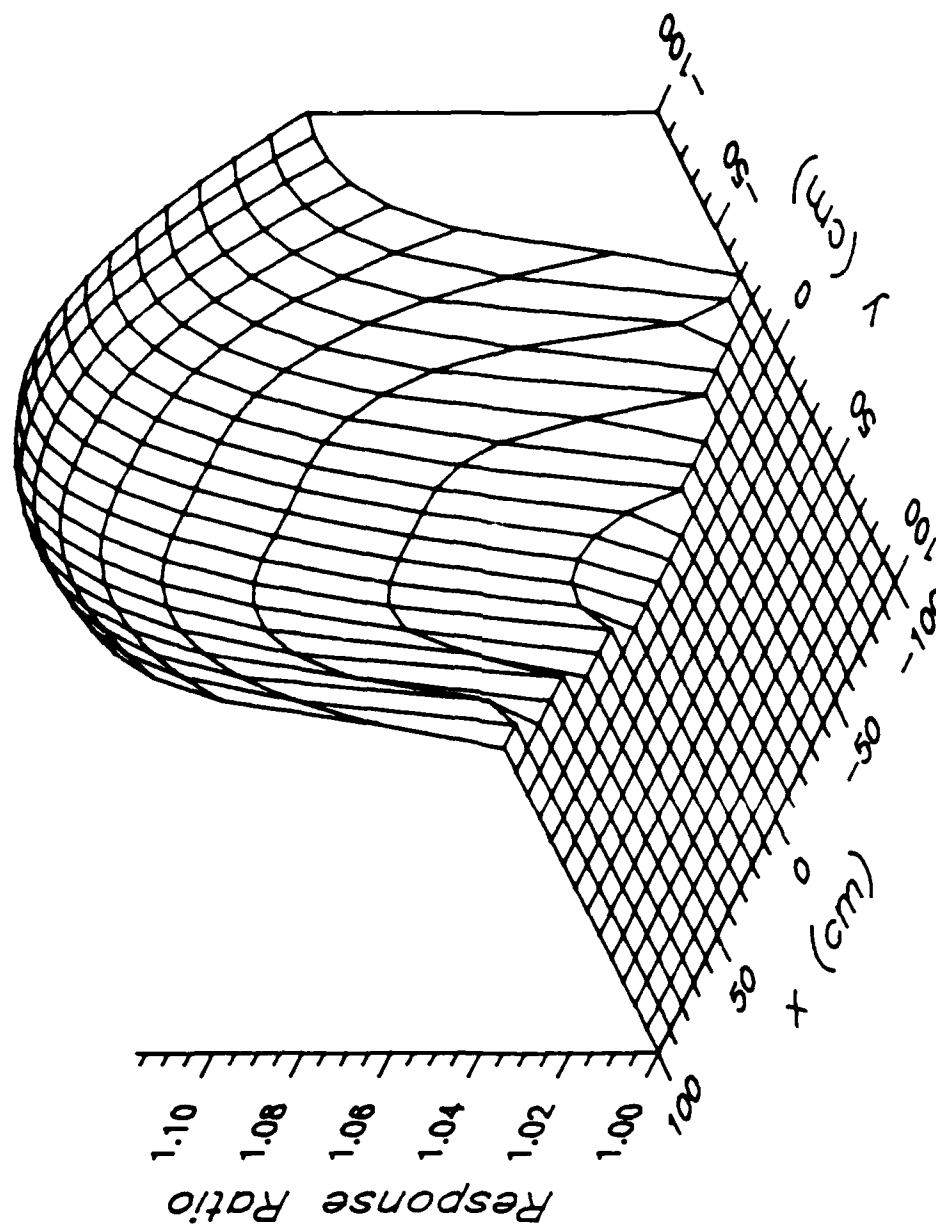


Figure VII.21. Spatial distribution of the single scattered mine to soil fluence response ratio for a 100 keV photon beam perpendicularly incident outside the edge of the TST mine. The TST mine is buried at a depth of 2.5 cm in NSL soil. The ratio is shown at a height of 34.6075 cm above the soil plane.

Conclusions Based on Signal Differences

The differences in the backscattered signals for mine present and absent suggest the examination of four detector types. These detector types are a simple, uncollimated detector to exploit differences in fluence; a collimated detector to exploit differences in the angular distribution of the fluence; an energy window detector to exploit the differences in the low energy spectra; and a segmented fluence detector to exploit differences caused by edge effects. Each of these detector types must be capable of rapidly detecting mines over a path wide enough to allow passage of an armored vehicle. This requirement results in detector configurations similar to that shown in Figure II.1, that is, large area detectors which allow rastering of an x-ray source beam. The existence of the raster gap and practical considerations of reasonable size result in configurations different than those employed in the simple physical arguments described above. The geometry of these more realistic configurations is examined later in this chapter. Despite the increase in geometric complexity, calculations for the more realistic configurations are shown to closely follow the general results presented above. Each of the more realistic detector types is modelled as two panels of detecting material located above and parallel to the soil surface, and separated by a gap to allow raster of the source beam. The collimated detector adds the capability to limit the acceptance angle of photons incident on the

detector. The energy window detector selects and accepts for counting, only those photons within a specific energy range striking the uncollimated panels. The segmented detector divides the panels into regions for comparisons of asymmetric fluence responses.

Except in the case of the small NaI(Tl) detector, used in the measurements to obtain images and to verify calculated predictions, only fluence response is considered. As long as the detector employed is capable of efficiently sensing photons in the energy range below 200 keV, the error introduced by considering only the fluence response is not major. Figure VII.22 displays the NaI(Tl) and fluence responses for the case of the TST mine buried at 2.5 cm in HTL soil as a function of source beam energy. The shapes of the response curves are very similar and results expressed in terms of ratios of fluence responses can be expected to closely follow detector response ratios. Differences will exist at low source energies. As an example, Figure VII.23 displays the ratio of the detector response to the fluence response for the case just discussed. The ratio is small at low energies because of the detector materials in front of the scintillation crystal and due to the lower level energy discrimination (35 keV in this example). The photons striking the detector are lower in energy than the source photons due to the incoherent scattering process, so that the figure is really a nonlinearly, energy-shifted version of the detector response versus energy curves, integrated

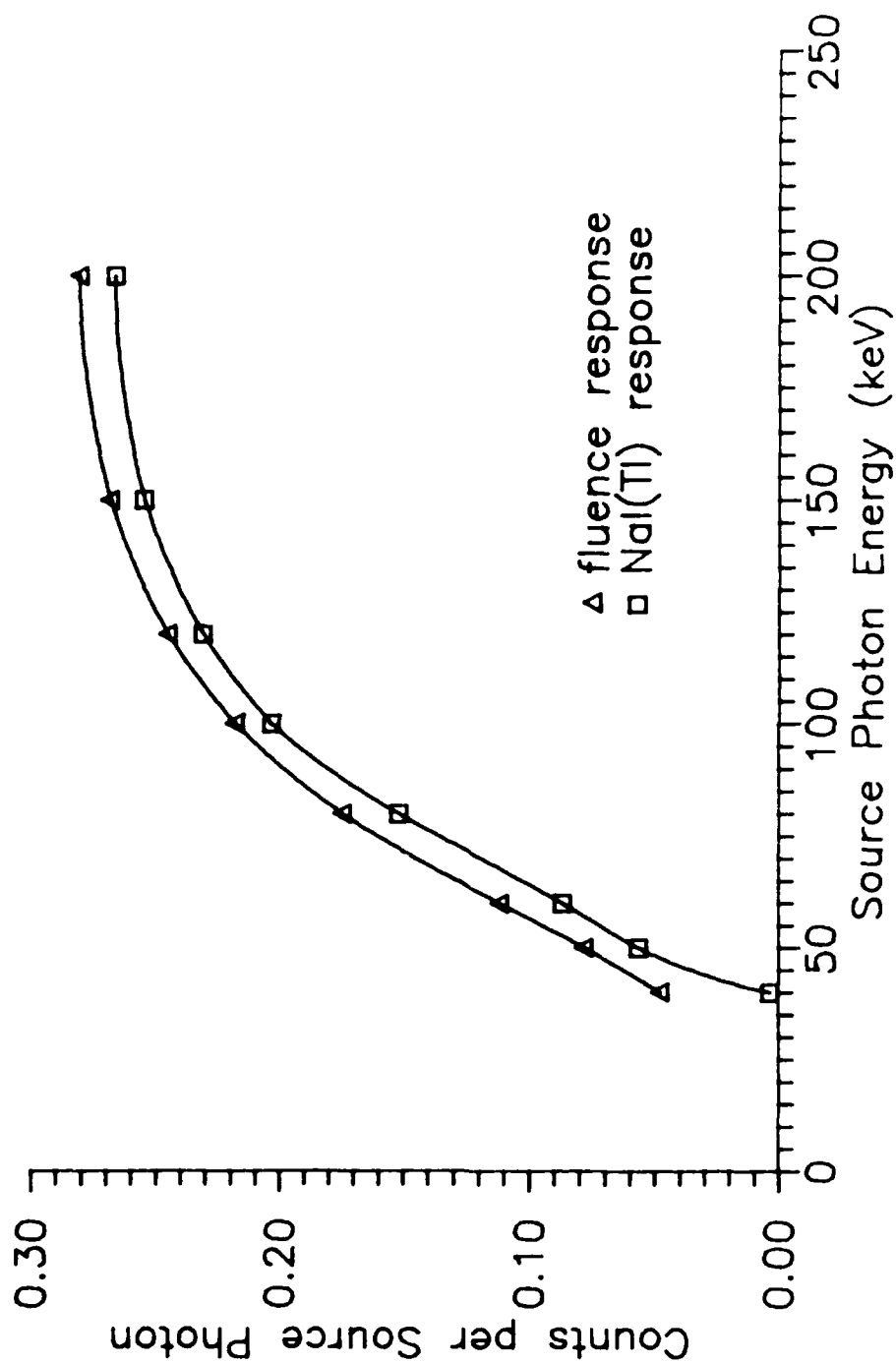


Figure VII.22. NaI(Tl) detector response and fluence response versus source beam energy. The responses (counts/source photon) are for perpendicular incidence of photon beams on the center of the TST mine buried at a depth of 2.5 cm in HTL soil. Both responses are for an infinite plane at a height of 34.6075 cm above the soil surface.

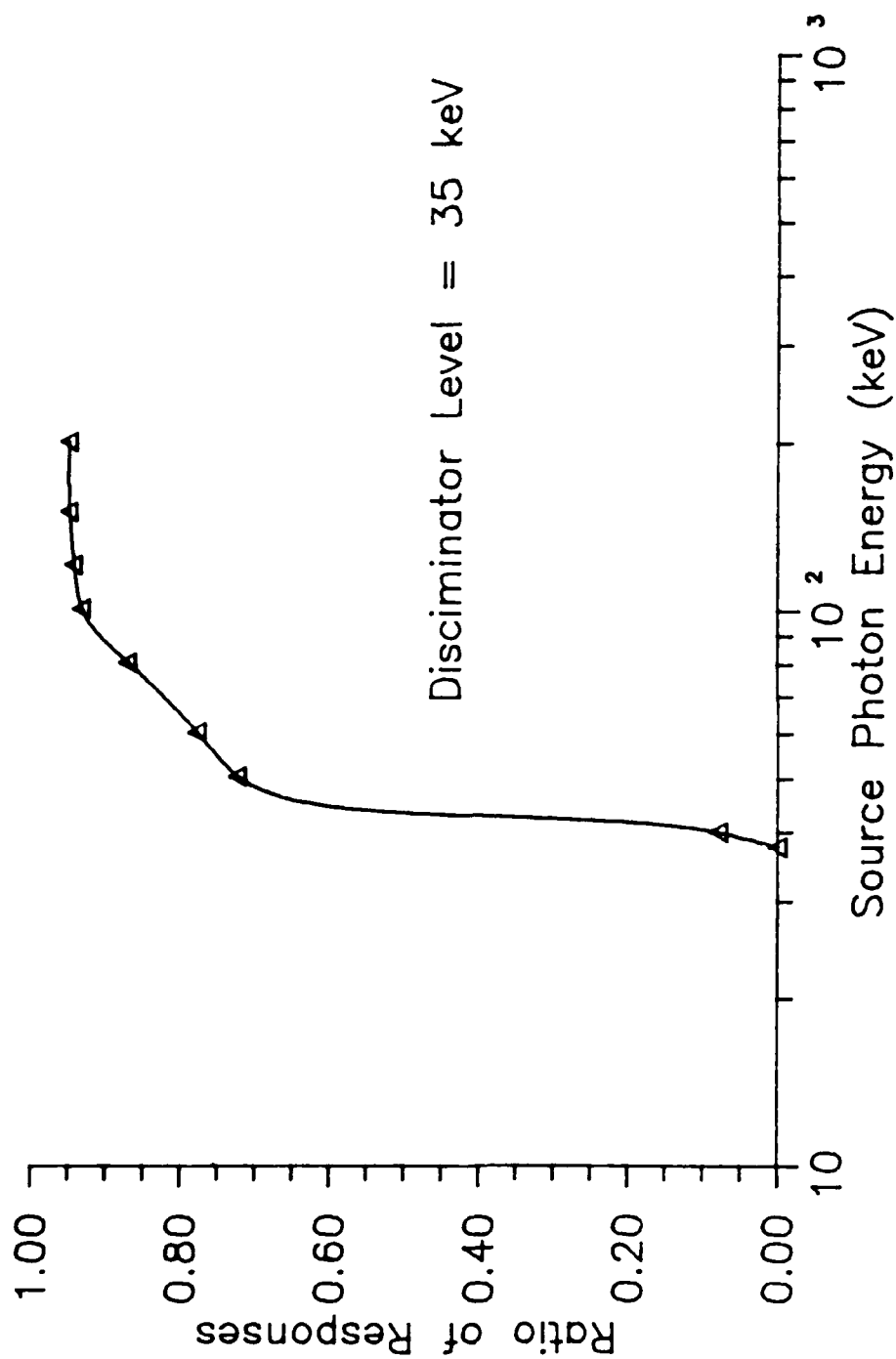


Figure VII.23. Ratio of NaI(Tl) detector response to fluence response as a function of source energy. This figure shows the ratio of the two responses displayed in Figure VII.22.

over all angles of incidence, presented in Chapter VI (compare this figure with Figure VI.4). The low ratio at low source energies is not of major consequence because such source photons do not contribute strongly to either of the responses. The energy window detector, which uses low energy photons as its detection mechanism, is a possible exception to these comments. If significant differences in the energy distributions of the mine and soil cases exist within energy bin widths (5 keV) used in the calculations, errors will be introduced as a result of the rapid variation in the detector to fluence response ratio at low energy.

Irradiation Geometry and Optimum Energy Considerations

A combination of practical concerns, and the physics of the backscatter problem limit the geometric relationship between detector and soil surface. With the large area, panel detector configuration as a basis, the irradiation geometry is examined. Optimum source energies are also discussed.

Height of Detector

The height of the detector above the soil surface must allow for operation over rough terrain. From a purely theoretical standpoint the optimum height would be determined as that which maximizes the ratio of mine present to mine absent response while providing the largest possible fluence striking the detector. This height depends on the

energy of the source beam and the panel geometry. Such considerations lead to optimum heights on the order of 15 to 25 cm for uncollimated detectors, dependent upon the width of the panels employed. As a practical concern, the height is determined by the rough terrain operation requirement. Heights of approximately 30 cm above the soil surface are probably the minimum acceptable to preclude damage to the detector. Even this may not be enough if large collimators are employed. With the exception of calculations to determine the effect of height variation, computations in this study have been performed for a detector height of 34.6075 cm. This height corresponds to that used in measurements and is near the minimum acceptable, and hence close to the practical optimum. A description of sensitivity to height variation of the detectors is provided in Chapter VIII.

Angle of Incidence

The optimum angle of incidence for the source beam on the soil is zero degrees (perpendicular). This angle provides the maximum penetration depth into the soil. All other angles effectively increase the apparent depth of burial of the mine, making detection more difficult. An objection to perpendicular incidence is that the maximum backscattered response is located on line with the source beam (see Figures VII.7 and VII.8), where a detector cannot be placed. However, the existence of the central minimum in the mine to soil response ratio, discussed above, makes

inclusion of this region unattractive. Table VII.2 shows an example of the effect of angles of incidence other than zero degrees on the mine to soil ratio for collimated and uncollimated fluence detectors. A number albedo detector is included in the table for reference. The detector geometry used in these calculations consists of two 30 cm wide panels separated by a raster gap of 30 cm, located 34.6075 cm above the soil surface and centered on the beam/soil intercept. This geometry allows the beam incident at 20 degrees to pass through the raster gap, while the 60 degree beam passes under the rear panel from behind, when used in conjunction with the source height employed in the measurements. Non-zero degree incident beams are shown to degrade the fluence response ratios. Energy window detectors are also adversely affected. Since the average soil penetration depth decreases with increasing angle of incidence, the low energy scatter contribution due to the mine decreases. Increasing the angle of incidence increases the number of reflected photons, primarily because their shallower penetration also produces easier escape to the soil surface. This increased scatter, however, is characteristic of the soil, not the buried mine. As a result, the mine to soil ratio in the energy window detector is lower for non-zero angles of incidence. This effect is shown by Figure VII.24 which displays the ratios of the integral energy spectra of mine present to soil cases for angles of incidence of zero and 60

TABLE VII.2

Mine to Soil Response Ratios
At Selected Beam Angles of Incidence

Detector Type	Mine to Soil Fluence Ratio ^a Angle of Incidence		
	0°	20°	60°
Number albedo	1.141 ±0.009	1.125 ±0.010	1.056 ±0.008
Uncollimated fluence ^b	1.183 ±0.017	1.155 ±0.016	1.056 ±0.013
Collimated fluence ^b			
Acceptance angle			
23.1°	2.173 ±0.160	1.968 ±0.179	1.702 ±0.113
19.9°	2.697 ±0.313	2.469 ±0.344	1.950 ±0.166
16.3°	2.748 ±0.466	3.015 ±0.648	2.523 ±0.300
11.5°	3.372 ±1.130	1.671 ±0.564	2.804 ±0.541

^aThe calculation example is for a 100 keV photon beam of radius of 1 cm, incident on NSL soil of density 1.54 g/cm³, with the TST mine at a depth of burial of 2.5 cm. In each case the beam is incident at the center top of the mine, and the detector height is 34.6075 cm.

^bThe detector consists of two 30 cm wide by 210 cm long panels, separated by a raster gap of 30 cm, parallel to the soil surface and centered on the beam/soil intercept position.

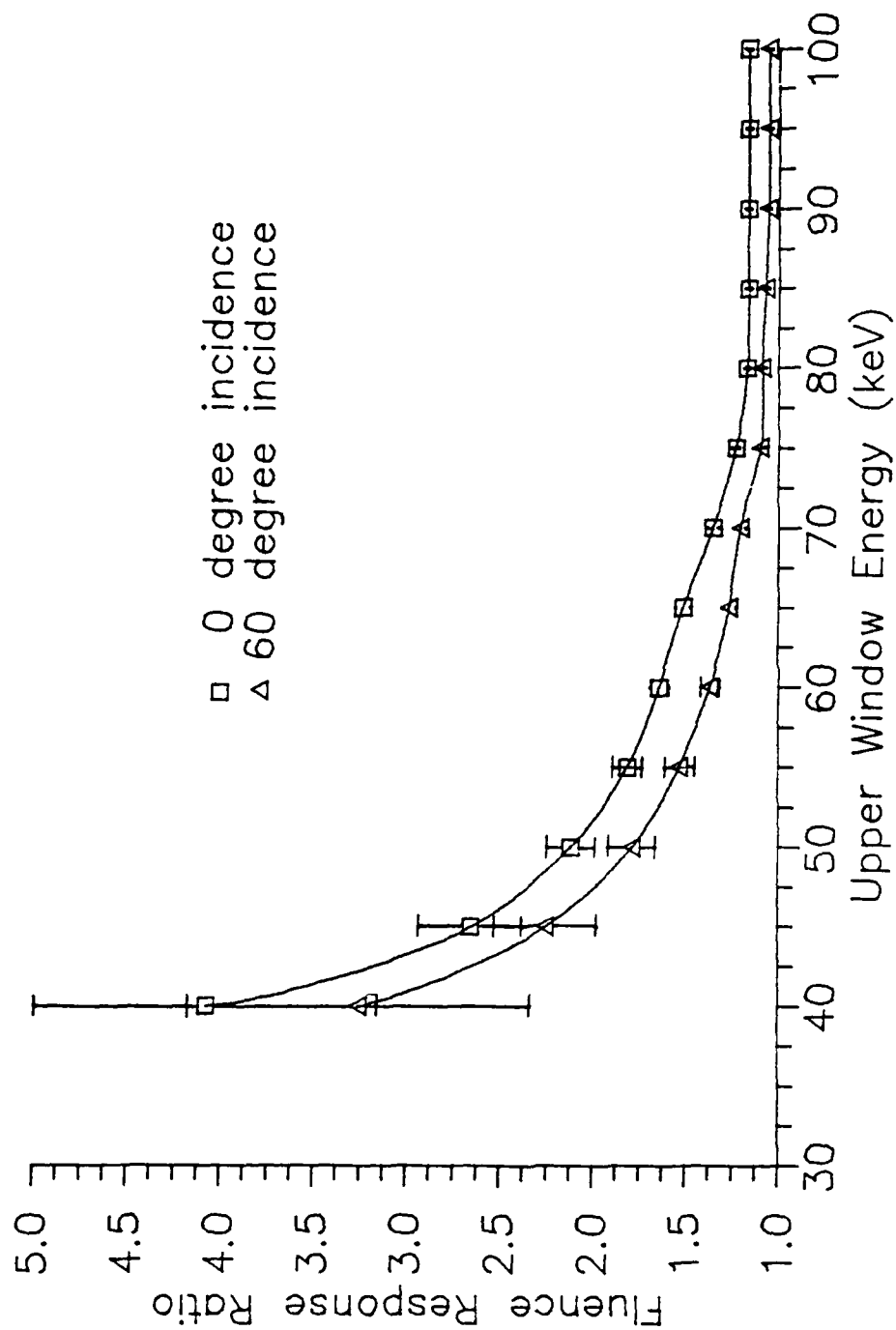


Figure VII.24. Ratios of integral energy spectra for 100 keV photons incident on the TST mine at 2.5 cm in NSL soil for the cases of 0 and 60 degree incidence. The lower energy window level is set at 35 keV.

degrees. The asymmetries produced by edge effects are masked by the asymmetries resulting from non-zero angles of incidence. Figure VII.25 shows the spatial variation in response on a plane located 34.6075 cm above the soil surface for the case of 60 degree incidence. Table VII.3 shows the ratio of the response of front to back panels for both the soil and mine cases, demonstrating this asymmetry. The high ratios are a result of the combination of the importance of photons scattered parallel to the soil surface and the forward peaking of the incoherent interaction. With this high angle of incidence, photons traveling parallel to the soil surface are forward scattered towards the front panel of the detector and backscattered towards the rear panel. The result is the large asymmetry between the panels. The higher fluence on the front panel is also due, in part, to the fact that the probability of forward scatter, unlike backscatter is, on a per electron basis, enhanced in lower atomic number materials at 100 keV (see Figure IV.7b). The large front to rear panel ratio, compared to the same quantity when only soil is present, suggests a fluence detector consisting of two segments. The ratio of the signals of the two panels would be compared to the expected ratio when only soil is present to indicate the presence of a mine. Unfortunately, the high angle of incidence makes this method less capable of detection at greater depths than perpendicularly incident photons beams. Table VII.3 also provides the front to rear panel ratio for the

TABLE VII.3

Front to Rear Panel Ratios of the Collimated Detector
for 100 keV Beams Incident on the TST Mine at 60 Degrees

Collimator Acceptance Angle	Front to Rear Panel Fluence		Ratio ^a
	Soil Only	DOB ^b =2.5 cm	DOB=7.5 cm
90.0°	1.095 ± 0.019	1.159 ± 0.020	1.088 ± 0.014
36.9°	1.661 ± 0.060	2.044 ± 0.072	1.754 ± 0.046
25.8°	4.671 ± 0.487	6.426 ± 0.599	4.655 ± 0.149
23.1°	6.102 ± 0.924	6.715 ± 0.787	5.618 ± 0.561
19.9°	5.030 ± 0.938	6.819 ± 1.015	5.266 ± 0.670
16.3°	3.777 ± 0.935	8.307 ± 1.701	3.590 ± 0.588
11.5°	2.774 ± 0.909	8.978 ± 2.958	2.514 ± 0.614

^aThe calculation example is for a 100 keV photon beam of radius of 1 cm, incident at 60 degrees on NSL soil of density 1.54 g/cm³, with the TST mine at depths of burial of 2.5 and 7.5 cm. In each case the beam is incident at the center top of the mine, and the detector height is 34.6075 cm. The detector consists of two 30 cm wide by 210 cm long panels, separated by a raster gap of 30 cm, parallel to the soil surface and centered on the beam/soil intercept position.

^bDepth of burial of the top surface of the mine in soil.

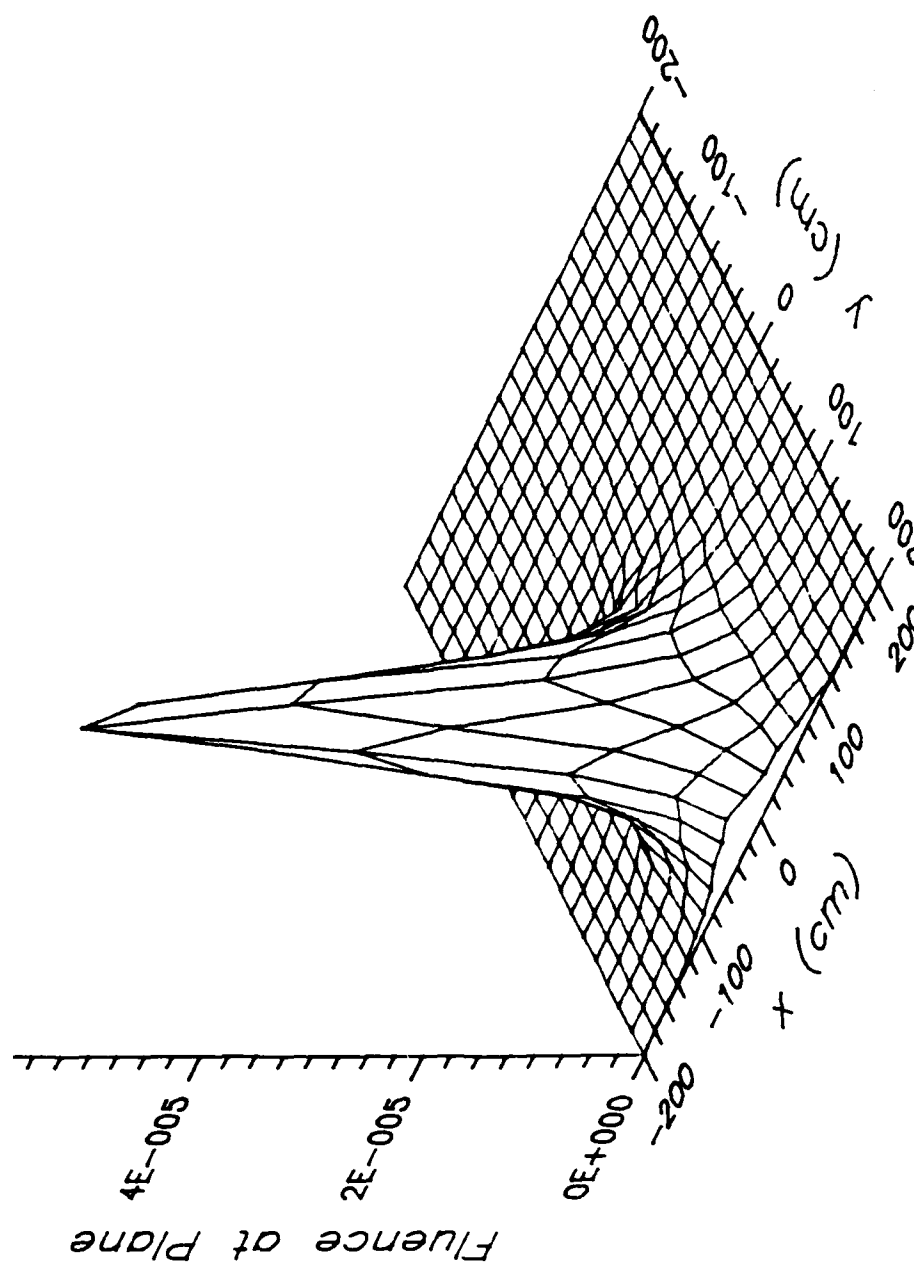


Figure VII.25. Spatial distribution of the fluence response from a 100 keV beam incident at 60 degrees on the TST mine at 2.5 cm in NSL soil. The fluence response (photons/(source photon-cm²)) is shown at a height of 34.6075 cm above the soil surface.

mine buried at 7.5 cm, demonstrating that the ratio at this depth is similar to that of soil at this depth.

Raster Gap Size

The size of the raster gap is an important variable for all of the detector types except the energy window detector. In the energy window detector, removal of the central section preferentially removes higher energy single scattered photons. Since the detector operates on differences in the lower energies, there is no major influence on the mine to soil ratio resulting from the gap. Calculations for a series of raster gap and panel width combinations show no statistically different results for gap sizes from 10 to 40 cm for the energy window detector. For the uncollimated fluence detectors, both segmented and unsegmented, the gap plays the role of removing the region of the central minimum in the mine to soil response ratio. Finding the optimum gap size involves maximizing the ratio between mine and soil response, while maintaining a reasonable fluence on the detector. Figure VII.26 shows a typical fluence response versus distance from the beam axis. The example is for a 100 keV beam striking the center of the TST mine buried at a depth of 2.5 cm in NSL soil. The rapid fall off in the response, coupled with the general increase in the mine to soil ratio with distance produce an optimization problem. This problem is addressed in conjunction with determination of the panel widths below.

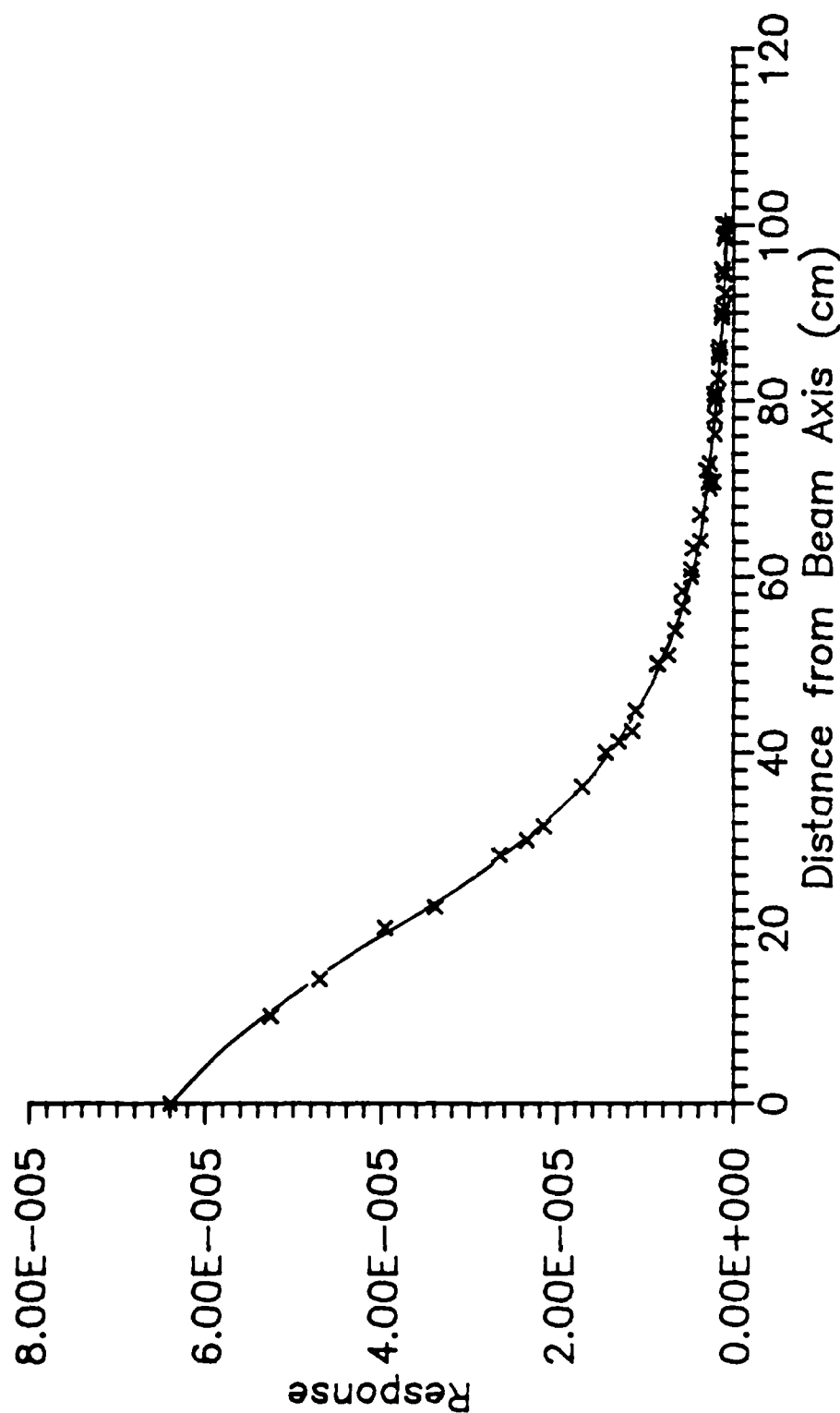


Figure VII.26. Fluence response versus distance from beam axis for 100 keV photons perpendicularly incident on the TST mine at 2.5 cm in NSL soil. The fluence response (photons/(source photon-cm²)) decreases rapidly with distance from the beam axis. The response is calculated at a height of 34.6075 cm above the soil plane.

The optimization of the gap size for the collimated fluence detector proceeds in the same fashion. The optimum gap size is very dependent upon the source energy, the soil type and density, and collimator acceptance angle since the technique differentiates between the multiple scattering properties of the medium. A decision based on the calculations is complicated by the poor statistics of the results caused by the very small fraction of the source photons which produce a response in a useful collimated detector. Attempts to use a correlated sampling technique within the Monte Carlo method, such as that employed by Coleman (1971), are inappropriate on two counts. First, the existence of air within the mine (not present in Coleman's work) violates the variance criterion for applying correlation techniques to the interaction coefficients. This criterion basically requires that the interaction coefficients of the materials in the correlation calculation be similar. The great difference in the densities of air and the other problem materials violates this requirement. The second problem with the method is that the correlation technique does not apply to any atomic number dependent quantities other than the interaction coefficients. Thus, even if the air layer were neglected, the scattering routines would have to be altered. No coherent scattering could be permitted, and the Klein-Nishina cross section would have to be substituted for the incoherent scattering cross section. Demonstrated inaccuracies with such substitutions in the energy range of

interest make that approach unattractive. Calculations with HTL soil containing 10% water by weight for the TST mine buried at 2.5 cm indicate that the optimum source energies are between 60 to 120 keV. With perpendicular incidence and a detector height of 34.6075 cm, the optimum gap size is approximately 30 to 40 cm with collimator acceptance angles of 20 to 26 degrees. Smaller collimator angles cannot be ruled out because the statistical uncertainties in the mine to soil ratio are very large. Relevant results from these calculations are provided in Table VII.4. The ratios displayed in this table are very large in comparison with those obtainable with the uncollimated fluence detector at this depth of burial of the mine. Virtually any energy between 50 and 200 keV is capable of providing mine detection at 2.5 cm. The same sets of calculations have been performed for a variety of depths of burial of the TST mine, several soil densities, two additional water contents of HTL soil, and NSL soil. Optimum energies for the collimated detector are approximately 60 to 120 keV. The other conclusions presented in this section are also valid over the range of variables investigated. Details of these calculations are provided in Chapter VIII. An additional consideration in selecting the raster gap size for a collimated detector is the capability to detect mines laid on the soil surface. This would be a particularly common situation in modern mechanized warfare. If the raster gap is larger than twice the diameter of the mine (the beam axis

TABLE VII.4

Results of Calculations for the Geometric Parameters
of the Collimated Fluence Detector

Energy (keV)	Gap Size (cm)	Mine to Soil Fluence Ratio ^a Collimator Acceptance Angle				
		90.0°	36.9°	25.8°	23.1°	19.9°
40	30	1.006 ± 0.020	0.996 ± 0.039	- _b	- _b	- _b
	40	1.022 ± 0.022	1.023 ± 0.065	- _b	- _b	- _b
50	30	1.047 ± 0.021	1.130 ± 0.046	1.353 ± 0.178	2.058 ± 0.773	- _b
	40	1.059 ± 0.023	1.161 ± 0.074	2.485 ± 1.260	1.826 ± 1.025	- _b
60	30	1.090 ± 0.022	1.178 ± 0.049	1.570 ± 0.184	3.975 ± 1.235	- _b
	40	1.076 ± 0.024	1.141 ± 0.071	2.895 ± 1.419	1.896 ± 1.092	- _b
80	30	1.149 ± 0.019	1.297 ± 0.042	1.867 ± 0.163	3.606 ± 0.588	5.034 ± 1.456
	40	1.126 ± 0.021	1.336 ± 0.066	2.749 ± 0.725	3.721 ± 1.457	2.330 ± 1.072
100	30	1.131 ± 0.016	1.240 ± 0.033	1.650 ± 0.114	2.474 ± 0.294	4.047 ± 0.876
	40	1.141 ± 0.019	1.285 ± 0.055	2.829 ± 0.582	2.738 ± 0.775	3.247 ± 1.189
120	30	1.155 ± 0.016	1.289 ± 0.035	1.679 ± 0.114	2.167 ± 0.234	2.262 ± 0.366
	40	1.130 ± 0.018	1.357 ± 0.053	3.025 ± 0.509	2.535 ± 0.556	2.958 ± 0.907
150	30	1.092 ± 0.015	1.169 ± 0.030	1.415 ± 0.084	1.907 ± 0.173	2.047 ± 0.277
	40	1.087 ± 0.016	1.332 ± 0.049	2.440 ± 0.333	2.262 ± 0.413	1.986 ± 0.494

TABLE VII.4 - continued

Energy (keV)	Gap Size (cm)	Mine to Soil Fluence Ratio ^a Collimator Acceptance Angle				
		90.0°	36.9°	25.8°	23.1°	19.9°
200	30	1.080 ±0.014	1.124 ±0.028	1.324 ±0.072	1.506 ±0.117	1.786 ±0.197
	40	1.080 ±0.015	1.261 ±0.044	2.147 ±0.239	2.441 ±0.357	2.247 ±0.427

^aThe calculations are for photon beams perpendicularly incident on HTL soil with 10% water content by weight and soil of density 1.80 g/cm³, with the TST mine at a depth of burial of 2.5 cm. The diverging source beams are 1.27 cm by 1.27 cm at the soil surface and are produced by a point source 64.48 cm above the soil surface. In each case the beams are incident at the center top of the mine, and the detector height is 34.6075 cm. Detector panels are 30 cm wide and 210 cm long, separated by raster gaps of either 30 or 40 cm, each centered on the source beam axis.

^bUncertainties are too large to allow meaningful comparisons.

to edge of detector distance exceeds the diameter of the mine), detection will be difficult because no medium (other than air) is available to scatter photons outside the walls of the mine. A compound detector, which includes an uncollimated portion placed inside the collimated panels (producing a smaller raster gap), could be used to overcome this problem. As shown in Chapter VIII, the uncollimated detector is well-suited to detection of surface laid mines (see Figures VIII.29 and VIII.30).

Detector Collimator Length

Because of the requirement for the mine detection system to travel over rough terrain, care must be taken to insure that the length of the collimator is not excessive for the detector height. The purpose of the collimator is to prevent single scattered photons from reaching the detector. There is a fixed geometric relationship between the height of the detector, the collimator length, the raster gap size, the collimator spacing, and the acceptance angle. In the case of a compound (collimated and uncollimated regions) detector, the raster gap discussed here is equivalent to twice the distance from the beam axis to the nearest edge of a collimated panel. If the raster gap is small, very long collimators are required at the panel edge nearest the beam to preclude significant amounts of single scatter from entering the detector. As the raster gap size increases, the required collimator lengths decrease. If the spacing between adjacent elements is large,

long collimators will again be needed. Figure VII.27 shows the relationships for a detector height of 34.6075 cm. This graph shows the required length of the collimator element closest to the beam axis to prevent single scattered photons from reaching the detector as a function of the raster gap size and the distance to the next nearest element. To obtain an overall 30 cm clearance above flat soil surfaces, the detector height must be increased to accommodate the collimator. As can be seen from the graph, unless care is taken with the geometry of the system, very long collimators will preclude practical employment at useful heights of the detector. With the small detector used in the experiments, employed at distances from the beam axis of approximately 20 cm (analogous to one-half of the raster gap size), collimator lengths of 3 to 5 cm are appropriate.

Detector Panel Dimensions

The length of the detector panels is determined by the requirement to cover the full width of an armored vehicle. This vehicle width is typically on the order of three meters, but the detector must extend beyond the sides of the vehicle in order to provide mine detection information in those locations. Given that detector heights of approximately 30 cm are to be used, Figure VII.26 indicates that this overhang on each end need not be more than about 70 cm. The rapid fall off in backscattered fluence with distance from the beam axis allows calculations performed for a truncated section of the detector about the axis to be

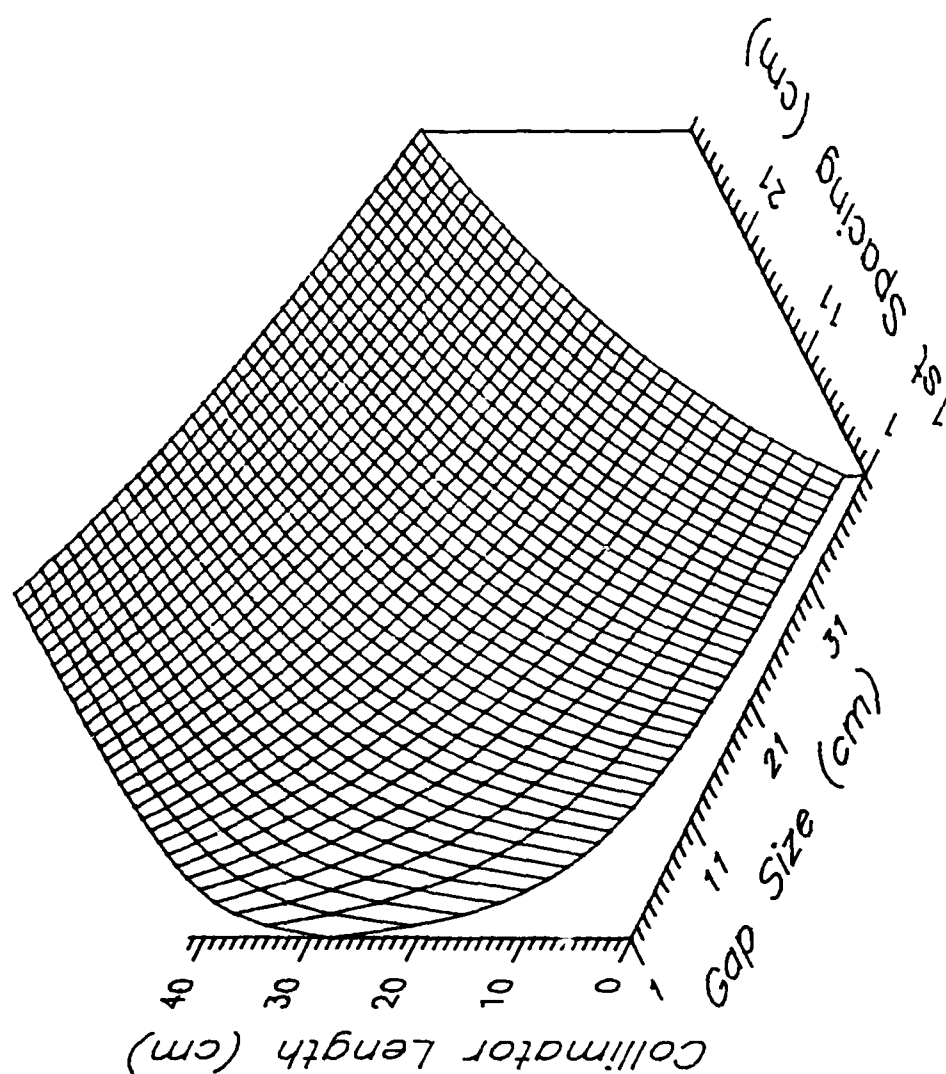


Figure VII.27. Relationship between the raster gap size, the length of the collimator, and the spacing of the first collimator element required to exclude single scattered photons from the detector.

accurate. Calculations performed in this research are for 210 cm long panels centered on the beam axis.

The optimum width of the detector panels depends on the beam energy, raster gap size, and operational considerations. Minimizing the width helps prevent the possibility of damage to the detector system while operating over rough terrain. The key advantage to larger widths lies in increasing the total fluence sensed, improving the detection statistics, and allowing lower x-ray generator power levels. For the uncollimated detectors there is the added advantage of reducing sensitivity to variations in height.

The optimum width of the collimated detector is not found through calculations because of the very low fluences striking small detector strips. Experiments using the NaI(Tl) detector, however, indicate that even very small detectors can be successfully used with this technique. The most important variables for the collimated detector are the size of the raster gap and the acceptance angle of the collimator, which have already been discussed. Widths of 30 cm have been used for collimated detectors in the calculations to allow meaningful comparisons of the low fluences sensed by these detectors per source photon.

Table VII.5 shows a typical set of calculations for an uncollimated fluence detector, used in determining panel width. The information provided by this table indicates that the improvement in the mine to soil ratio achievable by varying the panel width and raster gap size is small.

TABLE VII.5

Mine to Soil Fluence Ratio Dependence On Panel Width
and Raster Gap Size for an Uncollimated Detector

Raster Gap Size (cm)	Mine to Soil Fluence Ratio ^a (% of Backscattered Fluence Detected)		
	Panel width (cm)		
	10	30	50
10	1.112 ± 0.020 (23.5)	1.175 ± 0.024 (18.6)	1.174 ± 0.030 (12.5)
20	1.139 ± 0.016 (42.1)	1.175 ± 0.019 (31.2)	1.190 ± 0.023 (21.1)
30	1.147 ± 0.014 (54.6)	1.183 ± 0.017 (39.7)	1.176 ± 0.020 (26.5)
40	1.156 ± 0.012 (63.2)	1.176 ± 0.016 (45.1)	1.180 ± 0.019 (30.2)
50	1.153 ± 0.012 (68.6)	1.178 ± 0.015 (48.9)	1.176 ± 0.018 (32.7)
60	1.156 ± 0.012 (72.3)	1.176 ± 0.015 (51.3)	1.174 ± 0.018 (34.5)

^aThe calculations are for 100 keV photon beams perpendicularly incident on NSL soil of density 1.54 g/cm³, with the TST mine at a depth of burial of 2.5 cm. The diverging source beams are 1.27 cm by 1.27 cm at the soil surface and are produced by a point source at 64.48 cm above the soil surface. In each case the beams are incident at the center top of the mine, and the detector height is 34.6075 cm. Detector panels are 210 cm long and centered on the source beam axis.

Considerations regarding height sensitivity, examined quantitatively in Chapter VIII, encourage the use of small raster gaps to maximize the fluence striking the detector. Table VII.5 also provides the fraction of the total back-scattered fluence intercepted by the various detector configurations. Given the small differences in the mine to soil ratio, the 10 cm gap size is selected for calculations. Increase of panel width beyond 30 cm produces virtually no change in the mine to soil ratio, so the smallest width is used in the majority of the calculations for the uncollimated detector to satisfy the operational requirement to minimize the total size of the detector. Other widths are examined with respect to height sensitivity in Chapter VIII.

Segmented Detector Geometry

The geometry of the segmented detector is shown in Figure VII.28. The principle of operation of this detector is to remove an additional portion of the central minimum in the mine to soil ratio. A central section of each panel with respect to the beam axis is removed from the detector. Since the x-ray beam is rastered, the section removed must also be rastered. This could be accomplished electronically. Rather than simply comparing the backscattered responses with and without mine present, an amplification is achieved by comparing the ratios of the responses of each of the four detector segments. Over perfectly uniform soil and with beam intercept at the center of the mine, the ratios, taken with respect to any one of the segments, would be

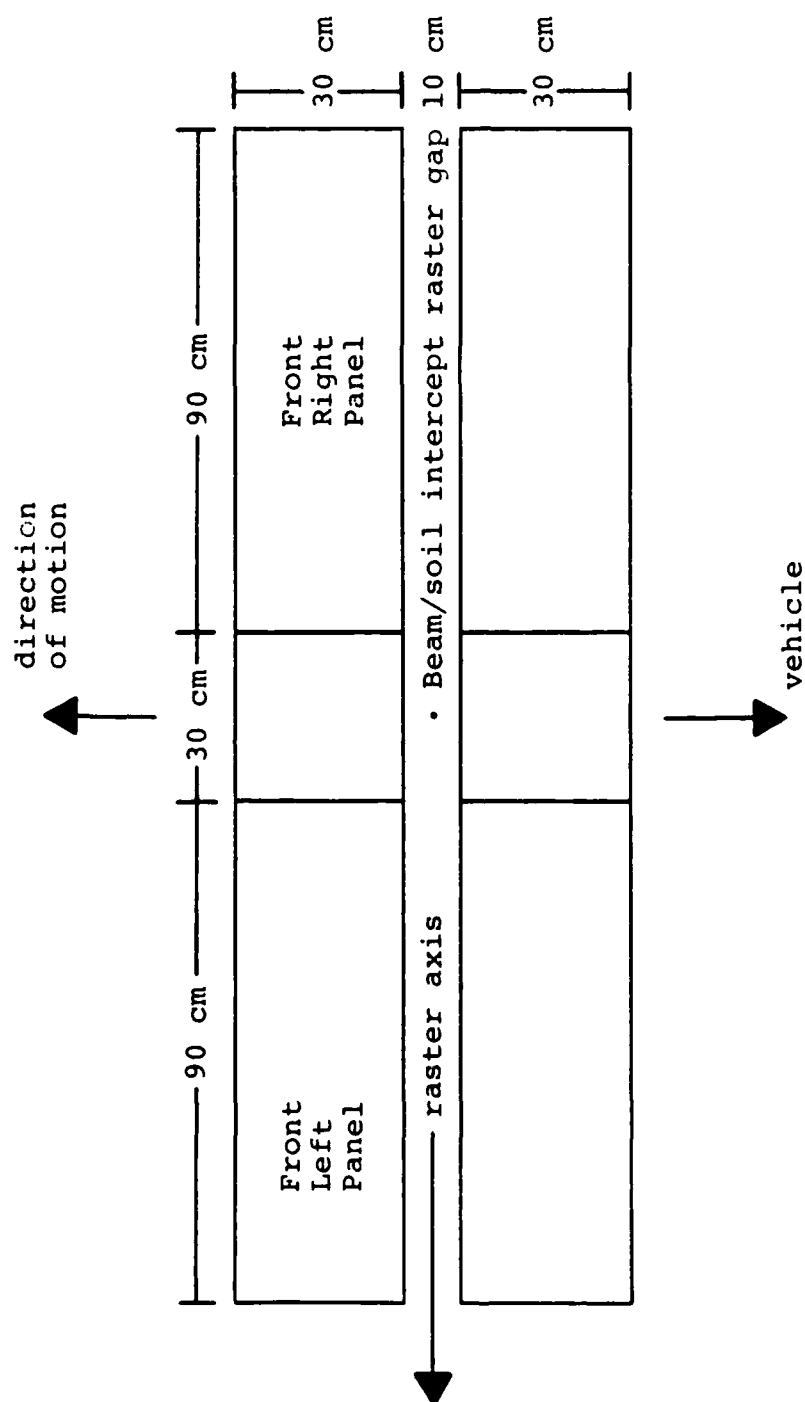


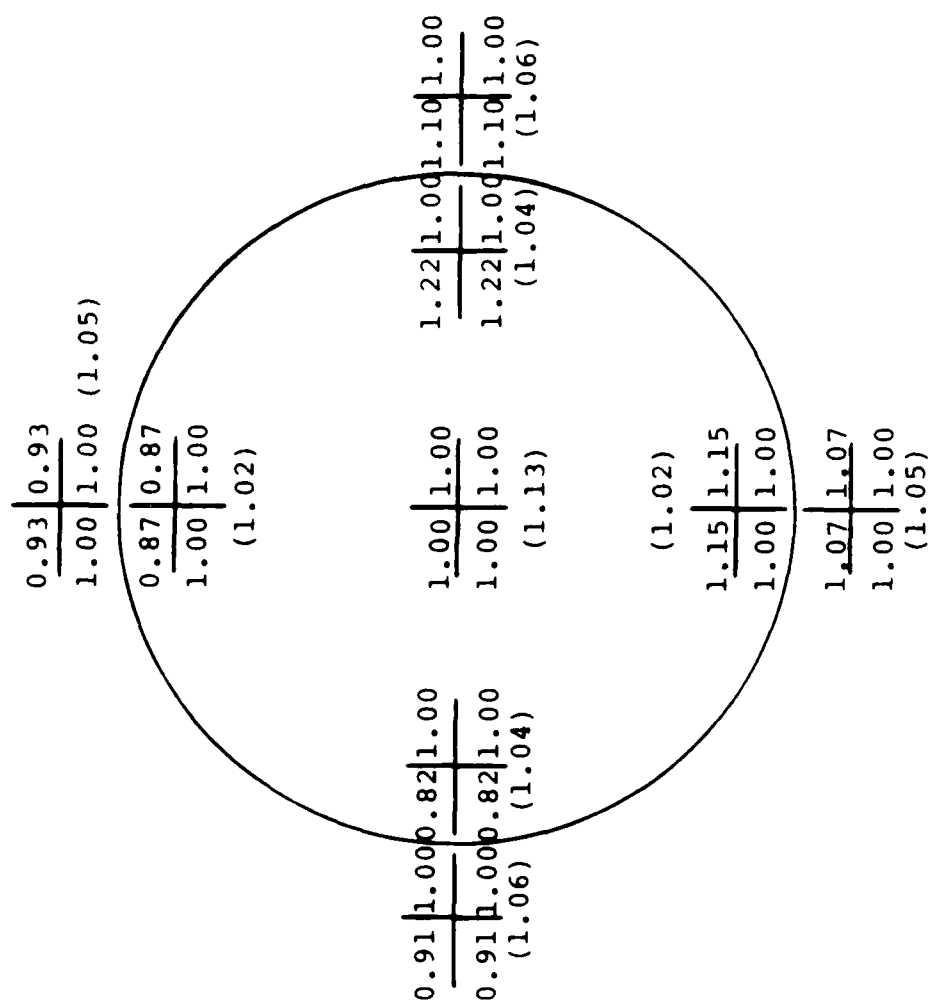
Figure VII.28. Geometry of the segmented fluence detector.

1.00. In all other cases, the ratios would not all be the same. The differences are the greatest when the beam intercepts are near the edge of the mine. In these locations, the edge effects, due to the air layer of the mine, discussed above, are dominant. The results of the consideration of the optimum panel widths suggest that a central 30 cm of each panel with respect to the beam be removed. Figure VII.29 shows the fluence response ratios for a 150 keV beam incident on the TST at a depth of burial of 2.5 cm in HTL soil as a matrix with right rear panel given a value of 1.00. The 150 keV energy is shown below to be approximately optimum for this detector. The mine to soil fluence ratio at 100 keV for an unsegmented, uncollimated detector with 30 cm wide panels and a 10 cm raster gap is also shown for the same intercepts.

Source Beam Collimation

Collimators are used to shape the x-ray beam. The primary considerations in the collimation process relate to image resolution and x-ray machine power requirements. The response from a given beam size striking the soil averages the effects of the materials through which the backscattered photons pass. Looser collimation, resulting in large beam dimensions, is less able to resolve differences between materials. Additionally, large beam sizes at the soil imply a greater angular spread of the beam. As seen in the discussion concerning angle of incidence, larger angles degrade the mine to soil ratio. The beam size used in the

Figure VII.29 Fluence response ratio matrices for the segmented detector for perpendicularly incident 150 kev photon beams on the TST mine at 2.5 cm in HTL soil. Each matrix value is with respect to the right rear panel of the segmented fluence detector. All intercepts, except that at the center of the mine, are located either 1.00 cm inside or outside of the mine wall. The ratios are calculated at a detector height of 34.6075 cm above the soil surface. Mine to soil ratios at 100 kev for an unsegmented, uncollimated detector at each intercept are indicated in parentheses.



experiments is 1.27 cm by 1.27 cm. This size, used in conjunction with a sampling interval of 2.54 cm, is capable of resolving the circular shape of the large antitank mine and providing edge effect information at mine/soil boundaries. Given the 64.48 cm height of the source, the angular spread of the beam is very small. Increasing the beam size to 5.08 cm by 5.08 cm, a factor of 16 in area, with this source height, produces only a 1.4% degradation of the mine to soil fluence ratio, in HTL soil examples. As a result beam sizes larger than those used in the experiments can be employed with little penalty in response ratio near the center of the mine, as long as the height of the source is not changed. Image resolution would suffer, however.

Source Energy Optimization

The method used to determine the optimum source energy for the collimated detector is addressed above in conjunction with geometry considerations. The optimum source energies of the other detector types depend less strongly on geometry, and are determined in this section. For the uncollimated detectors, both segmented and unsegmented, the technique employed is Monte Carlo calculations of the fluence responses for each of the three soil types with and without the TST mine, using the values of the geometric parameters discussed above. The calculations are for photon beams perpendicularly incident on the soils with various densities and moisture contents with the TST mine at a depth of burial of 0.0, 2.5, 5.0 and 7.5 cm. Diverging source

beams are 1.27 cm by 1.27 cm in size at the soil surface, and are produced by a point source at 64.48 cm above the soil surface. Detector panels, located 34.6075 cm above the soil, are 210 cm long and centered on the source beam axis. A beam/mine intercept at the center of the TST mine is used for the unsegmented detector; four intercepts inside and outside the mine are used for the segmented detector. Optimum energies for the energy window detector are examined by Monte Carlo calculations of the ratios of integral energy spectra at various source beam energies.

Figure VII.30 shows an example of an optimization curve for NSL soil for the uncollimated fluence detector. Curves obtained by this method are very similar to the number albedo versus energy graphs (Figures VII.2 and VII.3), as are the explanations for their shapes. The ratios are higher as a result of removal of the central minimum. The application of this same method to a range of soil conditions provides the results summarized in Table VII.6 for this detector type. A compromise energy of 100 keV provides reasonably good mine to soil ratios in all cases. Any energy within the range of 40 to 200 keV is capable of detecting mines buried flush to the soil surface. For this case, the lowest energy in the range provides the greatest ratio.

The uncollimated, segmented fluence detector presents a much wider range of optimum energies for the beam intercepts examined. These intercepts are located 1.00 cm from the

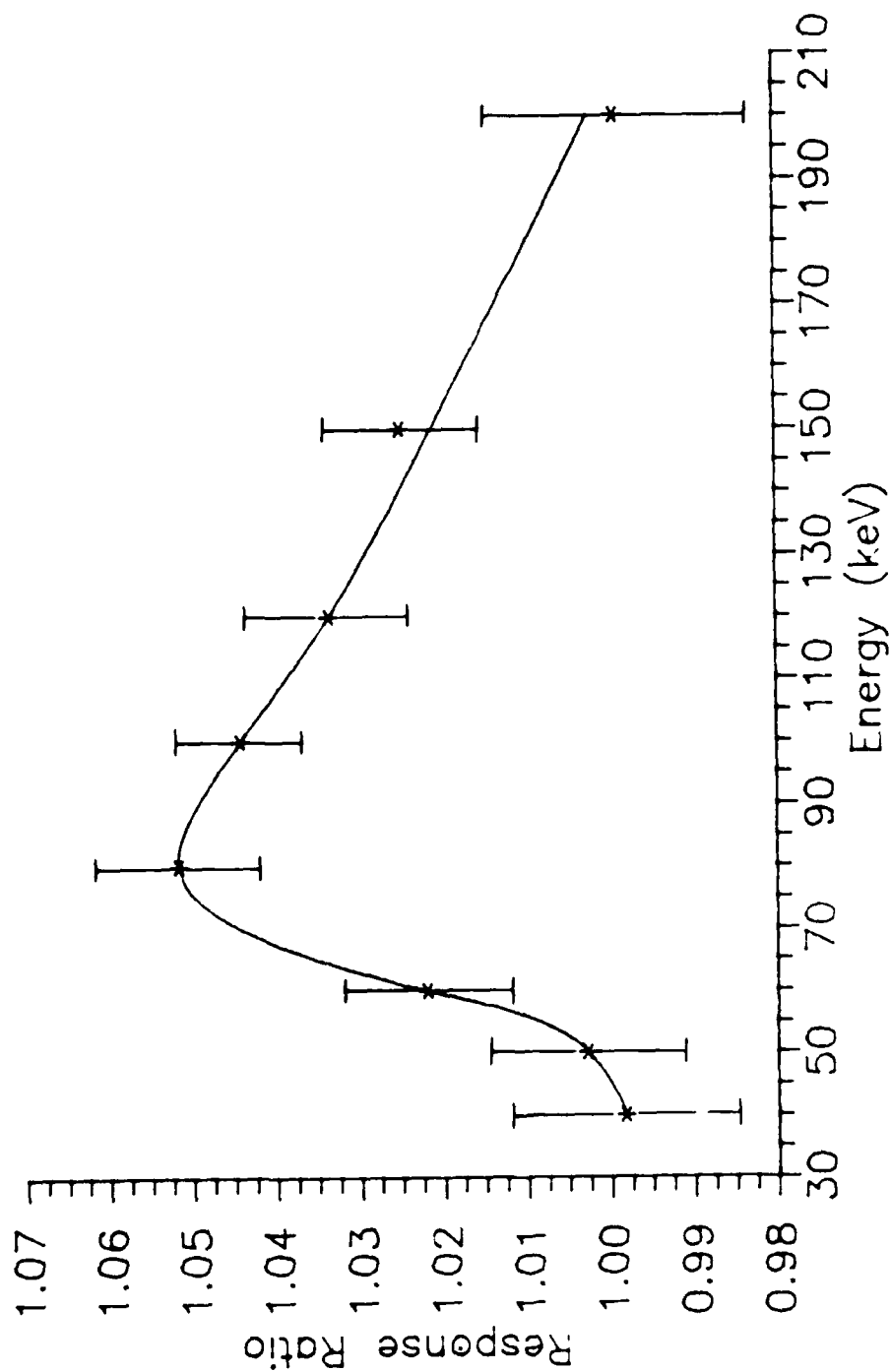


Figure VII.30. Source energy optimization curve for the uncollimated fluence detector with mine depth of burial of 5 cm, in NSL soil. The ratio of mine to soil fluence response striking an uncollimated detector consisting of two panels of 30 cm width and 210 cm length, separated by a raster gap of 10 cm and located 34.6075 cm above and parallel to the soil surface is shown as a function of source energy of perpendicularly incident beams. The beams intercept the mine at its center.

TABLE VII.6

Optimum Source Energies for the
Uncollimated Fluence Detector

Soil Type	Depth of Burial (cm)	Optimum Energy (keV)	Mine to Soil Fluence Response Ratio ^a
NSL	2.5	80	1.176 ± 0.018
	5.0	80	1.052 ± 0.016
	7.5	80	1.016 ± 0.016
HTL	2.5	100	1.133 ± 0.016
	5.0	120	1.042 ± 0.015
MCL	2.5	150	1.174 ± 0.026
	5.0	200	1.046 ± 0.015
HTL low density ^b	2.5	60	1.227 ± 0.021
	5.0	120	1.064 ± 0.015
	7.5	120	1.022 ± 0.014
NSL small air gap ^c	2.5	80	1.187 ± 0.014
	5.0	80	1.044 ± 0.015
HTL 10% H ₂ O	2.5	80	1.139 ± 0.011
HTL 20% H ₂ O	2.5	80	1.116 ± 0.015

^aSee text for description of calculation parameters.

^bDensity of 1.27 g/cm³.

^cAir layer in mine is 1.0 cm, instead of the normal 2.5 cm.

side of the mine in the positions shown in Figure VII.29. Because of symmetry, only four of the intercepts displayed in the figure produce different responses. For the purpose of this discussion, the intercepts will be referred to as inside or outside and front or lateral, where front is the direction of motion of the vehicle transporting the system (perpendicular to the long axis of the detector), and lateral is perpendicular to the direction of motion (along the direction of beam raster). The presence of soil in all beam intercepts outside of the mine results in optimum energies even for mines buried flush to the surface. There is a strong tendency towards higher energies in this technique, especially at greater depths of burial. The cone of forward scattered photons produced by scatter in the soil before the mine is reached, intercepts the edge of the mine producing dissimilar responses in the asymmetrically (with respect to the intercept position) located detector panels. The ratios produced are not large, but shift the optimum energy higher. Figure VII.31 shows an example of this behavior. Optimum energies for the segmented detector range from 80 keV to 200 keV or greater. It is not possible to find a single energy which provides good results for all cases, but 150 keV is the best for the range of soil types and densities examined. Table VII.7 provides a typical comparison of the ratios achieved by this method with the mine to soil ratios achieved by the unsegmented detector with 100 keV photons (compromise optimum for that detector)

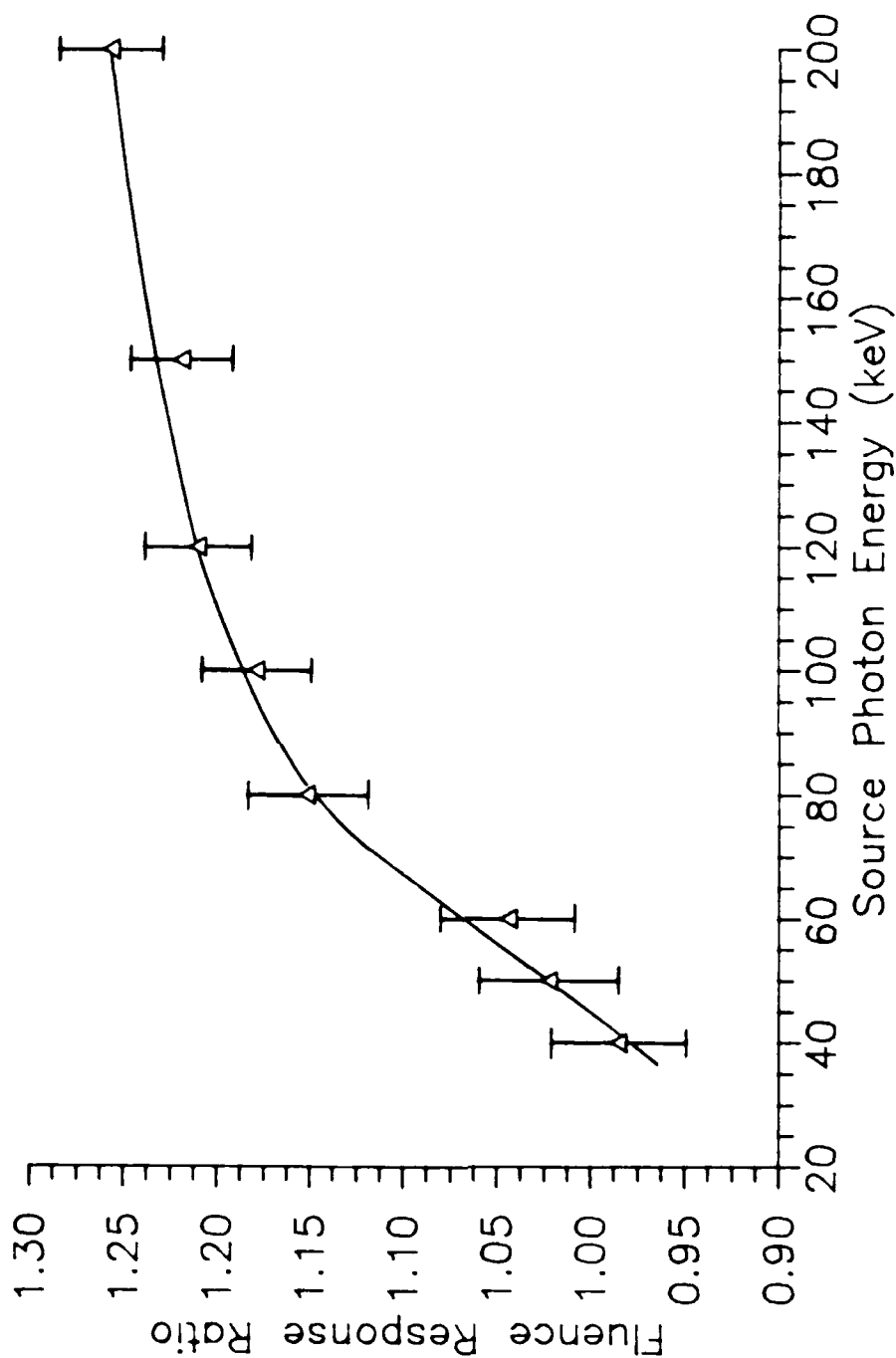


Figure VII.31. Source energy optimization curve for the segmented fluence detector with mine depth of burial of 2.5 cm in HTL soil. The ratio of right to left panel fluence response striking an uncollimated detector consisting of two panels of 30 cm width and 210 cm length, separated by a raster gap of 10 cm, and located 34.6075 cm above and parallel to the soil surface is shown as a function of source energy of perpendicularly incident beams. The beam intercepts are inside the mine wall and lateral (see text).

TABLE VII.7

Comparison of the Segmented and Unsegmented,
Uncollimated Fluence Detectors

Beam Intercept ^a and Depth of Burial (cm)	Fluence Response Ratio ^b		
	Segmented	At Intercept	Unsegmented At Mine Center
Inside Front			
0.0	1.654 ± 0.043	1.186 ± 0.017	1.753 ± 0.026
2.5	1.153 ± 0.026	1.024 ± 0.015	1.133 ± 0.016
5.0	1.052 ± 0.026	1.004 ± 0.014	1.037 ± 0.016
Outside Front			
0.0	1.201 ± 0.040	1.196 ± 0.018	1.753 ± 0.026
2.5	1.072 ± 0.029	1.050 ± 0.015	1.133 ± 0.016
5.0	0.974 ± 0.021	1.018 ± 0.015	1.037 ± 0.016
Inside Lateral			
0.0	2.107 ± 0.057	1.220 ± 0.018	1.753 ± 0.026
2.5	1.218 ± 0.027	1.037 ± 0.015	1.133 ± 0.016
5.0	1.064 ± 0.024	0.999 ± 0.014	1.037 ± 0.016
Outside Lateral			
0.0	1.511 ± 0.030	1.239 ± 0.018	1.753 ± 0.026
2.5	1.101 ± 0.023	1.056 ± 0.015	1.133 ± 0.016
5.0	1.035 ± 0.022	1.019 ± 0.015	1.037 ± 0.016

^aSee text for description of location of intercept positions.

^bThe calculations are for photon beams perpendicularly incident on HTL soil of density 1.70 g/cm³, with the TST mine at various depths of burial. The diverging source beams are 1.27 cm by 1.27 cm at the soil surface and are produced by a point source at 64.48 cm above the soil surface. The detector height is 34.6075 cm. Detector panels are 210 cm long and centered on the source beam axis. Beam energy for the segmented detector is 150 keV; for the unsegmented detector, 100 keV.

at the same intercept and at the mine center. The comparison at mine center is appropriate because that is the location at which the unsegmented detector works best, while the edges are where the segmented detector works best. The segmented detector is seen to improve detectability over the unsegmented detector only for beams incident on the inside edge of the mine, and, even then, not dramatically.

The optimum source energy for the energy window detector is found to be between 150 and 200 keV for depths of burial of 2.5 cm and 200 keV or greater at 5.0 cm. These conclusions are reached by comparing the mine to soil fluence ratios produced by a detector in the standard configuration with 30 cm wide panels and a 10 cm wide raster gap. Figure VII.32 shows a typical set of results. The lower energy of the window is set to 35 keV in this and the other comparison calculations. This value precludes counting only a very few photons and corresponds to the lower level discriminator setting used in the measurements. The spectra from which these results are derived are binned in 5 keV increments. Deviations in the mine to soil fluence ratio, and that obtained using a real detector, may occur because of the low energy of the source photons. As shown in Figure VII.23, variation between fluence and detector response at low energy can be large, even within a 5 keV increment. In many detectors, the higher energies are not attractive due to increased incoherent interactions which result in partial energy depositions. These events will mask the low energy scatter from the mine and soil.

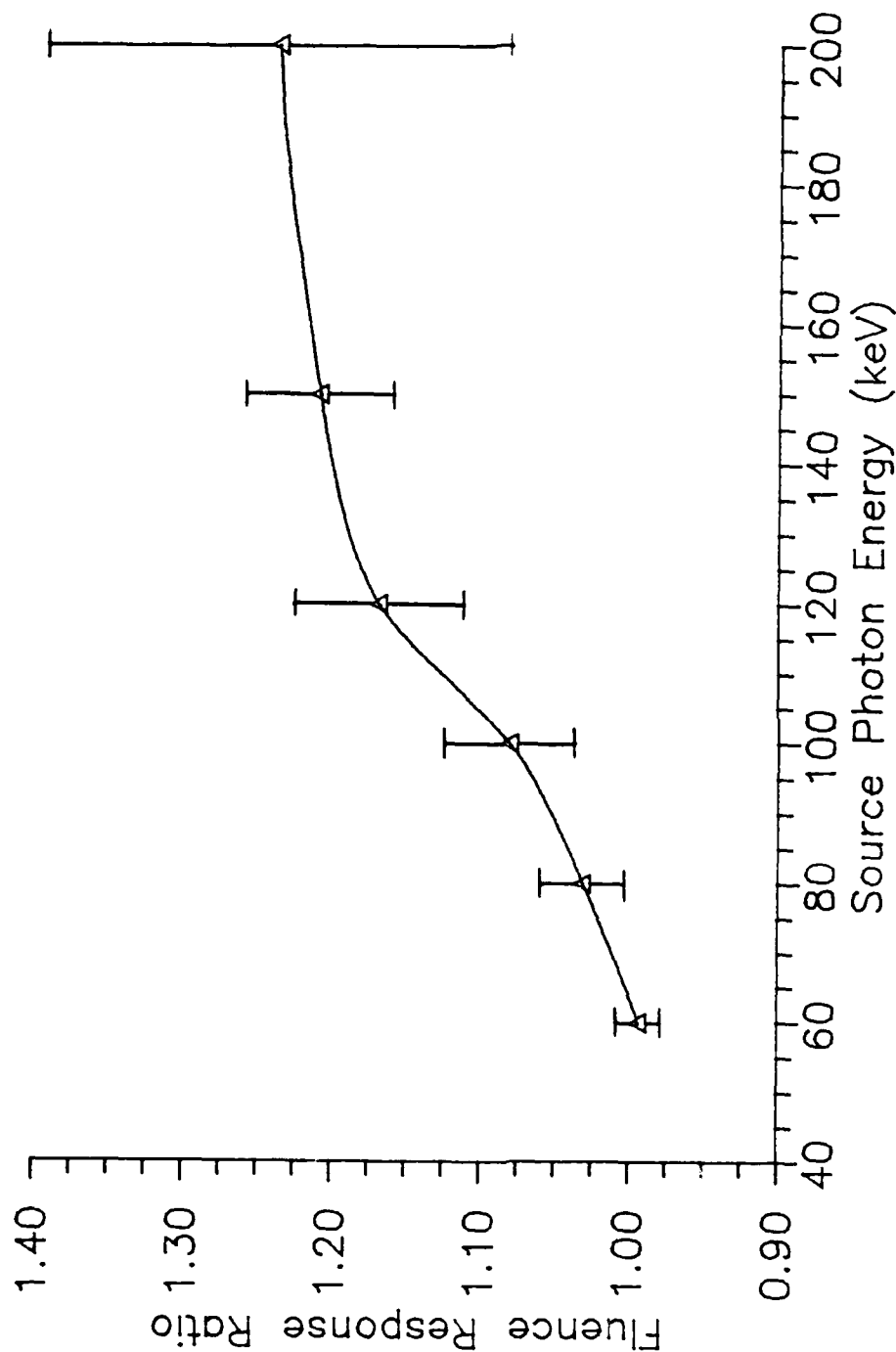


Figure 11.32. Source energy optimization curve for the energy window detector with mine depth of burial of 5 cm in HTL soil. The ratio of mine to soil fluence response at energies between 35 and 50 keV striking an uncollimated detector consisting of two panels of 30 cm width and 210 cm length, separated by a raster gap of 10 cm, and located 34.6075 cm above and parallel to the soil surface is shown as a function of source energy for perpendicularly incident beams. The beam intercept is at the center of the mine.

Depth of Burial

As a first comparison of the relative merit of the alternative detector types, the capability to detect mines buried at depth is examined. Mines are typically buried at shallow depths, normally flush with the surface, or in vegetated areas as deep as 8 cm. Regardless of these facts and the increasing importance of surface laid mines, a key criterion in all past research has been the ability to detect mines buried much deeper (Nolan et al., 1980). The most recently stated goal is for detection at 20.32 cm (8 inches), with the minimum useful depth being 5.08 cm (2 inches) (Moler, 1985). Table VII.8 compares the mine to soil fluence ratios for the optimum configurations of three of the four detectors at selected depths of burial in HTL soil with 10% water by weight. The moisture content and relatively high density of this soil make it a difficult medium for mine detection. The segmented detector, which is compared and shown to be approximately equivalent to the uncollimated, unsegmented detector in Table VII.7, is not included. The collimated detector is clearly superior for detection at depth. None of the configurations remotely approaches the capability of detection at the 20.32 cm goal. The unsegmented, uncollimated detector will be unable to detect mines even at the minimum useful depth of 5.08 cm without significant signal processing effort. The segmented, uncollimated detector improves upon the unsegmented detector only slightly. Detection at 5 cm remains

TABLE VII.8

Mine to Soil Fluence Ratio at Selected Depths
of Burial of the TST Mine

Depth of Burial (cm)	Detector Type		Energy Window ^c
	Uncollimated, Unsegmented ^a	Collimated ^b	
0.0	1.750 ±0.017	6.165 ±1.333	13.825 ±1.751
2.5	1.117 ±0.010	4.047 ±0.876	2.925 ±0.391
5.0	1.019 ±0.014	2.379 ±0.569	1.310 ±0.186
7.5	1.003 ±0.011	1.724 ±0.435	1.004 ±0.148
10.0	1.001 ±0.011	1.039 ±0.254	0.979 ±0.145

^aThe calculations are for 100 keV photon beams perpendicularly incident on HTL soil with 10% water by weight and density of 1.80 g/cm³, with the TST mine at various depths of burial. The diverging source beams are 1.27 cm by 1.27 cm at the soil surface and are produced by a point source at 64.48 cm above the soil surface. The detector height is 34.6075 cm. Detector panels are 30 cm wide and 210 cm long, separated by a raster gap of 10 cm, centered on the source beam axis.

^bThe calculations are for 100 keV photon beams perpendicularly incident on HTL soil with 10% water by weight and density of 1.80 g/cm³, with the TST mine at various depths of burial. The diverging source beams are 1.27 cm by 1.27 cm at the soil surface and are produced by a point source at 64.48 cm above the soil surface. In each case the beams are incident at the center top of the mine, and the detector height is 34.6075 cm. Detector panels are 30 cm wide and 210 cm long, separated by a raster gap of 30 cm, centered on the source beam axis. Collimator acceptance angle is 19.9 degrees.

TABLE VII.8 - continued

^cThe calculations are for 200 keV photon beams perpendicularly incident on HTL soil with 10% water by weight and density of 1.80 g/cm³, with the TST mine at various depths of burial. The diverging source beams are 1.27 cm by 1.27 cm at the soil surface and are produced by a point source at 64.48 cm above the soil surface. The detector height is 34.6075 cm. Detector panels are 210 cm long by 30 cm wide, and are centered on the source beam axis. The energy window extends from 35 to 50 keV.

difficult. The collimated detector is capable of detection at 7.5 cm. It is not capable of detection at 10 cm in this soil. It is shown later in Chapter VIII, when environmental parameters are examined, that this detector is capable of detection to greater depths in the low density soil surrounding a freshly buried mine. The energy window detector is capable of detection to 5 cm. It is, however, incompatible with an x-ray source, which provides a copious source of low energy photons to mask the low energy detection technique. Heavy filtration of the x-ray beam with a high atomic number material along with very good shielding against leakage radiation is the only recourse. Heavy filtration creates a spike-like spectrum at the K edge of the filter material. Depleted uranium offers the highest available K edge, 115.591 keV (Storm and Israel, 1970), for use as the filter material. This is far from the optimum energy for the technique of approximately 200 keV. Table VII.9 shows the results of calculations for the energy window detector at 100 keV. This energy would be close to the average of the fluence spectrum obtained if uranium filtration is used. The table indicates that detection at 5.0 cm should be possible even with this modification to the x-ray source used with energy window detector.

Polyenergetic Sources

With the exception of the energy window detector, discussions of parameter optimizations have all resulted from calculations using monoenergetic source beams. Since

TABLE VII.9

Mine to Soil Fluence Ratios Versus Depth of
Mine Burial for the Energy Window Detector
with Source Energy of 100 keV

Depth of Burial (cm)	Mine to Soil Ratio
0.0	10.174 \pm 0.514
2.5	2.052 \pm 0.114
5.0	1.144 \pm 0.076
7.5	1.088 \pm 0.073
10.0	1.015 \pm 0.060

^aThe calculations are for 100 keV photon beams perpendicularly incident on HTL soil with 10% water by weight and density of 1.80 g/cm³, with the TST mine at various depths of burial. The diverging source beams are 1.27 cm by 1.27 cm at the soil surface and are produced by a point source at 64.48 cm above the soil surface. The detector height is 34.6075 cm. Detector panels are 210 cm long by 30 cm wide, and are centered on the source beam axis. The energy window extends from 35 to 50 keV.

x-ray sources must be used to achieve rapid detection over wide paths, some discussion of the effect of polyenergetic sources is required. The presence of non-optimum energy photons will degrade the mine to soil ratios. This implies efforts to shape the source x-ray spectra to place a majority of the source photons near the monoenergetic optimum energy to lessen the effects of the other photons. The combination of two methods is generally used to shape spectra. Increasing the peak kilovoltage accelerating electrons across the x-ray tube increases the average and peak energies of the beam. Addition of filters to selectively remove low energy components (as discussed for the energy window detector) can also be used for this purpose. Filtration must be used with care, since too much filtration, while producing a more appropriate spectrum, also removes useful photons, increasing power requirements. Spectra calculated by the XRSPEC.PAS code for various filter and voltage combinations can be compared by using the fit technique described in Appendix H, with the response per source photon for a particular detector at a given depth of burial of the TST mine replacing the detector response at a specific detector position. This technique is applied to the calculation of power requirements in Chapter VIII.

Conclusions Based on Optimizations

The results of the optimization calculations presented above indicate that only the collimated detector offers the possibility of exceeding the minimum useful depth for mine

detection using an x-ray source. The uncollimated detectors are capable of detection only if the mine is close to the surface. The major problem with collimated and energy window detectors is that the magnitude of the backscatter signal sensed is small in comparison with that sensed by the uncollimated detector. The problem is worse with the energy window detector because the heavy filtration required further reduces the efficiency of the system. These considerations are directly related to a series of fundamental practical concerns about the feasibility of a mine detection system which center about the power requirements of the x-ray source. The key variables which influence the power requirement are the fluence spectrum, detection efficiency, the speed of forward motion, the width of the path scanned, noise characteristics, and beam size. Power calculations are made in Chapter VIII.

CHAPTER VIII

APPLICATION TO IMAGING

The production of images of buried nonmetallic antitank mines is the primary focus of this research. This chapter addresses the imaging process. Measurements using the General Electric Maxitron 300 X-Ray Therapy Unit, the Bicron NaI(Tl) detector, and the soil box with TST mine in locally obtained soil are compared to calculations performed by the MCPHOT.P code in conjunction with fluence spectra from the XRSPEC.PAS code and the detector response function provided by the DETNAI.P code. These comparisons are used to evaluate the capability of the calculation method to provide accurate predictions. Environmental parameters are examined using calculations to assess their impact on the imaging process. The parameters investigated are detector height variation, soil density, soil moisture content, and inhomogeneities such as wood, water, steel, and aluminum, which can be expected on the battlefield. These parameters are investigated for each of the detector types introduced in Chapter VII, except the segmented, uncollimated detector. Results for such a detector closely parallel those for the unsegmented, uncollimated detector. Images are produced both by measurement and by Monte Carlo calculations. Finally, the information derived from the calculations of

the preceding chapter and the imaging results are applied to estimations of the power requirements for the x-ray generator.

Comparisons with Measurements

The experimental apparatus described in Chapter III is used to perform a series of measurements to test the accuracy of the calculation techniques. The calculation techniques are described in detail in Chapters IV, V and VI, and Appendix H. Graphs of the calculated x-ray spectra used in the measurements described in this chapter are shown in Appendix F.

Spatial Distribution of Detector Response

Measurements of the spatial distribution of the detector response due to soil alone are made for three source spectra at 100, 150 and 200 kVp, filtered by varying amounts of lead, by varying the distance of the uncollimated NaI(Tl) detector from the beam axis. The spectra used are shown in Figures F.8, F.10 and F.12. Spectra are calculated by the XRSPEC.PAS code. Table VIII.1 summarizes the experimental and calculation parameters. Lead filtration is used in these experiments to keep the backscattered fluence rate at levels which can be handled by the NaI(Tl) detector without producing dead time effects. Initial attempts at comparisons with soil were very good at 100 kVp, but became progressively worse as beam energy increased. A series of experiments determined that the head leakage of the x-ray machine provides a considerable contribution to the source

TABLE VIII.1

Parameters for Spatial Distribution Comparison

Spectra:	100 kVp filtered by 4.75 mm Be, 0.25 mm Al equivalent (monitor ionization chamber), and 0.24 mm Pb
	150 kVp filtered by 4.75 mm Be, 0.25 mm Al equivalent (monitor ionization chamber), and 0.75 mm Pb
	200 kVp filtered by 4.75 mm Be, 0.25 mm Al equivalent (monitor ionization chamber), and 1.35 mm Pb
Detector height:	34.6075 cm
Source height:	64.48 cm
Beam angle of incidence:	0 degrees (perpendicular)
Beam dimensions:	diverging, 1.27 cm by 1.27 cm at soil surface
Soil type:	local, similar to NSL (used in calculations)
Soil density:	1.54 g/cm ³
Detector lower level discriminator setting:	equivalent to 35 keV

at the high beam energies. This result is a combination of the increased capability of high energy photons to leak through the standard shielding of the head of the x-ray machine and the lead filtration, which reduces beam intensity considerably. In order to correct for the head leakage contribution, additional measurements at each detector position are conducted at the higher energies by placing 1.03 cm of lead in the beam path. Due to this very large thickness of lead, the measurements taken in this configuration are now due only to head leakage. Subtraction of the head leakage from the original measurement data produces the detector response due to the source beam only. Figures VIII.1 through VIII.3 show the excellent agreement between calculation and measurement. The success of the code in predicting a problem in the experimental conditions testifies to its value. As a result of the discovery of the head leakage problem additional shielding now encloses the head.

Detector Response with Mine Present

A series of measurements with the TST mine buried flush to the soil surface with the beam intercept at the center of the mine provide an additional test of the calculation technique. The measurements are made with the 100 and 200 kVp spectra shown in Figures F.8 and F.12. Other parameters of the measurements are the same as those presented in Table VIII.1 with the exception of the height of the detector above the soil, which was 34.29 cm for the soil case, and

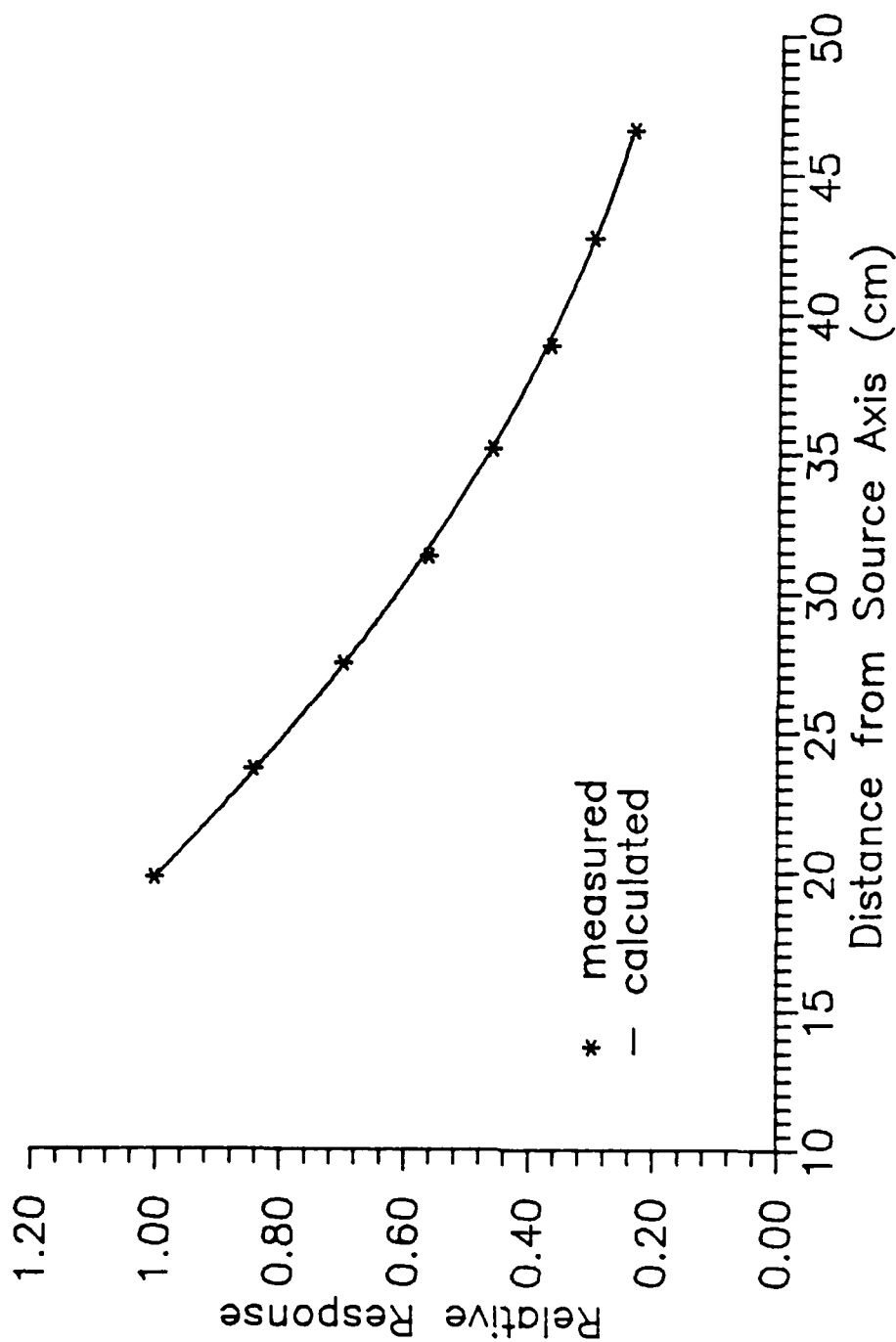


Figure VIII.1. Calculated and measured spatial distribution of detector response from backscatter from sandy soil at 100 kVp. Responses are normalized to 1.00 at 19.775 cm from the beam axis. Geometry and source details are provided in Table VIII.1. Uncertainties in measured results are too small to plot.

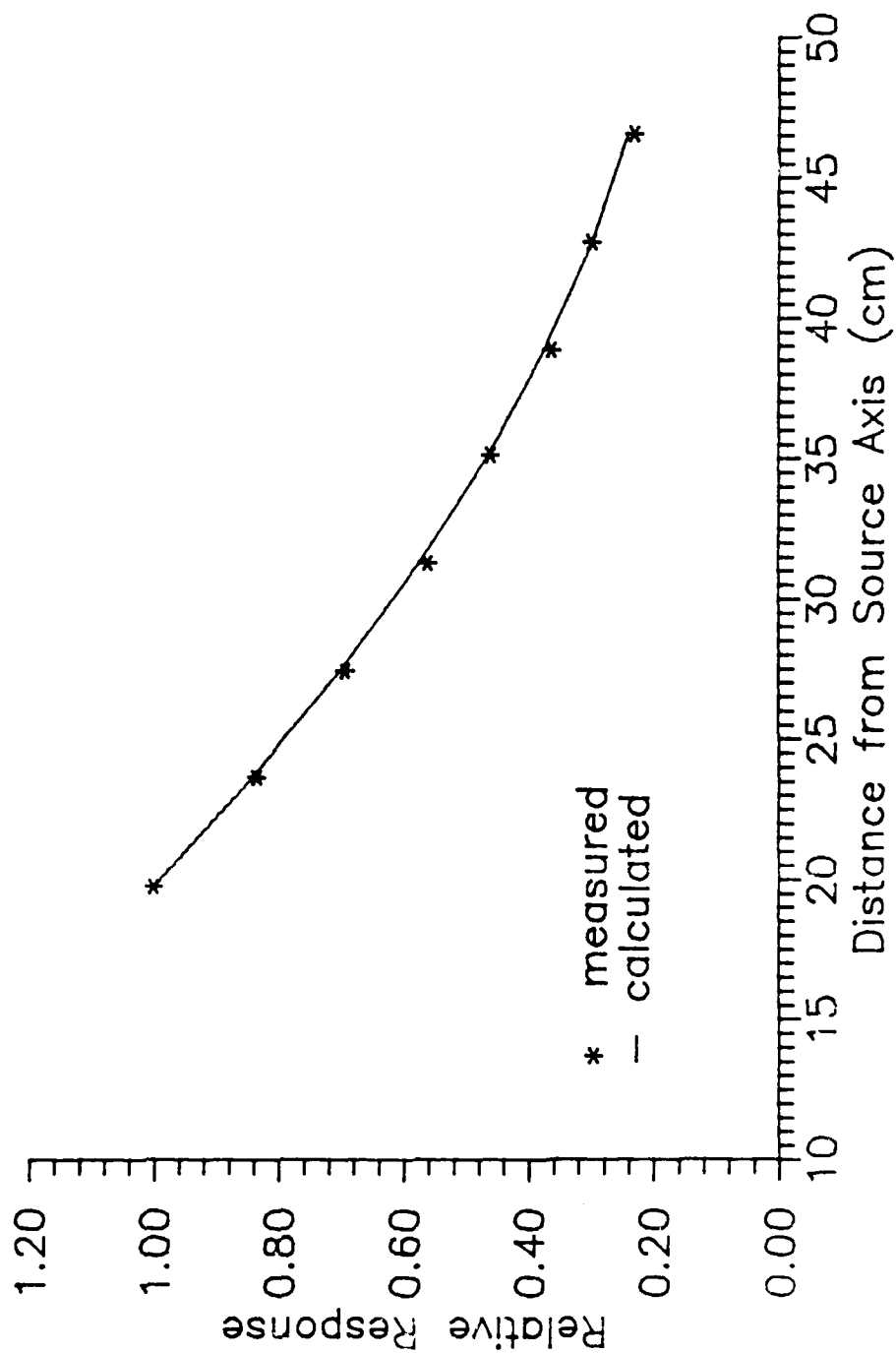


Figure 1. Calculated and measured spatial distribution of detector response versus distance from sandy soil at 150 kVp. Responses are normalized to 1.00 at the beam axis. Geometry and source details are provided in Table 1. The measured results are too small to plot.

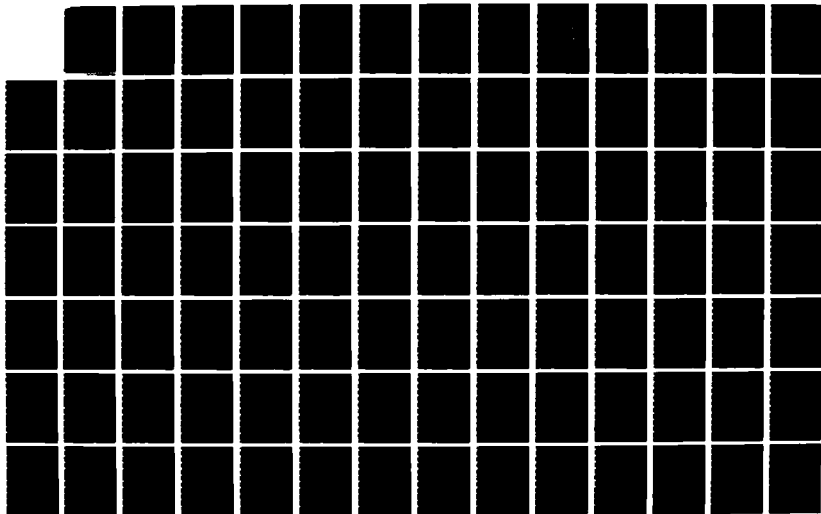
AD-A182 227

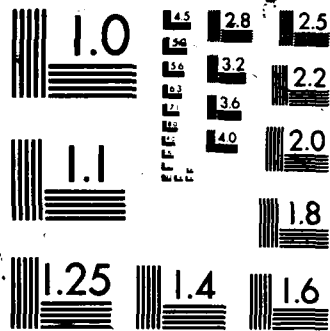
LANDMINE DETECTION BY SCATTER RADIATION RADIOGRAPHY(U)
ARMY MILITARY PERSONNEL CENTER ALEXANDRIA VA
J G CAMPBELL 02 JUL 87

4/6

UNCLASSIFIED

F/G 15/6 6 NL





XEROCOPY RESOLUTION TEST CHART

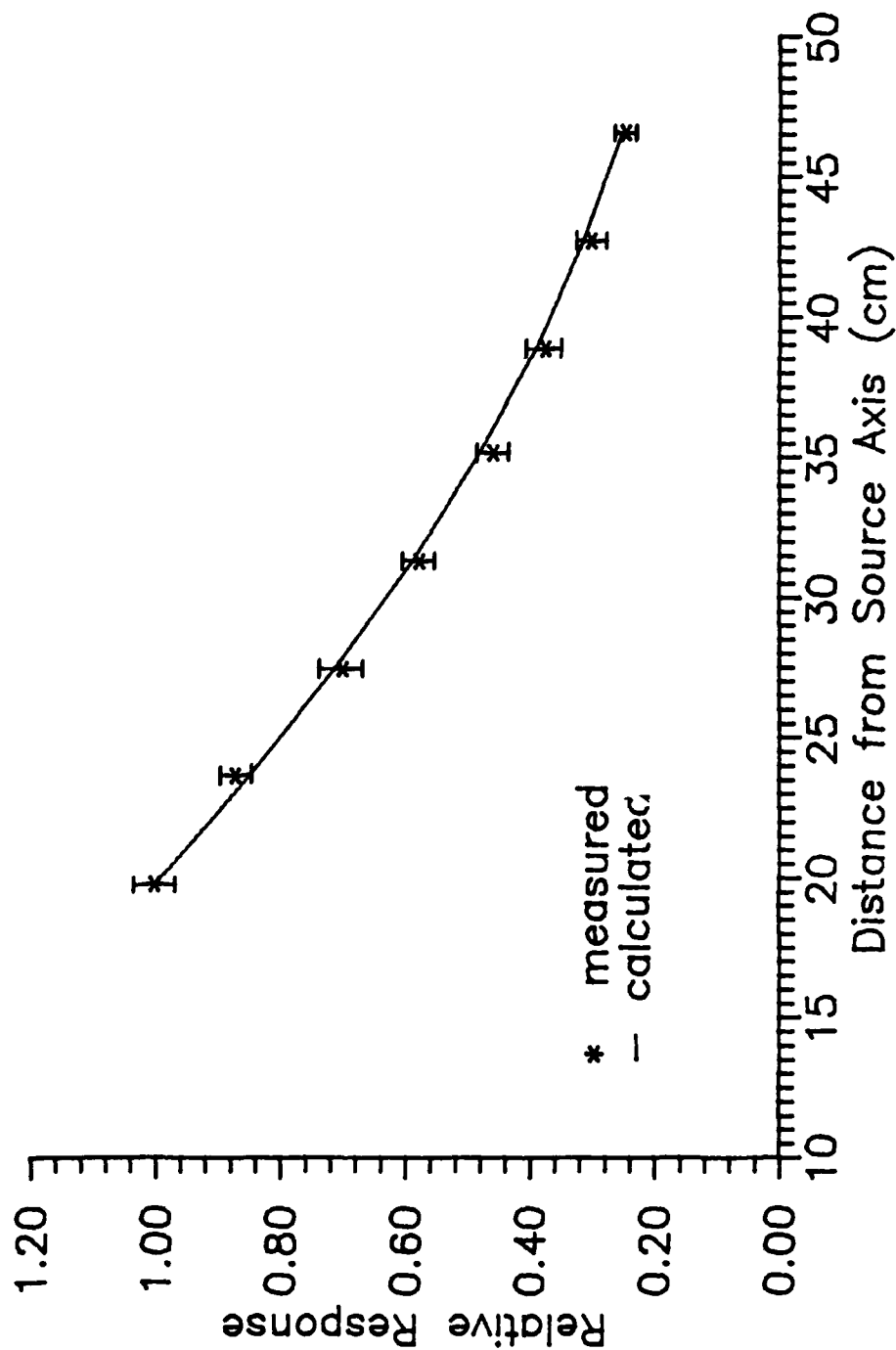


Figure VIII.3. Calculated and measured spatial distribution of detector response from backscatterer from sandy soil at 200 kVp. Responses are normalized to 1.00 at 19.775 cm from the beam axis. Geometry and source details are provided in Table VIII.1.

34.77 cm for the case with mine. Measurements were made at three detector positions for each source energy. The slight differences in height above the soil in the two measurements are due to the removal and addition of soil during placement of the mine. The calculations employ the interaction characteristics of sucrose as the explosive material. Measurement comparisons of the attenuation properties of TNT and sucrose, described in Chapter III (see Figure III.9), indicate sucrose is a good substitute material. Figure VIII.4 shows a comparison of calculations of the number albedo of sucrose and TNT at eight energies, indicating that the scattering properties of the two materials are also very similar. Exact agreement would exist if the data points lay directly on the line of slope equal to 1.00. Results of the measurement to calculation comparison are expressed as the ratio of mine to soil detector response in Table VIII.2. Agreement is seen to be very good. The relatively large uncertainties in the measured ratios derive from instabilities in the General Electric Maxitron 300, not quantum statistics. Correction for head leakage contributions is required in the 200 kVp measurements. As described in Chapter III, due to structural constraints, it is not possible to provide sufficient lead shielding to completely remove the head leakage contribution for higher beam energies.

These measurements confirm several key conclusions from the calculations described in Chapter VII. Those

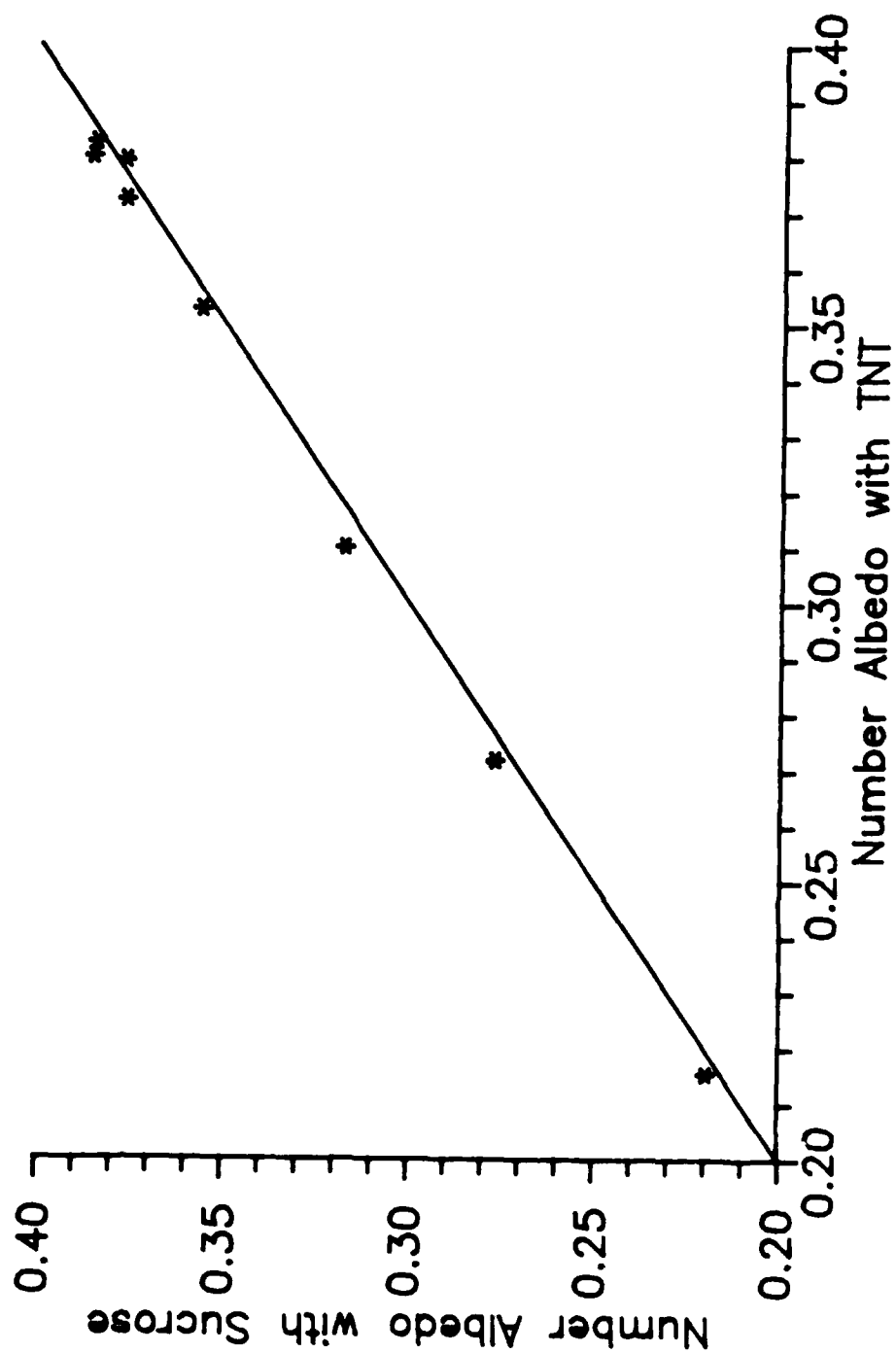


Figure VIII.4 Comparison of the number albedos of sucrose and TNT. Monte Carlo calculations for the TST mine containing sucrose and TNT are compared. Calculations are provided by the MCPHOT.P code.

TABLE VIII.2

Comparison of Calculated and Measured Mine to Soil
Detector Response Ratio with the TST Mine at 0.0 cm

Beam Energy (kVp)	Detector Position (cm) ^a	Detector Response Ratio Calculated	Ratio Measured
100	21.52	1.741 ± 0.053	1.670 ± 0.118
100	33.01	1.958 ± 0.046	1.842 ± 0.130
100	48.29	2.216 ± 0.060	2.034 ± 0.144
200	21.52	1.413 ± 0.019	1.374 ± 0.092
200	33.01	1.533 ± 0.039	1.516 ± 0.107
200	48.29	1.661 ± 0.030	1.629 ± 0.115

^a Measured from the beam axis.

calculations predict that for a surface buried mine, the low energy beams are more efficient at displaying contrast between mine and soil. This prediction is verified by the measurements. Additionally, the calculations predict that the mine to soil ratio has a relative minimum in its spatial distribution. The measurements confirm the increase in ratio with distance from the beam axis.

Edge Effects

Calculations predict the existence of edge effects when the source beam strikes near the wall of the mine. The first measured images are designed to test this prediction. To amplify the existence of any such effects, two non-mine targets are selected. These objects are annuli composed of lucite and steel. Each is buried with its top surface flush with the soil, and the soil in the center removed. The lucite annulus has an outer diameter of 15.24 cm, inner diameter of 12.70 cm, and height of 7.62 cm. The steel annulus has an outer diameter of 17.78 cm, an inner diameter of 15.24 cm, and a height of 7.62 cm. Both objects are, therefore, considerably smaller than an antitank mine. In order to resolve the 1.27 cm thick walls of each target, the backscattered fluence is sampled at an increment of the same size. The 100 kVp spectrum shown in Figure F.8 is used for the image. The detector is located 19.775 cm from the beam axis, and is uncollimated. All other experimental conditions are the same as indicated in Table VIII.1. The purpose of the air space in the centers of the annuli is to

test the edge effect predictions. Photons striking just inside the wall of the annuli nearest the detector should produce a reduced response, and those striking just outside the far wall should produce an enhanced response (for lucite) due to the arguments presented in Chapter VII. The increased depth of the air layer compared to that in an antitank mine should amplify the effect.

Figure VIII.5 shows a three dimensional representation, and Figure VIII.6, a two dimensional contour representation, of the image data for the lucite annulus. Since lucite has a lower average atomic number than soil, the walls of this annulus are more efficient photon scatterers than the surrounding medium. The detector is located in the positive y-direction (to the left front of the image in the three dimensional representation, to the right of image in the two dimensional representation). This positioning is analogous to that of the front panel of the large area detectors described in Chapter VII. The circular shape of the annulus is most apparent in the two dimensional representation. The depression in the response just inside the wall nearest the detector and the enhancement of the response for beams striking outside the wall furthest from the detector are the predicted edge effects. The edge effects at the walls are most clearly displayed in the two dimensional representation. The hachured regions indicate depressions in response.

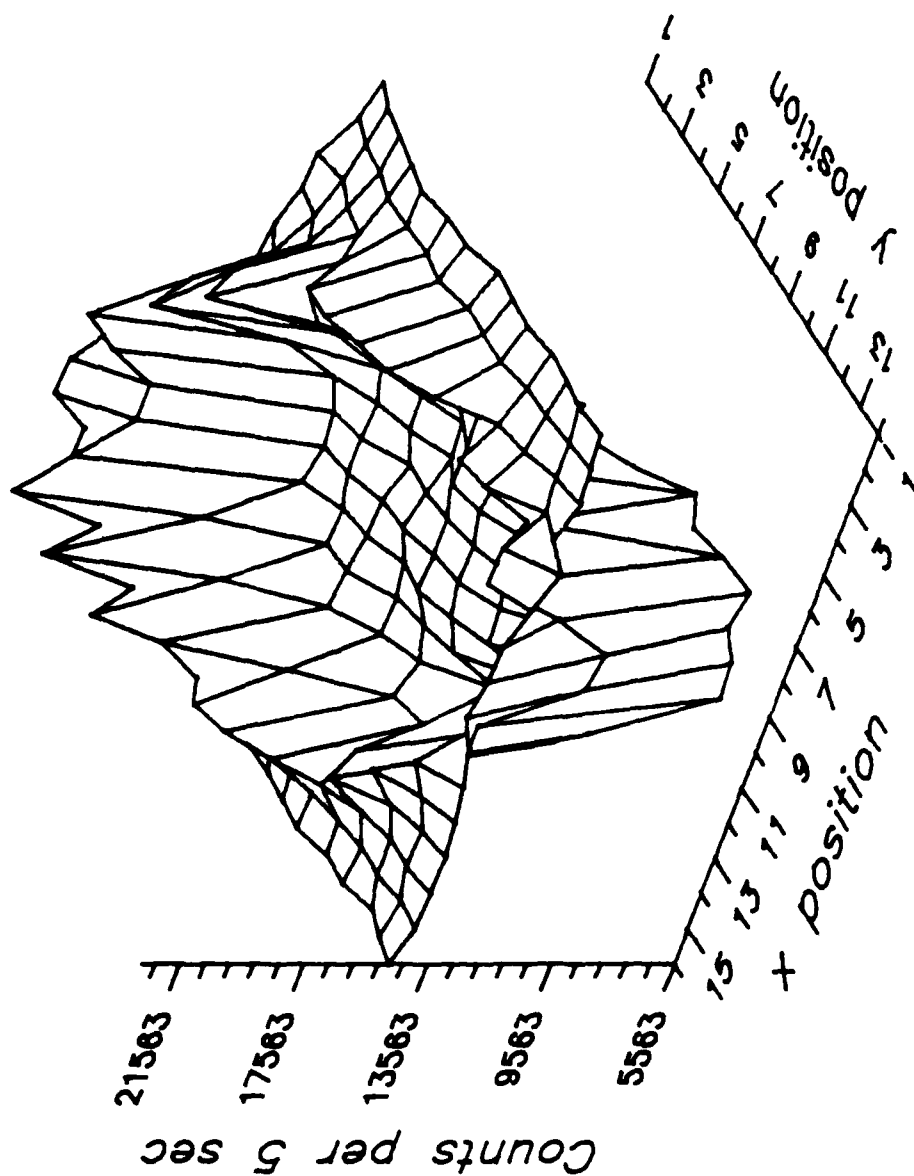


Figure VIII.5. Three dimensional image diagram of measured detector response for the lucite annulus experiment. The 100 kVp source spectrum is shown in Figure F.8.

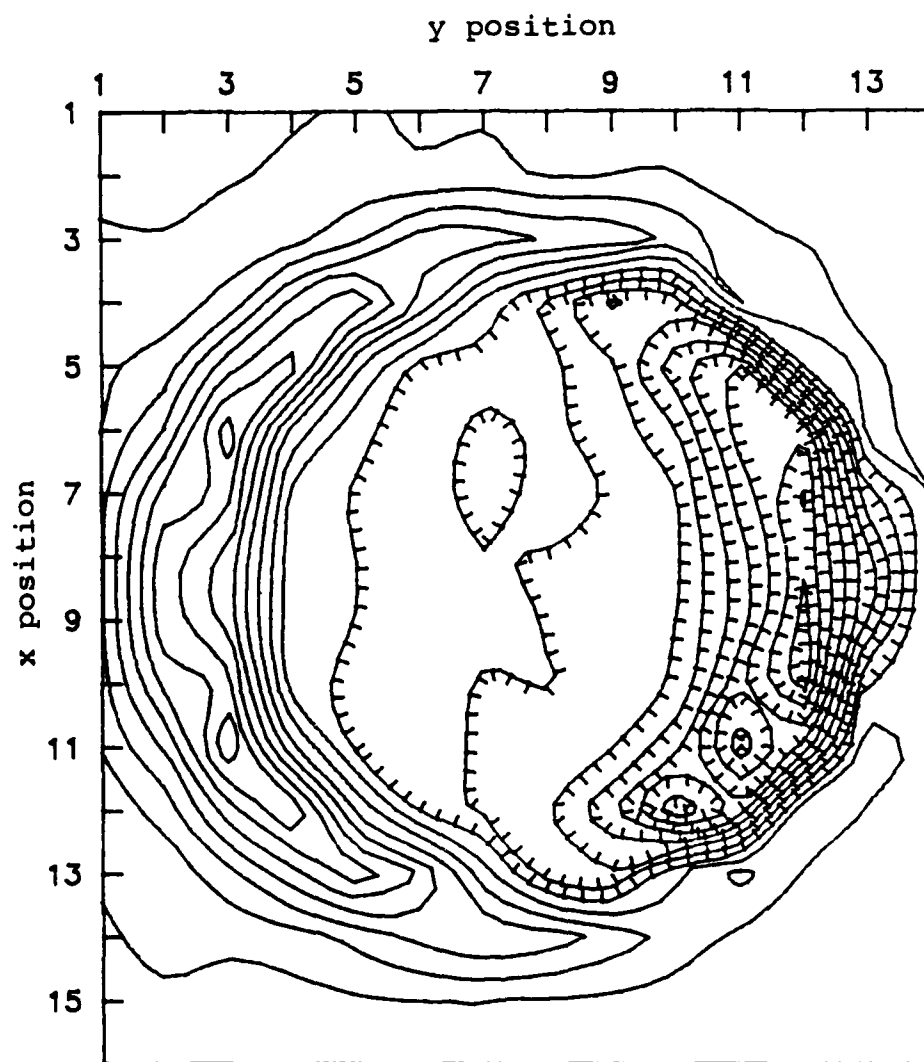


Figure VIII.6. Two dimensional image diagram of measured detector response for the lucite annulus experiment.

Figure VIII.7 shows a three dimensional representation of the measured detector response for the steel annulus. Since the steel walls of the annulus are less efficient photon scatterers than soil, a reduction in the response when they are struck by the beam is expected and observed. Figure VIII.8 is a two dimensional contour representation of this same image data. The depression in response clearly expresses the circular shape of the target. The depth of the depression is greatest near the wall nearest the detector. The enhancement at the far wall is not seen because of the high attenuation caused by 1.27 cm of steel, located between the photons striking just outside the wall and the detector.

Energy Window Detector

As discussed in Chapter VII, the energy window detector is not expected to perform well with an x-ray source due to the presence of low energy photons in the spectrum. Nevertheless, the technique should show some improvement in the mine to soil ratio over a detector which accepts photons of all energies. Experiments using lead filtration to preferentially remove low energy photons show the enhancement in the ratio. The experimental parameters are the same as those of Table VIII.1 with the exception of source spectra, which are shown in Figures F.9 and F.11. Separate measurements account for head leakage scatter radiation. Table VIII.3 provides the results of the measurements. The trend towards higher ratios with smaller, low energy windows is

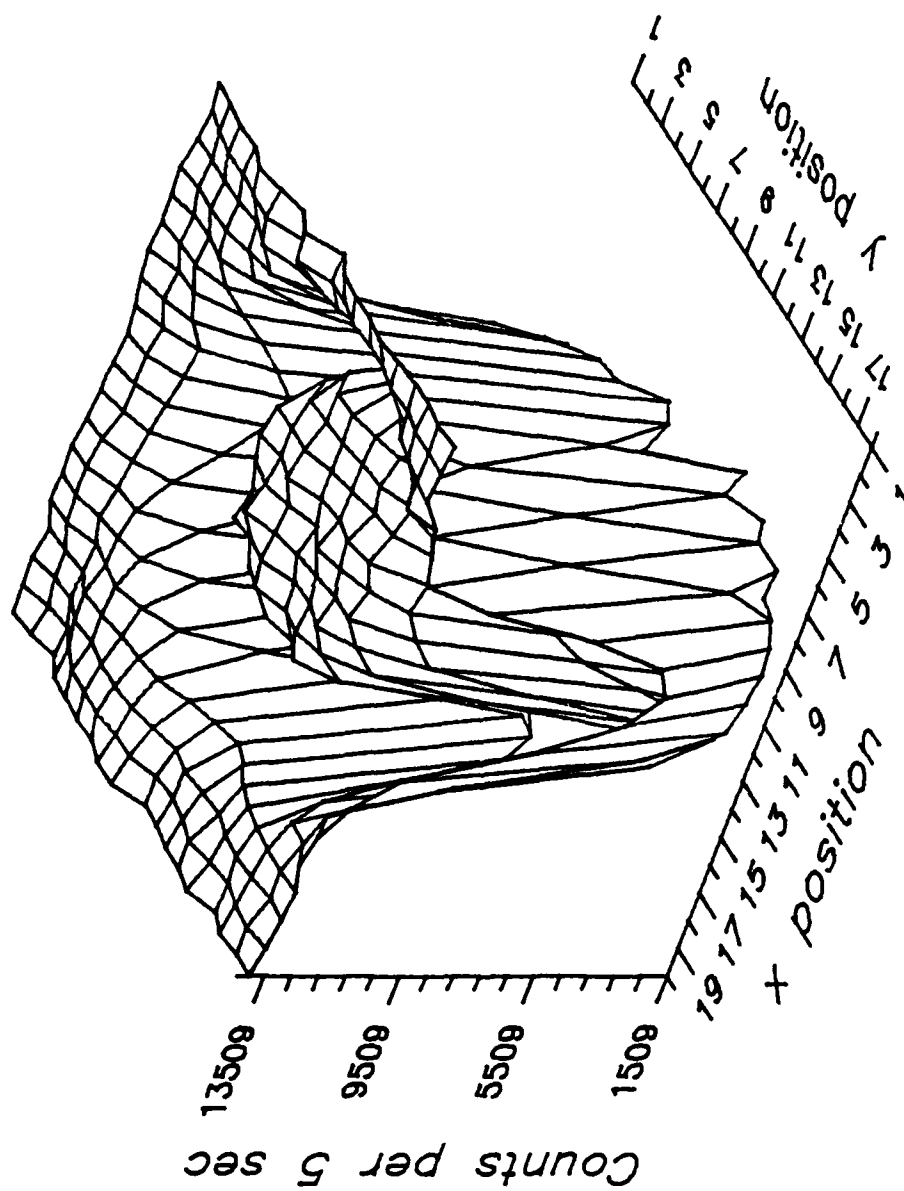


Figure VIII.7. Three dimensional image diagram of measured detector response for the steel annulus experiment. The 100 kVp source spectrum is shown in Figure F.8.

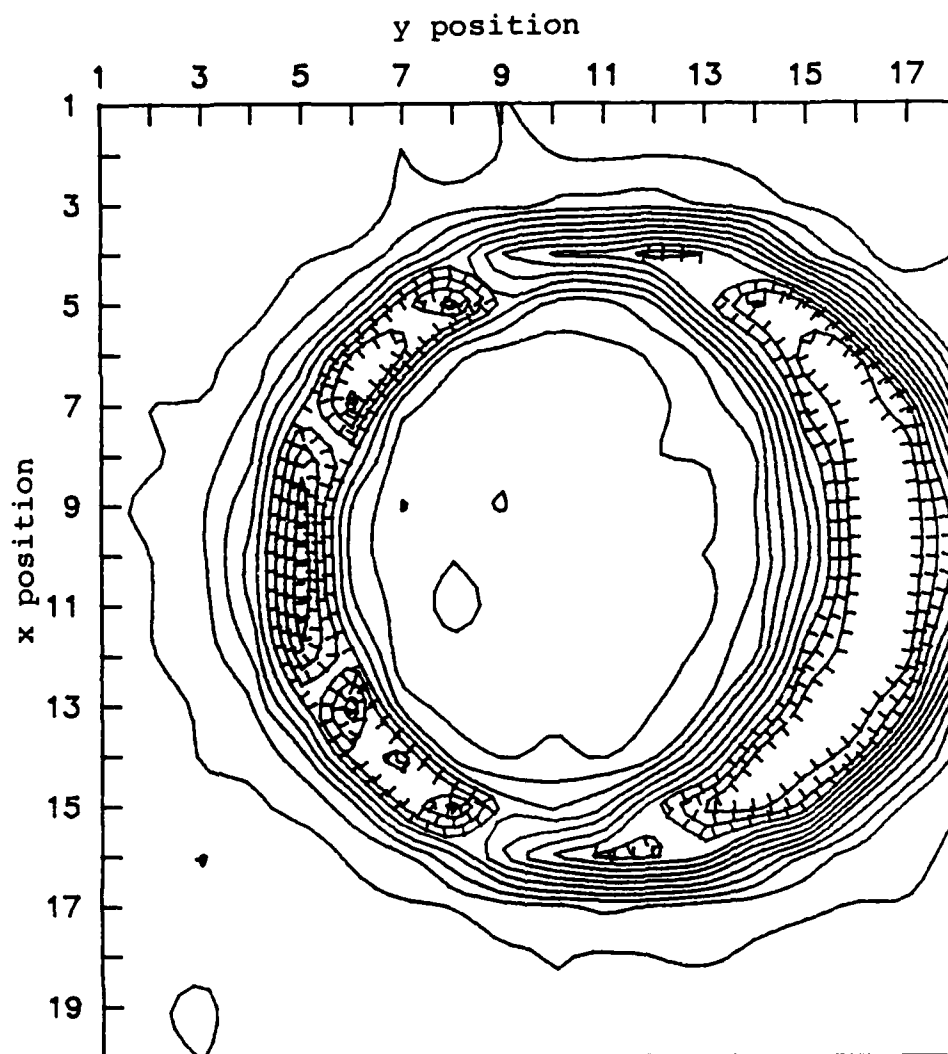


Figure VIII.8. Two dimensional image diagram of measured response for the steel annulus experiment.

TABLE VIII.3

Energy Window Measurements for
the TST Mine at 2.54 cm Depth of Burial

Source Energy (kVp)	Window (keV)	Mine to Soil Detector Response Ratio ^a
100 ^b	35.0 - 39.7	1.208 ± 0.172
	35.0 - 48.9	1.138 ± 0.062
	35.0 - 58.3	1.115 ± 0.026
	35.0 - 67.6	1.092 ± 0.027
	35.0 - open	1.092 ± 0.021
200 ^c	35.0 - 40.1	1.168 ± 0.034
	35.0 - 50.2	1.122 ± 0.018
	35.0 - 60.4	1.123 ± 0.014
	35.0 - 70.5	1.104 ± 0.008
	35.0 - open	1.075 ± 0.007

^aSee text for description of experimental configuration.

^bFiltered by 4.75 mm Be and 0.75 mm Pb. Source spectrum is shown in Figure F.9.

^cFiltered by 4.75 mm Be and 0.75 mm Pb. Source spectrum is shown in Figure F.11.

clear, but, as expected, the magnitudes of the ratios are much reduced from those produced by monoenergetic sources in Chapter VII as a result of the presence of low energy photons in each spectrum (see Figures F.9 and F.11) and partial energy deposition events in the small NaI(Tl) detector.

Environmental Parameters

In a fielded system, the mine detection process is complicated by a number of environmental influences. This section examines conditions which would be frequently encountered by a mine detection system on the battlefield.

Height Sensitivity

The calculations described in Chapter VII are all based upon a detector height of 34.6075 cm. This height is approximately the minimum possible to allow operation over moderately rough terrain without causing the detector panels to strike the ground. Implied in this precaution is the variation of height of the detector as the vehicle moves across such terrain. Of much less importance are the corresponding variation in the height of source and the resulting changes in the beam size intersecting the soil, provided perpendicular incidence and a fairly tightly collimated source beam are employed.

The optimum uncollimated detector, in terms of height sensitivity, has panels of infinite extent and no raster gap. This detector, disregarding air attenuation, would be completely insensitive to height variation because it would intercept the entire backscattered fluence independent of

height. Figure VII.26 indicates that because of the rapid decrease of the backscattered fluence with distance from the beam axis, panel widths of approximately 70 cm (without a raster gap) would be nearly equivalent to an infinite detector. Of course, a raster gap is required for the beam, and the central minimum in the mine to soil fluence ratio makes gaps on the order of 10 to 30 cm attractive. The principle reason for selecting a 10 cm gap for the uncollimated detector, in the discussion in Chapter VII, is to intercept a substantial fraction of the backscatter fluence. A 30 cm raster gap provides a slightly better mine to soil fluence ratio, but at the cost of allowing a sizeable fraction of the backscattered fluence to escape through the gap (see Table VII.5). Wide panels increase the probability of the detector striking the soil surface while moving over rough terrain. Figure VIII.9 shows the variation in the number of photons striking an uncollimated fluence gap detector per source photon for the case of 100 keV photons perpendicularly incident on the center of the TST mine at a depth of burial of 1.0 cm in NSL soil as a function of height of the detector above the soil. The raster gap is 10 cm, and the beam size is 1.27 cm by 1.27 cm when the source is at a height of 64.48 cm above the soil. The source is fixed at a height of 29.87 cm above the detector plane. Source height and beam size are varied to correspond to detector height. The response curves for selected panel widths are shown. The shapes of the curves are similar.

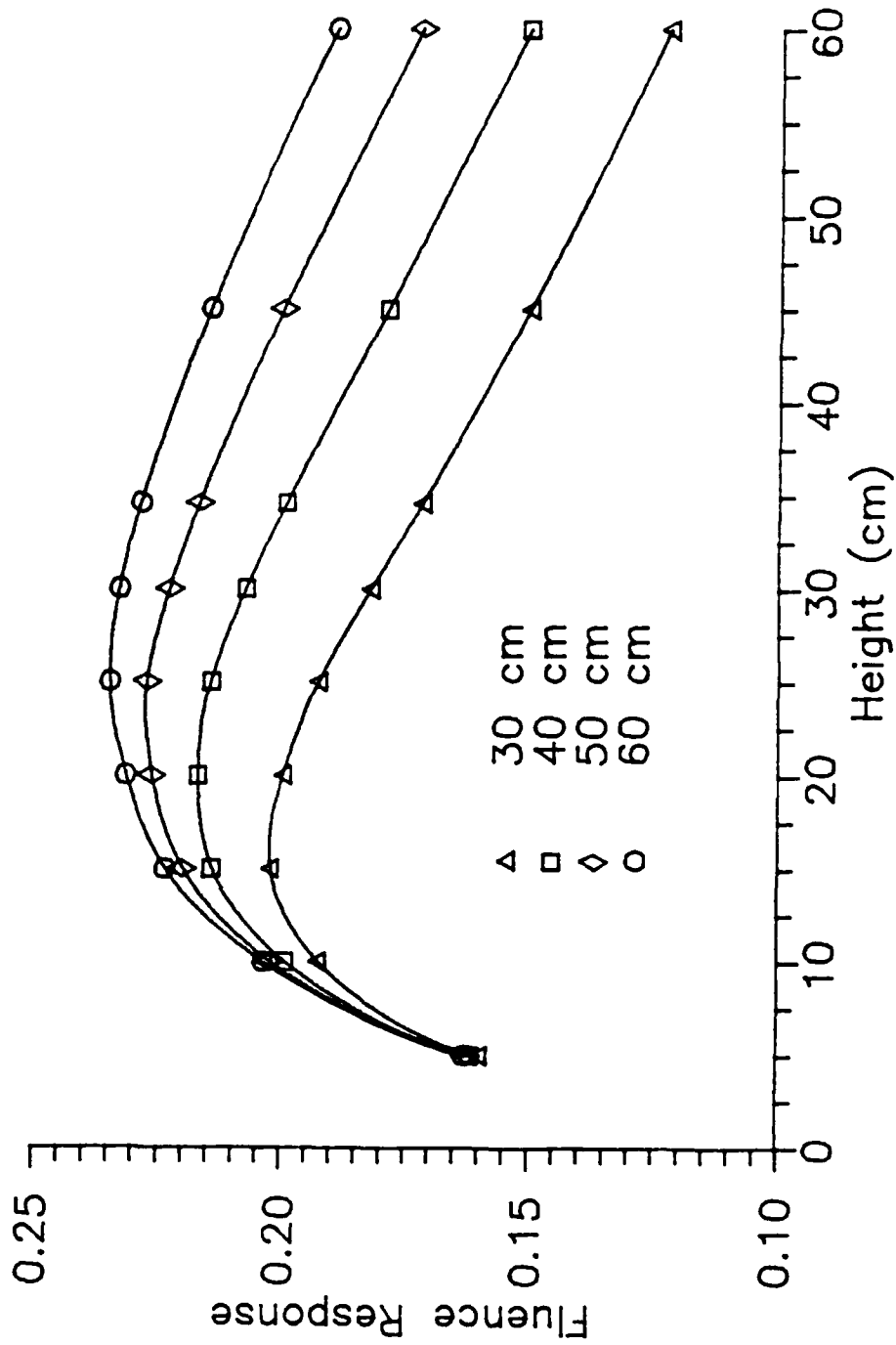


Figure VIII.9. Fluence response as a function of height above the soil surface for selected panel widths of the uncollimated detector. Calculations are for 100 keV photon beams perpendicularly incident on the center of TST mines at 1.0 cm depth of burial in NSL soil. The uncollimated detector consists of two panels of various widths and 210 cm length, separated by a raster gap of 10 cm. Fluence response units are photons/source photon.

All have relatively low response when the height is small. In this case the bulk of the photons are escaping through the raster gap. Since the gap size is the same in all the cases, the responses are also essentially the same. Each of the curves go through a maximum and then drop off at large heights above the soil. For large heights, the bulk of the photons are escaping beyond the detector panels. Not surprisingly, the broadest maximum and largest response is associated with the largest panels. The broader the maximum, the less the sensitivity of the detector configuration to height variation.

The collimated detector presents a different height sensitivity mechanism. The variation in height alters the size of the area of the soil surface from which the detector can receive photons. Tight collimation reduces the variation in the size of the area viewed. Since the detection mechanism depends on the differential attenuation by soil and explosive of multiply scattered photons reaching a collimated detector, large detector areas are not required to gather the bulk of the available photons. It is only the region near the beam side of the panel that is of great importance in a collimated detector which is configured to exclude the bulk of the single scattered fluence. Figure VIII.10 shows the sensitivity of collimated detector to height variation. The calculation is for the 100 keV photons perpendicularly incident on the center of the TST mine buried flush to the soil surface. The detector

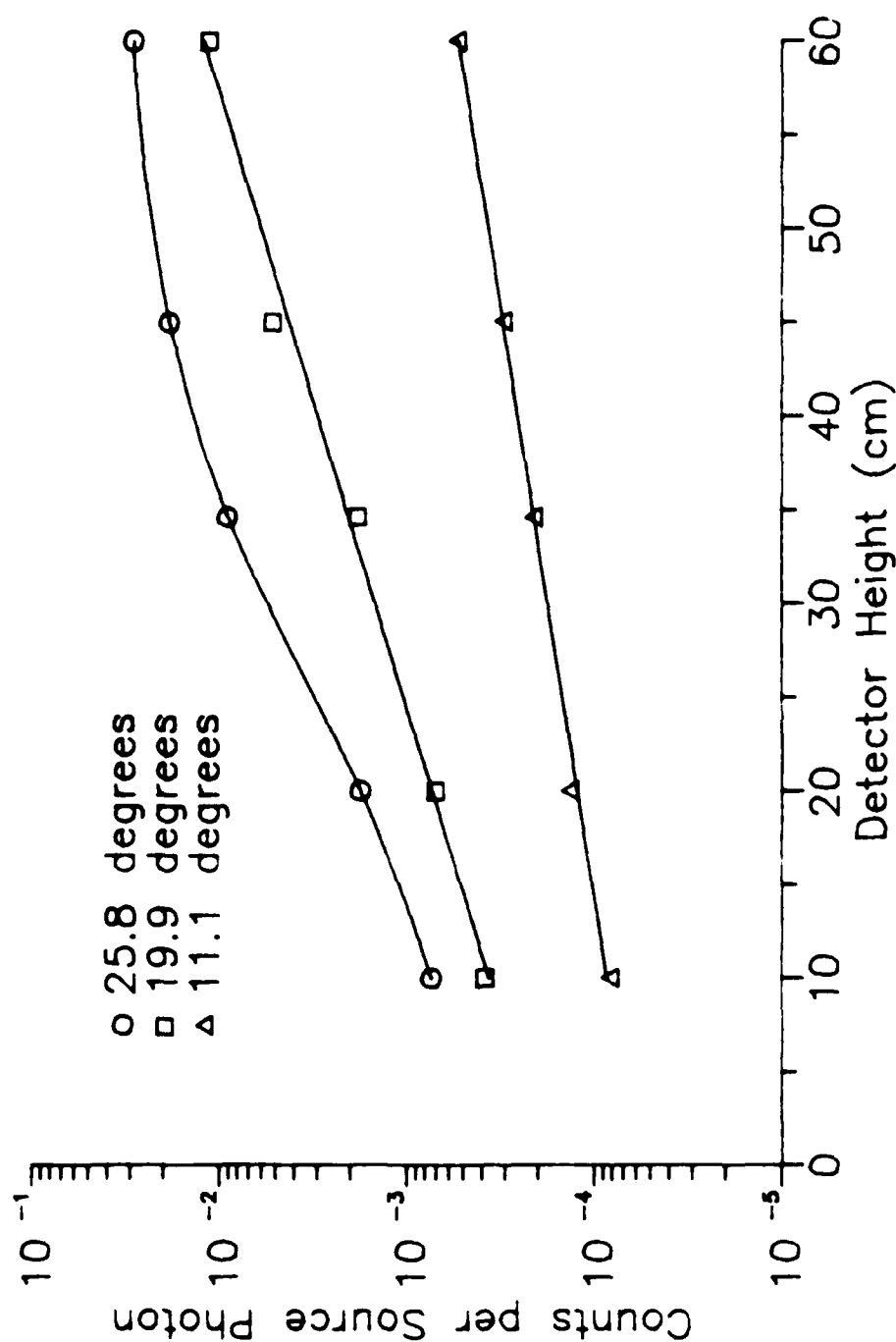


Figure VIII.10. Fluence response as a function of height above the soil surface for selected acceptance angles of the collimated detector. Calculations are for 100 keV photon beams perpendicularly incident on the center of TST mines buried flush to the surface in HTL soil. Collimated detectors consists of two panels of 30 width and 210 cm length, separated by a raster gap of 30 cm.

consists of two panels of width of 30 cm, separated by a 30 cm raster gap. The figure indicates this detector is very height sensitive. The sensitivity decreases as the acceptance angle becomes smaller. The sensitivity is even more serious than the figure indicates. The strong dependence of this detector on the geometry of the system with respect to soil is discussed above. Varying the height of the detector destroys the geometric relationship determined to provide optimum mine detection. This is particularly important when the detector height is above 34.6075 cm, that for which the geometry was optimized. Above this height the collimator begins to allow single scattered photons to enter the detector degrading its capability to detect mines. There are three options to remedy this problem. First, the collimator acceptance angle may be made very small, so that only photons backscattered close to perpendicular to the soil surface can reach the detector. The major problem arising from this remedy is the increase in the power requirements of the x-ray generator due to the further reduction in the number of photons reaching the detector. The second remedy is to insure a fixed height relationship to the soil through some servo mechanism or by restricting use of the detector to moderately flat surfaces such as roads. A third approach is signal processing based on correlation of single line scans. As shown later in this chapter, the operational requirements for the speed of the vehicle carrying the mine detection system and the width of the path to be searched

lead to very short single line scan times for the x-ray beam. During these short time periods, height variation over an object the size of a mine will be small. Each individual scan with a mine present will contain information characteristic of a chord through the mine. Correlation of such information from multiple scans to the size and shape of recorded mine images could be used to overcome height variations between scans.

Figure VIII.11 shows the height sensitivity of the energy window detector for the same example problem as discussed in the preceding paragraph. The sensitivity curve is seen to resemble that of the uncollimated fluence detector, but with a broader maximum, indicating less height sensitivity.

Soil Density Variation

Variations in soil density occur naturally, but are of special interest in mine detection. When a mine has been recently emplaced, the density of the soil surrounding the mine is reduced to approximately 75% of its in-place value (Roder and Van Konyenburg, 1975). This reduction allows photons scattered from deeper positions to be able to penetrate the overlying soil layer and reach the detector.

Figure VIII.12 shows the effect of reduced soil density on the uncollimated detector. The figure expresses this effect in terms of the ratio of the fluence response at reduced soil density to that for normal, in-place soil, as a function of source energy for perpendicularly incident beams

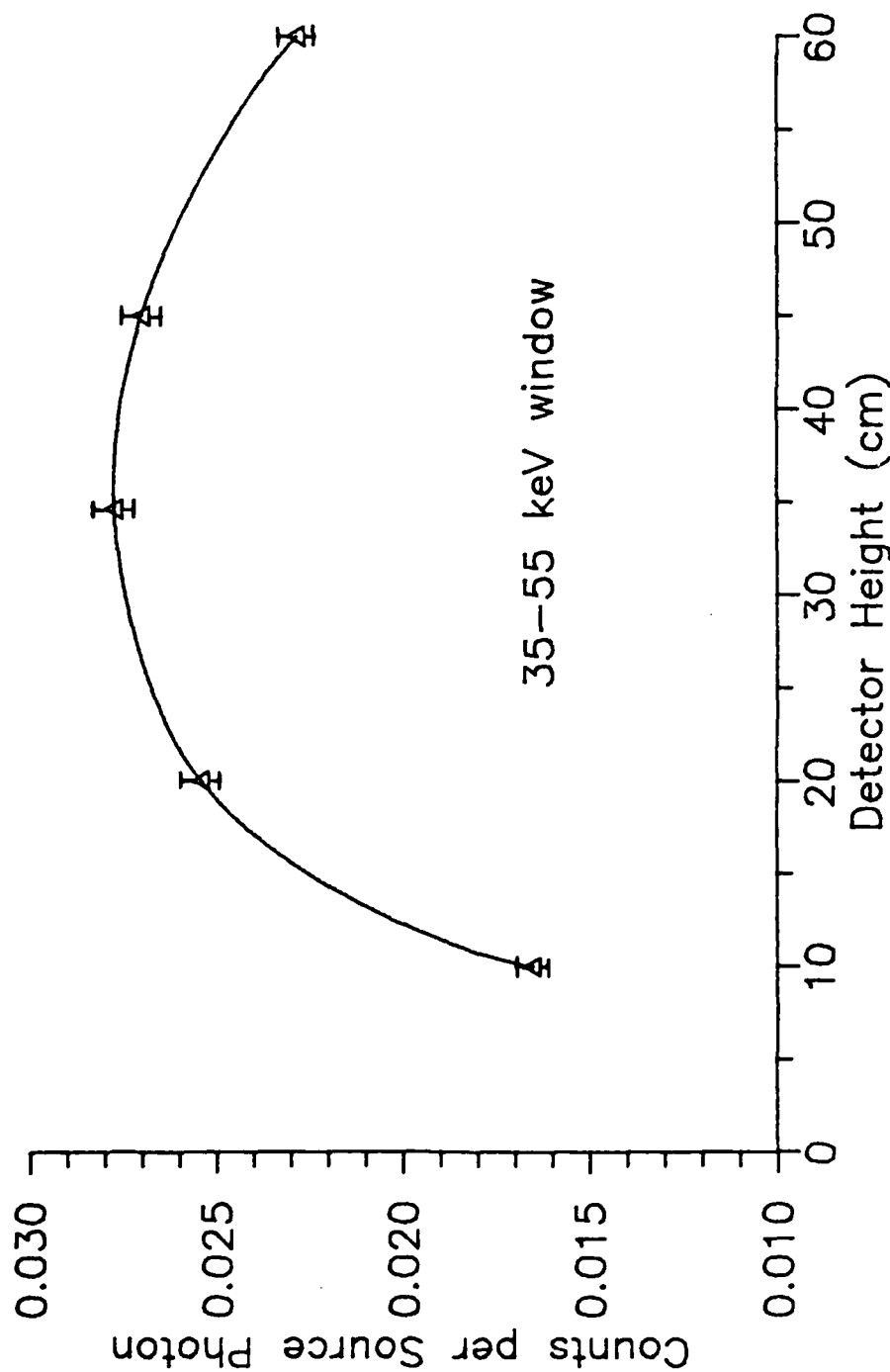


Figure VIII.11. Fluence response as a function of height above the soil surface for the energy window detector. Calculations are for 100 keV photon beams perpendicular-ly incident on the center of TST mines buried flush to the surface in HTL soil. The uncollimated detector with an energy window of 35 to 55 keV, consists of two panels of 30 cm width and 210 cm length, separated by a raster gap of 30 cm, and located at various heights above and parallel to the soil surface intercepts the backscattered fluence.

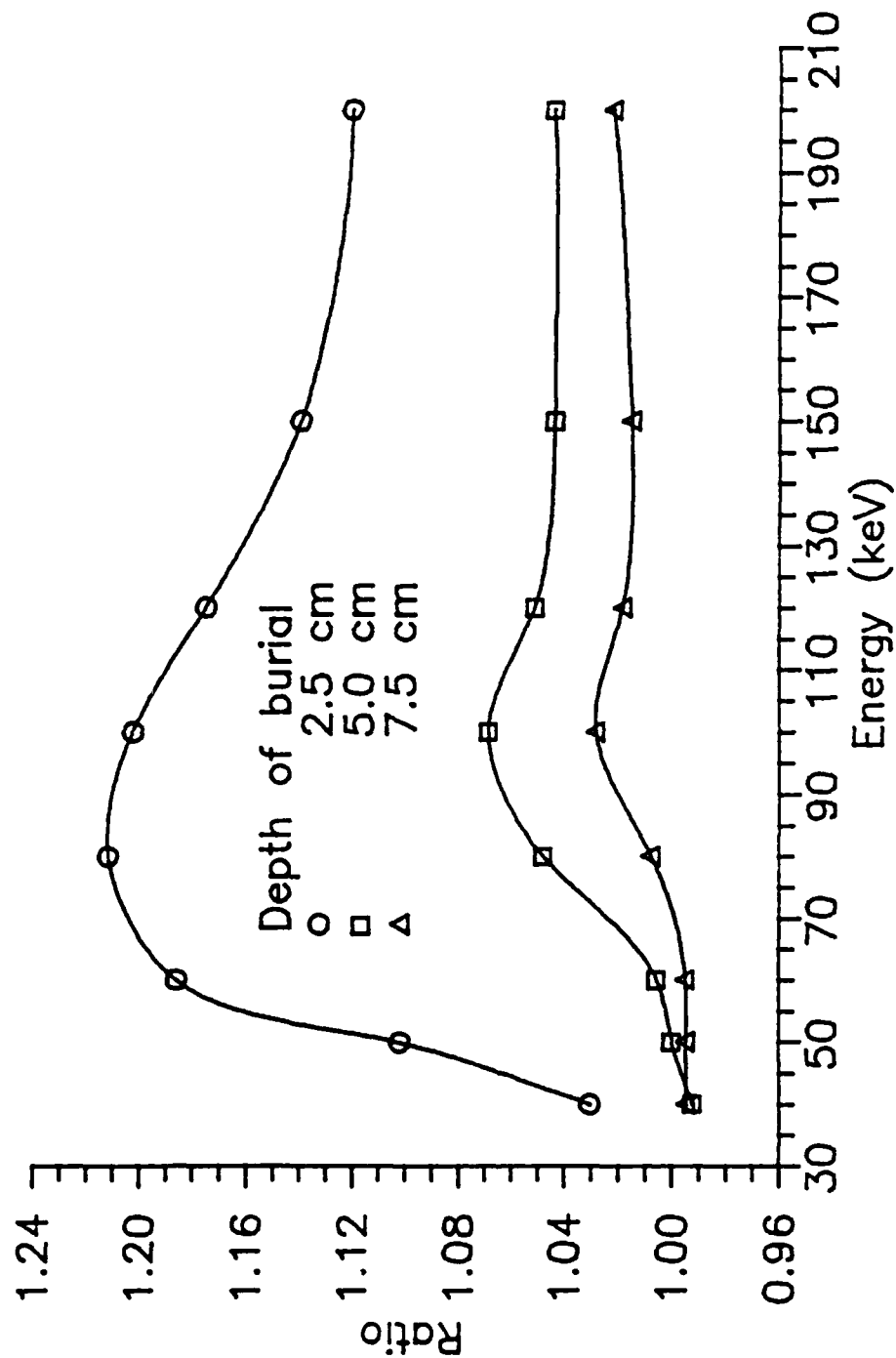


Figure VIII.12. Ratio of fluence responses for disturbed to in-place density of HTL soil with the TST mine at selected depths of burial as a function of source energy for the uncollimated detector. Calculations are for 100 keV photon beams perpendicularly incident on the centers of TST mines. The uncollimated detector consists of two panels of 30 cm width and 210 cm length, separated by a raster gap of 10 cm, and located 34.6075 cm above and parallel to the soil surface. Soil densities are 1.27 g/cm³ for disturbed soil, and 1.70 g/cm³ for in-place soil.

on TST mines at various depths of burial in HTL soil. The detector is located 34.6075 cm above the soil and consists of two panels, each 30 cm wide with a 10 cm raster gap. The disturbed soil density is 1.27 g/cm^3 ; the in-place soil density, 1.70 g/cm^3 . The ratio displayed in the figure should not be confused with the mine to soil fluence ratio. The ratio displayed, multiplied by the in-place mine to soil fluence ratio, gives the mine to soil fluence ratio in the reduced density soil. The peak in the density enhancement ratio lies in generally the same energy region as the peak in the mine to soil fluence ratio. For the mine buried at 2.5 cm, the peak is shifted somewhat to lower energy reflecting the new-found capability of relatively low energy photons to reach the soil surface. There is no change in the conclusions regarding optimum energy for the uncollimated detector, but detection becomes easier at 5.0 cm. Detection at 7.5 cm remains beyond the capability of the uncollimated fluence detector, even in low density soil.

The effect of reduced density on the collimated detector is much more dramatic. Table VIII.4 compares calculations for the collimated detector for in-place and disturbed soil. The conclusion reached is that detection is possible at 10.0 cm with the reduced soil density. In fact, detection is possible at any depth. The final entry in the table indicates that the collimated configuration detects density differences in the soil without the presence of the mine. This conclusion is consistent with results obtained by Texas

TABLE VIII.4

Mine to Soil Fluence Ratio from the Collimated
Detector with Recently Buried Mines

Depth of Burial (cm)	Mine to Soil Fluence Ratio ^a Collimator Acceptance Angle					
	25.8°		23.1°		19.9°	
	Density ^b		Density		Density	
	Normal	Low	Normal	Low	Normal	Low
0.0	3.007 ±0.203	3.086 ±0.208	4.453 ±0.512	4.562 ±0.531	6.165 ±1.333	6.469 ±1.394
2.5	1.650 ±0.114	2.030 ±0.145	2.474 ±0.294	3.344 ±0.402	4.047 ±0.876	6.079 ±1.316
5.0	1.197 ±0.095	1.461 ±0.111	1.516 ±0.206	2.099 ±0.269	2.379 ±0.569	3.368 ±0.770
7.5	1.028 ±0.084	1.268 ±0.071	1.142 ±0.165	1.673 ±0.223	1.724 ±0.435	2.778 ±0.650
10.0	1.005 ±0.072	1.190 ±0.083	0.926 ±0.121	1.554 ±0.188	1.039 ±0.254	2.396 ±0.528
15.0 without mine ^c	1.000	1.156 ±0.081	1.000	1.266 ±0.158	1.000	1.673 ±0.382

^aCalculations are for 100 keV photon beams perpendicularly incident on HTL soil with 10% water by weight. The beam intercepts TST mines at their centers. Diverging source beams are 1.27 cm by 1.27 cm at the soil surface and are produced by a point source at 64.48 cm above the soil surface. The detector consists of two panels, each 210 cm long by 30 cm wide, separated by a raster gap of 30 cm, located parallel to and 34.6075 cm above the soil surface.

^bThe density of the normal, undisturbed soil is 1.80 g/cm³; that of the disturbed soil is 1.35 g/cm³. The disturbed soil density is characteristic of that surrounding a recently emplaced mine.

^cThis calculation was made for a cylindrical hole of depth 15 cm and radius 15 cm filled with soil at 1.35 g/cm³ density.

Nuclear Corporation in their mine detection efforts (Roder and Van Konyenburg, 1975), as described in Chapter II. The possibility of dummy minefields being constructed by simply digging and refilling holes with loose soil exists with this detector, though imaging should be helpful in determining whether sizes and shapes are characteristic of mines.

The energy window detector also experiences an enhancement in its capability to detect mines due to reduced soil density. Table VIII.5 displays results for this detector for the same example considered above with the collimated detector. The energy window detector is capable of detection down to at least 5 cm, and probably to 7.5 cm, in soil recently disturbed by mine emplacement. Unlike the collimated detector, it is not subject to detecting refilled holes.

Soil Moisture Content

The addition of water lowers the effective atomic number of soil, making it a better scattering medium. As a result, each of the detector types, all of which depend on some form of differences in the scattering properties between the mine and soil, would be expected to be degraded in their ability to detect mines. This would be true if the average atomic number were the only change in the soil, but added water also results in higher density. As is seen in the preceding section, the collimated detector is particularly sensitive to density, so that mixed results for it might be expected.

TABLE VIII.5

Mine to Soil Fluence Ratio from the Energy Window
Detector with Recently Buried Mines

Depth of Burial (cm)	Mine to Soil Fluence Ratio ^a Energy Window Size (keV)			
	35 - 45 Density ^b		35 - 55 Density	
	Normal	Low	Normal	Low
0.0	19.863 ±1.890	19.960 ±1.900	6.529 ±0.219	6.605 ±0.221
2.5	2.634 ±0.274	3.951 ±0.411	1.732 ±0.064	2.214 ±0.083
5.0	1.163 ±0.147	1.508 ±0.180	1.120 ±0.048	1.302 ±0.050
7.5	1.016 ±0.133	1.129 ±0.144	1.044 ±0.456	1.094 ±0.047
10.0	1.007 ±0.114	1.076 ±0.121	1.022 ±0.039	1.046 ±0.040

^aCalculations are for 100 keV photon beams perpendicularly incident on HTL soil with 10% water by weight. The beam intercepts TST mines at their centers. Diverging source beams are 1.27 cm by 1.27 cm at the soil surface and are produced by a point source at 64.48 cm above the soil surface. The detector consists of two panels, each 210 cm long by 30 cm wide, separated by a raster gap of 30 cm, located parallel to and 34.6075 cm above the soil surface.

^bThe density of the normal, undisturbed soil is 1.80 g/cm³; that of the disturbed soil is 1.35 g/cm³. The disturbed soil density is characteristic of that surrounding a recently emplaced mine.

Table VIII.6 shows results, in terms of the mine to soil fluence ratio, for the uncollimated fluence detector for three different moisture contents of HTL soil with the TST mine at a depth of burial of 2.5 cm. The example is for 100 keV source photons incident perpendicularly on the mine center. The table shows a slight degradation in the mine to soil fluence ratio as a result of increasing water content for this detector.

Table VIII.7 shows results of calculations for the collimated detector for two different soil moisture contents of HTL soil as a function of source beam energy. At low energies the effect of additional moisture is to lower the mine to soil fluence ratio; at higher energies, to increase it. At the lower energies the dominant mechanism for change is the reduction in the photoelectric scattering cross section of the soil with increasing moisture content, resulting in increased incoherent scattering, which degrades the ratio. At higher energies, where the photoelectric cross section is already low, the dominant mechanism is the increased density of the soil with the higher water content. The increase in density serves to enhance the attenuation difference between the mine and soil.

Table VIII.8 shows the results of calculations for the energy window detector for HTL soil of three different soil moisture contents. The results indicate the mine detection capability of the energy window technique is degraded more by moisture than either of the other two detector configurations.

TABLE VIII.6

Mine to Soil Fluence Ratio of the Uncollimated
Fluence Detector for Three Water Contents of HTL
Soil with the TST Mine at 2.5 cm Depth of Burial

Source Beam Energy (keV)	Mine to Soil Fluence Ratio ^a Water content by Weight ^b		
	0%	10%	20%
40	1.007 ±0.024	1.011 ±0.016	1.010 ±0.016
50	1.058 ±0.021	1.047 ±0.017	1.042 ±0.017
60	1.108 ±0.021	1.094 ±0.013	1.081 ±0.018
80	1.138 ±0.018	1.138 ±0.016	1.116 ±0.015
100	1.133 ±0.016	1.116 ±0.013	1.099 ±0.012
120	1.142 ±0.018	1.113 ±0.013	1.088 ±0.013
150	1.103 ±0.014	1.081 ±0.012	1.068 ±0.012
200	1.075 ±0.016	1.067 ±0.012	1.047 ±0.012

^aCalculations are for photon beams perpendicularly incident on HTL soil with selected water content and densities. The beam intercepts TST mines at their centers. Diverging source beams are 1.27 cm by 1.27 cm at the soil surface and are produced by a point source at 64.48 cm above the soil surface. The detector consists of two panels, each 210 cm long by 30 cm wide, separated by a raster gap of 10 cm, located parallel to and 34.6075 cm above the soil surface.

^bSoil density varies with water content. The densities used in the calculation are 1.70 g/cm³ for the dry soil (0%), 1.80 g/cm³ for the 10% soil, and 1.90 g/cm³ for the 20% soil.

TABLE VIII.7

Mine to Soil Fluence Ratio of the Collimated Fluence
Detector for Two Water Contents of HTL Soil with the
TST Mine at 2.5 cm Depth of Burial

Source Beam Energy (keV)	Mine to Soil Ratio ^a			
	Collimator Acceptance Angle			
	25.8°		19.9°	
	Water Content by Weight ^b			
	10%	20%	10%	20%
40	1.068 ± 0.143	0.987 ± 0.134	- ^c	- ^c
50	1.353 ± 0.178	1.282 ± 0.165	- ^c	- ^c
60	1.570 ± 0.184	1.390 ± 0.163	- ^c	- ^c
80	1.867 ± 0.163	1.632 ± 0.148	5.034 ± 1.456	4.560 ± 1.395
100	1.650 ± 0.114	1.645 ± 0.102	4.047 ± 0.876	3.825 ± 0.654
120	1.679 ± 0.114	1.581 ± 0.107	2.262 ± 0.366	2.733 ± 0.471
150	1.415 ± 0.084	1.472 ± 0.088	2.047 ± 0.277	2.264 ± 0.308
200	1.324 ± 0.072	1.356 ± 0.077	1.786 ± 0.197	1.992 ± 0.242

^aCalculations are for photon beams perpendicularly incident on HTL soils with selected water content and densities. The beam intercepts TST mines at their centers. Diverging source beams are 1.27 cm by 1.27 cm at the soil surface and are produced by a point source at 64.48 cm above the soil surface. The detector consists of two panels, each 210 cm long by 30 cm wide, separated by a raster gap of 30 cm, located parallel to and 34.6075 cm above the soil surface.

^bSoil density varies with water content. The densities used in the calculation are 1.70 g/cm³ for the dry soil (0%), 1.80 g/cm³ for the 10% soil, and 1.90 g/cm³ for the 20% soil.

^cUncertainties too large for meaningful comparison.

TABLE VIII.8

Mine to Soil Fluence Ratio of the Energy Window
 Detector for Three Water Contents of HTL Soil with
 the TST Mine at 2.5 cm Depth of Burial for 100 keV
 Photon Beams

Energy Window (keV)	Mine to Soil Ratio ^a Water Content by Weight ^b		
	0%	10%	20%
35 - 45	3.076 ±0.421	2.635 ±0.274	2.174 ±0.174
35 - 55	1.939 ±0.089	1.732 ±0.064	1.599 ±0.048
35 - 65	1.532 ±0.040	1.412 ±0.030	1.247 ±0.018

^aCalculations are for 100 keV photon beams perpendicularly incident on HTL soils with selected water content and densities. The beam intercepts TST mines at their centers. Diverging source beams are 1.27 cm by 1.27 cm at the soil surface and are produced by a point source at 64.48 cm above the soil surface. The detector consists of two panels, each 210 cm long by 30 cm wide, separated by a raster gap of 10 cm, located parallel to and 34.6075 cm above the soil surface.

^bSoil density varies with water content. The densities used in the calculation are 1.70 g/cm³ for the dry soil (0%), 1.80 g/cm³ for the 10% soil, and 1.90 g/cm³ for the 20% soil.

Inhomogeneities

To this point, the only inhomogeneity considered in the calculations has been the mine itself. Other objects will be present in real applications. Calculations have been performed for wood, aluminum and iron. Since aluminum is similar in density and atomic number to common minerals, calculations for it also provide information concerning rock.

Figure VIII.13 shows the results of calculations, in terms of the object to soil fluence ratio of the uncollimated fluence detector, for objects composed of these three materials as a function of source beam energy. The irradiation condition is for the standard heights and beam sizes used throughout the calculation examples, for the object buried flush to the surface in NSL soil. The wooden object is a disk 8.57 cm in radius and 1.87 cm thick of density, 0.522 g/cm^3 . These dimensions correspond to a wooden disk used in imaging experiments. The aluminum and iron disks are 10 cm in radius and 2 cm thick. The figure shows that wood responds similarly, but less strongly than the mine at low energy, but unlike the mine, at higher energies, becomes indistinguishable from soil. The similarity to the mine at low energy is due to the low average atomic number of wood as compared to soil. The dissimilarity in response at high energy is due to the low density of the wood compared to explosive. The high energy photons pass through the wood without significant interaction. This

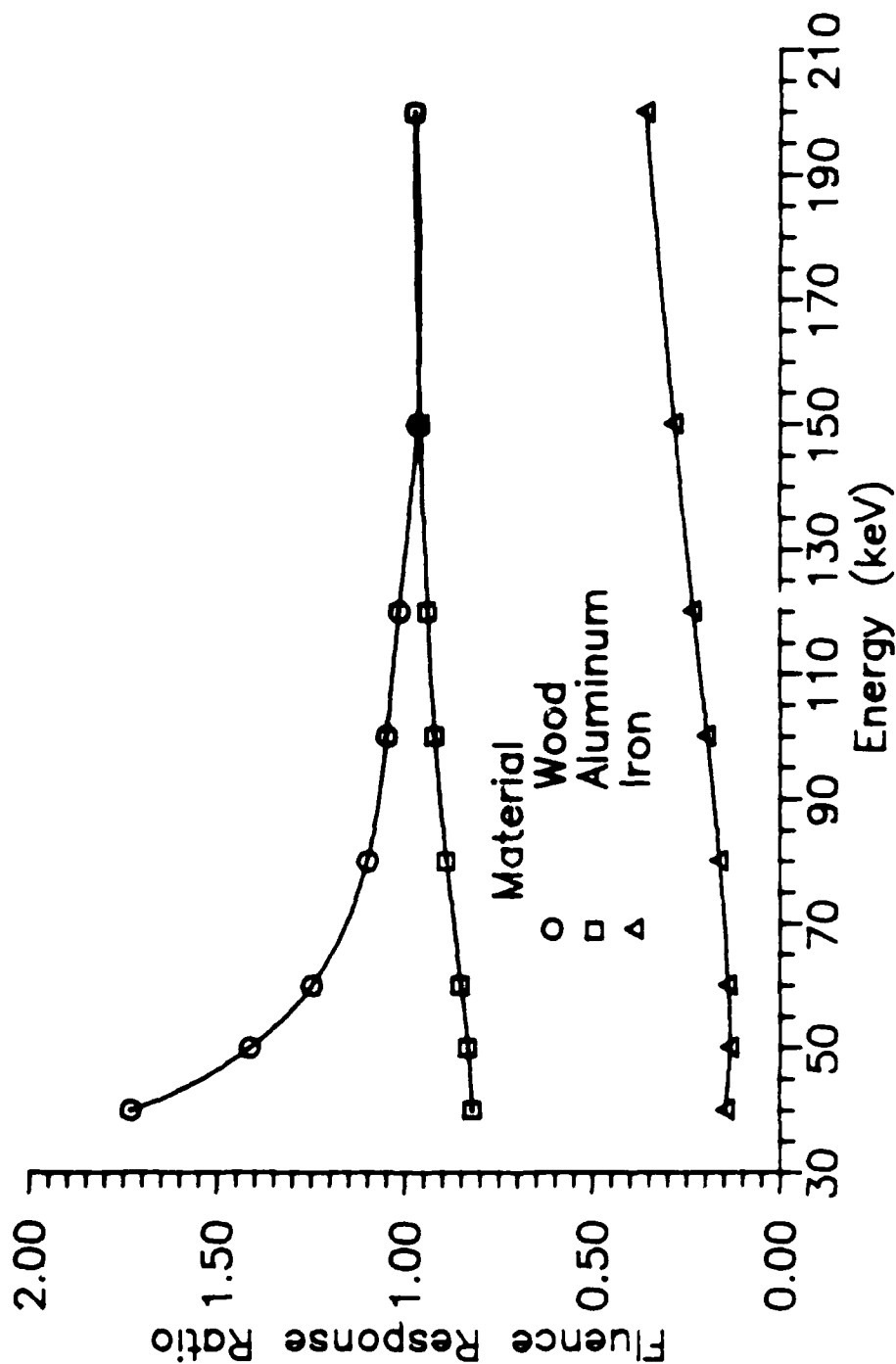


Figure VIII.13. Object to soil fluence response ratio for selected materials as a function of source energy for the uncollimated detector. Calculations are for 100 keV photon beams perpendicularly incident on the centers of selected objects (described in text) buried flush with the soil surface. The uncollimated detector consists of two panels of 30 cm width and 210 cm length, separated by a raster gap of 10 cm, and located 34.6075 cm above and parallel to the soil surface.

suggests that the wood might present edge effects like those seen for the low density air layer in the mine. A measured image, shown later in this chapter, reveals this to be the case. The atomic number of aluminum is slightly larger than that of typical soils. The figure shows that at low energy the response from aluminum is somewhat less than soil as would be expected by their relative atomic numbers. At higher energies, where the photoelectric effect cross section is small, the response of aluminum is essentially the same as soil. This suggests that rocks will create less problems in images if the source beam contains few low energy photons. The atomic number of iron is more than twice that of the average for normal soils. Accordingly, the severe reduction in response due to the iron disk is expected. The response remains low throughout the energy range of interest because the photoelectric effect interaction in iron is important throughout. The uncollimated detector will easily detect metal objects close to the surface.

The collimated detector is sensitive to differences in atomic number and density of the materials through which the photons pass on their way to the detector. The wooden disk does not respond as strongly as a mine because its low density fails to scatter photons as efficiently. The metal disks with both higher atomic number and higher density depress the response below that observed for the same objects with the uncollimated detector. Table VIII.9 shows

TABLE VIII.9

Object to Soil Fluence Ratios Produced by the
Collimated Detector for Selected Inhomogeneities

Collimator Acceptance Angle	Object to Soil Fluence Ratio ^a		
	Wood	Material Aluminum	Iron
90.0° ^b	1.041 ± 0.013	0.916 ± 0.012	0.197 ± 0.005
36.9°	1.054 ± 0.026	0.881 ± 0.023	0.175 ± 0.009
25.8°	1.280 ± 0.076	0.887 ± 0.060	0.121 ± 0.019
23.1°	1.400 ± 0.133	0.759 ± 0.088	0.081 ± 0.025

^a Calculations are for 100 keV photon beams perpendicularly incident on NSL with a density of 1.54 g/cm³. The beam intercepts the objects at their centers. Diverging source beams are 1.27 cm by 1.27 cm at the soil surface and are produced by a point source at 64.48 cm above the soil surface. The detector consists of two panels, each 210 cm long by 30 cm wide, separated by a raster gap of 30 cm, located parallel to and 34.6075 cm above the soil surface.

^b Same as an uncollimated detector.

the object to soil fluence ratio which is obtained by the collimated detector for each of the inhomogeneities.

The energy window detector is sensitive to any materials that significantly alter the capability of low energy photons to reach the detector. Table VIII.10 shows the object to soil fluence ratios produced by the three inhomogeneities for several energy window sizes. The wood response is similar, but reduced from that of the mine. It is larger than that achieved by the uncollimated or collimated fluence detectors. The depression in the response to aluminum and, especially iron, is much greater than those produced by either of the other two detectors. The higher atomic number materials and higher densities are not conducive to the scatter of low energy photons. It can be concluded that the energy window detector is very sensitive to inhomogeneities.

Imaging

Images are generated by rastering a source beam over a soil region containing a mine or other object. Images have been produced by Monte Carlo calculation and measurement using the apparatus described in Chapter III.

Monte Carlo Generated Images

The MCPHOT.P code is modified to allow simulation of raster of the source beam. Images are generated for the large area, uncollimated detector, for a variety of soils, depths of burial of the mine and other buried objects. Ten thousand photon histories are followed at each sampling

TABLE VIII.10

Object to Soil Fluence Ratios Produced by the Energy
Window Detector for Selected Inhomogeneities

Energy Window (keV)	Object to Soil Fluence Ratio ^a Inhomogeneity Material ^b		
	Wood	Aluminum	Iron
35 - 45	1.569 ± 0.211	0.567 ± 0.072	<0.0001
35 - 55	1.190 ± 0.046	0.722 ± 0.031	0.005 ± 0.001
35 - 65	1.094 ± 0.026	0.784 ± 0.020	0.032 ± 0.003

^aCalculations are for 100 keV photon beams perpendicularly incident on NSL soil with density of 1.54 g/cm³. The beam intercepts the objects at their centers. Diverging source beams are 1.27 cm by 1.27 cm at the soil surface and are produced by a point source at 64.48 cm above the soil surface. The detector consists of two panels, each 210 cm long by 30 cm wide, separated by a raster gap of 10 cm, located parallel to and 34.6075 cm above the soil surface.

^bSee text for description of objects used in calculations.

point. An increment of 2.54 cm, the same as used in the measurements with the TST mine, is employed. The positive y-direction is the simulated direction of forward motion of the vehicle carrying the system; raster of the beam occurs in the x-direction. The fluence response per source photon is calculated for each panel at each point within the array. The calculation area covers the central scan and one half of the mine. Symmetry is used to provide the remaining half. A minimum border of 5.08 cm around the mine is used in the images. The resulting arrays for mines require 17 x 9 separate calculations. Approximate single image calculation time using the DSI-32 coprocessor is 30 to 35 hours.

Figures VIII.14 through VIII.16 show the number of photons per source photon striking the panels of the uncollimated detector for the TST mine buried flush to the surface for three soils. The panels are each 205 cm long and 30 cm wide with a raster gap size of 10 cm. The detector panels are located 34.6075 cm above and parallel to the soil surface. The source is an 80 keV photon beam, which diverges from a point source located 64.48 cm above the soil surface. The beam size at the soil surface is 1.27 cm by 1.27 cm. This is the same configuration that is used earlier in this report to discuss geometric and environmental parameter variation. It is also similar to that used in the measurements. The 80 keV energy is chosen because it approximates the average source energy used in a number of measurements with the uncollimated Bicron NaI(Tl) detector.

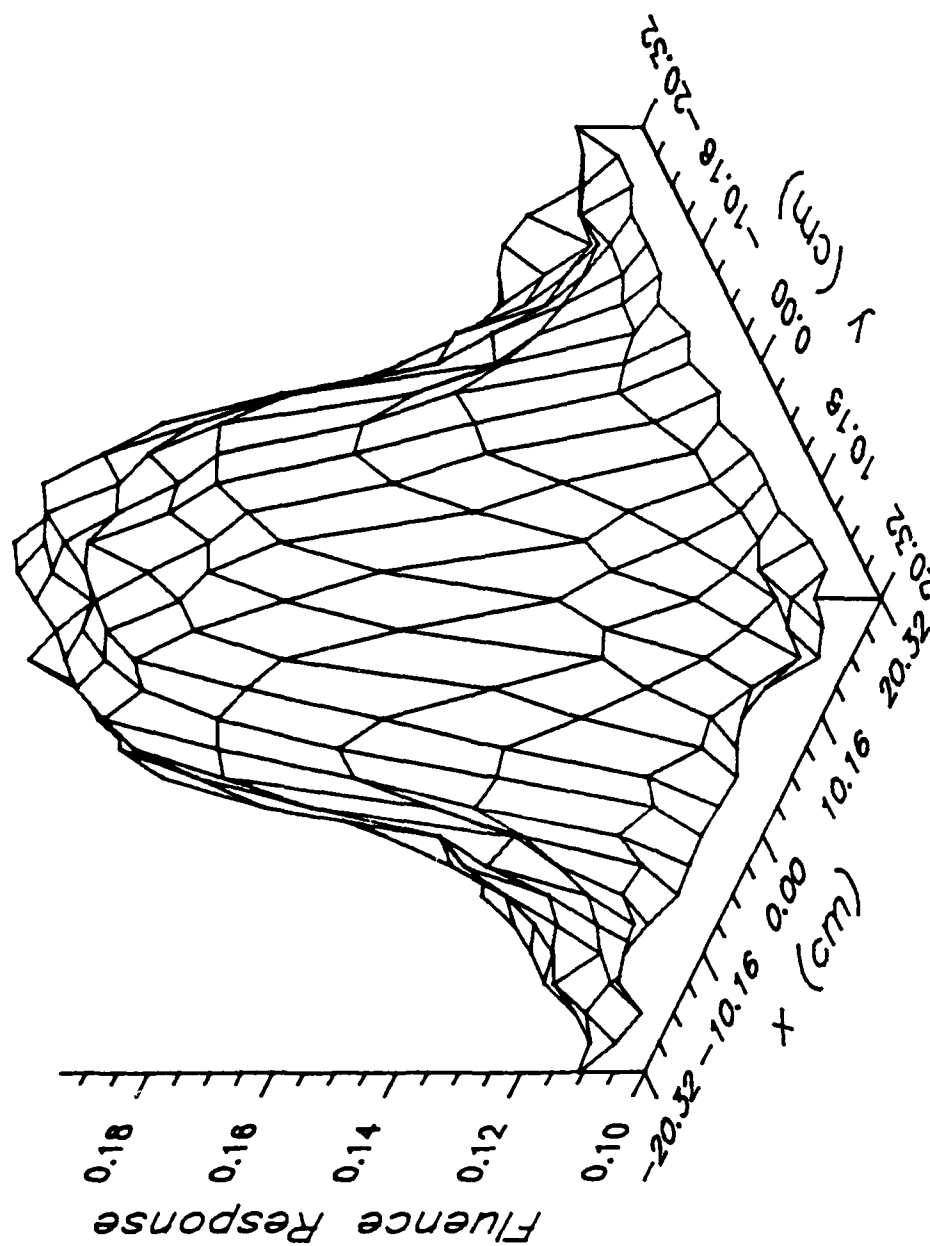


Figure VIII.14. Monte Carlo generated image for the TST mine buried flush to an NSL soil surface for the uncollimated fluence detector.

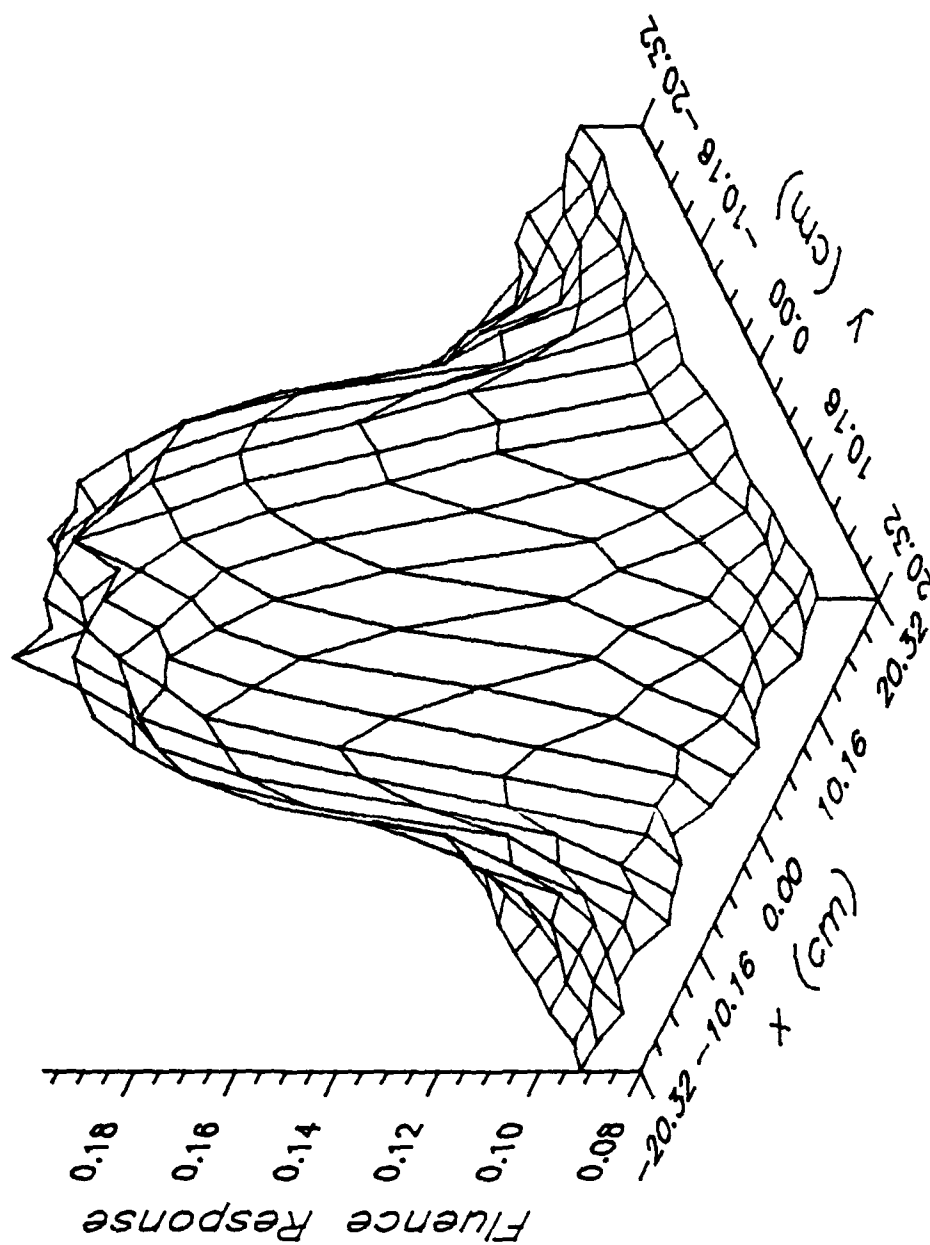


Figure VIII.15. Monte Carlo generated image for the TST mine buried flush to an HTL soil surface for the uncollimated fluence detector.

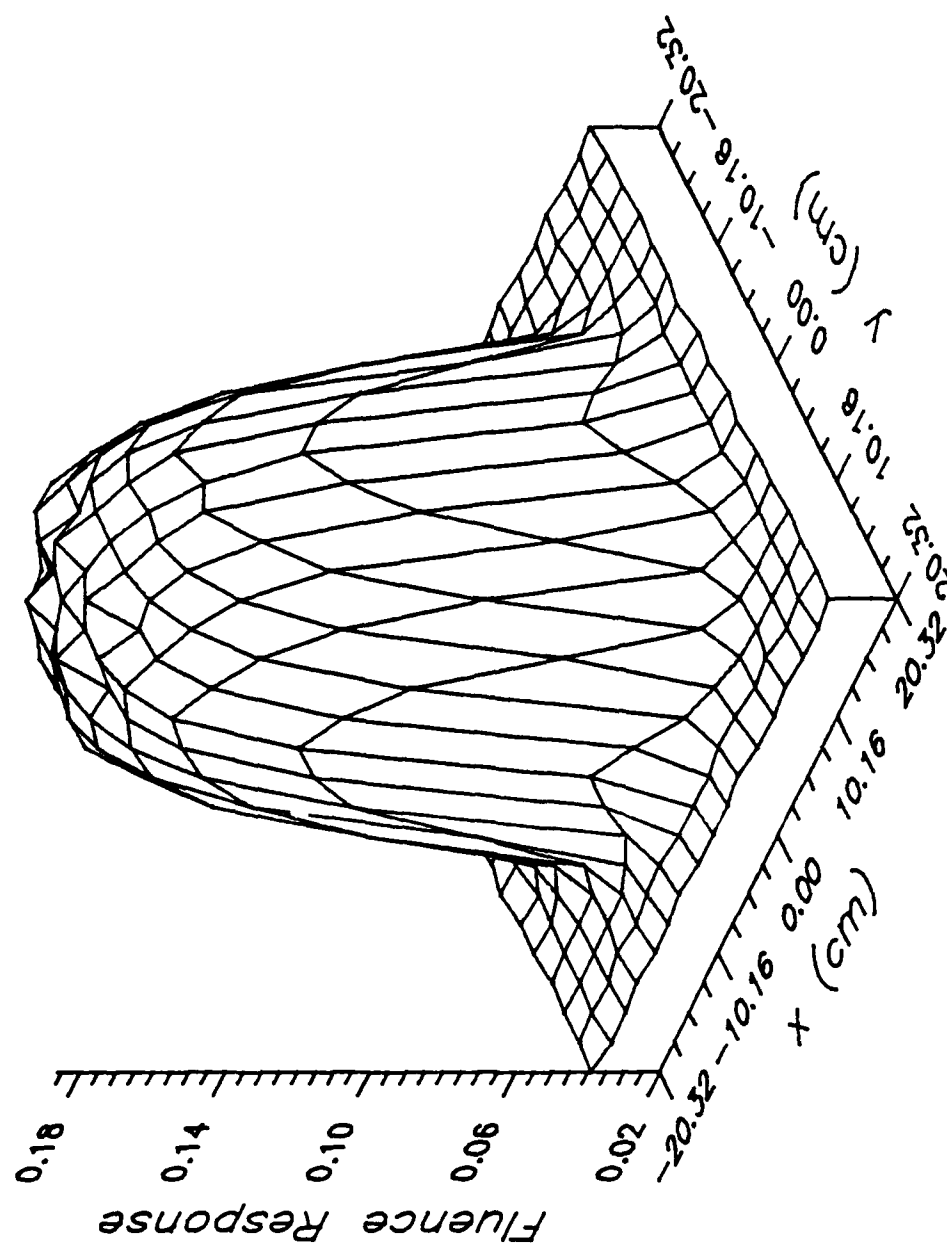


Figure VIII.16. Monte Carlo generated image for the TST mine buried flush to an MCL soil surface for the uncollimated fluence detector.

No attempt is made to provide polyenergetic calculations due to the rather significant time required to generate an image. Figure VIII.14 shows the NSL calculation; Figure VIII.15, the HTL soil calculation; and Figure VIII.16, the MCL soil calculation. In each figure the presence of the mine is clear, as would be expected from the large mine to soil fluence ratios from mines buried flush to the surface. The origin of the high ratio is clear if the responses for the two average soil calculations (NSL and HTL) are compared to that for MCL soil. The magnitudes of the response from the mines are nearly the same in all three cases. The magnitude of the responses from the soils are very different. This is the photoelectric effect contrast mechanism, more evident for MCL soil due to its higher average atomic number.

Figure VIII.17 shows the results of calculations for the TST mine at a depth of burial of 2.5 cm. Given the same numbers of photon histories as followed with the mine buried flush to the soil surface and the reduction in the difference between mine and soil responses, the statistical variation in backscatter fluence becomes more noticeable. Figure VIII.18 shows the application of a two-dimensional low pass filter to the image displayed in Figure VIII.17. This filter averages the response of nearest neighbors in the image to remove high frequency content. The image is reduced in size, losing the outer border which does not possess a full set of nearest neighbors. Figure VIII.19

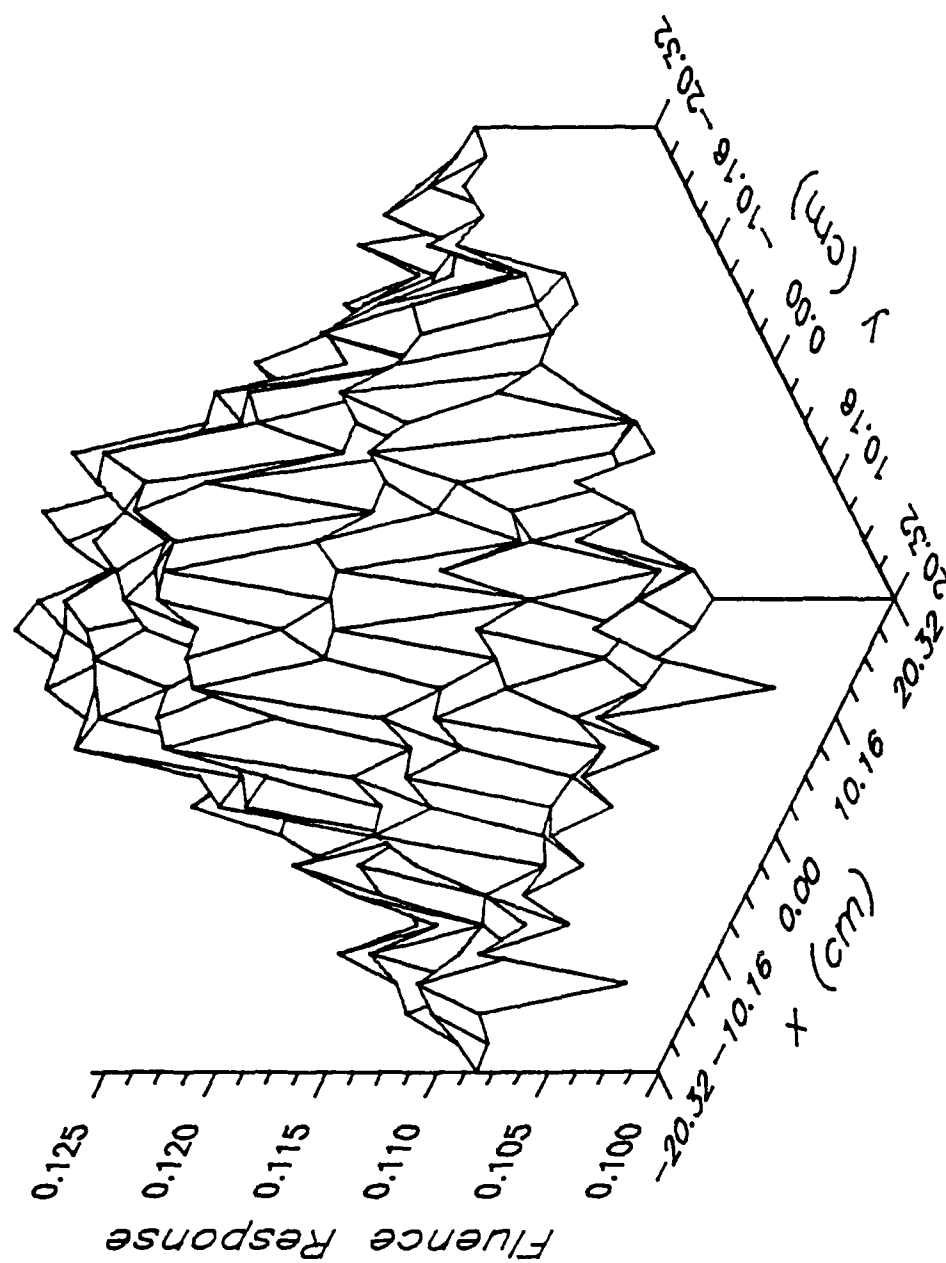


Figure VIII.17. Monte Carlo generated image for the TST mine at 2.5 cm depth of burial in NSL soil for the uncollimated fluence detector.

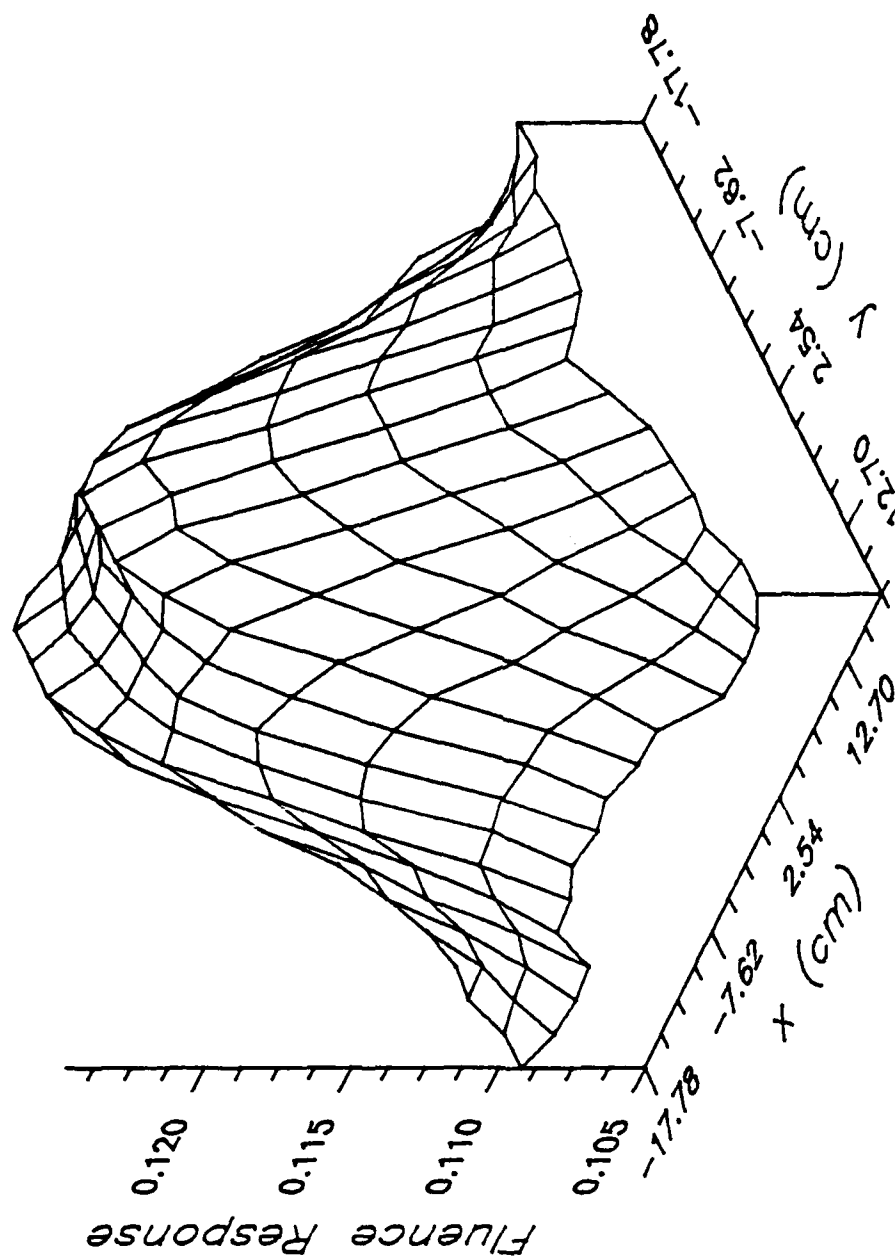


Figure VIII.18. Low pass filtered Monte Carlo image for the TST mine at 2.5 cm depth of burial in NSL soil for the uncollimated fluence detector. This figure is the result of two-dimensional low pass filtration of the image of Figure VIII.17.

shows the response from a TST mine buried at 5.0 cm in NSL soil. As the mine center intercept calculations indicate, the uncollimated detector has difficulty imaging below 2.5 cm.

Figure VIII.20 shows the response of a simulated water puddle. The puddle is modeled as a cylinder of radius of 10 cm and height of 5 cm, placed flush to the surface of HTL soil with 20% water by weight. The response image is very similar to that of the TST mine. The capability of imaging to determine the shape and size of objects is important in avoiding false alarms due to low atomic number soil inclusions such as water or tree roots. Figure VIII.21 shows the image response of a iron disk of 5 cm radius and 2 cm thickness buried flush to the surface in NSL soil, displaying the effect of a high atomic number inclusion.

Measured Images

Images of buried and surface laid mines, and other objects have been produced using the GE Maxitron 300 X-Ray Therapy Unit as the source with the Bicron NaI(Tl) detector. Chapter III describes these pieces of equipment, and the soil box positioning and computer control systems employed in the measurements. The geometry of the measurements closely follows that which is used in the calculations. With the exception of energy spectra, Table VIII.1 contains basic information concerning the irradiation geometry. All figures of measured images are for a detector positioned 21.5 cm from the beam axis. For the measured images which

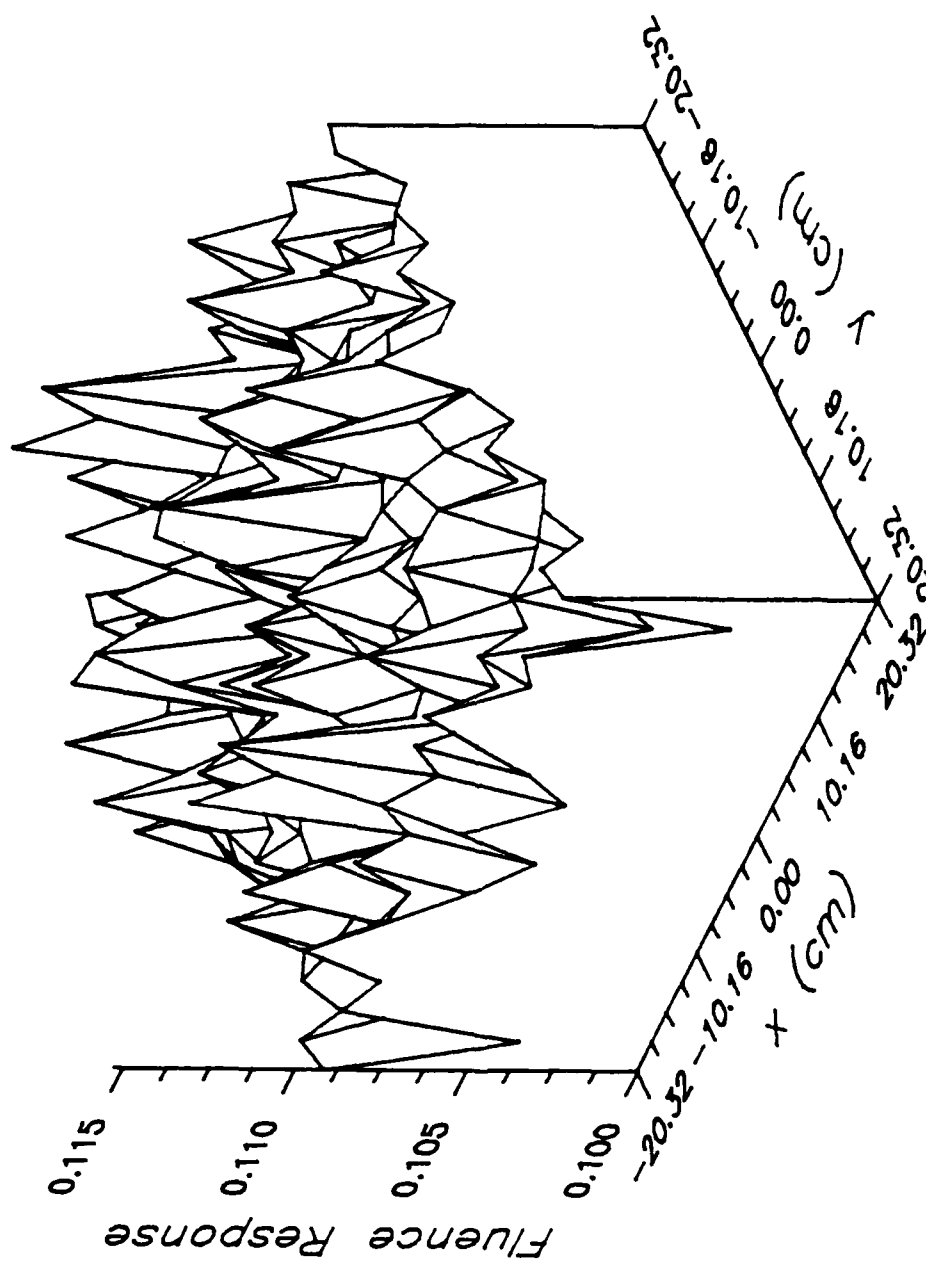


Figure VIII.19. Monte Carlo generated image for the TST mine at 5.0 cm depth of burial in NSL soil for the uncollimated fluence detector.

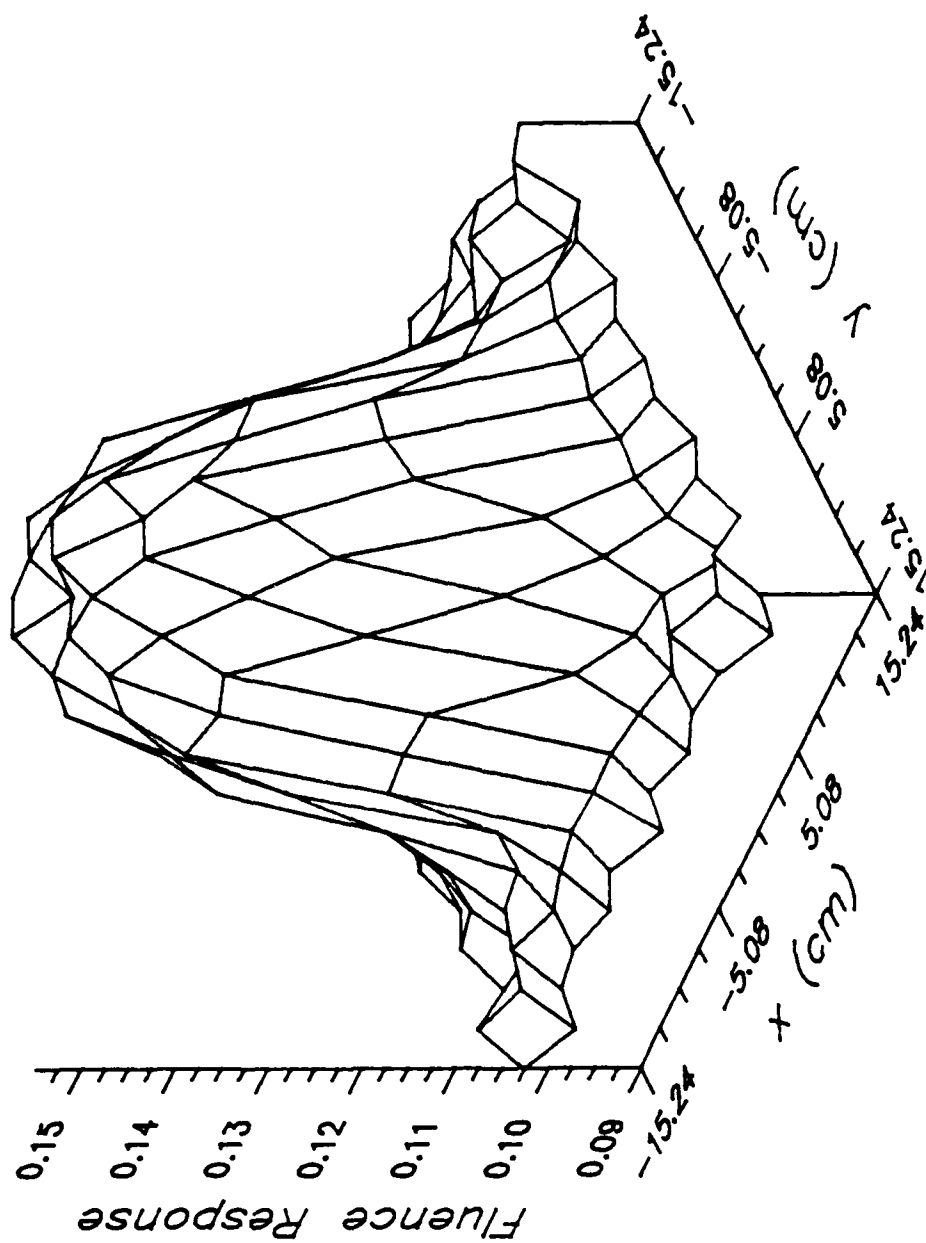


Figure VIII.20. Monte Carlo generated image for a simulated water puddle on HTL soil with 20% water content by weight for the uncollimated fluence detector. The water puddle is 10 cm in radius and 5 cm deep.

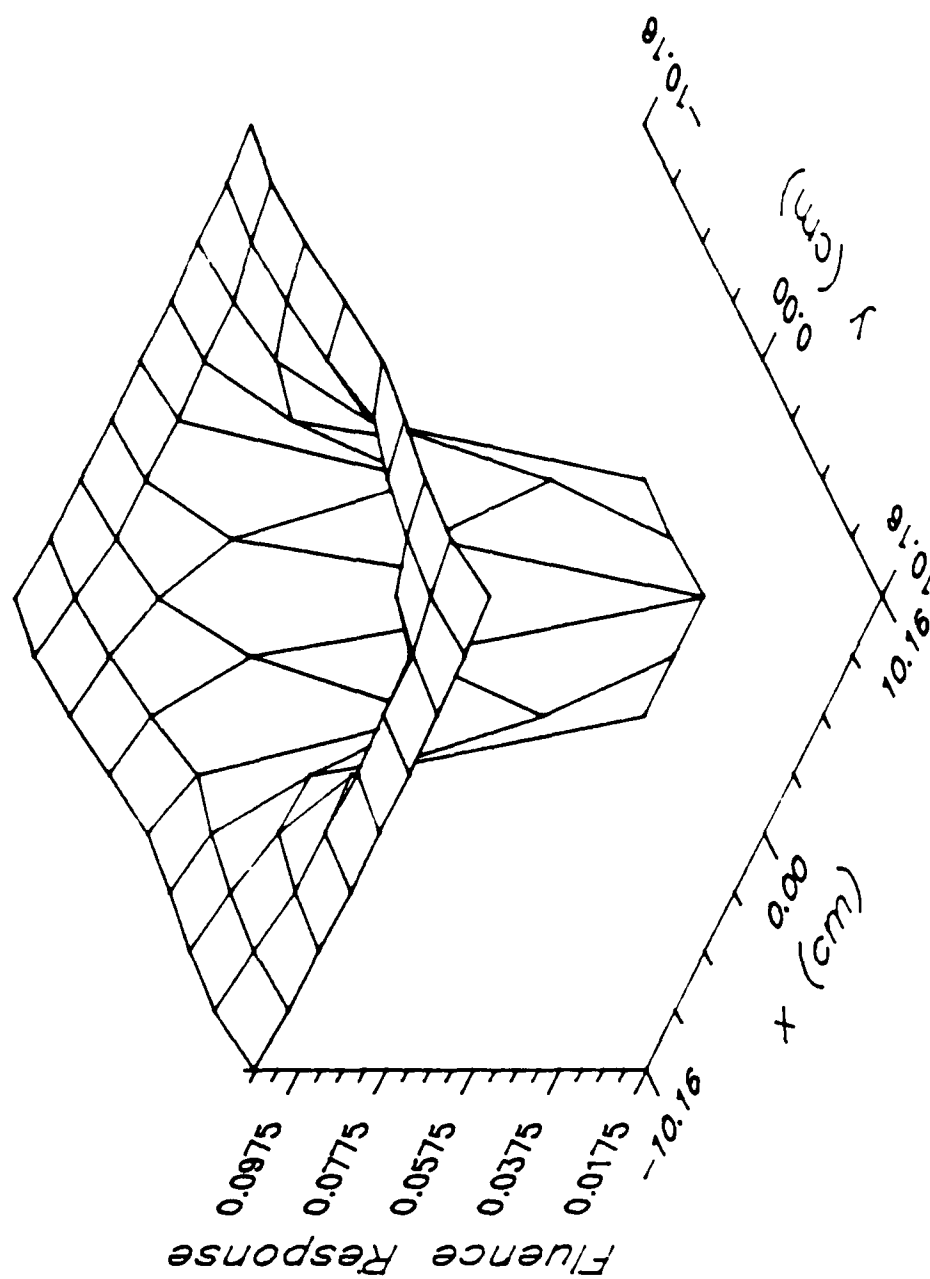


Figure VIII.21. Monte Carlo generated image for an iron disk buried flush to the surface of NSL soil for the uncollimated fluence detector. The disk is 5 cm in radius and 2 cm thick.

follow, specifics of the experimental conditions are provided in the captions of the figures. In all figures, the detector is located in the positive y-direction. With only a few exceptions, where image details of importance would be hidden, the detector is located to the left front of the three-dimensional representation. The exceptions are individually noted. In all cases, the detector is located to the right of the two-dimensional representations.

Figures VIII.22 through VIII.30 provide images produced by the uncollimated Bicron NaI(Tl) detector. Figures VIII.22 and VIII.23 are three- and two-dimensional image diagrams for the TST mine buried flush to the surface of the soil. The source is 100 kVp and is filtered by lead (Figure F.8). Edge effects at the near wall (depression in response) and far wall (enhancement of response) are seen. The mine to soil detector response ratio for central portions of the mine is approximately 1.8, making detection and imaging easy. Figure VIII.24 repeats the same image with the source spectrum at 200 kVp, also filtered by lead (Figure F.12). The images are similar in shape, but the central mine to soil ratio is much lower (approximately 1.4). The existence of more low energy photons in the first image spectrum is the cause of this difference. Figure VIII.25 shows the results of the 100 kVp beam (Figure F.8) incident on the TST mine at a depth of burial of 2.54 cm. The resulting image is similar to the Monte Carlo large area detector results in its noise content. Two-dimensional low

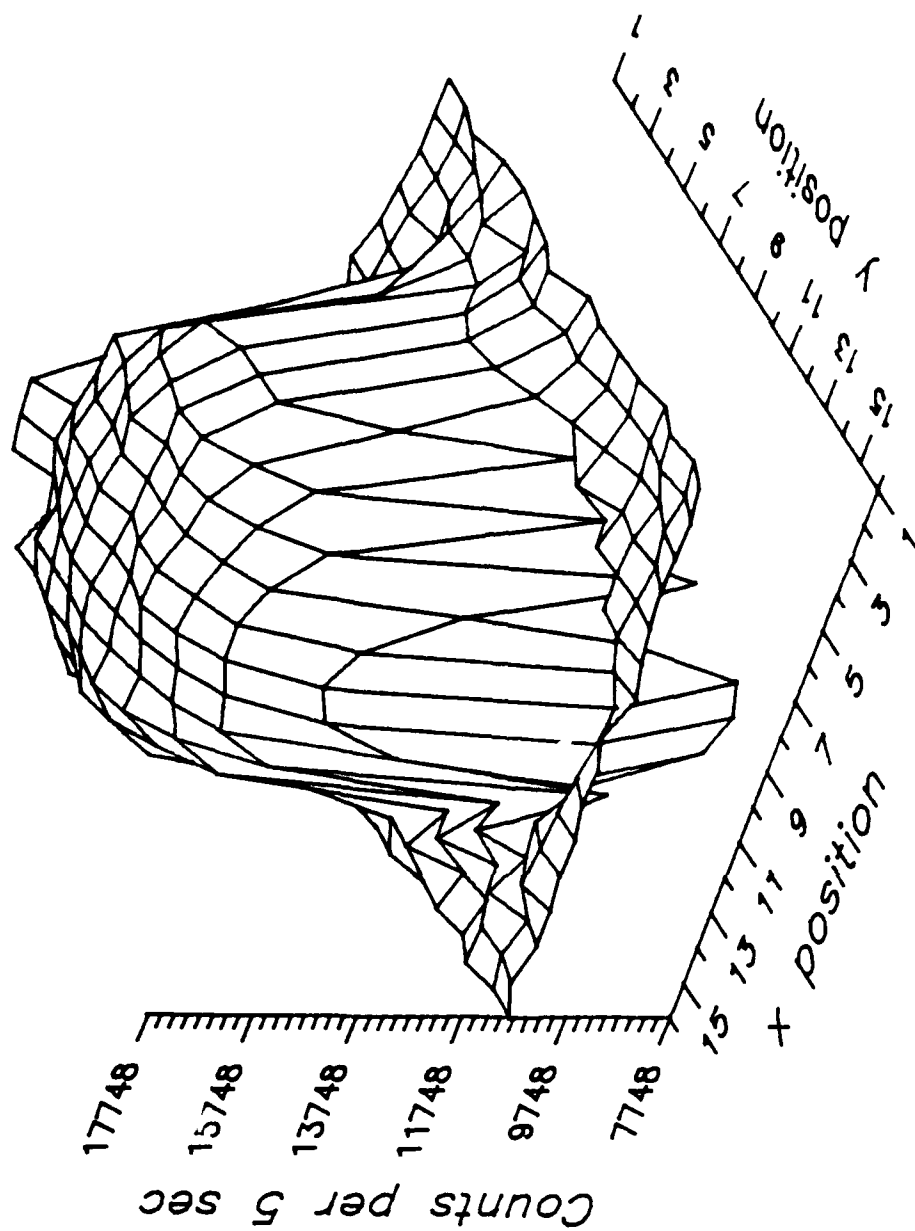


Figure VIII.22. Three-dimensional image diagram of the measured uncollimated detector response to a 100 kVp source beam filtered by Pb for the TST mine buried flush to the soil surface. The response is sampled at a 2.54 cm increment.

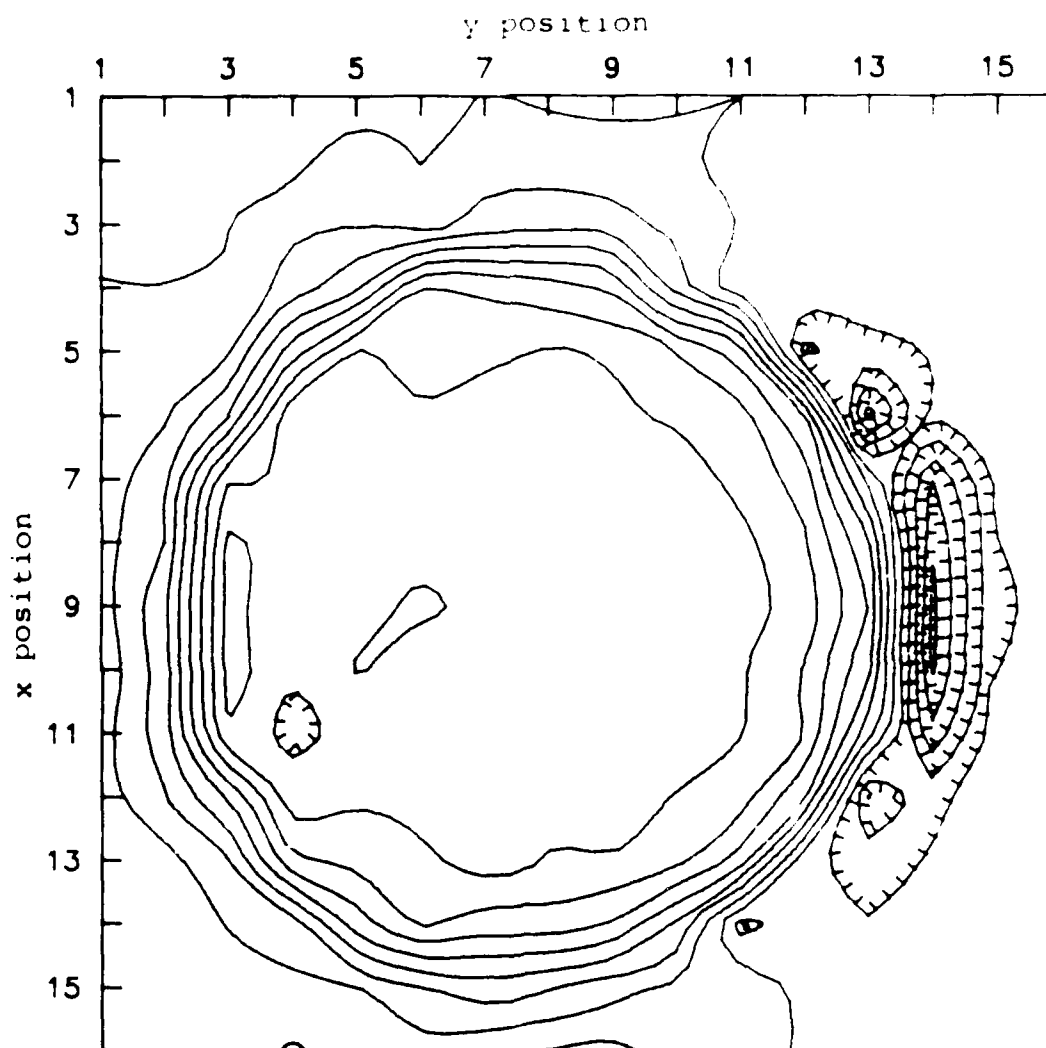


Figure VIII.23. Two-dimensional image diagram of the measured uncollimated detector response to a 100 kVp source beam filtered by Pb for the TST mine buried flush to the soil surface. The response is sampled at a 2.54 cm increment.

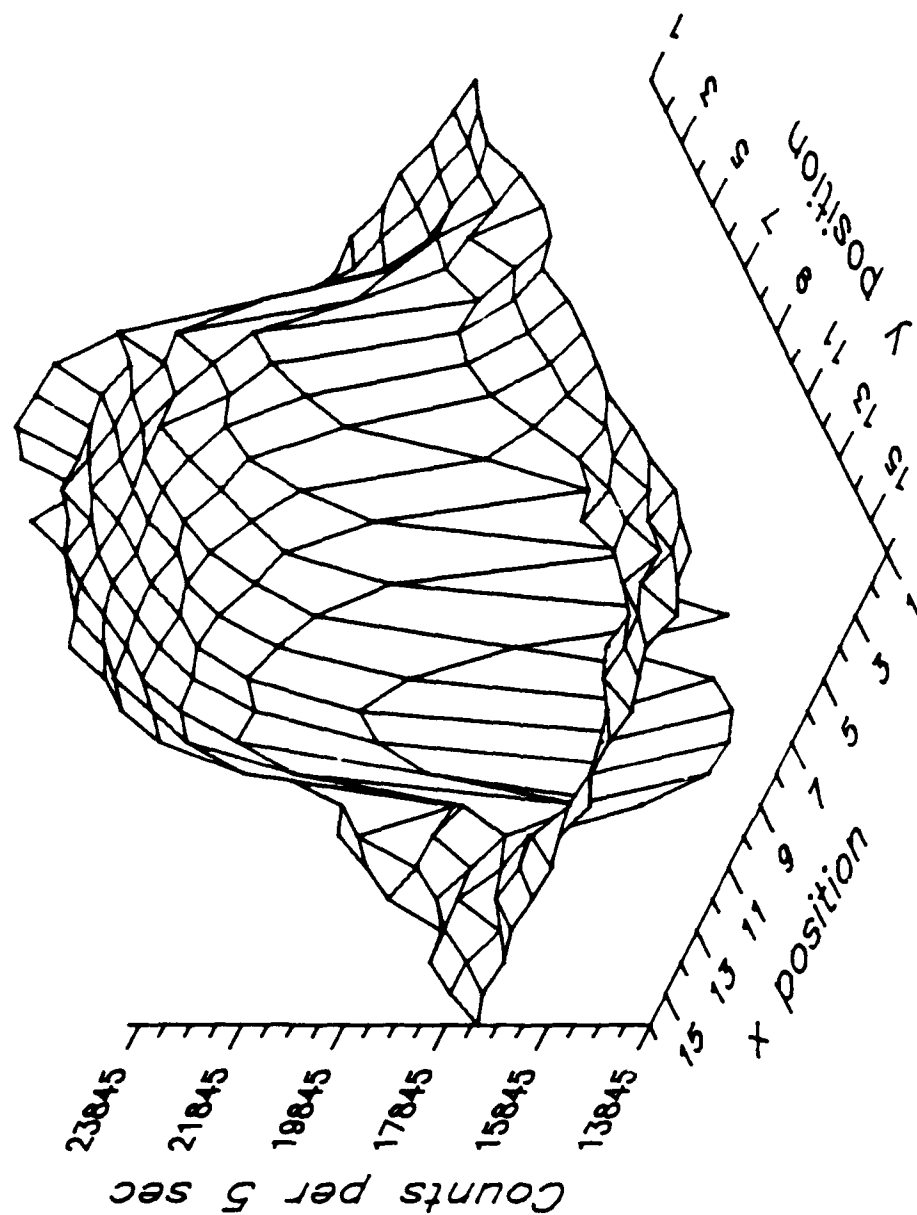


Figure VIII.24. Three-dimensional image diagram of the measured uncollimated detector response to a 200 kVp source beam filtered by Pb for the TST mine buried flush to the soil surface. The response is sampled at a 2.54 cm increment.

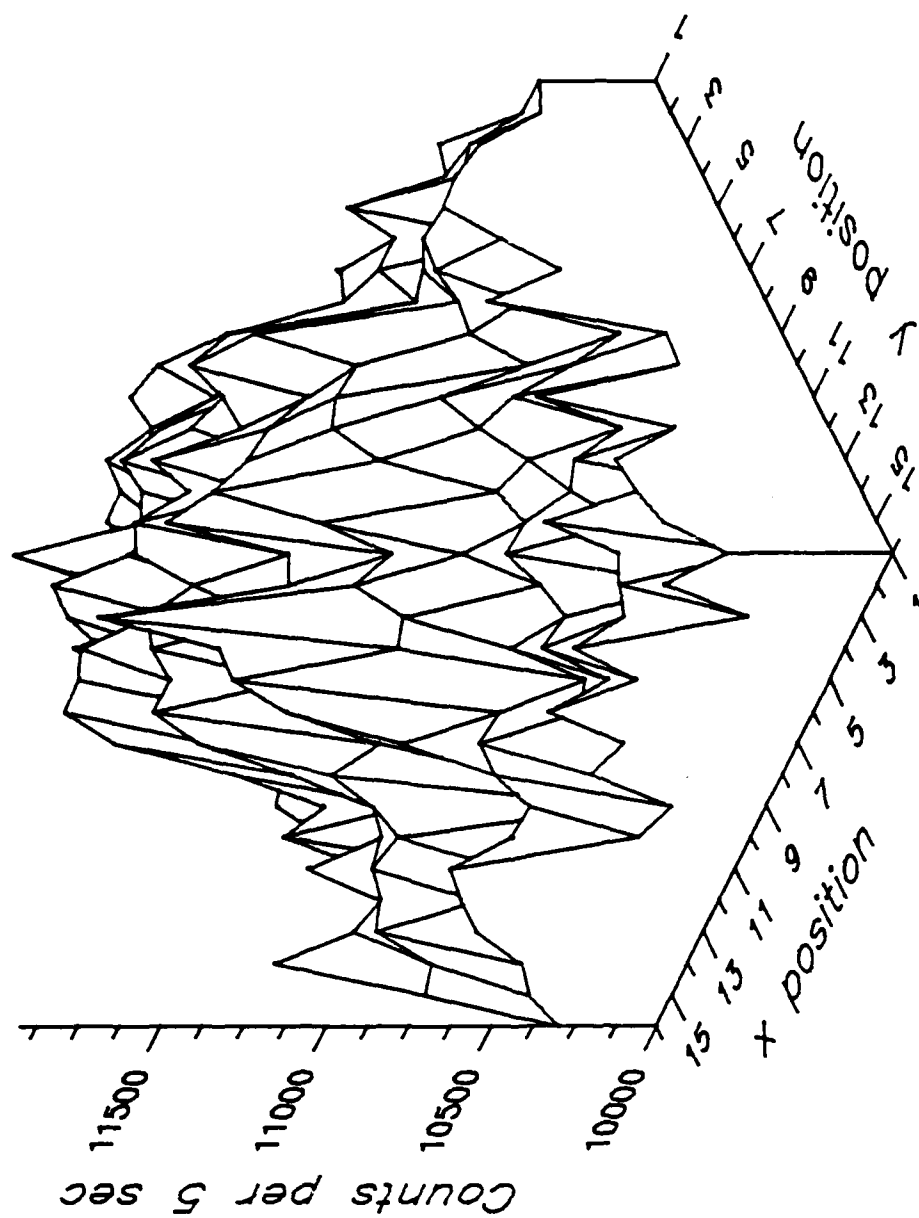


Figure VIII.25. Three-dimensional image diagram of the measured uncollimated detector response to a 100 kvp source beam filtered by Pb for the TST mine at a depth of burial of 2.54 cm. The response is sampled at a 2.54 cm increment.

pass filtration is applied to the noisy image to produce the result shown in Figure VIII.26. Figure VIII.27 shows the same case with a source beam energy of 200 kVp. The spectrum used in this image is shown in Figure F.12. The corresponding smoothed image is displayed in Figure VIII.28. Figures VIII.29 and VIII.30 are images of the TST mine laid on the top of the soil surface. In the three-dimensional diagram, the detector is located to the rear right of the image. This change in orientation is made to show the depression of the detector response behind the far wall of the mine. The reversal of the position of the depression in the edge effect is caused by shielding of the detector by the body of the mine. The spectrum of Figure F.8 is used for this measurement.

Figures VIII.31 through VIII.35 are images produced by collimating the Bicron NaI(Tl) detector. The distance from the detector to the source beam axis is 21.5 cm. The source spectrum is produced at 200 kVp with aluminum filtration (Figure F.3). Figure VIII.31 and VIII.32 are for the TST mine at a depth of burial of 2.54 cm. A collimator acceptance angle of 21.6° is used for this measurement. The mine to soil detector response ratio is approximately 2.0 near the center of the mine. This image is clearly superior to that produced by the uncollimated detector at this same depth of burial. The two-dimensional image best displays the circular shape of the mine. The gradual drop in response in the central portion of the mine in the positive

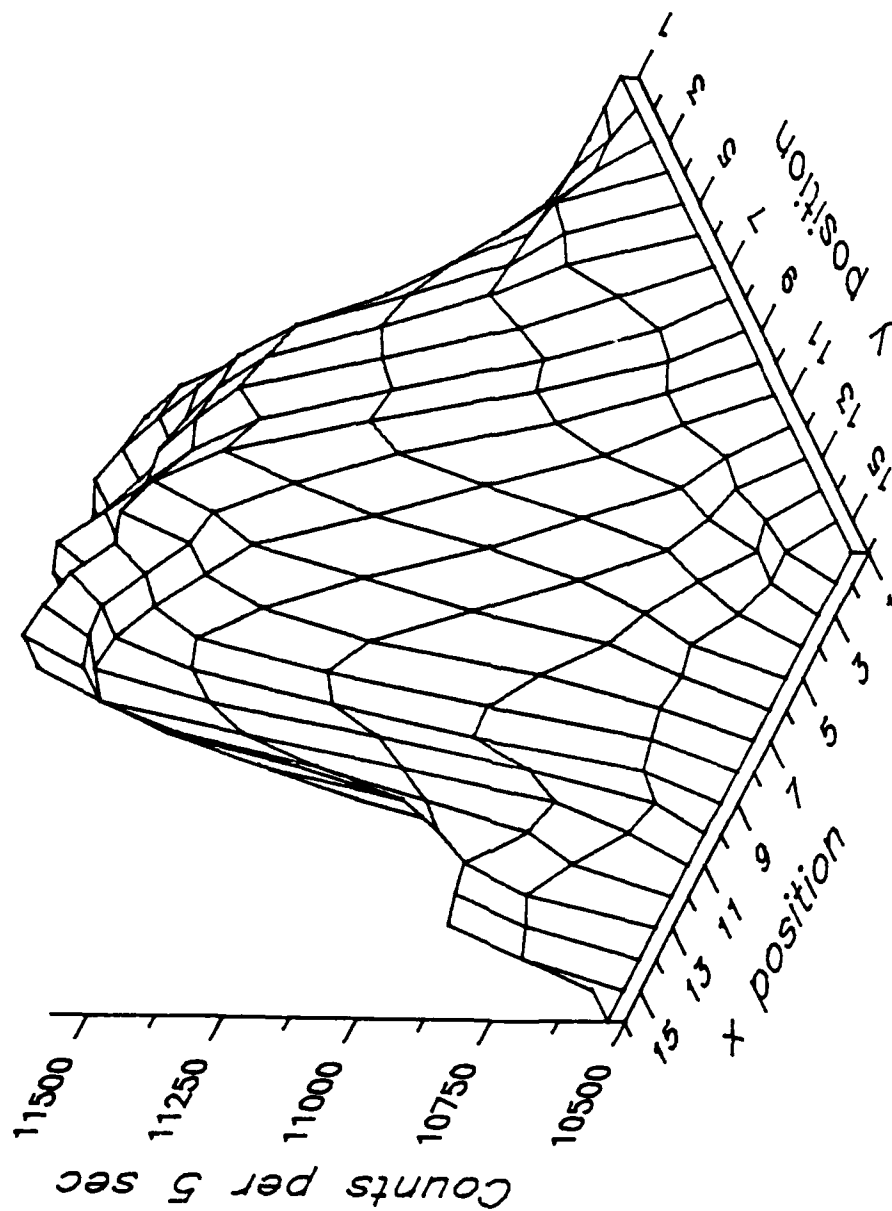


Figure VIII.26. Low pass filtered image diagram of the measured uncollimated detector response to a 100 kVp source beam filtered by Pb for the TST mine at a depth of burial of 2.54 cm. This figure is the result of two-dimensional low pass filtration of the image of Figure VIII.25.

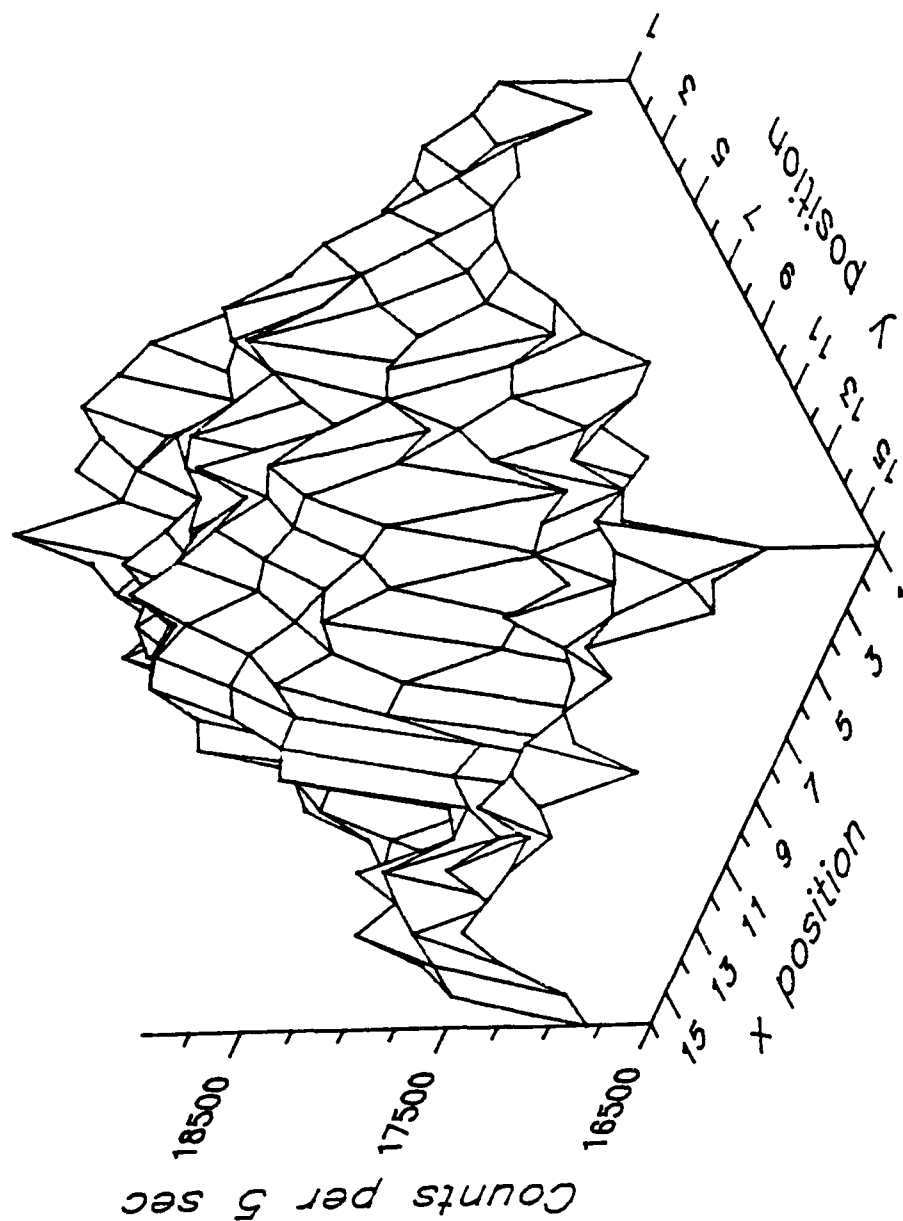


Figure VIII.27. Three-dimensional image diagram of the measured uncollimated detector response to a 200 kVp source beam filtered by Pb for the TST mine at a depth of burial of 2.54 cm. The response is sampled at a 2.54 cm increment.

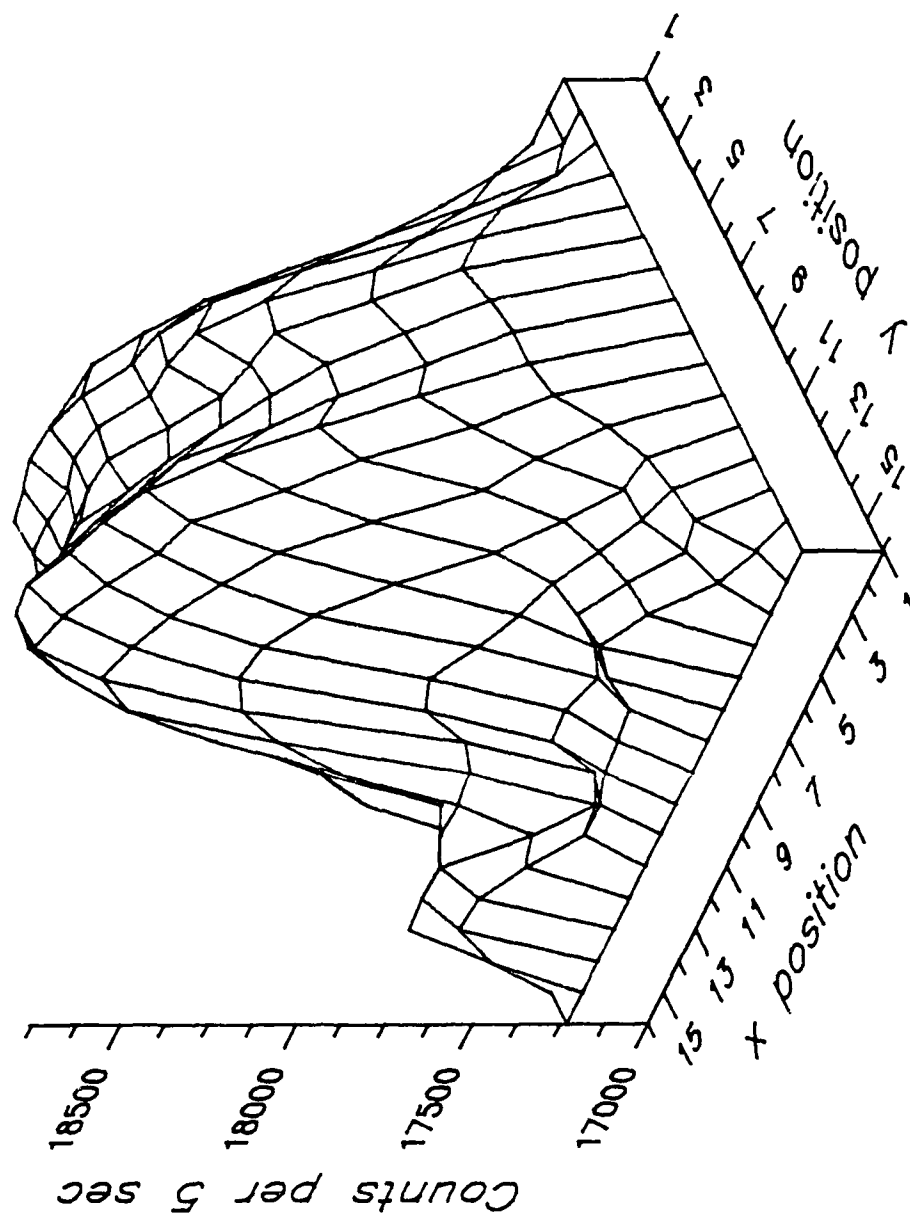


Figure VIII.28. Low pass filtered image diagram of the measured uncollimated detector response to a 200 kVp source beam filtered by Pb for the TST mine at a depth of burial of 2.54 cm. This figure is the result of two-dimensional low pass filtration of the image of Figure VIII.27.

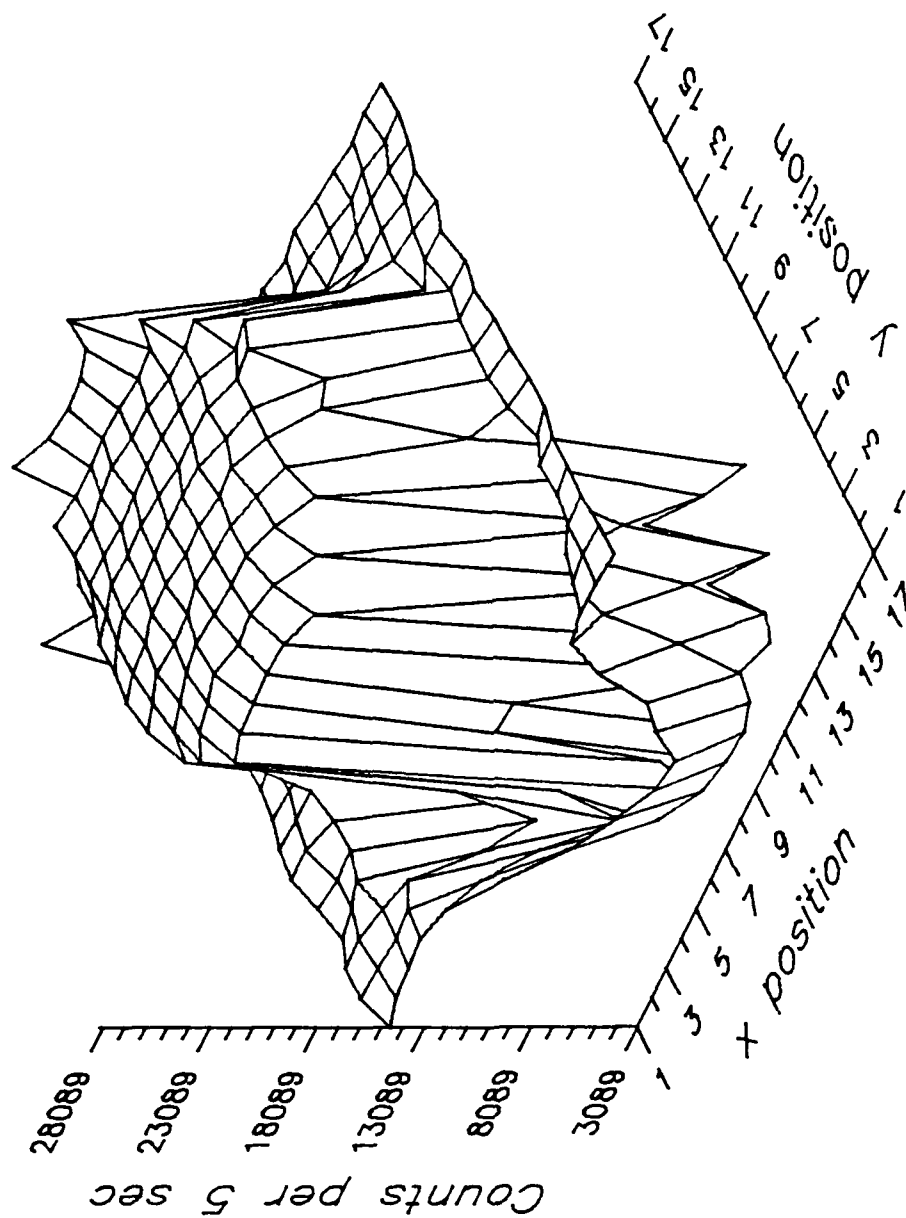


Figure VIII.29. Three-dimensional image diagram of the measured uncollimated detector response to a 100 kVp source beam filtered by Pb for the TST mine laid on the soil surface. The response is sampled at a 2.54 cm increment.

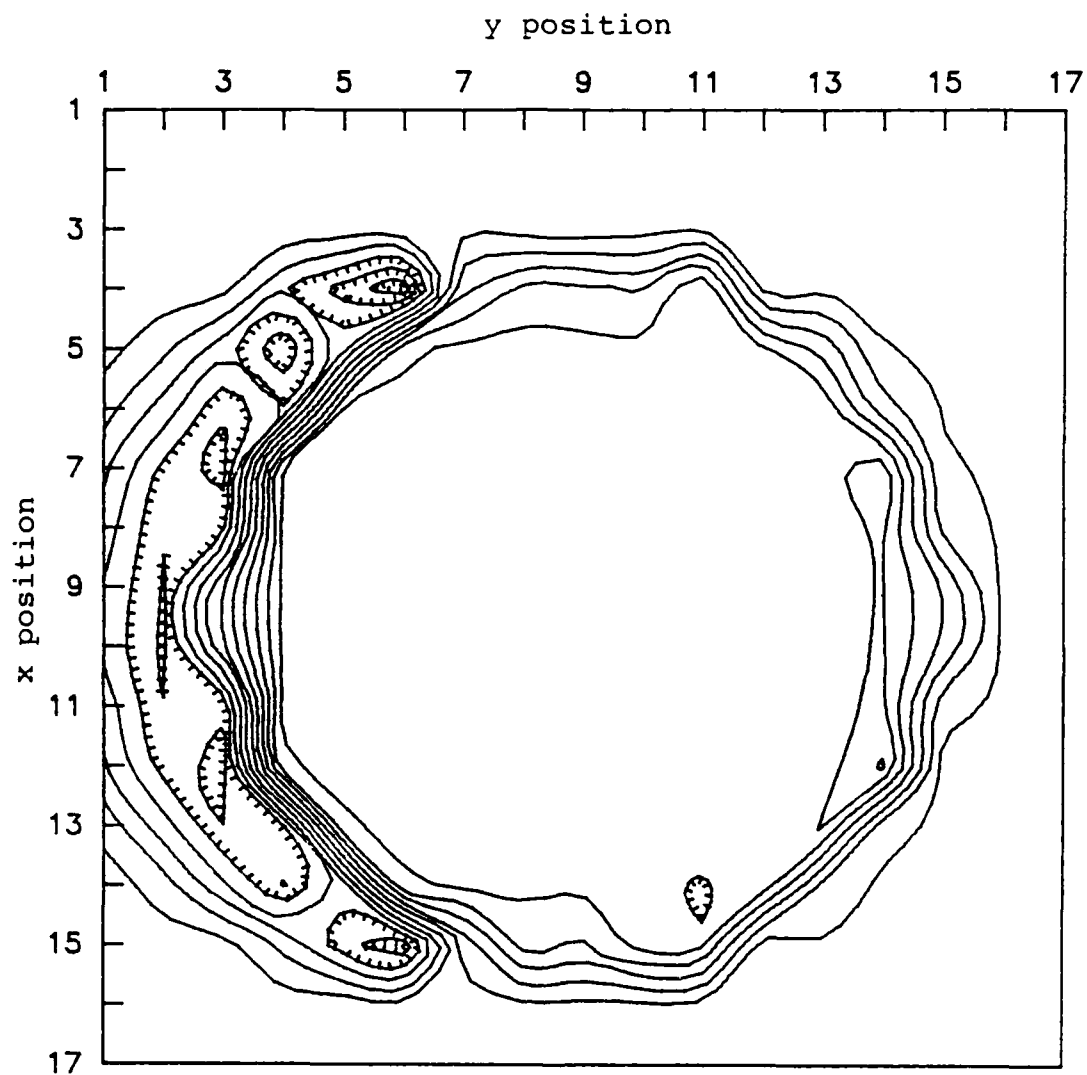


Figure VIII.30. Two-dimensional image diagram of the measured uncollimated detector response to a 100 kVp source beam filtered by Pb for the TST mine laid on the soil surface. The response is sampled at a 2.54 cm increment.

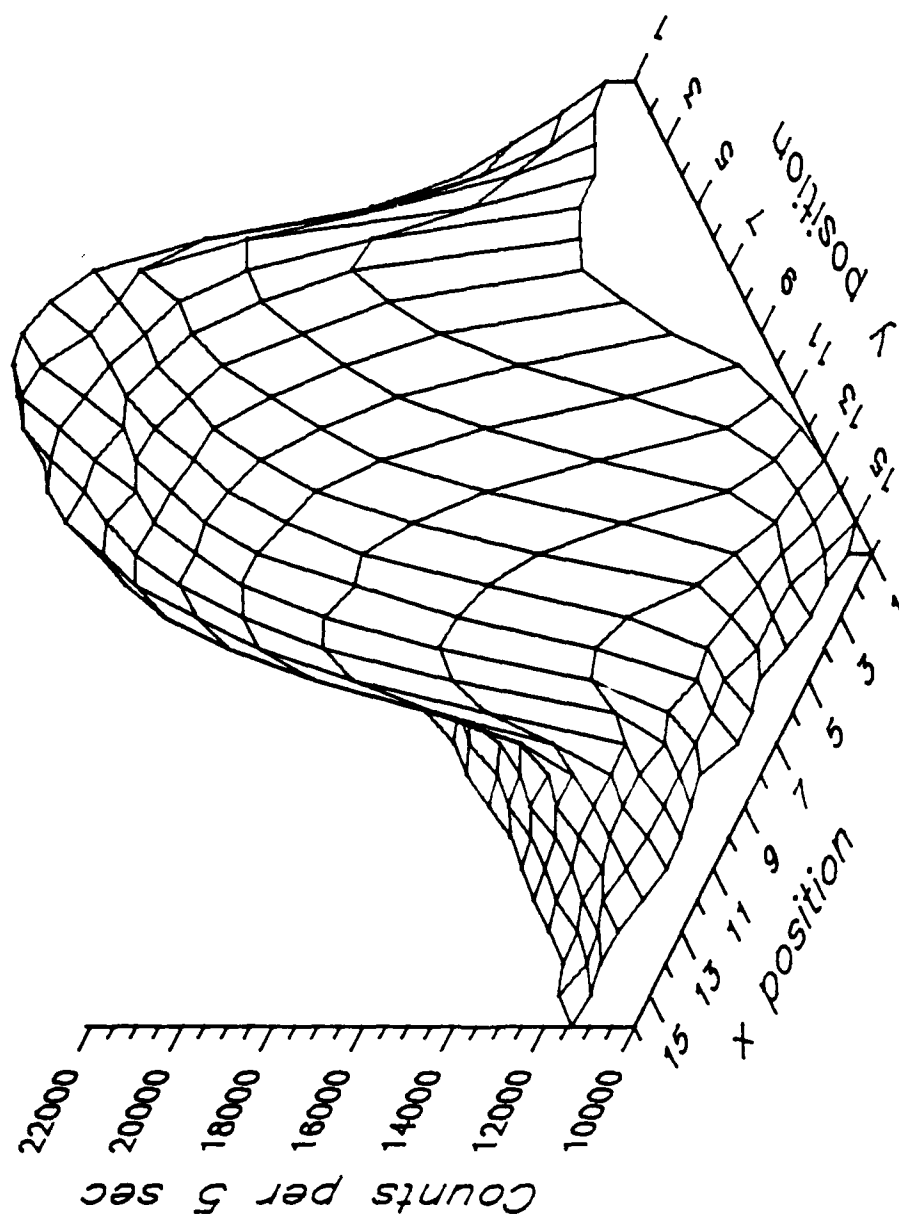


Figure VIII.31. Three-dimensional image diagram of the measured collimated detector response to a 200 kVp source beam filtered by Al for the TST mine at a depth of burial of 2.54 cm. The response is sampled at a 2.54 cm increment.

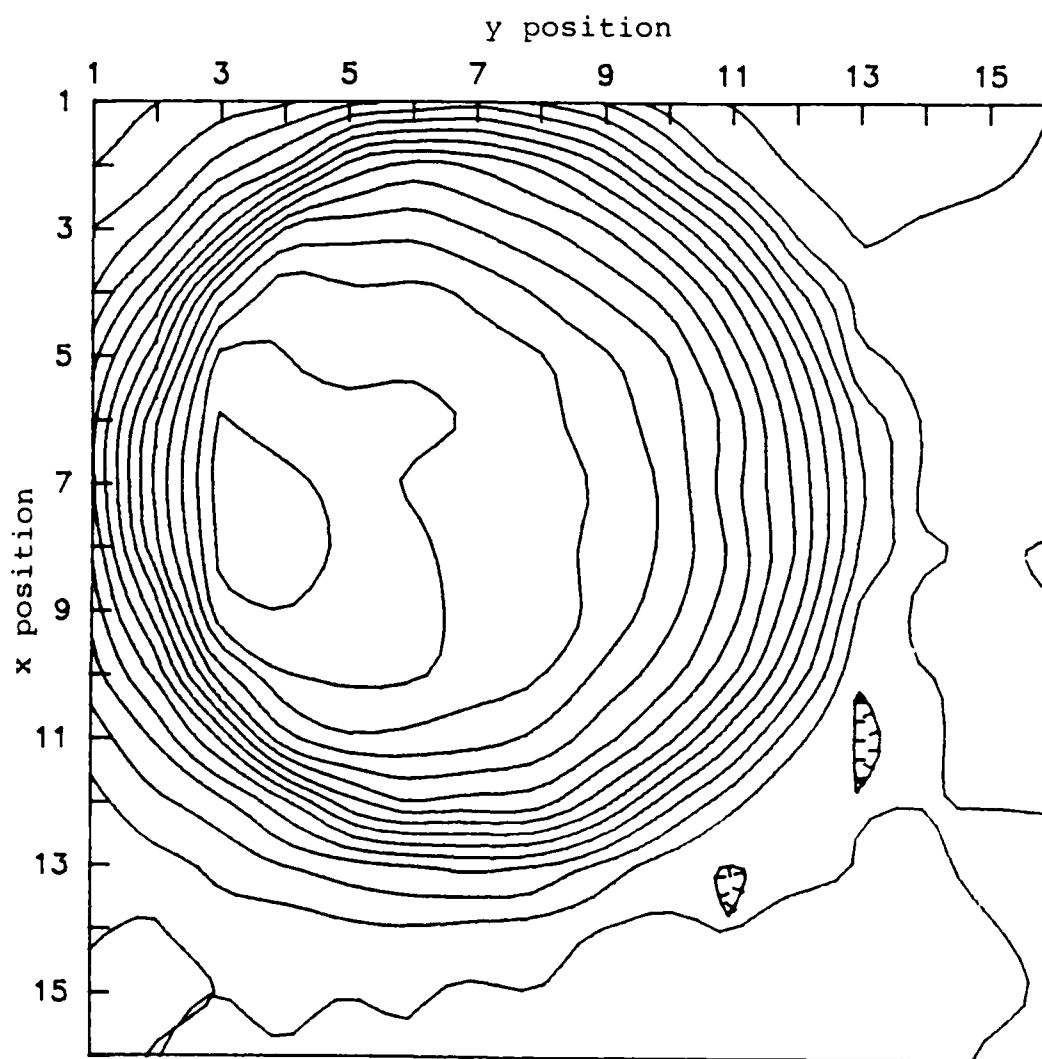


Figure VIII.32. Two-dimensional image diagram of the measured collimated detector response to a 200 kVp source beam filtered by Al for the TST mine at a depth of burial of 2.54 cm. The response is sampled at a 2.54 cm. increment.

y-direction is a result increasing numbers of photons crossing into soil after exiting the mine as the source beam moves closer to the wall nearest the detector. Figure VIII.33 shows the image formed for a mine at a depth of burial of 7.62 cm with the Bicron NaI(Tl) detector collimated to an acceptance angle of 18.1° . The mine to soil detector response ratio is approximately 1.2 at this depth. This is higher than the ratio achieved by the uncollimated detector at a depth of burial of 2.54 cm. Figures VIII.34 and VIII.35 show the response for a mine laid on the surface of the soil. As with the image of the surface-laid mine for the uncollimated detector, the three-dimensional image display has been rotated 180° to allow features that would otherwise be hidden to be seen. The considerably different image is a result of the multiple scatter requirement before detection. Just as in the uncollimated case, photons striking outside the mine wall furthest from the detector are shielded by the mine, producing a depression in the detector response associated with these beam intercepts. Photons striking inside the wall furthest from the detector initially show decreasing response as distance into the mine increases. The cause is photons traveling roughly parallel to the soil surface within the mine. Such photons increasingly escape the mine as the beam intercepts move towards the near wall and lateral paths exceed the distance to that wall. Upon escaping, they encounter primarily air, which only very rarely is able to scatter a photon to the

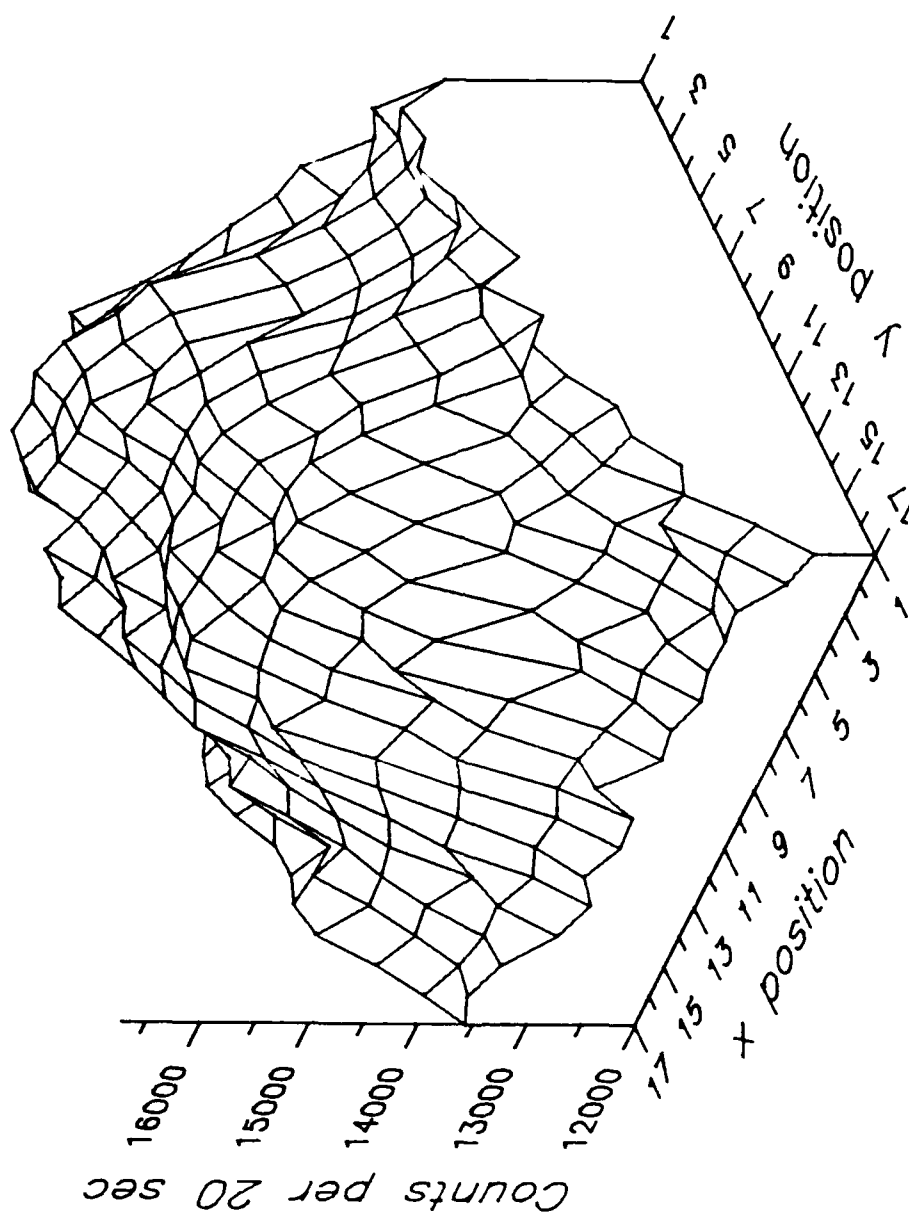


Figure VIII.33. Three-dimensional image diagram of the measured collimated detector response to a 200 kVp source beam filtered by Al for the TST mine at a depth of burial of 7.62 cm. The response is sampled at a 2.54 cm increment.

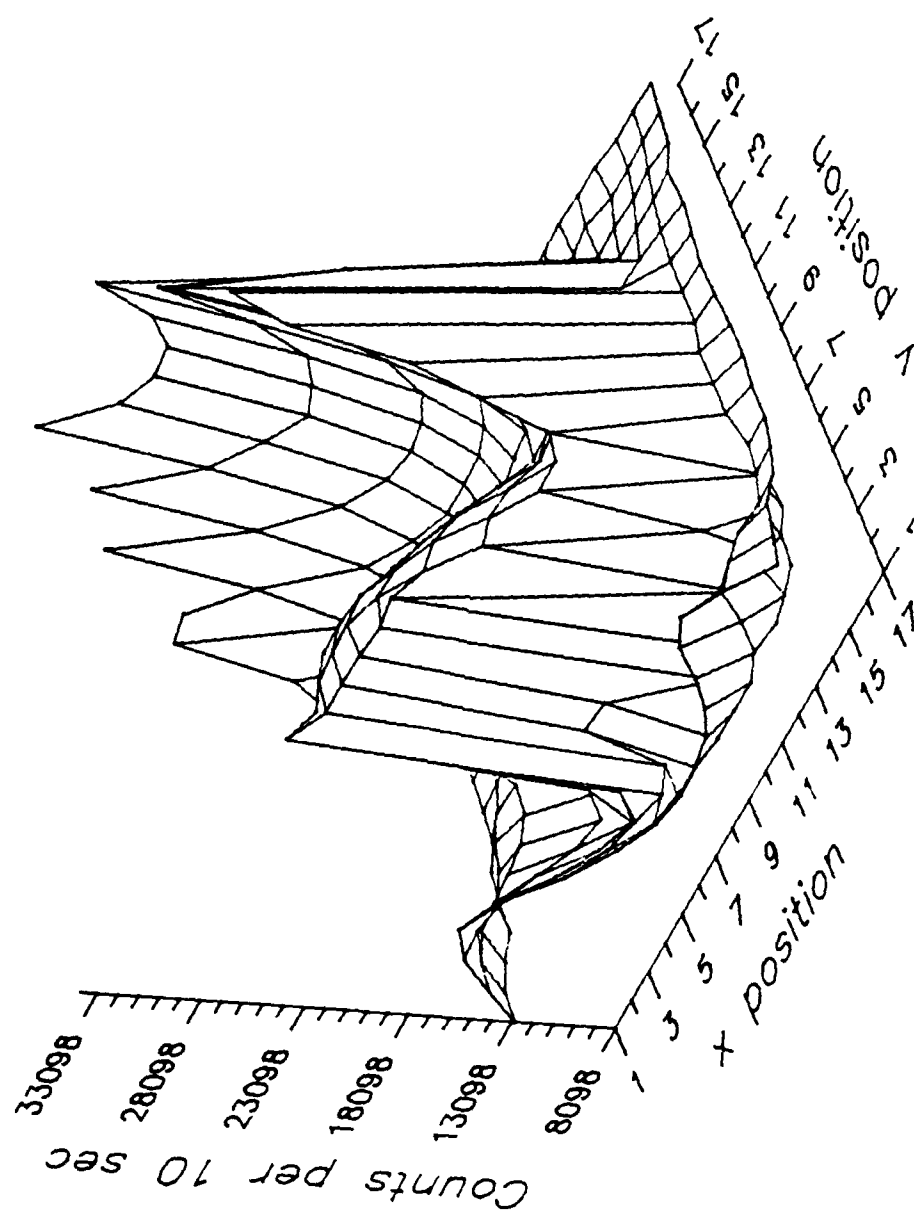


Figure VIII.34. Three-dimensional image diagram of the measured collimated detector response to a 200 kVp source beam filtered by Al for the TST mine laid on the soil surface. The response is sampled at a 2.54 cm increment.

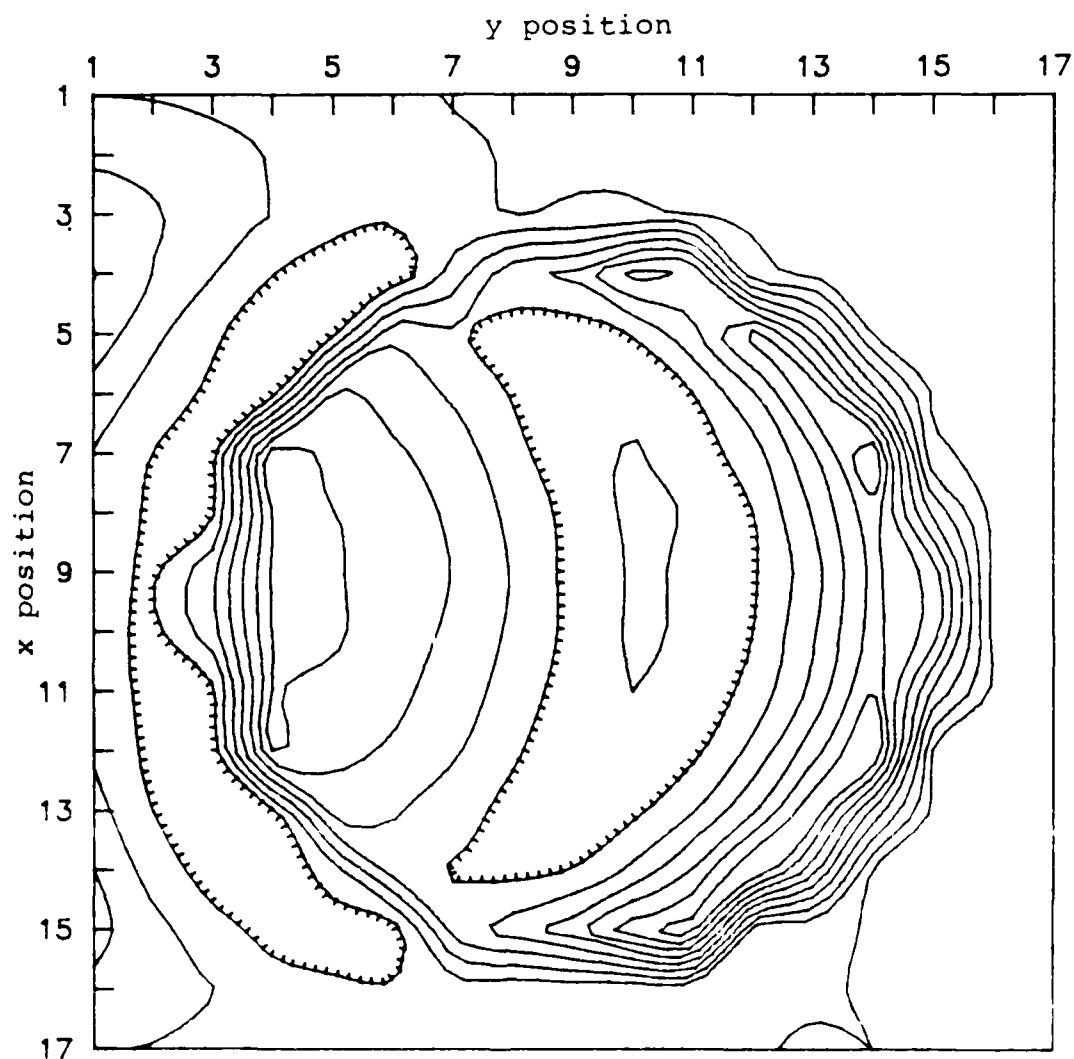


Figure VIII.35. Two-dimensional image diagram of the measured collimated detector response to a 200 kVp source beam filtered by Al for the TST mine laid on the soil surface. The response is sampled at a 2.54 cm increment.

detector. The increase in response at the edge of the mine nearest to the detector also is a result of the air.

Forward scattered photons from the mine which pass through the near wall are now able to traverse great distances in air before encountering soil. Many of these photons reach the region viewed directly by the collimated detector (28.1° in this case). Forward scattered photons in soil with a level surface, by contrast, are not nearly as likely to reach this position because of soil attenuation.

Figures VIII.36 through VIII.41 are images of the TST mine at a depth of burial of 2.54 cm with an array of stones, each approximately 1 cm^3 in volume, overlying a portion of the mine nearest to the detector. The series of images examines the effect of varying the source beam spectrum for the uncollimated detector, and then makes comparisons with the collimated detector. The spectrum used to produce the image in Figure VIII.36 has a beam energy of 100 kVp and is filtered by aluminum (see Figure F.4). As a result, it contains a sizeable low energy component, which is not efficient in penetrating the soil and scattering back through it. The low energy source photons are sensitive to the presence of the rock array, producing the deep response depressions in the image at the rock positions. The presence of the mine in the image is not obvious, although filtration is capable of improving the portion of the image not covered by rock to the point that detection is possible. The image in Figure VIII.37 is produced with a 150 kVp beam

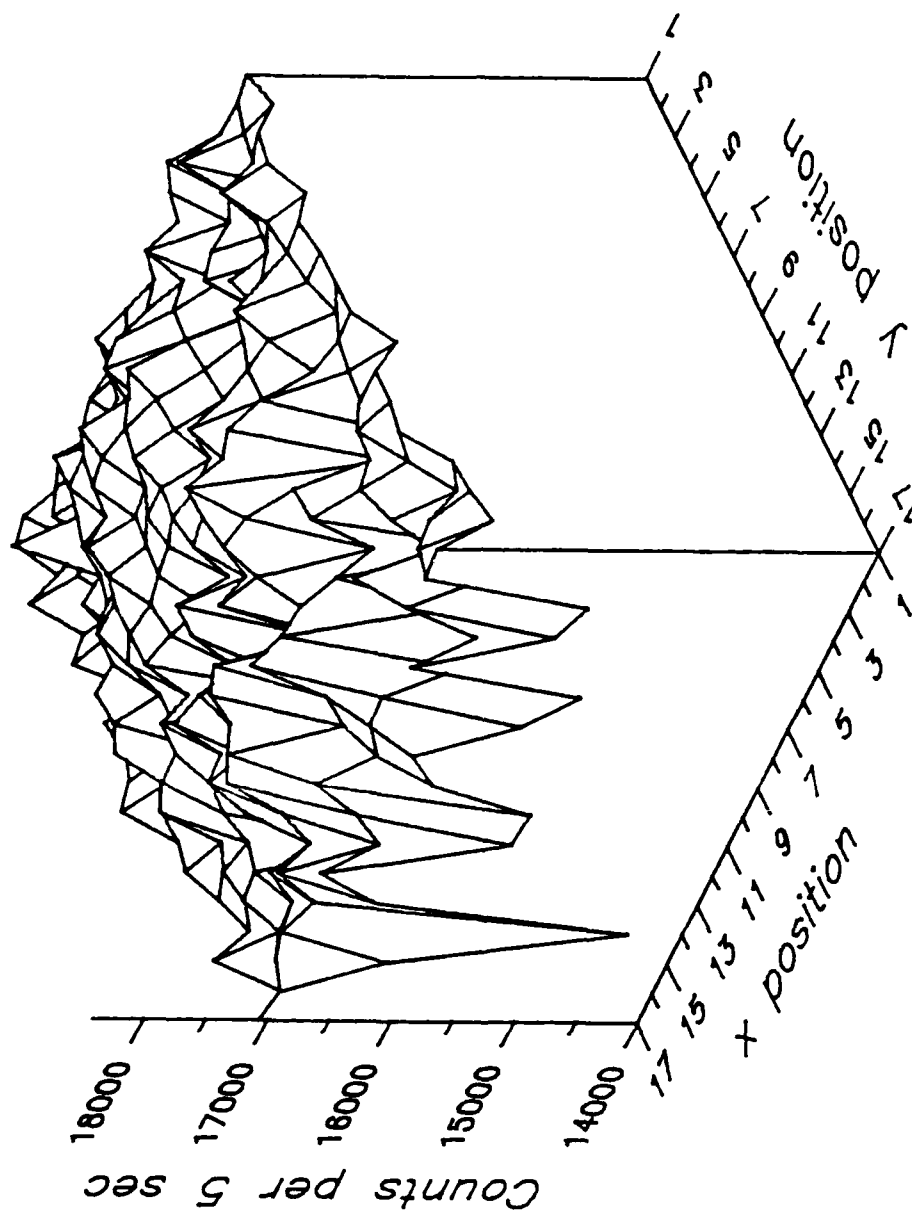


Figure VIII.36. Three-dimensional image diagram of the measured uncollimated detector response to a 100 kVp source beam filtered by Al for the TST mine at a depth of burial of 2.54 cm with overlying rock array. The response is sampled at a 2.54 cm increment.

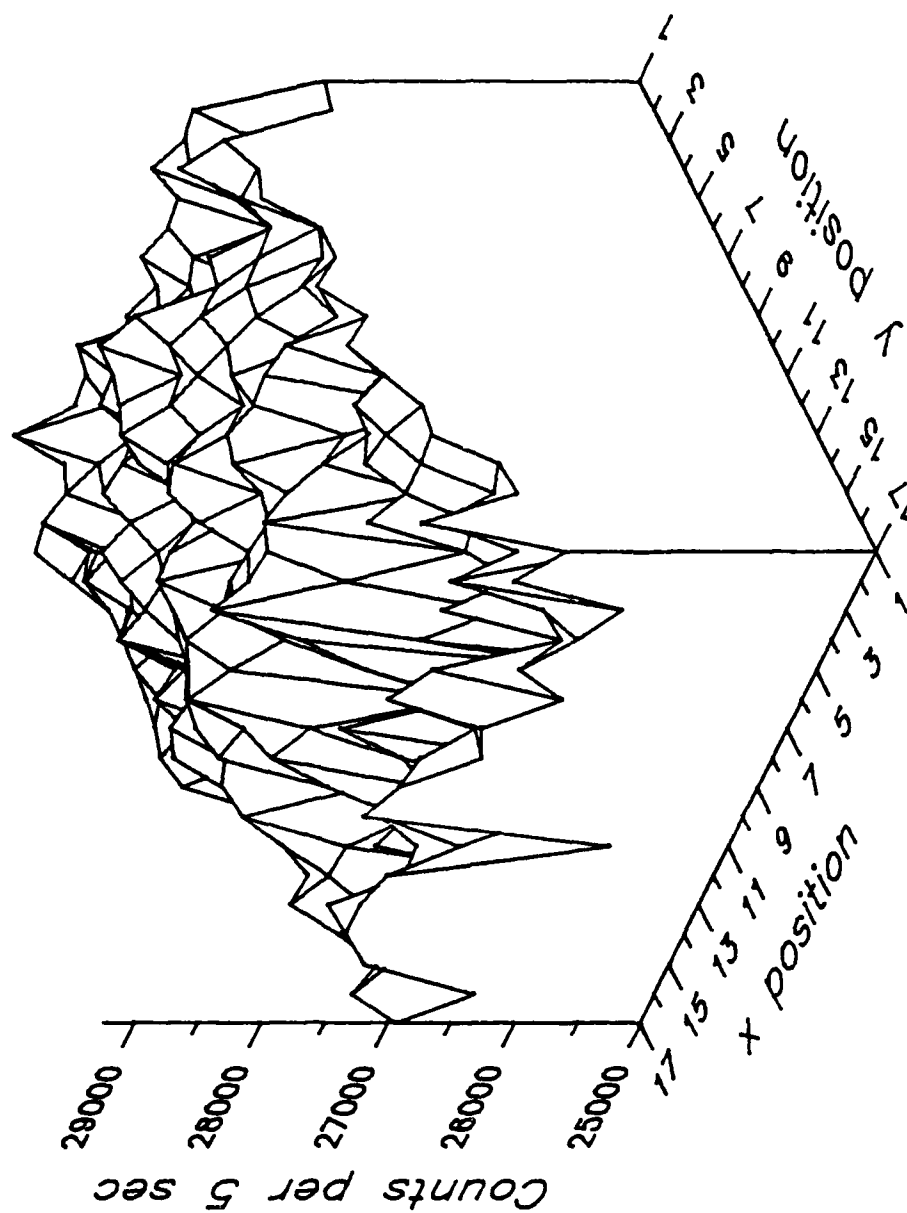


Figure VIII.37. Three-dimensional image diagram of the measured uncollimated detector response to a 150 kVp source beam filtered by Al for the TST mine at a depth of burial of 2.54 cm with overlying rock array. The response is sampled at a 2.54 cm increment.

also filtered by aluminum (see Figure F.5). While this spectrum still contains a significant low energy component, the presence of higher energy photons increases the response from the mine. The response depressions are still present. The images shown in Figure VIII.38 and VIII.39 are produced, respectively, with 150 and 200 kVp beams filtered by tin (see Figures F.6 and F.7). The tin filter hardens the spectra by preferentially removing the low energy components present before beam filtration. The 150 kVp spectrum more closely approximates the optimum energy for imaging in NSL soil and produces the higher mine to soil detector responses ratio near the center of the mine. Edge effects, not seen in the previous images in this series are present in both images. The edge effects at the wall of the mine nearest the detector are obscured by the presence of the rock array. The influence of the rock array is smallest in the 200 kVp image. Figures VIII.40 and VIII.41 complete this series of images by showing those produced by a collimated detector with an acceptance angle of 21.6° . The x-ray beams used are 150 and 200 kVp, both filtered by aluminum. The two fluence spectra are shown in Figures F.2 and F.3. The presence of the rock array is difficult to discern in either image. These images are vastly superior to those produced by the uncollimated detector. Between the two, the highest mine to soil detector response ratio is given by the 150 kVp spectrum. Spectral considerations play a much smaller role in the collimated detection technique. Because low energy

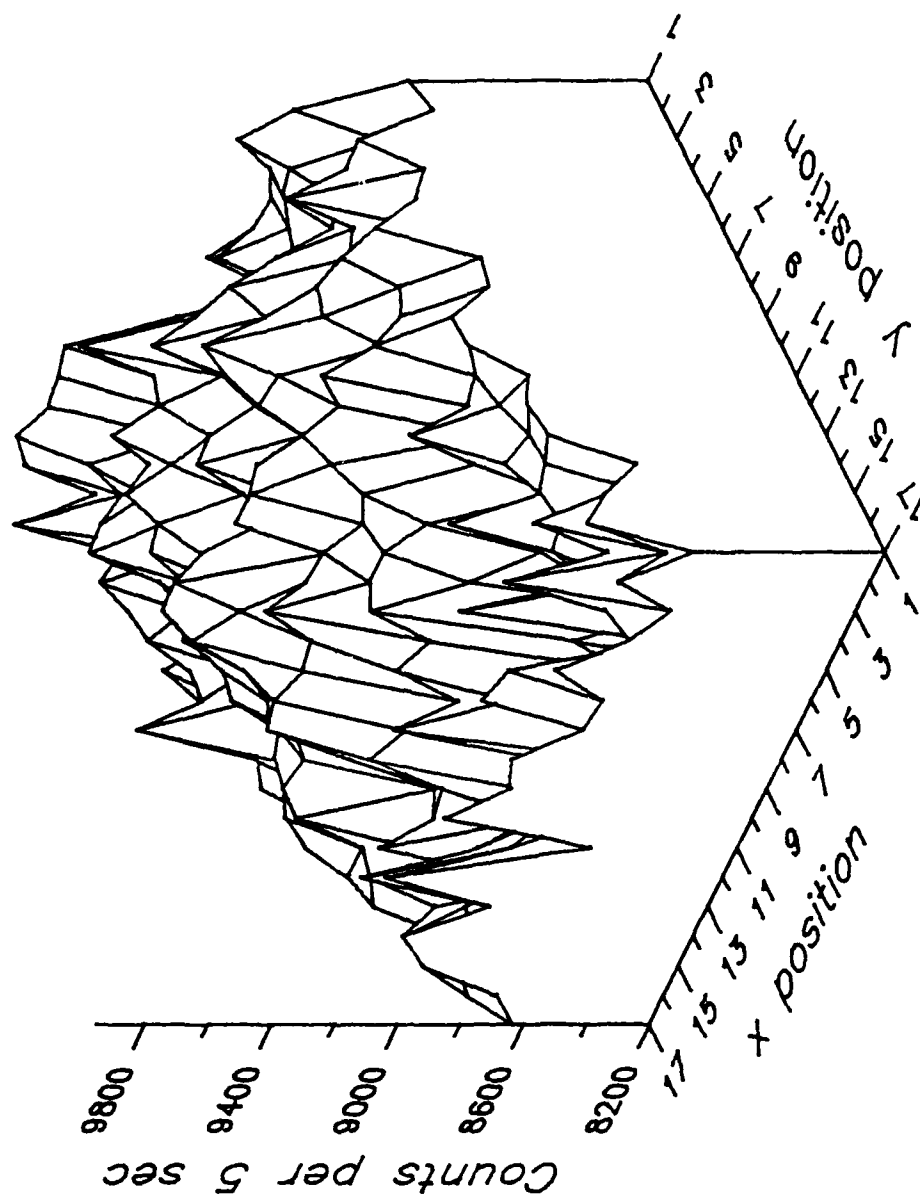


Figure VIII.38. Three-dimensional image diagram of the measured uncollimated detector response to a 150 kVp source beam filtered by $\frac{1}{2}$ in for the TST mine at a depth of burial of 2.54 cm with overlying rock array. The response is sampled at a 2.54 cm increment.

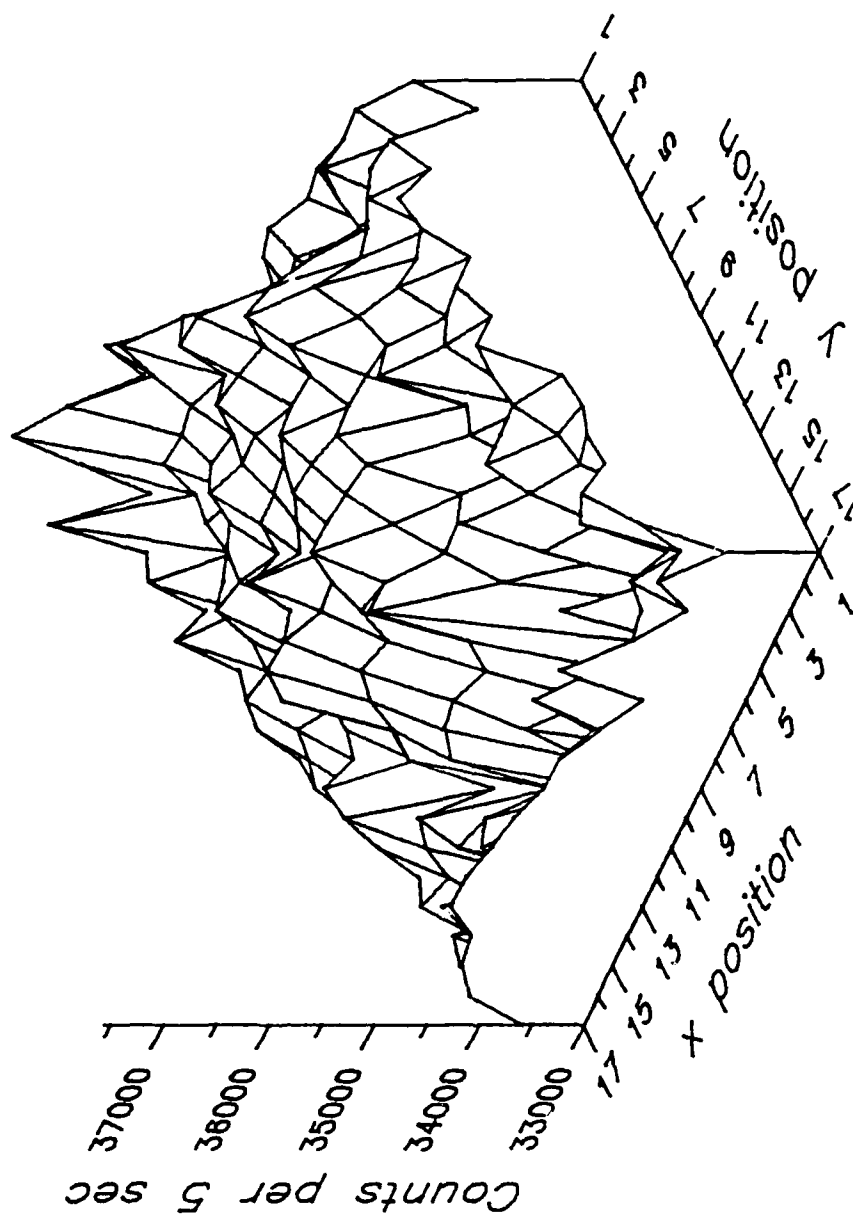


Figure VIII.39. Three-dimensional image diagram of the measured uncollimated detector response to a 200 kVp source beam filtered by Sn for the TST mine at a depth of burial of 2.54 cm with overlying rock array. The response is sampled at a 2.54 cm increment.

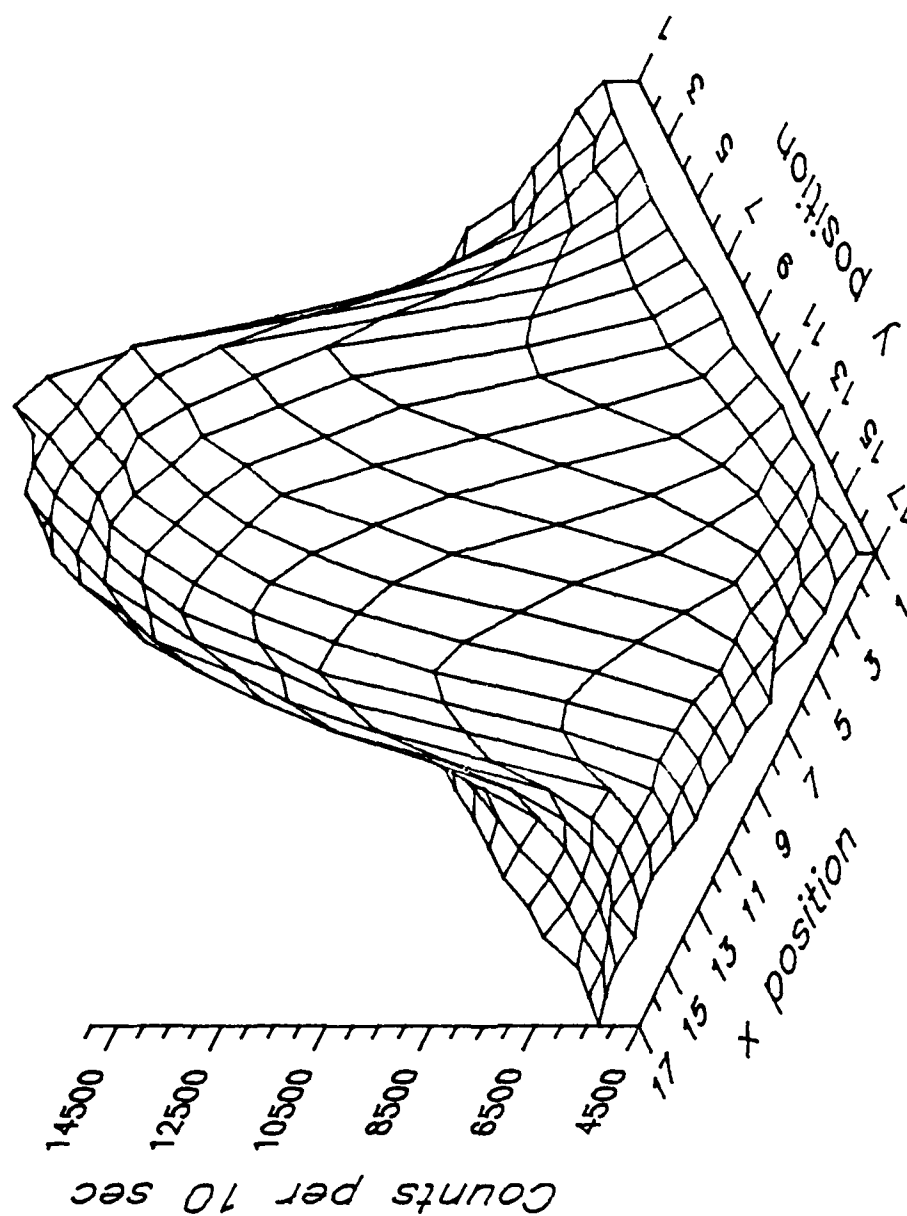


Figure VIII.40. Three-dimensional image diagram of the measured collimated detector response to a 150 kVp source beam filtered by Al for the TST mine at a depth of burial of 2.54 cm with overlying rock array. The response is sampled at a 2.54 cm increment.

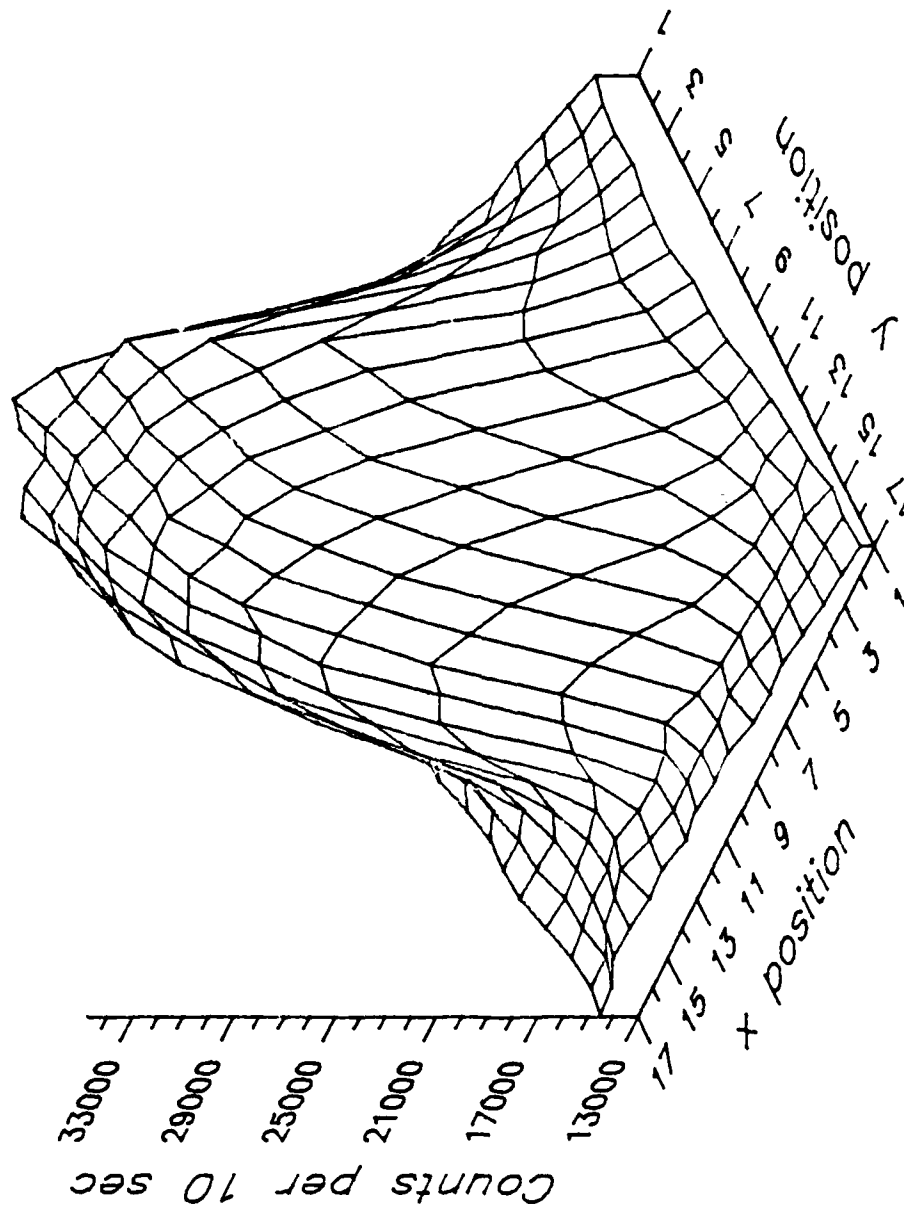


Figure VIII.41. Three-dimensional image diagram of the measured collimated detector response to a 200 kVp source beam filtered by Al for the TST mine at a depth of burial of 2.54 cm with overlying rock array. The response is sampled at a 2.54 cm increment.

photons are rarely able to perform the required multiple scattering through long paths in soil or explosive, the response at the detector is primarily due to the higher energy components. Since the detector operates on the difference in attenuation of the two materials, the lowest energy photons capable of reaching the detector in significant numbers provide the best detection mechanism. The higher energy photons, provide slightly less contrast between the two media, reducing the overall ratio in the 200 kVp case.

Figures VIII.42 through VIII.48 show the effect of irregularities in the soil surface on mine detection using the uncollimated and collimated detectors. Figure VIII.42 shows the positions with respect to the sampling array of six, 2.54 cm high mounds of soil protruding above a smooth soil surface. Buried beneath the soil at a depth of 2.54 cm and centered within the array is the TST mine. Figure VIII.43 shows an image produced for this configuration by a 200 kVp beam filtered by lead (Figure F.12) and used in conjunction with an uncollimated detector. The image is completely dominated by the effects of the soil surface irregularities. Figure VIII.44, which provides a two-dimensional representation of the image, shows more clearly that the image consists of minima and maxima of the same geometric pattern as the soil mounds. The positions of these image features with respect to the soil mound locations are determined by the average path lengths travelled by photons into soil

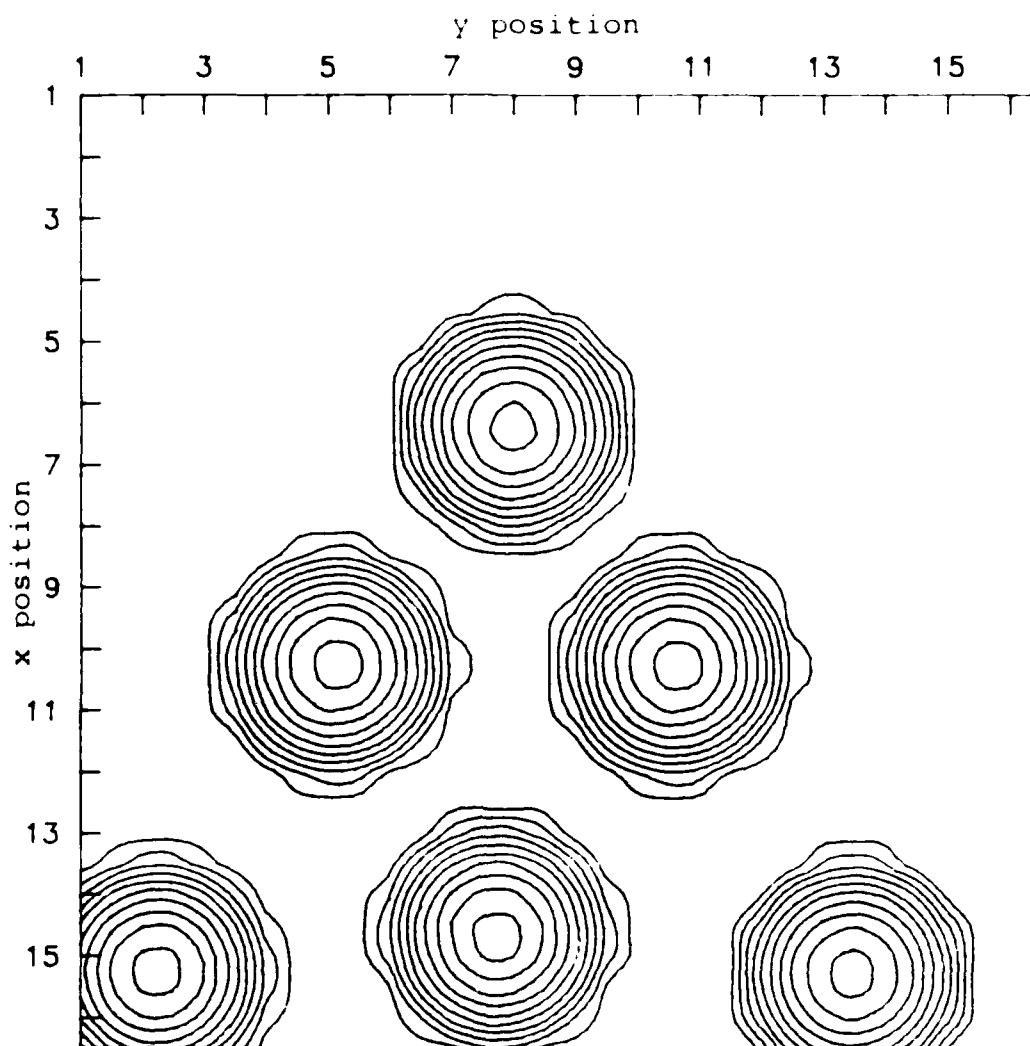


Figure VIII.42. Irregular soil surface used in measurements. The heights of the mounds above the soil surface are 2.54 cm. The irregular soil surface is shown on the same grid used in the images, which are displayed in subsequent figures.

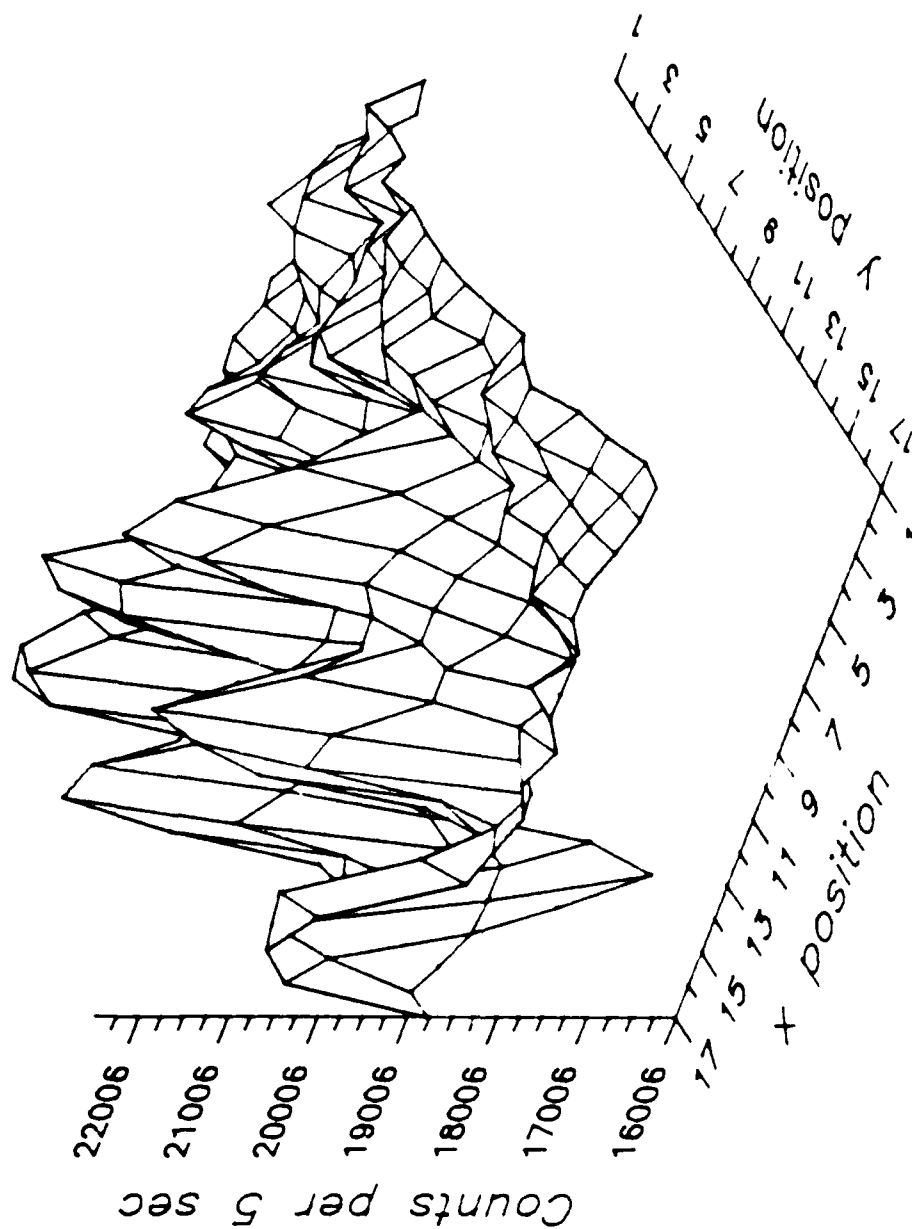


Figure VIII.43. Three-dimensional image diagram of the measured uncollimated detector response to a 200 kVp source beam filtered by Pb for the TST mine at a depth of burial of 2.54 cm with irregular soil surface. The response is sampled at a 2.54 cm increment.

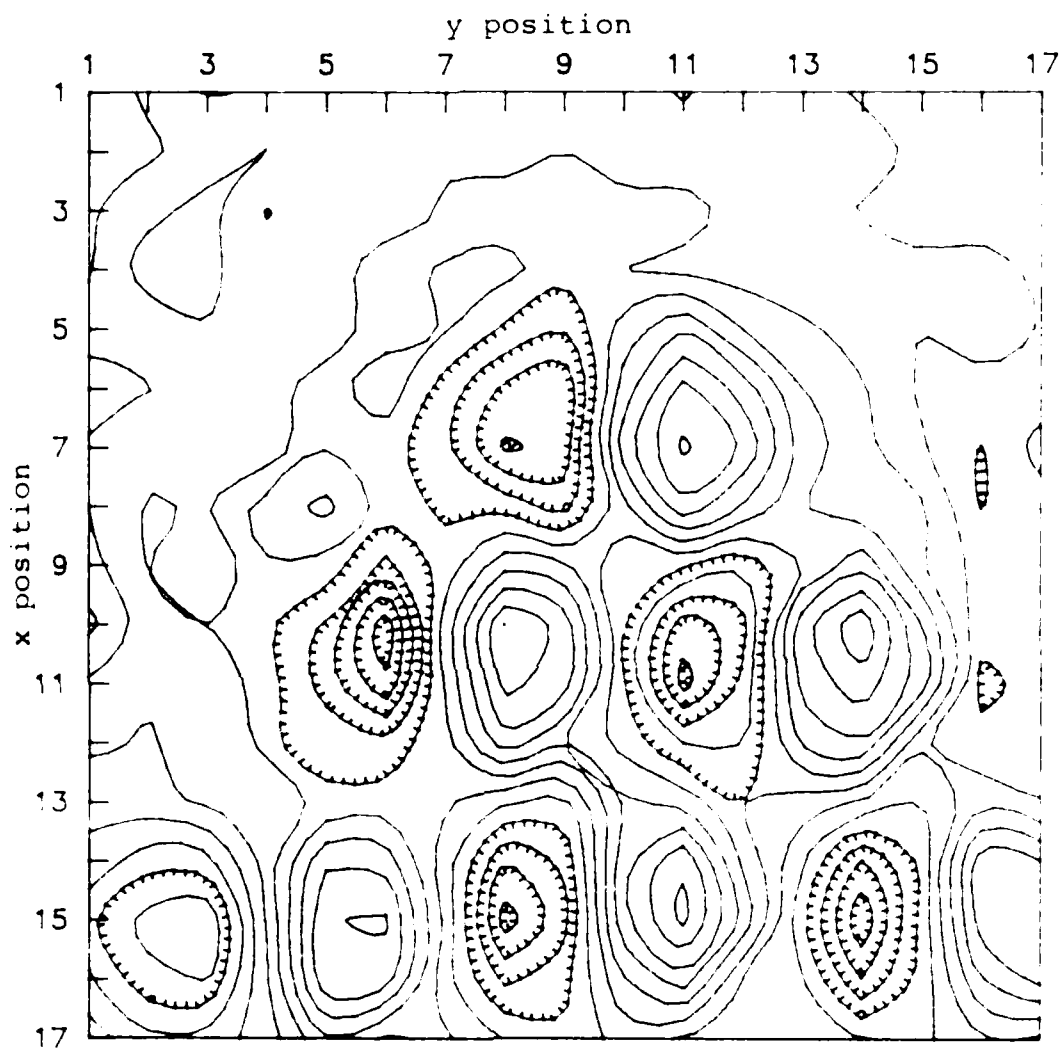


Figure VIII.44. Two-dimensional image diagram of the measured uncollimated detector response to a 200 kVp source beam filtered by Pb for the TST mine at a depth of burial of 2.54 cm with irregular soil surface. The response is sampled at a 2.54 cm increment.

before scattering. Scattering positions, which require the longest paths through soil to reach the detector produce the minima. Figures VIII.45 through VIII.47 show the use of a collimated detector with acceptance angle of 21.6° for three source beam energies filtered by aluminum. Figure VIII.45 is for a 100 kVp beam; Figure VIII.46 for a 150 kVp beam; and Figure VIII.47 for a 200 kVp beam. Spectra for these images are given by Figures F.1 through F.3. While each of these images produced by the collimated detector shows the influence of the irregular soil surface, there is no question as to the presence of the buried mine. Figure VIII.48 provides a two-dimensional image for the 200 kVp case with collimated detector to show that the distortions in the image shape of the mine are not large.

Figure VIII.49 shows the image response of a disk of wood buried flush to the soil surface as produced by a 100 kVp beam filtered by lead (Figure F.8) and an uncollimated detector. The edge effect at the side of the disk furthest from the detector is produced by the relative transparency of the low density wood to photons. Figure VIII.50 shows the response of the collimated detector with acceptance angle of 18.1 degrees to the same wood disk using the source spectrum shown in Figure F.3. The response is similar to that of a mine buried at approximately 7.5 cm. Figures VIII.51 and VIII.52 show the uncollimated and collimated images of an iron disk of radius of 5 cm and height of 2 cm buried flush to the soil surface. The same set of source

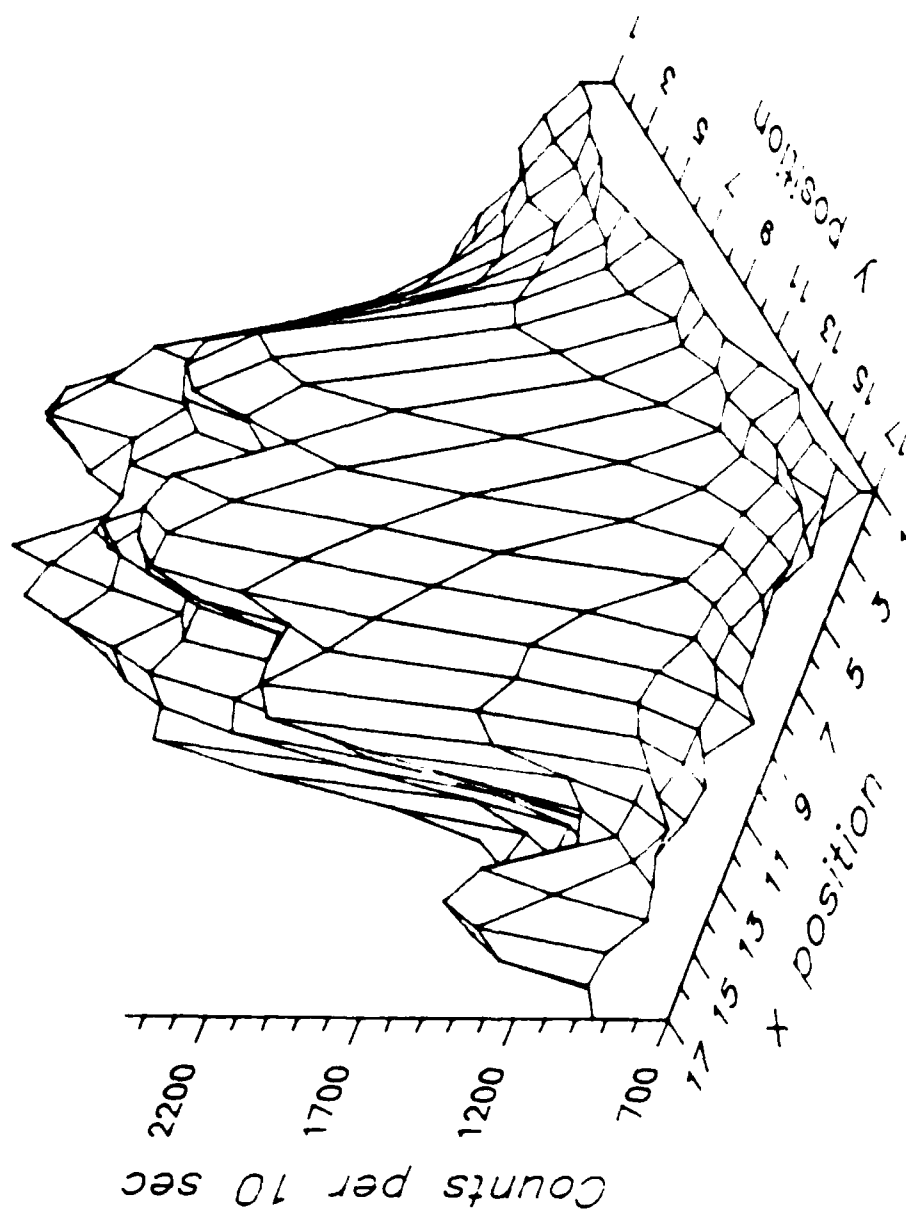


Figure VIII.45. Three-dimensional image diagram of the measured collimated detector response to a 100 kVp source beam filtered by Al for the TST mine at a depth of burial of 2.54 cm with irregular soil surface. The response is sampled at a 2.54 cm increment.

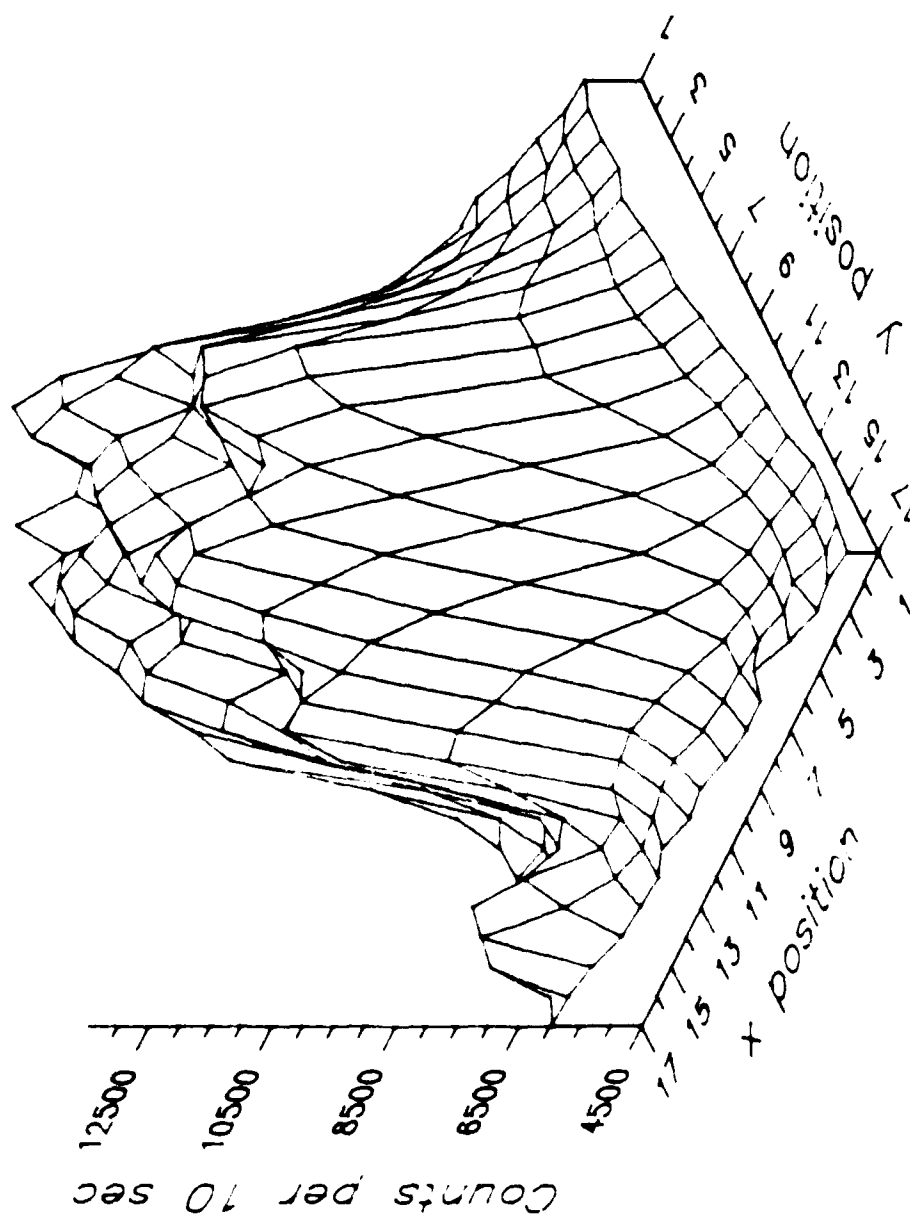


Figure VIII.46. Three-dimensional image diagram of the measured collimated detector response to a 150 kvp source beam filtered by Al for the TST mine at a depth of burial of 2.54 cm with irregular soil surface. The response is sampled at a 2.54 cm increment.

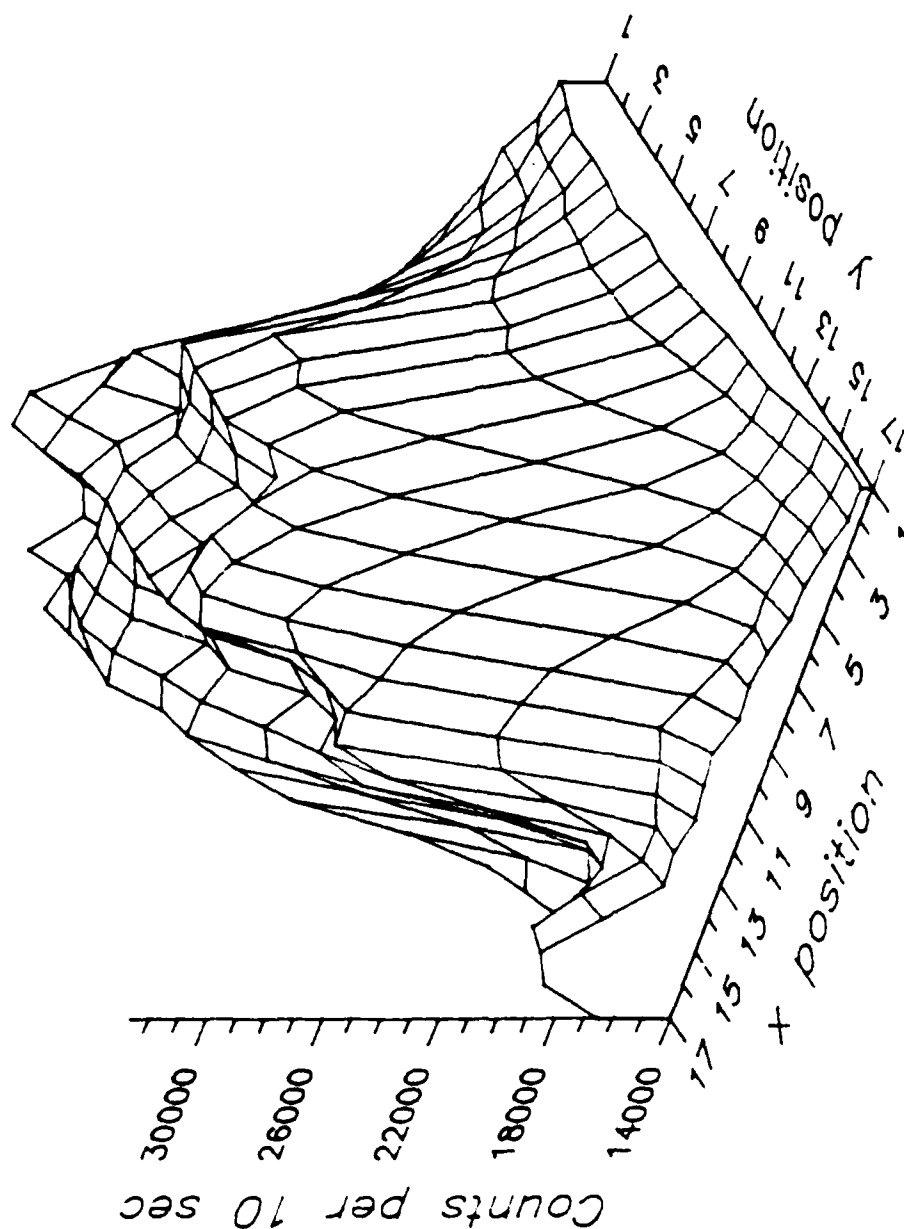


Figure VIII.47. Three-dimensional image diagram of the measured collimated detector response to a 200 kVp source beam filtered by Al for the TST mine at a depth of burial of 2.54 cm with irregular soil surface. The response is sampled at a 2.54 cm increment.

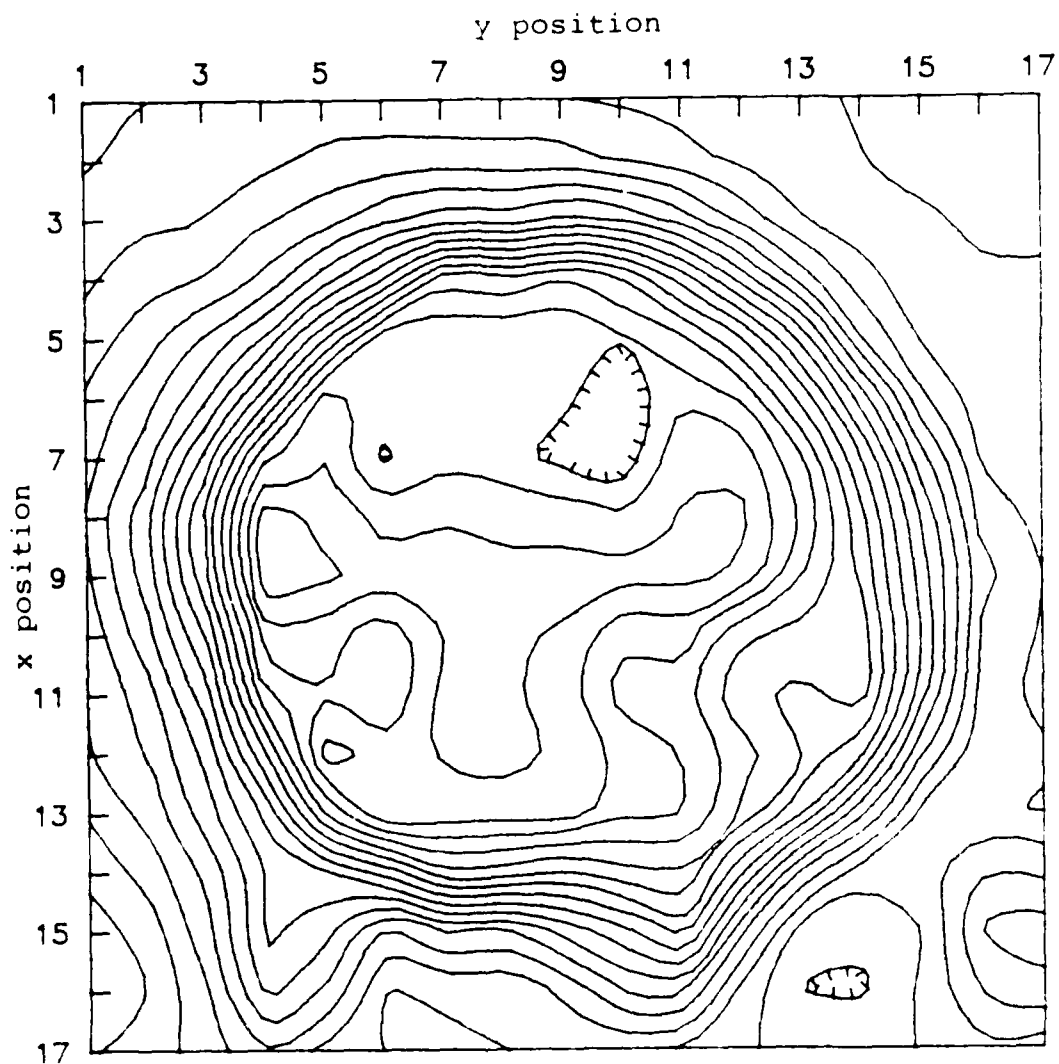


Figure VIII.48. Two-dimensional image diagram of the measured collimated detector response to a 200 kVp source beam filtered by Al for the TST mine at a depth of burial of 2.54 cm with irregular soil surface. The response is sampled at a 2.54 cm increment.

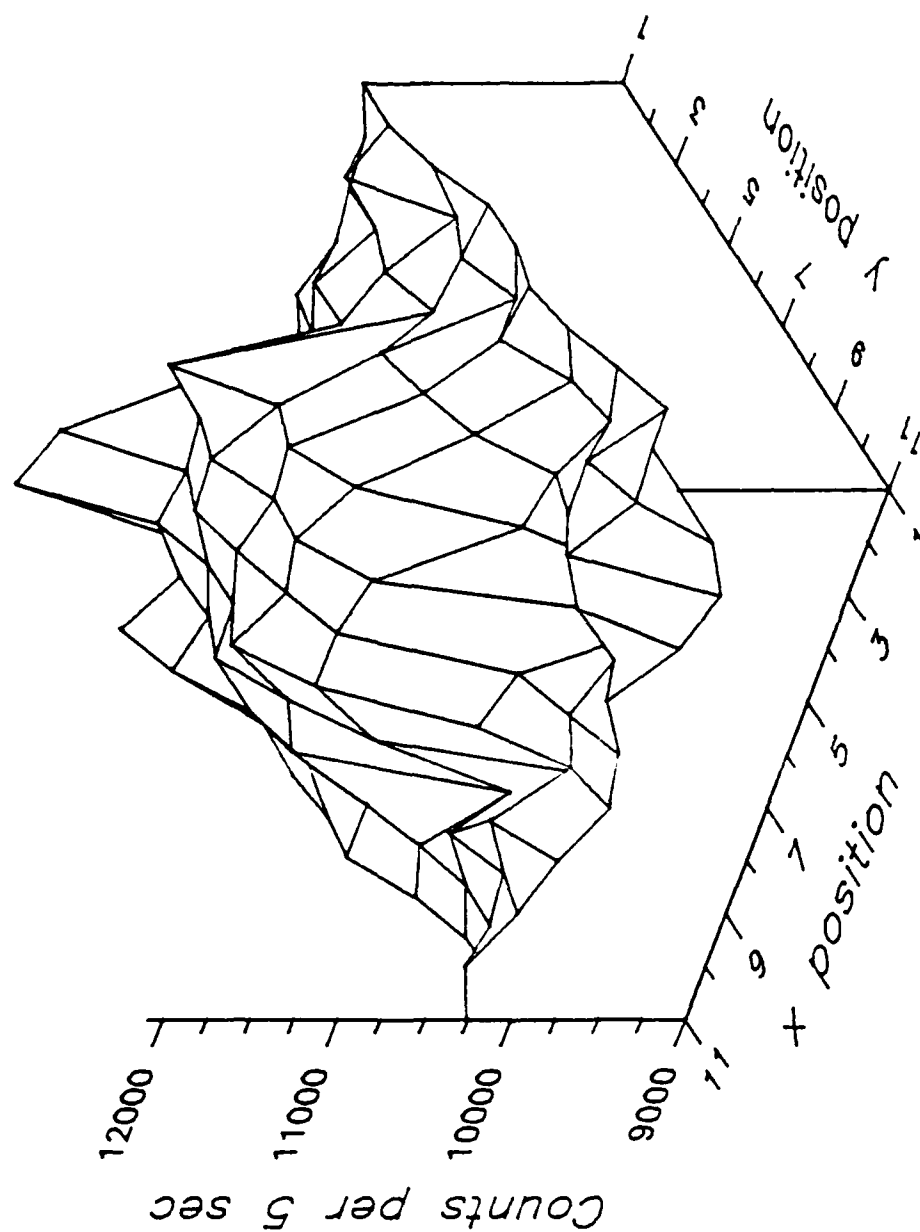


Figure VIII.49. Three-dimensional image diagram of the measured uncollimated detector response to a 100 kVp source beam filtered by Pb for a wood disk buried flush to the soil surface. The response is sampled at a 2.54 cm increment. The disk is 8.57 cm in radius and 1.87 cm thick.

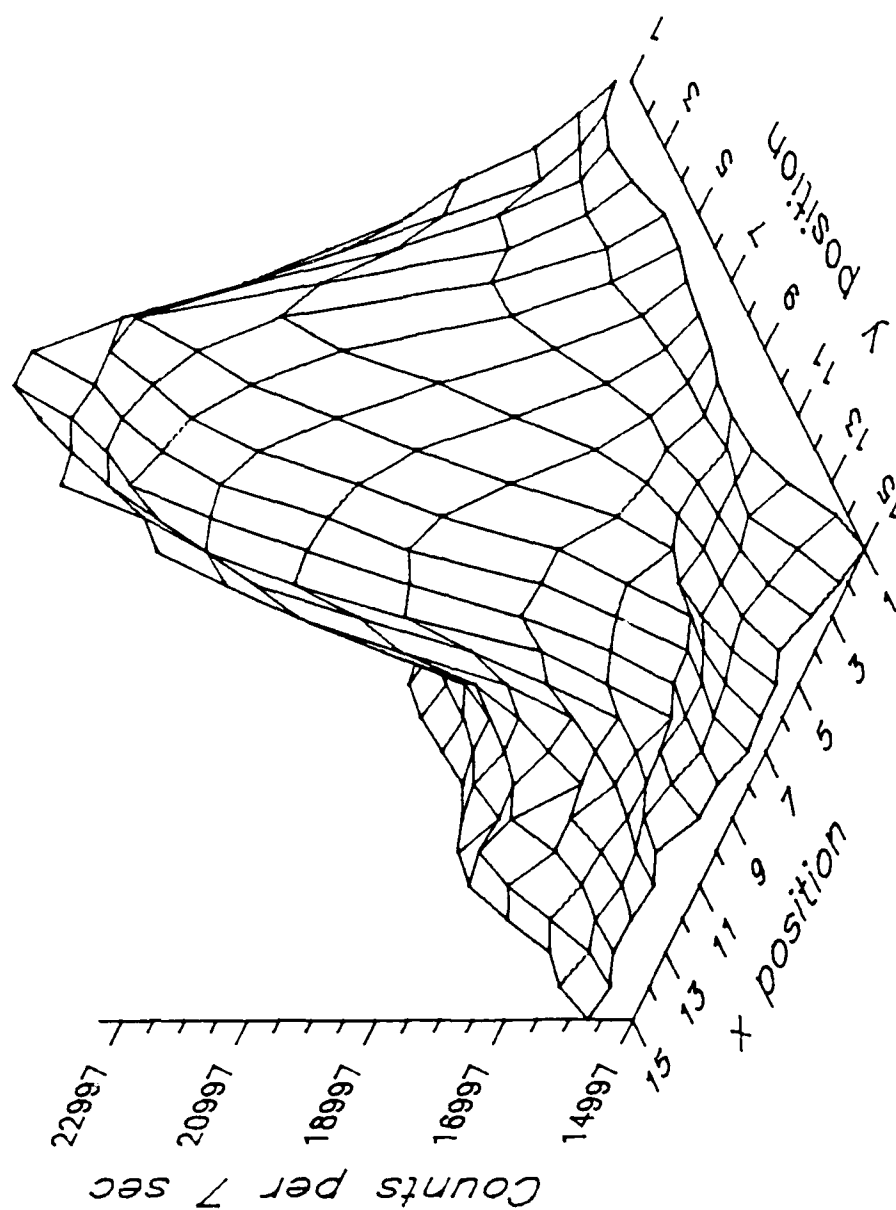


Figure VIII.50. Three-dimensional image diagram of the measured collimated detector response to a 200 kVp source beam filtered by Al for a wood disk buried flush to the soil surface. The response is sampled at a 1.905 cm increment. The disk is 8.57 cm in radius and 1.87 cm thick.

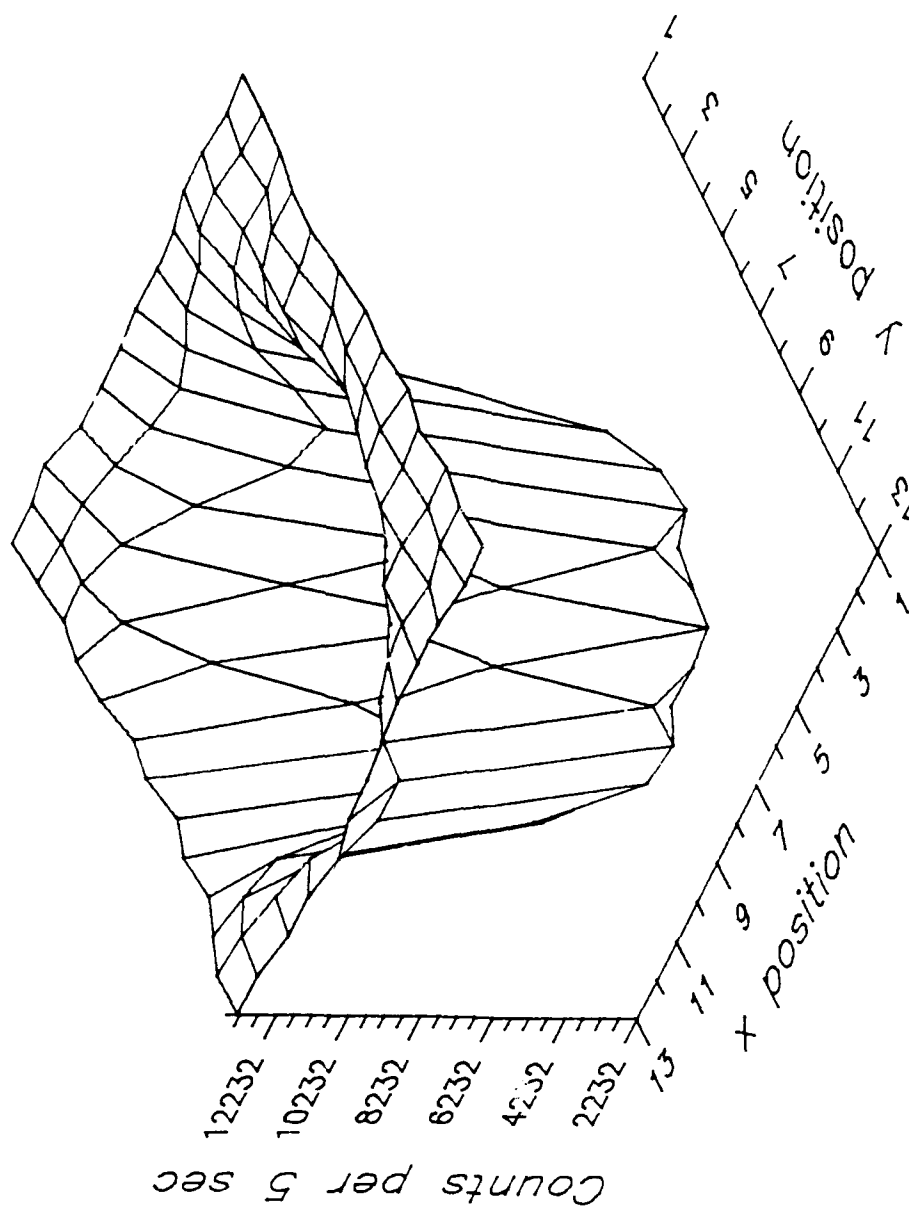


Figure VIII.51. Three-dimensional image diagram of the measured uncollimated detector response to a 100 kVp source beam filtered by Pb for a steel disk buried flush to the soil surface. The response is sampled at 1.27 cm increment. The disk is 5 cm in radius and 2 cm thick.

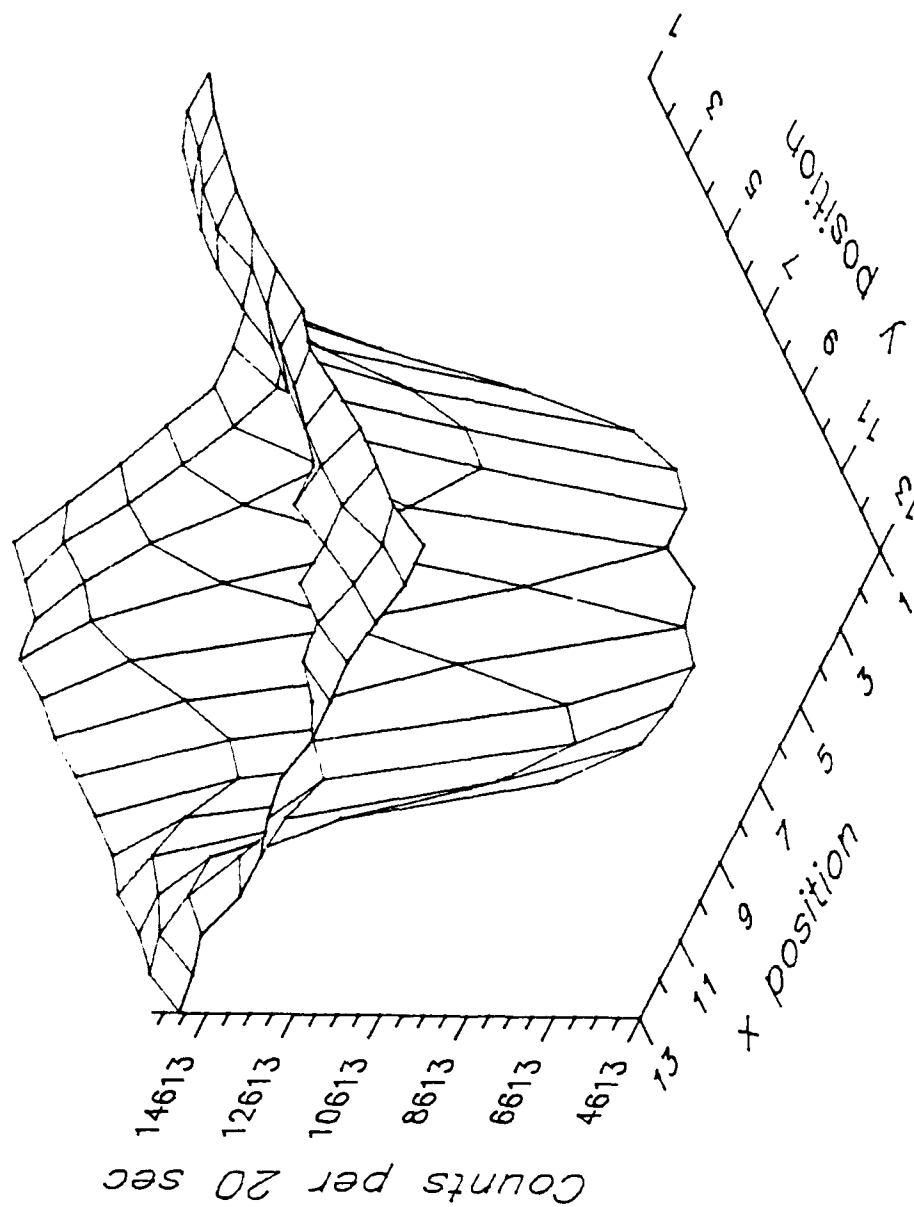


Figure VIII.52. Three-dimensional image diagram of the measured collimated detector response to a 200 kVp source beam filtered by Al for a steel disk buried flush to the soil surface. The response is sampled at a 1.27 cm increment. The disk is 5 cm in radius and 2 cm thick.

spectra (Figures F.8 and F.3) is employed in these and the remaining images discussed in this section. The strong depression in the backscattered response over the iron disk is due to the high probability of photoelectric absorption compared to that of soil. Figure VIII.53 and VIII.54 show the responses of the two detectors to a thin plastic container of water buried flush to the soil. The container has a radius of 5 cm and a depth of 7 cm. Except for its size in the x-y plane, the image resembles that of a mine. Figure VIII.55 shows the collimated detector response to a hole 15 cm in radius and 15 cm deep which has been refilled with soil of lower density than that which surrounds it. The depression in the response at the center of the image is a result of the density differences. Photons striking the higher density soil around the edges of the hole interact relatively near the surface. Many travel long lateral distances through the lower density soil before scattering to the detector. Photons striking the low density soil penetrate deeper into the soil. After scattering and travelling laterally through soil, many reach the high density region before scattering towards the detector. Because of their relatively greater depth in the soil, fewer photons are able to reach the detector. The low response at the edge of the hole nearest the detector is caused by this same effect. The result is a partial ring of high response. When viewed by a detector consisting of two panels, the image becomes a region of enhanced response with a central

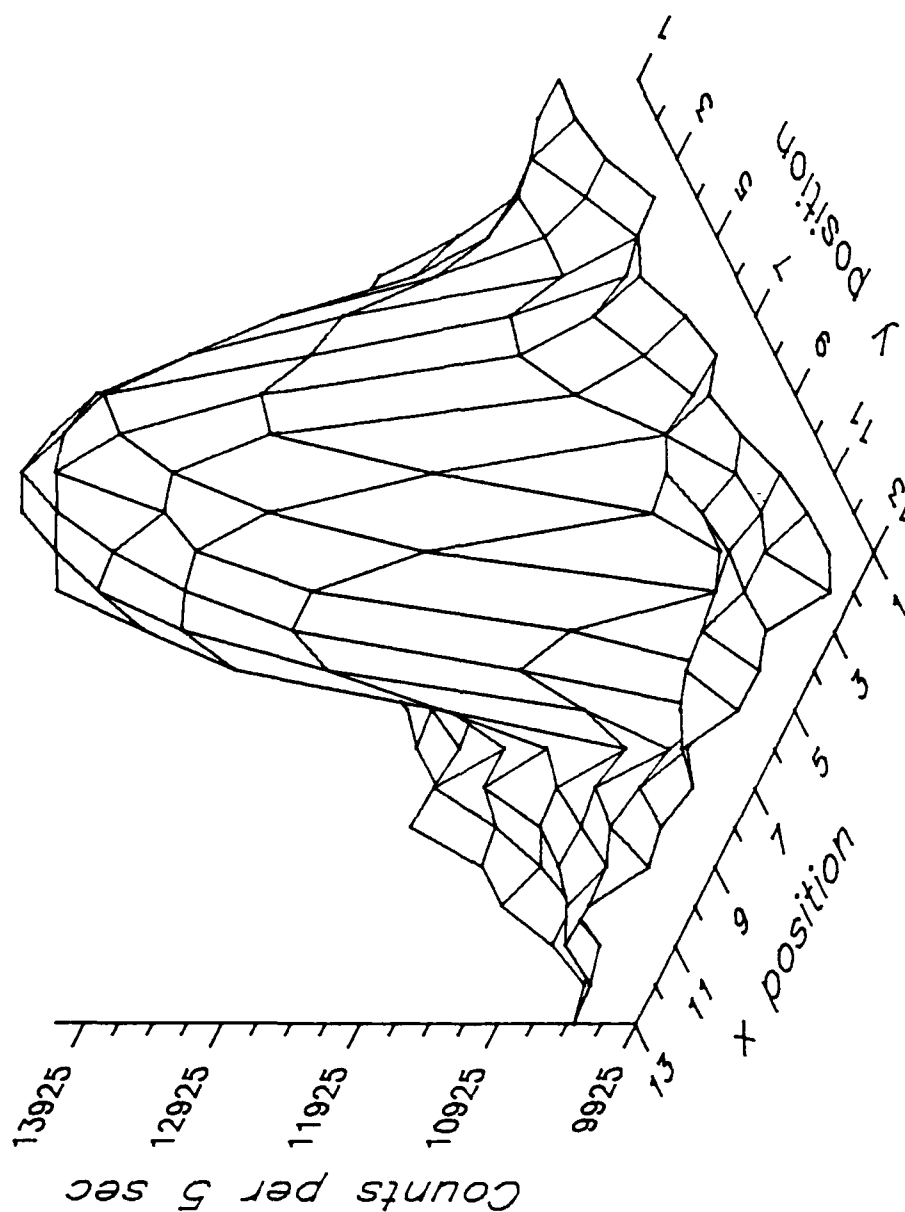


Figure VIII.53. Three-dimensional image diagram of the measured uncollimated detector response to a 100 kVp source beam filtered by Pb for water contained in a thin plastic container buried flush to the soil surface. The response is sampled at a 1.27 cm increment. The container is 5 cm in radius and 7 cm deep.

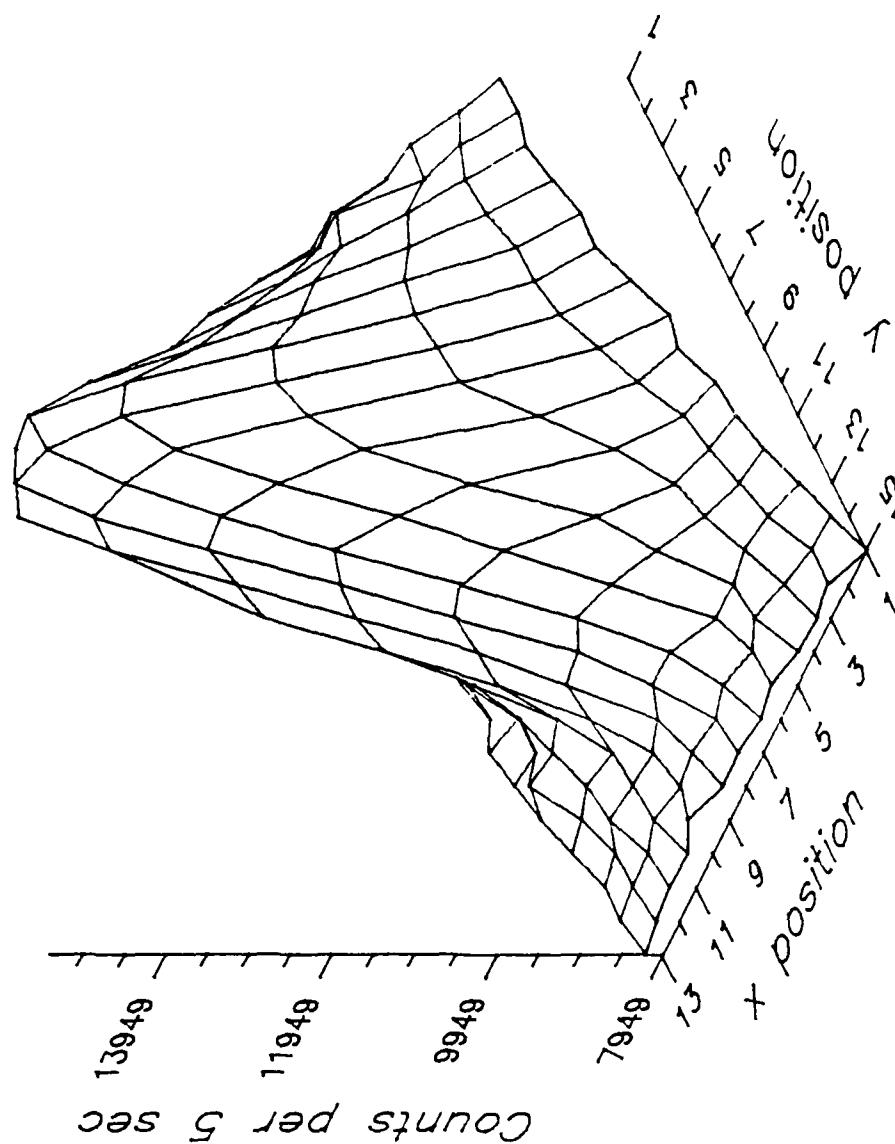


Figure VIII.54. Three-dimensional image diagram of the measured collimated detector response to a 200 kVp source beam filtered by Al for water contained in a thin plastic container buried flush to the soil surface. The response is sampled at a 1.27 cm increment. The container is 5 cm in radius and 7 cm deep.

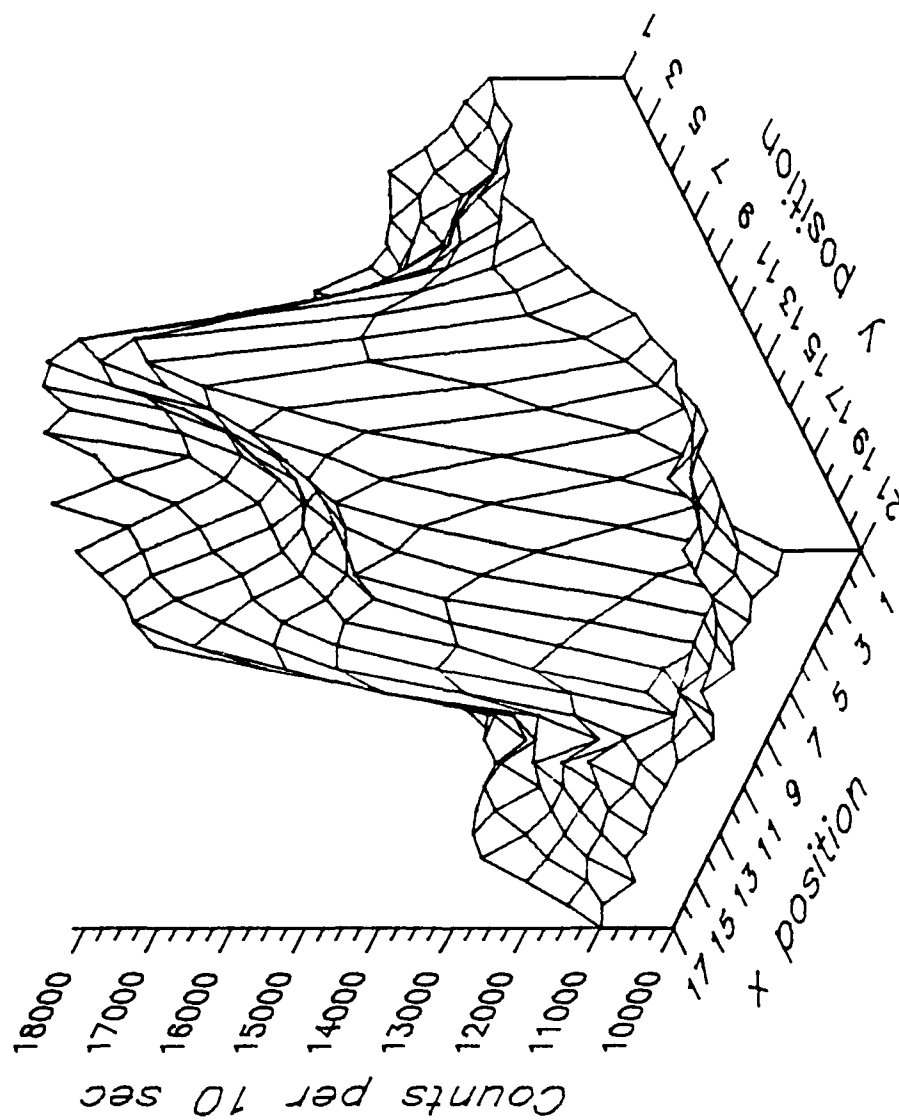


Figure VIII.55. Three-dimensional image diagram of the measured collimated detector response to a 200 kVp source beam filtered by Al for a hole filled with loose soil. The response is sampled at a 2.54 cm increment. The hole is 15 cm in radius and 15 cm deep.

relative minimum. This image is very different from that of a buried mine, but similar to that of a surface laid mine when viewed by a detector consisting of two panels. Each of these images for inhomogeneities are in accordance with the predictions made by calculations. The Monte Carlo calculated water and iron images for a large area detector resemble these measurements with the small NaI(Tl) crystal (see Figure VIII.20 for water and VIII.21 for iron). The mine-like response to a region of low density soil by the collimated detector is predicted in calculations made in Chapter VII in the discussion of depth of burial. Based upon these results, the false alarm shortcomings of x-ray backscatter radiation detectors constructed in the past (discussed in Chapter II) are understandable. The capability to produce images can do much to eliminate many false alarms on the basis of shape and size.

Dual Energy Subtraction

The dual energy subtraction technique uses source beams of two energies with backscatter imaging to correct for irregularities in materials overlying an object or region of interest (Jacobs et al., 1979). Subtracting the lower energy image, multiplied by an appropriate factor, from the higher removes information produced from backscatter from the upper layers of the material. Application of this technique to the mine detection problem is investigated as a possible means of removing the effects of surface irregularities and inhomogeneities in the soil above a buried mine.

The technique is not applicable to cases where the mine is positioned above the surface or buried flush to the top of the soil. In these cases, there are no irregularities or inhomogeneities other than the mine itself. Because the addition of a second energy beam greatly complicates the mine detection system and increases power requirements, principally by shortening the time the source beam intercepts a position on the mine at constant vehicle speed and by increasing the noise in the subtracted image, it is not desirable to use the technique in cases in which, despite the presence of irregularities or inhomogeneities, the signal from the mine is large enough to provide unmistakable detection. Examples of this situation for buried mines have been illustrated for the collimated detector with both inhomogeneities (Figures VIII.40 and VIII.41) and surface irregularities (Figures VIII.45 through VIII.48) for mines buried at 2.54 cm. For the uncollimated detector, which produces a small mine to soil ratio even at relatively shallow depths of burial, the technique would appear applicable. Eventually, even with the collimated detector, a depth will be reached where the mine to soil ratio is too small to allow unmistakable recognition due to irregularities or inhomogeneities.

Unfortunately, the dual energy technique is incompatible with the backscatter mine detection irradiation geometry. The problem lies with the positioning of the detector with respect to the source. As was described in

Chapter VII, the central minimum in the uncollimated mine to soil ratio and the very basis of the collimated detector, require significant separations of the detector from the source beam. Figure VIII.56 illustrates the problem for the dual energy technique arising from such separations. In the upper portion of the figure, typical scattering paths for a low and high energy photon are shown. The high energy photon penetrates further into the soil before scattering, resulting in a path to the detector quite different than that of the low energy photon. Extending this simple diagram to a polyenergetic beam of photons, the low energy beam and the low energy components of the high energy beam can be made to cancel by appropriate choice of a multiplying factor, but the high energy components of the high energy beam will still display the effects of the surface irregularities or inhomogeneities. A comparison of Figure VIII.57 and Figure VIII.44 shows the problem. Each figure shows the result of an imaging experiment with the irregular soil surface shown in Figure VIII.42. The image in Figure VIII.57 is from a 100 kVp source beam (Figure F.8); Figure VIII.44 from a 200 kVp source beam (Figure F.12). The peaks and valleys in the two images occur in different positions. Subtraction of the two images to remove the effect of the irregular soil surface is not possible. The lower portion of Figure VIII.56 displays an analogous problem with the collimated detector. Typical scattering paths of low and high energy photons which reach the detector are shown. The

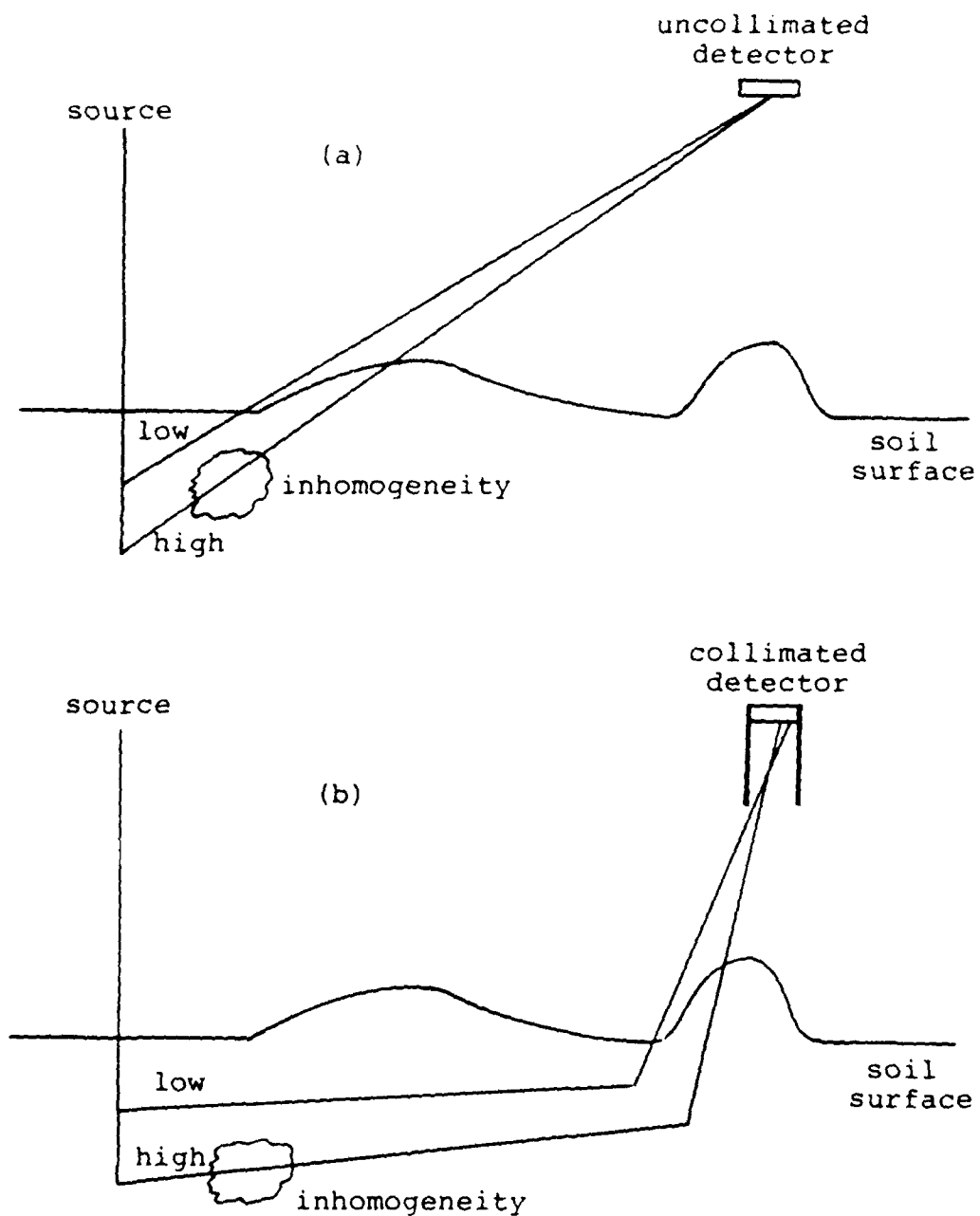


Figure VIII.56. Failure of the dual energy subtraction technique. (a) High and low energy photon paths to the uncollimated detector produce unrelated responses due to surface irregularities and inhomogeneities. (b) The same problem exists for the collimated detector.

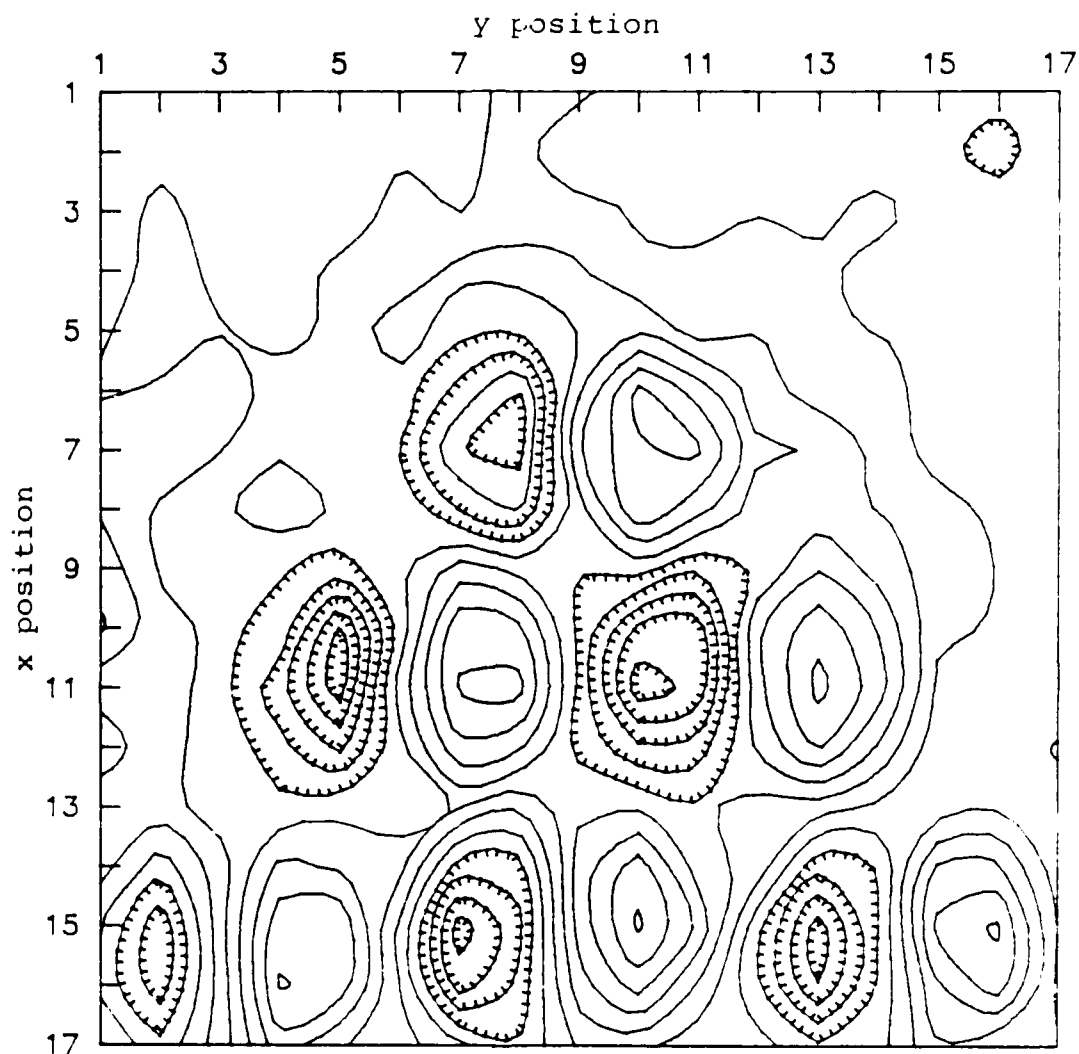


Figure VIII.57. Two-dimensional image diagram of the measured uncollimated detector response to a 100 kVp source beam filtered by Pb for the TST mine at depth of burial of 2.54 cm with irregular soil surface. The response is sampled at a 2.54 cm increment. Compare to Figure VIII.44.

deeper penetration of the high energy photon produces a very different path to the detector. The extension of these different paths to a polyenergetic spectrum, leads to the same conclusion as for the uncollimated detector; the high energy components of the higher energy beam are uncorrected. The previous application of this technique (Jacobs et al., 1979) used detectors positioned as close to the source as possible to produce nearly vertical paths through overlying materials.

Power Requirement

The data derived from calculations and imaging experiments provide the information required to make estimates of the power requirements for mine detection using backscatter radiation radiography. Two criteria are used to assess the capability of portable generators to provide the power required to produce images and detect buried mines. The first criterion derives from experience with the imaging experiments. Those experiments reveal that approximately 10000 counts with the mine present are required for each pixel in the image to produce readily recognizable patterns for mines buried at depth. This number of counts effectively determines the power requirement, but does not address the question of detectability, the second criterion. Detection is determined by the magnitude of the difference in the mine and soil responses in the presence of noise. The Neyman-Pearson criterion (Schwartz and Shaw, 1975) is used as the vehicle for the determination of detectability. These two

criteria are applied to the uncollimated and the collimated detectors. The segmented detector will produce results similar to the uncollimated detector. The energy window detector is too dependent on the properties of the detecting material to allow meaningful calculations based on fluence results.

Variables

The power estimate depends upon a large array of variables. Many of these have been condensed by the optimization calculations of Chapter VII into the fractions of source photons reaching the detector for a particular configuration and irradiation condition. The number of source photons emitted by the x-ray generator within the collimated beam per unit time and current is obtained by combining measurements of exposure rates with calculations of the XRSPEC.PAS code. The speed for the vehicle carrying the mine detection system, the size of the path to be searched, and acceptable values of the probabilities of detection and false alarm are variables which are determined by field operating requirements. Estimates of the range of acceptable values for these variables are provided by the U.S. Army (Moler, 1985). Table VIII.11 shows these values along with practical constraints on the size of portable power supplies. The number of samples characteristic of the mine, and the beam size to allow shape resolution are taken from the imaging experiments. The magnitude of the noise for soil in the experiments is approximately 6 to 7% of the

TABLE VIII.11

Operational Requirements for
a Vehicle-Mounted Antitank Mine Detection System

Characteristic ^a	Desired	Useful
Forward speed	1.34 m/s	0.23 m/s
Path width	3.05 m	1.83 m
Scanned width ^b	4.45 m	3.23 m
Detection probability	0.99	0.90
False alarm frequency ^c	<0.0025 /m	0.011 /m
Power	5 KW	100 KW

^aTable adapted from Moler, R.B., "Workshop Report, Nuclear Techniques in Mine Detection Research," (Belvoir Research and Development Center, Fort Belvoir, VA, 1985), p. 4.

^bThe scanned width must exceed the path width to allow mines to be detected near its ends. An extension of 0.7 m on each end is adequate.

^cUsing a mine diameter of 30 cm, the false alarm frequency can be translated into a false alarm probability. The desired probability is 0.00075; the useful probability is 0.00328.

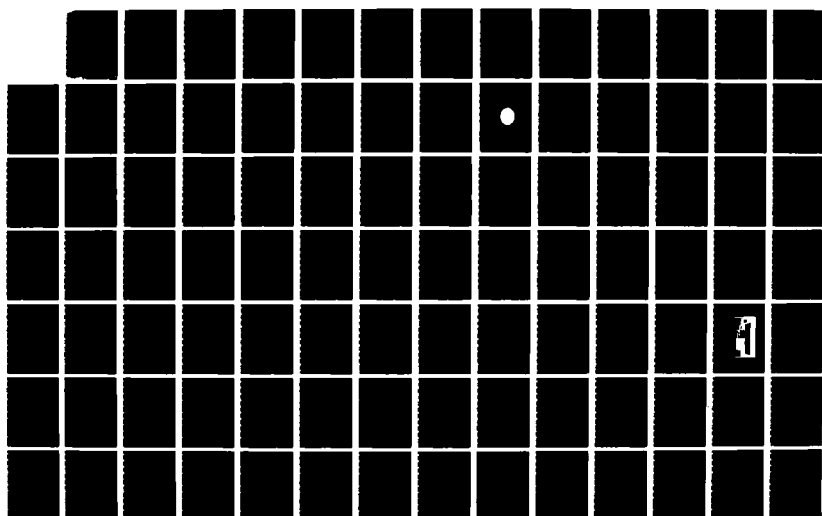
AD-A182 227

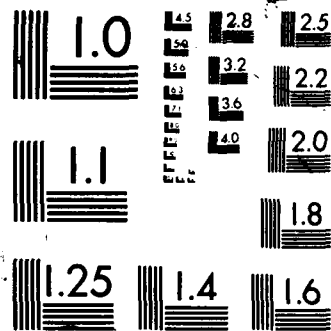
LANDMINE DETECTION BY SCATTER RADIATION RADIOGRAPHY(U)
ARMY MILITARY PERSONNEL CENTER ALEXANDRIA VA
J G CAMPBELL 02 JUL 87

5/6

UNCLASSIFIED

F/G 15/6 6 NL





XEROCOPY RESOLUTION TEST CHART

signal from smooth soil when approximately 10000 counts are obtained. This value is undoubtedly much smaller than that which will be experienced under field conditions due to height variations, surface irregularities and inhomogeneities. Accordingly, the magnitude of the noise is allowed to vary to determine the level at which detection at a specified probability level is no longer possible.

Fraction of Source Photons Reaching the Detector

The monoenergetic calculations of Chapter VII provide the fraction of photons reaching the detector per single energy source photon. These results are fit by cubic splines to provide the fraction per source photon as a function of source energy for a particular source spectrum, irradiation geometry and mine depth of burial with beam intercept at the center of the mine. Fluence spectra, calculated by the XRSPEC.PAS code, are then coupled to these functions to provide the fraction of the source photons reaching the detector per polyenergetic source photon.

Source Flux

The source flux per unit current is obtained by making exposure rate measurements at beam energies of interest. Calculations are made using the XRSPEC.PAS code to provide the ratio of fluence to exposure for the conditions of the measurement. Multiplication of the ratio by the measured exposure rate gives the flux at the point of measurement. This value is used to provide the flux normalization constant for the XRSPEC.PAS code for the measurement

conditions. The code can then be used for calculations with different beam filtrations at this same peak kilovoltage and at this single position. Values of the flux at other positions at this same peak kilovoltage are calculated using the inverse square law. Separate exposure rate measurements are required for each peak kilovoltage of interest to determine the appropriate flux normalization constant. The flux divided by the beam current applied during the exposure rate measurement provides the desired quantity for the power calculations. Since the voltage is specified by the beam energy, the beam current becomes the quantity of interest in fixing the power.

The ratios of fluence to exposure from the work of Fewell and Shuping (1977), produced by a similar single phase x-ray machine, are used to test the calculations of the XRSPEC.PAS code. Differences of less than 2% between the calculated and published fluence to exposure ratios are found for three spectra (Figures F.8 through F.10) from this paper. Table VIII.12 provides calculated results for the various spectra used in the measurements. These values are typical of x-ray generators having tungsten anodes, and are used in the power calculations. A significant improvement in the number of source photons available can be made by lowering the source to the height of the detector while maintaining the same beam size at the soil surface. There is virtually no change in the characteristics of the backscatter radiation due to the larger angular dispersion

TABLE VIII.12

Photon Output of the
GE Maxitron 300 X-Ray Therapy Unit

Beam Energy (kVp)	Filtration ^a	Flux per Current ^b (photons/cm ² -mAs)	Figure
100	1.01 mm Al	3.7002E+08	F.1
150	1.01 mm Al	7.7769E+08	F.2
200	2.67 mm Al	9.5862E+08	F.3
100	9.52 mm Al	9.4598E+07	F.4
150	9.52 mm Al	2.7062E+08	F.5
150	1.85 mm Sn	1.2016E+08	F.6
200	1.85 mm Sn	5.2068E+07	F.7
100	0.24 mm Pb ^c	3.2751E+07	F.8
100	0.75 mm Pb	3.2443E+06	F.9
150	0.75 mm Pb ^c	1.3955E+07	F.10
200	0.75 mm Pb	3.4953E+07	F.11
200	0.75 mm Pb ^c	3.4511E+07	F.12
200	1.35 mm Pb ^c	6.3004E+06	F.13

^aAll include 4.75 mm Be inherent filtration.

^bAt 64.48 cm from the anode.

^cAlso includes 0.25 mm Al equivalent monitor ionization chamber.

in the beam. While the maximum angular spread in the beam nearly doubles, it is still less than 1.4 degrees from perpendicular incidence. A source height of 34.6075 cm (the same as the detector) is used in the power calculations.

Pixel Dwell Time

The combination of forward speed and the raster of the beam determine the amount of time the beam spends on the mine. If an image is to be produced, the scan must be broken into smaller time segments to form pixels. The time the beam spends irradiating a single pixel is the pixel dwell time. Arguments presented in Chapter VII indicate that the size of the beam at the mine surface should not be much larger than the 1.27 cm by 1.27 cm used in the measurements to allow sufficient resolution to determine the circular shape of the mine. The time required for the beam to sweep through an area of this size can be calculated from the speed and raster lengths. Table VIII.13 provides the results of such calculations for a 1.27 cm by 1.27 cm beam using the desired and useful operational requirements given in Table VIII.11.

Calculation Technique

The fraction of source photons striking the detector is taken from Monte Carlo calculations for beam intercepts at the center of the mine. To be conservative, the fraction is adjusted so that the difference between mine and soil backscattered signals is reduced by 20% to account for lower responses at other beam intercepts near the center of the

TABLE VIII.13

Imaging Quantities Necessary to
Fulfill Operational Requirements

Quantity	Operational Requirement Level ^a	
	Desired	Useful
Number of pixels per line scan	350	254
Line scan rate	105.51 s ⁻¹	18.11 s ⁻¹
Single line scan time	9.48 ms	55.22 ms
Pixel dwell time	27.05 μs	217.11 μs

^aBased on vehicle speeds and scanned widths of Table VIII.11.

mine and for the effects of a real detector. The maximum number of independent 1.27 cm by 1.27 cm beam intercepts on the mine is more than 400. Many of these samples, however, will produce responses very unlike that of the center of the mine. Again, being conservative, only the central 50 samples are used in the detectability determination. This presupposes a system to recognize and group together high count pixels occurring in regions the size of a mine.

The fraction of source photons striking the detector multiplied by the flux per beam current, the pixel dwell time, and the area of the beam on the soil surface gives the number of photons reaching the detector divided by the beam current for a pixel near the center of the mine. Dividing this number into the required 10000 counts for imaging yields the required beam current. Using this current, the power and number of counts characteristic of soil can be calculated. To determine if this power level can also lead to mine detection, the Neyman-Pearson criterion is applied. This test maximizes the probability of detection while holding the false alarm probability to a fixed level by determining a threshold for deciding if a signal is present. The criterion is modified to allow a variable signal to noise ratio. The false alarm probability is given by

$$P_n = \frac{1}{2} \left[1 - \operatorname{erf} \left\{ \frac{\sqrt{m}}{\sqrt{2}} \frac{(d - A_s)}{f_s A_s} \right\} \right],$$

where P_n is the false alarm probability,

erf is the error function,

m is the number of samples,
 d is the decision threshold level,
 A_s is the number of counts due to irradiation of a
 single pixel of soil, and
 f_s is the reciprocal of the signal to noise ratio of
 soil.

Using the desired and useful false alarm probabilities of
 Table VIII.11, this equation is solved for the decision
 threshold level, d , which is then substituted into the
 expression for the probability of detection,

$$P_d = \frac{1}{2} \left[1 + \operatorname{erf} \left\{ \sqrt{\frac{m}{2}} \frac{(A_m - d)}{f_m A_m} \right\} \right],$$

where P_d is the probability of detection,
 A_m is the number of counts due to irradiation of a
 single pixel characteristic of a beam intercept
 near the center of the mine, and
 f_m is the reciprocal of the signal to noise ratio of
 the mine.

This formulation makes the probability of detection
 independent of the power level. This is the actual case
 since the majority of the noise is produced by height
 variations, soil surface irregularities or inhomogeneities.
 Increasing the power level simply increases the magnitude of
 these sources proportionately. Since the majority of the
 noise is produced by the soil, for mines buried below the
 surface, f_m and f_s are similar. They are set equal in the

power calculations. This quantity is allowed to vary to determine how the detection probability changes with noise. Tolerance levels are determined by the desired and useful levels of Table VIII.11.

A series of calculations are performed by a computer code, POWER.PAS. The error function is calculated from its complement, which is in turn computed from a routine provided by Press et al. (1986). This routine is also used to produce a table of the error functions used to find its inverse as a part of the solution of the false alarm equation for the decision threshold. The code also computes the minimum mine to soil ratio required to allow detection at the desired and useful operational levels.

Power Calculations

Several examples are used to examine the power requirement. The uncollimated detector is examined for depths of burial of 0.0, 2.5 and 5.0 cm; the collimated detector at 2.5 and 7.5 cm. Both detectors are examined at the desired vehicle speed and desired path width with the desired probabilities of false alarm and detection from Table VIII.11.

Table VIII.14 shows results for the uncollimated detector. A number of conclusions can be derived from the table. The generally reasonable power levels are a result of the high fraction of source photons reaching the uncollimated detector. The addition of filtration is seen to increase the power requirement. The low signal to noise ratios for the mines buried flush to the surface indicate

TABLE VIII.14

Power and Signal to Noise Ratio Requirements
for Imaging and Mine Detection
with the Uncollimated Detector

Source Beam ^b	Depth of Burial ^a					
	0.0 cm		2.5 cm		5.0 cm	
	Power ^c (KW)	SNR ^d	Power ^c (KW)	SNR ^d	Power ^c (KW)	SNR ^d
100 kVp 1.01 mm Al	0.256	0.795	0.642	12.642	0.680	217.628
150 kVp 1.01 mm Al	0.133	0.935	0.281	9.766	0.301	79.428
200 kVp 2.67 mm Al	0.110	1.070	0.207	9.074	0.222	57.142
100 kVp 9.52 mm Al	0.576	0.842	1.351	10.893	1.445	211.193
150 kVp 9.52 mm Al	0.260	1.015	0.508	8.917	0.548	67.751
150 kVp 1.85 mm Sn	4.482	1.729	6.289	7.485	6.780	27.579
200 kVp 1.85 mm Sn	1.350	2.081	1.777	8.333	1.901	30.864
100 kVp 0.24 mm Pb ^e	1.354	0.940	2.823	8.921	3.067	203.252
100 kVp 0.75 mm Pb	12.441	1.089	22.787	7.764	25.024	131.666
150 kVp 0.75 mm Pb ^e	4.207	1.206	7.174	7.628	7.851	69.735
200 kVp 0.75 mm Pb	2.149	1.502	3.257	8.306	3.521	51.256
200 kVp 0.75 mm Pb ^e	2.176	1.504	3.296	8.299	3.563	51.020
200 kVp 1.35 mm Pb ^e	11.602	1.716	16.581	8.756	17.840	51.282

TABLE VIII.14 - continued

^aCalculations are for perpendicularly incident beams of the indicated qualities originating from a diverging point source 34.6075 cm above an HTL soil surface. Beam size at the soil surface is 1.27 cm by 1.27 cm. The uncollimated detector consists of two panels, each 30 cm wide, separated by a 10 cm raster gap, and located 34.6075 cm above the soil surface.

^bAll include 4.75 mm Be inherent filtration.

^cThe power is that required to produce 10000 fluence counts on the detector per pixel near the center of the mine.

^dThe minimum signal to noise ratio (SNR) required to allow mine detection by a system transported on a vehicle moving at 1.34 m/s, searching a path 3.05 m wide, while maintaining a false alarm probability of 0.00075 and a detection probability of 0.99. See text for details of calculation.

^eAlso includes 0.25 mm Al equivalent monitor ionization chamber.

that they can be detected even in the presence of a great deal of noise. For this depth of burial, the softer spectra are less effected by noise. As depth of burial increases, the power increases due to the decreasing response from the mine. At a depth of burial of 2.5 cm, the minimum signal to noise ratio is on the order of half that observed for smooth soil in experiments. Detection in high noise environments may be difficult. At 5.0 cm, the minimum signal to noise ratio for detection often exceeds that due to quantum statistics alone; detection is highly unlikely at this depth. This conclusion is not altered by using the less stringent set of operational requirements. For the buried mines, the lowest signal to noise ratios occur for those spectra which contain significant numbers of photons near the monoenergetic optimums. The overall conclusion for the uncollimated detector is that it is capable of meeting operational imaging and detection requirements only for mines buried close to the surface (or above). Power level is not an issue; detection at depth is.

The low fraction of source photons reaching the collimated detector for useful acceptance angles immediately eliminates the majority of the heavily filtered spectra considered in this section. The combination of the low fraction per source photon and the reduction in the source strength by heavy filtration implies very large power levels. For example, the 150 kVp beam filtered by 1.85 mm of tin requires 700 KW for detection at the desired level

for a depth of burial at 7.5 cm. Lightly filtered beams become the only possible choice. Table VIII.15 shows results for two lightly filtered beams. While the power levels exceed the desired 5 KW level, they are well below the useful level of 100 KW. The signal to noise ratios at 2.5 cm are very low, allowing detection in considerable noise. The ratios at 7.5 cm are reasonable, especially considering the conservative nature of the calculation. The overall conclusion for the collimated detector is that it is capable of imaging and detection to depths of 7.5 cm in the presence of moderate amounts of noise. Greater depths are possible in loose soil surrounding a newly implaced mine.

TABLE VIII.15

Power and Signal to Noise Ratio Requirements
for Imaging and Mine Detection
with the Collimated Detector

Source Beam ^b	Depth of Burial ^a			
	2.5 cm Power ^c (KW)	SNR ^d	7.5 cm Power ^c (KW)	SNR ^d
150 kVp 1.01 mm Al	28.848	0.773	61.358	4.327
200 kVp 2.67 mm Al	17.162	0.941	33.951	5.571

^aCalculations are for perpendicularly incident beams of the indicated qualities originating from a diverging point source 34.6075 cm above an HTL soil surface. The soil contains 10% water by weight. Beam size at the soil surface is 1.27 cm by 1.27 cm. The collimated detector consists of two panels, each 30 cm wide, separated by a 30 cm raster gap, and located 34.6075 cm above the soil surface. The collimator acceptance angle is 23.1 degrees.

^bEach includes 4.75 mm Be inherent filtration.

^cThe power is that required to produce 10000 fluence counts on the detector per pixel near the center of the mine.

^dThe minimum signal to noise ratio (SNR) required to allow mine detection by a system transported on a vehicle moving at 1.34 m/s, searching a path 3.05 m wide, while maintaining a false alarm probability of 0.00075 and a detection probability of 0.99. See text for details of calculation.

CHAPTER IX

CONCLUSIONS

This research demonstrates how differences in the fundamental photon interaction characteristics of soil and explosive can be exploited by scatter radiation radiography to detect and image buried nonmetallic antitank landmines. Calculational techniques, centering on a Monte Carlo photon transport code, are used to optimize the geometry and energy characteristics of the problem. This code, along with others which calculate the x-ray source spectra and the detector response, are validated through a series of comparisons with results in the published scientific literature and by measurements.

An x-ray generator is the only reasonable choice for a source to provide intense beams capable of being rastered at high scan rate across a wide path while being transported forward at operationally compatible speeds. Detectors examined consist of large panels of sensing material located above and parallel to the soil surface. The height of the panels above the soil should be approximately 30 cm to preclude damage while operating over rough terrain. The optimum beam angle of incidence is zero degrees (perpendicular to the soil). The source beam should be approximately

1.27 cm by 1.27 cm at the soil surface to allow shape resolution of the mine. The optimum size of the raster gap depends on detector type.

Of the four types of detectors which have been examined for feasibility, only a large area detector, consisting of panels of sensing material separated by a 30 cm gap to allow beam raster and using collimation to remove the single scattered component, is capable of detecting mines at depths of burial greater than 5.0 cm. Higher mine to soil ratios can be obtained with larger raster gaps, but the reduction in backscattered fluence makes the power requirement unreasonable. Heavy filtration of the source beam to force its spectrum to possess a higher proportion of the monoenergetic optimum energy photons is counterproductive because of greatly increased power requirements. Lightly filtered 200 kVp beams are found to provide good results. The collimated detector is capable of mine detection and imaging to at least 7.5 cm. This conclusion is reached for realistically available portable power supplies with acceptable detection and false alarm probabilities for vehicle speeds and path widths compatible with operational requirements in the presence of moderate amounts of noise. In soil recently disturbed by burial of mines, larger depths are possible.

The major drawback of the collimated detector system is its sensitivity to height variation. This issue is discussed in the section below covering future research directions. Less important concerns include the ability of the

detector to sense soil density changes and an image response to surface laid mines which differs considerably from that of buried mines. The concern imposed by the detection of density differences is the possibility of constructing dummy minefields by simply digging holes and refilling them with loose soil. The image produced by such refilled holes differs considerably from that of a mine. Without an image, however, this situation would produce false alarms. The concern produced by the image of the surface laid mine is that it might be confusing to an operator looking for responses characteristic of buried mines. The image response for the surface laid mine is very strong, but has similarities to that of the refilled hole. Since surface laid mines are an important consideration on the modern battlefield, a composite detector, using an uncollimated detector as a supplement, could be useful.

An uncollimated detector consisting of two large area panels with a raster gap of 10 cm is marginally capable of detecting mines buried at only 2.5 cm. It is, however, an excellent detector for mines laid on the soil or buried flush to the surface. The lightly filtered beams, found to be necessary for the collimated detector to meet reasonable power requirements, are particularly useful when used with the uncollimated detector for mines either laid on the surface or buried flush to the soil. The very high back-scattered fluence available to this detector, as compared to the collimated detector, allows the possibility of combining

the two, using the region interior to the collimated panels. An additional benefit derived by this combination is ability to correlate two completely different detection mechanisms to increase detection probability.

Additional research should initially focus on the height sensitivity of the collimated detector. A clear definition of the mission requirements for the mine detection system is necessary to assess the extent of the problem. A large area collimated panel detector should be constructed and used in height variation experiments. Resolution of the height sensitivity problem may well lie within the realm of signal processing. The very short line scan times associated with the raster of the beam imply little opportunity for height variation induced by motion of the detector system over an object the size of a mine. Signal processing based on correlating features of individual line scans is worthy of investigation. Images produced by the collimated detector for surface laid mines and refilled holes should be evaluated to determine if uncollimated elements should be included. The overall topic of signal processing of real-time information, and translation of its results into information which is easily and rapidly capable of being interpreted, is a second major area of additional research. Provided that positive results are obtained in these two areas, actual construction of a prototype detector system to include x-ray source, and its testing over real surfaces, characteristic of operational requirements with

real (unarmed) mines, is the final step in determining the feasibility of scatter radiation radiography to detect nonmetallic antitank landmines.

APPENDIX A

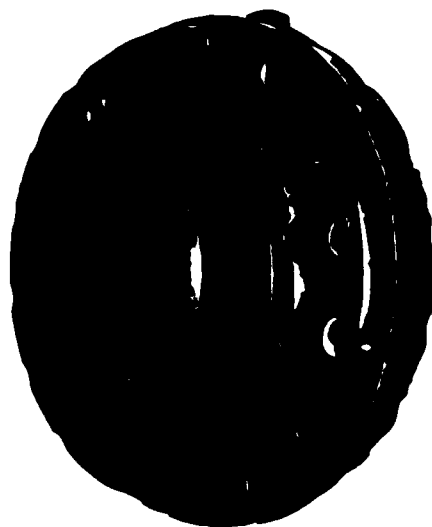
CHARACTERISTICS OF LANDMINES

A landmine is an explosive device placed in or on soil. While it is designed to destroy or damage vehicles, or to kill or incapacitate personnel, the primary purpose of mines is to reduce the mobility of enemy forces (U.S. Department of the Army, 1979a). Landmines are produced by dozens of countries. Their characteristics are extremely varied. Variables include size, geometry, composition, fuzing, and method of use. Mine sizes range from about that of a tennis ball to disks of diameters on the order of a meter. Two shapes predominate, the right circular cylinder and the rectangular parallelepiped, though other shapes, including irregular, exist. A typical landmine is shown in Figure A.1.

Mine Classifications

A number of different schemes can be used to classify mines. Mine cases may be metallic or nonmetallic. The explosive is usually trinitrotoluene (TNT), but other explosives are also employed (U.S. Department of the Army, 1979b, 1986). Mine construction ranges from very sophisticated industrial manufacture to crude, but often very

Figure A.1. Typical antitank mine. The device shown in the photograph is a U.S. Army training model of the East German PM-60 nonmetallic antitank mine.



effective devices built by soldiers in the field. Fuzing types range from simple pressure devices to integrated circuit controlled sensors. Mines may be buried or simply laid on the surface of the ground. They may be emplaced by individual soldiers, by specialized mine laying vehicles, or remotely by aircraft, artillery or rockets. Given this wide range of characteristics, it is understandable that there are a variety of classification schemes which may not be mutually exclusive.

Metallic or Nonmetallic

The classification metallic or nonmetallic refers to the composition of the case of the mine. The importance of the classification relates to mine detection. Devices capable of efficiently detecting metallic mines have been available since World War II (U.S. Department of the Army, 1986; Honeywell, 1981). Accordingly, most mines constructed at the present are nonmetallic, usually made of plastic. Field constructed, nonmetallic mines have cases made from wood (Radevich et al., 1965). Other nonmetallic case materials which have been used include ceramics, glass and cardboard. Nonmetallic mines are much more difficult to detect than metallic, and are the subject of this dissertation. Some metallic parts are present in virtually all mines, though the amount present in nonmetallic mines is usually less than 100 grams (U.S. Department of the Army, 1986).

Antitank or Antipersonnel

Antitank (AT) mines are designed to destroy or disable tanks. They are also employed against other tracked and wheeled vehicles. Their fuzing is generally designed to prevent an individual soldier from causing detonation. These are generally large mines, containing several kilograms of explosives. Of these two mine types, they represent the greatest threat to new U.S. operational concepts, and are also the subject of this dissertation. Antipersonnel (AP) mines are designed to kill or injure soldiers operating on foot. They are generally very small mines and may contain less than a tenth of a kilogram of explosive. Doctrine in most armies requires that anti-personnel mines be employed whenever antitank mines are emplaced to discourage their disarming by foot soldiers (U.S. Department of the Army, 1979a, Radevich et al., 1965). Alternatively, antihandling devices or boobytraps may be employed in conjunction with antitank mines for the same purpose.

Conventional and Scatterable

A conventional mine is placed in or on the ground by hand or by mechanical mine laying systems. Scatterable mines are delivered remotely by aircraft, artillery or rockets. Scatterable mines are employed to protect flanks, in enemy rear areas, or in response to enemy maneuver. (U.S. Department of the Army, 1979a). Scatterable mines will always be located on the surface of the ground;

conventional mines may be buried or surface laid. The pattern of mines produced by a scatterable delivery system is approximately random within the mined area. Conventional mines are often placed in some standard pattern, which includes gaps or lanes to allow friendly movement (U.S. Department of the Army, 1969, 1973; Radevich et al., 1965). These conventional minefields are carefully recorded and often marked to allow passage and removal when no longer required. Scatterable minefields, obviously, are not as well defined and do not contain gaps or lanes for movement. For this reason and because they are often employed in areas in which friendly forces may desire to operate in the future, scatterable mines self-destruct after a certain period of time. Scatterable antitank mines are usually much smaller than conventional antitank mines. Conventional mines do not have a self-destruct capability.

Surface or Buried

As has been discussed, mines may either be placed on the surface or buried. A major drawback to the use of mines is their logistical burden. Transportation and manpower requirements are large. Hand emplacement of buried mines is very time consuming. With the increasing tempo of modern warfare, it is likely that surface laid mines and scatterable mines will be frequently employed. While it may seem that a surface laid mine would be ineffective due to easy detection, extensive tests have shown this is not the case. The field of view provided to an armored vehicle driver

is quite restricted. This fact, combined with the presence of smoke, employed to assist movement of armored vehicles through open areas which may be covered by enemy fire, severely degrades the capability to detect mines (U.S. Department of the Army, 1979a). Moreover, there are many cases when mine detection is desired. A synergism exists when a minefield is covered by fire and the force attempting to breach the minefield is aware of its presence. The breaching vehicles are forced to slow their movement, dramatically increasing their vulnerability to direct covering fires. Even when a minefield is not covered by fire, the knowledge of the presence of mines may provide the necessary delay required to disrupt a coordinated attack.

Depths of burial of antitank mines may range down to approximately 15 cm in soil. In general, however, the depth of burial is much closer to the surface. Buried antipersonnel mines are always placed close to the surface. U.S. pressure fuzed antitank mines are generally buried flush with the soil surface and covered with a layer of soil for camouflage. The recommended depth of this layer ranges from 0 to a maximum of 5 cm depending on the source (U.S. Department of the Army, 1969, 1973, 1979a). For burial in sod, the turf is cut and rolled back for mine emplacement, and then replaced. In snow of less than 10 cm depth, mines are buried so that the pressure plate remains above the ground. For snow depths of 10 to 28 cm, mines are laid on the soil surface. For snow depths greater than 28 cm, mines are

supported so that they are 10 to 14 cm from the snow surface (U.S. Department of the Army, 1973).

Soviet instructions for the burial of landmines are similar to those described in the preceding paragraph (Radevich et al., 1965). In vegetated areas, the sod is cut to a depth of 5 to 8 cm, and peeled back. Soil is removed, the mine emplaced, and finally, the sod replaced covering the mine. In areas of solid soil or in well travelled dirt roads, 2 to 3 cm of the mine must protrude above the surface to allow the crushing action which begins the detonation chain in a pressure fused mine. In soft, nonvegetated soils, the mine is buried flush to the surface. In snow less than 25 cm deep, mines are placed on the soil surface. In depths of snow, greater than 25 cm, and less than 60 cm, snow is compacted under the mine so that the depth of snow (not compacted) above the emplaced mine is 10 to 15 cm. In depths greater than 60 cm, other materials are employed to build a firm foundation under the mine.

Mines emplaced by mechanical mine layers are generally more deeply buried than those emplaced by hand. The Soviet PMR-3 mechanical minelayer is capable of either surface placement or burials, in soft soils, of 30 to 40 cm (U.S. Department of the Army, 1979a). Large bombs converted for use as mines may be buried at even greater depths.

Fuzing Type

A wide variety of fuze types exist. For antitank mines, some aspect (or several) of the vehicle signature is

sensed by the fuze to begin the detonation sequence. Among the signatures available are velocity, ground pressure, specific impulse, local disturbance of the magnetic field of the earth, seismic impulse, noise, radio frequency radiation, visual recognition, and infrared radiation. Pressure fuzes are among the most common employed. They may operate on a single or multiple impulse method (to attack the third vehicle in a column on a road, for instance), or in a delay mode to defeat attempts to detonate mines with rollers preceding the vehicle. Other simple types include tilt rods and disturbance fuzes. Complex fuze types include magnetic anomaly, acoustic, vibration, active or passive infrared, and photon backscatter. Magnetic fuzes may be triggered by a threshold, a rate of change or by the magnetic signature associated with a particular vehicle type. Mines may also be detonated on command by an observer.

Employment of Landmines

Mines are employed in offensive, defensive and retrograde operations. In the offense they are primarily used to provide flank protection during movement, to block withdrawal routes of an enemy force under pursuit, and to protect against counterattacks. They also provide economy of force by defending areas which are only lightly held as a result of concentration elsewhere for the offensive operation. In the defense and in retrograde operations, they are employed as obstacles to delay and channelize enemy movement. In all operations they may be employed to harass and

demoralize the enemy. Mines are used to supplement other obstacles, especially natural terrain features. Whenever possible, the effectiveness of minefields is enhanced by direct and indirect fire weapon coverage. The density of mines by type within a minefield is determined primarily by the perceived enemy threat. Typical Soviet antitank minefields would contain 750 to 1000 mines per kilometer of front, placed in multiple belts (Honeywell, 1981).

APPENDIX B
HISTORICAL EXAMPLES OF MINE WARFARE
Mine Development

Forerunners of Modern Mines

Although the extensive use of landmines dates from World War II, mine warfare was employed as early as 20 A.D. with the Chinese use of buried gunpowder covered with scrap iron. Similar devices were used by the U.S. Army in the Seminole Wars, the Mexican Army in the defense of Chapul-tepec during the Mexican-U.S. War, the Russians during the Crimean War, and by the U.S. Army in the U.S. Civil War. The term "mine" derives from the use of tunnels employed in seige warfare in which the besieging force would excavate tunnels under fortifications. In the earliest uses, the timber supports for the tunnel were burned causing the collapse of the mine and structures above it. Such a mine was used at the seige of Antioch in the eleventh century. The use of gunpowder explosive charges in such tunnels greatly increased the effectiveness of the technique. The most famous such use was at the seige of Petersburg in the U.S. Civil War (U.S. Department of the Army, 1973).

The true forerunners of current mines made their first appearance during World War I in response to the newly

invented tank and to the increasing importance of mechanized vehicles. Though explosive devices were never employed in the form of extensive minefields, pipes filled with explosives and placed in roadways, and buried, modified artillery shells were used ((U.S. Department of the Army, 1986). In the years following World War I and before World War II, the German Army pioneered the development of landmines (Honeywell, 1981).

Mines of World War II

Modern mine development stems chiefly from German and Soviet innovations. The German Army developed a wide range of mine types including the Teller plate antitank mine, the bounding shrapnel antipersonnel mine, a variety of nonmetallic mines, mines employing shaped charges, and scatterable mines. The Soviets produced the first nonmetallic mine in response to a shortage of metal, rather than as an antidection mechanism; however, they also produced the first device, a tar paper cased mine, specifically designed for that purpose. The Soviets were also the first to use wooden cased mines, flame mines, projectile mines, and a wide variety of fuze types, including vibratory, magnetic influence, and an antidetector fuze to attack mine detectors based on frequency induction. Other nations copied and modified the German and Soviet designs (U.S. Department of the Army, 1973).

While modern mines are in some cases more sophisticated than those employed in World War II, they are, with the

exception of the newer scatterable mines and fuzing types, essentially the same technology as those employed in the 1940's.

Countermining Warfare in World War II

As discussed below, World War II saw the use of massive numbers of mines. Detecting and neutralizing mines became very important. At the beginning of the war, only visual inspection and hand probing were available for mine detection. Detectors were developed which were capable of locating metallic cased mines, but the increasing use of non-metallic mines late in the war, defeated these devices. To this date a reliable nonmetallic mine detector does not exist.

Mine Employment

While mines were used in all theaters of World War II the best examples of the massive use of mines in warfare are from the North African campaign and the Eastern front. The experience on the Eastern Front is particularly important with respect to the development of Soviet mine warfare doctrine. Experiences in Korea and Vietnam have shown that low density, random mining can be particularly effective.

North Africa

The battles fought in North Africa during World War II were noted for the important role mines played. The lack of natural obstacles in desert warfare encouraged the use of mines. Huge minefields were often necessary to tie together the few existing natural obstacles. The North African

campaign extended from June 1940 to May 1943. The early portions of the campaign were fought between British and Italian forces, with the German Africa Corp, commanded by Rommel, arriving in February, 1941.

During the spring of 1942, British forces at Ain El Galaza near Tobruck used one million mines in field of depths of thousands of meters to strengthen their defensive positions (Rommel, 1953). It was during this battle that Rommel developed a respect for and understanding of the utility of mines in the defense, which he would use in the future (Macksey, 1968). The British minefields in support of fortified positions were very effective in delaying, disrupting and sometimes defeating German attacks.

In June of 1941, Operation Battleaxe, a British attack against an inferior German force resulted in a total British defeat, largely because of the extensive use of mines. The mines slowed the attacking vehicles, making them easy targets for accurate German antitank weapon fire (Honeywell, 1981).

In August, 1942, the British defense at El Alamein employed 150,000 mines. In October, with the Germans then on the defensive, 500,000 mines, many captured from the British, were employed in "Devil's Gardens," large complex minefields with depths up to 6.4 kilometers. While these were formidable obstacles, the German failure to employ sufficient numbers of antipersonnel mines in the fields allowed the British to clear lanes or alter minefield patterns at night (Rommel, 1953).

Throughout the campaign both sides used mines to consolidate positions on newly captured terrain. Minefields were placed to cover all avenues of approach to secure positions against counterattack. In the desert mines became the most important means of restricting enemy maneuver.

Eastern Front

During World War II, the Red Army developed sound doctrine for the employment of mines in the defensive and offensive operations. Each individual Soviet unit position was protected by mines when available. Mining began only ten meters to the front of the most forward unit element, and was considered so important that it was even conducted under fire. When forced to withdraw mines were left behind to produce casualties in the attacking force. At Kiev and Vyborg in 1941 and Sevastopol in 1942, radio controlled mines were used as German forces entered the cities (Honeywell, 1981).

Soviet histories claim the use of 222 million mines during World War II. The immense transportation burden imposed by mine warfare was alleviated by requiring each soldier going to the front to carry a minimum of two anti-tank mines (Honeywell, 1981). The mass of the mines, on the order of ten kilograms each, is a strong testimonial to the importance the Red Army placed on mines. Field fabrication of mines using wooden cases also helped reduce the logistical problem.

At the pivotal battle of Kursk during the summer of 1943, mines played a decisive role. The German attack into the Kursk salient was expected; the Soviet forces, under Zhukov, were completely prepared (Zhukov, 1969). Six belts of fortified positions, each 175 km long, were protected by minefields of linear densities of up to 8000 mines per kilometer (Caidin, 1974). Minefields were positioned to channelize the attacking German forces into fire traps where concentrated direct fires and artillery were applied. German forces attempting to advance did not find it unusual to have to remove 40,000 mines per day in the sector of a Corps (Von Mellenthin, 1956). Such German efforts to remove minefields were met by heavy Soviet resistance, including snipers dedicated to protecting the fields. When German armor did manage to break through, the Soviets mined behind them and then counterattacked (Caidin, 1974). The first appearance of specialized engineer units designed to protect Soviet flanks in the offense with mines occurred at Kursk (Baxter, 1986).

At the end of the war, Soviet expertise in both mine and countermine warfare was unequalled. In most aspects (a notable exception is scatterable mines), this is also true today (Nolan et al., 1980; Honeywell, 1981).

Korea and Vietnam

In Korea, low density, random mining proved effective in slowing the movement of U.S. forces. Mine rollers, pushed by tanks and designed to detonate pressure mines,

were defeated by delays built into the fuzes. In Vietnam, virtually every road, bridge, culvert, landing zone, and railroad line was mined continuously (Nolan et al., 1980). Tremendous efforts were required to clear roads on a daily basis. To complicate the task, mines were almost always booby trapped, or employed command detonation. The experience in Vietnam showed that random mining was very effective.

APPENDIX C

OTHER MINE DETECTION AND NEUTRALIZATION METHODS

The range of technologies which have been applied to the mine detection problem is impressive. None, however, have been capable of providing real-time detection of non-metallic mines at a rate and reliability required for mechanized combat. Even the alternative of mine neutralization requires at least the initial detection of mines. The sources for the descriptions of the various detection and neutralization methods are from unclassified summaries of U.S. Army sponsored research (Nolan et al., 1980; U.S. Department of the Army, 1986). Descriptions of previous work on x-ray backscatter and related technologies are provided in Chapter II.

Detection Technologies

General Considerations

Mine detection includes all means to reveal the presence of mines or minefields. The most frequent mine detection method is, unfortunately, the detonation of a mine in its intended role. The surest detection method is the individual soldier probing for mines by hand. This method is extremely slow and is obviously not conducted unless mines are suspected to be present. It is clearly

incompatible with rapid maneuver by mechanized forces. Detection methods can be described as active or passive. Active systems input energy of some form into the soil and attempt to detect changes caused by the presence of the mine. Passive systems rely on characteristics of mines which produce emissions either from the mine itself or as a result of soil disturbances.

Microwaves

A number of active detector types based on microwaves have been examined. These systems consist of microwave transmitters and receivers. The balanced bridge concept uses two transmitters or receivers to compare the reflected signal produced by adjacent areas simultaneously. The reflected signal from the mine is much smaller than those produced by reflection from the soil surface and by direct coupling between transmitter and receiver. If the soil is uniform in the vicinity of the buried mine and the detector electronics are symmetric, the soil reflection and direct coupling signals should be of the same amplitude and phase. Any difference resulting from subtraction of these signals represents the buried mine. The hand held nonmetallic mine detector in use today in the U.S. Army operates on this principle. The major problems with this detector are surface irregularities, soil attenuation, and soil inhomogeneities. False alarms can be generated by tree roots or air pockets. When used with visual inspection and probing, the detector is useful. The detector operates by producing

sounds in a head set, which have a tendency to make the operator tone deaf after a short period of time. The detector is obviously not appropriate for maneuver by mechanized forces.

Microwave systems which have been investigated, but not fielded have been based on the concepts using wave guide beyond cutoff, depolarization, short-pulse radar, frequency modulated-continuous wave (FM-CW) radar, and harmonic radar.

The wave guide beyond cutoff concept uses two dipoles, one to transmit and the other to receive. The dipoles are arranged in open cavities connected by a metal sheet. When the metal sheet is less than one-half wavelength above the ground, the direct coupled and surface reflection signals are greatly reduced, improving the capability to detect the signal from the mine. The major drawback of this system is height sensitivity. When the metal plate is more than one-half wavelength above the soil, false alarms are generated. Accordingly, use of a system based on this concept is limited to relatively level soil surface with little vegetation. This concept was used to produce an unfielded vehicular detection system for use on roads.

The depolarization scheme uses horizontally polarized transmitted microwaves with an orthogonally arranged, horizontally polarized receiver. If the soil surface is level and the soil isotropic, no signal will be detected. Linear features of buried objects depolarize the microwaves and produce a signal. Problems, in addition to soil

irregularities, included weak depolarization signals generated by round objects, a very common mine geometry.

High resolution, short-pulse radar detectors were shown to be very height insensitive and capable of detection in moderate vegetation. The major problem with the technique was a very high false alarm rate. A continuous wave radar (FM-CW) using the same antenna as the short-pulse system was also investigated. Problems with the signal generator led to termination of the effort. The harmonic radar system detected mines by their reradiation of harmonics of the transmitted beam frequency. The prototype detectors were capable of detecting surface laid mines at ranges of 8 to 10 meters. No detection of buried mines is possible.

Neutrons

Research on inelastic scattering of neutrons produced by a deuterium-tritium generator for mine detection was conducted by Texas Nuclear Corporation from 1964 to 1967. The ratio of response to the 4.42 MeV gamma ray of ^{12}C to the 1.78 MeV gamma ray of ^{28}Si was used as the detection mechanism. The explosive of the mine contains large amounts of carbon, while silicon is a major constituent of most soils. Sodium iodide was used in the first version of the system. Major problems were false alarms due to the presence of water which enhanced production of an oxygen capture gamma ray, height sensitivity, radiological hazard, and poor signal to noise ratio. The shielding required for the detector produced a system of mass of approximately 1100 kg,

capable of covering a path width of only 20 cm. This mass did not include biological shielding. A technique was developed to subtract the contribution from neutron capture in oxygen. Attempts at improving the system centered on the use of the then newly available Ge(Li) solid state detectors. The only positive result of this change was reduction in the shielding weight. The very small size crystals then available was the primary cause for this reduction, not a hoped for improvement in resolution. The resolution advantages of the Ge(Li) detectors were of no practical use because of Doppler broadening of the inelastically produced gamma rays. Additionally, neutron irradiation destroyed the Ge(Li) detectors after only after a few hours of use. The use of larger Ge(Li) detectors and time of flight methods did not overcome the problems of the system.

The use of the thermal $^{14}\text{N}(n,\gamma)^{15}\text{N}$ reaction had been considered, but rejected because of two problems. First, the count rate for the 10.8 MeV gamma ray produced in the reaction was very low, and second, the resolution of a NaI(Tl) detector was not adequate to separate this gamma from a 10.6 MeV gamma ray of silicon. With the advent of Ge(Li) detectors, this second problem vanished. The low count rate problem remained. Solving it required a much higher thermal neutron flux than was feasible at the time. In 1970, Triangle Research Institute proposed the use of ^{252}Cf as the neutron source. This approach was rejected because of weight requirements of the biological shield and

the radiological hazard represented by battlefield destruction of the source.

Magnetic Resonance Techniques

In 1965, Southwest Research Institute attempted to apply electron paramagnetic resonance to mine detection. To produce the free electron densities necessary for signal production, the explosive of the mine was irradiated. On the basis of extrapolation from experiments at liquid nitrogen temperature using ^{60}Co as the irradiation source, it was estimated that an exposure rate on 10^{12}R/hr would be required. Accordingly, the program was terminated.

In 1972, Southwest Research Institute proposed to use nuclear magnetic resonance for mine detection. Differentiation between hydrogen in explosives and water in soil was demonstrated in laboratory experiments. An electromagnet was constructed which was capable of producing a homogeneous magnetic field at a distance of 10 cm from its coils. A detector system based on this technique was built in 1974. Problems included a 20 second time period to obtain a single measurement, and the inability to detect anything beyond 10 cm range of the field. This 10 cm limit included the distance from the coils in air to the soil surface, severely limiting the depth of detection in soil. These problems and failure of the device to operate properly during field tests caused termination of the effort.

Trace Gases

A wide range of techniques have been used in an attempt to detect buried mines by sensing TNT vapor. The vapor pressure of TNT corresponds to concentrations of the order of parts per billion. In the mine detection problem, the concentration is reduced by the presence of the mine case and soil. Soil permeabilities are such that 1 to 2 days are required for vapors to escape to the surface in sandy soils, and much longer in clay soils.

Early efforts, made by the Illinois Institute of Technology, used electrical discharge in a helium carrier gas for the vapor to produce a plasma containing nitrous oxide from the breakdown of TNT. Detection was based on spectroscopic examination for the characteristic emissions from nitrous oxide. Because trace amounts of nitrous oxide exist in air and because it can be formed in air at high temperatures, the vapors were first condensed. Air was then purged from the system, the condensate heated and flushed with helium gas to carry it into the detector. Laboratory experiments were able to detect at approximately 1 part in 10^{11} , but problems with lack of reproducibility, air contamination and residual condensate contamination caused termination of the project. Other efforts to detect TNT vapors included the electron capture concept, which relied on the high electron affinity of TNT; mass spectrometry; and plasma chromatography. None were capable of achieving the level of sensitivity required for timely mine detection.

Animals

Animals appear to be much more sensitive detectors of the vapors of TNT than any man-made device. The actual detection mechanism used by animals is unknown, but the sense of smell probably plays an important role. Properly trained dogs were shown to be able to detect mines over a wide range of environments. Field test showed detection rates as high as 90% with false alarm rates below 15%. The program was terminated by the Army because of perceived incompatibility of dogs and mechanized warfare, and their vulnerability.

A wide range of other animals have also been used in attempts to detect TNT. These include badger, coatimundi, coyote, deer, ferret, fox, hog, javelina, miniature pig, opossum, raccoon, three skunk species and timber wolf. A complex detection system, based on training rats to detect TNT vapor by direct stimulation of the pleasure center of the brain has been studied. TNT detection was accomplished by monitoring the electroencephalograph of the rat for a feature characteristic of activity in the pleasure center. The system is said to be ready for field testing, but primarily in an anti-terrorist explosives detection role.

Biochemical Methods

Experiments with bioluminescent bacteria were conducted by RPC Corporation, which demonstrated that certain bacteria produced visible light in the presence of TNT vapor which had been heated to 100°C. Bacteria were grown in nutrient

solutions and then transferred to an agar cartridge for use in a mine detection system. Air containing TNT vapor was drawn through the detector. The light output from the bacteria was detected by a photomultiplier. Attempts to increase the sensitivity of the bacteria to TNT vapor to levels required for mine detection application were unsuccessful.

A second biochemical approach was suggested by the observation that soil bacteria were able to chemically alter TNT, implying the existence of an enzyme responsible for the change. The enzyme was isolated by growing soil bacteria in nutrient media containing TNT. The enzyme, TNT reductase, is used as a catalyst in a reaction involving TNT and hydrogenated nicotinamide adenine dinucleotide (NADH), which produced a TNT dependent decrease in NADH. A luminescent system is used to measure the reduction in NADH. At present the method is not sensitive enough for application to mine detection and requires approximately 5 minutes for assay.

Infrared Methods

In 1953, work by the U.S. Army Engineer Research and Development Laboratories indicated that differences in the thermal properties of soil, and soil with buried mines might be used as a detection method. Differences in thermal conductivity and heat capacity in the two cases cause temperature differences. Because the thermal conductivity of a mine is less than that of moderately moist soil, the disturbed soil above the mine loses heat faster at night and

gains heat more rapidly during the day than surrounding undisturbed soil. In very dry soils, the thermal conductivities are approximately the same and no temperature differences occur. Additionally, very moist soils, air temperatures below freezing, shadows, long duration cloud cover, vegetation, and wind were also found to adversely affect this detection mechanism. Detection was best at night or first light due to thermal clutter during daylight hours. A number of infrared based detector systems were built and tested. Under favorable environmental conditions, the technique worked well for rapid detection of mines buried in roads.

Mine Neutralization

An alternative to the detection of mines is their neutralization. When a minefield is adversely encountered or detected by some other means, devices which destroy or move mines to clear a path through them can be employed. As was the case for the detection mechanisms, a wide range of methods have been tried.

Mechanical Systems

Three mechanical devices have been used by various armies to neutralize mines. In each case the device precedes the vehicle to which it is attached into a minefield. Rollers are heavy metal wheels designed to detonate pressure fuzed mines. Delayed fuzing or fuzing on a second pressure pulse are simple methods to defeat the roller (Shelkin, 1986). The number of mine encounters is limited before the

rollers themselves are rendered inoperable by detonating mines. The flail consists of chains or metal rods rotated at high speed which fragment buried mines. Very high power is required to maintain the necessary speed of rotation while penetrating soil. The plow pushes soil and buried mines out of the vehicle path. Very high power is also required for this system. Because of the power disadvantage described, each of these systems slows the speed of the pushing vehicle tremendously, increasing its vulnerability to direct fires. Accordingly, they are not normally attached to a vehicle and must be brought forward and attached when needed. Only the roller exists in the U.S. inventory.

Explosive Methods

Mines may be destroyed by a combination of pressure or impulse from an explosive detonation. Since pressure and impulse drop rapidly with distance from the point of detonation, explosives may be used in point or line charges to clear individual mines or paths through minefields. In a dispersed form explosives may be used to clear larger areas. Point methods include placement of explosive blocks on located mines, or the use of artillery or bombs against minefields. Line charge methods include rigid pipes of explosive which are pushed into minefields and detonated, or projected, flexible charges which are deployed by rocket over the minefield. Small numbers of line charges exist in the U.S. inventory. Area clearance devices which have been investigated are fuel-air explosives and dispersed high

explosives. The fuel-air explosive technique requires delivery of an explosive gas on the minefield, the mixing of the gas with atmospheric oxygen and detonation of the resulting cloud. A U.S. system using rockets to deliver the explosive has been developed and tested, but not fielded. The dispersed high explosive method is similar to the fuel-air explosive, but carries its own oxygen.

Magnetic Signature Duplicator

Devices have been built which project the magnetic signature of a vehicle. This projected signal detonates magnetically fuzed mines before they are encountered by the vehicle.

APPENDIX D
X-RAY TRANSMISSION CALCULATIONS
AND MEASUREMENTS

This appendix provides graphs of the results of calculations and measurements of x-ray exposure rate transmission. The measured transmission curves are the result of experiments using the Maxitron 300 X-Ray Therapy Unit (General Electric, 1962). Aluminum attenuators and an MDH Industries 1015 X-Ray Monitor arranged in the geometry recommended for half value layer measurements (Johns and Cunningham, 1983) are used to determine the transmission of exposure rate curves. Various combinations of peak kilovoltage and filtration are used. The calculated transmission curves derive from the XRSPEC.PAS code discussed in Chapter V. These calculations are made for each of the measured cases. The figures provided in this appendix show the fluence spectrum computed and a comparison of the measured and calculated exposure rate transmission curves.

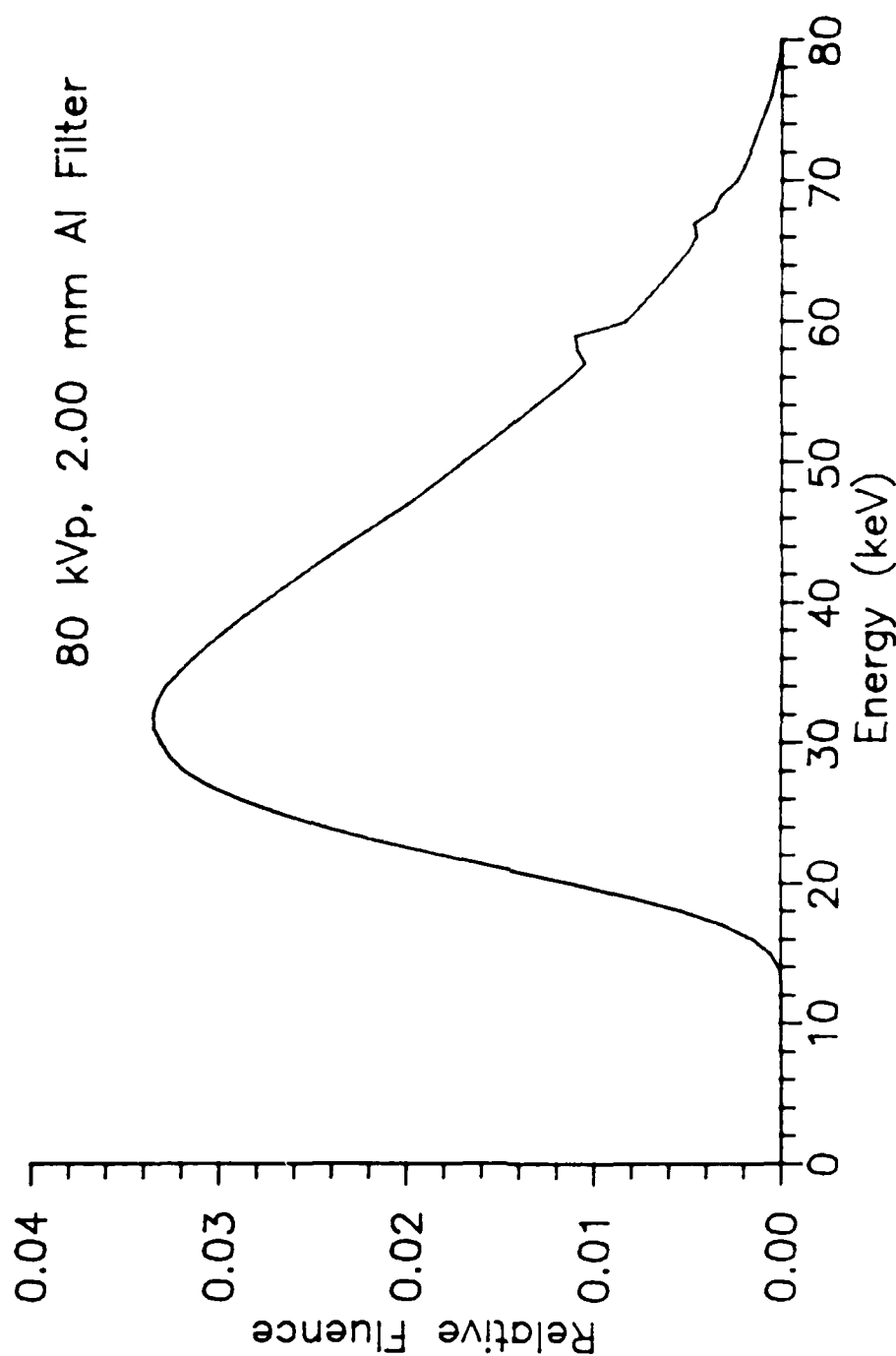


Figure D.1. X-ray fluence spectrum, 80 kVp, 2.00 mm Al. The x-ray spectrum at 80 kVp calculated by the XRSPEC.PAS code for the GE Maxitron 300 X-Ray Therapy Unit with 4.75 mm beryllium inherent filtration, 2.00 mm aluminum added filtration (includes 0.25 mm aluminum equivalent monitor ionization chamber) and air path length of 90.17 cm is shown. Fluence units are photons per cm^2 per keV. Total fluence is normalized to 1 photon per cm^2 .

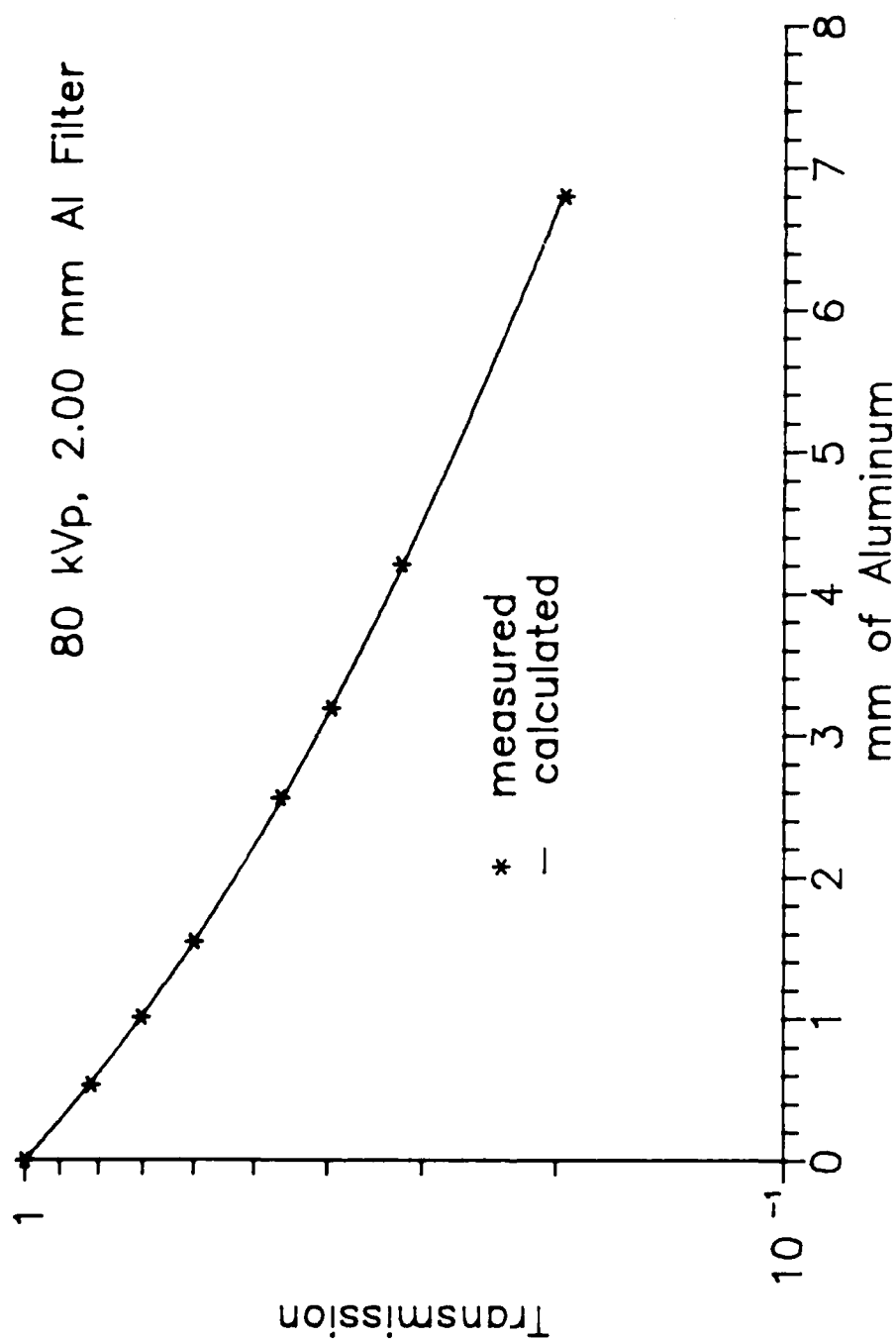


Figure D.2. Measured and calculated transmission of exposure rate, 80 kVp, 2.00 mm Al. A comparison of measured and calculated transmission of exposure rate of a 80 kVp beam produced by the GE Maxitron 300 X-Ray Therapy Unit with 4.75 mm beryllium inherent filtration, 2.00 mm aluminum added filtration and air path length of 90.17 cm is shown. The calculated transmission of exposure rate is based upon the spectrum shown in Figure D.1.

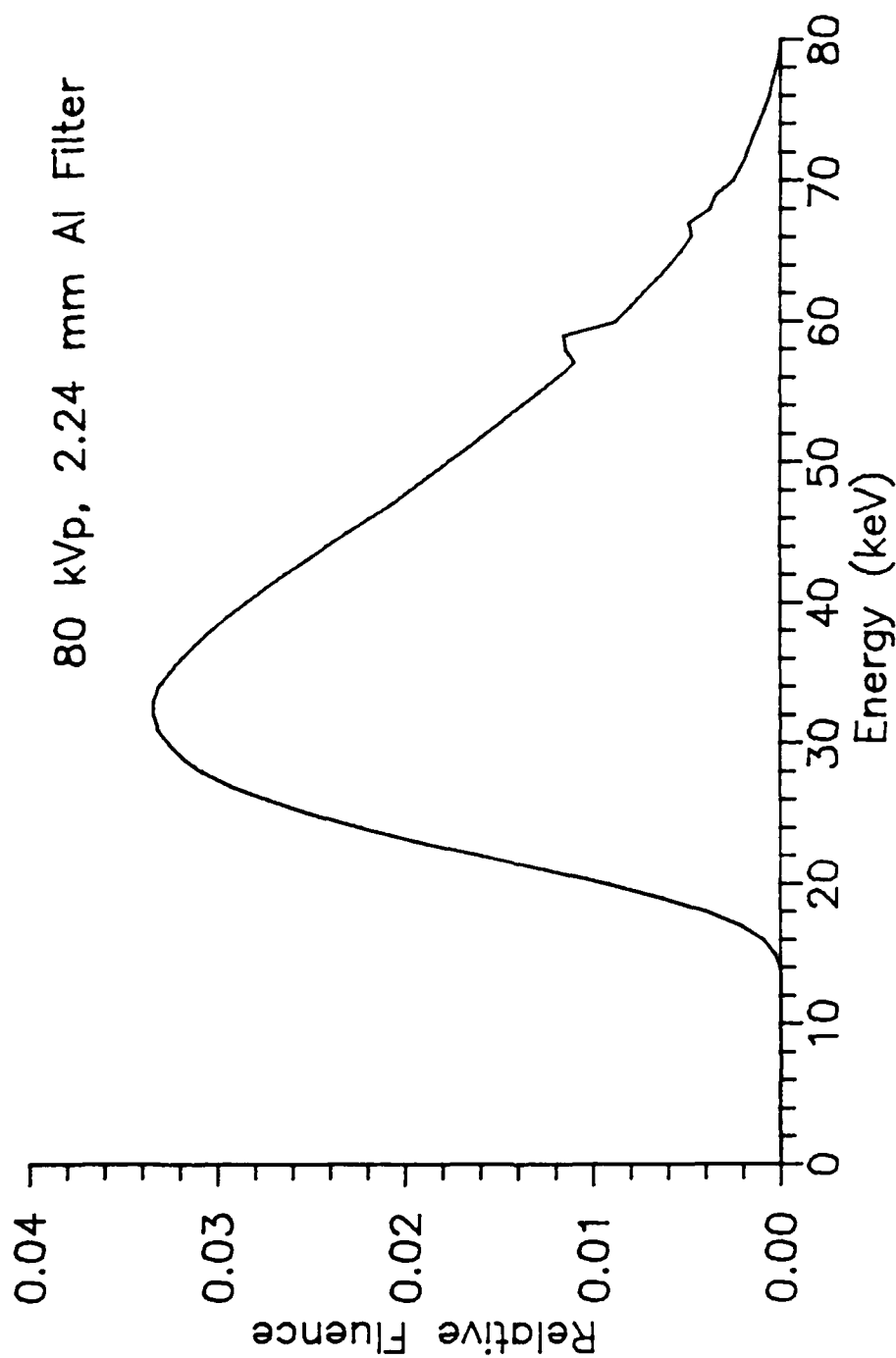


Figure D.3. X-ray fluence spectrum, 80 kVp, 2.24 mm Al. The x-ray spectrum at 80 kVp calculated by the XRSPEC.PAS code for the GE Maxitron 300 X-Ray Therapy Unit with 4.75 mm beryllium inherent filtration, 2.24 mm aluminum added filtration (includes 0.25 mm aluminum equivalent monitor ionization₂ chamber) and air path length of 90.17 cm is shown. Fluence units are photons per cm² per keV. Total fluence is normalized to 1 photon per cm².

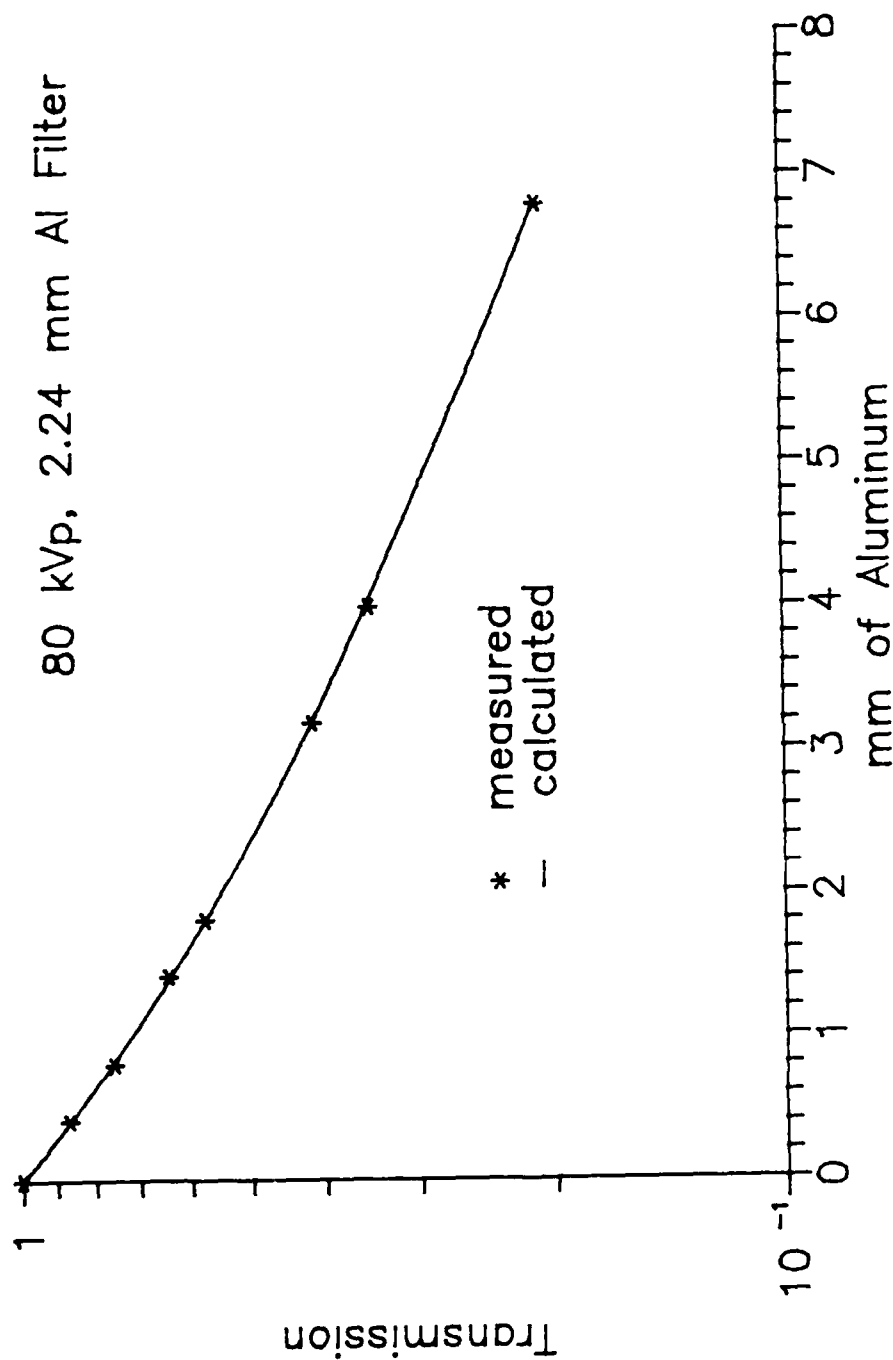


Figure D.4. Measured and calculated transmission of exposure rate, 80 kVp, 2.24 mm Al. A comparison of measured and calculated transmission of exposure rate of a 80 kVp beam produced by the GE Maxitron 300 X-Ray Therapy Unit with 4.75 mm beryllium inherent filtration, 2.24 mm aluminum added filtration and air path length of 90.17 cm is shown. The calculated transmission of exposure rate is based upon the spectrum shown in Figure D.3.

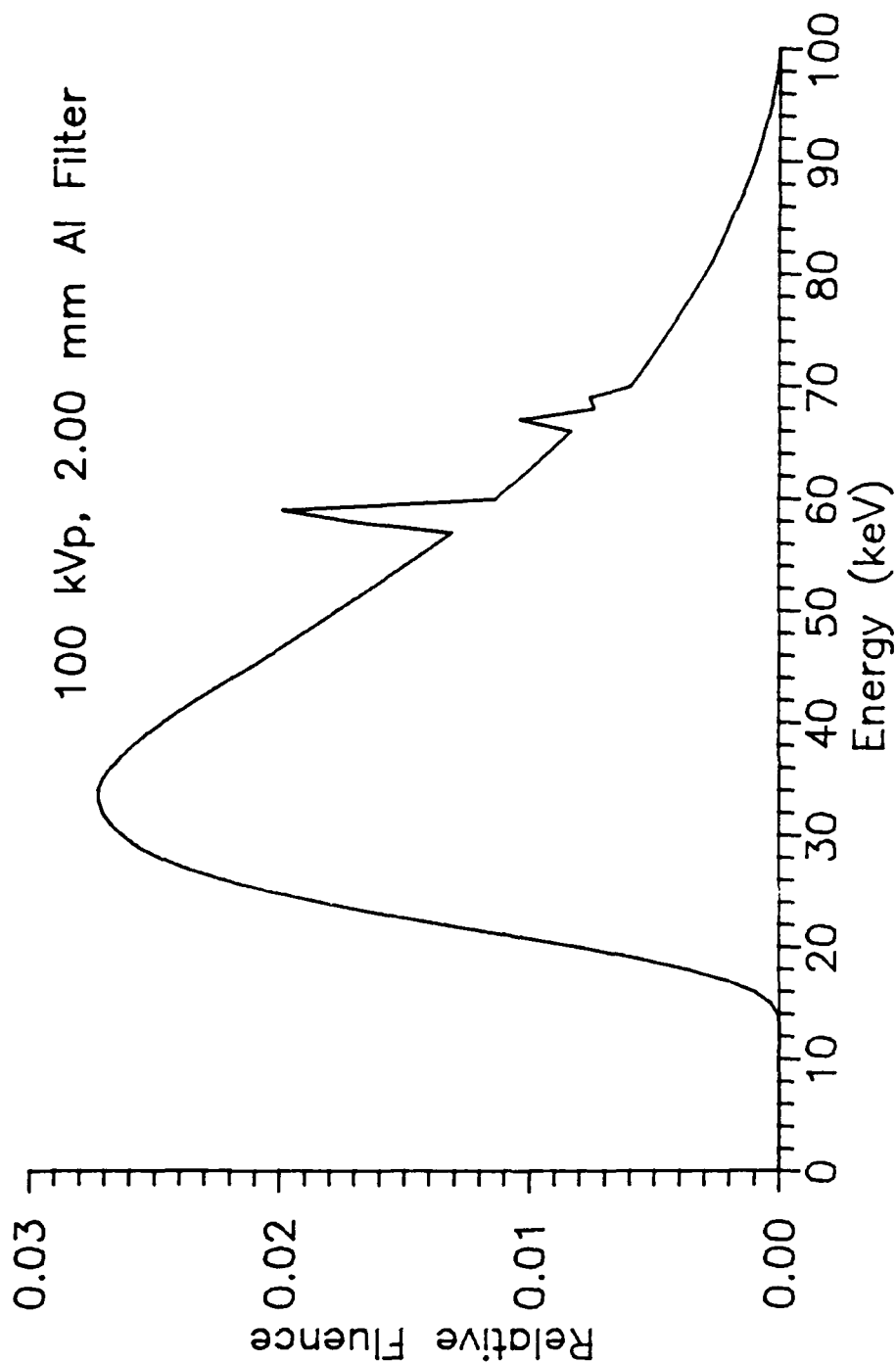


Figure D.5. X-ray fluence spectrum, 100 kVp, 2.00 mm Al. The x-ray spectrum at 100 kVp calculated by the XRSPEC.PAS code for the GE Maxitron 300 X-Ray Therapy Unit with 4.75 mm beryllium inherent filtration, 2.24 mm aluminum added filtration (includes 0.25 mm aluminum equivalent monitor ionization₂ chamber) and air path length of 90.17 cm is shown. Fluence units are photons per cm² per keV. Total fluence is normalized to 1 photon per cm².

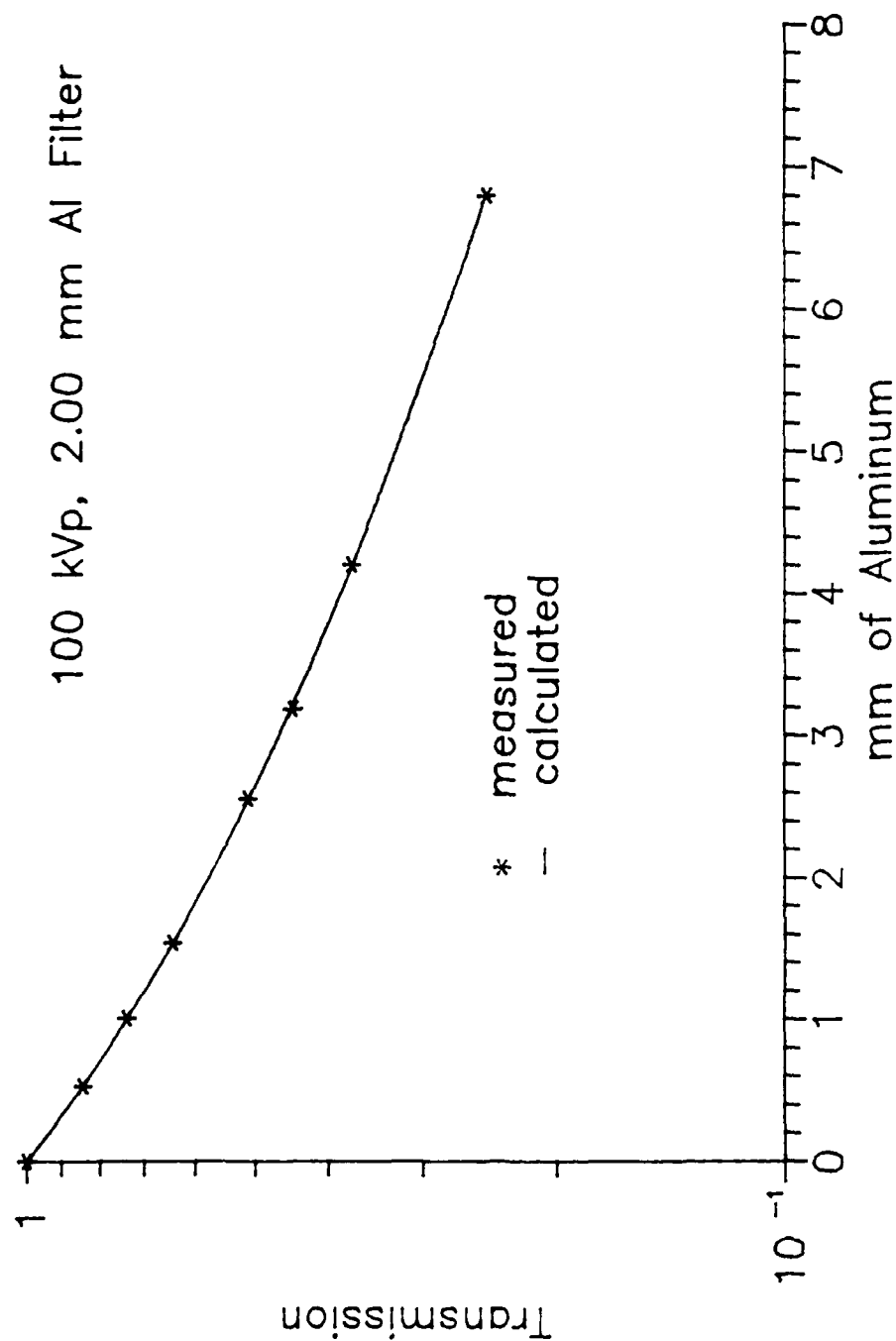


Figure D.6. Measured and calculated transmission of exposure rate, 100 kVp, 2.00 mm Al. A comparison of measured and calculated transmission of exposure rate of a 100 kVp beam produced by the GE Maxitron 300 X-Ray Therapy Unit with 4.75 mm beryllium inherent filtration, 2.00 mm aluminum added filtration and air path length of 90.17 cm is shown. The calculated transmission of exposure rate is based upon the spectrum shown in Figure D.5.

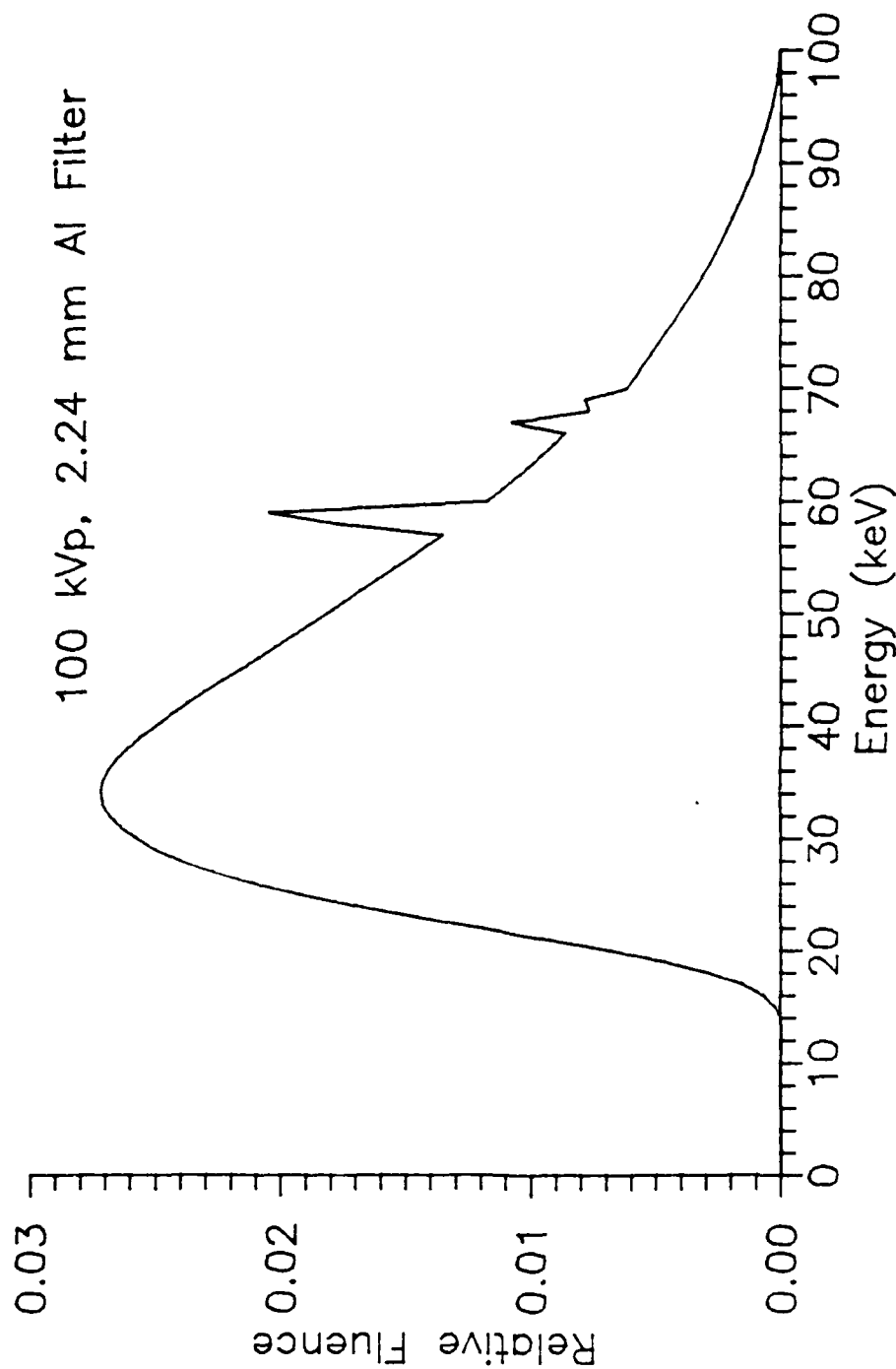


Figure D.7. X-ray fluence spectrum, 100 kVp, 2.24 mm Al. The x-ray spectrum at 100 kVp calculated by the XRSPEC.PAS code for the GE Maxitron 300 X-Ray Therapy Unit with 4.75 mm beryllium inherent filtration, 2.24 mm aluminum added filtration (includes 0.25 mm aluminum equivalent monitor ionization₂ chamber) and air path length of 90.17 cm is shown. Fluence units are photons per cm² per keV. Total fluence is normalized to 1 photon per cm².

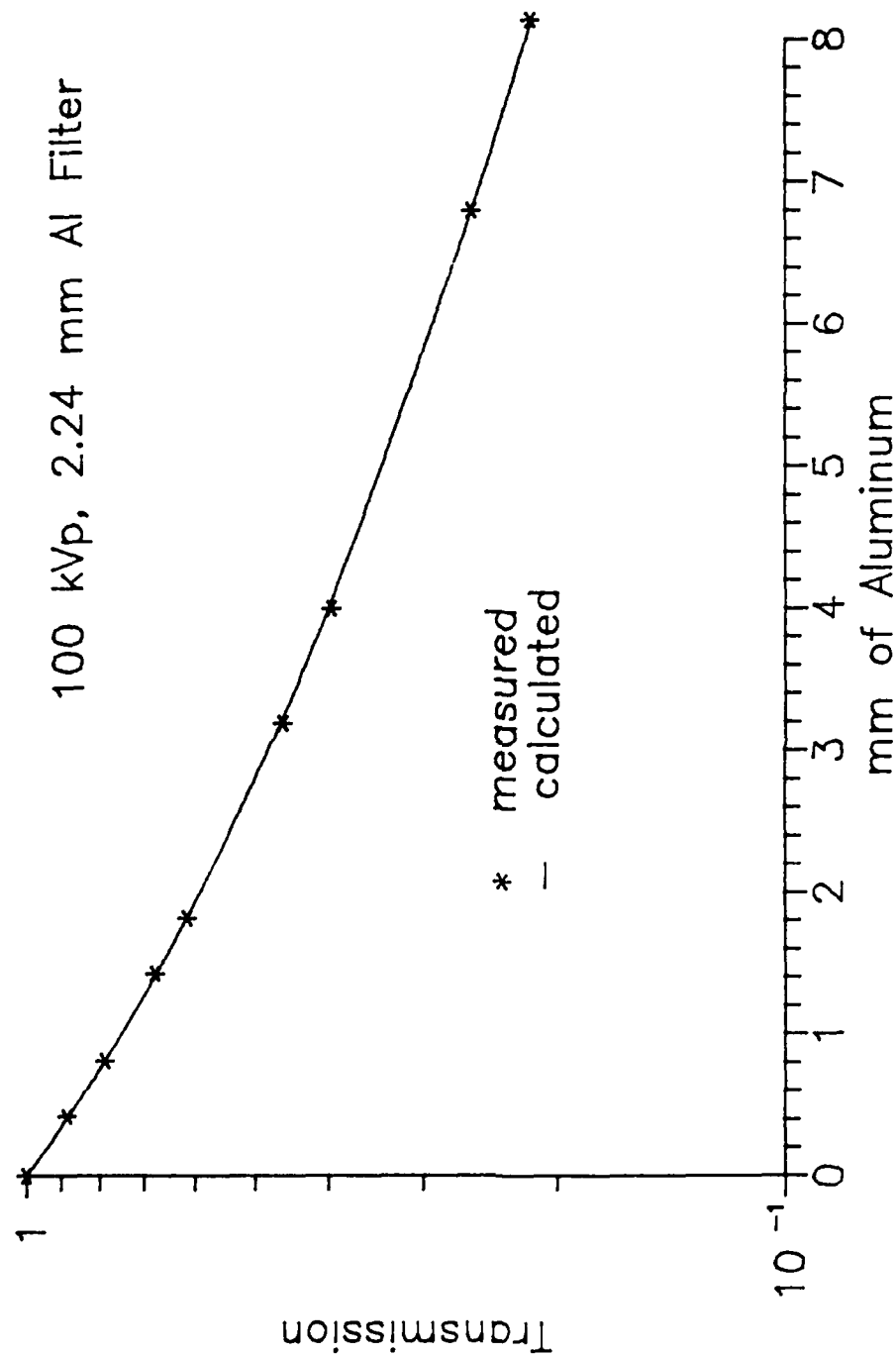


Figure D.8. Measured and calculated transmission of exposure rate, 100 kVp, 2.24 mm Al. A comparison of measured and calculated transmission of exposure rate of a 100 kVp beam produced by the GE Maxitron 300 X-Ray Therapy Unit with 4.75 mm beryllium inherent filtration, 2.24 mm aluminum added filtration and air path length of 90.17 cm is shown. The calculated transmission of exposure rate is based upon the spectrum shown in Figure D.7.

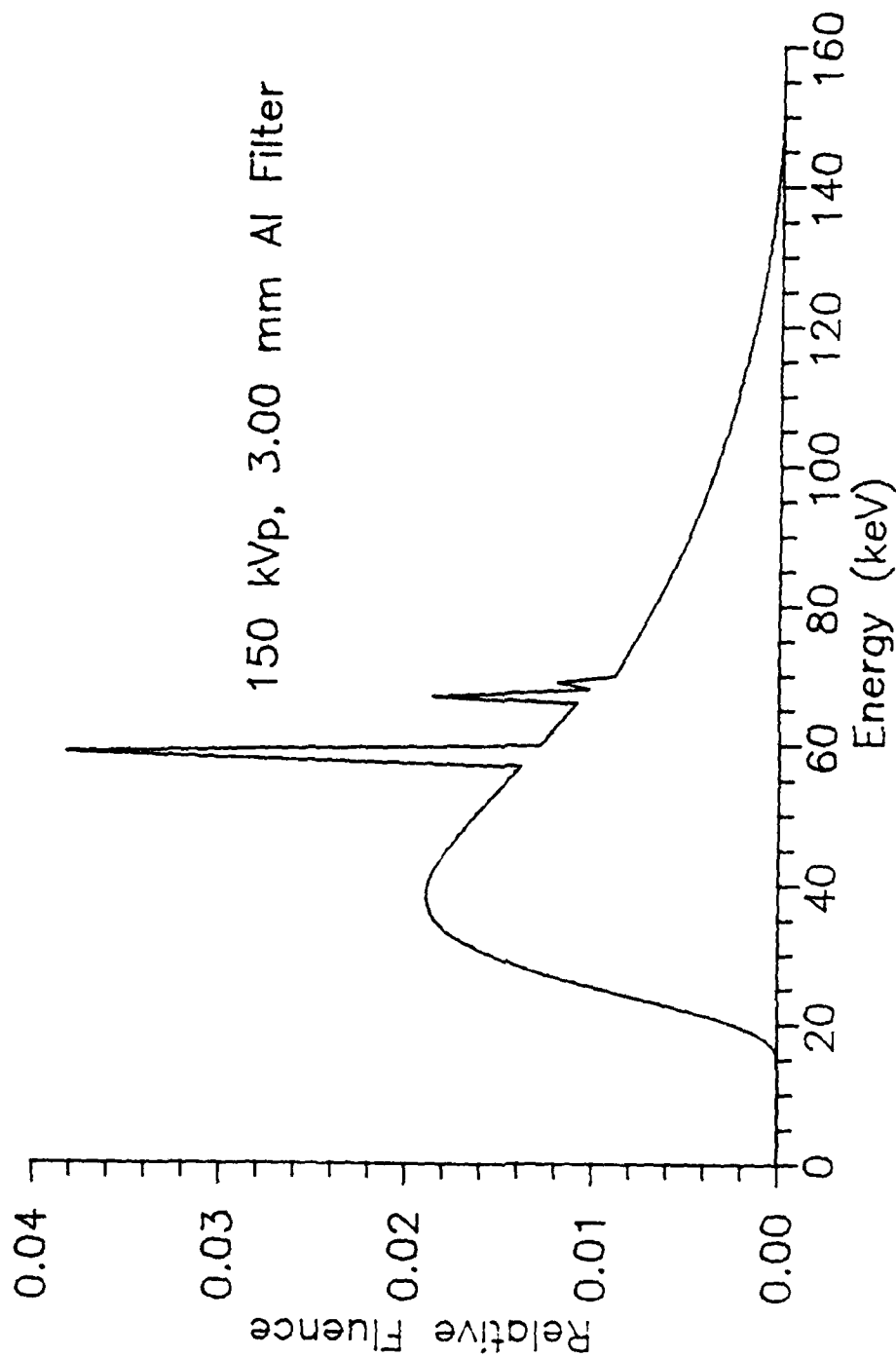


Figure D.9. X-ray fluence spectrum, 150 kVp, 3.00 mm Al. The x-ray spectrum at 150 kVp calculated by the XRSPEC.PAS code for the GE Maxitron 300 X-Ray Therapy Unit with 3.00 mm beryllium inherent filtration, 2.24 mm aluminum added filtration (includes 0.25 mm aluminum equivalent monitor ionization₂ chamber) and air path length of 90.07 cm is shown. Fluence units are photons per cm² per keV. Total fluence is normalized to 1 photon per cm².

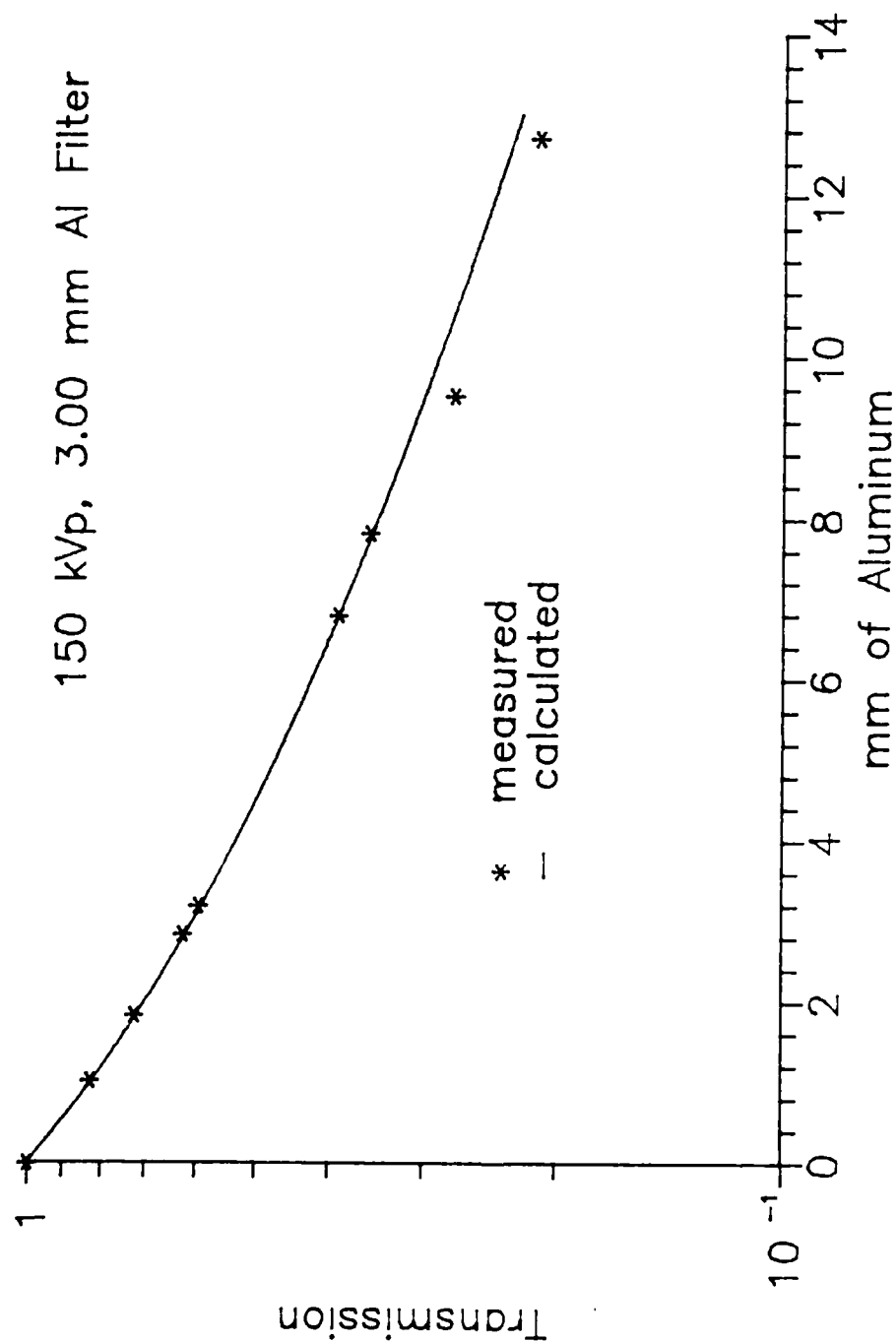


Figure D.10. Measured and calculated transmission of exposure rate, 150 kVp, 3.00 mm Al. A comparison of measured and calculated transmission of exposure rate of a 150 kVp beam produced by the GE Maxitron 300 X-Ray Therapy Unit with 4.75 mm beryllium inherent filtration, 3.00 mm aluminum added filtration and air path length of 90.07 cm is shown. The calculated transmission of exposure rate is based upon the spectrum shown in Figure D.9.

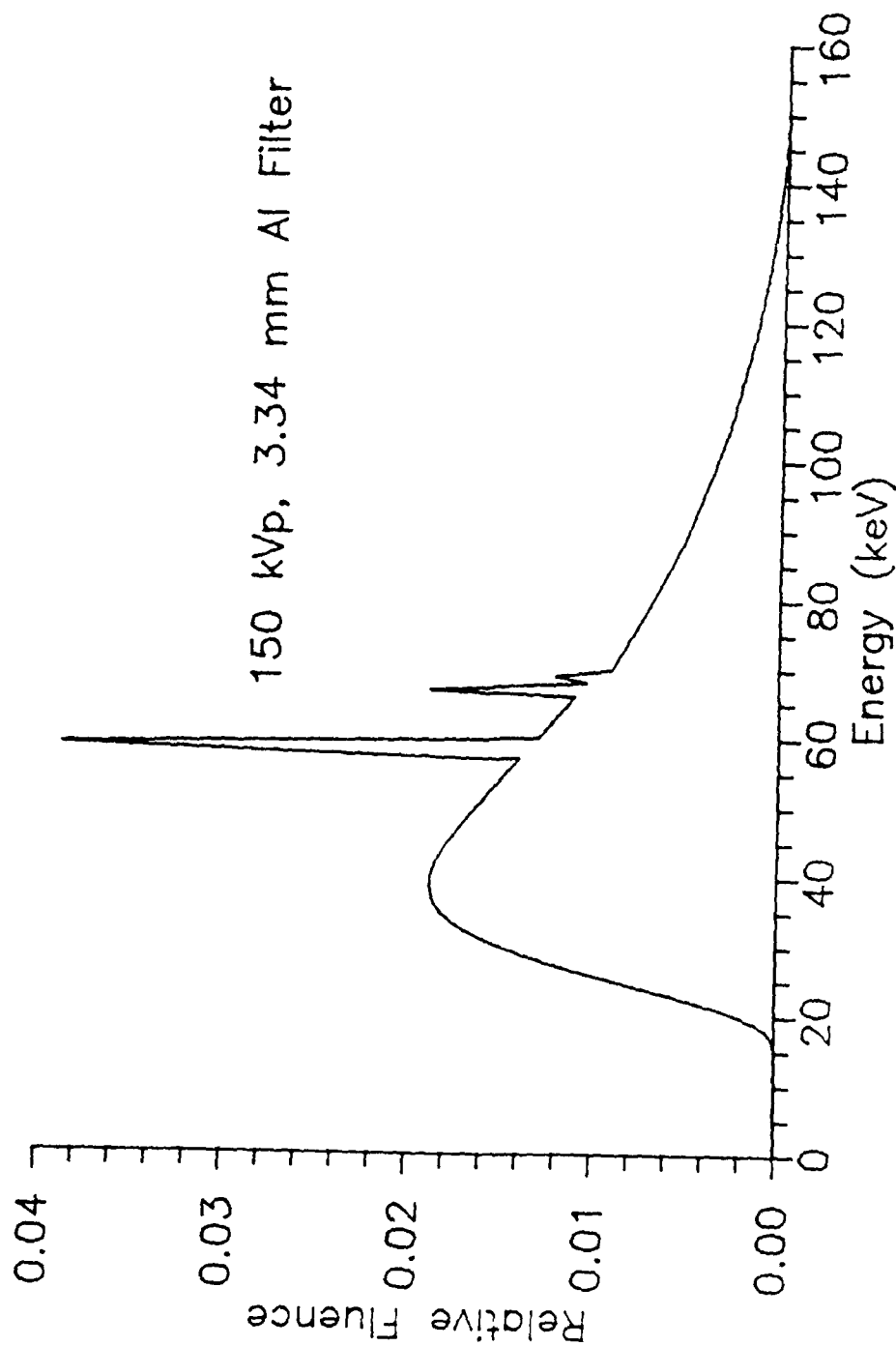


Figure D.11. X-ray fluence spectrum, 150 kVp, 3.34 mm Al. The x-ray spectrum at 150 kVp calculated by the XRSPEC.PAS code for the GE Maxitron 300 X-Ray Therapy Unit with 4.75 mm beryllium inherent filtration, 3.34 mm aluminum added filtration (includes 0.25 mm aluminum equivalent monitor ionization₂ chamber) and air path length of 90.07 cm is shown. Fluence units are photons per cm² per keV. Total fluence is normalized to 1 photon per cm².

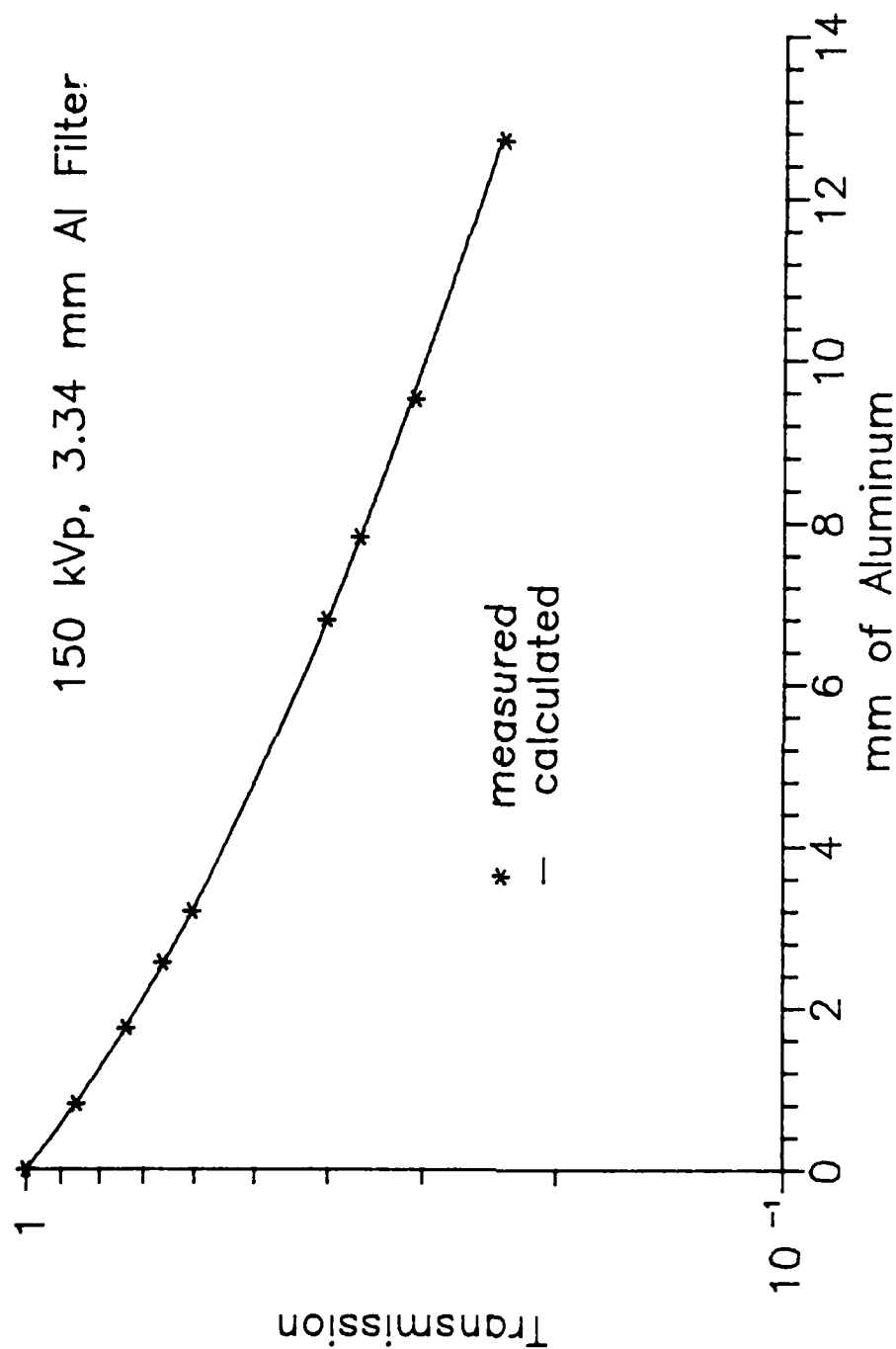


Figure D.12. Measured and calculated transmission of exposure rate, 150 kVp, 3.34 mm Al. A comparison of measured and calculated transmission of exposure rate of a 150 kVp beam produced by the GE Maxitron 300 X-Ray Therapy Unit with 4.75 mm beryllium inherent filtration, 3.34 mm aluminum added filtration and air path length of 90.07 cm is shown. The calculated transmission of exposure rate is based upon the spectrum shown in Figure D.11.

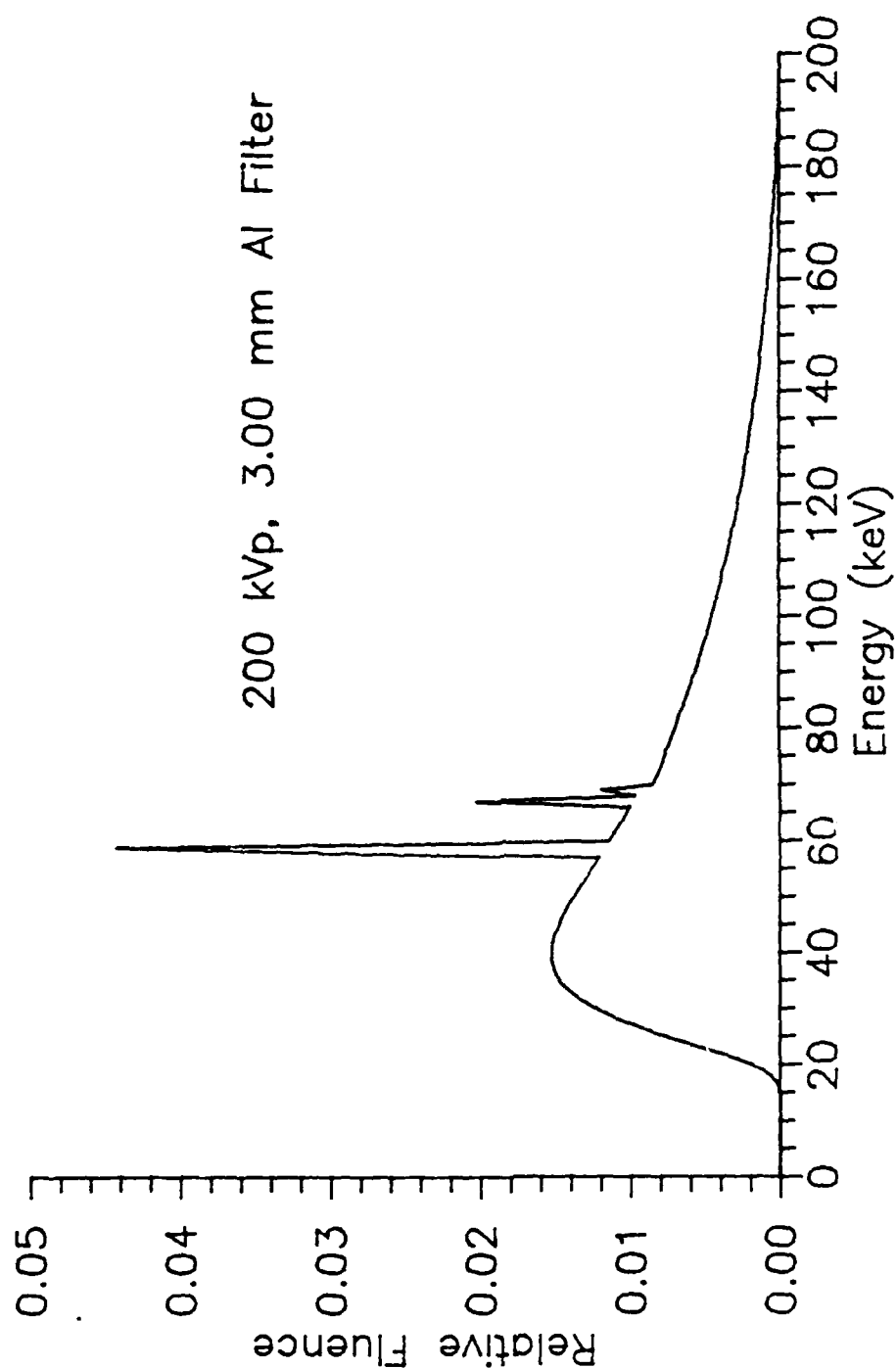


Figure D.13. X-ray fluence spectrum, 200 kVp, 3.00 mm Al. The x-ray spectrum at 200 kVp calculated by the XRSPEC.PAS code for the GE Maxitron 300 X-Ray Therapy Unit with 4.75 mm beryllium inherent filtration, 3.00 mm aluminum added filtration (includes 0.25 mm aluminum equivalent monitor ionization₂ chamber) and air path length of 90.07 cm is shown. Fluence units are photons per cm² per keV. Total fluence is normalized to 1 photon per cm².

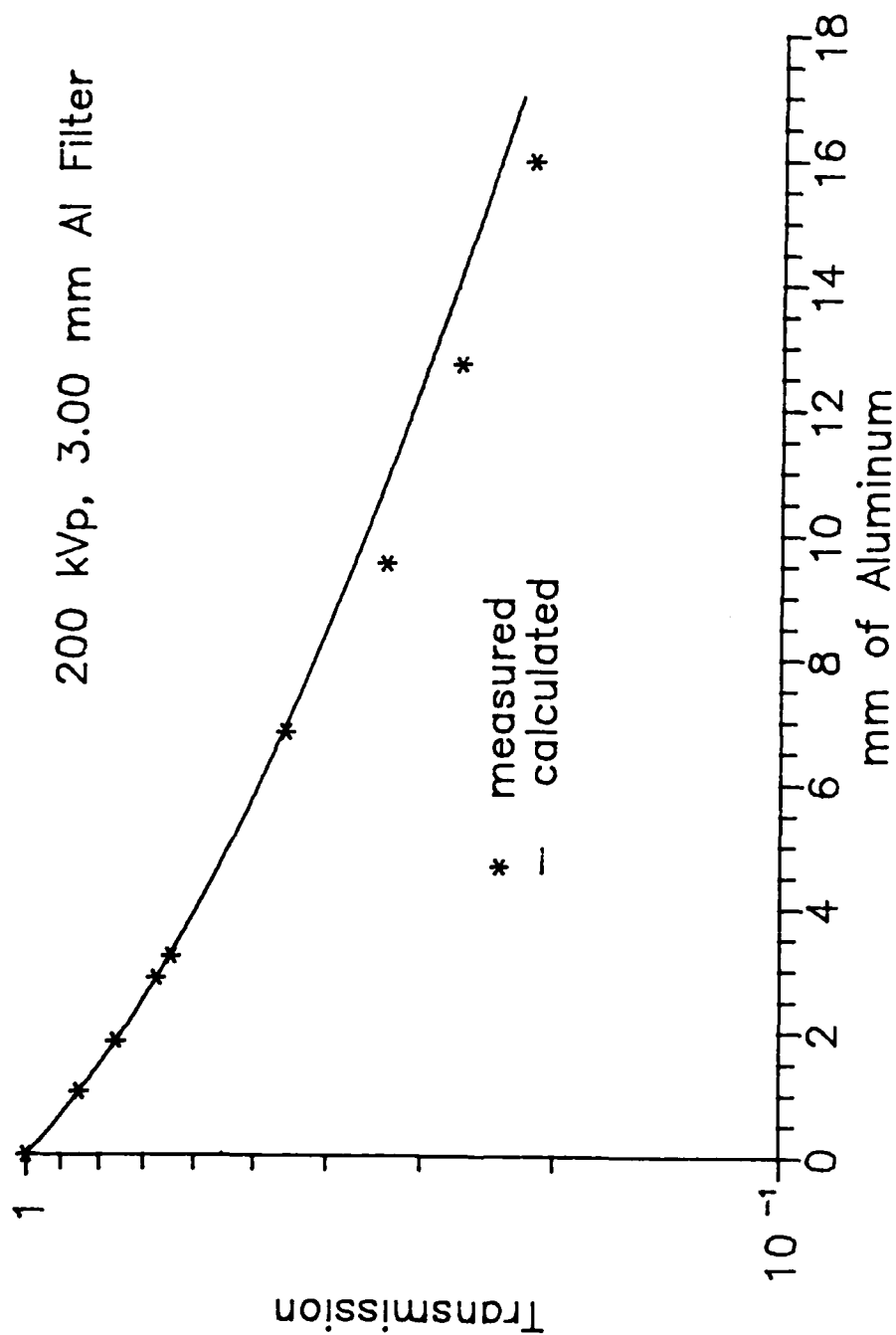


Figure D.14. Measured and calculated transmission of exposure rate, 200 kVp, 3.00 mm Al. A comparison of measured and calculated transmission of exposure rate of a 200 kVp beam produced by the GE Maxitron 300 X-Ray Therapy Unit with 4.75 mm beryllium inherent filtration, 3.00 mm aluminum added filtration and air path length of 90.07 cm is shown. The calculated transmission of exposure rate is based upon the spectrum shown in Figure D.13.

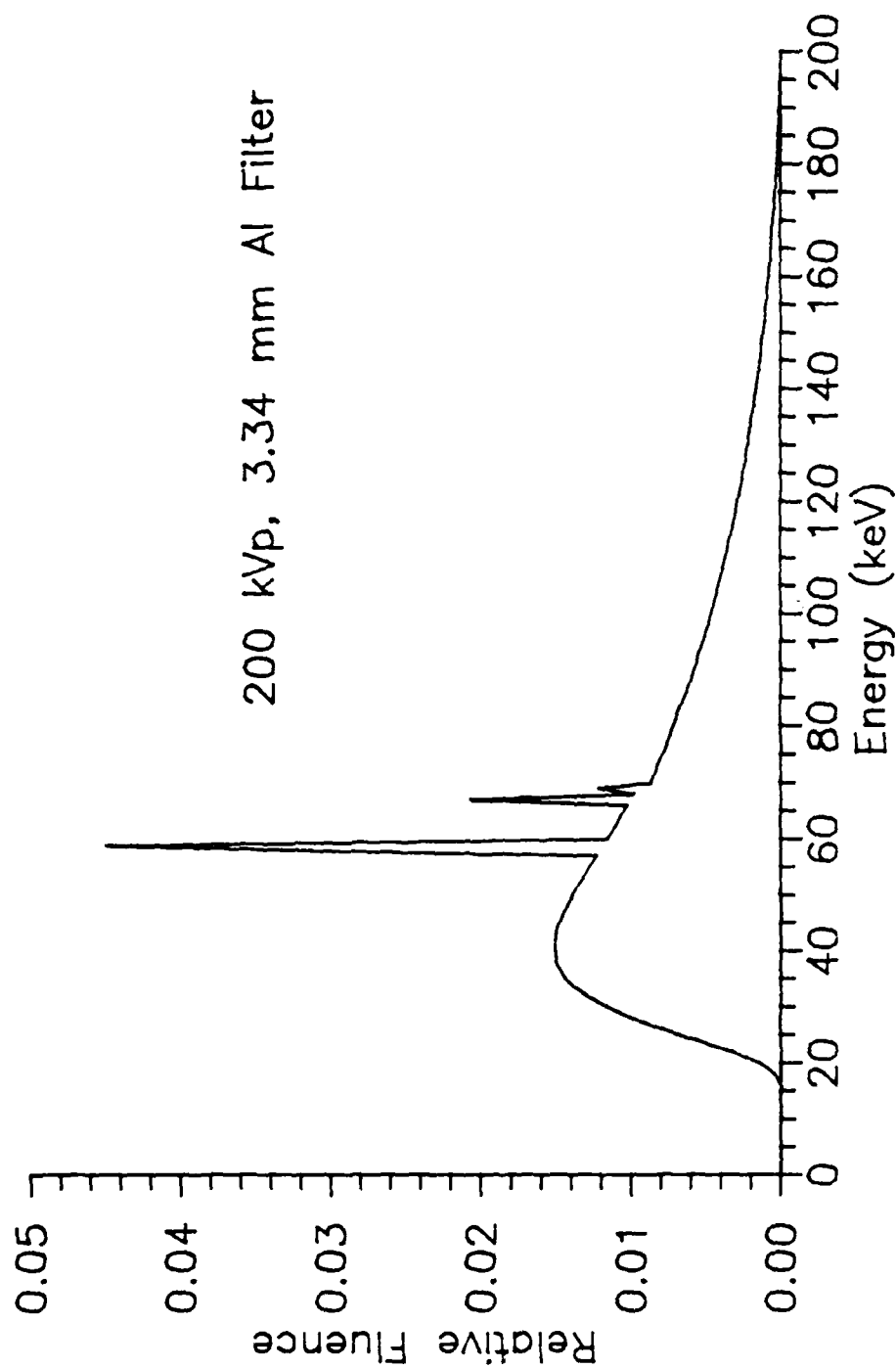


Figure D.15. X-ray fluence spectrum, 200 kVp, 3.34 mm Al. The x-ray spectrum at 200 kVp calculated by the XRSPEC.PAS code for the GE Maxitron 300 X-Ray Therapy Unit with 4.75 mm beryllium inherent filtration, 3.34 mm aluminum added filtration (includes 0.25 mm aluminum equivalent monitor ionization₂ chamber) and air path length of 90.07 cm is shown. Fluence units are photons per cm² per keV. Total fluence is normalized to 1 photon per cm².

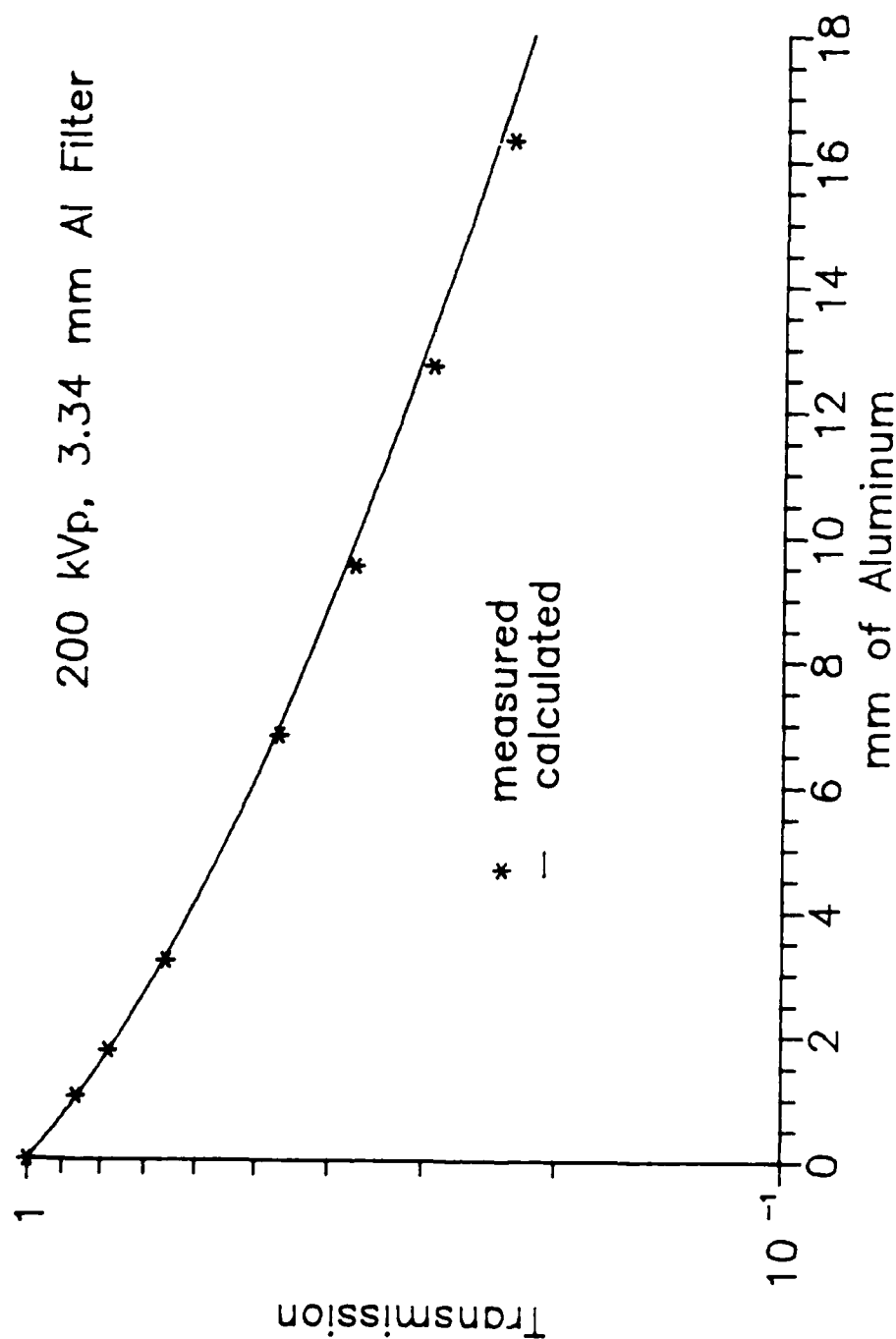


Figure D.16. Measured and calculated transmission of exposure rate, 200 kVp, 3.34 mm Al. A comparison of measured and calculated transmission of exposure rate of a 200 kVp beam produced by the GE Maxitron 300 X-Ray Therapy Unit with 4.75 mm beryllium inherent filtration, 3.34 mm aluminum added filtration and air path length of 90.07 cm is shown. The calculated transmission of exposure rate is based upon the spectrum shown in Figure D.15.

APPENDIX E

GADOLINIUM OXYSULFIDE DETECTOR

The use of terbium activated gadolinium oxysulfide x-ray intensifying screens for the mine detection system was suggested by the Belvoir Research and Development Center (Roder, 1985) as a method of providing a sensitive and inexpensive, large area detector. High sensitivity and large areas are desired to increase count rates in order to minimize the power requirements of the x-ray source. In accordance with these objectives, the detector shown in Figure E.1 was constructed by Moss (1986). As described below, this detector proves unsuitable for use in the mine detection system. Nevertheless, similar detectors based on different intensifying screen materials could prove useful. Large area coverage will be required for an operational antitank mine detection system. The analysis of such detectors would closely follow the description given in this appendix.

Detector Description

Detector Design

The active region of the detector consists of two sheets of 3M Corporation's Trimax 12 rare earth intensifying screen material (3M, 1985a). The 3M Trimax 12 set consists

Figure E.1. Gadolinium oxysulfide based detector.



of two screens. The screen which is normally placed nearest the x-ray source contains less gadolinium oxysulfide than the other. The screen nearest the source is called the front screen; the other, the back screen. To increase the sensitivity of the mine detection system, two back screens are used in the detector constructed by Moss. A diagram of the active region is shown in Figure E.2. The two intensifying screens are placed back to back with the phosphor sides facing away from each other. Normally, the two phosphor layers, covered by their protective coatings, face each other with an x-ray film sandwiched between. In the outward facing configuration, visible light photons resulting from x-ray interactions in the phosphor are collected by angled mylar reflectors, and directed to the face of a large photomultiplier tube. The lower half of the reflector is attached to thin cardboard to allow x-ray photons scattered by soil or buried materials to reach the screens without significant attenuation.

Screen Composition

The 3 M Trimax 12 screens were selected because of their large phosphor thickness and their emission spectrum (described below). For proprietary reasons, little information is available concerning the composition of the screens. To make matters worse, the two sets of screens purchased have back screens which differ in mass by more than 6%. Since the serial numbers of the two back screens reveal that they are from the same batch, considerable

Second Protective Layer
Second Phosphor Layer
Second Reflecting Layer
Second Base Layer
Cardboard Support Layer
First Base Layer
First Reflecting Layer
First Phosphor Layer
First Protective Layer

Figure E.2. Active region of the detector. The layers of the active region of the detector are shown (not to scale). This portion of the detector is constructed from two 3M Trimax 12 terbium activated gadolinium oxysulfide x-ray intensifying screens. Thicknesses, compositions and densities of the layers are given in Table E.1.

variability in composition is indicated. Communications with 3M Corporation indicate that this variation in mass is not unusual (Frank, 1986). Additional information concerning the screen composition was provided in those communications and by 3M product brochures (3M, 1985a). Unfortunately, that information is incompatible with the measured masses of the screens. 3M Corporation suggests that the discrepancy may be due to entrained air in the phosphor layer (Frank, 1986).

Given the mass variability and the apparent discrepancies in the compositions and thicknesses, x-ray attenuation measurements were performed to determine the actual thicknesses of gadolinium oxysulfide in the screens. Preliminary Monte Carlo calculations indicated that the attenuation properties of the screens depend almost entirely on only the gadolinium oxysulfide in the phosphor layer. With this in mind, a model of the screen was constructed using the information provided by 3M for all layers except the phosphor. To determine the phosphor layer composition and thickness, a modification of a method used by Venema (1979) to address the same lack of information for x-ray intensifying screens due to proprietary reasons is employed. Venema assumes that screens under investigation are composed of pure gadolinium oxysulfide. He then measures the attenuation produced by the screens when subjected to an x-ray source, and based upon these results, calculates the thicknesses of the gadolinium oxysulfide in mg/cm^2 . The method used in this

research uses the same technique as a first estimate of the gadolinium oxysulfide thickness and then employs an iterative method to include the effects of the other materials present in the screen.

In order to perform the calculations for the iterative procedure, an accurate knowledge of the x-ray source spectrum used is required. The XRSPEC.PAS code is used for this purpose. Preliminary measurements with the desired spectrum are made to verify the spectrum using attenuation of exposure rate by aluminum. Other examples of this type of measurement check are given in Appendix D. The calculation of the fluence spectrum used in the measurements to determine the phosphor layer composition is shown in Figure E.3 along with its exposure rate transmission curves. The agreement between the measured and calculated curves is excellent. Additional exposure rate transmission measurements with this spectrum are made with Trimax 12 sheets in the beam. The XRSPEC.PAS is used to calculate the exposure rate transmission produced by screens of pure gadolinium oxysulfide of thicknesses varying from 0.05 mm to 0.50 mm in increments of 0.01 mm. The measured transmission values are then compared to the calculations to determine the thickness of pure gadolinium oxysulfide which produces the observed results. This value is used as a first estimate of the gadolinium oxysulfide thickness. Using a mass balance equation, the masses, volumes and thicknesses of the binder material in the phosphor layer are calculated using the

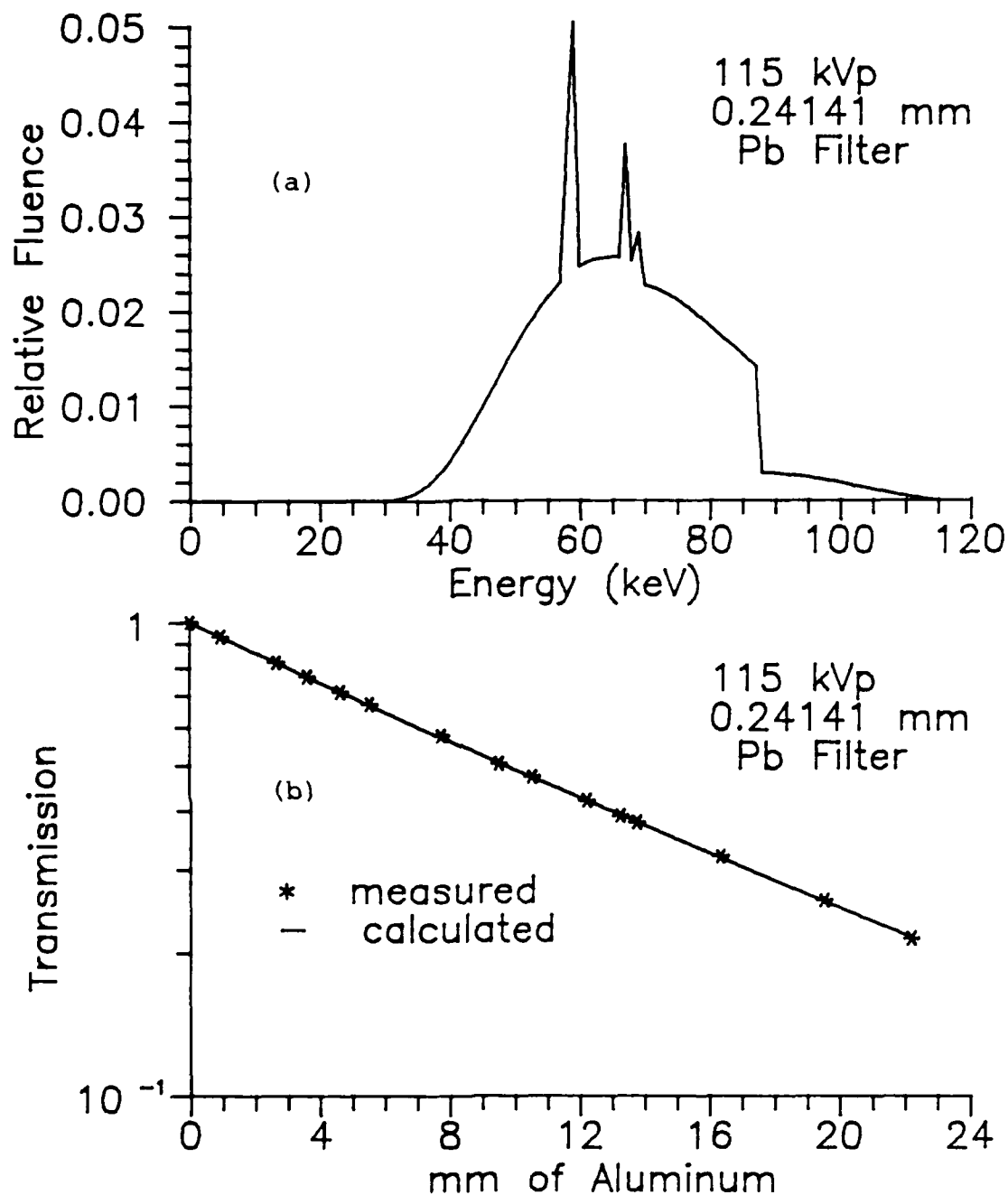


Figure E.3. Spectrum and transmission curve at 115 kVp. (a) The x-ray spectrum at 115 kVp calculated by the XRSPEC.PAS code for the GE Maxitron 300 X-Ray Therapy Unit with 4.75 mm beryllium inherent filtration, 0.25 mm aluminum equivalent monitor ionization chamber, 0.2414 mm lead added filtration, and air path length of 91.44 cm is shown. Fluence is normalized to 1 photon per cm^2 . (b) A comparison of measured and calculated transmission of exposure rate of the spectrum in (a) is shown.

gadolinium oxysulfide thickness estimate and the model of the other portions of the screens. Using these calculated values for the binder material the entire screen model, minus the gadolinium oxysulfide, is introduced into the XRSPEC.PAS calculations. Thicknesses of gadolinium oxysulfide are added to these calculations and varied until the computed exposure rate transmission matches that of the experiments. Using this second value for the thickness of the gadolinium oxysulfide, the mass balance equation is again used to obtain a second estimate of the binder thickness. The entire process continues until convergence is obtained. Convergence is very rapid, and the final result confirms that Venema's assumption of pure gadolinium oxysulfide is fairly good; the difference between this assumption and the final result of the iterative process is only 2.2%. Table E.1 gives the thicknesses and densities of the screen used in the detector (one back screen was divided into halves to produce the two layers).

Detector Response Matrix Calculation

Calculation Technique

A Monte Carlo code, DETECT.PAS, written in Turbo Pascal (Borland, 1985), is used to construct the detector response matrix for the gadolinium oxysulfide based screen materials. The code is a modification of the MCPHOT.PAS photon transport code discussed in Chapter IV. The major differences between the codes, other than materials and geometry, is that photoelectric interactions with subsequent fluorescent emission are modelled in DETECT.PAS.

TABLE E.1

Gadolinium Oxysulfide Screen Model

Screen Layer	Composition	Thickness (cm)	Density (g/cm ³)
Protective	Lucite	0.00100	1.000
Phosphor	Gd ₂ O ₂ S in lucite	0.02694	4.526
Reflecting	TiO ₂	0.001905	4.260
Base	Lucite	0.0254	1.000

Photoelectric events are eliminated in the MCPHOT.PAS code by a weighting scheme which allows only scattering interactions to be considered. This is justifiable because of the low atomic number of the materials present in the mine and soil. In the case of the detector response calculation, energy deposition is the quantity of interest and photoelectric events become extremely important. Additionally, in a thin detector containing a relatively high atomic number material (64 for gadolinium oxysulfide), fluorescent emission also plays an important role. Detailed photoelectric interaction cross sections and information concerning fluorescent emissions are taken from Storm and Israel (1970). Atomic fluorescence yields are taken from Fink et al. (1966). The method used to model fluorescent emission is that suggested by Carter and Cashwell (1977). Using their recommendations, titanium in the reflecting layer, and gadolinium in the phosphor layer are permitted to have fluorescent emissions. The terbium in the phosphor layer is neglected because it is present in very small quantities (less than 0.3 atom % replacing gadolinium), and because it is very close to gadolinium in the energies of its fluorescently emitted photons (the atomic number of terbium is 65). Only K characteristic emissions of titanium are considered since its L x rays have energies on the order of only 500 eV, and can be considered to be effectively absorbed at the locations of the photoelectric interactions which precede their production. An effective L edge of gadolinium is

taken by averaging the three actual edge energies. Five characteristic photons are allowed from gadolinium and three from titanium, provided edge energies are exceeded. These photon energies are given in Table E.2. The probabilities of emission of a particular photon are computed using the method recommended by Carter and Cashwell. Secondary fluorescence following $K_{\alpha 1}$ or $K_{\alpha 2}$ emission is included in the model. All fluorescent emissions are isotropic.

General Results of Calculations

The DETECT.PAS code is used to perform calculations of the energy deposited in the phosphor layers of the screen configuration shown in Figure E.2. The screen layer compositions, thicknesses and densities used in the code are shown in Table E.1. A 0.3 cm thick cardboard layer, which provides support, separates the two screens. Ten thousand photon histories were followed for 20 photon energies incident on the screen at nine different angles. The quantity recorded in the response matrix is the energy deposited in the phosphor layers per incident photon at a particular energy and angle. As discussed below, this quantity is directly proportional to the electronic signal produced in the complete detector system by an incident photon.

Two phenomena occur at the K edge energy of gadolinium (50.239 keV) which profoundly influence the detector response. At the edge energy the cross section for photoelectric interaction in gadolinium increases rapidly. This results in an increase in the number of photoelectric

TABLE E.2
 Energies of Fluorescent Photons Used
 in the DETECT.PAS Code

X-Ray	Energy (keV)	
	Titanium	Gadolinium
Weighted average of 3 L x rays	not considered	6.642
$K_{\alpha 1}$	4.510	42.996
$K_{\alpha 2}$	4.504	42.309
$K_{\beta 1}$, weighted average of M2,M3,M4 to K transitions	4.931	48.6485
$K_{\beta 2}$, weighted average of N2,N3 to K transitions	not applicable	49.9595

interactions occurring in the phosphor layer. At this same energy, K fluorescent x rays are first capable of being produced. Below the K edge energy, only L characteristic photons can be emitted. They are produced with a much lower probability than the K x rays, and their low energies result in many being absorbed before escaping the phosphor layer in which they originate. In contrast, because of their higher energies and the thinness of the phosphor layers, many K characteristic photons escape the phosphor layers in which they originate. Most of the K x rays escaping into the hemispheres of the screens which face one another are absorbed in the other (non-origin) screen. Those escaping into the hemispheres facing outward from the screen layers are lost, carrying away a substantial portion of the initial photon's energy. Complicating the K x ray loss phenomenon is the fact that the first phosphor layer (the layer closest to the source of the incident photon) effectively shields the second phosphor layer. This shielding effect is a function of incident photon energy. An asymmetry in energy deposition in the phosphor layers occurs which is greatest at low energies. In general, more energy is deposited in the first phosphor layer than in the second. This effect also occurs at energies above the K edge, but with an additional asymmetry. Since more photoelectric events are occurring in the first phosphor layer, more K fluorescent photons are being produced. As a result, the loss of K x rays into the reflected direction (into the hemisphere from

which the incident photon entered the screen) is much greater than into the transmitted direction. As energy increases above the K edge, the asymmetry between energy deposition in the two phosphor layers decreases, losses in the reflected direction decrease (except at very large angles of incidence), and losses in the transmitted direction increase. To further complicate the situation, two other phenomena are also occurring. As the angle of incidence of the photons increases, the probability of backscatter from the first screen also increases, reducing the number of photons capable of depositing energy in either screen. Increasing the angle of incidence also decreases the depth at which interactions occur in the first phosphor layer. If the interaction is photoelectric, followed by K fluorescent emission, the probability of escape from the phosphor layer is enhanced. Additionally, as photon energy increases, the probability of transmission without interaction or after an incoherent scattering event increases. This is a result of the decrease in the photoelectric interaction cross section with energy.

Description of the Detector Response Matrix

The combination of these phenomena produces a rather complex detector response function. It is somewhat easier to present these effects graphically in terms of the fraction of incident photon energy which is deposited in a particular layer or lost. The response of the detector at three angles of incidence for energies from 15 keV to 300

keV is used to demonstrate the effects. For each angle, four graphs are shown. These graphs display the fraction of incident photon energy absorbed in the phosphor layers of the detector, the fractions of incident photon energy absorbed in each layer of the detector, the fraction of incident photon energy lost into the reflection hemisphere, and the fraction of the incident photon energy lost into the transmission hemisphere. The fraction of incident photon energy deposited in non-phosphor layers of the detector is generally less than 0.01 and is not shown.

Perpendicular Incidence

Figure E.4 shows the fraction of the incident photon energy absorbed in the phosphor layers of the detector for the case of perpendicular incidence. At very low energies (below 0.020 MeV), virtually all of the incident energy is captured by the phosphor layers as a result of the very high photoelectric cross section of gadolinium. Figure E.5 indicates that the first phosphor layer absorbs nearly all the energy, shielding the second phosphor layer from any significant number of interactions. Figure E.6 shows that the fraction of incident photon energy lost in the reflected direction is small (and remains so, up to the K edge). All that can escape in this energy range are a few L x rays and contributions from the few coherent and incoherent scattering events. Figure E.7 shows that virtually no photon energy is able to penetrate the screen, as would be expected by the very high absorption of the first phosphor layer.

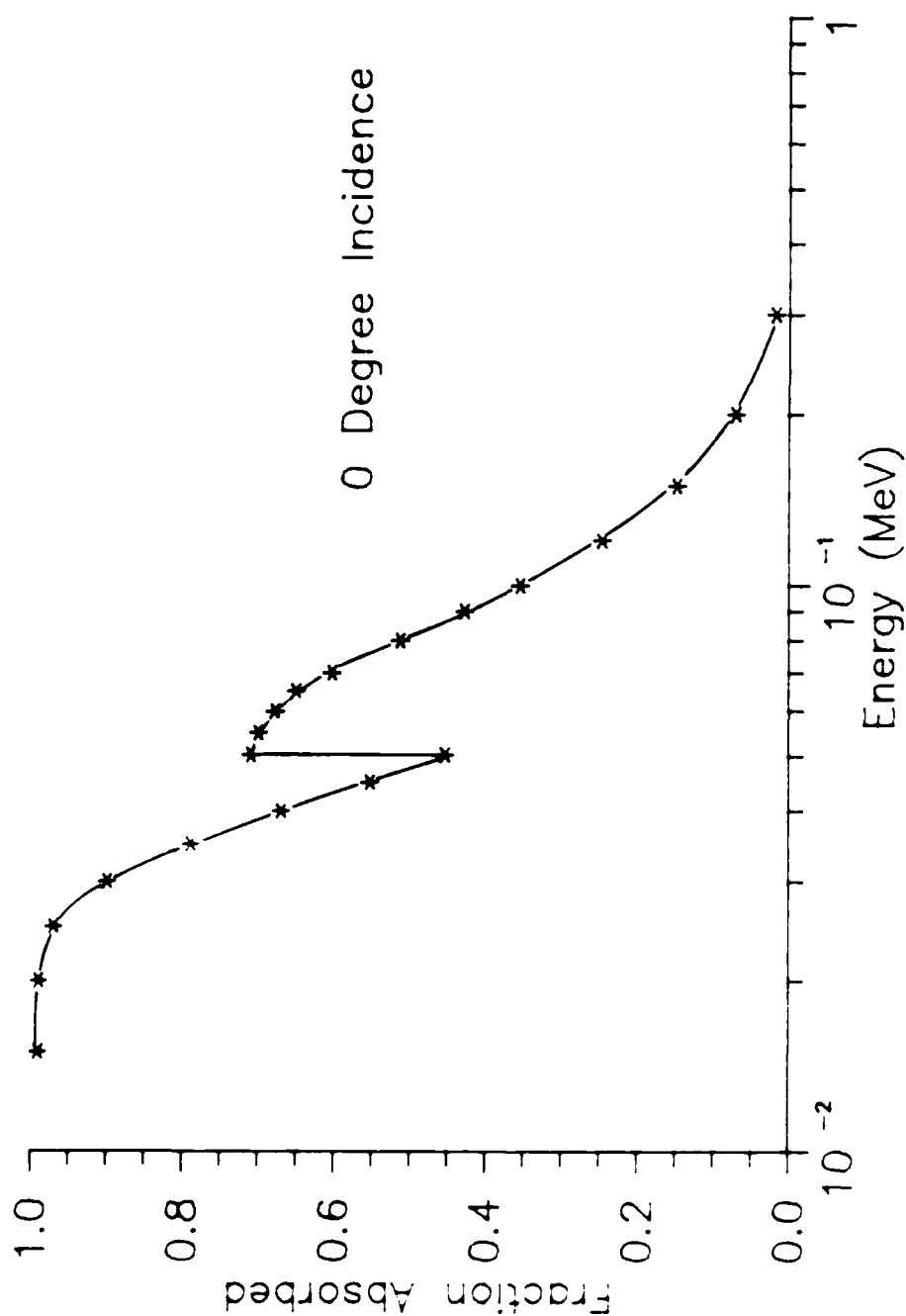


Figure E.4. Fraction of incident energy absorbed, perpendicular incidence. The fraction of incident x-ray photon energy absorbed in the two phosphor layers of the detector system constructed from two halves of 3M Trimax 12 screen B 184048 as a function of incident x-ray photon energy (MeV) for the case of perpendicular incidence is shown.

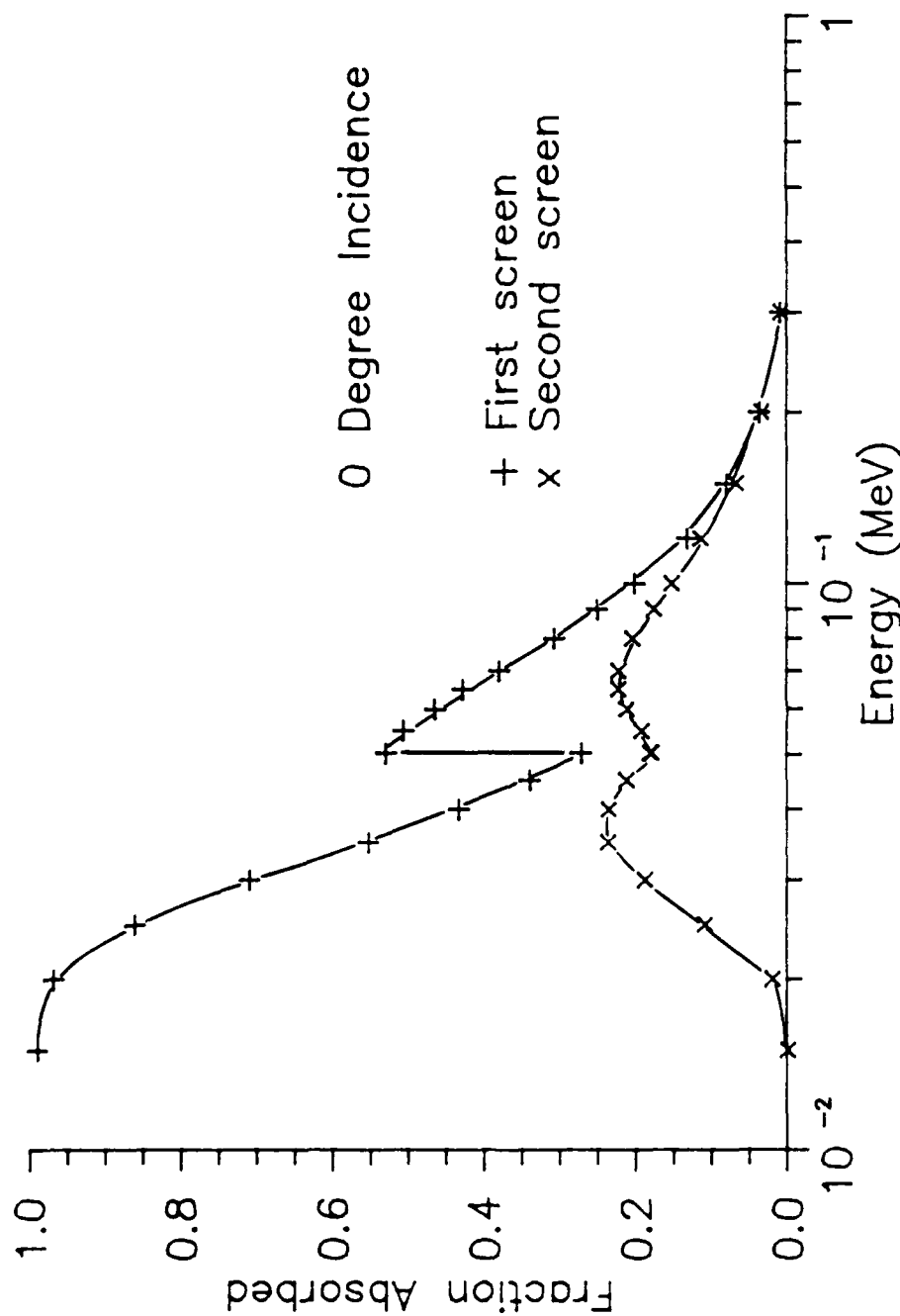


Figure E.5 Fraction of incident energy absorbed in each screen, perpendicular incidence. The fraction of incident x-ray photon energy absorbed in the two phosphor layers of the detector system constructed from two halves of 3M Trimax 12 screen B 184048 as a function of incident x-ray photon energy (MeV) for the case of perpendicular incidence is shown. The first screen is that nearest the incident photon when it first encounters the detector.

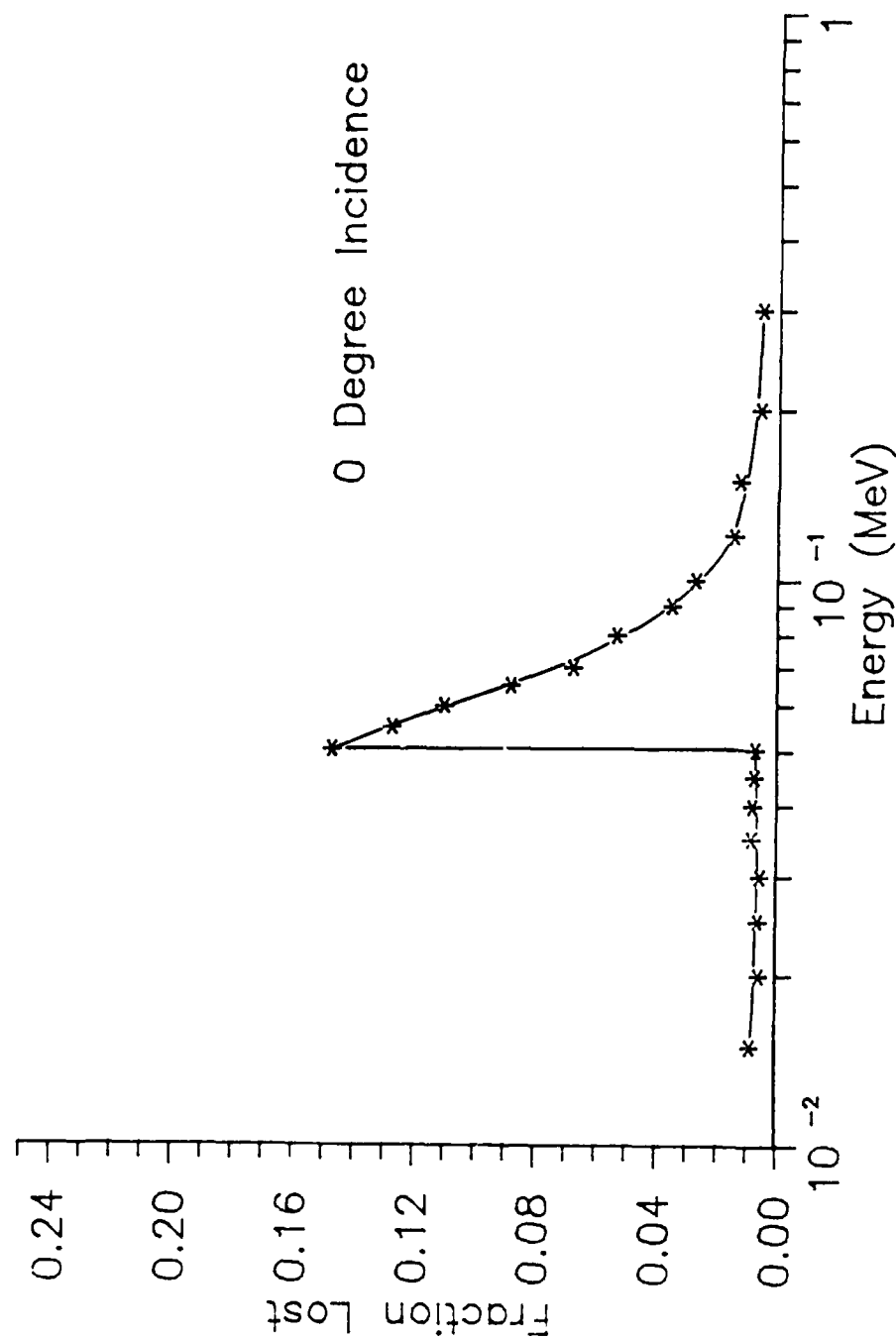


Figure E.6. Fraction of incident energy reflected, perpendicular incidence. The fraction of incident x-ray photon energy escaping into the reflection hemisphere of the detector system constructed from two halves of 3M Trimax 12 screen B 184048 as a function of incident x-ray photon energy (MeV) for the case of perpendicular incidence is shown.

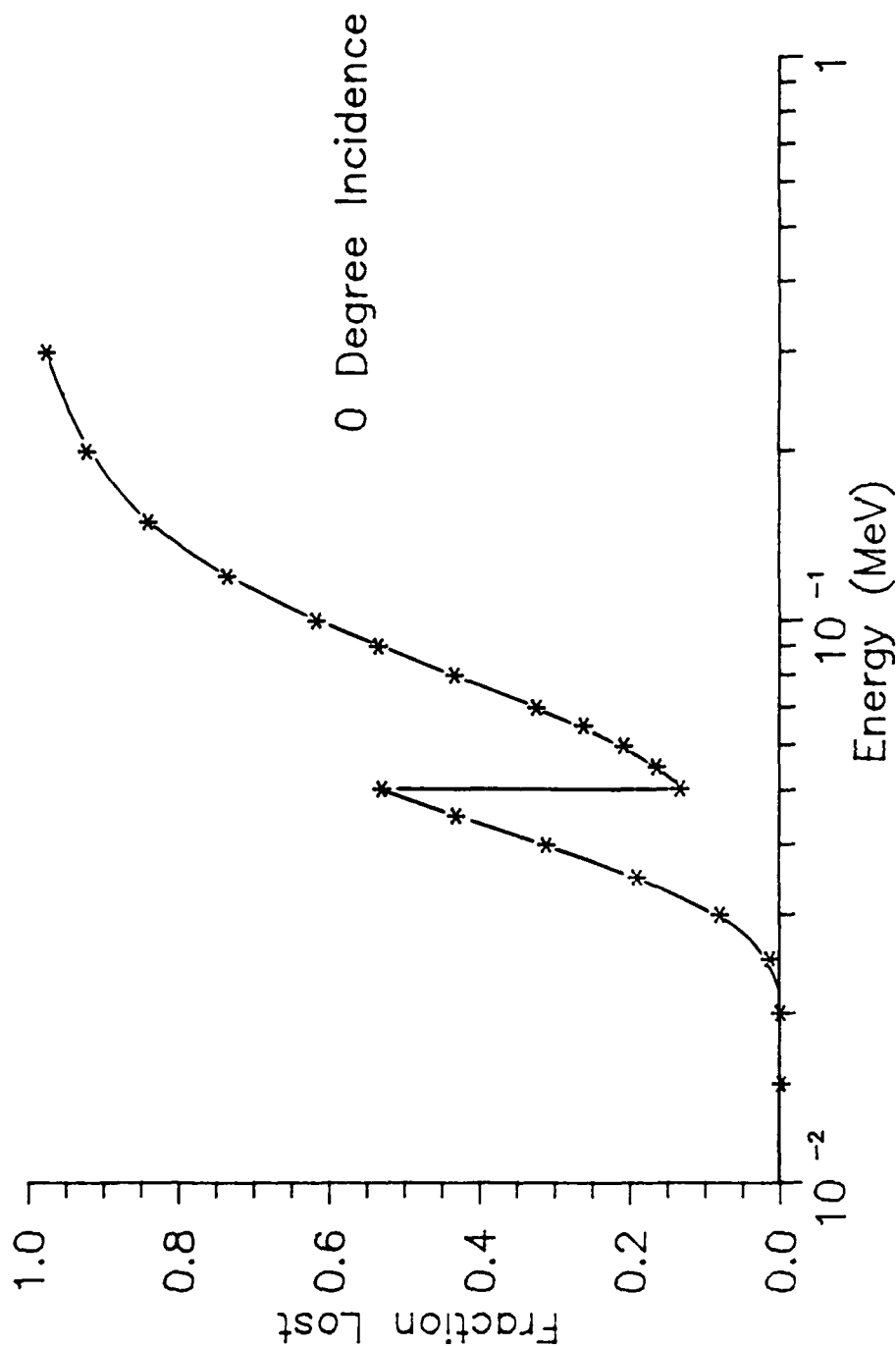


Figure E.7. Fraction of incident energy transmitted, perpendicular incidence. The fraction of incident x-ray photon energy escaping into the transmission hemisphere of the detector system constructed from two halves of 3M Trimax 12 screen B 184048 as a function of incident x-ray photon energy (MeV) for the case of perpendicular incidence is shown.

As incident photon energy increases (0.020 MeV to below the K edge), the photoelectric interaction cross section is still dominant, but is decreasing rapidly in magnitude. As a consequence, fewer photons and less energy are absorbed in the first phosphor layer. The second phosphor layer begins to see and absorb more photons as they increasingly survive absorption in the first. These effects are seen in Figure E.5. The fraction of energy absorbed in the first phosphor layer decreases, and the fraction absorbed in the second phosphor layer increases. The fraction of energy reflected (Figure E.6) remains low, but the fraction transmitted increases with energy (Figure E.7). The net result, as seen in Figure E.4, is a decrease in the fraction of energy absorbed. The increase of absorption in the second phosphor layer is insufficient to make up for the loss of absorption in the first and the increasing transmission losses. In fact, at about 0.035 MeV, the photoelectric cross section has fallen so low that the fraction absorbed in the second phosphor layer also begins to fall (Figure E.5).

At the K edge there is a sudden large increase in the photoelectric interaction cross section as a result of reaching the threshold energy for ionizing the K shell of gadolinium. There is an immediate, discontinuous increase in the fraction of incident energy absorbed in the phosphor layers (Figure E.4). Figure E.5 shows that the fraction absorbed in the first phosphor layer increases greatly, again shielding the second phosphor layer, which reaches a

relative minimum in the fraction of energy it absorbs. At the K edge, there is a sharp increase in the fractional energy loss into the reflection hemisphere (Figure E.6). This is a result of the production of K x rays and their isotropic emission. These K x rays all have energies just below the K edge and, therefore, find surviving travel through the phosphor layers easier than the incident photons which were the cause of their existence. Many are captured in the second screen, but many also escape into the reflection hemisphere. As expected, the fraction of energy transmitted drops sharply at the K edge (Figure E.7) as a result of both the increased absorption in the phosphor and the increased reflection loss.

As energy increases above the K edge, the photoelectric cross section resumes its decrease. The fraction of energy absorbed in the phosphor layers decreases (Figure E.4) monotonically (at least to 0.3 MeV). The change in curvature at energies greater than 0.150 MeV is a result of the increasing importance of incoherent scattering. Figure E.5 shows a replay of the discussion above, concerning the partition of the absorbed energy between the two phosphor layers. The first phosphor layer becomes more and more transparent, resulting in a monotonic loss in fraction of absorbed energy. The second phosphor layer, from the K edge to about 0.070 MeV, experiences an increase in fraction absorbed because of reduced shielding by the first layer. Above 0.070 MeV, the increasing transmission losses reduce the fraction absorbed

in both layers. As both phosphor layers become more and more transparent, the fractions absorbed in each become almost equal. The fraction of incident energy escaping into the reflection hemisphere (Figure E.6), composed overwhelmingly of K fluorescent photons, decreases continuously as a result of their decreasing production and greater average depth of production (primarily in the first phosphor layer). The escaping K fluorescent photons are also responsible for the relative flatness of the curve near the edge energy. In an interaction in which a K fluorescent photon is lost, the energy deposited in the phosphor layer is that of the incident x-ray photon minus the energy of the escaping K x ray. If the incident energy is near that of the edge, very little energy is deposited. The amount of energy deposited increases as the incident x-ray energy increases, partially compensating for the decrease in the photoelectric cross section. The dominant effect in this energy range is transmission loss (Figure E.7), which increases rapidly with energy.

45 Degree Incidence

Figure E.8 shows the fraction of incident energy absorbed by the layers for 45 degree incidence. The low energy region (below 0.025 MeV) is flatter and extends further than in the perpendicular incidence case. Again, virtually all the incident energy is captured by the phosphor layers with the first layer absorbing almost all the energy shielding the second (Figure E.9). The

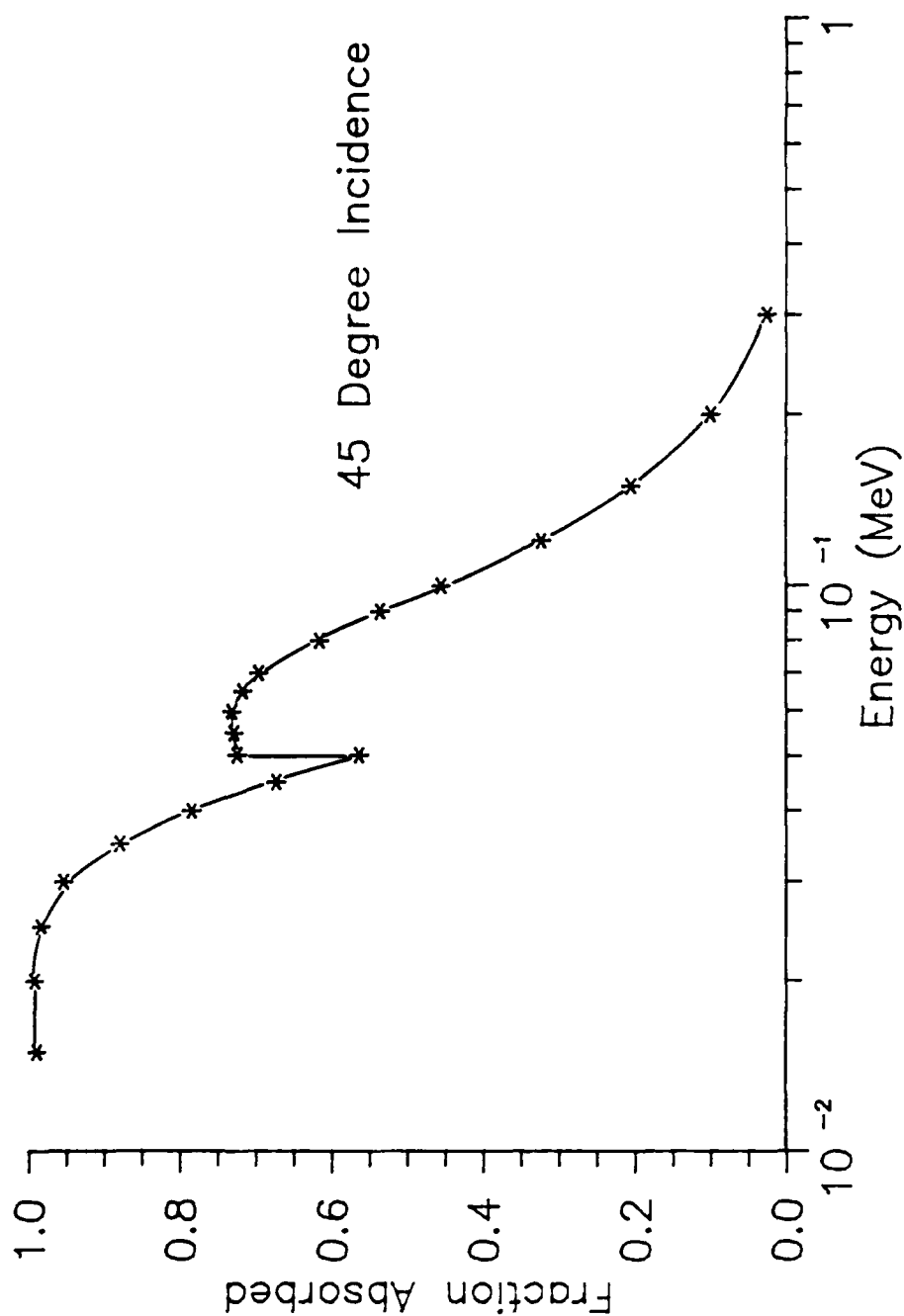


Figure E.8. Fraction of incident energy absorbed, 45 degree incidence. The fraction of incident x-ray photon absorbed in the two phosphor layers of the detector system constructed from two halves of 3M Trimax 12 screen B 184048 as a function of incident x-ray photon energy (MeV) for the case of 45 degree incidence is shown.

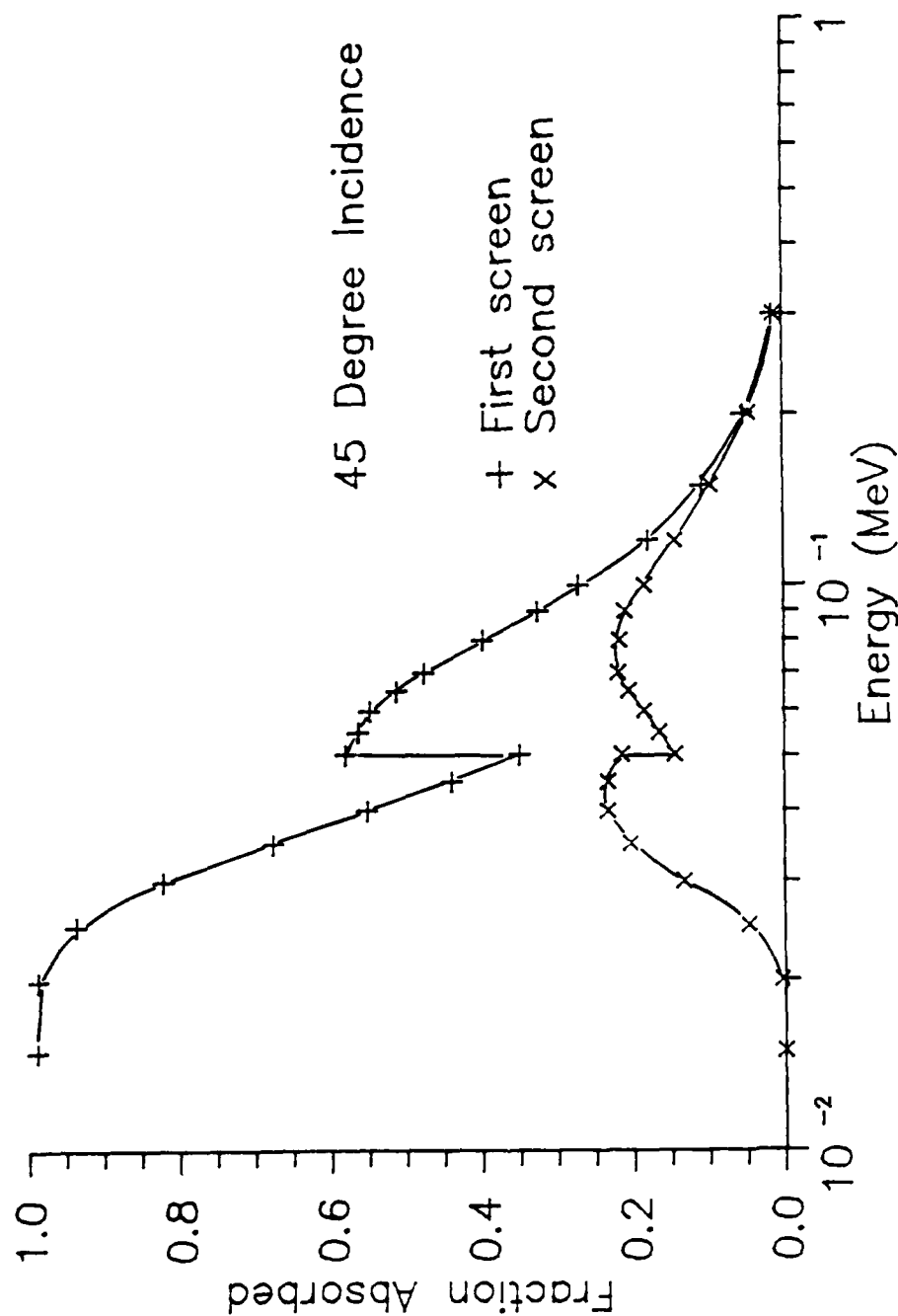


Figure E.9. Fraction of incident energy absorbed in each screen, 45 degree incidence. The fraction of incident x-ray photon energy absorbed in the two phosphor layers of the detector system constructed from two halves of 3M Trimax 12 screen B 184048 as a function of incident x-ray photon energy (MeV) for the case of 45 degree incidence is shown. The first screen is that nearest the incident photon when it first encounters the detector.

energy region is larger because the incident photons are effectively encountering a phosphor layer 1.4142 times thicker than in the perpendicular incidence case. Once again, the fraction lost to the reflection hemisphere remains small below the K edge (Figure E.10), and virtually no photons are capable of penetrating the screens (Figure E.11).

As incident photon energy increases (from 0.025 to just below the K edge), the fraction of incident energy absorbed decreases (Figure E.8) for the reasons previously addressed for the perpendicular case. The decrease, however, is slower, and the fraction of incident energy absorbed at the bottom of the K edge is larger than in the perpendicular case. The reason for these results is the increased apparent thicknesses of the phosphor layers to incident photons. Comparison of Figures E.5 and E.9 shows that the increasing energy absorption is greatest for the first phosphor layer and that, in fact, the second phosphor layer, up to about 0.040 MeV, actually absorbs a lower fraction at 45 degree incidence than it did in the case of perpendicular incidence due to the improved shielding by the first screen. Above 0.040 MeV, the second phosphor layer at 45 degrees is more efficient than it was at 0 degrees, as a result of finally beginning to see significant numbers of photons transmitted through the first phosphor layer. The peak in the second phosphor layer fraction shifts to about 0.042 MeV. Above this energy (and below the K edge), the fraction

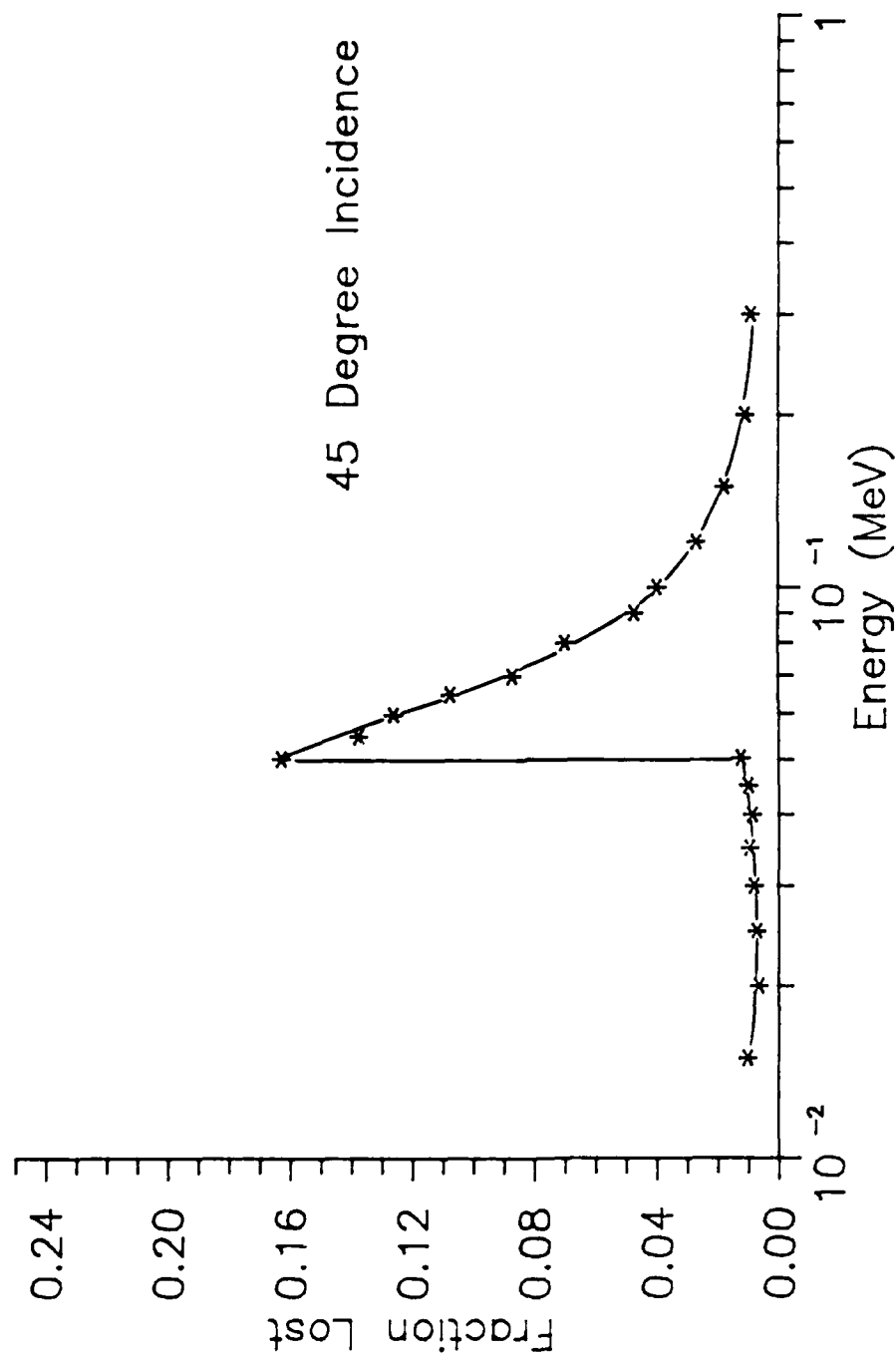


Figure E.10. Fraction of incident energy reflected, 45 degree incidence. The fraction of incident x-ray photon energy escaping into the reflection hemisphere of the detector system constructed from two halves of 3M Trimax 12 screen B 184048 as a function of incident x-ray photon energy (MeV) for the case of 45 degree incidence is shown.

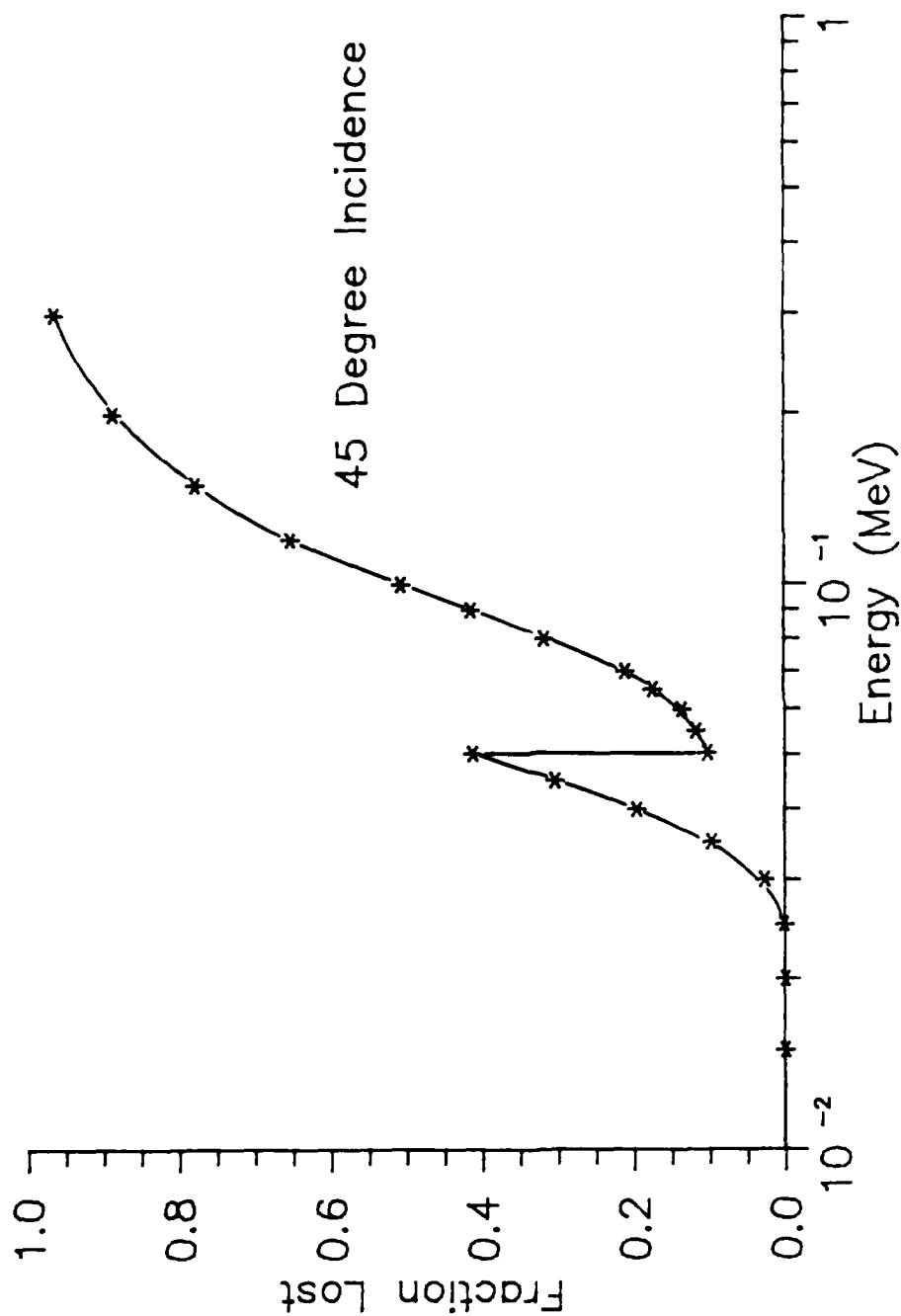


Figure E.11. Fraction of incident energy transmitted, 45 degree incidence. The fraction of incident x-ray photon energy escaping into the transmission hemisphere of the detector system constructed from two halves of 3M Trimax 12 screen B 184048 as a function of incident x-ray photon energy (MeV) for the case of 45 degree incidence is shown.

of energy absorbed in both phosphor layers decreases due to increasing transmission losses. Comparison of Figures E.7 and E.11 reveals that at any given energy, the transmission losses are smaller at 45 degree incidence than at 0 degrees, as would be expected from the increased phosphor absorption.

At the K edge (Figure E.8), there is again a discrete jump in the fraction of energy absorbed in the phosphor layers as a result of the increase in the photoelectric cross section. Comparison of Figures E.5 and E.9 shows that the first phosphor layer at 45 degrees absorbs a higher fraction of the incident energy, and the second phosphor layer, a lower fraction (as a result of better shielding by the first) than at 0 degree incidence. In fact, there is a small step decrease in the fraction absorbed by the second phosphor layer at the edge. Comparison of Figures E.6 and E.10 shows an increase at 45 degree incidence in the fraction of energy lost to the reflection hemisphere as a consequence of increased incident photon absorption in the first phosphor layer and hence increased K fluorescent photon production. Fluorescent emission losses in this direction are also enhanced by shallower average depth in the phosphor at which photoelectric interactions take place. The net result of increased absorption in the first phosphor layer, decreased absorption in the second, and increased losses into the reflection hemisphere is a slight increase in fractional energy absorption at the K edge over the 0 degree incidence case. As would be expected, there is a

slight decrease in the fraction of energy transmitted when compared to the 0 degree case (Figures E.7 and E.11).

Above the K edge, comparison of Figures E.4 and E.8 shows a major difference in curvature. While the perpendicularly incident case resulted in a monotonically decreasing function above the K edge, the 45 degree case gives a relative maximum at about 0.058 MeV. The effect is not rooted in any increase of efficiency of the screen with increasing energy, but rather with a loss of efficiency in the vicinity of the K edge at larger angles of incidence. The site of this loss of efficiency is the first phosphor layer. As has been previously discussed, as the angle of incidence increases, the apparent phosphor thickness the incident photon encounters becomes larger, resulting in more absorptions and more K fluorescent photons and an average shallower depth of production. Thus as angle of incidence increases, the fraction of energy loss into the reflection hemisphere increases. This increase is augmented by increasing backscatter from the screen surface with increasing angle of incidence, but the main effect is the loss of K fluorescent photons, which is greatest at energies near the K edge (Figure E.10). The effect is magnified by the fact that events in which the incident photon energy is close to that of the K edge, and in which the K x ray escapes, deposit very little energy in the phosphor. The result is the relative maximum observed in Figure E.8. Once this maximum is passed, the remaining effects have been

previously explained. Transmission losses increase (Figure E.11) as a result of decrease in the photoelectric cross section.

75 Degree Incidence

Figure E.12 shows the fraction of incident energy absorbed in the phosphor layers for the case 75 degree incidence. The low energy region (below 0.035 MeV) is flat and greatly extended. The apparent thickness of the phosphor layer to an incident photon is now 3.864 times the true thickness. Virtually all photons are stopped in the first phosphor layer; the second layer is well shielded (Figure E.13). Reflection losses are higher than in previous cases due to backscatter from the screens, but are still relatively low (Figure E.14). Transmission losses in this energy region do not occur (Figure E.15).

From 0.035 MeV to the K edge, the fraction of energy absorbed in the first screen decreases with the falling photoelectric cross section; the fraction absorbed by the second layer increases as photons manage to reach it through the first layer (Figure E.13). The second layer fraction does not pass through a maximum in this energy range as it did in the previously discussed cases. The extreme shielding afforded by the first layer accounts for this effect at 75 degree incidence. Reflection and transmission losses remain low (Figures E.14 and E.15).

At the K edge, an inversion in previous results is seen. The low energy side has higher fractional energy

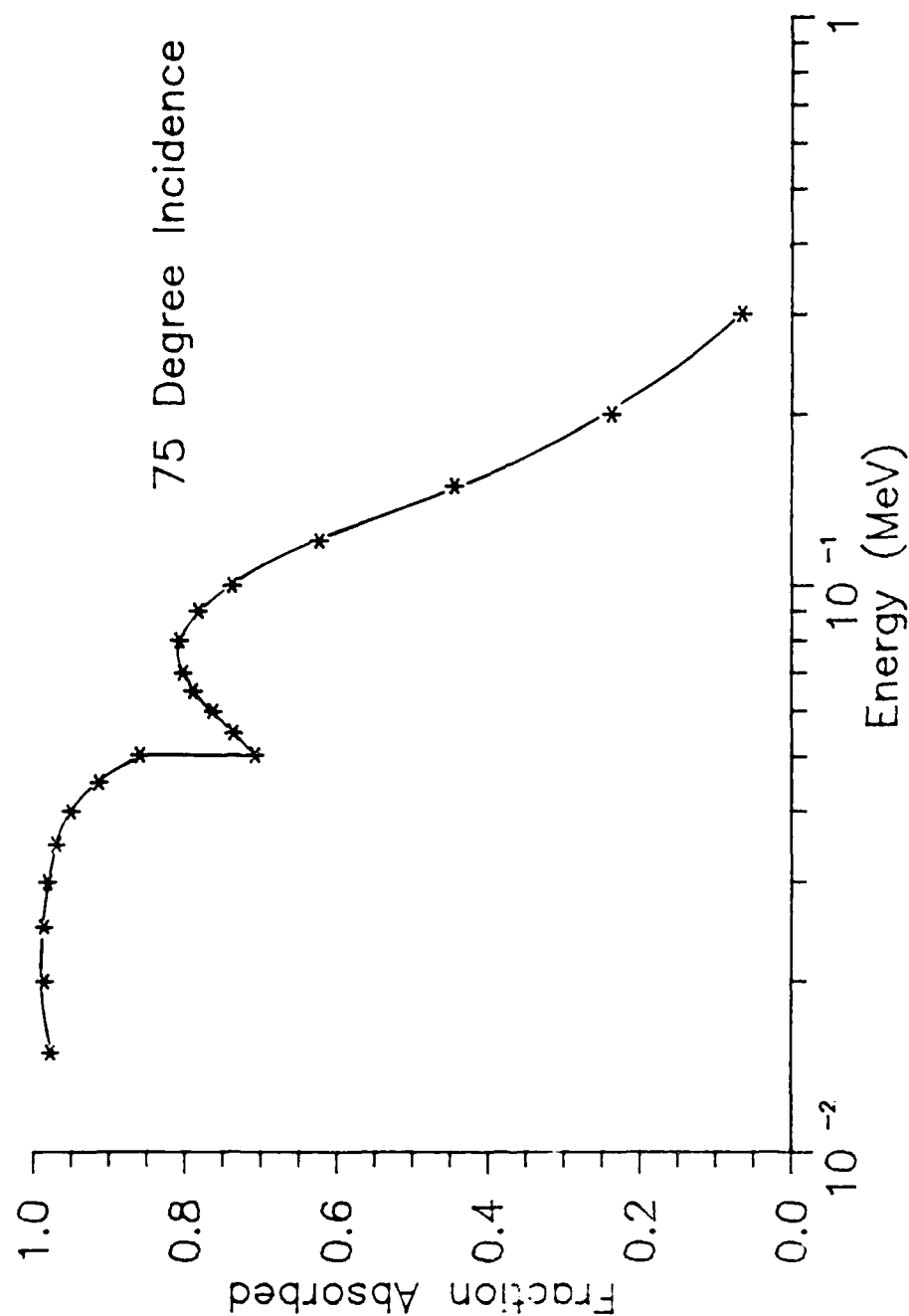


Figure E.12. Fraction of incident energy absorbed, 75 degree incidence. The fraction of incident x-ray photon absorbed in the two phosphor layers of the detector is shown. The curve is constructed from two halves of 3M Trimax 12 screen B 184048 as a function of incident x-ray photon energy (MeV) for the case of 75 degree incidence is shown.

AD-R182 227

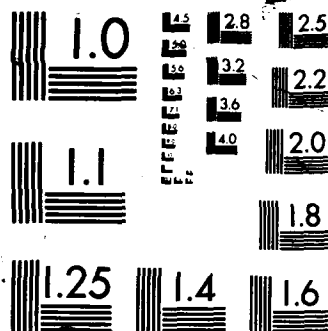
LANDMINE DETECTION BY SCATTER RADIATION RADIOGRAPHY(U)
ARMY MILITARY PERSONNEL CENTER ALEXANDRIA VA
J G CAMPBELL 02 JUL 87

6/6

UNCLASSIFIED

F/G 15/6 6 NL

END
8-87
BTR



XERO COPY RESOLUTION TEST CHART

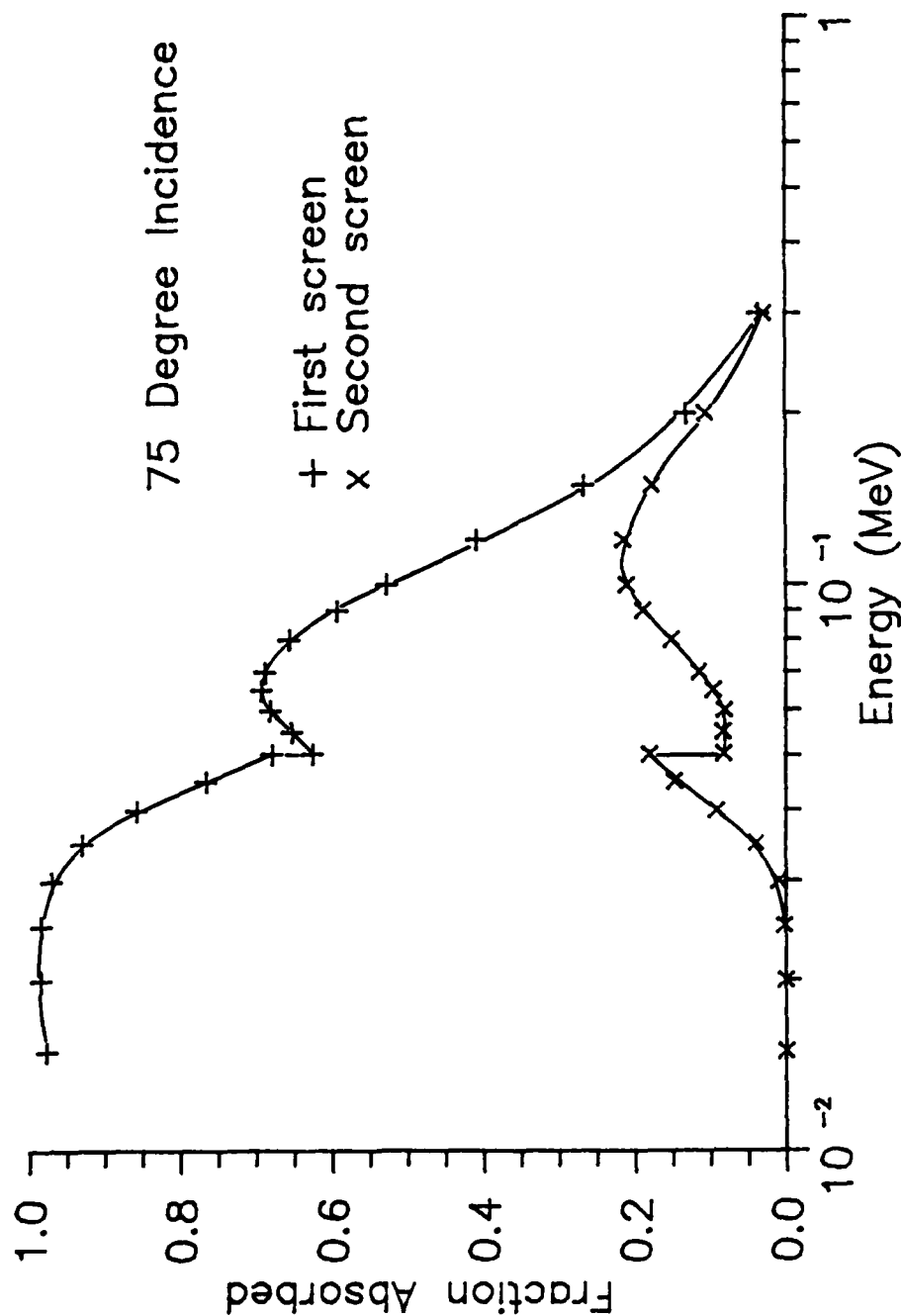


Figure E.13. Fraction of incident energy absorbed in each screen, 75 degree incidence. The fraction of incident x-ray photon energy absorbed in the two phosphor layers of the detector system constructed from two halves of 3M Trimax 12 screen B 184048 as a function of incident x-ray photon energy (MeV) for the case of 75 degree incidence is shown. The first screen is that nearest the incident photon when it first encounters the detector.

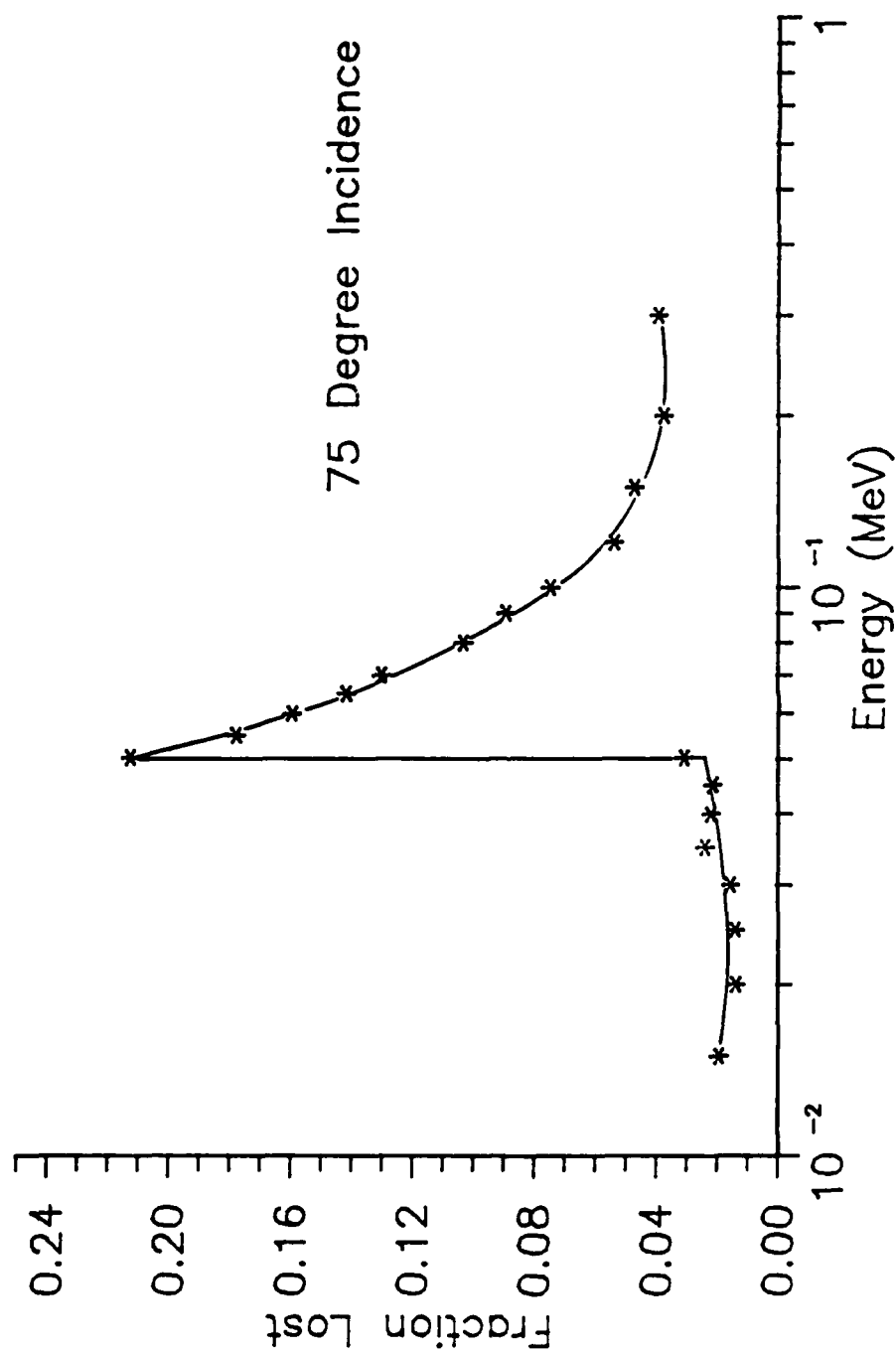


Figure E.14. Fraction of incident energy reflected, 75 degree incidence. The fraction of incident x-ray photon energy escaping into the reflection hemisphere of the detector system constructed from two halves of 3M Trimax 12 screen B 184048 as a function of incident x-ray photon energy (MeV) for the case of 75 degree incidence is shown.

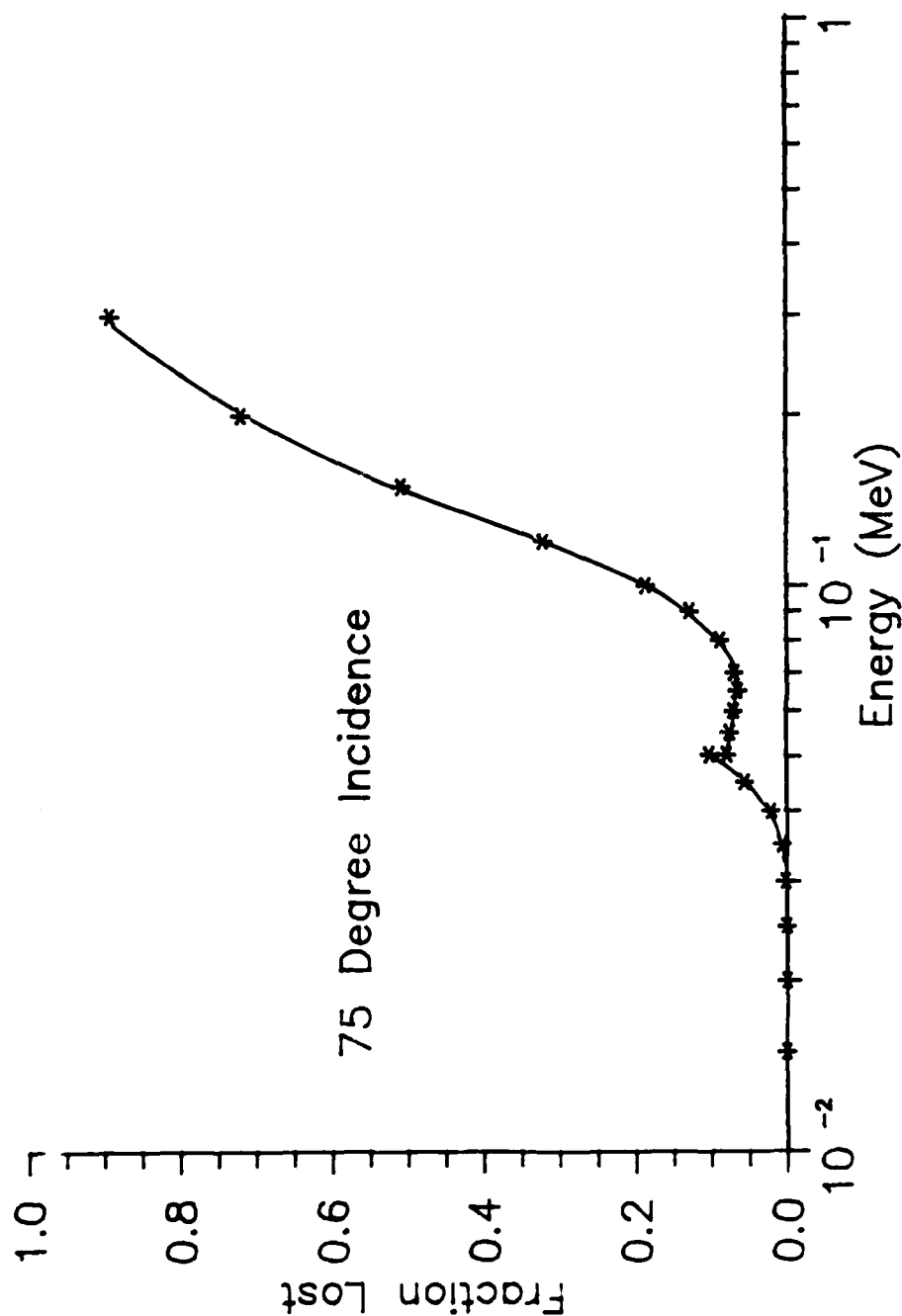


Figure E.15. Fraction of incident energy transmitted, 75 degree incidence. The fraction of incident x-ray photon energy escaping into the transmission hemisphere of the detector system constructed from two halves of 3M Trimax 12 screen B 184048 as a function of incident x-ray photon energy (MeV) for the case of 75 degree incidence is shown.

absorption than the high energy side. Figure E.13 shows that the first phosphor layer displays this same behavior. This is a result of the same effect responsible for the maximum above the K edge energy in the 45 degree case, the loss of K fluorescent photons with corresponding small energy deposition for incident photons with energies near the K edge energy. Figure E.14 shows that at the K edge, approximately 21% of the incident energy is lost into the reflection hemisphere. This energy loss is a combination of K fluorescent x rays (dominant portion) and backscatter. The fraction of energy deposited in the second layer decreases also (Figure E.13). The cause is the same as in previous discussions: shielding by the first phosphor layer. It is more obvious that a good deal of that shielding is in the form of fluorescent emission into the reflection hemisphere. Transmission losses remain low (Figure E.15). Above the K edge, the effects are the same as discussed for the case of 45 degree incidence, but enhanced by the larger apparent phosphor thickness seen by the incident photons.

Comparison with Published Results

Chan and Doi (1984) have performed Monte Carlo calculations for x-ray intensifying screens. While their calculations are for only a single screen composed of pure phosphor, they do show graphs of the fraction of energy absorbed per incident x-ray photon for the cases of zero and 80 degree incidence. The shapes of these curves for the Lanex Regular screen, which is based on gadolinium oxysulfide

(Kodak, 1980), including complex features such as the inversion at the K edge for large angles of incidence, correspond very well to results presented in this section.

Response Matrix Relationship to Detector Electronics

Deposition of energy in the phosphor is a single step in a chain of events which leads to the electrical signal produced by the detector system. The x-ray photon energy deposited within the phosphor layer is converted into kinetic energy of electrons within the layer. Some of these electrons interact with the terbium impurity ions in the phosphor layer, resulting in the emission of a discrete spectrum of visible light photons. A discrete spectrum is obtained because the interaction producing the visible light photons is with electrons in the 4f shell of terbium, which is shielded from external charge distributions (Anderson, 1984). The intrinsic conversion efficiency (defined as watts of optical power output divided by watts of x-ray power absorbed) for production of visible light photons in terbium activated gadolinium oxysulfide screens is given as 0.18 by Buchanan et al. (1972) for excitation by electrons. A value of 0.15 is generally favored for excitation by x-rays (3M, 1985a; Anderson, 1984). Regardless of the value used, the visible light output is directly proportional to the energy deposited in the phosphor. Given the amount of energy deposited in the phosphor and its conversion efficiency into optical energy, the number of visible light photons which are produced depends only upon the

energies of the discrete visible energy photons emitted and their relative intensities. The atom percentage of terbium replacing gadolinium determines the relative intensities of the components of the visible spectrum emitted. The majority of terbium activated gadolinium oxysulfide intensifying screens use a 0.3 atom % of terbium replacing gadolinium. The result is emission dominated by photons in the green region of the visible spectrum (Buchanan et al., 1972; Kodak, 1980). Figure E.16 shows a typical emission spectrum for screens of this type. The Trimax 12 screens contain less than 0.3% atom percent terbium which alters the relative intensities, producing more photons from the blue region of the visible spectrum (Frank, 1986). Figure E.17 shows the emission spectrum from a Trimax 12 phosphor (3M, 1985b). The number of visible photons produced is, therefore, also directly proportional to the energy deposited in the phosphor. Figure E.18 shows the average number of visible photons produced (based on the intensity weighted average energy of the visible emission spectrum of the Trimax 12 screens and an intrinsic conversion efficiency of 0.15) per x-ray photon incident on the screens as a function of energy of the incident x-ray photon. Results similar to this figure but for thinner screens and, therefore, of lower magnitude are reported by Dick and Motz (1981). The next step in the chain of events is the efficiency of the mylar reflector surrounding the screens to direct the visible photons onto the photocathode of the photomultiplier tube.

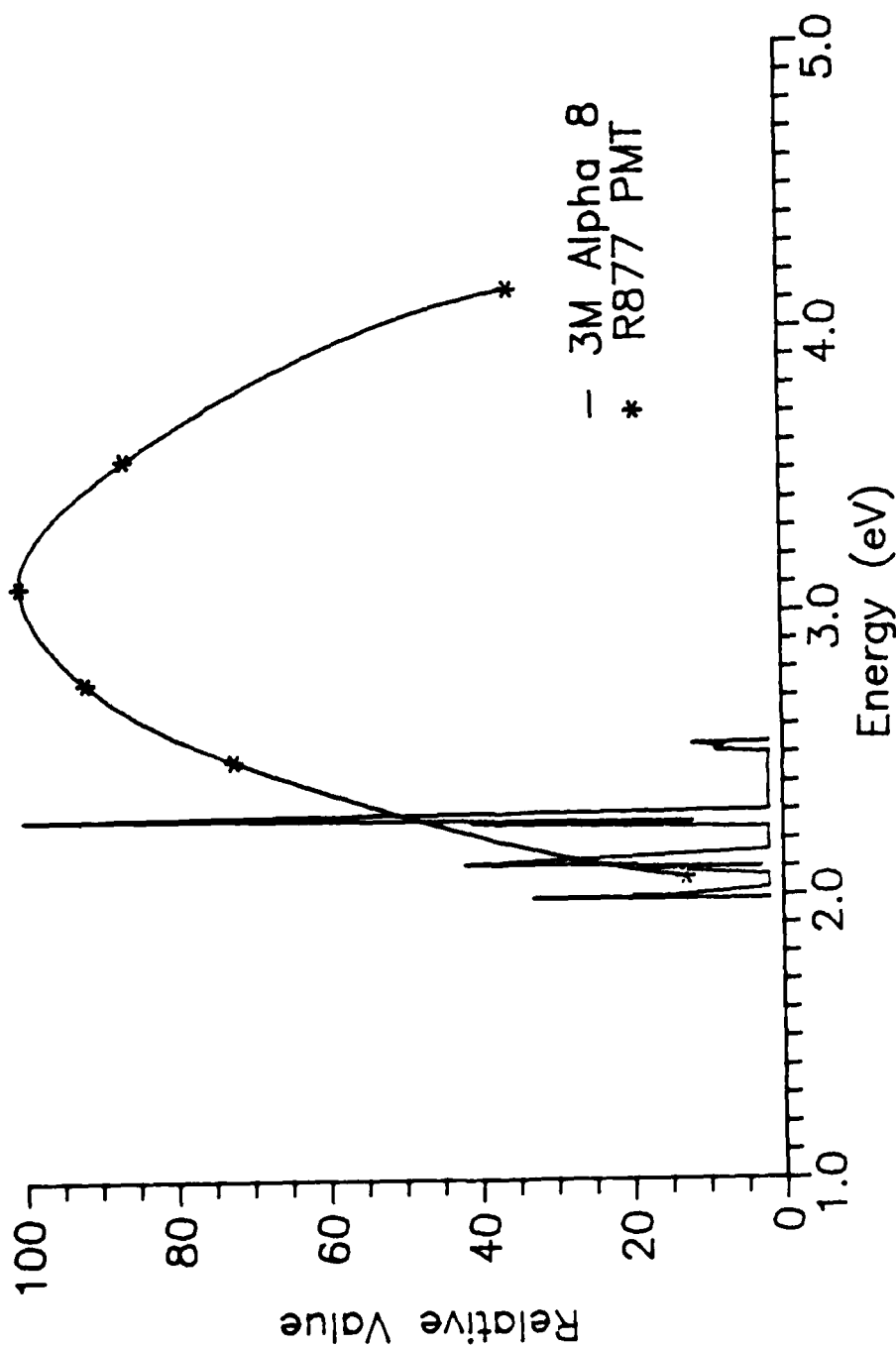


Figure E.16. Emission spectrum of gadolinium oxysulfide with 0.3 atom % terbium. The relative intensities of the discrete line emission spectrum of a terbium activated gadolinium oxysulfide x-ray intensifying screen containing 0.3 atom % terbium replacing gadolinium (here, the 3M Alpha 8 screen) and the relative sensitivity of the Hamamatsu R877 photomultiplier tube versus photon energy (eV) are shown.

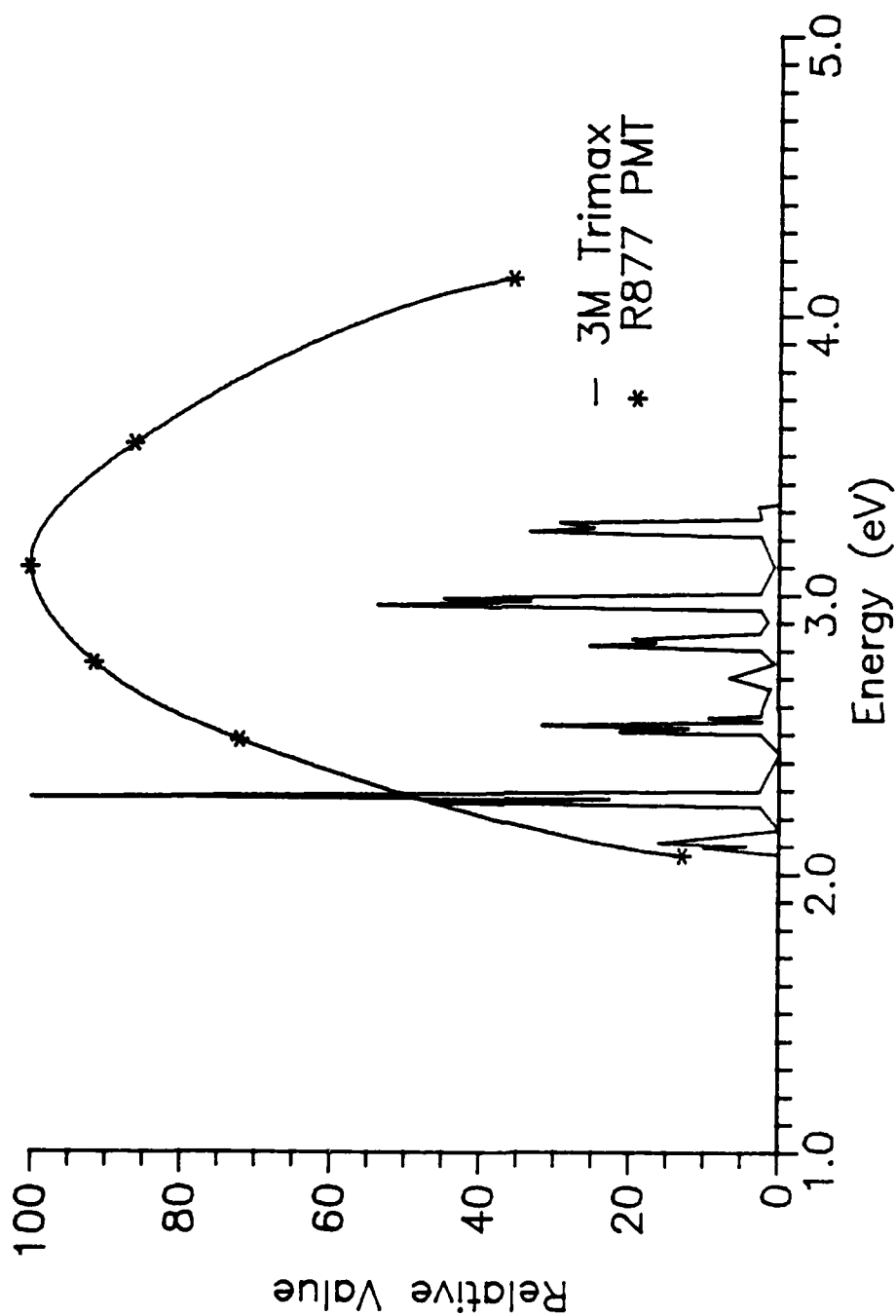


Figure E.17. Emission spectrum of 3M Trimax 12 screens. The relative intensities of the discrete line emission spectrum of the 3M Trimax 12 terbium activated gadolinium oxysulfide x-ray intensifying screen containing 0.3 atom % terbium replacing gadolinium and the relative sensitivity of the Hamamatsu R877 photomultiplier tube versus photon energy (eV) are shown.

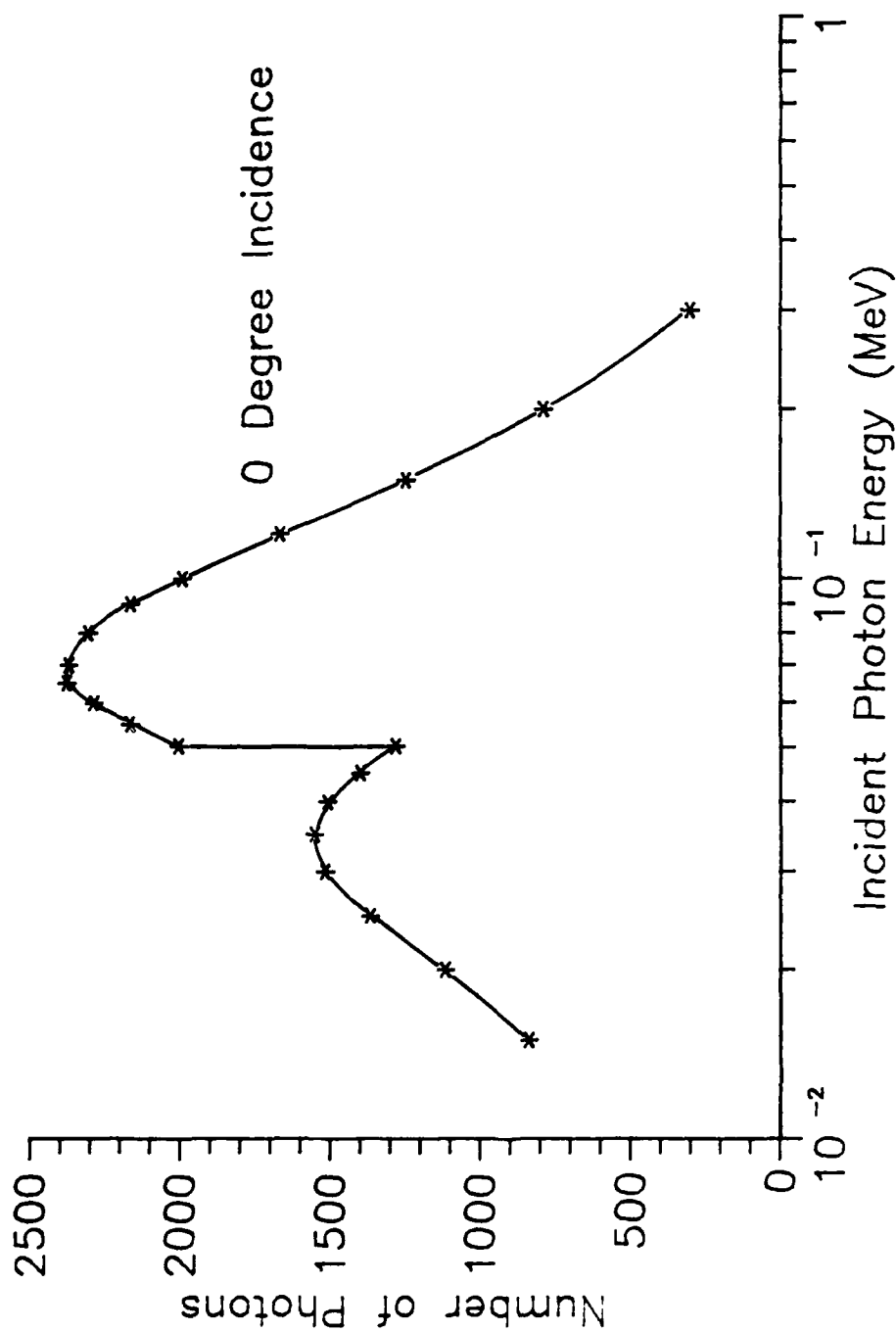


Figure E.18. Average number of visible photons produced per incident x-ray photon. The average number of visible photons produced in the phosphor layers of a detector system constructed from two halves of Trimax 12 screen B 184048 per incident x-ray photon as a function of incident x-ray photon energy (MeV) for the case of perpendicular incidence is shown.

Regardless of the value of this collection efficiency, it will be a constant. The next step is the conversion of the visible light energy to electron kinetic energy by the photocathode of the photomultiplier tube. Given a constant relative intensity, incident visible spectrum, this will also be a constant, as will be the amplification of the electron signal as it passes through the dynodes of the photomultiplier tube. The signal output from the anode of the photomultiplier, therefore, is directly proportional to the energy deposited in the phosphor layer of the screen material. Accordingly, the usefulness of a response matrix, which provides the amount of energy deposited within the phosphor layers per incident x-ray photon, becomes apparent. The response matrix (with appropriate interpolation routines) can be coupled directly to the fluence output of the MCPHOT.PAS code to produce results directly proportional to the measured electrical signal output of the detector system. The difference in emission spectrum, noted above, allows selection of a high efficiency photomultiplier tube with a better match of the spectral sensitivity of the photocathode. Figures E.16 and E.17 also show the spectral sensitivity of the Hamamatsu R877 photomultiplier tube used in measurements with the screens (Hamamatsu, 1985).

Shortcomings of the Detector

The gadolinium oxysulfide based detector is designed to obtain high count rates to assist in reducing the x-ray generator power requirements by improving counting statistics

for deeply buried mines. Double layers of the intensifying screens with areas of 255 cm^2 each are employed to maximize light output. The geometry of the reflecting coating on the interior of the detector is designed to direct a large fraction of the visible light created by the screens to the photocathode of the photomultiplier tube. A large diameter bialkali photomultiplier tube is selected for its high sensitivity and its ability to match the spectral characteristics of the visible light falling on the photocathode. The combination of these items produces a detector which is extremely sensitive to photon radiation in the energy range of interest for mine detection. The detector is readily capable of distinguishing between different scattering materials placed in an x-ray beam in the mine detection geometry. However, the count rates so obtained bear no relationship to the calculated detector response matrix. A series of measurements were made to define the causes for this discrepancy. Two causes are found, high sensitivity and the fluorescence decay time of the terbium activated gadolinium oxysulfide phosphor used in the Trimax 12 screens.

Sensitivity

The high sensitivity of the detector system is a result of two design factors. The first factor is the high visible light output of the intensifying screens. This high output is due to the inherently high efficiency of the screens to absorb x-ray photon energy and emit visible light, and the

large area of the screens. The second factor is the high sensitivity of the photomultiplier tube, due primarily to its large photocathode area. The high sensitivity of the detector system leads to two undesirable effects.

In all detector systems, there is a minimum amount of time which must separate two pulses (a pulse being the electronic signal eventually generated by a photon interacting in the phosphor), if they are to be recorded as individual events. In other words, if two events occur too closely spaced in time, the second event will be lost because of this deadtime effect. The situation can become particularly severe in high count rate situations. The results of measurements indicate that the deadtime for the detector system is best represented by a paralysable model (Knoll, 1979). For a detector characterized by a paralysable deadtime model, operated in sufficiently high radiation environment, the count rate will decrease as the intensity of the radiation field is increased.

Dark pulses refer to noise generated by the photomultiplier tube when no source is present. The primary cause of this effect is thermionic emission of electrons from the photocathode. Electrons in the conduction band of the photocathode possess thermal kinetic energy. Within the conduction band there is a distribution of energies and some electrons will have enough energy to overcome the work function of the photocathode and escape. This process occurs to some extent in all photomultiplier tubes. Because

thermionic emissions lead to pulses resulting from single electrons, the pulse height (voltage) associated with such events is very small. This effect is normally handled by setting the lower level discriminator voltage of the single (or multi) channel analyzer to reject all pulses below a given small amplitude. As a result these small, single electron produced pulses are not counted, while the large pulse amplitude events generated by the many electrons produced by the incident radiation (through the chain of events beginning with absorption of the incident radiation in the phosphor layers of the detector) are counted. In general, bialkali photomultiplier tubes (such as the tube being used in the detector system) produce less of these noise events than other tube types, but are very sensitive to exposure to high levels of illumination, resulting in large increases in the rate of dark pulses which may persist for hours. Figure E.19 shows the dark pulse count rate produced by the detector system after exposure to a scatter x-ray field generated by the GE Maxitron 300, operating at 115 kVp with a 0.2414 mm lead filter, as a function of time after the x-ray machine was turned off. The persistence in the dark pulse rate is indicative of the very high light output of the terbium activated gadolinium oxysulfide phosphor. Simply adjusting the lower level discriminator to remove this effect is not a straight-forward correction because of the effect described in the following paragraph.

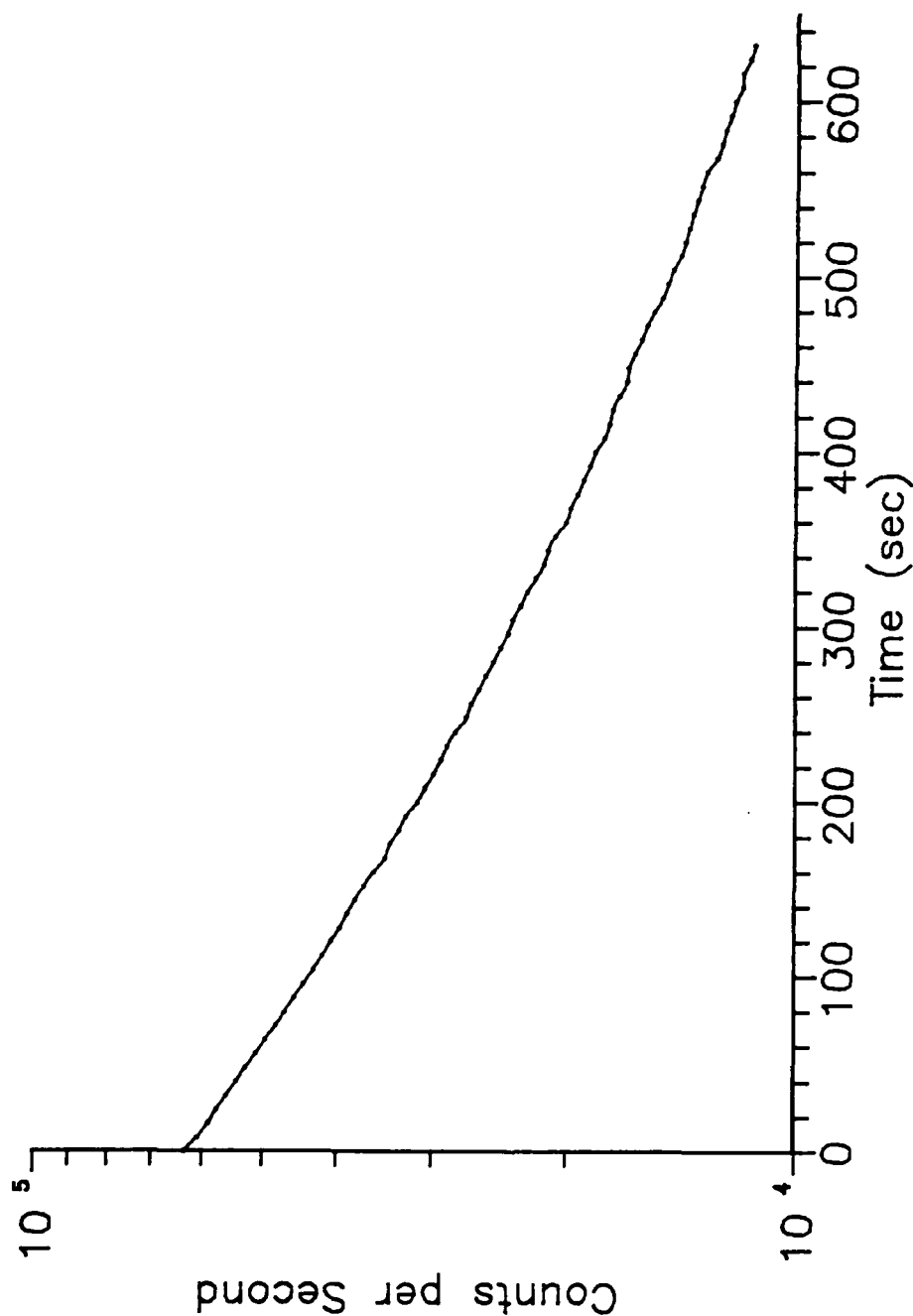


Figure E.19. Dark pulse count rate versus time. Dark pulse count rate of the terbium activated gadolinium oxysulfide detector system after exposure to a scatter x-ray field generated by the GE Maxitron 300 X-Ray Therapy Unit operating at 115 kvp with a 0.2414 mm lead filter as a function of time after the x-ray machine was turned off is shown.

Fluorescence Decay Constant

The fluorescence decay constant refers to the amount of time required for the induced luminescence from the phosphor to decay by a factor of $1/e$ ($e = 2.7182818...$). For scintillation counting, especially at high count rates, the pulse decay time should be short, so that fast signal pulses can be generated. The results of pulse height spectra measurements indicate that the fluorescence decay time (which may include phosphorescence or delayed fluorescence) for terbium activated gadolinium oxysulfide is long, on the order of tenths of seconds. This long decay constant leads to a long time period (relative to any realistic high count rate electronics) during which visible light is emitted from the phosphor layers. This results in the pulse of electrons produced at the photocathode extending over a long period of time. In low count rate situations, the ultimate result is very small pulse amplitudes characteristic of single electron events, that is, having exactly the same characteristics as the dark pulses described above. Hence, there is no simple way to discriminate against noise events. As count rate increases the number of visible light photons reaching the photocathode within a short time interval increases, and multiple electron pulses are generated, leading to larger pulse height amplitudes. This is the phenomenon of pulse pile up. It should be understood that in general, these larger pulse pile up amplitudes are produced (ultimately) by different incident photon

interactions in the phosphor layers. In order to display this effect, low activity radionuclide sources were used to construct pulse height spectra. Low activity was used to avoid the photomultiplier tube persistence demonstrated in Figure E.19. At these low levels, count rates were stable and very reproducible, as were dark pulse count rates measured without the sources. Figure E.20 displays the results of these pulse height spectra measurements. Three pulse height spectra are displayed in the figure, those of the dark pulse rate or background, ^{137}Cs , and ^{133}Ba . The radionuclide count rates include background, and the barium source is stronger than the cesium source in terms of flux intercepted by the detector.

Several points described above are demonstrated by these spectra. The background and source pulses are predominately small, and the pulse height spectra similar. Neither amplification nor discrimination can separate the bulk of the dark pulses from the source pulses. For the very small pulses, which occur with high count rates, the greatest count rate is associated with the smallest true intensity. This is an example of paralysable deadtime behavior. Above the deadtime region the amplitude of the tails of the spectra decrease continuously and have count rate magnitudes related to each other in the same relative order as their intensities. These two effects are a result of the pile up of small pulses described above. Essentially, the radionuclide pulse height spectra show that the

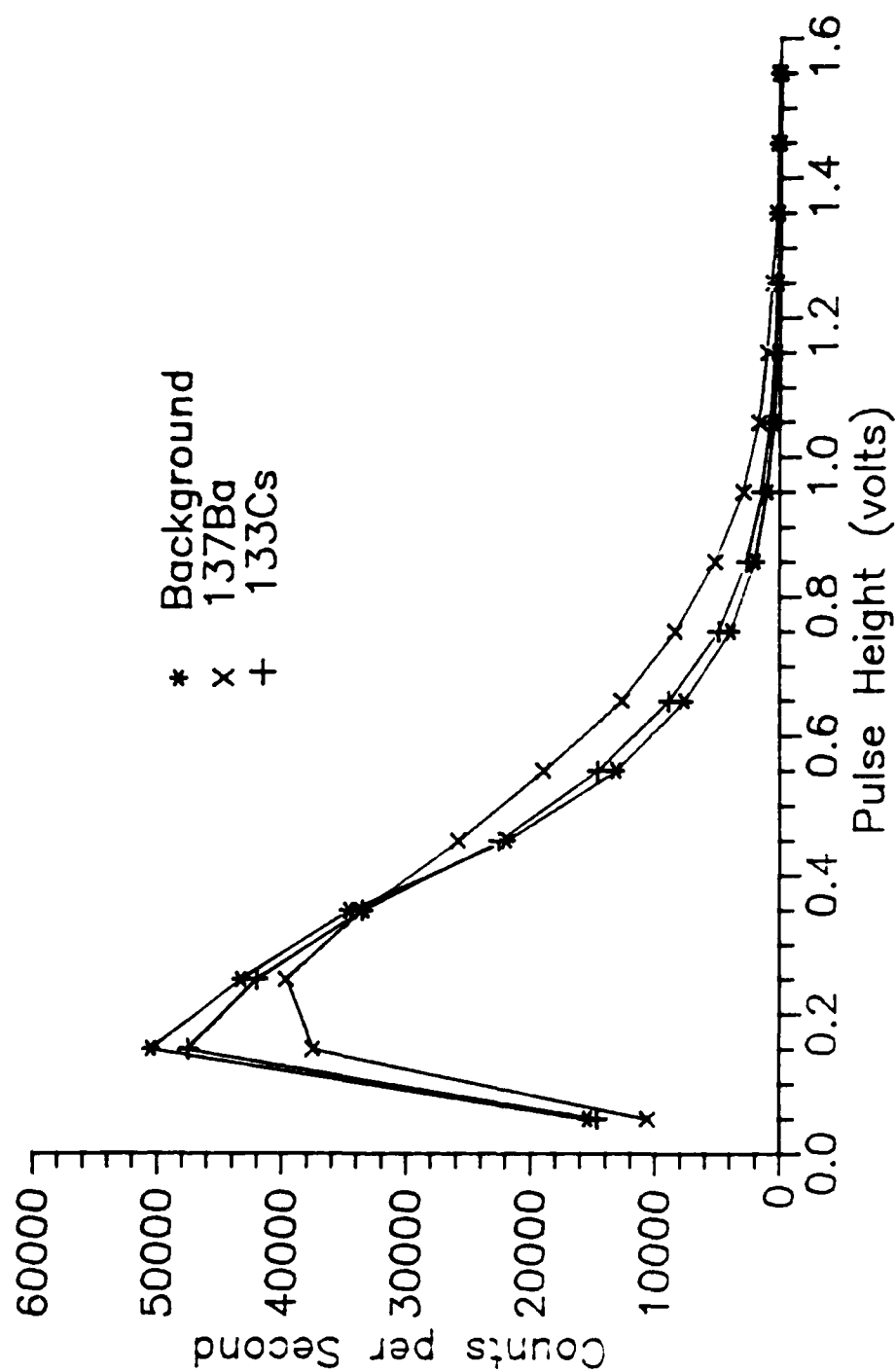


Figure E.20. Measured pulse height spectra. The pulse height spectra using the terbium activated gadolinium oxysulfide detector system for background (dark pulses) and two radionuclide sources are shown.

probability of a given number of visible photons reaching the photocathode within the detector resolving time decreases continuously as a function of that number. For the dark pulses, the interpretation is that the probability that a given number of electrons are thermionically emitted from the photocathode within the detector resolving time decreases continuously as a function of that number.

Corrective Actions

Some corrective actions can be taken to allow the detector to function as a tool for the measurements, however, the long fluorescence decay constant makes any detector based on this phosphor unusable in a real operating landmine detector system. The reason for this conclusion lies in the rapid scanning rate required to meet reasonable rates of travel for the vehicle carrying the detector system. Pixel irradiation times in such a real system are estimated to be on the order of 10 to 100 microseconds (Moler, 1985). Corrections, which can be applied to the terbium activated gadolinium oxysulfide detector, to allow its use in imaging measurements for laboratory experiments are reducing the detector sensitivity, reducing the dark pulses, and applying low energy discrimination. The simplest methods to reduce sensitivity are to reduce the area of the detector and the diameter of the photomultiplier tube. This will result in lower count rates and decreased photomultiplier tube persistence. Since the amount of thermionic emission is directly proportional to the area of the photocathode, reduction in

the size of the photomultiplier tube will also benefit this problem. Cooling the photomultiplier tube would also reduce thermionic emission. Nothing can be done to alter the fluorescence decay constant, but it can be converted to a possible advantage. By setting the lower level discriminator at a point on the tail of the curve, well beyond any deadtime region, count rates will increase with intensity of the incident radiation fields. In fact the increase is, in general, greater than linear due to pulse pile up effects. Used in this mode, the detector could actually amplify differences between soil only and soil with buried mine situations. Prediction of the detector response by calculations under these operating conditions would be extremely difficult. Nevertheless, measurements were made using radionuclide sources for comparison with calculated values.

Comparisons of Measured and Calculated Responses

Calculation Technique

A simple Monte Carlo code was written to simulate the isotropic emission of photons from radionuclide sources. The code is run until emissions produced 10000 intersections with the detector screens. Energies of source photons are assigned based on the frequency of emission per decay characteristic of the radionuclide. Emissions which resulted in photons missing the detector were simply counted separately. The photons striking the detector plane were coupled to the calculated detector response matrix using their energies and

angles of incidence. To allow higher energy photons to be considered, the detector response matrix was extended to 1.00 MeV using the DETECT.PAS code. The sources used in the calculations were ^{133}Ba and ^{137}Cs . Energies and frequencies of emission per decay were taken from Unger and Trubey (1982). These two nuclides were chosen for their very different photon emission characteristics.

The ^{133}Ba source emits low energy photons while the emissions of the ^{137}Cs source are dominated by a 0.6616 MeV gamma. Because of the high energy of this photon, significant deposition of energy in the phosphor layers of the detector occurs only for large angles of incidence. Two types of calculation results are provided, the ratio of the detector responses of the two nuclides and response versus distance from the detector curves. Table E.3 shows the ratios of various radiation field quantities for the two nuclides used. The largest contributing factor in the uncertainties given in the table lies in the activities of the sources. As can be seen from these numbers, the detector response function plays a major role in increasing the relative importance of the low energy photons of the barium source.

Measurements

The detector responses for each nuclide were measured at the face (3.016 cm from the plane of the face of the front screen) of the detector with a lower level discriminator level setting of 1.10 volts (far out on the pulse pile

TABLE E.3
Calculated Ratios of Radiation Field Quantities,
 ^{133}Ba to ^{137}Cs

Quantity	Ratio ^a
Activity ^b	0.744 ± 0.032
Fluence rate (flux)	2.075 ± 0.088
Energy fluence rate	0.522 ± 0.022
Detector response	4.725 ± 0.223

^aSources located 3.016 cm from the center of the detector plane.

^bOn August 14, 1986.

up tail). The measured value for the ratio was 4.892 ± 0.346 , which compares well with the calculated value of 4.725 ± 0.223 . Response versus distance curves were made under the same conditions as the first ratio comparison above. These curves are shown in Figures E.21 and E.22. In these figures, each set of calculated data has been normalized to the measured data by multiplication by a constant. The value of the constant for a data set is determined by calculating the single best value for the measured to calculated ratio considering unequal uncertainties in each ratio (Knoll, 1979). The cesium results are good; the barium results show significant departure from measured values closer to the detector, probably reflecting the non-linear nature of the pulse pile up with variation of source strength. This effect would be expected to play a larger role for barium than cesium because of the higher flux of the source and the higher response of the detector to its lower energy photons.

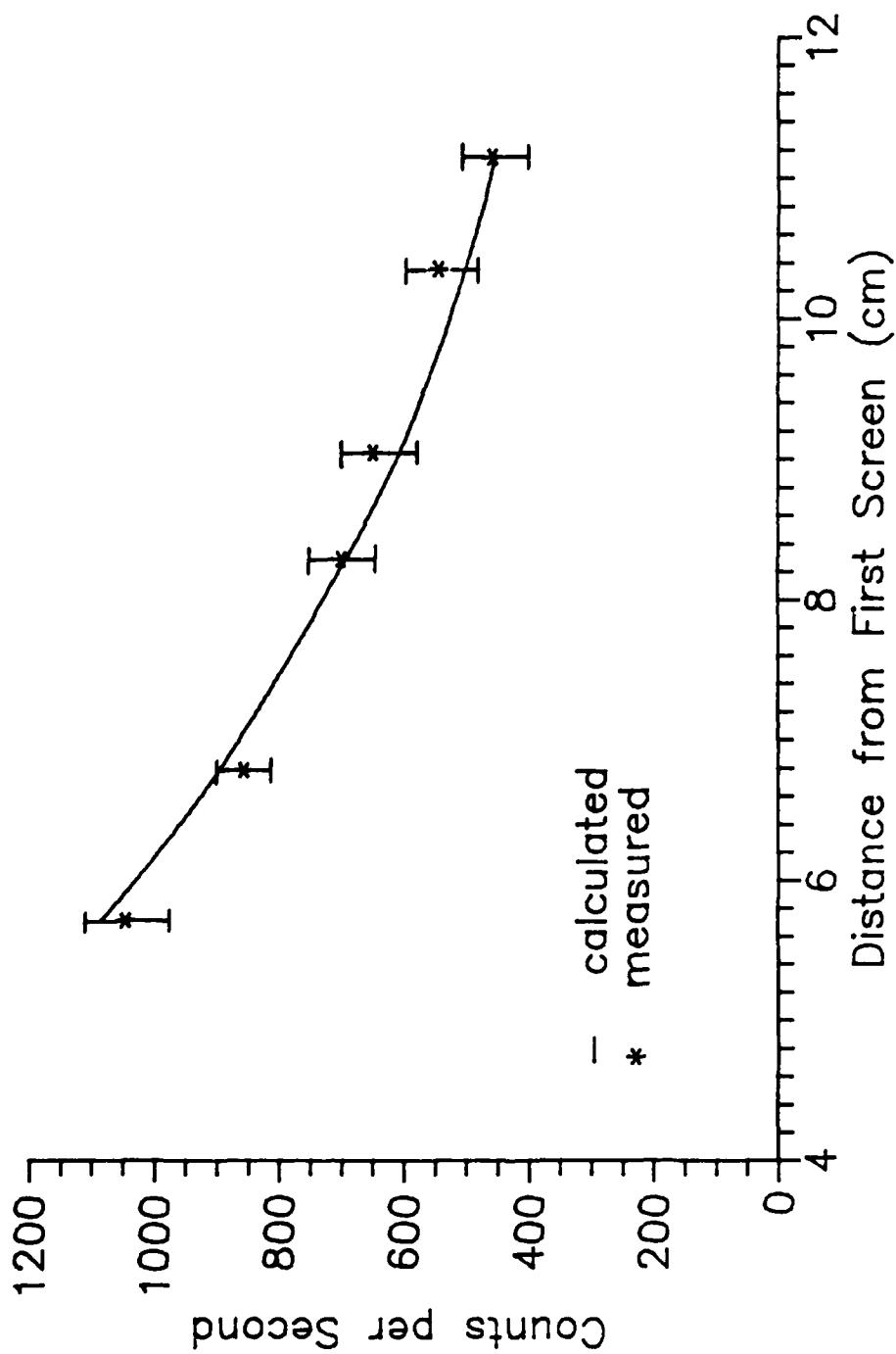


Figure E.21. Response versus distance for ^{137}Cs . A comparison of the measured and calculated response of the terbium activated gadolinium oxysulfide detector for a ^{137}Cs point source as a function of distance from the detector plane is shown.

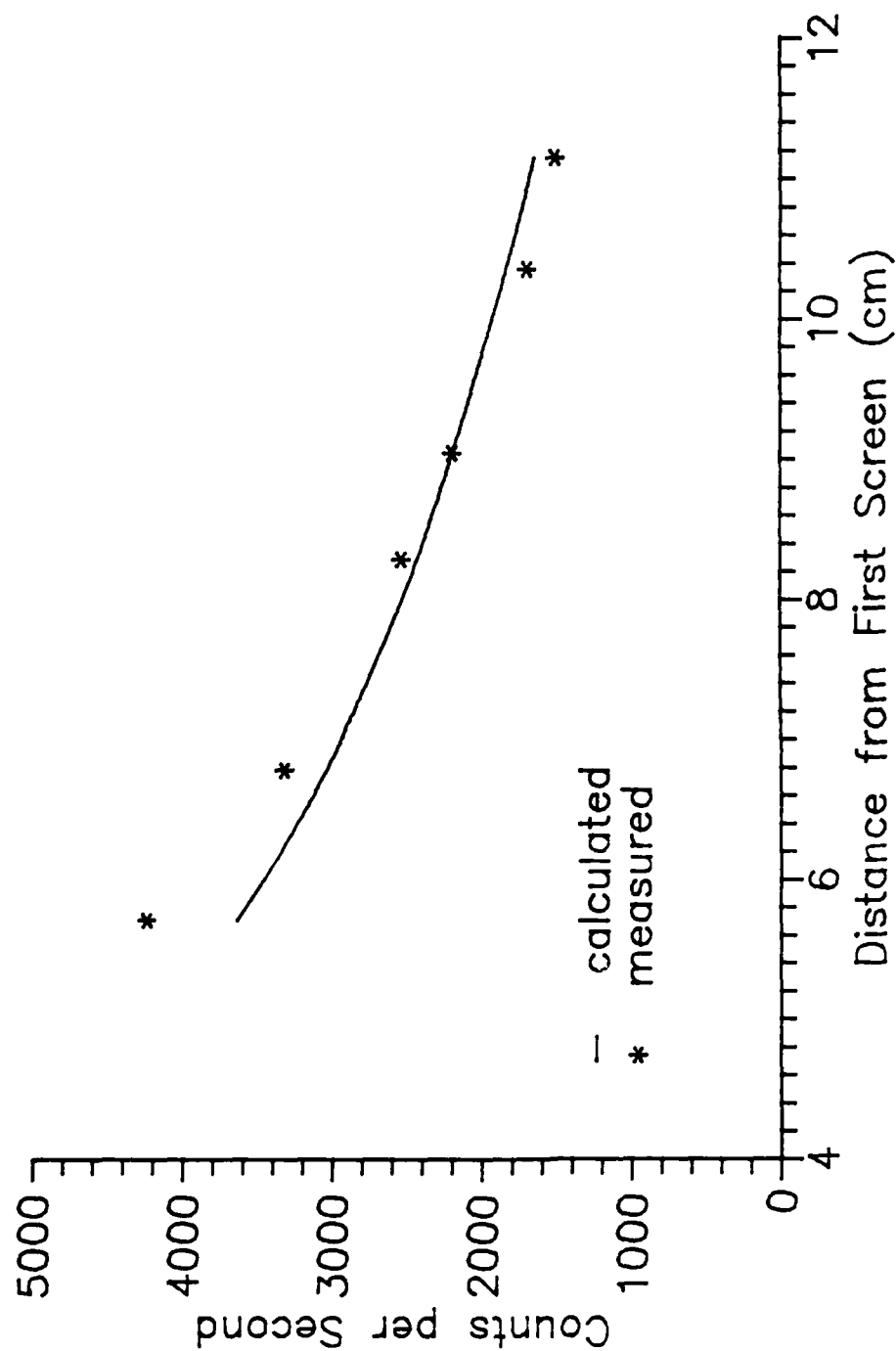


Figure E.22. Response versus distance for ^{133}Ba . A comparison of the measured and calculated response of the terbium activated gadolinium oxysulfide detector for a ^{133}Ba point source as a function of distance from the detector plane is shown. Uncertainties in measured data are too small to plot.

APPENDIX F
X-RAY SPECTRA USED IN MEASUREMENTS

This appendix contains a catalog of calculations of the x-ray spectra used in the experimental portion of the research described in Chapter VIII. These spectra are also used for the discussion of power requirements contained in that same chapter. The calculations of the spectra are provided by the XRSPEC.PAS code described and validated in Chapter V and Appendix D.

The source of the x-ray spectra used in the experiments is the GE Maxitron 300 X-Ray Therapy Unit (General Electric, 1962). It is described in Chapter III. The spectra displayed in this appendix are for peak kilovoltages of 100, 150 and 200 kVp. Beam filtration varies from very light to very heavy, providing a fair representation of the range of possible beam qualities available from this machine. The spectra are displayed in terms of the fluence per unit energy (photons per cm^2 per keV) as a function of photon energy. All spectra are normalized to a total fluence of 1 photon per cm^2 .

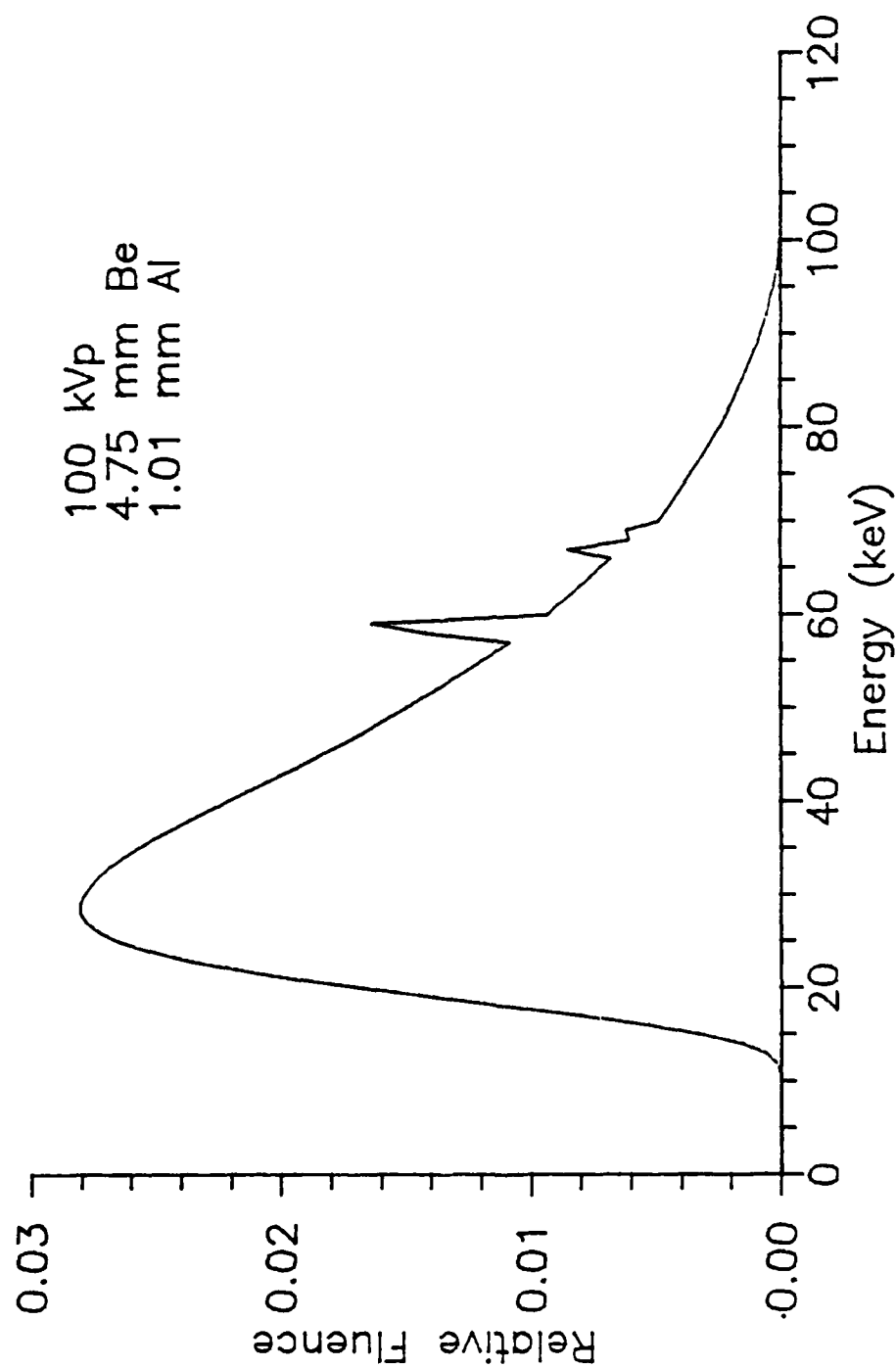


Figure F.1. X-ray fluence spectrum, 100 kVp, 1.01 mm Al. The x-ray fluence spectrum at 100 kVp calculated by the XRSPEC.PAS code for the GE Maxitron 300 X-Ray Therapy Unit with 4.75 mm beryllium inherent filtration, 1.01 mm aluminum added filtration and air path length of 60 cm is shown. Fluence units are photons per cm^2 per keV. Total fluence is normalized to 1 photon per cm^2 .

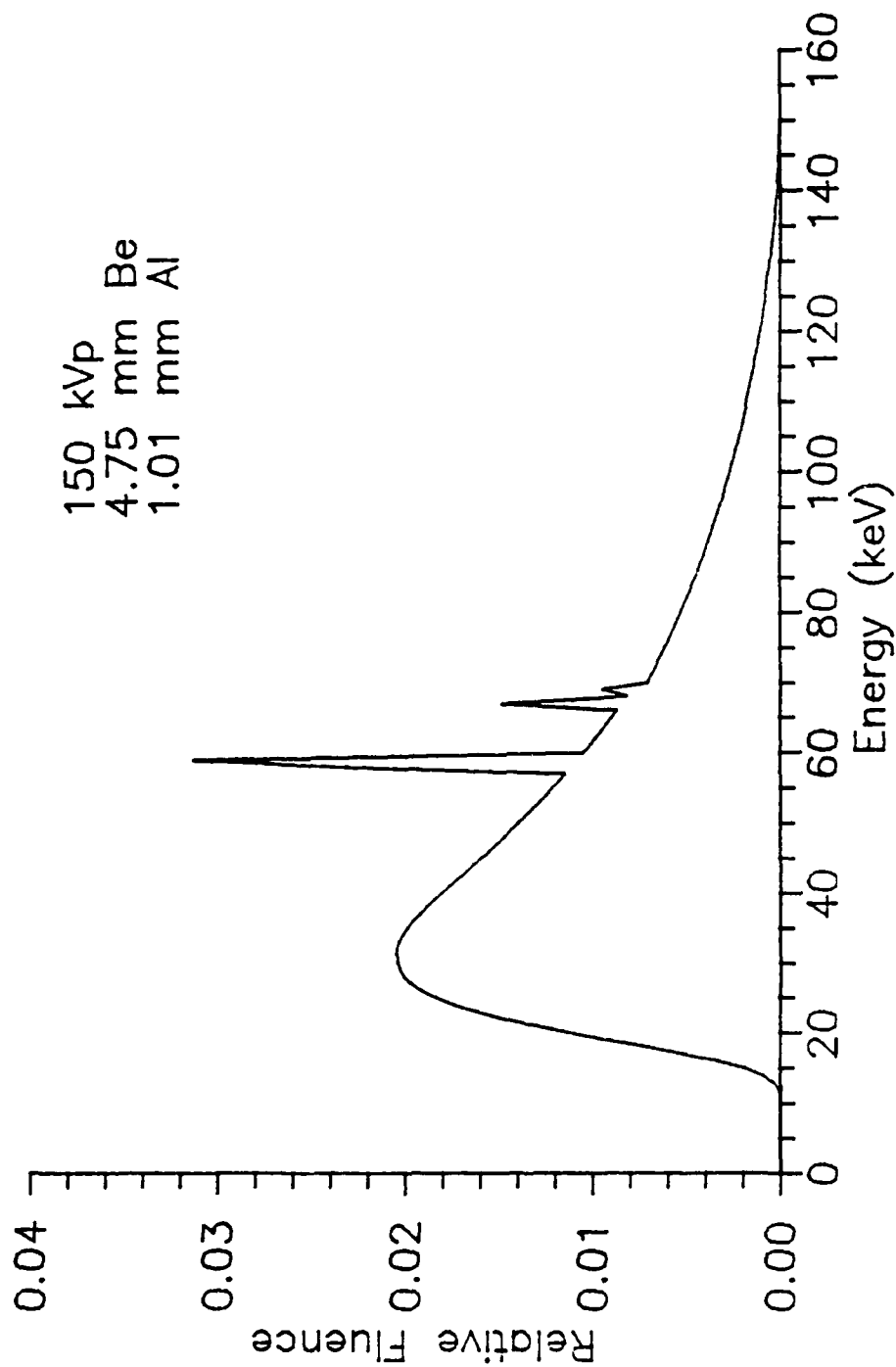


Figure F.2. X-ray fluence spectrum, 150 kVp, 1.01 mm Al. The x-ray fluence spectrum at 150 kVp calculated by the XRSPEC.PAS code for the GE Maxitron 300 X-Ray Therapy Unit with 4.75 mm beryllium inherent filtration, 1.01 mm aluminum added $\frac{1}{2}$ filtration and air path length of 60 cm is shown. Fluence units are photons per cm^2 per keV. Total fluence is normalized to 1 photon per cm^2 .

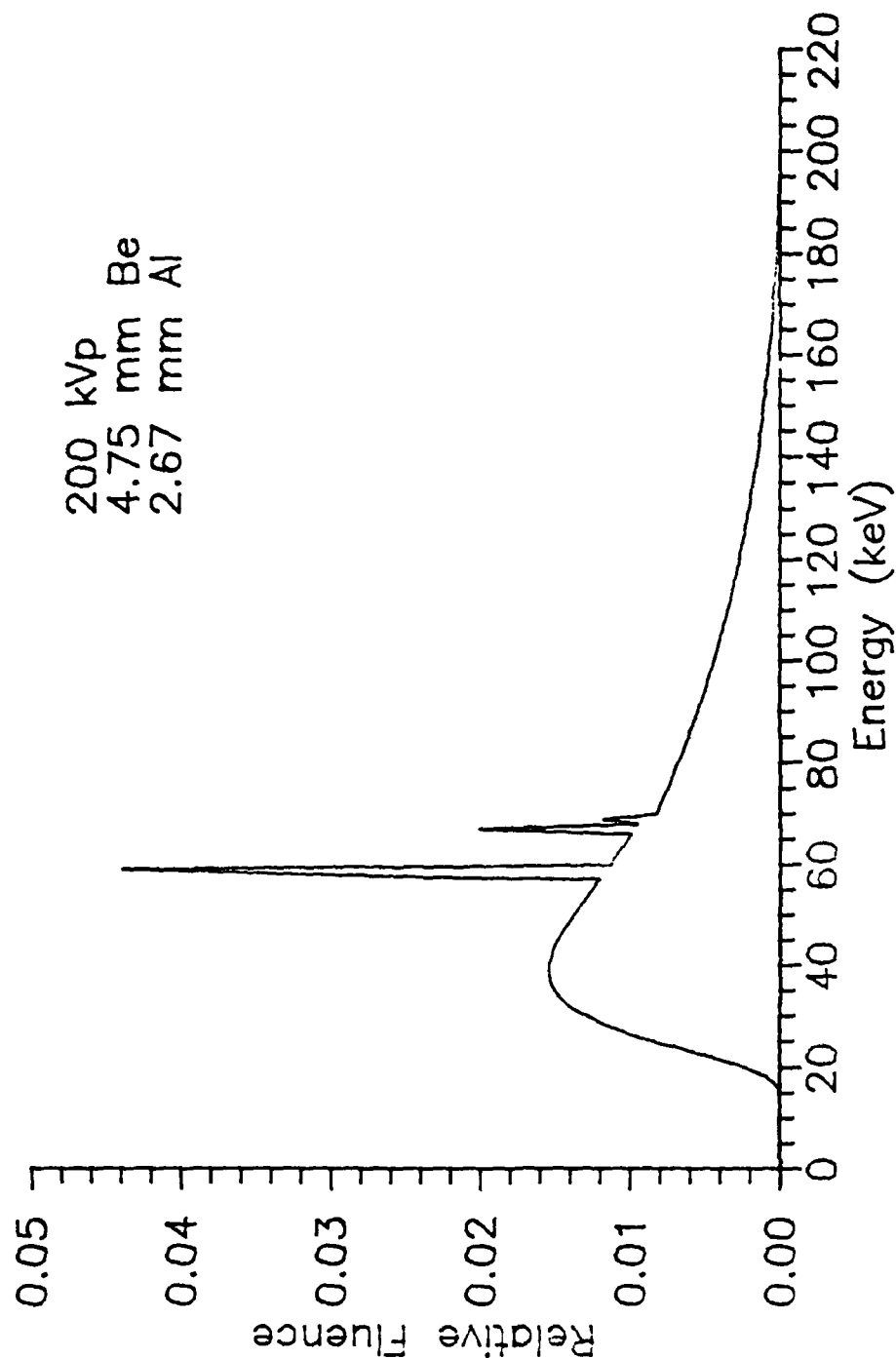


Figure F.3. X-ray fluence spectrum, 200 kVp, 2.67 mm Al. The x-ray fluence spectrum at 200 kVp calculated by the XRSPEC.PAS code for the GE Maxitron 300 X-Ray Therapy Unit with 4.75 mm beryllium inherent filtration, 2.67 mm aluminum added filtration and air path length of 60 cm is shown. Fluence units are photons per cm^2 per keV. Total fluence is normalized to 1 photon per cm^2 .

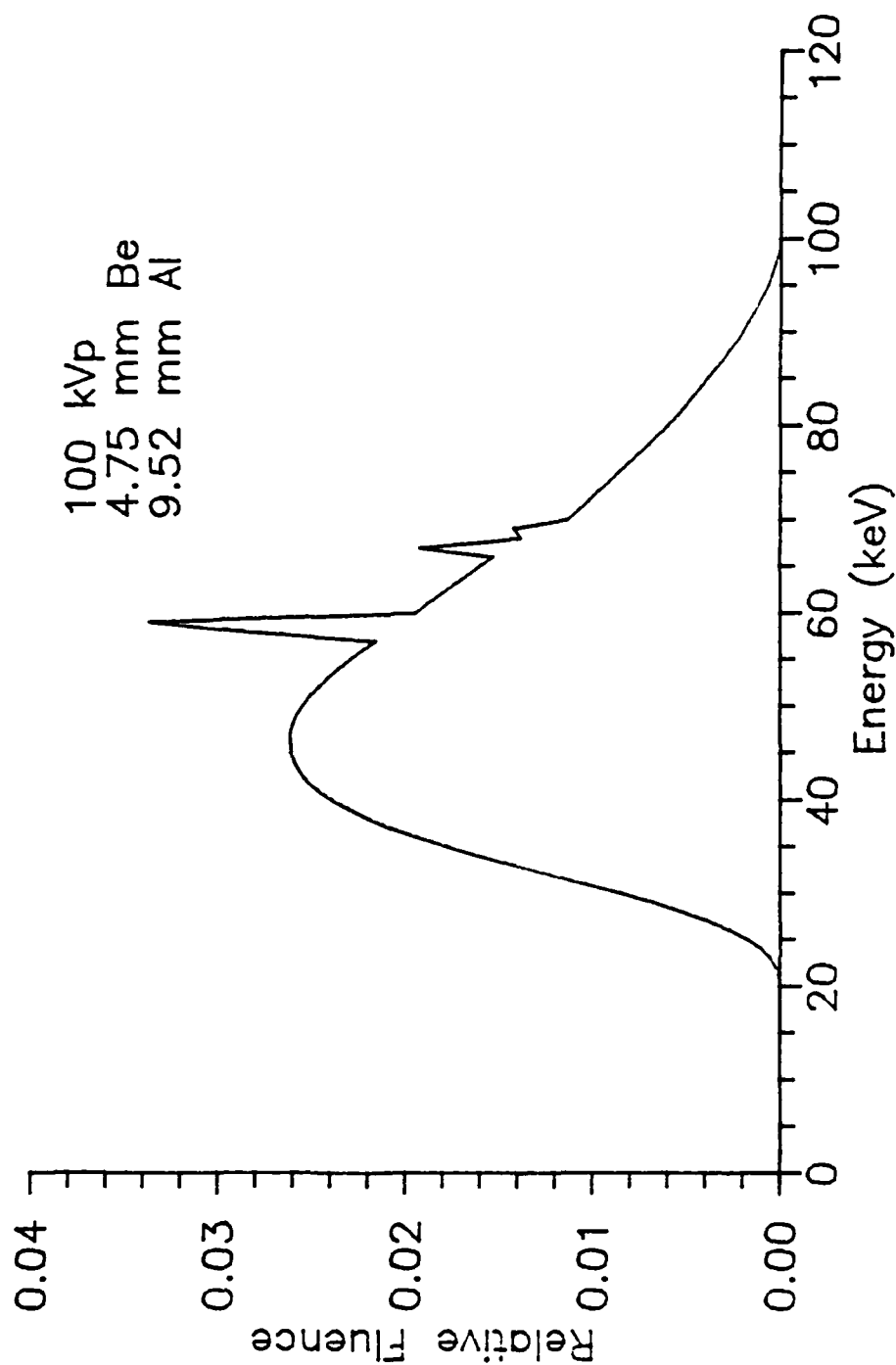


Figure F.4. X-ray fluence spectrum, 100 kVp, 9.52 mm Al. The x-ray fluence spectrum at 100 kVp calculated by the XRSPEC.PAS code for the GE Maxitron 300 X-Ray Therapy Unit with 4.75 mm beryllium inherent filtration, 9.52 mm aluminum added $\frac{1}{2}$ filtration and air path length of 60 cm is shown. Fluence units are photons per cm^2 per keV. Total fluence is normalized to 1 photon per cm^2 .

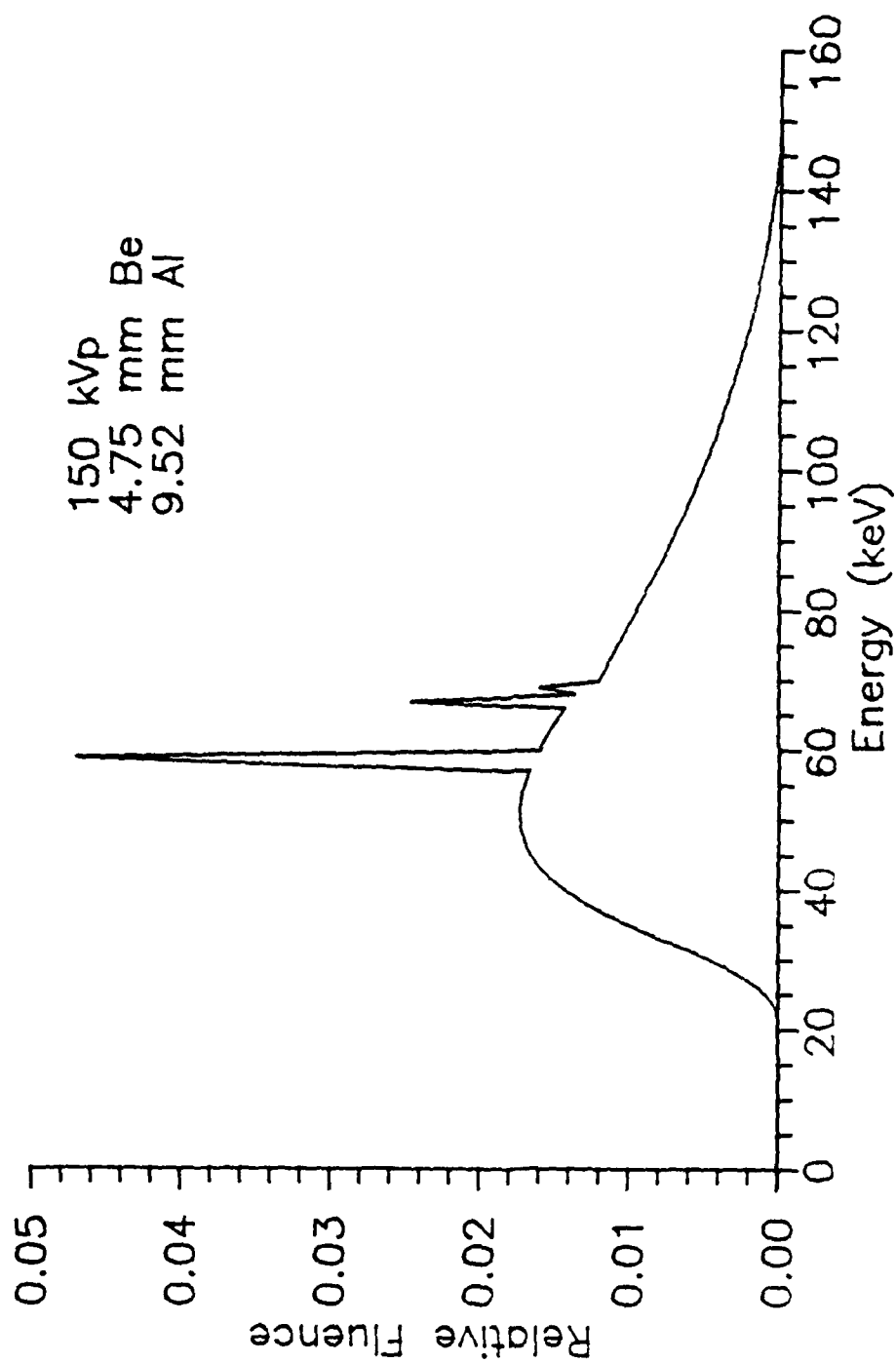


Figure F.5. X-ray fluence spectrum, 150 kVp, 9.52 mm Al. The x-ray fluence spectrum at 150 kVp calculated by the XRSPEC.PAS code for the GE Maxitron 300 X-Ray Therapy Unit with 4.75 mm beryllium inherent filtration, 9.52 mm aluminum added filtration and air path length of 60 cm is shown. Fluence units are photons per cm^2 per keV. Total fluence is normalized to 1 photon per cm^2 .

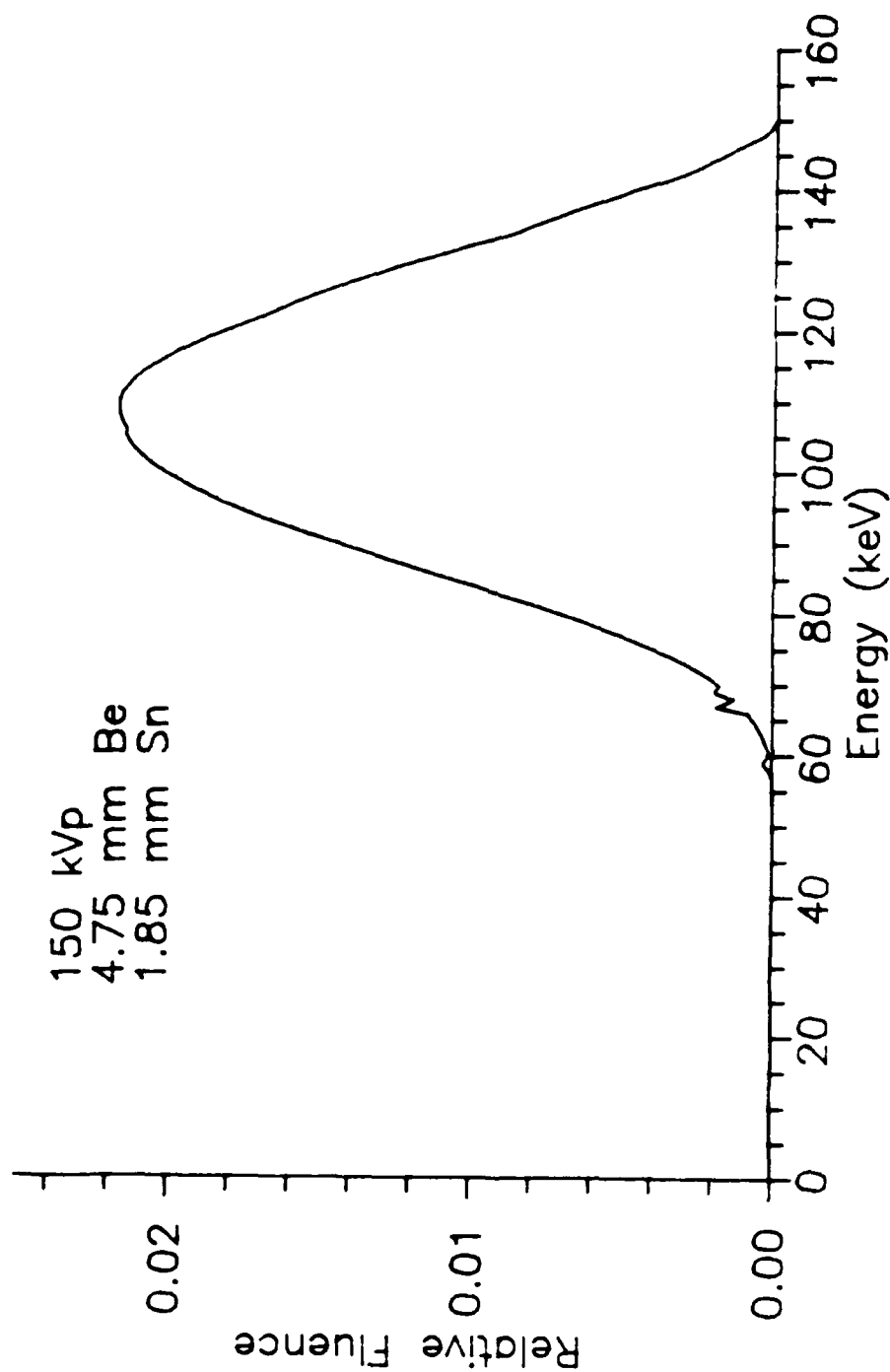


Figure F.6. X-ray fluence spectrum, 150 kVp, 1.85 mm Sn. The x-ray fluence spectrum at 150 kVp calculated by the XRSPEC.PAS code for the GE Maxitron 300 X-Ray Therapy Unit with 4.75 mm beryllium inherent filtration, 1.85 mm tin added filtration and air path length of 60 cm is shown. Fluence units are photons per cm^2 per keV. Total fluence is normalized to 1 photon per cm^2 .

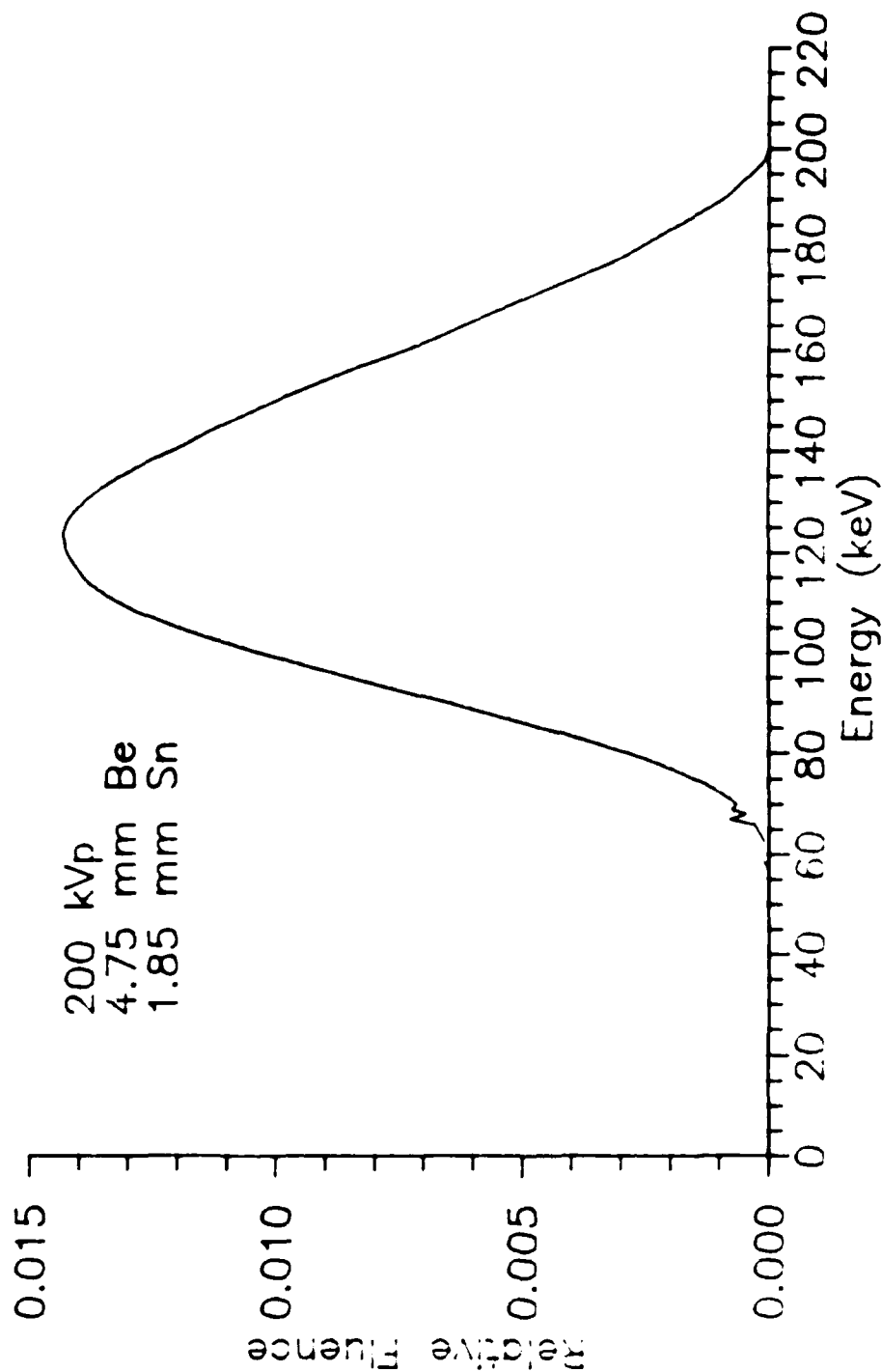


Figure F.7. X-ray fluence spectrum, 200 kVp, 1.85 mm Sn. The x-ray fluence spectrum at 200 kVp calculated by the XRSPEC.PAS code for the GE Maxitron 300 X-Ray Therapy Unit with 4.75 mm beryllium inherent filtration, 1.85 mm tin added filtration and air path length of 60 cm is shown. Fluence units are photons per cm^2 per keV. Total fluence is normalized to 1 photon per cm^2 .

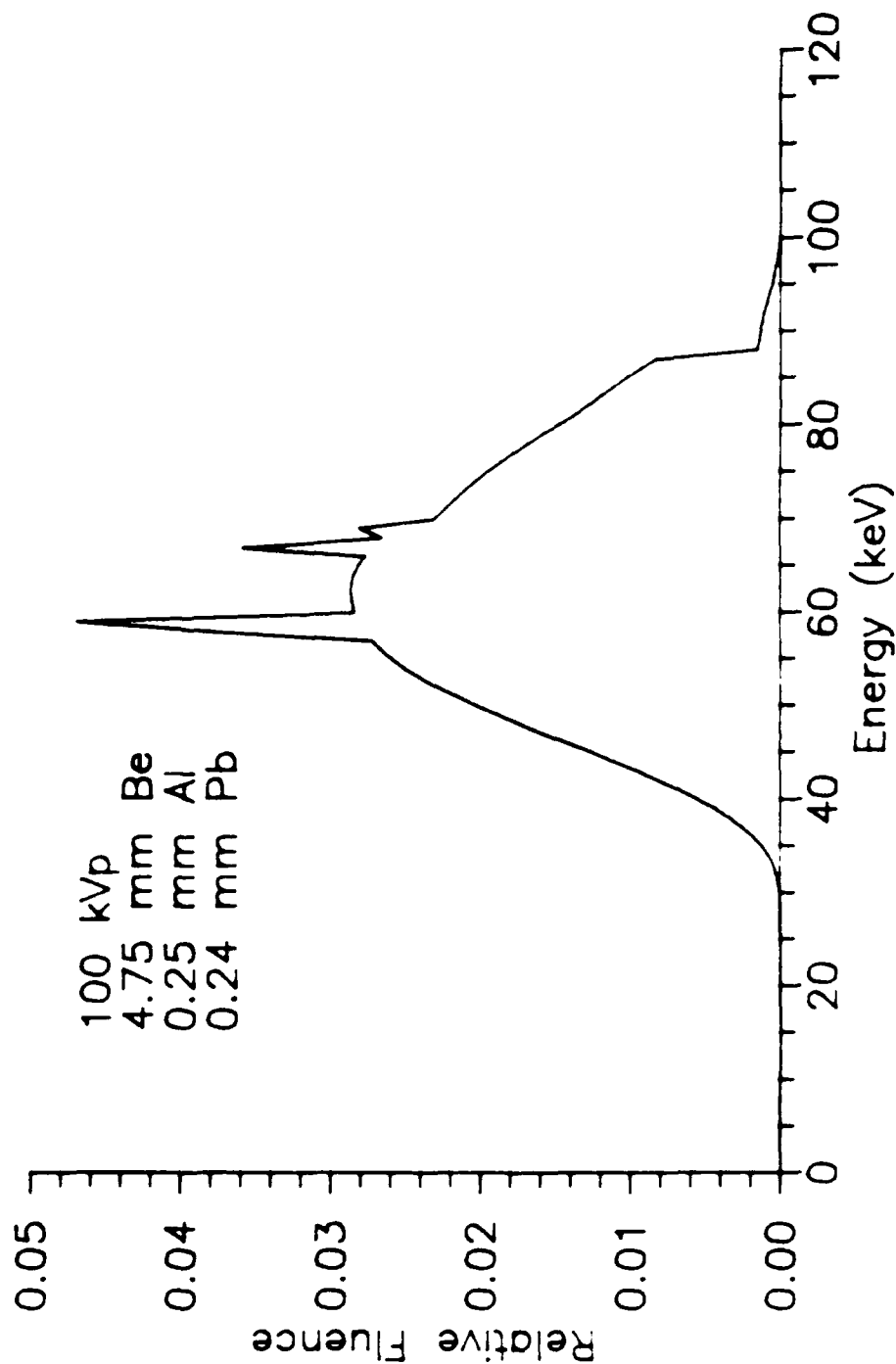


Figure F.8. X-ray fluence spectrum, 100 kVp, 0.25 mm Al, 0.24 mm Pb. The x-ray fluence spectrum at 100 kVp calculated by the XRSPEC.PAS code for the GE Maxitron 300 X-Ray Therapy Unit with 4.75 mm beryllium inherent filtration, 0.25 mm aluminum equivalent monitor ionization chamber, 0.24 mm lead added filtration and air path length of 60 cm is shown. Fluence units are photons per cm^2 per keV. Total fluence is normalized to 1 photon per cm^2 .

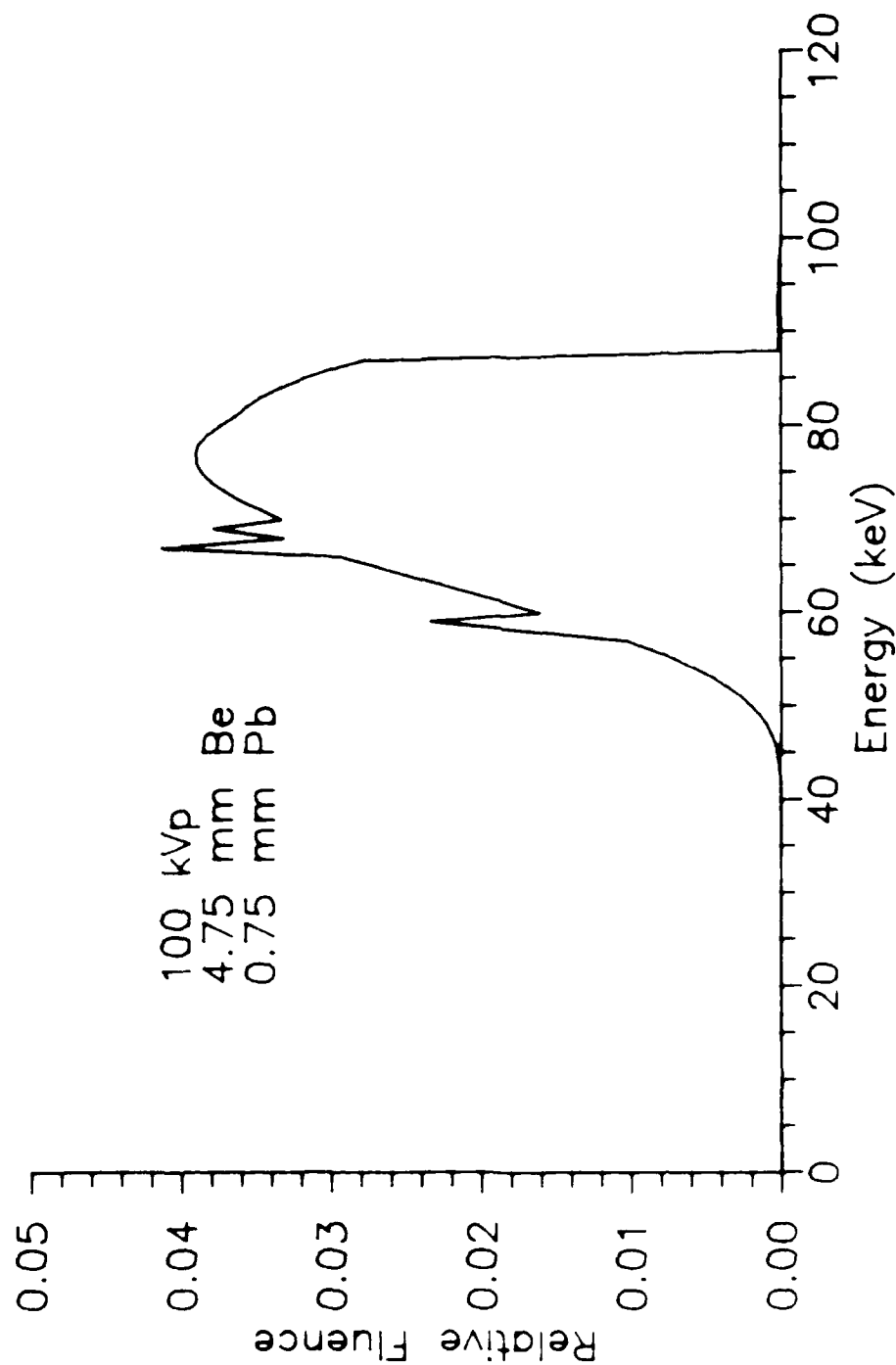


Figure F.9. X-ray fluence spectrum, 100 kVp, 0.75 mm Pb. The x-ray fluence spectrum at 100 kVp calculated by the XRSPEC.PAS code for the GE Maxitron 300 X-Ray Therapy Unit with 4.75 mm beryllium inherent filtration, 0.75 mm lead added $\frac{1}{2}$ filtration and air path length of 60 cm is shown. Fluence units are photons per cm^2 per keV. Total fluence is normalized to 1 photon per cm^2 .

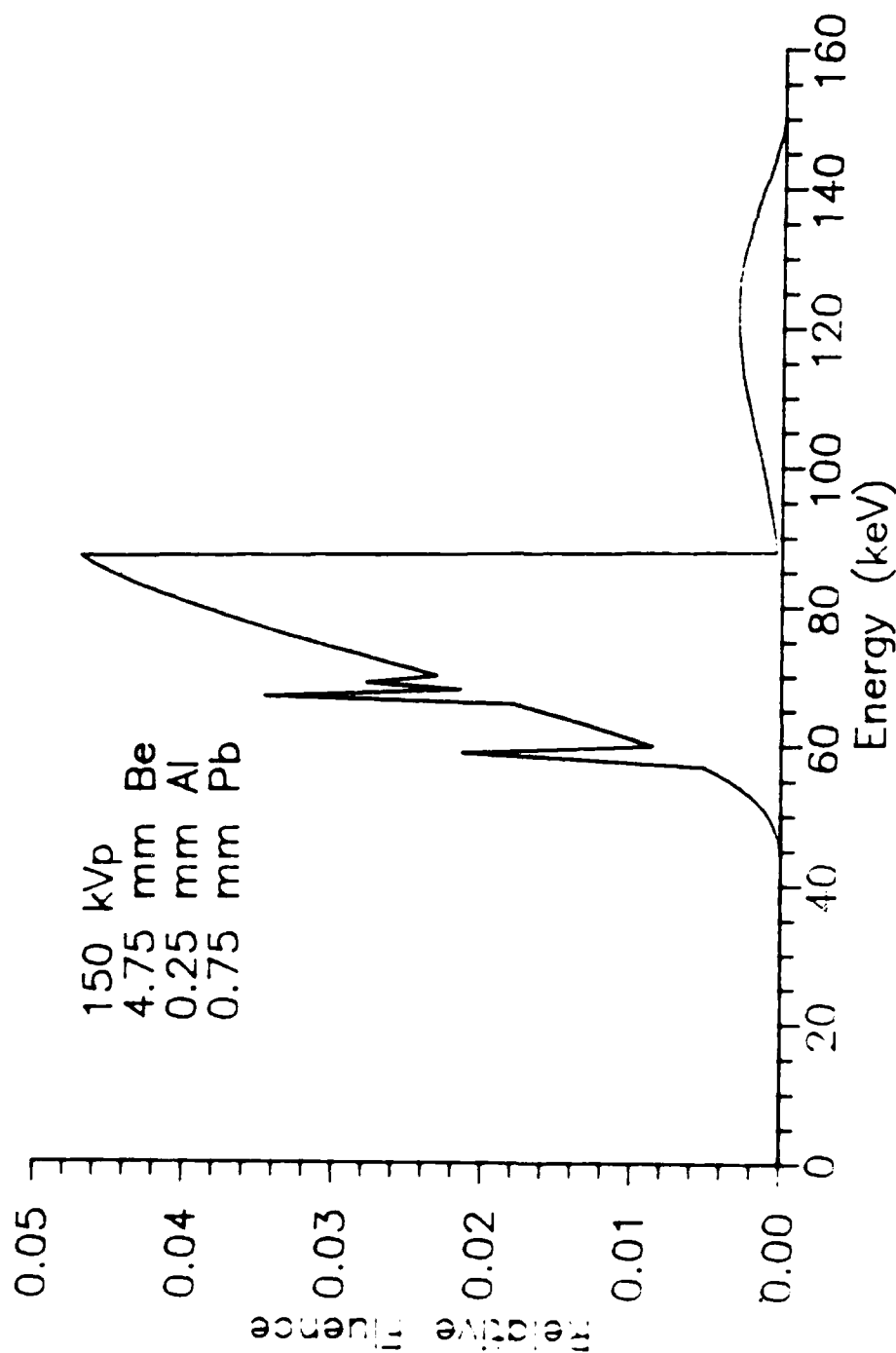


Figure F.10. X-ray fluence spectrum, 150 kVp, 0.25 mm Al, 0.75 mm Pb. The x-ray fluence spectrum at 150 kVp calculated by the XRSPEC.PAS code for the GE Maxitron 300 X-Ray Therapy Unit with 4.75 mm beryllium inherent filtration, 0.25 mm aluminum equivalent monitor ionization chamber, 0.75 mm lead added filtration and air path length of 60 cm is shown. Fluence units are photons per cm^2 per keV. Total fluence is normalized to 1 photon per cm^2 .

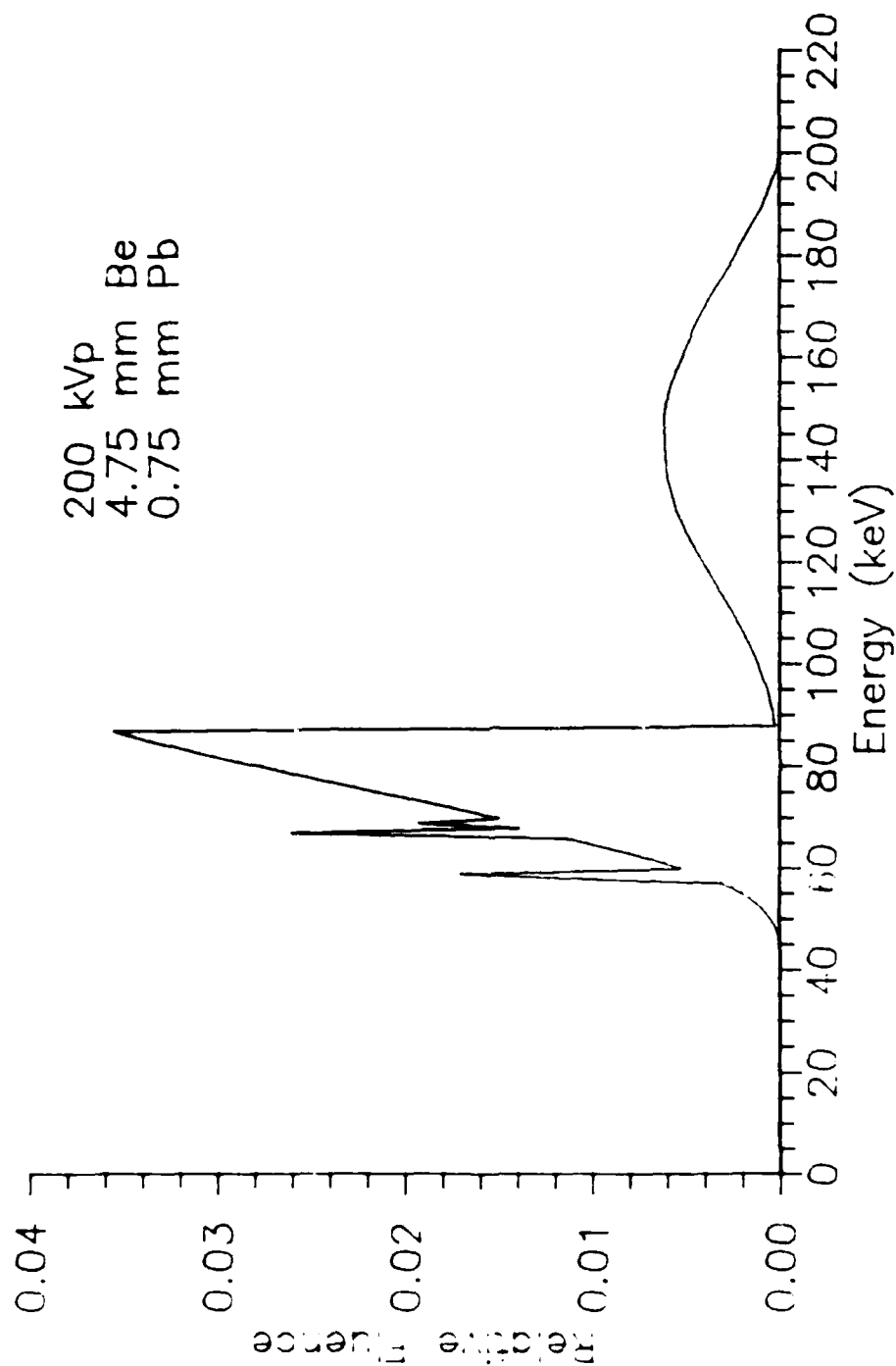


Figure F.11. X-ray fluence spectrum, 200 kVp, 0.75 mm Pb. The x-ray fluence spectrum at 200 kVp calculated by the XRSPEC.PAS code for the GE Maxitron 300 X-Ray Therapy Unit with 4.75 mm beryllium inherent filtration, 0.75 mm lead added filtration and air path length of 60 cm is shown. Fluence units are photons per cm² per keV. Total fluence is normalized to 1 photon per cm².

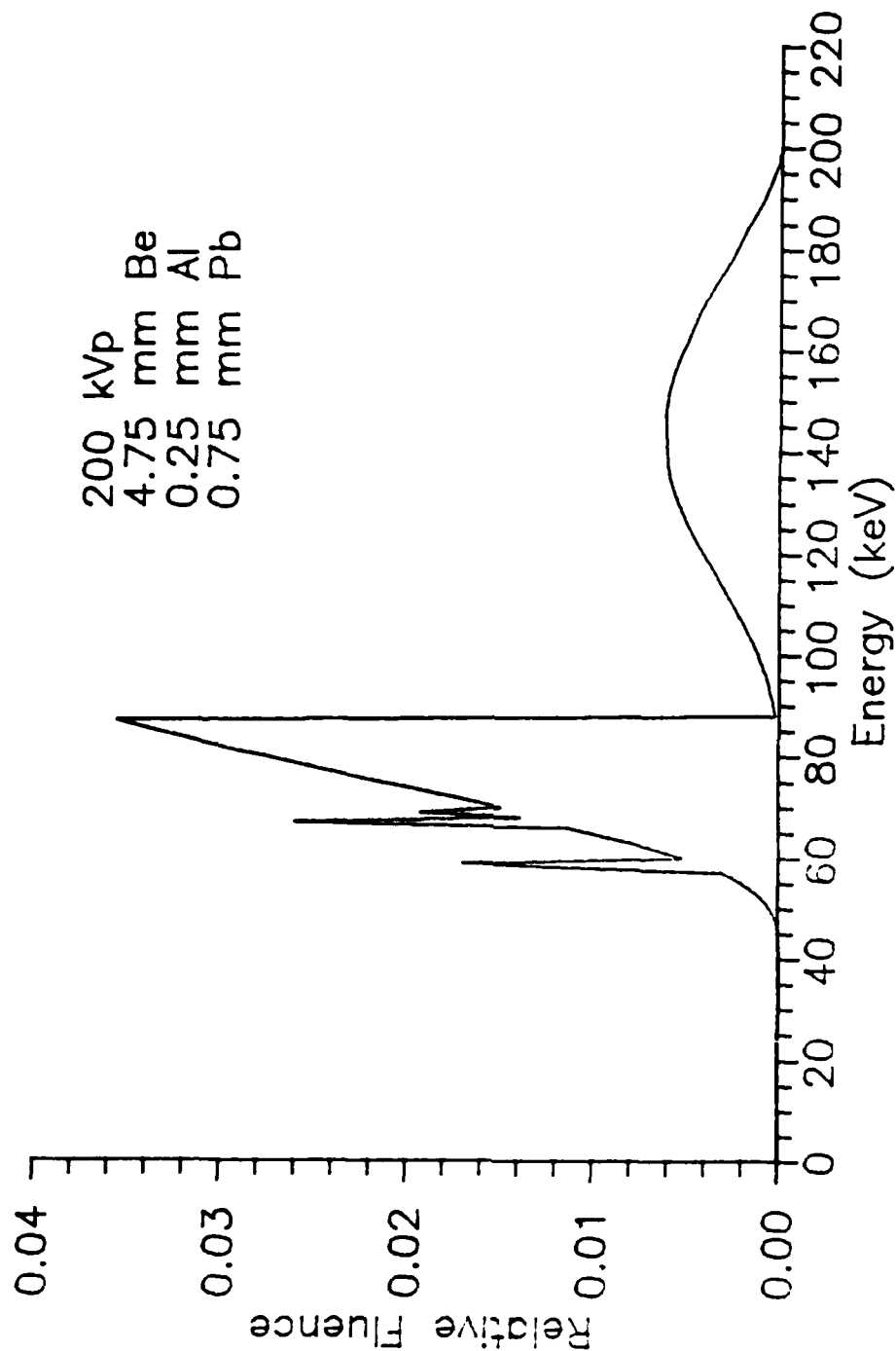


Figure F.12. X-ray fluence spectrum, 200 kVp, 0.25 mm Al, 0.75 mm Pb. The x-ray fluence spectrum at 200 kVp calculated by the XRSPEC.PAS code for the GE Maxitron 300 X-Ray Therapy Unit with 4.75 mm beryllium inherent filtration, 0.25 mm aluminum equivalent monitor ionization chamber, 0.75 mm lead added filtration and air path length of 60 cm is shown. Fluence units are photons per cm^2 per keV. Total fluence is normalized to 1 photon per cm^2 .

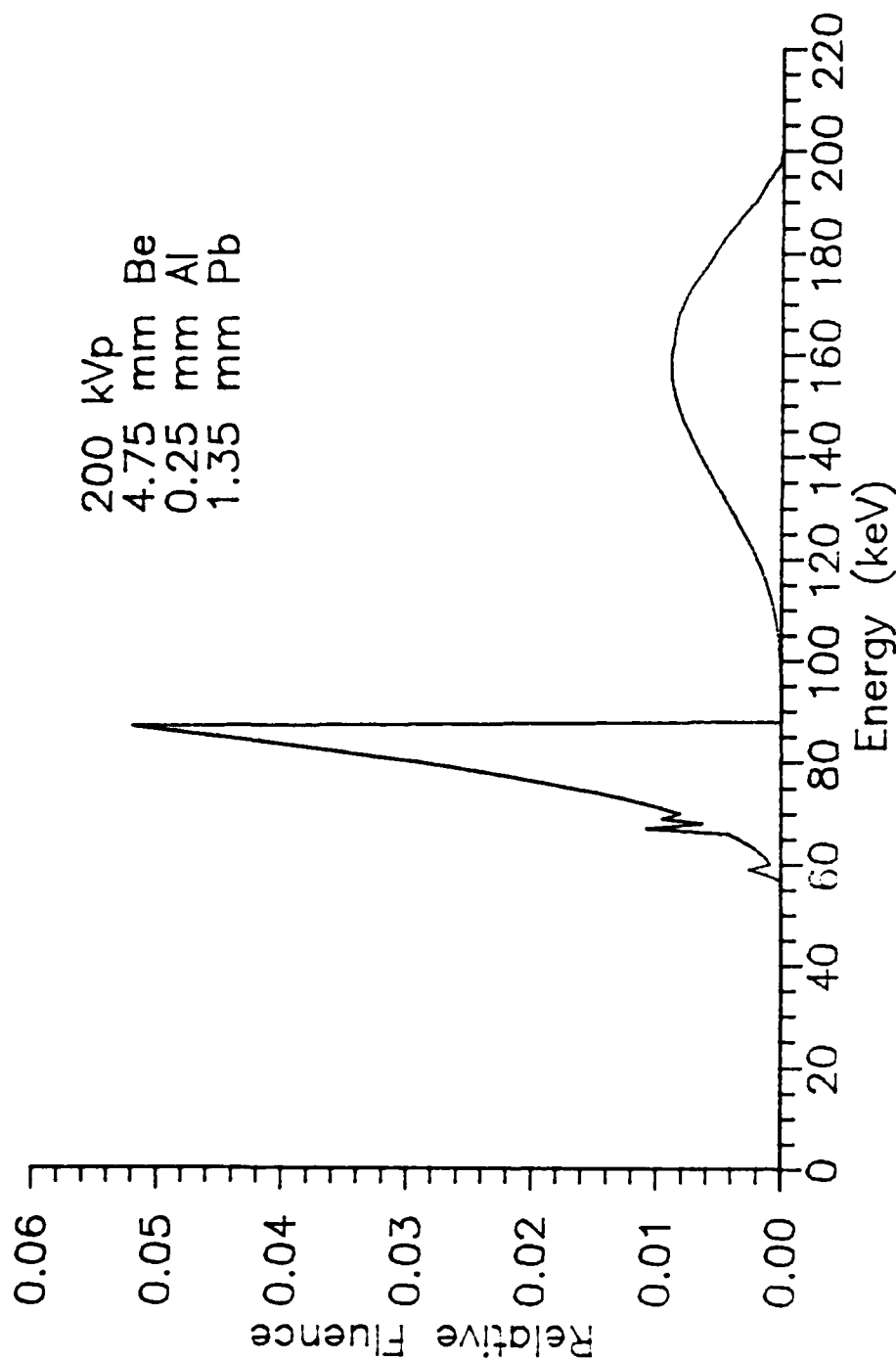


Figure F.13. X-ray fluence spectrum, 200 kVp, 0.25 mm Al, 1.35 mm Pb. The x-ray fluence spectrum at 200 kVp calculated by the XRSPEC.PAS code for the GE Maxitron 300 X-Ray Therapy Unit with 4.75 mm beryllium inherent filtration, 0.25 mm aluminum equivalent monitor ionization chamber, 1.35 mm lead added filtration and air path length of 60 cm is shown. Fluence units are photons per cm^2 per keV. Total fluence is normalized to 1 photon per cm^2 .

APPENDIX G

COMPUTER CODES

The application of the computer to the mine detection problem has been important to the research effort. Computer calculations have been used to determine optimum parameters for the problem and for analyzing data generated in experiments.

Computer Hardware

Personal Computers and Monte Carlo Calculations

The research described in this dissertation makes extensive use of Monte Carlo photon transport calculations. These types of computations are normally performed on large mainframe computers using established codes. Advances in computer technology have made such calculations feasible on personal computers. Calculation time is still far short of that achievable by modern mainframe computers, but advantages in cost, flexibility and detailed understanding of the problem make the small computer attractive.

Detailed understanding of the problem is sometimes lost with large sophisticated standard mainframe codes. The alternative of writing the Monte Carlo code encourages understanding of sampling procedures and the physics of photon interactions. The ability to make mistakes without

incurring any cost above wasted time encourages experimentation with the code. This ability to make mistakes is, of course, a major disadvantage if they go undetected. Comparisons with published data, experimental measurements, and standard codes run on mainframe computers are important to avoiding coding and logic errors.

The flexibility to write a code specific to the problem at hand can do much to overcome speed advantages of mainframe computers used with standard codes. The standard codes are generally large and somewhat unwieldy because they must have the capability to provide almost any imaginable desired type of output over a very large range of problem types and parameters. An additional flexibility is accrued because a small computer can be dedicated entirely to the problem at hand and not have to compete in a multiple user environment.

Computer Selection

A Compaq Deskpro (Compaq, 1984a), equipped with 640 kilobytes of random access memory, two 360 kilobyte floppy diskette drives, a 20 megabyte hard disk drive, a 8087-2 math coprocessor and a Definicon Systems DSI-32 32032 coprocessor (Definicon, 1986) with 32081 math coprocessor and 1 megabyte of random access memory, was used for the calculations presented in this dissertation. An IBM Personal Computer (Norton, 1986), equipped with 640 kilobytes of random access memory, two 360 kilobyte floppy diskette drives, a 8087 math coprocessor, and an IEEE

General Purpose Interface Bus, was used for gathering data from measurements. Analysis of measurement data was performed on both computer systems.

The Compaq Deskpro with math coprocessor is an excellent tool for floating point intensive calculations, but increased speed was desired to allow a wider range of Monte Carlo calculations to be performed. Two options for increasing the speed of calculations were examined. First, accelerator boards operating with high speed 80286 central processor units and high speed math coprocessors were examined. The fastest of these accelerator boards (Petzold, 1986), the PC-elevATor family, produced by Applied Reasoning Corporation, were tested using a MCPHOT.PAS problem as a benchmark (Lickly, 1986). Results of the benchmark showed only a modest gain in speed when compared to the Compaq Deskpro. The reason for the poor showing by these devices lies in the relative inefficiency of the 80286/80287 combination to perform floating point intensive calculations (Petzold, 1986). The second option examined was the Definicon Systems DSI-32 coprocessor. This device uses a 10 MHz 32032 central processing unit with a 32081 math coprocessor to achieve speeds comparable to mid-sized VAX minicomputers (Marshall et al., 1985). The DSI-32 coprocessor plugs into an expansion slot in the Compaq Deskpro. The disadvantage to the system is the requirement to recode programs to run on the new central processing unit. To ease the recoding process from Turbo Pascal, a Pascal compiler was selected.

The same MCPHOT.PAS benchmark, converted to MCPHOT.P, was run on the DSI-32. This comparison is no longer purely between hardware, since two different compilers are now being used. Results of this and other benchmark tests are shown in Table G.1. The DSI-32 has been used for the majority of the Monte Carlo calculations performed in this research.

Comparison with the Cray X-MP/48 Supercomputer

As described in Chapter IV, one Monte Carlo photon transport problem was run on a Cray X-MP-48 supercomputer to test the MCPHOT.P code results against the MCNP transport code (Briesmeister, 1986), a recognized standard mainframe code, which, like the MCPHOT.P code, is capable of performing calculations with fully developed coherent and incoherent scattering routines. While the purpose of that comparison was to assess the accuracy of the MCPHOT.P code, insights into the relative speed of calculations are also of interest. The comparison is not completely fair to the Cray computer, since its computation time is dominated by the efficiency of the MCNP code, which is designed to do much more than the relatively simple problems presented. The Cray/MCNP combination was faster than the DSI-32/MCPHOT.P combination by a factor of only 35.43. The Cray central processing time, using the MCNP code, which would have been required for Monte Carlo calculations of this research effort is estimated to be on the order of 60 hours.

TABLE G.1
Benchmarks for Monte Carlo Transport Codes

Computer	Code	Speed Factor ^a
IBM PC/XT with 8087	MCPHOT.PAS	1.00
IBM PC/AT (6 MHz) with 5.33 MHz 80287	MCPHOT.PAS	1.57
Compaq Deskpro with 8087-2	MCPHOT.PAS	1.98
PC-elevATor with 8 MHz 80286 and 8 MHz 80287	MCPHOT.PAS	2.75
PC-elevATor with 10 MHz 80286 and 8 MHz 80287	MCPHOT.PAS	3.17
PC-elevATor with 12.5 MHz 80286 and 8 MHz 80287	MCPHOT.PAS	4.12
Definicon DSI-32	MCPHOT.P	7.65
Cray X-MP/48	MCNP	271.04

^aSpeed factor is with respect to the IBM PC. It is calculated by dividing the program execution time on the IBM PC by the execution time for other computer and code combinations.

Computer Software

Brief descriptions of the computer codes written for this research are provided. Descriptions of the validation of the major codes are provided within the chapters of the dissertation. A separate document (Campbell, 1987) contains listings of the major codes used in this research.

Computer Languages

Computer codes for the research are written in Microsoft BASIC, version 2.10 (Compaq, 1984b); Turbo Pascal, version 3.01A (Borland, 1985); or Green Hills Pascal, version GS-1.2a (Green Hills, 1985). In the file naming scheme used, file extensions identify the language in which a particular program is written. The extension, BAS, refers to a BASIC program; PAS, to a Turbo Pascal program; and, P, to a Green Hills Pascal program. All files with the extension, COM, are object code, generated by the Turbo Pascal compiler. These object codes are primarily used on the IBM Personal Computer for processing imaging data. All other file extensions refer not to programs, but to data.

Radiation Transport Codes

SGLMIN.PAS is a single scatter photon transport code. It is described in detail in Chapter IV.

MCPHOT.PAS and MCPHOT.P are Monte Carlo photon transport codes. They are described in detail in Chapter IV.

PBSCAT.PAS is a Monte Carlo photon transport code used to calculate scatter and fluorescent emission contributions to the x-ray source beam from lead filters employed in some of the experiments.

RNDMAVE.PAS, RNDMXSQ.PAS, RNDMCOR.PAS, and RNDMPSD.PAS test sequences of random numbers from random number generators by finding averages, performing chi squared tests, calculating the autocorrelation, and computing power spectral density.

ANCOHER.PAS provides an analytical calculation of the solid angle differential coherent scattering cross section of a material as a function of the cosine of the scattering angle.

COHINT.PAS evaluates an integral required for Monte Carlo sampling for the direction of a coherently scattered photon (described in Appendix H).

COHER.PAS provides a Monte Carlo calculation of the solid angle differential coherent scattering cross section as a function of the cosine of the scattering angle using the sampling method of Carter and Cashwell (1977), and Williamson and Morin (1983a, 1983b). Comparisons between the results of ANCOHER.PAS and COHER.PAS are used to validate the Pascal coding of the method.

KLEIN.BAS provides an analytical calculation of the solid angle differential Klein-Nishina cross section and the solid differential incoherent scattering cross section per electron for materials of interest as functions of scattering angle.

INCOH.PAS provides a Monte Carlo calculation of the solid angle differential scattering cross section as a function of the cosine of the scattering angle. The method

of Carter and Cashwell (1977) using the Kahn method for sampling the Klein Nishina distribution (Kahn, 1956) is employed. Comparisons of these results with calculations by the KLEIN.BAS code are used to validate the Pascal coding of the sampling method.

X-Ray Spectra Codes

XRSPEC.PAS calculates x-ray spectra produced by the GE Maxitron 300 X-Ray Therapy Unit (General Electric, 1962). It is described in detail in Chapter V.

XRSPEC3.PAS is a modification of the XRSPEC.PAS code used to investigate the effects on the x-ray spectra produced by the external collimator.

XRSPEXM.PAS is a modification of the XRSPEC.PAS code. It is used for the calculation of exposure rate attenuation of TNT and Norfolk Sandy loam soil. These results are then used for comparisons with measurements for the explosive substitute and the locally available soil.

XRSPDET.PAS is a modification of the XRSPEC.PAS code. It is used in combination with measurements to determine the thickness of the phosphor layer of a gadolinium oxysulfide based intensifying screen.

XRGRAPH.COM provides graphical output of the results of a spectrum calculation by the XRSPEC.PAS code.

DMUDE.PAS calculates the differential of the linear attenuation coefficient of a material with respect to energy for use in Laplace transform pair calculations of x-ray spectra.

XRGREEN.PAS calculates x-ray spectra by Greening's Laplace transform pair method (Greening, 1950).

FITARCH.PAS calculates the fitting parameters for the Archer-Wagner Laplace transform pair (Archer and Wagner, 1982) using the Levenberg-Marquardt method (Press et al., 1986).

FITRUBIO.PAS calculates the fitting parameters for the Rubio-Mainardi modification of the Archer-Wagner Laplace transform pair (Rubio and Mainardi, 1984) by the Levenberg-Marquardt method.

ARCHER.PAS computes the transmission of exposure rate by the Archer-Wagner method, given the fitting parameters found by the FITARCH.PAS code. The output of this code is compared to the original exposure rate transmission measurements as a check of the FITARCH.PAS code results.

Detector Response Codes

DETECT.PAS is a Monte Carlo code which is used to calculate the detector response matrix for the gadolinium oxysulfide x-ray intensifying screen based detector. The code is described in Appendix E.

DETNAI.PAS and DETNAI.P are Monte Carlo codes employed to calculate the plane detector response function for the Bicron Corporation NaI(Tl) detector used in the measurements. The codes are described in Chapter VI.

DETCOR.PAS corrects the plane detector response function calculated by the DETNAI.PAS code for the shield and finite size of the actual detector. The correction technique is described in Chapter VI.

DETNAIP.PAS is a Monte Carlo code which is used to determine the lead shielding requirements for the NaI(Tl) detector.

NAISPEC.PAS is a Monte Carlo code which calculates NaI(Tl) energy spectra on a one keV increment.

SPRESOL.PAS modifies the output of the NAISPEC.PAS code to account for the energy dependent resolution of the NaI(Tl) detector using the recommendations of Berger and Seltzer (1972).

DETISO.PAS is a Monte Carlo code which calculates the response of a detector to an isotropic point source. It is used to compare the results of detector response matrix calculations to experiments with radionuclide sources.

COLLIM.PAS computes the relationship between detector collimator acceptance angle, collimator height and width of the gap in the large area fluence detector.

Imaging Codes

COUNTER.BAS controls detector system electronics for count rate measurements with the GE Maxitron X-Ray Therapy Unit. It is used without soil box motion for multiple measurements at a single position. The code was written by Moss (1986).

OPS.BAS controls the detector system electronics and soil box positioning system for measurements with the GE Maxitron 300 X-Ray Therapy Unit to produce images of buried objects. This code was also written by Moss (1986).

SURFIMG.COM provides three-dimensional displays of measured image data. It accepts the output of the OPS.BAS code.

IMAGE.COM provides two-dimension gray scale displays of measured image data. It accepts the output of the OPS.BAS code.

FILIMG.PAS provides filtration and three-dimensional graphs of measured image data. Both high and low pass filtration techniques are available.

FOURIMG.PAS calculates the two-dimensional fast Fourier transform (FFT) of measured image data.

IMGDIF.PAS finds the difference between two image measurements and also provides filtration of results if desired. This code is used to remove the x-ray machine head leakage contribution and for investigations of the dual energy subtraction technique.

POWER.PAS calculates power requirements and assesses detection probability. The techniques and underlying assumptions used in this code are discussed in Chapter VIII.

Utility Codes

MIXCS.BAS converts tabulated elemental cross section data to mass interaction coefficients for compounds and mixtures. Energy mesh structure is that of the cross section data (Hubbell et al., 1975; Storm and Israel, 1970).

MUCBS.BAS uses cubic spline interpolation to convert the wide energy mesh mass interaction coefficients created by the MIXCS.BAS code to a fine energy mesh used by the photon transport and detector response codes.

MUCBSX.BAS converts the wide energy mesh mass interaction coefficients created by the MIXCS.BAS code to the one keV increment mass attenuation coefficients used by the XRSPEC.PAS code.

MIXFS.BAS creates files of atomic form factors and incoherent scattering functions for compounds and mixtures.

SURFACE.PAS produces a three-dimensional display of the spatial distribution of fluence or detector response calculated by the photon transport codes.

READF.PAS manipulates the fluence and detector response outputs of the photon transport codes. Manipulations include filtration, symmetry operations, integration, and addition, subtraction and division of matrices.

POSDATA.PAS reads spatial response files created by MCPHOT.PAS and MCPHOT.P codes, applies any available symmetries to improve statistics, and creates a file of response versus distance from beam axis for a monoenergetic source beam.

PTRESP.PAS, PTRESPLN,PAS, AND PTRESPSP.PAS use, respectively, least squares polynomial fits, least squares log-log fits and cubic spline fits of detector response versus energy at a particular detector position used in combination with x-ray spectra produced by the XRSPEC.PAS code to give the detector or fluence response at a position due to the polyenergetic source beam.

Photon Interaction Data Files

COEF.# are files of the photon interaction cross sections from Hubbell et al. (1975), and Storm and Israel (1970), where detailed photoelectric edge data is required. In the file extension, # is the atomic number of the element.

MURHO.EXT are files of photon mass interaction coefficients for compounds and mixtures created by the MIXCS.BAS code. The file extension code (EXT) identifies the material.

MUCBS.EXT are files of fine energy mesh mass interaction coefficients created by the MUCBS.BAS code and used in the photon transport codes.

MUCBSM.EXT are files of fine energy mesh mass interaction coefficients used in the photon transport codes. They differ from the MUCBS.EXT files in their energy range. The MUCBS.EXT files contain data from 1 keV to 1 MeV. The MUCBSM.EXT files contain data from 1 keV to 0.205 MeV. The reduction of the data set allows faster table look-up.

FFISF.# are files of the atomic form factor and incoherent scattering function from the tables of Hubbell et al. (1975).

FFISF.EXT are files of atomic form factors and incoherent scattering functions for mixtures created by the MIXFS.BAS code.

AFF.EXT are files of the integral associated with Monte Carlo sampling of the scattering direction after a coherent interaction.

MUCBSX.EXT are files of the one keV energy increment mass attenuation coefficients used by the XRSPEC.PAS code.

Table G.2 summarizes the elements and materials for which these files are available. All materials which have MUCBSM.EXT and MUCBSM.EXT files also have FFISF.EXT and AFF.EXT files.

Commercial Software

A number of commercially available programs have been used in the research. The Microsoft Basic (Compaq, 1984), Turbo Pascal (Borland, 1985) and Green Hills Pascal (Green Hills, 1984) languages have previously been mentioned, but some additional discussion of Turbo Pascal is required. This language has been very important to the research effort. The extremely rapid compilation of programs, and error finding capabilities coupled to the program editor allowed debugging activities and coding variations that would have been inconceivable with most languages. All programs intended for use on the Definicon DSI-32 were first run under Turbo Pascal and then converted to Green Hills Pascal. All editing for either language was done with the Turbo Pascal editor.

Programmer's Utilities by Turbo Power Software (1985) was valuable in optimizing the MCPHOT.PAS code for speed. In particular, the Pascal structure analyzer, the execution profiler and the execution timer were found to be very powerful tools. Using these tools, speed improvements of 20%-35% were made in the photon transport codes.

TABLE G.2
Photon Interaction Data Files

Material	File Extension Code	Availability by File Type ^a		
		MUCBS	MUCBSM	MUSBSX
Air	AIR	x	x	x
Aluminum	AL	x	x	x
Beryllium	BE	x	x	x
Concrete ^b	CON	x	x	
Copper	CU			x
Dinitrobenzene	DNB	x	x	
FTB soil ^c	FTB	x	x	
GAD soil ^d	GAD	x	x	
Gd ₂ O ₂ S phosphor ^e	GOS	x	x	x
HTL soil ^f	HTL	x	x	
HT1 soil ^g	HT1	x	x	
HT2 soil ^h	HT2	x	x	
Iron	FE	x	x	x
Lead	PB	x	x	x
Lucite	LUC	x	x	x
MCL soil ⁱ	MCL	x	x	
NSL soil ^j	NSL	x	x	x
Rubber	CUS	x	x	
SiO ₂	SIO	x	x	
Sucrose	SUC	x	x	x
NaI	NAI	x	x	
TiO ₂	TDO	x	x	x
Teflon	TEF	x	x	
Trinitrotoluene	TNT	x	x	x
Tungsten	W			x
Water	WAT	x	x	
Wood	WOD	x	x	

^aSee text of this appendix for a description of these file types.

TABLE G.2-continued

- ^bConcrete composition is from Chilton et al. (1984).
- ^cSoil characteristic of Fort Belvoir, VA.
- ^dGlobal average soil.
- ^eGadolinium oxysulfide in a lucite binder.
- ^fHagerstown loam.
- ^gHagerstown loam with 10% water by weight.
- ^hHagerstown loam with 20% water by weight.
- ⁱMalatula clay loam
- ^jNorfolk sandy loam.

DoubleDos by SoftLogic Solutions (1986) allows simultaneous operation of the Definicon DSI-32 performing Monte Carlo calculations and word processing on the Compaq Deskpro. An unexpected bonus in using this program is a 10% speed increase in programs run on the DSI-32 when another program is running concurrently on the 8086 of the Compaq Deskpro.

Three commercial graphics programs were also used. SCIPLOT by Techdata (Denison, 1984) provided rapid graphing capability with a wide range of curve fitting techniques. GRAPHER by Golden Software (1986) was used to generate publication quality two-dimensional graphs. SURFER, also by Golden Software (1987), was used to produce publication quality contour and three-dimensional graphs.

APPENDIX H

MONTE CARLO TECHNIQUES

This appendix provides supplemental information concerning Monte Carlo techniques used with the photon transport and detector response codes. Techniques for sampling the coherent and incoherent angular scattering distributions, details of the random number generators, methods for modelling fluorescent emission, and discussion of the extension of the monoenergetic calculations to polyenergetic spectra are provided. Unless otherwise indicated, definitions of the symbols used in this appendix are provided in Chapter IV.

Angular Scattering Distributions

Momentum Transfer Variable

The momentum transfer variable, x , defined in Chapter IV, is written in an alternate form for use in the techniques employed for sampling angular scatter distributions. Using the relationship between the energy and wavelength of a photon, and a half angle formula from trigonometry, the momentum transfer variable can be written as

$$x = k\alpha(1-\omega)^{1/2},$$

where k is a constant given by

$$k = \frac{m_e c}{\sqrt{2} h} ,$$

where α is the energy of the photon in electron rest mass units,

m_e is the rest mass of the electron,

c is the speed of light in vacuum,

h is Planck's constant, and

ω is the cosine of the scattering angle.

The maximum value of the momentum transfer variable occurs when ω is equal to -1, and is given by

$$x_{\max} = \sqrt{2} k \alpha .$$

Incoherent Scattering

The method for sampling the incoherent angular scattering distribution is that suggested by Carter and Cashwell (1977). The probability density function for the incoherent angular scattering distribution is

$$p(\Omega) = \frac{\frac{d\sigma_{\text{inc}}}{d\Omega}}{\sigma_{\text{inc}}} .$$

This relationship can be rewritten in terms of the solid angle differential Klein-Nishina cross section and the incoherent scattering function as

$$p(\Omega) = \frac{\frac{d\sigma_{KN}}{d\Omega}}{\sigma_{inc}} S(x, Z).$$

Multiplying this expression by unity in the form of several factors and rearranging gives

$$p(\Omega) = S(x_{max}, Z) \frac{\sigma_{KN}}{\sigma_{inc}} \frac{S(x, Z)}{S(x_{max}, Z)} \frac{\frac{d\sigma_{KN}}{d\Omega}}{\sigma_{KN}}$$

The probability density function is now in a generalized form for applying rejection sampling. The expression contains three parts, a term which is independent of the scattering angle, a term involving the ratio of incoherent scattering functions, and a new probability density function. This new probability density function is that of the angular scattering distribution of the Klein-Nishina cross section. The ratio of the incoherent scattering functions is always a number between 0 and 1, since $S(x, Z)$ is a monotonically increasing function (see Figure IV.6).

Determining the incoherent scattering angle begins by sampling the Klein-Nishina probability density function for the scattering angle (described below). This trial sampled value, along with the energy of the incident photon, is used to calculate a trial sample momentum transfer variable. A table of the momentum transfer variables and associated incoherent scattering function values of the appropriate material is entered. The values of the incoherent scattering function at x and x_{max} are found. The ratio of these

incoherent scattering function values ($S(x,Z)/S(x_{\max},Z)$) is calculated and compared to a random number. If the random number is less than the value of the ratio, the sampled angle is accepted and used to calculate the energy of the scattered photon through Compton's relationship. If the random number exceeds the value of the ratio, the sampled angle is rejected, and another attempt is made.

Sampling the Klein-Nishina Distribution

As indicated in the previous paragraph, the first step in sampling the incoherent angular scattering distribution requires sampling the Klein-Nishina angular scattering distribution. The method used in the transport and detector response codes to perform this sampling is that of Kahn (1956). The technique employed is a further generalization of the rejection technique. The formula for the solid angle Klein-Nishina cross section given in Chapter IV can be algebraically manipulated to the form,

$$\frac{d\sigma_{KN}}{d\Omega} = \frac{r_e^2}{2} \left(\frac{\alpha'}{\alpha}\right)^2 [\omega^2 - 1 + \frac{\alpha}{\alpha'} + \frac{\alpha'}{\alpha}] .$$

Since the probability density function is given by

$$p(\Omega) = \frac{\frac{d\sigma_{KN}}{d\Omega}}{\sigma_{KN}} ,$$

and σ_{KN} is a constant, an alternate form is

$$p(\omega) = \left(\frac{\alpha'}{\alpha}\right)^2 [\omega^2 - 1 + \frac{\alpha}{\alpha'} + \frac{\alpha'}{\alpha}] / G ,$$

where G is a constant. Kahn introduces a change of variable at this point to

$$z = \frac{\alpha}{\omega}, \quad .$$

This parameter can take on values between 1 and $1 + 2\alpha$, corresponding to scatter at zero and 180 degrees. The resulting probability density function for z is given by

$$p(z) = \frac{1}{G'z^2} (\omega^2 - 1 + \frac{1}{z} + z),$$

where G' is another constant. Kahn applies the rejection method to two independent components of this distribution. The distribution becomes

$$p(z) = K [A_1 H_1(z) g_1(z) + A_2 h_2(z) g_2(z)],$$

where K is a constant,

$$A_1 = (1 + 2\alpha)/(9 + 2\alpha),$$

$$h_1(z) = 4(1/z - 1/z^2),$$

$$g_1(z) = 1/(2\alpha),$$

$$A_2 = 8/(9 + 2\alpha),$$

$$h_2(z) = (1/z + \omega^2)/2, \text{ and}$$

$$g_2(z) = (1 + 2\alpha)/(2\alpha z^2).$$

These components are chosen so that $g_1(z)$ and $g_2(z)$ are themselves probability density functions, and so that the $h_1(z)$ and $h_2(z)$ functions have maximum values of 1 in the range of z . Sampling begins by selecting a random number

and comparing it to A_1 . If the random number is less than A_1 , $g_1(z)$ is used as the probability density function for selecting a value of z ; otherwise, $g_2(z)$ is used. The trial sample value of z is computed by

$$z = 2\rho_2^\alpha + 1,$$

if $g_1(z)$ is used, and by

$$z = \frac{1 + 2\alpha}{2\rho_2^{\alpha+1}},$$

if $g_2(z)$ is used. In these expressions, ρ_2 is the second random number selected in the scheme. These expressions are the result of solving an equation of the form

$$\rho_2 = \frac{\int_1^z g_1(z') dz'}{\int_1^{1+2\alpha} g_1(z') dz'}$$

for z and a similar equation for $g_2(z)$. In either case, in the next step, a third random number is selected and compared to the value of the associated $h_n(z)$ function. If the random number is smaller, the trial sample value for z is selected; if not, the process begins again. If the sample value is retained, the energy of the scattered photon is calculated from z . The scattering angle is then calculated from the incident and scattered energies by the Compton energy/angle relationship.

Coherent Scattering

The method used for sampling the coherent angular scattering distribution is that suggested by Carter and

Cashwell (1977) and Williamson and Morin (1983a, 1983b).

The probability density function for the coherent scattering angular distribution is

$$p(\Omega) = \frac{\frac{d\sigma_{\text{coh}}}{d\Omega}}{\sigma_{\text{coh}}} .$$

which can also be written as

$$p(\Omega) = \frac{r_e^2}{2} \frac{(1+\omega^2)F^2(x, Z)}{\sigma_{\text{coh}}} .$$

A change of variables to the square of the momentum transfer variable is made through

$$p(x^2) = p(\Omega) \left| \frac{d\Omega}{dx^2} \right| = 2\pi p(\omega) \left| \frac{d\omega}{dx^2} \right| ,$$

where the Jacobian in the last formula is $1/(k_\alpha)^2$.

Multiplication by unity in the form of several factors yields

$$p(x^2) = \frac{2\pi r_e^2 Z^2 A(x_{\text{max}}^2, Z)}{(k_\alpha)^2 \sigma_{\text{coh}}} \frac{(1+\omega^2)}{2} \frac{F^2(x, Z)}{Z^2 A(x_{\text{max}}^2, Z)} ,$$

where $A(x^2, Z)$ is given by

$$A(x^2, Z) = \int_0^{x^2} \frac{F^2(x, Z)}{Z^2} dx^2$$

Z in these equations is the atomic number of the material. The original probability density function now consists of three terms, a term independent of the scattering angle, a term which ranges in value from 1/2 to 1, and a new probability density function written in terms of an integral of

the atomic form factor squared. In order to sample this distribution, tables of values of the integral must be constructed for all materials of interest. This integral is calculated using the trapezoidal rule by the COHINT.PAS code. Sampling by the rejection method proceeds by calculating the value of the square of the maximum value of the momentum transfer variable, which depends only on the energy of the incident photon. Using this value the tables of the coherent integral are entered, and the value of the integral is determined by log-log interpolation. A random number is selected and then multiplied by this value of the integral to provide a trial sample value of the integral associated with x . The table is then reentered with this trial integral value and a trial value of the associated square of the momentum transfer variable is obtained. This value is used to calculate a trial sample cosine of the scattering angle by then applying

$$\omega = 1 - \frac{x^2}{(\alpha k)^2} .$$

A second random number is obtained and compared to the value of

$$\frac{1 + \omega^2}{2} ,$$

using the trial sample value of the cosine of the scattering angle. If the random number is less than this quantity, the sample value is accepted; if not, another attempt is made.

Random Number Generators

MCPHOT.PAS Generator

The MCPHOT.PAS code uses a real number modification of a multiplicative congruential random number generator suggested by Cheney and Kincaid (1980). The generator is implemented by the following algorithm.

BEGIN.

random seed <-- (fraction[(a*random seed)/b])*b

random number <-- random seed/c

END.

In the algorithm, $a = 16807.0$; $b = 2147483647.0$; and $c = 2147483648.0$. The fraction operation provides the real fractional portion of the bracketed quantity.

MCPHOT.P Generator

The MCPHOT.P code uses an integer based linear congruential random number generator designed for 32-bit word computers (Dyck et al., 1984). A straight forward algorithm for this technique would be of the following form.

BEGIN.

random seed <-- [random seed*a + c] (mod m)

random number <-- random seed/m

END.

The algorithm actually employed takes advantage of the automatic performance of $(\text{mod } 2^n)$ integer calculations by computers, where n is the bit-word length of the computer and m is 2^{n-1} . Because of the method by which computers manipulate integers, these calculations can produce either

positive or negative numbers. If a negative number is generated, it is converted to a positive number by adding the magnitude of the largest negative integer, which is equivalent to the largest positive number plus one. The algorithm used is as follows.

BEGIN.

random seed \leftarrow random seed $\times a + b$.

if random seed < 0 , then

random seed \leftarrow random seed + 2147483647 + 1.

random number $\leftarrow c \times$ random seed.

END.

In this algorithm, $a = 843314861$; $b = 453816693$; and $c = 0.46566128752458\text{E}-9$. The number, 2147483647, is $2^{31}-1$.

These constants are from Forsythe et al. (1977).

Flourescent Emission

Fluorescent emission routines, based on the recommendations of Carter and Cashwell (1977), are used in the detector response codes. The calculated probabilities of emission associated with the fluorescent emission photons used in this research are shown in Table H.1. Data for the calculations is from Storm and Israel (1970), with the exception of total yields, which are taken from Fink et al. (1966) or Bambynek et al. (1972). The more current data of Bambynek et al. are used wherever available. Data for the L shell yields are poorly known. Fortunately, the low energies of the L fluorescent photons makes this shortcoming unimportant in the mine detection problem.

TABLE H.1
Fluorescent Emission Probabilities

Energy Range	X-Ray	Element			
		Ti	I	Gd	Pb
Less than the average L edge	none	0.000000	0.00000	0.00000	0.00000
Between L and K edges	L	not considered	0.07963	0.15462	0.29554
Above the K edge	$K_{\alpha 1}$	0.09476	0.39457	0.39467	0.38022
	$K_{\alpha 2}$	0.04823	0.21287	0.21944	0.22661
	$K_{\beta 1}$	0.01619	0.10828	0.11783	0.12586
	$K_{\beta 2}$	none	0.02107	0.02577	0.03000
Secondary after $K_{\alpha 1}$ or $K_{\alpha 2}$	L	not considered	0.03333	0.06600	0.13000

Application to Polyenergetic Sources

Available Methods

The MCPHOT codes calculate fluence and detector responses resulting from the scattering of monoenergetic source beams. The x-ray source required for mine detection is polyenergetic. A method for converting the monoenergetic source results to a polyenergetic source is required. Three solutions to this problem are available.

First, the source energy spectrum could be sampled from within the MCPHOT codes. This method would be the most accurate if sufficient photon histories could be followed. The method is rejected because the large number of histories required to properly sample the spectrum and transport the photons is beyond reasonable computation time on the computer used in this research. Also, because the method is specific to one source spectrum, it lacks the generality of the other two options.

A second method is a multigroup solution. This is the typical method used for polyenergetic transport. The source spectrum is divided into a series of energy groups, and the results of calculations for a single energy representative of the group are weighted by the number of source photons within the group. Accuracy in such a solution depends greatly on the number of groups employed.

The third method, and the one chosen in this research, is a fitting method. If monoenergetic calculations are made at a series of source energies, and response for a given

detector configuration is plotted as a function of source energy, a smooth curve can be fit to the data to provide an empirical relationship between the response and the source energy. The success of this strategy depends upon the continuous nature of the variation of photon interaction cross section as a function of energy. This empirical relationship can then be coupled to the x-ray spectrum to provide the detector response to the polyenergetic source.

Application of the Fit Method

The sodium iodide detector employed in the measurements is used as an example of how the fit method can be applied. For the sodium iodide detector, the only exceptions to the continuous nature of the photon interactions occur as a result of the K edge of iodine and the lower level discriminator setting (see Figure VI.4). Figure H.1 shows a typical set of response versus source energy calculations for a single detector position, and polynomial least squares and cubic spline fits to the results of the calculations. While the effects of the two discontinuities are present, they are not severe. The effect of the K edge of iodine is difficult to detect. The K edge related discontinuities involve the detector response to photons interacting by the photoelectric effect in the crystal with subsequent escape of an iodine K x ray leaving less than the energy required by the lower level discriminator to produce a count. As was seen in the detailed discussion of the detector response in Chapter VI, if the discriminator level setting is greater

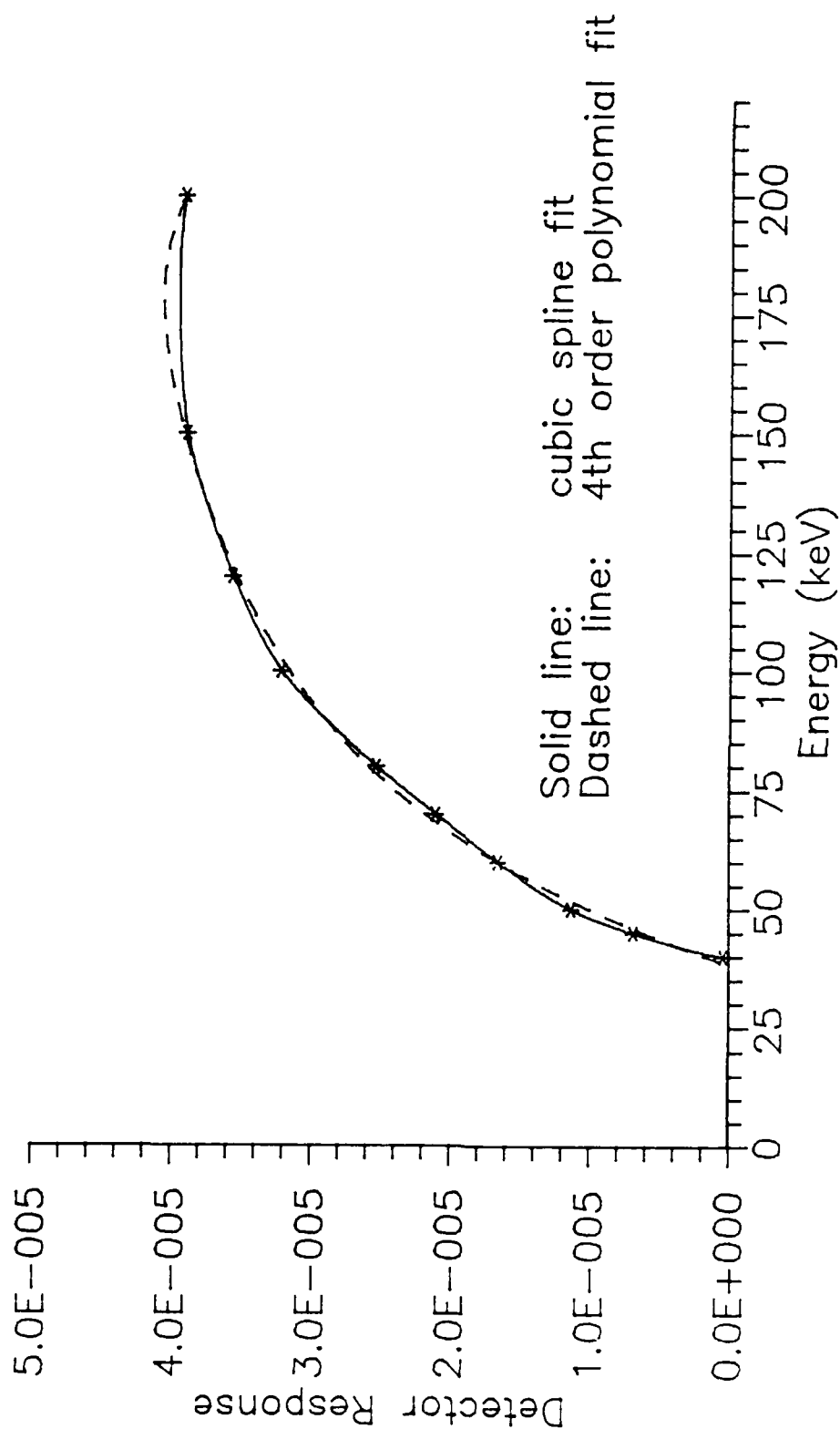


Figure H.1. The fit technique. A typical example of the fit technique for the detector response (in counts per source photon per cm^2 of detector face area) as a function of source energy for the Bicron Model .5M.39Q/.5L-X NaI(Tl) detector. The solid line is a cubic spline fit to the data; the dashed line, a fourth order polynomial least squares fit.

than the K edge energy (as is the case in the measurements), there is only one region of discontinuity above the energy corresponding to the discriminator level setting rather than two for a setting corresponding to energies below the K edge. Further, the region of discontinuity is actually a staircase because of the four possible K x rays which are emitted, which softens the transition. Also, the detector response discussion was in terms of the energy of the photons striking the detector. The discussion now centers around the relationship with the energy of the source photons. The incoherent scattering process serves to further decouple the source energy from the discontinuities arising from K edge effects, smearing the scattered photon energy. The effect of the discontinuity in the detector response matrix at the energy corresponding to the lower level discriminator setting is of little consequence because of the small magnitude of the response near this energy. The fitted response versus energy relationships (a different relationship exists for each detector position of interest) can be coupled directly to any energy spectrum to predict the response at a given position.

The fit method has the advantage of conserving computer time while providing a more accurate solution than the multigroup method. The number of monoenergetic calculations used to determine the fitted curve is important to the accuracy of the solution. Eight to ten energies are used in this research and appear to be more than adequate to express the desired relationship accurately.

REFERENCES

- Ahuja, S. D.; Steward, P. G.; Roy, T. S.; and Slessinger, E. D. "Estimated Spectrum of a 4 MV Therapeutic Beam." Med. Phys. 13:368-373, 1986.
- Aitken, D. W.; Beron, B. L.; Yenicay, G.; and Zulliger, H. R. "The Fluorescent Response of NaI(Tl), CsI(Tl), CsI(Na) and CaF₂(Eu) to X-Rays and Low Energy Gamma Rays." IEEE Trans on Nucl. Sci. 14:468-477, 1967.
- Anderson, D. W. Absorption of Ionizing Radiation. Gaithersburg, MD: Aspen, 1984.
- Anghaie, S. Accuracy Improvement for Gamma-Ray Techniques in Two-Phase Measurements. Ph.D. Thesis, The Pennsylvania State University, University Park, PA, 1982.
- Archer, B. R. "Analysis of Errors in Spectral Reconstruction with a Laplace Transform Pair Model." Phys. Med. Biol. 30:411-418, 1985.
- Archer, B. R., and Wagner, L. K. "A Laplace Transform Pair Model for Spectral Reconstruction." Med. Phys. 9:844-847, 1982.
- Baird, L. C. "X-Ray Spectra Vs. Attenuation Data: A Theoretical Analysis." Med. Phys. 8:319-323, 1981.
- Bambynek, W.; Craseman, B.; Fink, R. W.; Freund, H. U.; Mark, H.; Swift C. D.; Price, R. E.; and Rao, P. V. "X-Ray Fluorescence Yields, Auger, and Coster-Kronig Transition Probabilities." Rev. of Mod. Phys. 44:716-813, 1972.
- Battista, J., and Bronskill, M. "Compton-Scatter Tissue Densitometry: Calculation of Single and Multiple-Scatter Photon Fluences." Phys. Med. Biol. 23:1-23, 1978.
- Battista, J.; Santon, L.; and Bronskill, M. "Compton-Scatter Imaging of Transverse Sections: Corrections for Multiple-Scatter and Attenuations." Phys. Med. Biol. 22:229-244, 1977.
- Baxter, W. P. Soviet AirLand Battle Tactics. Novato, CA: Presidio Press, 1986.

- Bear, B. E. Chemistry of the Soil. New York: Reinhold, 1955.
- Bell, G. E. "Spectral Distribution in the Continuous X-Ray Spectrum and the Specification of X-Ray Quality." Brit. J. Radiol. 9:680-688, 1936.
- Berger, M. J., and Raso, D. "Monte Carlo Calculations of Gamma-Ray Backscattering." Radiation Research 12:20-37, 1960.
- Berger, M. J., and Seltzer, S. M. "Response Functions for Sodium Iodide Scintillation Detectors." Nucl. Instr. and Meth. 104:317-332, 1972.
- Bloomquist, R. N., and Gelbard, E. M. "An Assessment of Existing Klein-Nishina Monte Carlo Sampling Methods." Nucl. Sci. Engr. 83:380-384, 1983.
- Borland International. Turbo Pascal Reference Manual. Scotts Valley, CA: Borland International, 1985.
- Briesmeister, J. F. MCNP - A General Monte Carlo Code for Neutron and Photon Transport. Los Alamos, NM: Los Alamos National Laboratory, 1986.
- Buchanan, R. A.; Finkelstein, S. I.; and Wickersheim, K. A. "X-Ray Exposure Reduction Using Rare-Earth Oxysulfide Intensifying Screens." Radiol. 105:185-190, 1972.
- Bulatov, B. P., and Andrushin, N. F. "Gamma-Ray Energy and Number Albedos." Sov. J. At. Energy 22:307-308, 1967.
- Caidin, M. The Tigers Are Burning. New York: Hawthorn, 1974.
- Campbell, J. G., "Computer Code Listings for Backscatter Radiation Radiography Applications to Landmine Detection." Unpublished Report. University of Florida, Gainesville, FL, 1987.
- Carter, L. L., and Cashwell, E. D. Particle-Transport Simulation with the Monte Carlo Method. Technical Information Center Publication TID-26607. Oak Ridge, TN: Energy Research and Development Administration, 1977.
- Chan, H. P., and Doi, K. "Studies of X-Ray Absorption and Quantum Noise Properties of X-Ray Screens by Use of Monte Carlo Simulation." Med.Phys. 11:37-46, 1984.
- Cheney, W., and Kincaid, D. Numerical Mathematics and Computing. Monterey, CA: Brooks/Cole Publishing, 1980.

- Chilton, A. B.; Shultis, J. K.; and Shaw, R. E. Principles of Radiation Shielding. Englewood Cliffs, N.J.: Prentice-Hall, 1984.
- Clarke, R. L., and Van Dyk, G. "A New Method for Measurement of Bone Mineral Content Using Both Transmitted and Scattered Beams of Gamma-Rays." Phys. Med. Biol. 18:532-539, 1973.
- Coleman, W. A. "Monte Carlo Calculation of the Effect of Subterranean Perturbations on Reflexed X-Rays." Nucl. Sci. Engr. 46:12-21, 1971.
- Compaq Computer Corporation. Compaq Deskpro Personal Computer Operations Guide. Houston, TX: Compaq Computer Corporation, 1984a.
- Compaq Computer Corporation. BASIC Version 2 Reference Guide. Houston, TX: Compaq Computer Corporation, 1984b.
- Compton, A. H. "A Quantum Theory of the Scattering of X-Rays by Light Elements." Phys. Rev. 21:483-502, 1923.
- Definicon Systems. DSI-32 Manual. West Lake Village, CA: Definicon Systems, 1986.
- Dell, J. R., and Ebert, P. J. "NaI(Tl) Escape Peak to Photopeak Ratios." Nucl. Instr. and Meth. 68:335-336, 1969.
- Denison, J. T. SCILOT. Houston, TX: Techdata Engineering Programs, 1984.
- DePuy, W. E. "Toward a Balanced Doctrine." Army 34(11):18-25, 1984.
- Dick, C. E., and Motz, J. W. "Image Information Transfer Properties of X-Ray Fluorescent Screens." Med. Phys. 8:337-346, 1981.
- Dohring, W.; Reiss, K. H.; and Fabel, H. "Lokale in vivo Dichtesbestimmungen der Lunge mit Hilfe der Compton-Streuung." ("Compton Scatter for Local in vivo Assessment of Density in the Lung.") Pneumonologie 150:345-359, 1974. Abstract in English.
- Dyck, V. A.; Lawson, J. D.; and Smith, J. A. FORTAN 77, An Introduction to Structured Problem Solving. Reston, VA: Reston Publishing, 1984.
- Dyson, N. A. "Characteristic X Rays--A Still Developing Subject." Phys. Med. Biol. 20:1-29, 1975.

Epp, E. R., and Weiss, H. "Energy Spectrum of Primary Diagnostic X Rays." Phys. Med. Biol. 11:225-238, 1966.

Evans, R. D. The Atomic Nucleus. Eleventh printing. New York: McGraw-Hill, 1955.

Farmer, F. T., and Collins, M. P. "A New Approach to the Determination of Anatomical Cross-Sections of the Body by Compton Scattering of Gamma-Rays." Phys. Med. Biol. 16:577-586, 1971.

Farmer, F. T., and Collins, M. P. "A Further Appraisal of the Compton Scatter Method for Determining Anatomical Cross-Sections of the Body." Phys. Med. Biol. 19:808-818, 1974.

Fewell, T. R., and Shuping, R. E. "Photon Energy Distribution of Some Typical Diagnostic X-Ray Beams." Med. Phys. 4:187-197, 1977.

Fink, R. W.; Jopson, R. C.; Mark, H.; and Swift, C. D. "Atomic Fluorescence Yields." Rev. of Mod. Phys. 38:513-540, 1966.

Forsythe, G. E.; Malcom, M. A.; and Moler, C. B. Computer Methods for Mathematical Computations. Englewood Cliffs, NJ: Prentice-Hall, 1977.

Frank, W. X-Ray Products Division, 3M Corporation, St. Paul, MN. Personal communications, May 23 and June 3, 1986.

Garnett, E. S.; Kennett, T. J.; Kenyon, D. B.; and Webber, C. E. "A Photon Scattering Technique for Measurement of Absolute Bone Density in Man." Radiol. 106:209-213, 1973.

General Electric Corporation. Maxitron 300 X-Ray Therapy Unit Operation, Maintenance. General Electric X-Ray Department, 1962. Milwaukee, WI, General Electric Directions No. 12338C.

Golden Software, Inc. Grapher. Golden, CO: Golden Software, 1986.

Golden Software, Inc. Surfer. Golden, CO: Golden Software, 1987.

Green Hills Software, Inc. Green Hills Software User's Guide, Pascal Language. Glendale, CA: Green Hills Software, 1984.

- Greening, J. R. "The Determination of X-Ray Energy Distributions by the Absorption Method." Brit. J. Radiol. 20:71-78, 1947.
- Greening, J. R. "The Determination of X-Ray Wavelength Distributions from Absorption Data." Proc. Phys. Soc. (London) 63A:1227-1234, 1950.
- Grodstein, G. W. "X-Ray Attenuation Coefficients from 10 KeV to 100 MeV." National Bureau of Standards, 1957. Washington, DC, NBS Cir. No. 583.
- Hamamatsu Corporation. Catalog: Photomultiplier Tubes. Hamamatsu City, Japan: Hamamatsu Corporation, 1985.
- Hanson, H. P., and Salem, S.I. "Effective Depth of X-Ray Production." Phys. Rev. 124:16-21, 1961.
- Hanson, J. A.; Duke, P. R.; Figley, M. M.; and Butler, J. "Compton Scatter Densitometry with Polychromatic X-Ray Beams." Med. Phys. 10:517, 1983.
- Hendee, W. R. Medical Radiation Physics, 2nd ed. New York: Year Book Medical Publishers, 1984.
- Holder, L. D. "A New Day for Operational Art." Army 35(3):22-32, 1985.
- Honeywell Defense Systems Division. Countermining Warfare Analysis Final Report. Hopkins, MN: Honeywell, 1981. Available from NTIS, Springfield, VA.
- Hough, B. K. Basic Soils Engineering. New York: Ronald Press, 1957.
- Huang, P. H.; Kase, K. R.; and Bjarngard, B. E. "Spectral Characterization of 4 MV Bremsstrahlung by Attenuation Analysis." Med. Phys. 8:368-374, 1981.
- Hubbell, J. H. "Photon Mass Attenuation Coefficients from 1 keV to 20 MeV." Int. J. Appl. Radiat. Isot. 33:1269-1290, 1982.
- Hubbell, J. H.; Veigele, W. J.; Briggs, E. A.; Brown, R. T.; Cromer, D. T.; and Howerton, R. J. "Atomic Form Factors, Incoherent Scattering Functions, and Photon Scattering Cross Sections." J. Phys. Chem. Ref. Data 4:471-538, 1975.
- International Commission on Radiological Units and Measurements. Physical Aspects of Irradiation, Recommendations of the International Commission on Radiological Units and Measurements. Report 10b (NBS Handbook 85). Washington, DC: National Bureau of Standards, 1964.

- Jacobs, A. M.; Towe, B. C.; and Harkness, J. E. "Backscatter X-Ray Radiography: Medical Applications." Proc. of the SPIE, Medical Imaging II:206-211, 1979.
- Jaeger, R. G., ed. Engineering Compendium on Radiation Shielding. Vol. II. New York: Springer-Verlag, 1975.
- Jammer, M. The Conceptual Development of Quantum Mechanics. New York: McGraw-Hill, 1966.
- Johns, H. E., and Cunningham, J. R. The Physics of Radiology. 4th ed. Springfield, IL: Thomas, 1983.
- Jones, D. E. A. "The Determination from Absorption Data of the Distribution of X-Ray Intensity in the Continuous X-Ray Spectrum." Brit. J. Radiol. 13:95-101, 1940.
- Joseph, P. M. "Mathematical Method for Determining kVp from X-Ray Attenuation Measurements." Med. Phys. 2:201-207, 1975.
- Kahn, H. Applications of Monte Carlo. Report AECU-3259. Santa Monica, CA: The Rand Corp., 1956.
- Knoll, G. F. Radiation Detection and Measurement. New York: Wiley, 1979.
- Koch, H. W., and Motz, J. W. "Bremsstrahlung Cross Section Formulas and Related Data." Rev. Mod. Phys. 31:920-955, 1959.
- Kodak Corporation. "Technical Information for General Publication: Kodak Lanex Regular Screen/4864, Kodak Lanex Medium Screen/4863, Kodak Lanex Fine Screen/4869." Kodak Technical Information Coordination Office, Kodak Park, NY, 1980.
- Kondic, N. N., and Hahn, O. J. "Theory and Application of the Parallel and Diverging Beam Method in Two-Phase Systems." 4th International Heat Transfer Conference, Paris 7:MT-1.4, 1970.
- Kramers, H. A. "On the Theory of X-Ray Absorption and of the Continuous X-Ray Spectrum." Philos. Mag. J. Sci. 46:836-871, 1923.
- Lale, P. G. "The Examination of Internal Tissues Using Gamma-Ray Scatter with Possible Extension to Megavolt Radiography." Phys. Med. Biol. 4:159-167, 1959.
- Lale, P. G. "Examination of Internal Tissues by High-Energy Scattered X-Radiation." Radiol. 90:510-517, 1968.

- Lederer, C. M., and Shirley, V. S. Table of Isotopes. New York: Wiley, 1978.
- Lickly, A. Applied Reasoning Corporation, Cambridge, MA. Personal communications, June 6 and 11, 1986.
- Macksey, K. Africa Corps. New York: Ballintine, 1968.
- Marshall, T. G.; Scolaro, G.; Rand, D. L.; King, T.; and Williams, V.P. "The DSI-32 Coprocessor Board." Byte, 10: 120-136, 1985.
- Melocik, G. Bicron Corporation, Newbury, OH. Personal communication, November 21, 1986.
- Minato, S. "Low Energy Components of Scattered Gamma Radiation." Nucl. Sci. Engr. 51:32-40, 1973.
- Moler, R. B. "Workshop Report, Nuclear Techniques in Mine Detection Research." Fort Belvoir, VA: Belvoir Research and Development Center, 1985.
- Moss, D. C. "An X-Ray Backscatter Imaging System: Hardware and Software Development." Unpublished Master of Science Degree Project Report. University of Florida, Gainesville, FL, 1986.
- Nolan, R. V.; Egghart, H. C.; Mittleman, L.; Brooke, R. L.; Roder, F. L.; and Gravitte, D. L. MERADCOM Mine Detection Program: 1960-1980. Fort Belvoir, VA: U.S. Army Mobility Equipment Research and Development Command, 1980.
- Norton, P. Inside the IBM PC. New York, NY: Prentice-Hall, 1986.
- Odeblad, E., and Norhagen, A. "Electron Density in a Localized Volume by Compton Scattering." Acta Radiologica 45:161-167, 1956.
- Petzold, C. "Accelerator Boards, Power for a Price." PC Magazine 5(15):125-165, 1986.
- Plyaskin, V. Ya.; Lysukhin, I. F.; Ruvinskiy, V. A. Engineer Support of Combined-Arms Combat. Moscow: Voenizdat, 1970. Translated from Russian and published by the U. S. Army Foreign Science and Technology Center, Charlottesville, VA, 1973.
- Preiss, K., and Livnat, R. "Detection of Plastic Mines by Gamma-Ray Backscatter." Trans. Israel Nucl. Soc. 1:30-33, 1973.

- Press, W. H.; Flannery, B. P.; Teukolsky, S. A.; and Vetterling, W. T. Numerical Recipes, the Art of Scientific Computing. New York: Cambridge University Press, 1986.
- Radevich, P. G.; Shuraviev, V. V.; and Volkov, I. V. Manual on the Laying and Clearing of Minefields. Moscow: Military Publishing House of the Ministry of Defense, USSR, 1965. Translated from Russian and published by the U. S. Army Foreign Science and Technology Center, Charlottesville, VA, 1965.
- Raso, D. J. "Monte Carlo Calculations on the Reflection and Transmission of Scattered Gamma Rays." Nucl. Sci. Engr. 17:411-418, 1963.
- Reiss, K. H., and Schuster, W. "Quantitative Measurements of Lung Function in Children by Means of Compton Backscatter." Radiol. 102:613-617, 1972.
- RisCassi, R. W. "A Historic Juncture of Doctrine Advances, Technological Change." Army 36(10):178-193, 1986.
- Roder, F. L. Belvoir Research and Development Center, Ft. Belvoir, VA. Personal communication, July 11, 1985.
- Roder, F. L., and Van Konyenburg, R. A. Theory and Application of X-Ray and Gamma-Ray Backscatter to Landmine Detection. Report 2134. Fort Belvoir, VA: U.S. Army Mobility Equipment Research and Development Center, 1975.
- Rommel, E. The Rommel Papers. Edited by Liddell Hart, B. H. New York: Harcourt, Brace, 1953.
- Rubio, M., and Mainardi, R. T. "Determination of X-Ray Spectra Including Characteristic Line Intensities from Attenuation Data." Phys. Med. Biol. 29:1371-1376, 1984.
- Saylor, W. L. "The X-Ray Spectrum from a 2 MVp Alternating Potential Generator." Phys. Med. Biol. 14:87-91, 1969.
- Schwartz, M., and Shaw, L. Signal Processing: Discrete Spectral Analysis, Detection and Estimation. New York: McGraw-Hill, 1975.
- Sharma, R. C.; Garg, S. P.; and Somasundaram, S. "Monte Carlo Calculations for Thin NaI(Tl) Crystals at Energies Below 100 keV." Nucl. Instr. and Meth. 101:413-422, 1972.

- Shelkin, M., and Purdy, J. P. "The Counter Obstacle Vehicle." The Military Engineer 78:362-364, 1986.
- Sidorenko, A. A. The Offensive, A Soviet View. Washington, DC: U.S. Government Printing Office, 1973.
- Silberstein, L. "Determination of the Spectral Composition of X-Ray Radiation from Filtration Data." J. Opt. Soc. Am. 22:265-280, 1932.
- Silberstein, L. "Spectral Composition of an X-Ray Radiation Determined by its Filtration Curve." Phil. Mag. 15:375, 1933.
- SoftLogic Solutions, Inc. DoubleDos. Manchester, NH: SoftLogic, 1986.
- Soole, B. W. "The Attenuation of X-Radiation Generated at Constant Potentials Sufficient to Excite K-Radiation in a Tungsten Target." Phys. Med. Biol. 16:427-437, 1971.
- Stanton, L.; Day, J. L.; Lightfoot, D. A.; Villafana, T.; and Rauch, P. L. "Rapid Computation of Diagnostic X-Ray Bremsstrahlung Spectra." Radiol. 130:477-484, 1979.
- Storm, E., and Israel, H. I. "Photon Cross Sections from 1 keV to 100 MeV for Elements Z=1 to Z=100." Nuclear Data Tables, Section A A7:565-681, 1970.
- Sundararaman, V.; Prasad, M. A.; and Vora, R. B. "Computed Spectra from Diagnostic and Therapeutic X-Ray Tubes." Phys. Med. Biol. 18:208-218, 1973.
- Suvorov, V. Inside the Soviet Army. London: Hamilton, 1982.
- 3M Corporation. "Trimax Intensifying Screens." X-Ray Products Brochure. St. Paul, MN, 1985a.
- 3M Corporation. "Spectral Emission of Screens and Log Sensitivity of Film." Information paper. St. Paul, MN, 1985b.
- TurboPower Software. Programmer's Utilities. Campbell, CA: TurboPower Software, 1985.
- Uli, P. J. "Soviet Engineers." The Military Engineer 78:510-513, 1986.
- Unger, L. M., and Trubey, D. K. Specific Gamma-Ray Dose Constants for Nuclides Important to Dosimetry and Radiological Assessment. Report ORNL/RSIC-45/R1. Oak Ridge, TN: Oak Ridge National Laboratory, 1982.

U.S. Department of the Army. Engineer Field Data. Field Manual 5-34. Washington, DC: U.S. Government Printing Office, 1969.

U.S. Department of the Army. Mine-Countermine Operations Manuscript. Fort Belvoir, VA: U.S. Army Engineer School, 1973.

U.S. Department of the Army. Engineer Combat Operations. Field Manual 5-100. Washington, DC: U.S. Government Printing Office, 1979a.

U.S. Department of the Army. TRADOC Threat Monograph, A Comparison of Selected NATO and Warsaw Pact Engineer Organizations and Equipment. Fort Monroe, VA: U.S. Army Training and Doctrine Command, 1979b.

U.S. Department of the Army. Operations. Field Manual 100-5. Washington, DC: U.S. Government Printing Office, 1982.

U.S. Department of the Army. Sensing and Neutralizing Mines. Ft. Belvoir, VA: U.S. Army Belvoir Research, Development and Engineering Center, 1986.

Venema, H. W. "X-Ray Absorption, Speed, and Luminescent Efficiency of Rare Earth and Other Intensifying Screens." Radiol. 130:765-771, 1979.

Von Mellenthin, F. W. Panzer Battles. Norman, OK: University of Oklahoma Press, 1956.

Walker, W. A. "The Deep Battle." Army 36(7):37, 1986.

Weast, R. C. ed. Handbook of Chemistry and Physics. Cleveland, OH: Chemical Rubber Company, 1967.

West, H. W.; Cress, D. H.; Ford, M. B. "Mine/Countermine Research." The Military Engineer 77:472-474, 1985.

Whitney, C. A. "Generating and Testing Pseudorandom Numbers." Byte 9:128-129, 442-451, 1984.

Wichmann, B., and Hill, D. "Building a Random-Number Generator." Byte 12-127-128, 1987.

Williamson J. F., and Morin, R. L. "An Efficient Method of Sampling the Coherent Angular Scatter Distribution." Phys. Med. Biol. 28:57-62, 1983a.

Williamson, J. F., and Morin, R. L. "Concerning an Efficient Method of Sampling the Coherent Angular Scatter Distribution." Phys. Med. Biol. 28:991-992, 1983b.

Zhukov, G. K. Marshall Zhukov's Greatest Battles. New
York: Harper and Rowe, 1969.

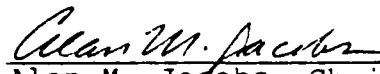
BIOGRAPHICAL SKETCH

John G. Campbell is the son of retired U.S. Army Colonel John Campbell, Jr., and Mary Elizabeth Campbell. He was born in Chicago, Illinois, in 1947. Growing up as a member of a military family, he has lived in many places within the United States, Europe and the Middle East. He graduated from high school in Jacksonville, Alabama, in 1965, and attended the University of Missouri, where he received a Bachelor of Science degree in physics in 1969, and a Master of Science degree in nuclear engineering in 1970.

He was commissioned as Second Lieutenant of Infantry in the U.S. Army in 1969. His military education includes the airborne and jumpmaster courses, the Infantry Officers' Basic Course, the Engineer Officers' Advanced Course, and the Command and General Staff College. His military assignments include service in Vietnam, Korea and many places within the United States.

He married Rebecca J. Eggerman, herself a member of a military family, in 1974. He is currently a Lieutenant Colonel of the Corps of Engineers. After leaving the University of Florida, he will be an Associate Professor in the Department of Physics at the United States Military Academy at West Point, New York.

I certify that I have read this study and that in my opinion it conforms to acceptable standards of scholarly presentation and is fully adequate, in scope and quality, as a dissertation for the degree of Doctor of Philosophy.



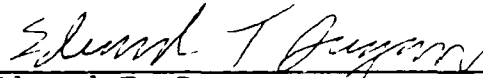
Alan M. Jacobs, Chairman
Professor of Nuclear Engineering
Sciences

I certify that I have read this study and that in my opinion it conforms to acceptable standards of scholarly presentation and is fully adequate, in scope and quality, as a dissertation for the degree of Doctor of Philosophy.



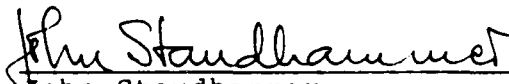
Edward E. Carroll, Jr.
Professor of Nuclear Engineering
Sciences

I certify that I have read this study and that in my opinion it conforms to acceptable standards of scholarly presentation and is fully adequate, in scope and quality, as a dissertation for the degree of Doctor of Philosophy.



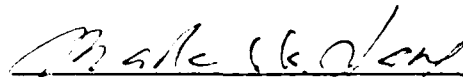
Edward T. Dugan
Associate Professor of Nuclear
Engineering Sciences

I certify that I have read this study and that in my opinion it conforms to acceptable standards of scholarly presentation and is fully adequate, in scope and quality, as a dissertation for the degree of Doctor of Philosophy.



John Staudhammer
Professor of Electrical
Engineering

I certify that I have read this study and that in my opinion it conforms to acceptable standards of scholarly presentation and is fully adequate, in scope and quality, as a dissertation for the degree of Doctor of Philosophy.



Mark C. Yang
Professor of Statistics

This dissertation was submitted to the Graduate Faculty of the College of Engineering and to the Graduate School and was accepted as partial fulfillment of the requirements for the degree of Doctor of Philosophy.

August 1987

Dean, College of Engineering

Dean, Graduate School

END

8-87

DTIC